Université Sorbonne Paris Cité

Université Paris.Diderot

École doctorale d'Astronomie et Astrophysique d'Ile de France
Laboratoire AIM, CEA Saclay

Thèse de Doctorat

Discipline : Astronomie et Astrophysique

Étude des processus physiques dans le milieu interstellaire des Nuages de Magellan

The physical processes in the interstellar medium of the Magellanic Clouds

Mélanie Chevance

Thèse dirigée par : Suzanne Madden

Soutenue le 10 octobre 2016

Jury

Jacques Le Bourlot,	Université Paris Diderot - Paris 7	Président du jury
Gordon Stacey,	Cornell university	Rapporteur
Juergen Stutzki,	Physikalisches Institut, Universität zu Köln	Rapporteur
Alexander Tielens,	Leiden Observatory, Leiden University	Examinateur
Laurent Verstraete,	Institut d'Astrophysique Spatiale, Université Paris Saclay	Examinateur

Abstract

The interstellar medium (ISM) plays a major role in galaxy evolution. Feedback from stars, in particular, drives several processes responsible for the global properties of a galaxy. However, the efficiency of these processes is related to the properties and structure of the different gas and dust ISM phases and remains uncertain.

Due to the increased sensitivity and resolution of the new far-infrared (FIR) and submillimeter facilities (such as the *Herschel* Space Observatory, *SOFIA* and *ALMA*, in particular), it now becomes possible to study in detail the interplay between star formation and the surrounding ISM phases. This work focuses on the physical properties of the gas in the Magellanic Clouds. The Large Magellanic Cloud and the Small Magellanic Cloud, our closest neighbors, both at subsolar metallicity, are good laboratories to study the interaction between star formation and environment.

The 30 Doradus region, in the Large Magellanic Cloud, one of the most massive and active star forming region known in our neighborhood, is first studied in detail. We use the FIR and mid-infrared tracers, provided by the space telescopes *Herschel* and *Spitzer*, to bring constrains on the pressure, radiation field and 3D structure of the photo-dissociation regions (PDR) in this extreme region, using the Meudon PDR code. This modeling allows us to estimate the fraction of molecular gas not traced by CO, also known as the "CO-dark" molecular gas.

We apply this method to other star forming regions of the Magellanic Clouds, which are characterized by different environmental conditions. Our study allows us to evaluate key diagnostics of the gas heating and cooling of low metallicity resolved starburst regions. This is a first step toward understanding similar but unresolved regions, in high-redshift galaxies.

Résumé

Le milieu interstellaire (MIS) joue un rôle important dans l'évolution des galaxies. Les radiations et vents stellaires, ainsi que les supernovae par exemple, sont à l'origine de nombreux processus ayant un impact sur les propriétés globales des galaxies. Cependant, l'efficacité des ces processus est liée aux propriétés et à la structure des différentes phases du MIS, et est souvent incertaine.

Grace à la sensibilité et résolution accrues des nouveaux télescopes observant dans l'infrarouge lointain (FIR) et le submillimetrique (comme par exemple le *Herschel* Space Observatory, *SOFIA* et *ALMA*), il est désormais possible d'étudier en détail les interactions réciproques entre la formation stellaire et les différentes phases du MIS environnant. Ce travail est axé sur les propriétés physiques du gaz dans les Nuages de Magellan. Le Grand Nuage de Magellan et le Petit Nuage de Magellan, nos plus proches voisins, tout deux à métallicité sub-solaire, sont de bons laboratoires pour étudier les interactions entre la formation stellaire et l'environnement.

La région 30 Doradus, dans le Grand Nuage de Magellan, l'une des plus massives et des plus actives régions de formation stellaire connues dans notre voisinage, est étudiée en détail. Les observations des télescopes spatiaux Herschel et Spitzer sont utilisées pour contraindre la pression, le champ de radiation ainsi que la structure tri-dimensionnelle des régions de photo-dissociation (PDR), en combinaison avec le code PDR de Meudon. Cette modélisation permet également d'estimer la fraction de gaz moléculaire qui n'est pas détectée par le traceur généralement utilisé CO.

Cette méthode est ensuite appliquée à d'autres régions de formation stellaire dans les Nuages de Magellan, présentant différents environnements. Cette étude permet d'évaluer les diagnostiques clés du chauffage et du refroidissement du gaz à faible métallicité dans des régions actives de formation stellaire, avec une bonne résolution spatiale. Ceci constitue une première étape pour mieux comprendre les observations non résolues de telles régions dans des galaxies lointaines.

Contents

List of Figures

List of Tables

Résumé étendu en français

Introduction

Les processus par lesquelles les galaxies se forment et évoluent sont fortement liés à leur environnement (par les interactions gravitationnelles entre galaxies ou les collisions de galaxies par exemple), ainsi qu'aux rétroactions engendrées par la formation d'étoiles (émission de champs de radiations ionisants, vents stellaires, supernovae). Ainsi, mieux connaitre l'histoire de la formation stellaire est une des clés pour comprendre l'évolution des galaxies. Cependant, les mécanismes exacts mis en jeu lors de la formation des étoiles, leur efficacité, en particulier dans les environnements primordiaux, ainsi que leur évolution restent incertains.

Le milieu interstellaire (MIS) est un des acteurs importants de l'évolution des galaxies. Ses propriétés et sa structure, soumises au cycle de la matière entre le gaz, la poussière et les étoiles, connaissent des changements perpétuels. L'observation détaillée des différentes phases du MIS permet de sonder les différents états physiques et chimiques du gaz et de la poussière dans les galaxies. Les propriétés du MIS dans les galaxies naines à faible métallicité, c'est à dire avec une faible fraction d'éléments lourds (notée $Z_\odot$), ont souvent été considérées comme proches de celles existant dans un univers jeune, en raison notamment de leur composition chimique, pauvre en élément lourds, qui les différencie notablement des galaxies à métallicité solaire. Elles constituent donc des environnements particulièrement intéressants pour étudier l'interaction entre le MIS et la formation stellaire. Cependant, en raison de leur petite taille et de leur faible luminosité, les galaxies naines sont généralement difficiles à étudier dans l'univers lointain.

Cette thèse est axée sur un échantillon de régions de formation stellaire dans le Grand Nuage de Magellan (noté LMC pour Large Magellanic Cloud) et dans le Petit Nuage de Magellan (noté SMC pour Small Magellanic Cloud), les deux galaxies naines les plus proches de notre Voie Lactée. En raison de leur métallicité modérée ($0.5\,Z_\odot$ pour le LMC et $0.2\,Z_\odot$ pour le SMC), les conditions rencontrées dans le MIS de ces galaxies diffèrent de celles présentes dans la Voie Lactée. Elles constituent donc des laboratoires idéaux pour étudier en détail l'impact de l'environnement sur la formation stellaire et, réciproquement, la rétroaction stellaire sur le MIS à faible métallicité. Dans les régions actives de formation stellaire, la présence d'étoiles jeunes émettant de forts rayonnements ultraviolets, conjuguée avec une abondance de poussière réduite, tendent à modeler la structure du MIS différemment des galaxies à plus forte métallicité, ce qui affecte notre description classique des différentes phases du MIS. Les propriétés générales du MIS ainsi que les caractéristiques spécifiques à faibles métallicité sont décrites au Chapitre I.

Chacune des différentes phases du MIS peut être caractérisée à travers différentes observations, notamment le continuum infrarouge et les raies d'émission du gaz. Une partie du continuum in-

frarouge est émis par la poussière, absorbant les rayonnements ultraviolets (UV) et visibles émis par les étoiles. Les raies de structure fine dans l'infrarouge lointain ont été initialement détectées grâce au Kuiper Airborne Observatory (*KAO*) et à l'Infrared Space Observatory (*ISO*) dans les galaxies naines. L'étude des raies d'émission IR dans les galaxies permet de sonder le gaz et la poussière dans les différentes phases du MIS (phases ionisées, neutres – en particulier les régions de photodissociation – ou moléculaires), et d'obtenir ainsi des informations sur les processus en jeu. Les récentes observations des télescopes spatiaux *Spitzer* et *Herschel* ont fait considérablement évoluer notre compréhension de la composition et des processus physiques du MIS. Les nouveautés apportées par les observations *Herschel* et les nouveaux télescopes désormais disponibles (Stratospheric Observatory for Infrared Astronomy, *SOFIA*, et Atacama Large Millimeter/sub-millimeter Array, *ALMA*) pour l'observation du MIS en IR et submillimétrique sont décrits au Chapitre II.

Le travail présenté ici s'appuie sur la combinaison des observations photométriques et spectroscopiques des télescopes spatiaux *Herschel* et *Spitzer* avec des modèles de régions de photodissociation (PDR), présentés au Chapitre III, afin d'examiner les conditions physiques et la structure du MIS. Les résultats ainsi obtenus pour la région 30 Doradus du LMC sont présentés au Chapitre IV. Cette région de formation stellaire extrêmement active constitue en effet une cible idéale pour l'étude détaillée des interactions entre la formation stellaire et le MIS alentour. Cette modélisation permet de déterminer la fraction de "gaz moléculaire sombre", c'est à dire la quantité de H_2 qui n'est pas détectée via les raies d'émission de CO, traceur habituel de H_2 (Chapitre V). Cette méthode est ensuite appliquée à d'autre régions de formation stellaire du LMC et du SMC au Chapitre VI. La diversité des environnements représentés constitue une première étape vers une meilleure compréhension de la formation stellaire et des processus physiques dans le MIS à plus large échelle, pour des galaxies plus lointaines.

Chapitre 1 : Le milieu interstellaire des galaxies naines

Ce chapitre présente un aperçu de nos connaissances actuelles sur le milieu interstellaire. La composition d'une galaxie et certains des processus physiques intervenant dans le milieu interstellaire y sont décrits. Les galaxies naines et leurs spécificités sont aussi présentées, en particulier celles du Grand Nuage de Magellan (LMC) et du Petit Nuage de Magellan (SMC) qui sont les objets de notre étude.

Description générale

Une galaxie est composée d'étoiles, de gaz et de poussière, gravitationnellement liés, à l'intérieur d'un halo de matière noire. Le gaz et la poussière forment ce qu'on appelle le milieu interstellaire (MIS). Il sont chauffés par les photons émis par les étoiles (le champ de radiation interstellaire), principalement dans les domaines visible et ultraviolet (UV), par les rayons cosmiques et les rayons X. Les divers processus de refroidissement résultent en un ensemble de raies d'émission et d'émission continue, dans les domaines visible et infrarouge (IR). L'observation d'une galaxie dans un large intervalle de longueurs d'ondes permet ainsi d'avoir accès à une vue la plus complète possible de ses composants, et de pouvoir modéliser les différents processus physiques affectant la propagation de la lumière dans la galaxie (voir le Chapitre II).

Le gaz interstellaire est majoritairement composé d'hydrogène et d'hélium, avec une faible fraction d'éléments plus lourds, quantifiée par la métallicité du milieu. Selon la théorie du Big Bang, l'univers primordial était originellement composé uniquement d'hydrogène et d'hélium (ainsi que de lithium et de béryllium à l'état de traces). Les éléments plus lourds ont été formés par fusion au cœur

des étoiles ainsi que lors d'explosions de supernovæ. Ainsi, la composition chimique d'une galaxie s'enrichit progressivement à travers le cycle de la naissance et de la mort des étoiles. Néanmoins, la relation entre métallicité et le temps n'est pas linéaire et est compliquée par d'éventuelles éjections de gaz riche en métaux et l'accrétion de gaz primordial venant du milieu intergalactique.

Taux de formation stellaire

Des études détaillées dans notre Galaxie ont montré que les étoiles sont généralement formées par effondrement de nuages moléculaires, principalement composés d'hydrogène moléculaire H_2. En revanche l'efficacité de ce processus diffère suivant les galaxies. Le taux de formation stellaire (star formation rate, SFR, en anglais), est une caractéristique importante des galaxies. A grande échelle, Kennicutt (1998) a déterminé une relation empirique, connue sous le nom de loi de Schmidt-Kennicutt, entre la densité de surface du taux de formation d'étoiles, Σ_{SFR}, et la densité surfacique de gaz, Σ_{gas} :

$$\Sigma_{SFR} \propto (\Sigma_{gas})^n,$$

avec $n \approx 1.4$. Cependant, certains environnements semblent dévier de cette loi, comme par exemple certaines galaxies naines (Cormier et al. 2014), en particulier le Petit Nuage de Magellan (Bolatto et al. 2011), ou les régions externes de galaxies spirales (Bigiel et al. 2010).

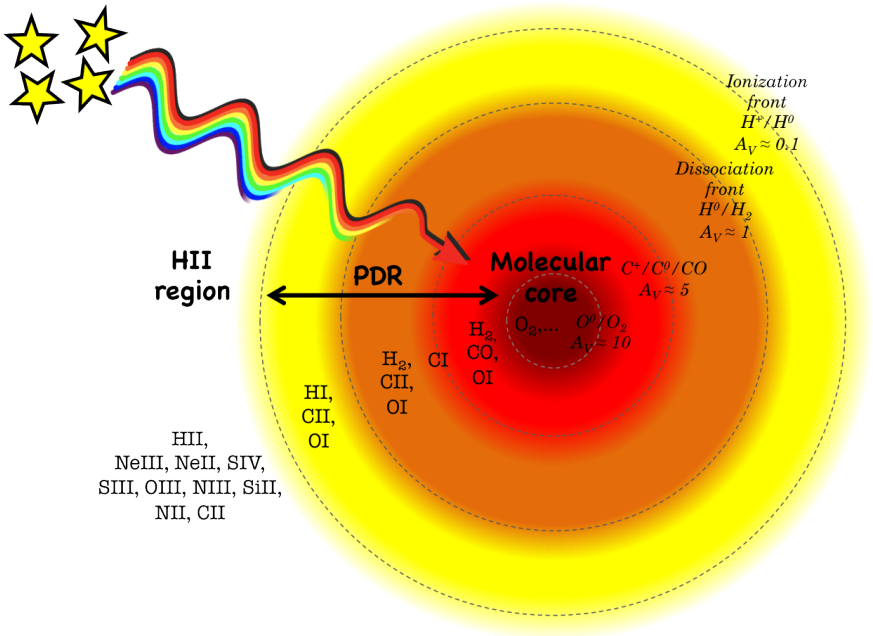

Figure 1: *Zoom sur la structure d'une PDR. Différents éléments observés avec les télescopes spatiaux Spitzer et Herschel, ainsi que les principales transitions ($H^+/H^0/H_2$, $C^+/C^o/CO$ et O^0/O_2), sont indiqués.*

Le gaz du milieu interstellaire

Le gaz représente 99% de la masse du MIS et joue un rôle important dans l'évolution des galaxies. Il existe sous différentes phases, en fonction des conditions physiques locales, qu'on distingue souvent en fonction de l'état d'ionisation prédominant de l'hydrogène : une phase ionisée, une phase neutre et une phase moléculaire (Figure 1).

La phase à laquelle nous nous intéressons particulièrement dans cette étude est la phase neutre dans les régions de transition entre les régions H II (phase ionisée) et les nuages moléculaires. Elle est appelé région de photodissociation (PDR ; Tielens & Hollenbach 1985; Hollenbach & Tielens 1999).

Le chauffage et la chimie y sont dominés par les photons UV durs (FUV), d'énergie comprise entre 6 eV et 13.6 eV. L'hydrogène est donc prédominant sous sa forme atomique. La structure des PDR est schématisée Figure 1.

Lorsque le rayonnement FUV est suffisamment écranté, des molécules peuvent se former. De nombreuses molécules, et en particulier H_2, se forment sur les grains avant de s'évaporer dans le gaz du MIS. Le principal mécanisme de refroidissement des molécules se fait à travers l'émission de photons dans les transitions rotationnelles ou vibrationnelles dans l'IR ou le domaine visible. Pour H_2, qui est une molécule symétrique, les transitions rotationnelles sont difficiles à observer. Les transitions vibrationnelles dans le proche IR sont observées dans le gaz moléculaire chaud et dense, mais cela ne représente qu'une faible fraction de la masse de gaz moléculaire d'une galaxie. On a donc recours en général à d'autres traceurs, comme par exemple CO, pour estimer la masse totale de gaz moléculaire (voir Chapitre V).

La poussière du milieu interstellaire

La présence de poussière dans le MIS a plusieurs effets sur le transfert radiatif à travers une galaxie. On observe notamment le rougissement et l'extinction de la lumière émise par des étoiles lointaines, la réflexion de la lumière par diffusion sur les grains, une émission continue dans l'IR due à la poussière froide et la polarisation de la lumière par des gros grains alignés sur le champ magnétique.

Ces effets sont visibles sur la densité spectral d'énergie (SED) de la galaxie. En particulier, l'émission de la poussière domine l'émission totale entre 10 μm et 1mm. Les modèles de SED, tels que ceux présentés par Galliano et al. (2011), utilisés dans notre étude, prennent en compte les différentes contributions des étoiles, du gaz et de la poussière pour reproduire la SED observée et en déduire différents paramètres physiques tels que la masse de poussière, ses propriétés ainsi que l'intensité du rayonnement stellaire. Cette modélisation est décrite plus en détails au Chapitre III.

Les grains de poussière sont composés en grande partie de carbone, oxygène, magnésium, silicium, soufre et fer. Différents type de grains, présentant différentes propriétés optiques ont été identifiés : les silicates, les grains carbonés et les PAH (Polycyclic Aromatic Hydrocarbons). Les PAH sont des molécules planes, contenant entre 20 et 1000 atomes de carbone environ. La taille typique des grains varie entre 5 et 250 nm, et entre 0.4 et 1 nm pour les PAH. L'effet photoélectrique sur les PAH pourrait être le principal mécanisme de chauffage dans certains environnements (voir par exemple Weingartner & Draine 2001a; Rubin et al. 2009; Lebouteiller et al. 2011), mais ils sont vraisemblablement détruits par la proximité d'une étoile jeune, ou en présence de chocs (par exemple Lebouteiller et al. 2007; Verstraete 2011).

Chauffage et refroidissement du gaz

Le gaz du MIS est principalement chauffé par le champ de radiation des étoiles par photo-ionisation : l'électron éjecté emporte une partie de l'énergie du photon incident sous la forme d'énergie cinétique, qui est ensuite transférée à d'autres atomes et électrons par collisions. Dans les régions H II, le chauffage est dominé par l'ionisation de H. Dans les régions H I, il est dominé par l'effet photoélectrique sur les PAH et les petits grains : un photon FUV incident sur un grain produit des électrons de plusieurs eV dans le grain qui, s'ils sont injectés dans le gaz avec suffisamment d'énergie cinétique, chauffent le gaz par collisions. H_2 contribue également au chauffage du gaz neutre, par absorption d'un photon UV puis désexcitation par fluorescence de la molécule (pompage UV de H_2). Dans le gaz moléculaire, le gaz peut-être chauffé par la photo-dissociation des molécules et l'effet photoélectrique sur les grains.

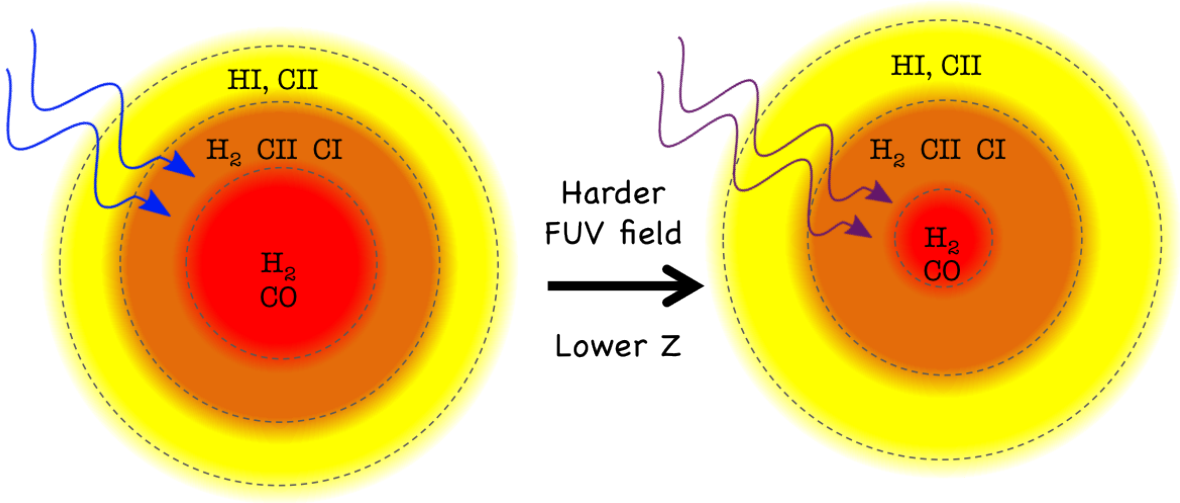

Figure 2: *Illustration de l'effet de la métallicité sur la structure d'un nuage moleculaire, inspiré de Wolfire et al. (2010). La profondeur physique des différentes couches de gaz (H I, H_2 sans CO, et H_2 avec CO dans le coeur moléculaire) varie avec l'augmentation de la dureté du champ de radiation et la diminution de la métallicité.*

Le refroidissement du gaz se fait principalement par émission radiative. En particulier, les raies de refroidissement émises dans les domaines IR et submillimétrique, faiblement affectées par l'extinction par la poussière, sont de bons indicateurs des conditions physiques et de la structure des différentes phase du gaz. Les raies de structures fines dans l'IR lointain (par exemple, [O III] 52 et 88 μm, [N II] 122 et 205 μm, [C II] 158 μm, [O I] 63 et 145 μm, [C I] 370 et 609 μm, etc) permettent d'estimer le flux de radiation incident, la température, la densité et le facteur de remplissage (fraction de la surface d'un pixel effectivement occupée par les différentes phases du gaz). Elles ont été observées par de nombreux télescopes, comme *COBE* (COsmic Background Explorer ; Wright et al. 1991), le télescope spatial *Herschel* et d'autres, jusqu'au télescope *SOFIA* (Stratospheric Observatory for Infrared Astronomy) aujourd'hui.

Caractéristiques des galaxies naines

Dans cette étude, nous nous intéressons aux conditions physiques et à la structure du gaz du MIS dans les environnements particuliers que constituent les galaxies naines. Les galaxies naines sont communément définies comme petites en taille, avec une faible luminosité, et une faible masse. Parmi celles-ci, on distingue plusieurs morphologies (Grebel 2001), en fonction de leur forme et de leurs propriétés, mais cette classification n'est en général pas unique.

Notre étude se focalise en particulier sur nos plus proches voisins, le LMC et le SMC, respectivement à ~ 50 kpc et ~ 61 kpc. Leur métallicité est d'environ $0.5\,Z_\odot$ pour le LMC (Pagel 2003), proche de la métallicité moyenne du MIS durant le pic de formation stellaire dans l'univers ($z \sim 1.5$; Madau et al. 1996), et $0.2\,Z_\odot$ pour le SMC (Russell & Dopita 1992). Ainsi, nous avons la possibilité d'étudier les conditions physiques des PDR dans différents environnements, à différentes métallicités, avec une bonne résolution spatiale.

Une métallicité réduite a en effet de nombreuses conséquences sur la physique et la chimie du MIS. En particulier, la quantité de poussière, liée à la quantité de métaux, est faible. L'atténuation des rayons UV est donc elle aussi amoindrie et le milieu est plus poreux. La structure les nuages est elle aussi modifiée, comme schématisé sur la Figure 2. Alors que certaines galaxies naines montrent des

taux de formation d'étoiles important, CO y est difficile à détecter (par exemple, Taylor et al. 1998; Leroy et al. 2009; Schruba et al. 2012; Cormier et al. 2014). Ce paradoxe soulève la question suivante : est-ce que la formation stellaire se passe différemment à faible métallicité et un réservoir important de H_2 n'est pas nécessaire pour nourrir cette formation, ou bien est-ce que CO devient inefficace à tracer le réservoir total de gaz moléculaire dans ces conditions, laissant invisible une grande partie de gaz moléculaire sombre ?

Chapitre 2 : Observations infrarouges et submillimétriques des Nuages de Magellan

Dans ce chapitre, nous présentons les principaux instruments avec lesquelles ont été collectées les données utilisées pour cette étude.

Le télescope spatial *Herschel*

Le *Herschel* Space Observatory (Pilbratt et al. 2010), développé par l'Agence Spatiale Européenne, est le successeur de plusieurs observatoires infrarouges. Dès 1974, le Kuiper Airborne Observatory (*KAO*) entre en service à bord d'un avion. Puis le télescope InfraRed Astronomical Satellite (*IRAS*), lancé en 1983, ouvre la voie à l'astronomie infrarouge depuis l'espace, suivi par *ISO* (InfraRed Space Observatory) en 1995 et le *Spitzer* Space Telescope en 2003. Entre 2009 et 2013, *Herschel*, avec un diamètre de 3.5 m, a apporté une meilleure résolution spatiale et spectrale par rapport à ses prédécesseurs, dans l'intervalle de longueurs d'ondes 55-672 μm. Ses principales missions concernent l'étude de la formation et l'évolution des premières galaxies, l'observation des premiers stades de la formation des planètes et des étoiles ainsi que la compréhension des processus physiques et chimiques dans le MIS.

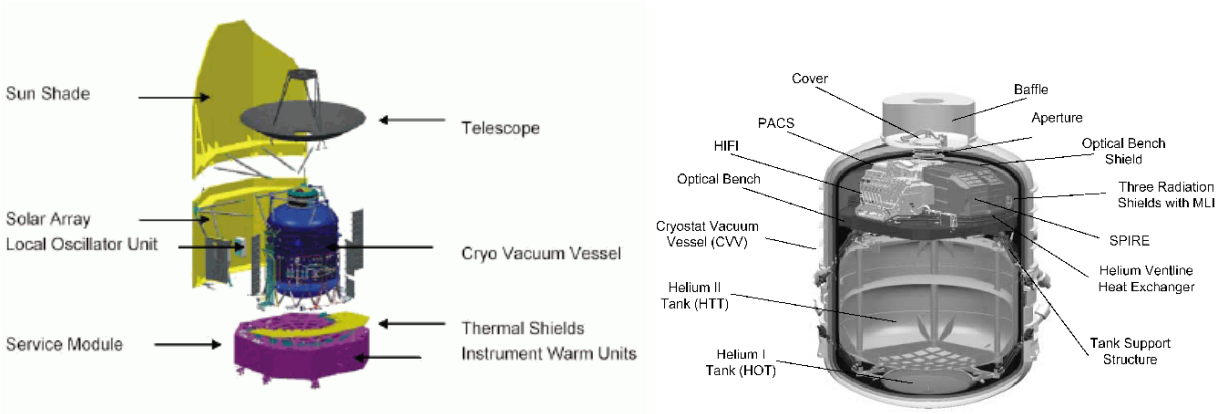

Figure 3: *Shéma du télescope spatial Herschel détaillant les principaux composants (gauche) et vue en coupe du cryostat, montrant la répartitions des trois instruments (droite).*

Le télescope *Herschel* était composé d'un cryostat d'hélium liquide (Figure 7), abritant le banc optique avec les trois instruments suivant :

- le **Photodetector Array Camera and Spectrometer** (PACS; Poglitsch et al. 2010) est composé d'un photomètre imageur et d'un spectromètre de moyenne résolution ($\lambda/d\lambda \approx 940-5500$). Le spectromètre PACS est un IFU (Integral Field Unit), composé de 5×5 pixels spatiaux couvrant

un champ de 47″×47″ et opérant dans le domaine de longueur d'onde 55 à 210 μm. La résolution angulaire obtenue est comprise entre 9.5″ et 13″. Le photomètre PACS permet d'observer simultanément dans la bande rouge (125-250 μm) et dans la bande bleue ou verte (respectivement 60-80 μm et 85-125 μm). Les deux matrices de bolomètres de 32×32 pixels (pour la bande rouge) et de 64×32 pixels (pour les bandes bleue et verte) permettent de couvrir chacune un champ de $\sim$ 1.75′×3.5′. La résolution angulaire est principalement dominée par la limite de diffraction du télescope.

- le **Spectral and Photometric Imaging REceiver** (SPIRE; Griffin et al. 2010) est composé d'un photomètre imageur et d'un spectromètre à transformée de fourrier (FTS). The spectromètre couvre un intervalle de longueur d'onde 194-671 μm, avec une résolution angulaire comprise entre 16″ et 43″ et un champ de vue de 2′. Le photomètre SPIRE comprend trois matrices de bolomètres centrées approximativement sur 250 μm, 350 μm et 500 μm permettant une résolution spatiale de 18″ à 36″.

- le **Heterodyne Instrument for the Far Infrared** (HIFI; de Graauw et al. 2010), un spectromètre hétérodyne à très haute résolution, fonctionnant dans les intervalles de longueur d'onde 157-212 μm et 240-625 μm.

Présentation des observations

L'étude présentée ici s'appuie en partie sur des données du programme *Dwarf Galaxy Survey* (DGS ; PI : S. Madden) et du programme *Star formation and activity in infrared bright galaxies at 0<z<1* (SHINING ; PI : E. Sturm). Ce sont 50 galaxies naines qui ont été observées avec les instruments PACS et SPIRE pour un total de 230 heures. La présentation de cet échantillon, couvrant une large gamme de métallicité et de taux de formation stellaire est décrite par Madden et al. (2013).

Pour le LMC et le SMC particulièrement, 11 régions ont été observées par le spectromètre PACS et 9 par le spectromètre SPIRE/FTS par le DGS et le programme "Open Time" mené par Hony et al. Ces observations sont complétées par des observations photométriques de *Herschel* et *Spitzer* (programmes HERITAGE, Meixner et al. 2010 et SAGE, Meixner et al. 2006) couvrant en grande partie le LMC et le SMC.

Les Nuages de Magellan ont aussi été cartographiés en HI à 21 cm par le Australian Telescope Compact Array et le radio télescope Parkes 64m par Kim et al. (2003) pour le LMC et Stanimirovič et al. (1999) pour le SMC, avec une résolution angulaire de $\sim$ 1′. Notre étude s'appuie également sur les données CO(1-0) du télescopes Mopra (Wong et al. 2011 pour le LMC et Muller et al. 2010 pour le SMC), avec une résolution de 45″, ainsi que sur les observations de CO(3-2) du Atacama Submillimeter Telescope Experiment (ASTE) (Minamidani et al. 2011).

Les analyses détaillées des PDR et du gaz moléculaire sombre dans la région de 30 Doradus, construites à partir de ces observations, sont présentées aux Chapitre IV et V. Les autres régions du LMC et du SMC sont présentées au Chapitre VI.

Traitement des données

Les données *Herschel* ont été réduites à l'aide de HIPE (Herschel Interactive Processing Environment, Ott 2010). Les informations détaillées concernant les étapes de la réduction se trouvent sur `http://herschel.esac.esa.int/hcss-doc-14.0/`. Pour la spectroscopie PACS, après calibration du signal par HIPE v.12, le logiciel PACSman décrit par Lebouteiller et al. (2012) a été utilisé pour

l'analyse du flux. Cela permet, entre autre, de propager les erreurs pour chaque pixel, grâce à une méthode Monte-Carlo. Les données SPIRE/FTS ont été réduites avec HIPE v.11.0.2825 et l'analyse du flux est décrite dans Lee et al. (2016).

Les différentes cartes photométriques et spectrométriques, à différentes longueurs d'ondes et obtenues avec différents instruments, ont dues être convoluées pour être comparées entre elles. Les procédures développées par Aniano et al. (2011), disponibles sur http://www.astro.princeton.edu/~ganiano/Kernels.html, ont été utilisées pour les cartes PACS.

Autres observatoires infrarouges et submillimétriques

Le télescope spatial *Spitzer*

Le télescope spatial *Spitzer*, lancé par la NASA en 2003, est composé d'un miroir primaire de 83 cm, refroidi à l'hélium liquide jusqu'au 15 mai 2009. *Spitzer* est maintenant entré dans la "phase chaude" de son fonctionnement. Trois instruments étaient embarqués à bord de *Spitzer* : le spectrographe infrarouge IRS (InfraRed Spectrograph), la caméra infrarouge IRAC (InfraRed Array Camera), seul instrument encore en activité, et le photomètre imageur MIPS (Multiband Imaging Photometer for *Spitzer*).

Le télescope *SOFIA*

Les observations spectroscopiques de la région de 30 Doradus de PACS ont été complétées grâce à l'observatoire stratosphérique *SOFIA* (Stratospheric Observatory For Infrared Astronomy), un télescope de 2.5 m de diamètre, embarqué à bord d'un Boeing 747SP modifié (Figure 4). Huit instruments peuvent être installés alternativement au plan focal du télescope. Nos observations ont étés réalisées à l'aide du spectromètre FIFI-LS (Field Imaging Far Infrared Line Spectrometer ; P.I.: A. Krabbe), dont les caractéristiques techniques (résolutions spatiale et spectrale notamment) sont très proches de celles de PACS. Cet instrument a néanmoins l'avantage de couvrir un intervalle de longueur d'onde légèrement plus grand (51-203 μm) ce qui donne accès en particulier à la raie de structure fine [O III] 52 μm.

Figure 4: *Gauche : SOFIA lors de la campagne 2016 à Christchurch, Nouvelle-Zélande. Droite : les antennes d'ALMA sur le plateau de Chajnantor au Chili.*

L'interféromètre *ALMA*

Des observations du LMC à haute résolution sont nécessaires pour améliorer notre compréhension du MIS. Atacama Large Millimeter/submillimeter Array (*ALMA*) est un radiotélescope, composé d'un

réseau de 66 antennes de 7 m et 12 m, installé sur le plateau de Chajnantor au Chili. Il opère dans les domaines des longueurs d'ondes millimétriques et submillimétriques, provenant de la poussière froide et du gaz moléculaire dans les galaxies proches ou plus lointaines, à hautes résolutions spatiale et spectrale.

Chapitre 3 : Modélisations du milieu interstellaire

La modélisation du MIS est un problème complexe qui implique de nombreux processus intervenant à différentes échelles, dans une large gamme de longueurs d'onde. Ce chapitre décrit plusieurs modèles permettant d'explorer les différentes phases du MIS et permettant de mieux comprendre les processus physiques à l'origine des observations du MIS.

Modélisation de l'émission de la poussière

Une partie du rayonnement d'une galaxie émis par les étoiles dans le domaine UV-visible est absorbé par la poussière et ré-émis dans le domaine MIR-FIR. Ainsi, la luminosité IR est fortement liée à la population stellaire. Mesurer cette luminosité IR est donc un élément important pour contraindre les modèles PDR qui couplent le rayonnement émis au gaz et à la poussière.

Pour cela, nous avons utilisé le modèle semi-empirique décrit par Galliano et al. (2011) pour réaliser un ajustement de la SED observée, du domaine MIR au domaine millimétrique, par une combinaison de modèles réalistes de poussières. A ces longueurs d'ondes, la majeur partie de l'émission est due aux gros grains en équilibre avec le champ de radiation et le détail du spectre d'émission et la répartition spatiale ont peu d'influence sur le spectre résultant. Ce n'est pas le cas pour les petits grains ($\lesssim 10$ nm) qui sont hors équilibre et qui sont ajustés séparément. Le modèle se décompose en deux étapes :

1. la première étape consiste à modéliser la SED de la poussière pour un élément de masse du MIS, contrôlée par les propriétés microphysiques des grains et caractérisée par une intensité donnée du champ de radiation.

2. la deuxième étape permet de reproduire la macrophysique, en combinant plusieurs éléments de masse, soumis à une gamme de conditions d'illumination, tenant compte des différents environnements présent dans le champ de vue du télescope.

Une fois les observations reproduites par le modèle, la luminosité FIR, L_{FIR}, est l'intégration de la SED modélisée entre 60 μm et 200 μm.

L_{FIR} associé au gaz neutre uniquement : L_{FIR}^{PDR}

Alors que nous nous intéressons ici tout particulièrement à la modélisation des PDR, L_{FIR} est susceptible d'être émis par la poussière dans le gaz ionisé, et pas seulement par les grains et les PAH dans la phase neutre. Ainsi, afin de contraindre les propriétés physique des PDR comme au Chapitre IV il est nécessaire de décomposer au préalable L_{FIR} en une composante du gaz ionisé et une composante du gaz neutre.

Pour cela, nous avons utilisé le fait que l'émission des PAH est un bon traceur des PDR (Sellgren et al. 1990; Tielens & Hollenbach 1993) et que [O III] est présent uniquement dans le gaz ionisé. Nous faisons donc l'hypothèse que L_{FIR} se décompose linéairement tel que :

$$L_{FIR} = L_{FIR}^{PDR} + L_{FIR}^{IG} = \alpha \times L_{PAH} + \beta \times L_{[O\,III]},$$

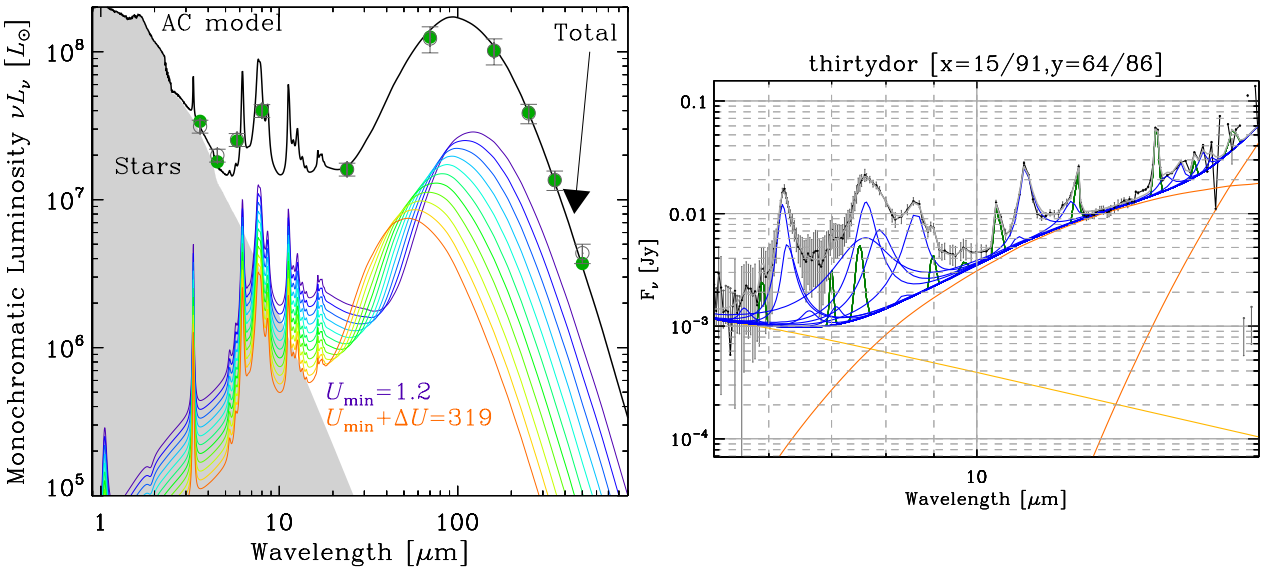

Figure 5: *Gauche : décomposition d'une SED du LMC en un ensemble de SED uniformément éclairées (tiré de Galliano et al. 2011). Les points verts sont les flux Spitzer et Herschel (Meixner et al. 2006, 2010). Le modèle total (en noir) est la somme d'une composante stellaire (en grisé) et de l'intégrale d'un ensemble de SED uniformément éclairées (en couleurs) caractérisées par différentes intensité lumineuses (U). Droite : exemple de la décomposition spectrale du spectre IRS (en noir) pour 30 Doradus. Les bandes d'émission des PAH sont en bleu, les raies atomiques et ionisées sont en vert. Le continu stellaire est représenté en jaune et la poussière en orange.*

où les valeurs α et β sont calculées de manière unique pour toute la carte par régression multi-linéaire pixel à pixel. Il est implicitement supposé ici que la fraction massique des PAH par rapport à la poussière est constante dans les PDR et nulle dans les régions H II. Ce modèle simple permet de reproduire la luminosité L_{FIR} observée avec une incertitude maximale de 30%.

PAH

Les PAH jouent un rôle important pour le chauffage par effet photoélectrique du gaz comme source de photoélectrons (e.g. Tielens & Hollenbach 1985; Bakes & Tielens 1994). L'émission des PAH (L_{PAH}) peut donc être utilisée pour caractériser le chauffage du gaz, comme présenté en Section IV.1.3. Nous comparerons les résultats donnés par deux méthodes d'estimation de L_{PAH} décrites dans cette section.

La première méthode s'applique aux spectres IRS, entre 5 et 40 μm. Elle consiste à ajuster les bandes d'émission des PAH, les raies ioniques, les raies H_2 et l'émission continue due à la poussière et à l'émission stellaire, par des composantes individuelles à l'aide du programme MILES (Mid-Infrared Line Extraction Software). Un exemple pour un pixel de la carte de 30 Doradus est présenté en Figure 5. La deuxième méthode peut être appliquée lorsque les spectres IRS ne sont pas disponibles mais seulement les cartes photométriques de l'instrument IRAC par exemple, ce qui est le cas pour la plupart des régions du LMC et du SMC étudiées. Nous avons alors suivi la méthode utilisée par Lebouteiller et al. (2012) pour estimer L_{PAH} à partir de l'émission dans la bande IRAC 3 ou IRAC 4, dominées par l'émission des PAH et le continu de poussière. Le continuum de la poussière est soustrait après extrapolation basée sur l'émission en bandes IRAC 1 et IRAC 2. L'émission restante, due principalement à l'émission des PAH à 6.2 μm pour la bande 3 et à 7.7 μm et 8.6 μm pour la

bande 4 est alors multipliée par un factor correctif pour obtenir l'émission totale des PAH. Ce facteur correctif est estimé à partir des spectres IRS de 13 galaxies à flambée d'étoiles (Brandl et al. 2006).

Modèles PDRs

L'intensité des raies émises par un nuage de gaz, I_ν, reflète les conditions physiques du gaz à l'endroit où elles ont été émises, mais aussi celles rencontrées sur toute la ligne de visée jusqu'au détecteur. Il est donc important de prendre en compte l'absorption, α_ν, l'émission par des sources internes, ϵ_ν, ainsi que la diffusion, σ_ν pour résoudre l'équation du transfert radiatif le long de la direction de propagation, mesurée par le chemin optique, s :

$$\frac{dI_\nu}{ds} = -(\alpha_\nu + \sigma_\nu)I_\nu + \epsilon_\nu + \sigma_\nu J_\nu,$$

avec J_ν l'intensité moyennée sur 4π stéradian.

Dans les conditions rencontrées en astrophysique, la matière et le champ de radiation ne sont généralement pas à l'équilibre thermodynamique. Cependant, il est courant de considérer un Equilibre Thermodynamique Local (ETL) de la matière. Dans ce cas, la solution du transfert radiatif dépend uniquement du profil de température et de densité. C'est une bonne approximation à haute densité, mais elle ne permet pas de reproduire de façon fiable tous les environnements.

Un modèle PDR cherche à décrire la structure et les conditions physiques du MIS. Pour cela, de nombreuses quantités physiques sont calculées localement à l'intérieur du nuage, telles que la pression du gaz, la température du gaz et des grains, les propriétés des grains, les abondances relatives des différents constituants du gaz ainsi que les populations de leurs niveaux électroniques, etc. Il faut ainsi résoudre de manière itérative l'équilibre chimique, l'équilibre thermique et le transfert radiatif, couplés par de nombreux processus physiques.

Le modèle PDR de Meudon

Le code PDR de Meudon a été choisi pour notre étude en raison de l'attention particulière portée aux PDR et du traitement précis des mécanismes de formation et de destruction de H_2. Le modèle PDR de Meudon considère un modèle plan-parallèle à une dimension, illuminé par un champ de radiation isotrope provenant d'un seul ou des deux côtés. Deux hypothèses peuvent être faites : soit une densité d'hydrogène (n_H) constante, soit une pression (P) constante. La version 1.4 de ce code est disponible à `http://pdr.obspm.fr/PDRcode.html` et les versions les plus récentes ont été décrites par Le Petit et al. (2006); Le Bourlot et al. (2012); Bron et al. (2014). Les spécificités de la version 1.6.0, en développement, utilisée pour la modélisation des régions du LMC, sont décrites dans la Section III.3.3.

Méthodologie et limites

Cette section présente la méthode utilisée pour contraindre les paramètres physiques du modèle à l'aide des observations *Herschel* et *Spitzer*. Les résultats pour les différentes régions du LMC sont présentés aux Chapitres IV et VI.

Un grand nombre de modèles a été réalisé en faisant varier les paramètres d'entrée G_{UV} (intensité du champ de radiation incident sur le nuage du côté de l'observateur, donné en unité du champ de Mathis, Mathis et al. 1983 ; sur le côté opposé, nous avons choisi $G_{UV} = 1$), P (pour un modèle à pression constante) et A_V^{max} (extinction totale du nuage). Les intensités modélisées M_j reproduisant

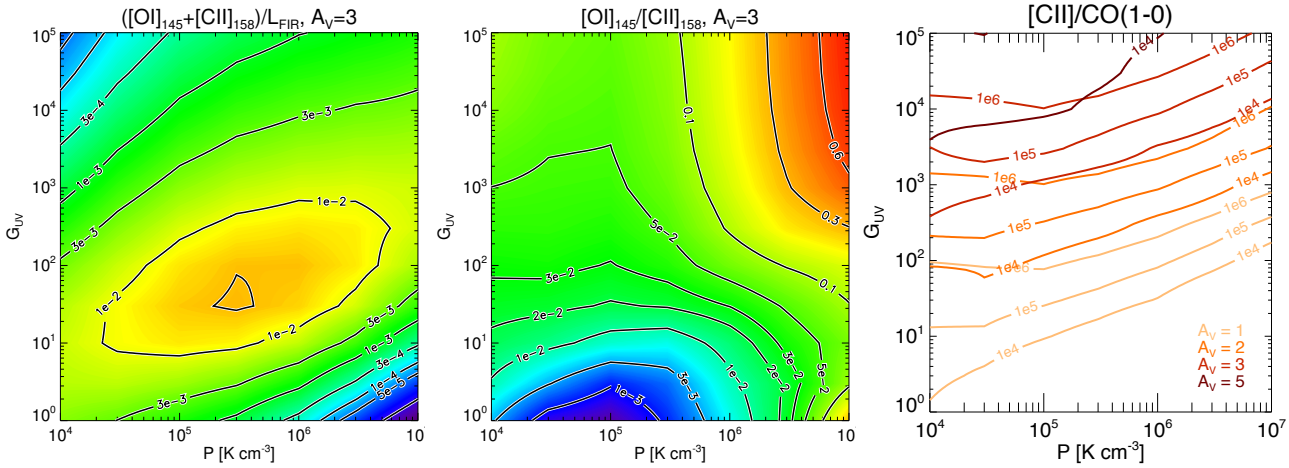

Figure 6: *Gauche : rapport ([O I] 145 µm+[C II] 158 µm)/L_{FIR} émis par un nuage simulé de* $A_V^{max} = 3$*, en fonction de* G_{UV} *et P. Centre : rapport [O I] 145 µm/[C II] 158 µm pour le même nuage simulé. Droite : rapport [C II]/CO(1-0) en fonction de* G_{UV}*, P and* A_V^{max}*. Les différentes couleurs représentent différents* A_V^{max}*.*

au mieux les intensités observées $I_j(x,y)$ pour un pixel (x,y) donné sont déterminées en minimisant la fonction :

$$\chi^2 = \sum_{j=1}^{N} \left(\frac{I_j(x,y) - M_j}{\sigma_j(x,y)} \right)^2 ,$$

avec $\sigma_j(x,y)$ l'incertitude associée à l'intensité observée $I_j(x,y)$. Pour les valeurs observées, des rapports de raies sont utilisés préférentiellement aux intensités absolues afin de s'affranchir du facteur de remplissage, défini comme la fraction de la surface d'un pixel couverte par les PDR, qui peut être différent de 1, comme supposé dans le modèle. Les rapports ([O I] 145 µm+ [C II])/L_{FIR} et [O I] 145 µm/[C II] sont utilisés pour contraindre G_{UV} et P, combinés avec [C II]/[C I] 370 µm qui permet de contraindre également A_V^{max} (Figure 6). Le facteur de remplissage surfacique peut alors être calculé par le rapport : $\Phi_A = \frac{[\mathrm{C\,II}]_{predict}}{[\mathrm{C\,II}]_{observ}}$.

Plusieurs remarques doivent être faites quant à la robustesse des résultats obtenus par cette méthode. Dans la plupart des cas, une dégénérescence est présente entre une solution à grand G_{UV}/faible P et une solution à faible G_{UV}/haute P. Cependant, la valeur plus faible du χ^2 et le fait que, par confrontation avec le rapport [C II]/[C I], la solution à faible G_{UV}/haute P requiert un A_V^{max} plus faible pour une opacité de [O I] 63 µm plus élevée font que la solution à grand G_{UV}/faible P est privilégiée. Pour le cas particulier de 30Dor, la compatibilité de la distance du gaz ionisé à R136, calculées par Pellegrini et al. (2011) avec celle des PDR à R136 calculés avec notre modèle renforce cette hypothèse. Le modèle utilisé est plan-parallèle, mais la géométrie exacte des nuages, qui n'est pas connue, influerait sur la taille calculée. Un modèle plus réaliste devrait prendre en compte une distribution de nuages de différentes tailles, à différentes distances de la source d'ionisation. Enfin, nous avons considéré que les nuages sont vus de face. L'introduction d'un angle entre la ligne de visée et la perpendiculaire à la surface des nuages changerait notre détermination de Φ_A. Ces deux valeurs sont dégénérées et il n'est pas possible de les déterminer indépendamment avec les données actuellement disponibles.

Chapitre 4 : Un environnement extrême : 30 Doradus dans le LMC

Ce chapitre applique le modèle décrit précédemment aux observations de la nébuleuse 30 Doradus dans le LMC. Il s'agit d'un environnement extrême de formation d'étoiles qui a été observé à travers tout le spectre électromagnétique. C'est donc une des meilleures cibles pour étudier en détail l'effet d'un champ de radiation fort sur le MIS environnant à demi-métallicité solaire.

La nébuleuse 30 Doradus

Description

La nébuleuse 30 Doradus dans le LMC (abrégée par la suite par "30Dor"), aussi connue sous le nom de nébuleuse de la Tarentule (Figure 7), a été premièrement classifiée comme une nébuleuse par Louis-Nicolas de Lacaille en 1751. Elle est considérée comme la région H II la plus grande et la plus massive de notre Groupe Local (son diamètre est d'environ 200 pc ; Lebouteiller et al. 2008) et est aussi une région de formation d'étoiles très active, avec un taux de formation d'étoiles spécifique environ 2.4×10^4 fois plus important que celui de la Voie Lactée (Doran et al. 2013). Grâce à sa proximité (~ 50 kpc), cette région constitue une cible idéale pour étudier les interactions entre la gaz, le rayonnement stellaire et la poussière dans un environnement à métallicité réduite ($0.5\,Z_\odot$; Rolleston et al. 2002; Pagel 2003).

En raison de ses possibles similarités avec les galaxies lointaines (mode de formation d'étoiles par "flambée d'étoiles", et métallicité sub-solaire), cette région a été étudiée dans tous les domaines de longueur d'onde. La population stellaire de l'amas d'étoile dominant, et tout particulièrement de son coeur le plus dense, Radcliff 136 (R136; Feast et al. 1960), a fait l'objet de nombreuses caractérisations (par exemple, Massey & Hunter 1998; Selman & Melnick 2013; Sabbi et al. 2013; Evans et al. 2011; Walborn et al. 2014; Cignoni et al. 2015; Crowther et al. 2016) permettant d'établir, entre autres, son âge (1-2 Myr) et d'identifier le type spectral de nombreuses étoiles.

Le gaz ionisé, neutre et moléculaire, ainsi que la poussière du MIS ont aussi été étudiés en détail dans cette région (par exemple Israel et al. 1982; Stacey et al. 1991; Poglitsch et al. 1995; Pineda et al. 2009; Pellegrini et al. 2010; Paradis et al. 2010; Pellegrini et al. 2011; Pineda et al. 2012; Indebetouw et al. 2013). Notons en particular les relevés SAGE (Surveying the Agents of Galaxy Evolution ; Meixner et al. 2006) et HERITAGE (HERschel Inventory of The Agents of Galaxy Evolution ; Meixner et al. 2013) qui couvrent plus largement le LMC et le SMC.

Diagnostiques empiriques

Certains rapports de raies FIR permettent d'évaluer les conditions physiques du MIS. Nous comparons ici 30Dor avec d'autre sources du DGS (Cormier et al. 2015) et des galaxies riches en métaux (Brauher et al. 2008). En particulier, le rapport [O III] 88 μm/[N II] 122 μm élevé permet de mettre en évidence le rayonnement UV dur proche de R136. D'autre part, en comparant le rapport mesuré [C II] 158 μm/[N II] 122 μm avec le rapport théorique attendu dans la phase ionisés, nous avons montré que plus de 90% de [C II] est émis par la phase PDR. C'est un résultat important qui nous permet d'utiliser l'émission [C II] comme contrainte pour le modèle PDR (Chevance et al. 2016). En revanche, comme montré par le rapport [O I] 145 μm/[O I] 63 μm proche de 0.1, les effets d'opacité de la raie [O I] 63 μm peuvent être importants et rendre son interprétation difficile. Enfin, contrairement à d'autres galaxies à flambées d'étoiles, l'émission de la raie [O III] 88 μm domine sur [C II] 158 μm. En

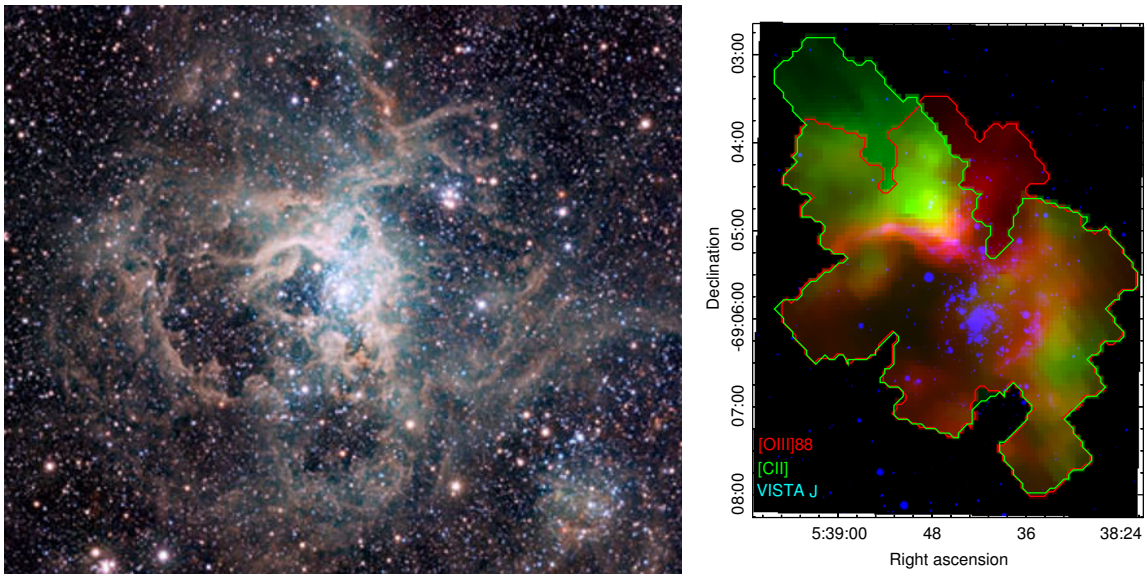

Figure 7: *Gauche : la nébuleuse 30Dor observée dans le cadre du VISTA (Visible and Infrared Survey Telescope for Astronomy) Magellanic Cloud Survey à l'Observatoire Paranal (ESO). Droite : la nébuleuse 30Dor observée par le télescope spatial Herschel, montrant le gaz ionisé ([O III] 88 µm en rouge) et les PDR ([C II] 157 µm en vert) grâce au spectromètre PACS. Les étoiles sont imagées avec VISTA (bande J, en bleu).*

conclusion, l'environnement autour de R136 est très différent de celui des galaxies à plus forte métallicité et montre également des propriétés extrêmes comparées à celles d'autres galaxies du DGS.

La luminosité IR, qui provient de l'émission thermique des grains, est souvent considérée comme un traceur du chauffage du gaz neutre, chauffé en majeur partie par les photoélectrons éjectés par les petits grains de poussière. D'autre part, [C II] et [O I] 63 µm sont les principales raies de refroidissement du gaz neutre. Le rapport ([O I] 63 µm/[C II]/L_{FIR}) peut donc être vu comme une mesure de l'efficacité du chauffage par effet photoélectrique. Dans 30Dor, nous avons montré que ce rapport est très hétérogène et que L_{FIR} provient en réalité en partie du gaz ionisé. Il est donc nécessaire d'isoler la composante du gaz neutre de celle du gaz ionisé, comme décrit au Chapitre III. Alternativement, plusieurs études ont montré que l'émission des PAH est une bonne mesure de l'éjection des photoélectrons dans la phase neutre (par exemple, Croxall et al. 2012; Lebouteiller et al. 2012). Pour 30Dor, une même efficacité de chauffage par effet photoélectrique est estimée (∼ 1%), que ce soit pour les petits grains ou les PAH.

Modèle PDR de 30Dor

Dans cette partie sont décrits les résultats du modèle PDR de 30Dor, tels que présenté dans Chevance et al. (2016). Les données photométriques de *Herschel* et *Spitzer* sont utilisées pour calculer L_{FIR}, ensuite décomposée comme décrit au Chapitre III pour ne garder que la composante du gaz neutre. Les rapports ([O I] 145 µm+ [C II])/L_{FIR}, [O I] 145 µm/[C II] et [C II]/[C I] 370 µm permettent alors de contraindre les paramètres d'entrée du modèle PDR : G_{UV}, P et A_V^{max}. Les cartes finales de G_{UV} et P, à la résolution de 12″, sont présentées en Figure 8. A_V^{max} est compris entre 1.7 et 3.4 mag sur l'ensemble de la carte. La comparaison du champ de rayonnement incident, G_{UV}, avec le champ de rayonnement émis, G_{stars}, nous a permis d'estimer la distance de la surface des PDR à l'amas R136 (Figure 8). La corrélation marquée entre le rapport [O III] 88 µm/[C II] et le facteur de remplissage Φ_A

peut être interprété comme un signe de la porosité élevée du MIS dans cette région particulière.

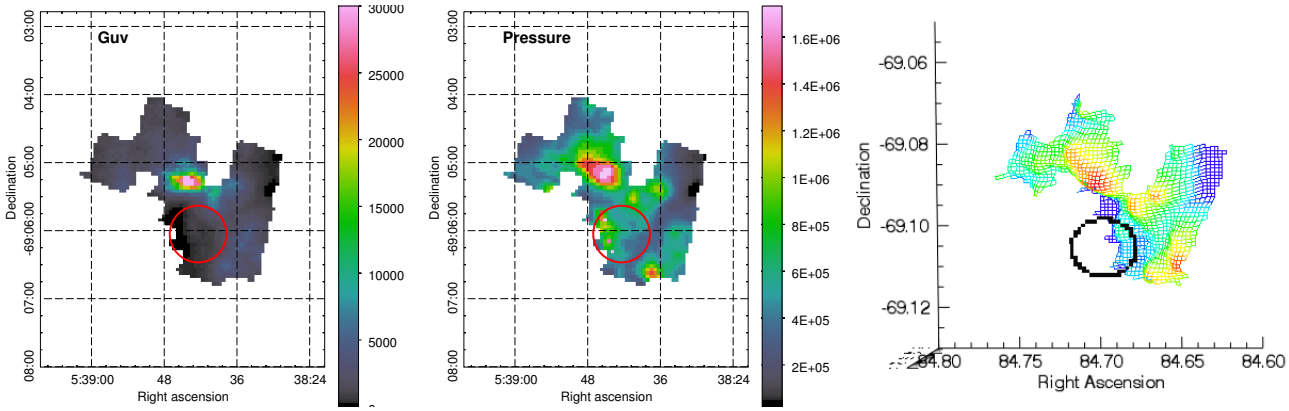

Figure 8: *Gauche : carte du champ de radiation incident (en unités du champ de Mathis). Le cercle rouge représente la position de R136. Centre : carte de la pression (cm^{-3} K). Droite : vue tridimensionnelle de la répartition des PDR autour de R136 (cercle noir). Les couleurs représentent la distance au plan z=0 dans lequel se situe R136.*

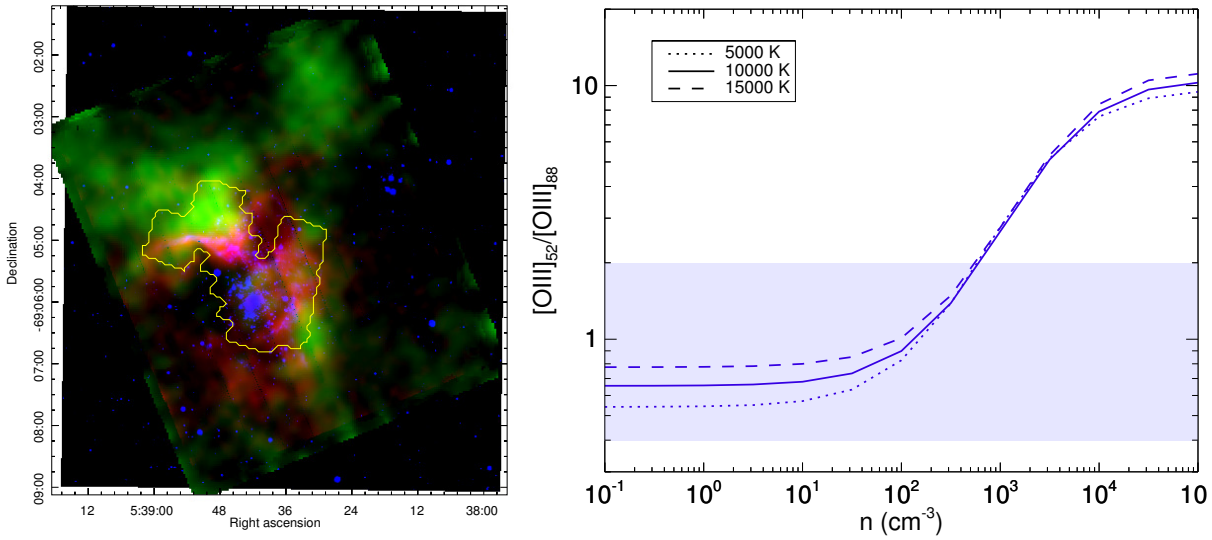

Figure 9: *Gauche : Vista bande J (bleu), FIFI-LS [O III] 52 µm (rouge) et [C II] 158 µm (vert). Le contour jaune la région observée par PACS pour la raie [O I] 145 µm. Droite : rapport théorique [O III] 52 µm/[O III] 88 µm en fonction de la densité électronique pour trois températures différentes. La zone bleue indique l'intervalle des valeurs observées.*

Nouvelles observation *SOFIA*

Pour le cycle 4 des observations *SOFIA*, 7 h d'observation nous ont été accordées pour compléter la cartographie de 30Dor, à plus grande échelle. Ces observations ont été réalisées avec le spectromètre FIFI-LS, entre le 28 juin et le 4 juillet 2016 (P.I. : Chevance). Nous avons entièrement observé une région de 90 pc × 75 pc, centrée sur R136, en [O III] 52 µm (inaccessible avec PACS), [O III] 88 µm et [C II] 158 µm (Figure 9) et nous avons agrandi la carte de [O I] 145 µm. La raie [O I] 63 µm, fortement absorbée par l'atmosphère, est à peine détectée.

Ces nouvelles observations permettent premièrement une mesure de la densité électronique du gaz ionisé grâce au rapport des raies [O III] (Figure 9). Dans un second temps, nous aurons la possibilité de déterminer G_{UV}, P et A_V^{max} en utilisant le modèle PDR puis d'estimer la fraction de gaz H_2 non tracé par CO (voir Chapitre V) en fonction de la distance à R136, ce qui n'était pas possible avec la couverture spatial réduite des données PACS. Ceci est une étape importante qui permettra de mieux interpréter les observations des galaxies lointaines, non résolues spatialement.

Chapitre 5 : Etude du gaz moléculaire

H_2, marqueur de la formation stellaire

Bien que H_2 soit la molécule la plus abondante dans l'Univers et qu'elle soit l'ingrédient principal de la formation stellaire, la majeur partie du gaz moléculaire H_2 n'est en général pas observable directement. En effet, la molécule de dihydrogène est symétrique et n'a pas de moment électrique permanent, H_2 n'est donc pas observable directement dans le gaz moléculaire froid. D'autres molécules sont en revanche plus facile à observer à basse température. C'est le cas en particulier de CO, qui est la deuxième molécule la plus abondante ($CO/H_2 \sim 10^{-4}$). CO est donc souvent utilisée comme traceur de la masse du gaz moléculaire dans la Voie Lactée (par exemple, Heyer & Dame 2015 et les références citées dans cet article). En effet, une relation de proportionnalité peut être supposée entre l'intensité de CO(1-0) et la densité de colonne de H_2, en introduisant le facteur de proportionnalité X_{CO} :

$$N(\mathrm{H_2})\,[\mathrm{cm^{-2}}] = \mathrm{X_{CO}} \times I_{\mathrm{CO(1\text{-}0)}}\,[\mathrm{K\ km\ s^{-1}}].$$

En terme de masse de H_2, on peut également définir α_{CO} comme suit :

$$M_{mol}\,[M_\odot] = \alpha_{\mathrm{CO}} \times L_{\mathrm{CO(1\text{-}0)}}\,[\mathrm{K\ km\ s^{-1}\ pc^2}].$$

Par des calculs théoriques, on trouve une relation proche de cette dernière en appliquant le théorème du viriel à un nuage à l'équilibre. Dans notre galaxie, $X_{CO,MW} = 2 \times 10^{20}\,\mathrm{cm^{-2}}$ $(\mathrm{K\ km\ s^{-1}})^{-1}$ et $\alpha_{CO,MW} = 4.3\,\mathrm{M_\odot\ pc^{-2}}$ $(\mathrm{K\ km\ s^{-1}})^{-1}$ (Bolatto et al. 2013). Cependant, aux faibles densités de colonnes, une fraction de H_2 pourrait ne pas être tracée par CO (Grenier et al. 2005; Planck Collaboration 2011a).

Cas à faible métallicité

Le champ de radiation intense (par exemple, Madden et al. 2006) et l'abondance réduite de poussières (par exemple, Rémy-Ruyer et al. 2014) dans les galaxies naines modifient la structure du MIS. L'émission CO est en général faible comparée aux traceurs de la formation stellaire (par exemple, Hughes et al. 2010; Wong et al. 2011; Madden et al. 2013; Cormier et al. 2014, 2015) comme illustré sur la Figure 10. Cela pourrait s'expliquer par une efficacité de formation d'étoiles accrue, ou bien par le fait que CO n'est pas un bon traceur du réservoir de gaz moléculaire à faible métallicité.

De nombreuses études théoriques ont montré une évolution de la structure des nuages moléculaires lorsque la métallicité diminue (par exemple, van Dishoeck & Black 1986; Maloney & Black 1988; Hollenbach & Tielens 1999; Röllig et al. 2006; Wolfire et al. 2010; Glover & Mac Low 2011; Krumholz & Gnedin 2011; Glover & Clark 2012; Sternberg et al. 2014). En effet, l'auto-écrantage de H_2 est efficace à faible densité de colonne, alors que le rayonnement FUV dur combiné à une abondance de poussières réduite repousse la transition $C^+/C^o/CO$ plus profondément dans le nuage. La relation entre X_{CO} et la métallicité a été étudiée observationnellement (Bolatto et al. 2008; Leroy et al. 2011; Genzel et al. 2012; Schruba et al. 2012), mais reste incertaine (Figure 10).

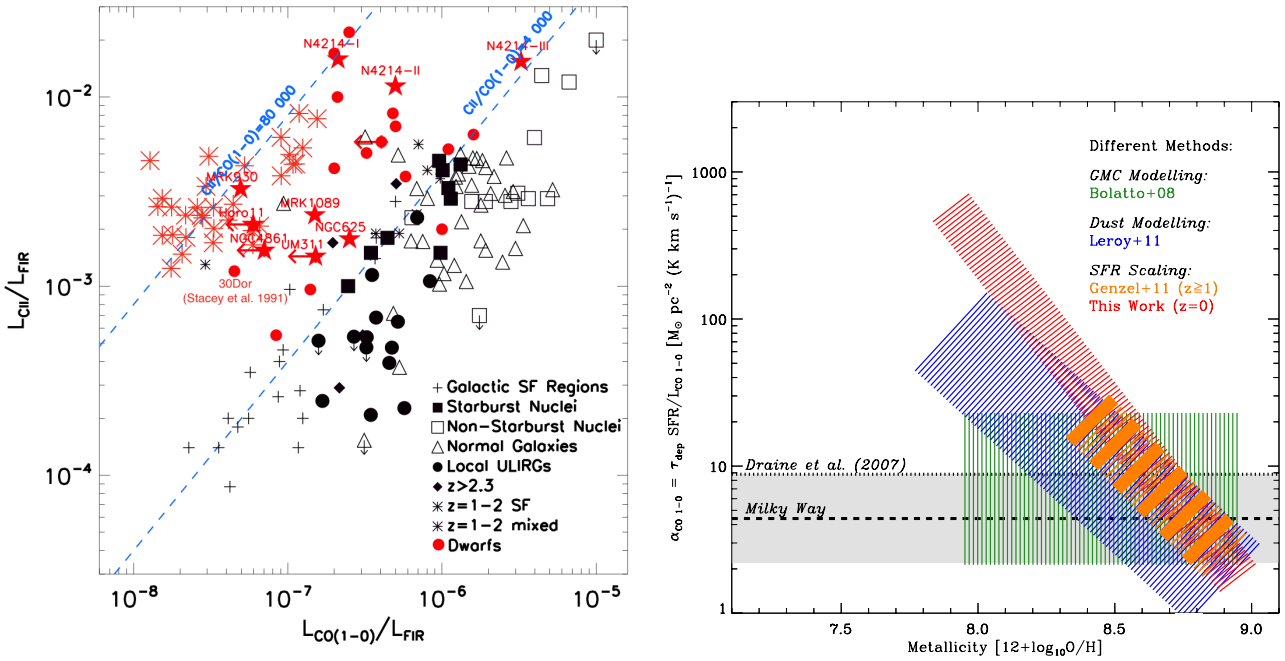

Figure 10: *Gauche : [C II]/L_{FIR} en fonction de CO/L_{FIR}. Adapté de Stacey et al. (1991, 2010); Hailey-Dunsheath et al. (2010); Madden et al. (2013); Cormier (2012). Les galaxies normales et à flambées d'étoiles sont en noir (Stacey et al. 1991, 2010; Hailey-Dunsheath et al. 2010), principalement situées sous la ligne bleue représentant [C II]/CO = 4000. Les cercles et les étoiles rouges sont les galaxies naines de l'échantillon DGS (Madden et al. 2013), principalement au-dessus de [C II]/CO = 4000. Les astérisques rouges représentent 30Dor, avec un rapport moyen [C II]/CO ≈ 80000. Droite : figure tirée de Schruba et al. (2012) montrant la variation observée de α_{CO} en fonction de la métallicité. Les différentes couleurs représentent les résultats obtenus par différentes approches.*

Mesure du gaz moléculaire sombre en CO

Différentes méthodes pour déterminer la masse totale de gaz moléculaire sont décrites dans la Section V.2.1 :

- théorème du viriel et dispersion des vitesses,
- estimation de la densité de colonne grâce aux isotopes de CO,
- estimation de la masse de H_2 grâce à la masse de poussières,
- modélisation de l'émission diffuse en rayons gamma,
- hypothèse d'une efficacité de formation d'étoiles constante,
- modélisation de la structure des nuages par un code PDR.

Résultats pour 30Dor

En complément des observations *Herschel* et *Spitzer* de 30Dor, la transition CO(3-2) a été observée par le télescope ASTE (Minamidani et al. 2011) avec une résolution angulaire de 22″, et la transition CO(1-0) par le télescope Mopra (Wong et al. 2011) avec une résolution de 45″. Les observations H I (Kim et al. 2003) sont à une résolution de 1′ et H_α à 5″ (MCELS; communication privée R.Leiton).

En combinant toutes ces observations, nous avons déterminé la masse de gaz moléculaire dans la région de 30Dor par deux méthodes. Grâce aux résultats du modèle PDR à la résolution de 22″ et 45″, en appliquant la méthode décrite à la Section III.4.2, nous avons estimé A_V^{max} entre 1.7 et 3.4

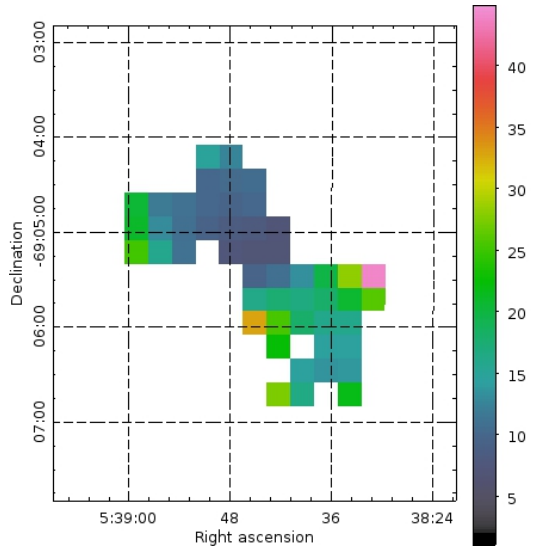

Figure 11: *Rapport entre notre estimation du facteur* X_{CO} *adapté pour 30Dor,* $X_{CO,30Dor}$*, en utilisant les résultas du modèle PDR à une résolution angulaire de 22″, et une valeur standard communément utilisée pour la Voie Lactée,* $X_{CO,MW} = 2 \times 10^{20}\, cm^{-2}\ (K\ km\ s^{-1})^{-1}$. $X_{CO,30Dor}$ *est en moyenne entre 5 et 20 fois supérieur à* $X_{CO,MW}$.

mag, et nous en avons déduit une masse de H_2 approximativement entre 50 et 550 $M_\odot/pc^2$. La masse calculée à partir de l'émission CO(1-0) et $X_{CO,MW}$ représente seulement 1 à 20% de cette valeur. On peut donc redéfinir un facteur de conversion plus adapté à cette région par : $X_{CO,30Dor} = \frac{N(H_2)_{model}}{I_{CO(1-0)}}$ (Figure 11), dont la valeur est comprise entre 1×10^{20} cm^{-2} (K km s^{-1})$^{-1}$et 4×10^{20} cm^{-2} (K km s^{-1})$^{-1}$ sur l'ensemble de la carte.

Remarques

D'autres traceurs pourraient être de meilleurs traceurs de la masse totale de H_2 que CO à faible métallicité. La présence de [CII], co-existant avec H_2 dans les galaxies irrégulières a été suggérée par Madden et al. (1997). Une récente étude par Nordon & Sternberg (2016) montre que la densité de colonne de C^+ associée à H_2 est plus importante que celle associée au gaz atomique.

D'autres études, théoriques et observationnelles, ont montré que [CI] pourrait également constituer un bon traceur de H_2 à faible métallicité (par exemple, Offner et al. 2014; Glover & Clark 2016, Madden et al. en préparation), en particulier pour les galaxies lointaines (Papadopoulos et al. 2004).

Effets de la résolution spatiale

Pour les galaxies lointaines, la résolution spatiale diminue et des environnements différents sont intégrés dans un seul champ de vue, ce qui peut induire des masse de H_2 erronées. Si la répartition du gaz n'est pas homogène, on peut se demander si le résultat sera dominé par les régions diffuses, plus étendues, ou bien par les régions plus denses et plus lumineuses. A la distance de la galaxie d'Andromède (~ 780 kpc ; Ribas et al. 2005) notre carte de 30Dor tiendrait dans un seul pixel du spectromètre PACS. Les valeurs obtenues pour G_{UV}, P et la masse de H_2 seraient alors proches des valeurs moyennes obtenues à la résolution de 22″ et l'effet de la résolution spatiale est ici peu marqué. Cependant, la région imagée par *Herschel* est relativement réduite et homogène et on s'attend à plus de différences en incluant les régions plus lointaines et diffuses observées par *SOFIA*.

Aux petites échelles, les observations de Indebetouw et al. (2013) avec *ALMA* ont révélé un facteur X_{CO} proche de deux fois la valeur galactique pour les nuages moléculaires. Cependant, le milieu internuage, plus diffus, n'est pas pris en compte, ce qui augmenterait encore cette valeur. De nouvelles

observations avec le télescope *ALMA* sont en cours (P.I. Chevance) pour résoudre la structure des nuages moléculaires dans 30Dor et évaluer les effets de la résolution, notamment sur la valeur du paramètre A_V^{max} et la fraction de gaz moléculaire sombre en CO.

Chapitre 6 : L'impact de l'environnement

30Dor est un environnement relativement extrême et les propriétés du MIS à quelques parsecs d'un amas d'étoiles sont vraisemblablement différentes du reste du LMC. Nous allons donc étudier dans ce chapitre la structure et les conditions physique du MIS dans d'autres régions de formation d'étoiles du LMC et du SMC, pour tenter de comprendre quels paramètres contrôlent la fraction de gaz moléculaire sombre.

Présentation de l'échantillon

La métallicité du LMC est considérée comme relativement constante spatialement, et proche de $0.5\,Z_\odot$ (Rolleston et al. 2002; Pagel 2003). En revanche, la densité, le champ de radiation, l'extinction, varient en différents endroits de la galaxie. L'effet de la métallicité peut être vu en comparant le LMC avec le SMC, à $0.2\,Z_\odot$ environ (Russell & Dopita 1992). En plus de 30Dor, 8 régions du LMC et 2 du SMC ont été observées par *Herschel* au cours du relevé DGS et du programme de Hony et al. (Figure 12). Quelques caractéristiques des différentes régions de formation d'étoiles (N11, N44, N157, N158, N159, N160, N180 et une région plus "diffuse" et le LMC ainsi que N66 et N83 dans le SMC) sont décrites dans la Section VI.1.1.

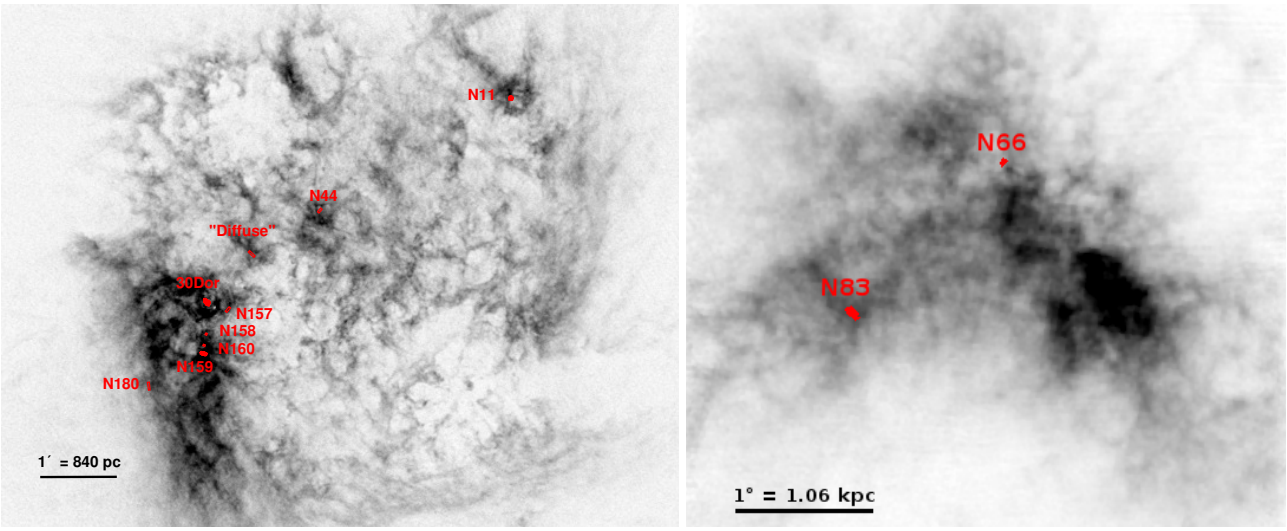

Figure 12: *Carte en H I du LMC (gauche ; Kim et al. 2003) et SMC (droite ; Stanimirovič et al. 1999). Les couvertures spatiales des cartes PACS et SPIRE des régions étudiées ici sont délimitées en rouge.*

Modèle PDR

Analyse des régions individuelles

Chaque région a été modélisée individuellement suivant la méthode décrite à la Section III.4.2. A la différence de 30Dor, comme les abondances des différents éléments ne sont pas connues avec

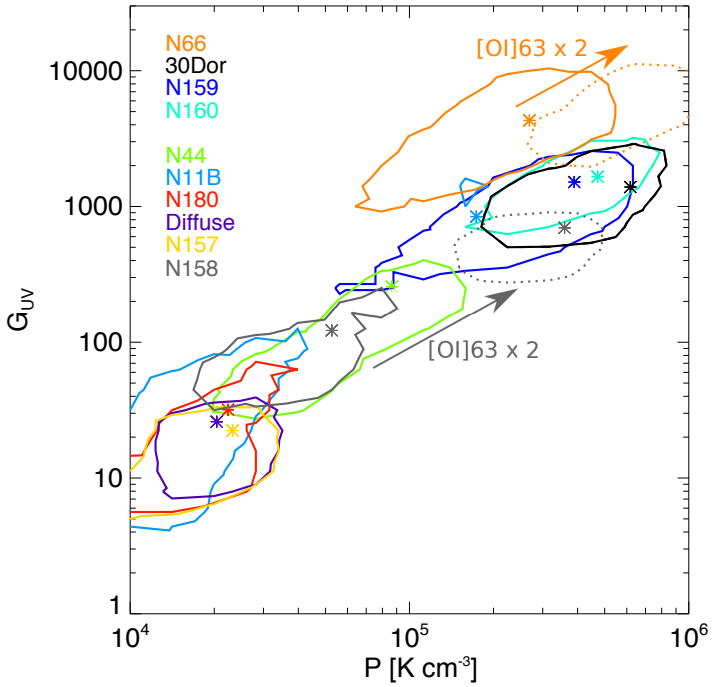

Figure 13: *Paramètres G_{UV} and P, pour les régions de formation d'étoiles du LMC et du SMC. Les contours indiquent la localisation de 75% des pixels pour une région donnée. Les astérisques indiquent les meilleures solutions pour les cartes intégrées. Les contours pointillés orange et gris indiquent la position de 75% des pixels pour N66 et N158, respectivement, en multipliant l'intensité de [O I] 63 µm par un facteur deux pour prendre en compte un possible effet d'opacité. Pour N66 et N158, la raie optiquement fine [O I] 145 µm n'a pas été observée.*

précision pour chacune de ces régions, nous avons choisi de diminuer toutes les abondances par un facteur 2 ou 5 (pour le LMC et le SMC respectivement) par rapport aux abondances solaires. De plus, la taille limitée des régions couvertes en [O III] 88 μm en particulier ne permet pas une correction de L_{FIR} pour prendre en compte une éventuelle contamination par le gaz ionisé. Nous avons donc utilisé directement L_{FIR} comme contrainte pour le modèle PDR, ce qui est généralement fait dans les autres études, et supposé que la totalité de l'émission [C II] provient bien des PDR, ce qui est en général bien vérifié dans les régions de formation d'étoiles (par exemple, Lebouteiller et al. 2012; Okada et al. 2015). Les résultats de cette modélisation sont présentés en Figure 13.

Remarques sur la résolution

Nous avons également déterminé les paramètres permettant de reproduire les intensités observées intégrées pour chaque région (représentés par un astérisque sur la Figure 13). Les solutions sont globalement décalées vers les hautes pressions et forts champs de radiation comparé aux valeurs moyennes obtenues à la résolution de 12″.

De plus, même à la résolution de 3 pc (12″), le MIS n'est pas homogène et plusieurs phases (nuages moléculaires dense et milieu diffus inter-nuages) sont probablement présentes dans un seul champ de vue (les nuages observés avec *ALMA* ont des diamètres de l'ordre du parsec ou inférieur ; Indebetouw et al. 2013). Les futures observations ALMA permettront de déterminer si les émission [C II], [C I] et CO sont associées aux mêmes structures.

Le gaz moléculaire sombre en CO

Résultats préliminaires

Avec la même méthode que celle utilisée pour 30Dor, nous avons déterminé la fraction de gaz moléculaire sombre en CO pour chaque région en comparant la masse de H_2 déterminé par le modèle PDR avec $\alpha_{CO,MW} \times L_{CO}$, pour essayer de comprendre comment la diversité des conditions physiques affecte cette valeur. Les résultats sont regroupés dans la Table 1 et couvrent une large gamme de

Table 1: Résultats de la modélisation des régions de formation d'étoiles (intégrées) des Nuages de Magellan.

Région	G_{UV}	P [cm^{-3}]	A_V^{max} [mag]	M_{H_2} [$M_\odot\,pc^{-2}$]	$\alpha_{CO}/\,\alpha_{CO,MW}$	$M_{dark\ gas}$ [$M_\odot\,pc^{-2}$]	$F_{dark\ gas}$ %
Diffuse	26	2.04×10^4	1.2	93	2.84	60.4	65
N11B	842	1.74×10^5	1.9	77	2.62	47.8	62
N44	257	8.65×10^4	1.8	280	2.54	169.0	61
N157	240	2.33×10^4	0.9	297	14.60	276.0	93
N158	122	5.27×10^4	1.2	312	13.50	289.0	92
N159	1513	3.89×10^5	2.1	143	1.19	22.7	16
N160	1659	4.70×10^5	1.7	132	3.81	97.2	74
N180	31.8	2.24×10^4	1.2	95.6	3.77	70.2	73
30Dor	1390	6.18×10^5	2.7	194	10.20	175.0	90
N66	4305	2.69×10^6	3.0	35	–	–	–

Remarque : α_{CO} et $M_{dark\ gas}$ n'ont pas été déterminés pour N66 dû au manque de contraintes observationnelles.

valeurs, de 16 à 93%. À part N159, toutes les régions ont une fraction de gaz moléculaire sombre (F_{dark}) supérieure à 50% , ce qui ne peut donc pas être expliqué par une simple relation linéaire de α_{CO} avec la métallicité. De plus, ces valeurs ne semblent corrélées ni avec G_{UV} ni avec G_{UV}/P. Notre échantillon étant relativement petit, la dépendance de la fraction de gaz moléculaire sombre avec d'autres paramètres, tels que l'âge de la région par exemple, ne peut être confirmé pour l'instant.

Projet d'observations *ALMA* pour le cycle 4

Une bonne résolution spectrale et spatiale est essentielle pour résoudre individuellement les nuages moléculaires et calculer la masse de gaz moléculaire. Ainsi, nous avons proposé d'observer [CI] 609 μm et ^{12}CO(2-1) dans les régions N44 et N159 avec l'interféromètre *ALMA* (P.I. Chevance). Ces deux régions présentent des caractéristiques bien distinctes, et notamment des fractions de gaz moléculaire sombre en CO très différentes (61% et 16% respectivement). Les résolutions spectrale et spatiale élevées d'*ALMA* nous permettrons de comparer les structures des nuages moléculaires dans ces deux environnements et d'étudier le potentiel du rapport [CI]/^{12}CO(2-1) comme traceur du réservoir de gaz moléculaire.

Conclusions et perspectives

Résumé des résultats

Le but de cette thèse a été d'étudier en détail les conditions physiques et la structure du milieu interstellaire (MIS) dans des régions de formation d'étoiles dans le LMC et le SMC. Nous nous sommes intéressés à l'impact d'un fort champ de radiation sur le MIS à faible métallisé pour mieux comprendre comment les processus physiques dans le MIS sont affectés par une réduction de l'abondance en métaux. Nous avons tout particulièrement étudié les régions de photodissociation (PDR), dans lesquelles un important réservoir de gaz moléculaire H_2, l'ingrédient élémentaire de la formation

stellaire, est attendu dans des environnements à faibles métallicité. Il ne serait alors pas détecté par le traceur classique, CO, ainsi qu'anticipé par les études théoriques (par exemple, Röllig et al. 2006; Wolfire et al. 2010; Glover & Mac Low 2011).

Notre échantillon d'étude comporte des régions du *Herschel* DGS (Madden et al. 2013), complété par des régions du *Herschel* OT2 (Hony et al.). Le large domaine de longueurs d'ondes couvert par *Herschel* et *Spitzer* nous a permis de sonder une large diversité de phases du MIS, du gaz ionisé au gaz moléculaire, et ainsi de déterminer les propriété physiques du MIS dans des régions de formation d'étoiles du LMC et du SMC. J'ai décrit brièvement le modèle d'émission de la poussière présenté par Galliano et al. (2011) qui m'a permis d'estimer spatialement en particulier L_{FIR} et la masse de poussière. J'ai ensuite présenté le modèle PDR de Meudon (Le Petit et al. 2006) utilisé pour déterminer les paramètre G_{UV}, P et A_V^{max} dans les régions étudiées. Les dégénérescences entre différents paramètres (G_{UV} et P, la géométrie des nuages, leur profondeur et le facteur de couverture) ont été examinées. Grâce à ce modèle, j'ai pu déterminer la structure du MIS dans la nébuleuse 30 Doradus dans le LMC, ainsi que sa répartition tridimensionnelle autour du super amas R136. J'ai également pu montrer que ~90% de la masse de H_2 n'est pas tracée par CO avec l'hypothèse d'un facteur de conversion égal à celui de la Voie Lactée. Une fois cette méthode établie pour 30 Doradus, je l'ai étendue à neuf autre régions de formation stellaire dans le LMC et le SMC, et j'ai montré que la fraction de gaz sombre en CO varie entre 16% et plus de 90%.

Perspectives

Une bonne résolution spatiale est importante pour déterminer la masse de gaz moléculaire. Cependant, pour les galaxies lointaines à faible métallicité, la résolution et la sensibilité limitées des instruments actuelles ne permettent pas d'appliquer la plupart des méthodes décrites au Chapitre V. Il est donc crucial d'étudier en détail les galaxies proches pour être en mesure d'interpréter les observations non résolues de galaxies lointaines. Les observations ALMA en cours, à 0.2 pc, vont nous permettre de mieux comprendre les variations du facteur X_{CO} en fonction des conditions locales ainsi que de contraindre la géométrie des modèles.

Par la suite, il sera intéressant de comparer notre échantillon de régions de formation d'étoiles du LMC avec des régions de formation d'étoiles de la Voie Lactée et d'autre galaxies à métallicité solaire du Groupe Local. Un des buts sera de calibrer les potentiels traceurs du gaz moléculaire, dans une large gamme d'environnements locaux, comme gabarits pour l'interprétation des galaxies lointaines.

De nouveaux observatoires sont maintenant disponibles dans les domaines infrarouge (*SOFIA*) et submillimétrique (*ALMA*, *NOEMA*) et permettent des observations du gaz et de la poussière à des résolutions et des sensibilités accrues. Ils seront bientôt complémentés par le James Webb Space Telescope (*JWST*; 2018), le Square Kilometer Array (*SKA* ; ~ 2020) et peut-être par un prochain télescope spatial infrarouge, *SPICA* (~ 2027).

Introduction

The processes of galaxy formation and evolution from the primordial Universe to present days involve the environment, such as gravitational interactions and merger events, for example. Feedback processes from stars, in the form of ionizing radiation, stellar winds, supernovae, etc, are also thought to be responsible for the global properties of a galaxy. Hence, knowledge of the star formation history is one of the keys towards understanding galaxy evolution. However, the exact mechanisms of star formation, in particular in primordial environments, and the physical processes controlling star formation efficiency and its evolution, remain largely uncertain.

The interstellar medium (ISM), as one of the main components of galaxies, plays a major role in this evolution. Due to the interplay and the cycling of matter between gas, dust and stars, the structure and properties of galaxies are continuously evolving. Detailed observations of the different phases of the ISM probe the current physical and chemical states of a galaxy.

The chemical state of low metallicity dwarf galaxies is such that their ISM properties have often been thought to resemble early universe conditions. Because of their low metal-abundance, they have notable differences compared to more metal-rich galaxies However, due to their small size and low luminosity they can be difficult to study outside of our local Universe.

In this study, we focus on a sample of star-forming regions of the Large Magellanic Cloud (LMC) and the Small Magellanic Cloud (SMC), our closest neighbors. With moderate metallicity ($0.5\,Z_\odot$ for the LMC and $0.2\,Z_\odot$ for the SMC), these galaxies show very different ISM conditions from the Milky Way. As such they are ideal laboratories to study in detail the impact of the environment on the star formation and, reciprocally, the stellar feedback on the metal-poor ISM. In active star-forming regions in particular, the presence of young stars irradiating their environment with hard and intense radiation fields, combined with the reduced dust abundance is expected to shape the structure of the ISM in a different way from metal-rich star-forming galaxies and affect our classical view of the multiphase ISM. I will describe some of the general properties of the ISM along with the specific characteristic of dwarf galaxies in Chapter I.

The different phases in the ISM can be observationally traced through a variety of diagnostics. The ultraviolet (UV) and visible radiation emitted by stars are absorbed by dust and re-emitted in the infrared (IR) domain. Moreover, bright far-infrared (FIR) fine structure lines, revealing the gas cooling, were originally detected from the Kuiper Airborne Observatory (*KAO*) and the Infrared Space Observatory (*ISO*) in dwarf galaxies. Thus, studying the IR emission from the galaxies enables us to probe gas and dust in the different ionized, neutral and molecular phases and provides information on many physical processes at play in the ISM. With the recent observations from *Spitzer* and *Herschel*, our understanding of the composition and physical processes in the ISM has considerably evolved. In Chapter II, I will describe in particular the novelty of *Herschel* observations and present briefly the new observational facilities *SOFIA* (Stratospheric Observatory for Infrared Astronomy)

and *ALMA* (Atacama Large Millimiter/sub-millimeter Array), now accessible to probe the ISM in IR and submillimeter wavelengths.

My work investigating the physical conditions and structure of the ISM is based on the combination of *Herschel* and *Spitzer* spectroscopy and photometry data with PDR models, described in Chapter III. In this chapter, I also present the dust and PAH modeling, used as tracers of the gas heating. This is applied to the region of 30 Doradus in the LMC, as a first test-bed (Chapter IV) to set up the methodology. This extremely active star-forming region represents an ideal target to study the interplay between the stellar radiation field and the surrounding ISM in detail. The physical properties (incident radiation field, pressure) and structure (depth of the clouds, 3-dimensional repartition around the cluster) of the gas are determined. Based on this modeling, I estimate the total molecular gas mass in this region and the fraction of "CO-dark" gas, the amount of H_2 not traced by CO (Chapter V) The same method is extended to other star-forming regions of the LMC and SMC in Chapter VI. These different environments present great contrast in term of star formation activity, density, age and metallicity. The detailed study focusing on relatively small star-forming regions in the Magellanic Clouds is a first step toward a better understanding of star formation and physical processes in the ISM on more global scales.

Chapter I

The interstellar medium of dwarf galaxies

Contents

In this chapter, we aim to present a brief overview of our current knowledge on the composition, structure and physics of the interstellar medium (ISM) of galaxies. We will first describe some general characteristics of galaxies and present the properties of gas and dust, the two components of the ISM. Then, we will focus on the observational probes which will be used as diagnostic tools in the following study. We then describe properties of dwarf galaxies, and in particular the Large Magellanic Cloud (LMC) and Small Magellanic Cloud (SMC), which are the focus of this study

I.1 General views of a galaxy

I.1.1 Galaxy composition

A simple description of a galaxy is a gravitationally bound ensemble of stars and interstellar gas and dust, embedded in a dark matter halo. While stars are on average separated by ~ 2 pc in the solar neighborhood, galaxies are not empty: the available space between the stars is filled by the interstellar medium (ISM) composed of gas and dust. Interstellar gas, which is for the most part composed of hydrogen and helium, with a small fraction of heavier elements, can be found in a large variety of phases, depending on the physical conditions of the local environment. It can consist, for example, of diffuse warm ionized gas, often filling large fraction of the galaxy, and small, dense and cold molecular clouds. Dust is present throughout the galaxy. The relative importance of these components (stars, gas and dust), in terms of mass and luminosity, varies for different galaxies, depending on the morphology of the galaxy and its stellar activity in particular. For the Milky Way, Table I.1 summarizes the contribution of each component to the total mass and luminosity of the Galaxy.

Table I.1: Masses and luminosities of the different components of the Milky Way. Adapted from Tielens (2005).

Component	Mass [$M_\odot$]	Luminosity [$L_\odot$]
Stars	1.8×10^{11}	$\sim 4.8\times10^{10}$
Gas	4.5×10^{9}	$\sim 2\times10^{8}$
Dust	$\sim 4.5\times10^{7}$	$\sim 1.7\times10^{10}$
Total	$\sim 2\times10^{11a}$ - $\geqslant 10^{12b}$	$\sim 6.5\times10^{10}$

$^{(a)}$ Visible matter only. $^{(b)}$ Including dark matter.

This gas and dust is heated by photons originating from stars (the interstellar radiation field), mainly in the ultraviolet (UV) and visible wavelength range, by cosmic rays (mainly energetic protons) and X-rays, emitted by galactic and extragalactic hot gas. A number of cooling processes, depending on the local physical conditions (in particular density and temperature), result in the emission of a variety of lines and continuum, in the optical and infrared (IR) wavelength domain. As a result, galaxies emit radiation over the entire electromagnetic spectrum, and the energy at each wavelength results from several complex processes. For example, as presented in Figure I.1, the image of a galaxy such as the LMC or the SMC at various wavelengths shows very different structures. Stars will be mostly seen in the UV or visible wavelength, where they emit the most energy. Young stars, in particular, will mostly emit in the UV. On the other hand, dust can absorb the UV-to-visible light, creating dark zones in the visible image, and re-emit IR continuum, which is detected by the space telescopes *Herschel* and *Spitzer*, for example. Therefore, to have a complete view of a galaxy, it is

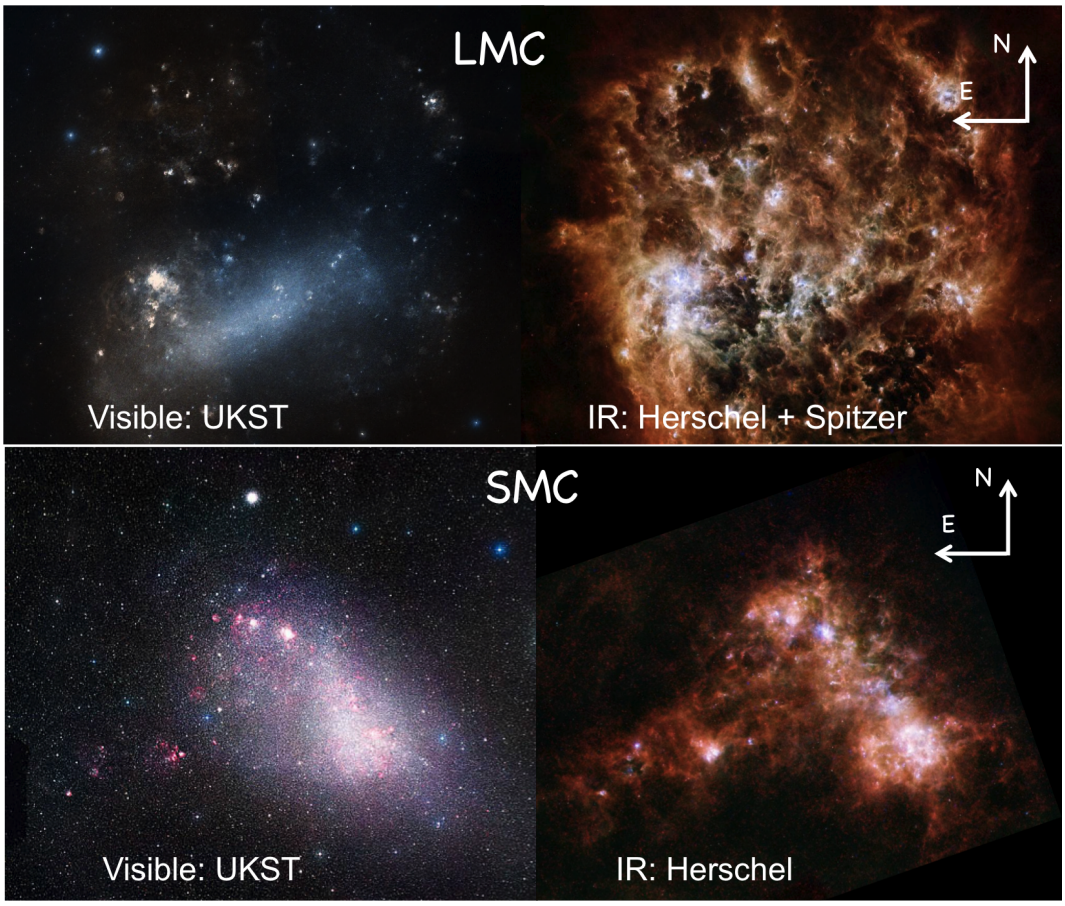

Figure I.1: *Top: the LMC observed by the UK Schmidt Telescope (UKST; left) in visible, revealing mostly the stars; and by the space telescopes Herschel and Spitzer in IR (right), revealing an important component of dust and cold gas. Bottom: the SMC observed by the UKST (left) in visible and Herschel Space Observatory in IR (right). Credits: Anglo-Australian Observatory/Royal Observatory Edinburgh and ESA/NASA/JPL-Caltech/STScI.*

crucial to have access to the largest possible wavelength range. We will describe some of the instruments we use for our study in Chapter II. The modeling of the spectral energy distribution (SED) of a galaxy, i.e. the distribution of the emitted energy as a function of the wavelength, requires taking into account all of the physical processes affecting the radiation in the galaxy in order to disentangle the different components and their physical properties. This will be detailed in Section I.3.3.

I.1.2 Definition of metallicity

Metallicity, noted Z, is the mass fraction of the elements heavier than helium, which are called metals. The mass fractions of hydrogen and helium are usually noted X and Y respectively, so that:

$$X + Y + Z = 1. \tag{I.1}$$

According to the Big Bang theory, the primordial universe was first composed almost entirely of hydrogen and helium. The primordial mass fractions were then $X_P \approx 0.744$, $Y_P \approx 0.256$ and $Z_P = 0$ (Izotov et al. 2012). The lightest elements (lithium and beryllium) were also formed during primordial nucleosynthesis and exist as trace elements. All of the other elements up to iron are mainly formed

by fusion in stellar cores and released in the ISM through stellar winds or during the death of stars, i.e. supernovae (SN). High mass stars ($\gtrsim 8\,M_\odot$) can form elements up to iron, while Solar-type stars only synthesize helium, carbon, nitrogen and oxygen. Elements heavier than iron are produced during supernova events.

Thus, it is believed that the first stars to form must have been extremely metal-poor. Metal enrichment of a galaxy is achieved progressively through the cycles of birth and death of stars. Hydrogen is slowly converted into heavier elements in stars and today's mass fractions in the solar neighborhood are measured as: $X_\odot \approx 0.7154$, $Y_\odot \approx 0.2703$ and $Z_\odot = 0.0142$ (Asplund et al. 2009). Thus, the metallicity traces the history of the stellar activity, giving an idea of the number of cycles of star formation the ISM has experienced. Metallicity is then expected to increase with the age of the galaxy. However, as massive stars are short-lived compared to lower mass stars, the relation between metallicity and time is not expected to be linear. In addition, outflows of chemically enriched gas and infall of primordial gas from the extragalactic medium can affect this simple view.

Metallicity determination

Metallicity is generally approximated by the ratio of the abundance of one metal element to the hydrogen abundance. Oxygen is often used as a proxy for the metallicity and the number $12+\log(O/H)$ is used to describe the metallicity value. In the solar neighborhood, $12+\log(O/H) = 8.69$ (Asplund et al. 2009), while $12+\log(O/H) = 8.58$ in the LMC ($\sim 0.5\,Z_\odot$; Rolleston et al. 2002). However, abundances do not scale similarly for all elements and deficiency of specific elements can be observed. Similarly, metallicity values are not necessarily valid on global galaxy scales. They depend on the medium probed (which is different for different measurement methods) and on the efficiency and mixing timescale. For example O is produced by massive stars, which have a rather short lifetime, and is thus injected early-on in the ISM via supernova explosions. However, C and N, produced by high and intermediate mass stars, can thus be injected later on in the ISM. Hence the ratios C/O and N/O are expected to be low after a recent star burst for example.

Several ways exist to measure elemental abundances, as reviewed by Kunth & Ostlin (2000). These include: spectroscopy of ionized gas in H II regions (Izotov et al. 2006) or planetary nebulae (Pagel 1997); photometry of resolved stellar populations (e.g. Lee et al. 1993; the abundance ratio [F/H] is determined by the color of the red giant branch population); spectroscopy of individual stars (only possible in the Milky Way and nearest galaxies; e.g. Haser et al. 1998 in the Magellanic Clouds); etc.

I.1.3 Galaxy evolution and star formation histories

The main epoch of galaxy formation is believed to be approximately at redshift $z \sim 1-2$ (Madau et al. 1996). In the hierarchical scenario of structure formation (Dekel & Silk 1986), massive galaxies form by a succession of merging of smaller building blocks (bottom-up theory). This scenario is compatible with the Cold Dark Matter (CDM) cosmology models. In this case, dwarf galaxies could be the base of today's more massive galaxies. However, this scenario is debated. Evidence for downsizing (Cowie et al. 1996) have been found, where stellar growth moves to lower mass systems as the universe expands, i.e. more massive galaxies are formed at higher redshift.

While dwarf galaxies may not necessarily be the building blocks for galaxy evolution, they may be considered to be chemically young objects, as they are often metal-poor. By this aspect, they could be compared to the unevolved systems of the early universe, which have experienced few star formation episodes. However, the reality is more complex, since all dwarf galaxies show evidence

for intermediate-age or old stellar population for example. Studying the star formation history of the different types of dwarf galaxies could bring clues to our understanding of galaxy evolution. One possible explanation to reconcile the presence of an old stellar population with a low-metallicity ISM could be the existence of galactic outflows removing the enriched gas from the dwarf galaxy (e.g. Babul & Rees 1992), and/or infalls of pristine gas from the inter-galactic medium. However, the exact processes remain uncertain.

The stellar content of galaxies can be studied in particular via UV and optical observations. Photometric observations, with the *Hubble Space Telescope* (*HST*) for example, are important to recover the star formation histories of galaxies. However, UV and optical wavelengths are affected by extinction due to dust, particularly in spiral galaxies which contain more dust than dwarf galaxies. Various stellar populations can be identified by comparing the photometry of stellar populations to stellar evolutionary models, adapted for the age and metallicity (Schaller et al. 1992; Bertelli et al. 1994) after correction for the reddening by dust. For example, recent star formation ($\leqslant 500$ Myr) is revealed by the presence of main-sequence stars, red supergiants, Wolf-Rayet (WR) stars, which have short lifetimes, and thus must have formed recently to be still observable today. Older populations ($\geqslant 1$ Gyr) are traced by asymptotic giant branch (AGB) stars and red giant branch stars, or by horizontal branch stars (e.g. RR Lyrae stars) for $\geqslant 10$ Gyr populations. Extragalactic cluster population analysis are challenging due to the mixing of several populations and the difficulty to resolve clusters in distant objects. Recently, very detailed spectroscopic studies of the super star cluster (SSC) R136 in the 30 Doradus nebula of the LMC (at the VLT, Evans et al. 2011; and with *HST*, Crowther et al. 2016) bring new insight on the star formation history of this region.

More generally, most dwarf galaxies host a mix of old ($\geqslant 1$ Gyr) and young ($\leqslant 0.5$ Gyr) stellar populations (e.g. I Zw 18, Tosi et al. 2007; SMC, Zaritsky et al. 2000; LMC, Westerlund 1997). Most irregular and Blue Compact Dwarf (BCD) galaxies show active star-forming complexes, dense SSCs and/or massive O-B associations, embedded in a more extended, older stellar population (e.g. Hodge et al. 1991). The presence of a young population has an impact on the physical processes of the ISM. Indeed, young stars produce a high proportion of hard UV photons. The hardness of the radiation field is expected to decrease after a few Myr, as the stellar population evolves off the main sequence (e.g. Levesque et al. 2010). The combination of a high fraction of young massive stars and lower dust content due to low metallicity results in a harder radiation field throughout dwarf galaxies (e.g. Campbell et al. 1986) and maybe explains the high ionization lines observed in H II regions of metal-poor environments (e.g. Thuan & Izotov 2005; Madden et al. 2006). In more metal rich environment, metals in the atmosphere of massive stars already absorb and reduce the fraction of hard photons emitted (Kewley et al. 2001).

For the main part, two main modes of star formation are observed in galaxies: a continuous star formation and/or short episodic events of star formation activity called bursts. Spiral galaxies, or gas-rich dwarf galaxies with a sufficient gas reservoir, can sustain continuous star formation at a relatively constant rate over long periods of time, contributing to progressive metal enrichment. On the other hand, gas-poor dwarf galaxies (mainly ellipticals and spheroidals) show a rather continuous star formation at a decreasing rate, or episodic star formation (Hunter 1997). Star formation may stop anytime if no gas is accreted between the star formation episodes.

BCDs show very violent (up to 10 $M_\odot\,yr^{-1}$, Thuan & Martin 1981) and episodic (every 10^8 yr; Hodge et al. (1989); lasting for a few 10^6 yr) star formation bursts. This mode of formation produces massive stars such as Wolf-Rayet (WR) stars, which are extreme, massive and evolved stars characterized by broad emission lines from high velocity winds. They exhibit active star formation

activity over a brief period, in the last 10 Myr, expelling matter in the ISM, and contributing to metal enrichment. As the strength of stellar winds depends on the metal content of the stellar atmosphere (e.g. Kudritzki et al. 1987; Vink et al. 2000), the number of WR stars is expected to decrease with the metallicity (Vink & de Koter 2005; Gräfener & Hamann 2008). This is indeed the case in the metal-rich Milky Way (630 WRs), compared to the LMC (140 WRs) and the SMC (only 12 WRs; Hainich et al. 2015).

In spiral galaxies, spiral density waves generally trigger the gravitational collapse and fragmentation of giant molecular clouds (GMCs; Lada & Lada 2003), and hence the star formation. In dwarf galaxies, these density waves generally do not exist and other mechanisms must take place. Other local processes may trigger star formation such as gravitational instabilities, random gas motions, feedback from supernovae, mechanical energy from stellar winds (Hunter 1997). Moreover, the effect of environment has a role on the star formation history, and particularly for dwarf galaxies. The effect of gravitational interactions, for example, can be particularly violent compared to more massive galaxies. This can explain in some cases the peculiar observed properties such as asymmetric stellar and gas distributions, complex velocity fields, etc. One typical example is the characteristic shape of the SMC, most likely resulting from tidal interactions with the LMC and the Milky Way. Merger events of gravitational interactions could explain partially the observed star formation activity, by the accretion of gas triggering new star formation episodes for example. However many dwarf galaxies do not show any signs of interactions such as tidal debris, and seem isolated (Portas et al. 2011).

I.1.4 Star formation rate

Detailed studies in the Milky Way have shown that stars are formed by gravitational collapse of dense molecular clouds, essentially made of molecular hydrogen H_2. An important characteristic of a galaxy is its efficiency in making stars. We define the star formation rate (SFR) $\psi(t)$ as the total mass of stars formed per unit of time (in units of $M_\odot\,yr^{-1}$). The SFR can be inferred from the H_α emission-line luminosity at 656 nm. Indeed, H_α luminosity gives the number of ionizing photons emitted by young massive stars (O stars) and absorbed locally. Since O stars are very hot ($\sim$ 30000 to 52000 K) and very luminous (more than 10000 times the Solar luminosity) they consume their hydrogen very rapidly and live only for $\sim 10^6$ yr. Hence, assuming a standard distribution of stars, the initial mass function (IMF), which gives the number of stars formed for each luminosity and spectral type, we can estimate the total star formation rate from the O star formation rate, via H_α (e.g. Kennicutt et al. 2008). Another star formation tracer can be the far-utraviolet (FUV) luminosity, tracing OB stars in low density low surface-brightness galaxies (e.g. Lee et al. 2011). However, H_α and UV observations are affected by dust absorption and have to be corrected to estimate the total number of ionizing photons. The dust absorbing optical and UV photons is heated and reradiates this energy in the mid-infrared (MIR) wavelength range. Therefore the MIR luminosity at 24 μm, for example, can be calibrated to estimate the amount of dust-obscured on-going star formation (Kennicutt. et al. 2007). This approach has been calibrated for star-forming regions of 33 nearby galaxies of the *Spitzer* Infrared Nearby Galaxies Survey (SINGS; Kennicutt et al. 2003) by Calzetti et al. (2007), leading to:

$$SFR(M_\odot yr^{-1}) = 5.3\times10^{-42}[L(H_\alpha) + (0.031\pm0.006)\times L(24\,\mu m)], \quad \text{(I.2)}$$

with luminosities in erg s^{-1}. This calibration was used for the LMC and SMC by Jameson et al. (2016), resulting in an RMS background value of the SFR map of 1×10^{-4} $M_\odot\,yr^{-1}\,kpc^{-2}$ in the LMC and 4×10^{-4} $M_\odot yr^{-1}\,kpc^{-2}$ in the SMC. Alternatively, some studies make use of the FUV luminosity,

which traces predominantly O and early B stars (e.g Bigiel et al. 2008; Leroy et al. 2008) or pre-main sequence stars, using the calibration determined by Leroy et al. (2008):

$$SFR(\mathrm{M_\odot yr^{-1}}) = 8.1\times10^{-2}L(FUV) + 3.2\times10^{-3}L(24\,\mu\mathrm{m}). \quad \text{(I.3)}$$

A more direct method, which is more appropriate for small-scale studies, consists in counting the newly assembled O- and B-type stars, although this requires high resolution and accurate photometry (e.g. Hony et al. 2015). Another estimation of the SFR comes from young stellar objects (YSOs), which are young stars still in the process of forming and thus show an excess of IR emission from circumstellar dust. Therefore, YSO candidates can be selected based on mid-IR *Spitzer* observations for example (e.g. Gruendl & Chu 2009 in the LMC) and are thought to trace the current star formation activity, as compared to the SFR derived from H_α and the 24 μm flux, which give an averaged value over the last $\sim$ 10 Myr (e.g. in the LMC, Indebetouw et al. 2008; Chen et al. 2010, 2014).

Large galaxies, containing more gas, are likely to form a larger number of stars than smaller galaxies in a given amount of time. A more useful quantity to compare various galaxies can then be the specific star formation rate (sSFR) which is defined as the SFR per unit of stellar mass (SFR/M_{stars}, in $\mathrm{yr^{-1}}$). Alternatively, another interesting quantity to look at is the star formation efficiency (SFE), which is defined as the SFR per unit gas (SFR/M_{gas}, in $\mathrm{yr^{-1}}$). The inverse of this quantity can be interpreted as the time required to consume the H_2 gas reservoir. Thus, the molecular gas depletion time, τ_{dep}, is defined as 1/SFE.

On larger scales, especially for high redshift galaxies, the study of star formation becomes more difficult. The idea is then to find an empirical law linking the gas reservoir and the star formation (Schmidt 1959). Kennicutt (1998) determines a relation between the star formation rate surface density, Σ_{SFR} and the gas (atomic+molecular) surface density, Σ_{gas}, known as the Schmidt-Kennicutt law:

$$\Sigma_{SFR} \propto (\Sigma_{gas})^n, \quad \text{(I.4)}$$

with $n \approx 1.4$. This relation is based on H_α observations as a star formation activity tracer, and HI and CO observations as gas tracers, for a large sample of disk galaxies.

Moreover, this relation presents a threshold at low gas column densities ($\sim 10^{20} - 10^{21}$ H cm^{-2}; Kennicutt 1989). This can be understood as a stability criteria (Toomre 1964): below a certain critical density, the gas is stable and large-scale density perturbations at the origin of star formation cannot develop inside the galaxy disk. In dwarf irregular galaxies, Hunter et al. (1998) derive a somewhat lower value of this critical density by a factor of $\sim$ 2, suggesting that stars form in more stable gas compared to spiral galaxies.

I.2 Gas phases in the ISM

The gas represents 99% of the mass of the ISM. It plays an important role in the evolution of galaxies. It is mainly composed of hydrogen and helium and, by a much smaller fraction, of heavier elements such as carbon, oxygen and nitrogen, injected by stars during SN explosions or stellar winds for example. It is common to describe the ISM structure with a simple three-phase model, based on the dominant state of hydrogen: an ionized phase (where H^+ dominates), a neutral atomic phase (where H dominates) and a molecular phase (where H_2 dominates). This is illustrated in Figure I.2. We enumerate here briefly some of the properties of the gas in these three phases, summarized in Table I.2. A more complete description of the physics and chemistry of the ISM can be found in Hollenbach & Tielens (1999), Tielens (2005) and Osterbrock & Ferland (2006).

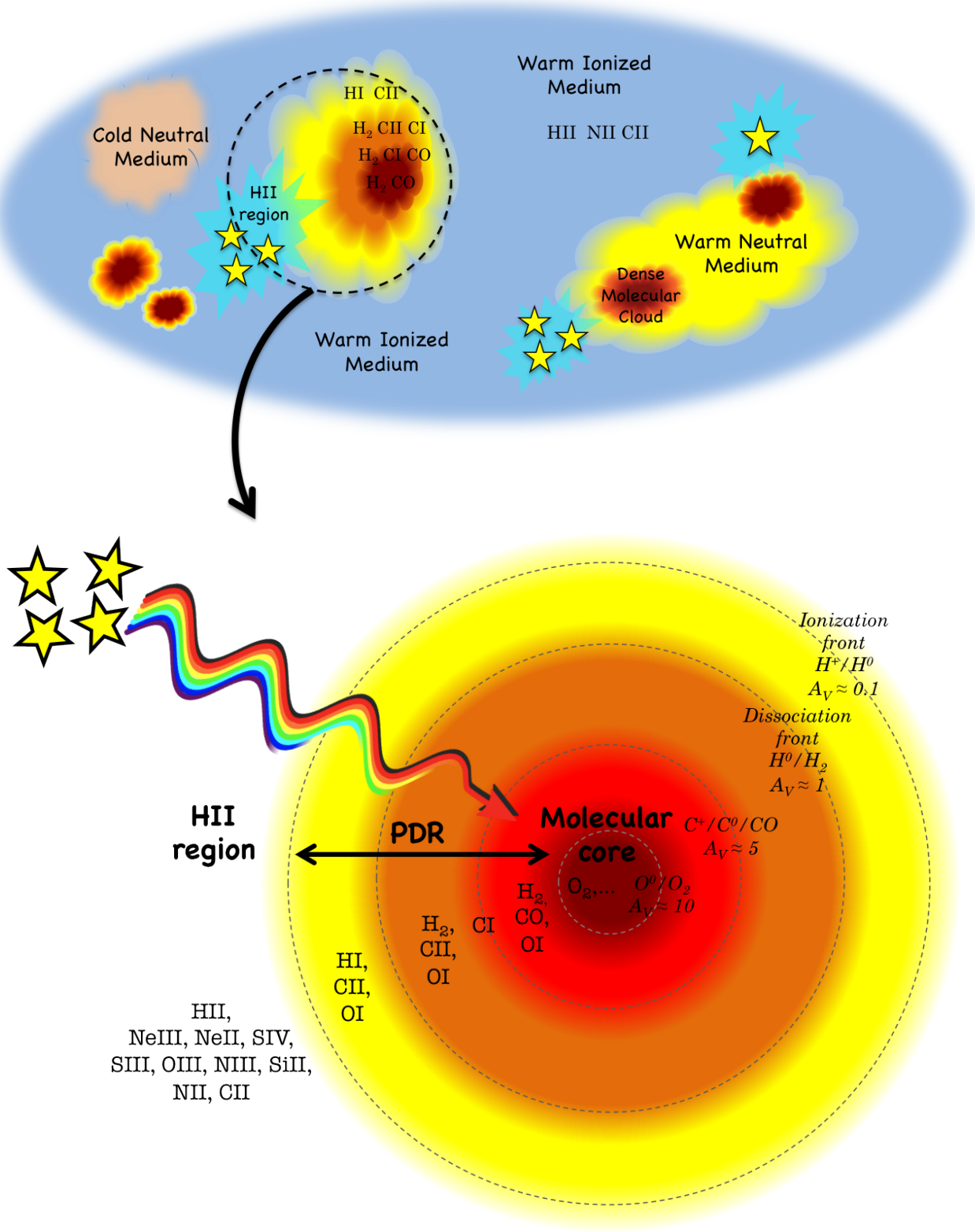

Figure I.2: *Top: schematic of the different phases found in the ISM of a galaxy: the ionized phases (WIM and H II regions), the neutral phases (WNM and CNM) and the molecular clouds. Bottom: zoom-in view of the structure of a PDR. The different elements observed with the Spitzer and Herschel IR space telescopes, as well as the main transitions ($H^+/H^0/H_2$, $C^+/C^0/CO$ and O^0/O_2) are indicated.*

I.2.1 Ionized phase

When the UV photons from stars interact with the surrounding ISM, photons with energies $h\nu \geqslant 13.6$ eV (the ionization potential of hydrogen) ionize the gas, creating what are called H II regions, in which hydrogen is almost fully ionized. H II regions are typically found around hot young stars of type O and B, and are thus directly linked to recent star formation. They have a characteristic temperature of $\sim 10^4$ K and span a wide range of densities, from 1 cm^{-3} up to 10^5 cm^{-3}. Escaping photons from the H II regions can ionize more diffuse regions of low density ($\sim 10^{-1}$ cm^{-3}) and large filling factor, called the warm ionized medium (WIM). The WIM represents $\sim 95\%$ of the ionized gas phase, and fills $\sim 25\%$ of the volume of our Milky Way (Tielens 2005).

In the ionized phase, the primary heating sources of the gas are the photo-ionizing photons emitted by OB stars and electrons emitted by dust grains via the photo-electric effect (see Section I.4.1). The diffuse ionized gas can be traced through optical and UV ionic absorption lines against background sources and through emission in the H_α recombination line at 656 nm, when H^+ recombines with an electron. The ionized gas is also a strong source of thermal radio emission. In denser H_2 regions, emission in forbidden fine structure lines (such as [Ne II] 13 μm, [O III] 88 μm, [S IV] 10.5 μm, etc) participate in the gas cooling as well. Low ionization species typically probe more diffuse gas phases, while high ionization species probe denser gas phases, where higher energy photons are more likely to be absorbed. H II regions are also often characterized by bright MIR continuum emission emitted by heated dust grains.

Alternatively, a hot component of ionized gas (the Hot Ionized Medium; HIM) can be produced by supernovae explosions. This gas is ionized and heated to $\sim 10^5 - 10^6$ K by shock waves originating from the supernovae or from stellar winds. Cooling processes are thermal X-ray emission and line emission from highly ionized species.

I.2.2 Atomic phase

The atomic phase is characterized by the existence of atomic H as the dominant form of hydrogen, where photons have energies lower than 13.6 eV and molecules are nonexistent. Hence in this phase, neutral atomic species (H^0, O^0, C^0), as well as ionic species (C^+, Si^+, S^+) with ionization potential lower than that of hydrogen, co-exist. Two phases can be distinguished: a diffuse inter-cloud phase, the Warm Neutral Medium (WNM), and denser, cold clouds (the Cold Neutral Medium, CNM). The WNM is characterized by a typical temperature of ~ 8000 K and a typical density of ~ 0.5 cm^{-3} and fills a large volume in galaxies. The CNM has a typical temperature of ~ 80 K and a typical density of ~ 50 cm^{-3}, and is confined in much smaller volumes.

Two main processes contribute to the gas heating: the photoelectric effect involving dust grains, and the FUV pumping of H_2 (see Section I.4.1). Other heating mechanisms (cosmic rays, X-rays) usually play only a limited role. Observationally, the neutral gas can be mapped via the H I line at 21 cm. This line results from the transition of an electron between two hyperfine levels of the ground state of atomic hydrogen.

Photodissociation regions (PDRs)

The transition zone between an H II region and a molecular core is defined as a Photodissociation Region (PDR; Tielens & Hollenbach 1985; Hollenbach & Tielens 1999). In this region, the penetrating FUV photons have energies $6 < h\nu < 13.6$ eV and the heating and the chemistry are predominantly regulated by FUV photons. PDRs can then also be referred to as Photon-dominated Regions (Sternberg & Dalgarno 1995). They include the cold and dense neutral medium as well as part of the molecular

gas. By distinction to the diffuse neutral gas, PDRs are associated with star formation, and famous examples are the Orion nebula or the Horse Head nebula for instance (Figure I.3).

Figure I.2 illustrates the structure of a PDR. FUV photons emitted by the stars penetrate the cloud, ionizing the edge of the cloud. Deeper into the cloud, beyhond the ionizing front, all photons with energies > 13.6 eV have been absorbed and only lower energy photons can penetrate, ionizing the carbon and photo-dissociating the molecules. Even deeper into the cloud ($A_V \approx 1$ mag), when the flux of H_2 dissociating photons has been attenuated, H_2 can form, aided by the efficient self-shielding (see Section I.2.3). At $A_V \approx$ 4-5 mag, the incident carbon-ionizing photons are attenuated as well so that the transitions from C^+ to C^o and then CO become possible. The far edge of the PDR is determined by the transition from atomic to molecular oxygen, which marks the beginning of the molecular core.

Most of the FUV photons penetrating the PDR are absorbed by dust and heat the gas via the photoelectric effect, described in Section I.4.1. The gas in PDRs cools mainly through far-infrared (FIR) fine structure line emission of the most abundant ionic and atomic species (e.g. [CII], [CI], [OI]; see Figure I.2). The MIR and FIR continuum emission by dust, the PAH features (Section I.3.2) and molecular lines (CO rotational lines, rotational-vibrational transitions of warm H_2) are also usually bright in the PDRs.

Figure I.3: *Left: optical image of the HII region in M42 from the Hubble Space Telescope. The ionization front and the PDR region beyond it, known as the Orion bar, are visible as a bright ridge in the bottom left of the image (credit: NASA, C. R. O'Dell and S. K. Wong). Right: the Horse Head Nebula, embedded in the Orion molecular cloud (Data: G. C. Iaffaldano; Processing: R. Colombari). The diffuse glow behind the horse head is ionized by a nearby bright star. A part of the dark molecular cloud on the bottom of the image constitutes the horse head, in which stars are forming.*

I.2.3 Molecular phase

The molecular phase is where the gas is the coldest (T∼10 K) and the densest ($n \geqslant 200\,\mathrm{cm}^{-3}$), and is characterized by the presence of molecules. The most abundant molecule is H_2, although other molecules are also found in molecular clouds such as CO, CS, HCN, O_2, H_2O, etc, where the shielding by dust, and self-shielding of H_2 particularly, protect the molecules from the FUV radiation field. H_2 has the property of being efficient in self-shielding: H_2 photo-excitation transitions (the Lyman-Werner bands in particular) become optically thick so that the molecule can be shielded from incident starlight by other molecules. CO on the other hand, the second most abundant molecule, does not

Table I.2: Physical characteristics of the different ISM phases. Adapted from Tielens (2005). Typical means of detection are listed in the last column.

Phase	T[a] [K]	n[b] [cm^{-3}]	ϕ_v[c] [%]	M[d] [$10^9 M_\odot$]	Σ[e] [$M_\odot pc^2$]	Observation
H II regions	10^4	1 - 10^5	–	0.05	0.05	H_α recombination line Thermal radio emission FIR fine structure lines MIR continuum emission from dust
Warm Ionized Medium	8000	0.1	25	1.0	1.1	H_α recombination line Thermal radio emission Ionic absorption lines
Hot Ionized Medium	10^5 - 10^6	0.003	~ 50	–	0.3	Thermal X-rays and radio emission Ionized metals absorption/emission lines
Warm Neutral Medium	8000	0.5	30	2.8	1.5	H I absorption/emission line FIR fine structure lines
Cold Neutral Medium	80	50	1	2.2	2.3	H I emission line FIR fine structure lines
Molecular clouds	10	$\geqslant$ 200	0.05	1.3	1.0	CO rotational lines

[a] Typical temperature. [b] Typical density. [c] Representative filling factor in the Milky Way. [d] Representative mass in the Milky Way. [e] Mass surface density in the solar neighborhood.

have efficient self-shielding capabilities and mostly relies on the shielding by dust. As a result, the transition H/H_2 and the transition C^+/C^o/CO are not necessarily co-spatial. In particular, the latter depends largely on the amount of dust along the line of sight, and will be shifted deeper into the cloud in low-metallicity environments. This explains the increasing fraction of "CO-dark" molecular gas that can be present in galaxies: the fraction of H_2 existing outside of the CO-emitting molecular clouds, as the metallicity decreases (this is described in more details in Chapter V).

More than 200 molecules have already been identified in the ISM (Tielens 2005). Much of the molecular gas is confined in discrete GMCs which cover a large range of properties in term of mass, size and temperature, with typical sizes of a few tens of parsecs and typical masses of $10^3 - 10^6 M_\odot$. Molecular clouds are thought to be self-graviting rather than in pressure equilibrium with the other phases of the ISM. They have typical life-time of $\sim 10^7$ Myr and are considered to be the sites of active star formation. A spectacular example of a molecular gas structure can be seen as the dark protusion forming the Horse Head nebula in Figure I.3. Emission by cold dust can also be detected in molecular clouds, in the FIR-to-submm wavelength range.

The formation of H_2, as well as many other molecules, occurs on the surface of dust grains, at cold temperature, before being evaporated. Other molecules can form directly in the gas phase through collisions. Molecular gas is mainly heated by the FUV flux and the low energy cosmic rays (≈ 100 MeV) which can penetrate deep into the clouds. Molecules can be formed in an excited state, or be excited through shocks and collisions. The main cooling mechanism of molecules is through rotational and vibrational transitions in the IR and submillimeter (submm) wavelength domains. The observed large widths of emission lines from molecular clouds, larger than expected from thermal velocity of the gas, indicate significant turbulence effects, providing support against gravitational collapse of the cloud. Magnetic pressure also plays a role, especially inside dense cores, as the

strength of the magnetic field increases with density.

Observations

Although the abundance ratio H_2/CO is $\sim 10^4 - 10^5$, the CO transitions ($J = 1-0$ at 2.6 mm, $J = 2-1$ at 1.3 mm, $J = 3-2$ at 870 μm, etc) are often used as tracers of the molecular gas reservoir. Indeed, H_2 is a symmetric molecule and does not have a dipolar momentum. As a consequence, it is very difficult to observe directly through its rotational transitions. Near-infrared (NIR) rotational-vibrational transitions can be observed in warm (~ 1000 K) and dense ($\sim 10^4$ cm^{-3}) gas, but represents only a small fraction of the total molecular gas mass of a galaxy. A simple conversion factor, X_{CO}, is generally assumed between the observed CO intensity, I_{CO} and the H_2 column density, $N(H_2)$:

$$X_{CO} = N(H_2)/I_{CO}. \tag{I.5}$$

The value of X_{CO} can be observationally determined through different techniques. One of the most common is through CO(1-0) observations of cold clouds (e.g. Solomon et al. 1987). A typical value for the Galactic conversion factor, $X_{CO,MW}$, is 2×10^{20} cm^{-2} (K km s^{-1})$^{-1}$. However, this value is likely to a be function of the environment (metallicity, radiation field), and the Galactic conversion factor does not necessarily apply to other galaxies. The derivation of the X_{CO} factor, and where it fails to trace the full H_2 reservoir, will be discussed in more detail in Chapter V.

I.3 The dust phase in the ISM

I.3.1 The effects of dust

The presence of dust in the ISM is revealed through several visible effects. For example, a reddening and extinction of the light from distant stars is due to the presence of small dust grains along the line of sight. Reflection nebulae are the result of starlight scattering by dust. Dust also emits light: the bright IR emission of the ISM is due to continuum emission by cold dust grains. Additionally, polarization due to large dust grains aligned with the magnetic field, can be observed. These processes are illustrated in Figure I.4.

Extinction by dust grains

One on the major effects of dust in a galaxy is the absorption of the stellar radiation as it propagates through the galaxy. The attenuation of the starlight along a given line of sight is related to the optical depth, $\tau(\lambda)$, which is proportional to the dust column density along the line of sight. The extinction can also be expressed as $A(\lambda)$, in magnitudes. The monochromatic intensity, I_λ, received by an observer is related to the source intensity, I^0_λ, by:

$$I_\lambda = I^0_\lambda e^{-\tau(\lambda)} = I^0_\lambda \times 10^{-A(\lambda)/2.5} \tag{I.6}$$

Hence, the extinction is related to the optical depth via the relation $A(\lambda) = 1.086 \times \tau(\lambda)$.

Extinction is not uniform and depends on the dust composition, grain size and shape. Indeed, for a homogeneous cloud of size l, composed of spherical dust grains of radius a, the dust optical depth is expressed as:

$$\tau(\lambda) = n_d \, Q_{ext}(a, \lambda) \pi a^2 l, \tag{I.7}$$

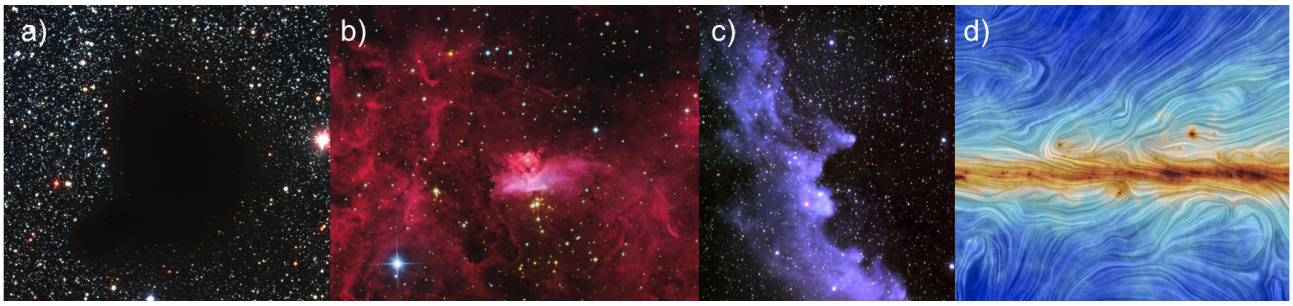

Figure I.4: *a) Background stars are extincted by the "Dark Cloud", Barnard 68; at the edge, the light is reddened by dust absorption (credit: ESO). b) The emission nebula NGC 6357, showing bright IR emission from dust (credit: Johannes Schedler, Panther Observatory). c) The light from the bright star Rigel is reflected by surrounding dust, creating the Witch Head reflexion nebula, IC 2118 (credit: NASA/STScI Digitized Sky Survey/Noel Carboni). d) Planck observations reveal the direction of the polarized light emitted by dust in the Milky Way (Planck collaboration 2016). The colors indicate the dust column density while the texture show the orientation of the magnetic field, orthogonal to the direction of the submm polarization.*

where n_d is the dust density and $Q_{ext}(a,\lambda)$ is the extinction efficiency at wavelength λ for a grain of radius a. Extinction is due to both absorption and scattering, so Q_{ext} can be decomposed into an absorption efficiency, Q_{abs} and a scattering efficiency Q_{sca} : $Q_{ext} = Q_{abs} + Q_{sca}$. Figure I.5 represents the absolute extinction, $A(\lambda)/A_V$ as a function of wavelength measured for our Milky Way, for the LMC and the SMC. A_V is the total extinction in the V band[1]. The different curves can be modeled using different mixtures of grains (e.g. Weingartner & Draine 2001a). The total-to-selective extinction ratio, R_V, is defined as:

$$R_V = A_V/(A_B - A_V), \tag{I.8}$$

where A_B and A_V are the extinction in the band B and V respectively. R_V can be seen as the slope of the extinction curve in the band V. In the Milky Way, $R_V \simeq 3.1$ in the diffuse ISM while $R_V \simeq 4-6$ in denser molecular clouds.

Mie theory provides numerical solutions for scattering and absorption of spherical and homogeneous dust grains, by solving Maxwell's equations of propagation through a dust grain. This has been extended to more realistic non-spherical grains by Draine & Lee (1984). In the IR, when the grain size is small compared to the wavelength, absorption dominates over scattering. From theory as well as from laboratory experiment, $Q_{abs}(\lambda)$ in the ISM can often be approximated by a power law in the IR wavelength domain, and thus:

$$Q_{ext} \sim Q_{abs} \sim \lambda^{-\beta}, \tag{I.9}$$

where β is called the emissivity index. For a crystalline grain, $\beta = 2$, and it is typically considered between 1 and 2 for ISM grains. Hence, the emissivity index, β drives the slope of the extinction curve in Figure I.5, in the high-wavelength domain.

Dust emission

Large dust grains, bathed in the interstellar radiation field, can be considered to be in thermal equilibrium: the dust grain absorbs the same amount of energy as it emits per unit time, which determines

[1]The photometric bands U, B and V (for Ultra-violet, Blue and Visible) where first standardized by Johnson & Morgan (1953). They represent broad (~60-90 nm) photometric windows centered on 365 nm, 445 nm and 551 nm respectively.

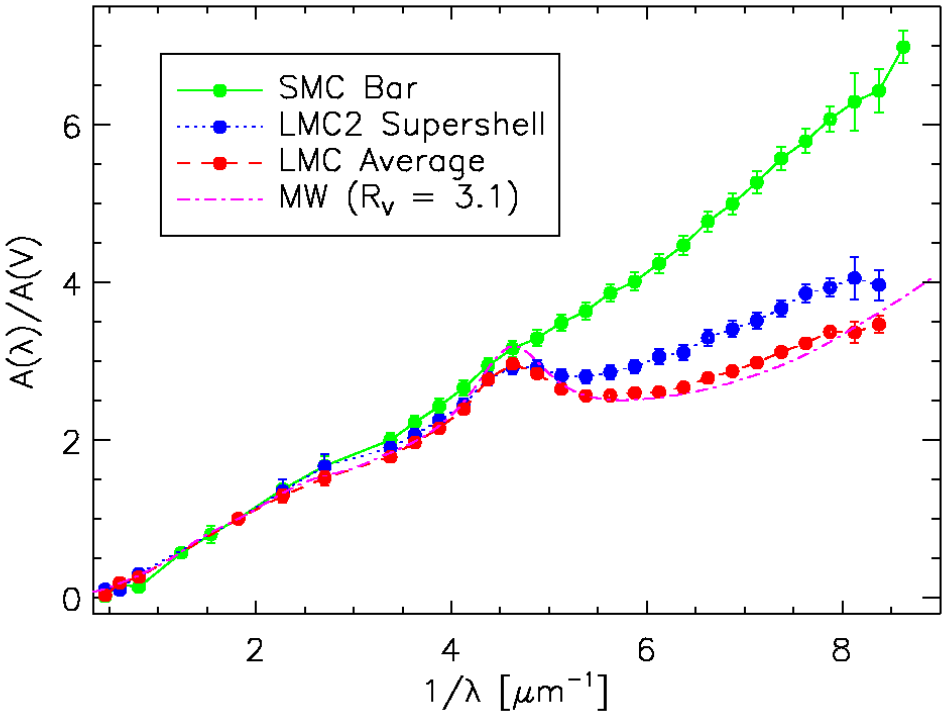

Figure I.5: *Extinction curves of the Milky Way (dashed pink, $R_V = 3.1$), LMC (red, $R_V = 3.4$ and blue, $R_V = 2.8$) and SMC (green, $R_V = 2.7$), from Gordon et al. (2003). The important absorption feature at 2175Å is due to the presence of carbon rich particles (graphite, amorphous carbon). The extinction in the UV-optical wavelength regimes is due to intermediate to big (~ 100-2000 Å) grains.*

an equilibrium temperature, T_d. This temperature depends in particular on the shape of the radiation field and on the absorption efficiency, Q_{abs}. Assuming Equation I.9 in the IR, the energy density of the radiation emitted by a dust grain is given by the Stefan-Boltzmann's law and is $\propto T_d^{4+\beta}$, with β generally $\sim 1-2$. As a consequence, hot grains emit much more energy than cold grains.

Application of the Wien's displacement law for a blackbody gives us an idea of the location, λ_{max}, of the peak of the SED:

$$\lambda_{max} T_d \sim 3000\ \mu\text{mK}. \tag{I.10}$$

Hence, for hotter grains, the peak of the SED is shifted to shorter wavelengths, while for colder grains it is shifted to larger wavelength. These are very simplistic considerations, as dust grains in the ISM are distributed in sizes and temperature, however it can be useful to have a rough idea of the dust properties.

For very small grains ($\lesssim 100$ Å), the absorption of a single photon considerably affect the internal temperature of the grain, which is comparable to the photon energy. This leads to a sudden rise in temperature. Then, the grain has, in general, time to cool down to its equilibrium before interacting with another photon. This produces the temperature profiles as shown in the lower two panels of Figure I.6, where temperature fluctuations are important compared to the average temperature. An extreme example is for PAHs (~ 4-10 Å; see below), where the temperature can reach 2000 K after FUV photon absorption and decays very rapidly in ~ 2 s (Tielens 2005).

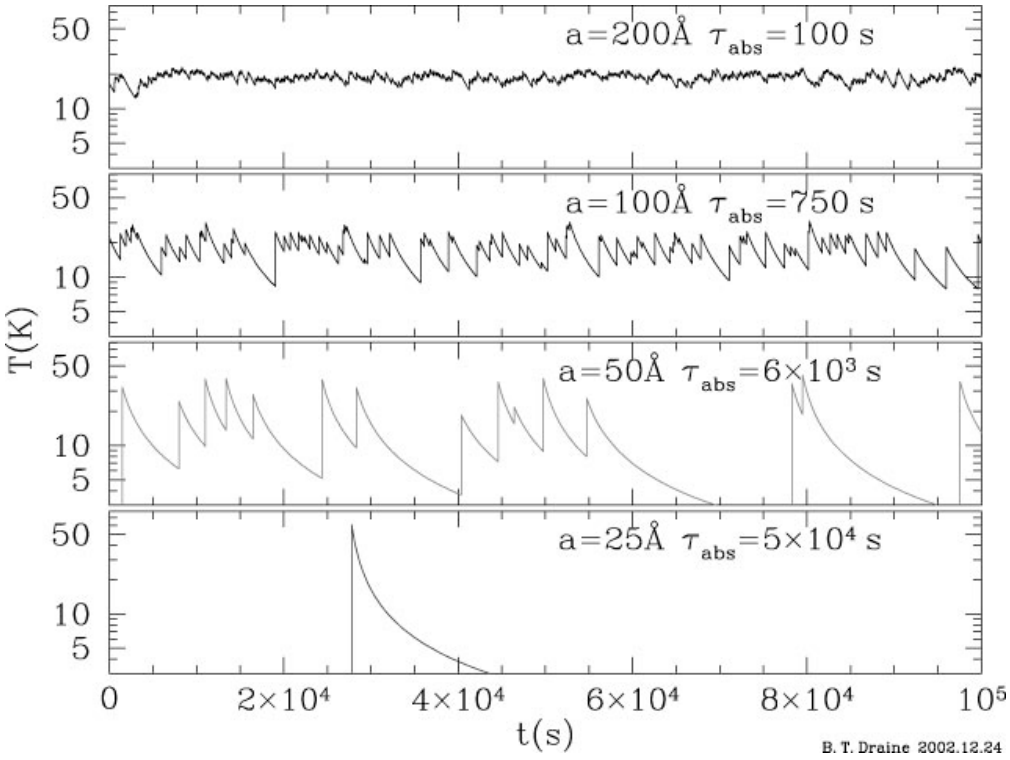

Figure I.6: *Variation of the temperature of small grains (radius a between 25Å and 200Å) as a function of time during approximately one day (figure from Draine 2003). τ_{abs} is the mean time between photon absorptions, i.e. the mean time between the peak temperature fluctuations.*

I.3.2 Dust composition

Chemical composition

Dust grains are built from elements depleted from the gas phase ISM. The difference between the measured gas phase metal abundance and what is expected to be ejected from stars through stellar wind is called elemental depletion. Measurements of elemental depletions can be used to estimate the fractions of metals locked up in the grains (e.g. Savage & Sembach 1996). C, O, Mg, Si, S and Fe are among the main constituents of dust grains. Several types of dust grains, with different properties have been identified: silicates, carbon grains (including graphite grains and amorphous carbon grains) and Polycyclic Aromatic Hydrocarbons (PAHs; see below). The composition of interstellar dust is still debated and is believed to vary between different environments, but these three families are considered to be the most important and the most abundant dust components.

The dust emissivity is tightly linked to its composition. For example, the dust masses determined via modeling of the SED using graphite for dwarf galaxies are often too high to be compatible with elemental abundances (Galliano et al. 2011). However, using more emissive dust grains such as amorphous carbons, enriched in H atoms, may solve this contradiction. The geometry or porosity of the grains also changes their emissivity (grains are usually considered spherical in the models while other geometries, such as "fluffy" structures resulting from grain collision and accretion may be more realistic; e.g. Siebenmorgen et al. 2014).

Size distribution

As noted in Equation I.7, dust extinction efficiency and the resulting starlight extinction depend as well on the grain radius a. A simple model of the grain size distribution is the MRN model, proposed by Mathis, Rumpl, & Nordsieck (1977), considers a power-law size distribution:

$$n(a) \propto a^{-3.5}, \tag{I.11}$$

with a the radius of the grains, varying between 5 and 250 nm. This grain size distribution reproduces the interstellar extinction curve of the Milky Way between 0.11 and 1 μm but does not include PAHs. For our study, we will consider a dust model from Galliano et al. (2011), adapted from Zubko et al. (2004), which uses a combination of silicate, carbon grains and PAHs to reproduce simultaneously the extinction, emission and elemental abundances of the Galactic ISM. The size distribution ranges over approximately 3 orders of magnitude. This model is described in more details in Section III.1.1.

Polycyclic Aromatic Hydrocarbons (PAHs)

From the mid-1970s, observations from ground-based and airborne observatories in the MIR revealed unidentified broad features in the spectra of bright sources with associated gas and dust. A few years later, the high sensitivity of the space observatories *ISO* (Infrared Space Observatory) and then *Spitzer* unveiled the presence of these IR emission features in almost all objects (H II regions, planetary nebulae, reflection nebulae, young stellar objects, nuclei of galaxies, ultra luminous galaxies, the general ISM of galaxies...).

Duley & Williams (1981) first suggested that the features at 3.3 μm and 11.3 μm could arise from vibrational transitions of C-H bonds on aromatic carbon atoms attached to small ($\lesssim$ 100Å) amorphous carbon particles. Vibrations in individual, molecule-sized PAHs where later proposed as origins of these MIR features by Leger & Puget (1984) and Allamandola et al. (1985). The PAHs are planar

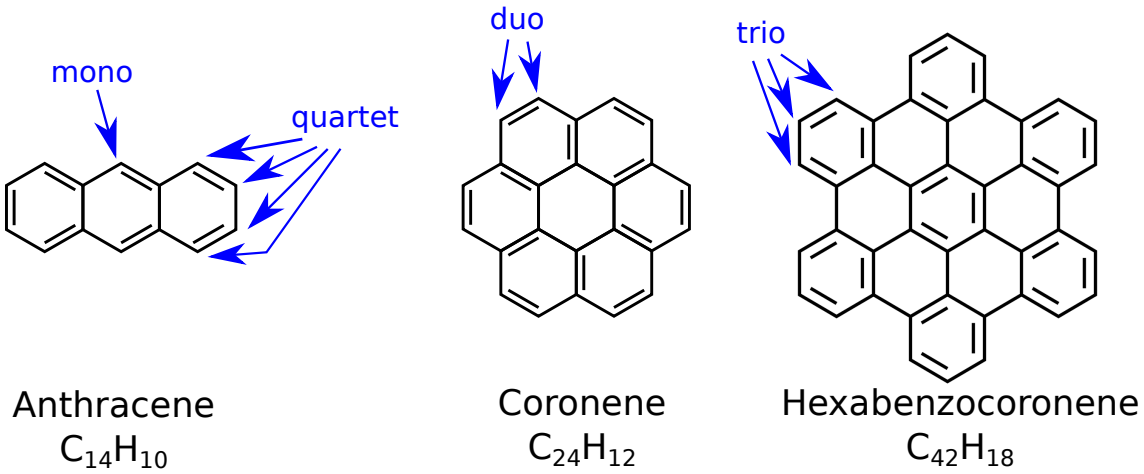

Figure I.7: *Molecular structure of three PAHs. Examples of the position of singlet, doublet, triplet and quartet H atoms are indicated in blue.*

molecules made of ~ 20 to ~ 1000 carbon atoms organized into hexagonal rings, such as presented in Figure I.7.

Several vibrational processes are at the origin of the multiple broad band features visible on the spectrum of the Orion nebula (Figure I.8). Stretching modes of the C-H and C-C bonds, in-plane and out-of-plane bending modes of C-H or combinations of these modes are responsible for the main MIR features: the 3.3 μm feature associated with the C-H stretching mode, the 6.2 μm feature produced by C-C stretching mode, the 7.7 μm band produced by a combination of C-C stretching and in-plane C-H bending modes, the 8.6 μm band associated with in-plane C-H bending modes, the features at 11.3, 12.0, 12.7, 13.6 and 14.4 μm are associated with out-of-plane C-H bending modes of H atoms in respectively "solo", "duo", "trio", "quartet" and "quartet" sites (relatively to the number of adjacent C-H groups, see Figure I.7; Tielens 2008). Several weaker features can also be identified. The exact position and shape of the observed features are sensitive to the local physical conditions. The relative intensities of the bands are susceptible to vary between galaxies as well as within individual objects (e.g. Smith et al. 2007; Galliano et al. 2008).

The role of PAHs on the thermodynamics, dynamics and chemistry of the ISM is very important. In diffuse clouds of the Milky Way, they represent about 20% of the total carbon abundance (e.g. Zubko et al. 2004; Draine & Li 2007). Typical PAH size ranges between 0.4 to 1 nm in radius. Photoelectric effect on PAHs could be the major heating mechanism in some environments (e.g. Weingartner & Draine 2001a; Rubin et al. 2009; Lebouteiller et al. 2011; see also Sect. IV.1.3). Habart et al. (2001), using *ISO* observations, find a photoelectric efficiency for PAHs of 3% in isolated clouds, decreasing with increasing grain size. On the other hand, PAHs are thought to be destroyed in highly irradiated environments, in the vicinity of young stars or in shocks (e.g. Lebouteiller et al. 2007; Verstraete 2011 and reference therein).

I.3.3 Spectral energy distribution

A number of different processes affect the light emitted by a galaxy (emission by a large population of stars, absorption and re-emission by various types of grains, absorption and re-emission by gas...). This results in a complex spectral energy distribution (SED), which reflects the physical conditions and processes at play in the galaxy as illustrated in Figure I.9. In particular, between ~ 10 μm and

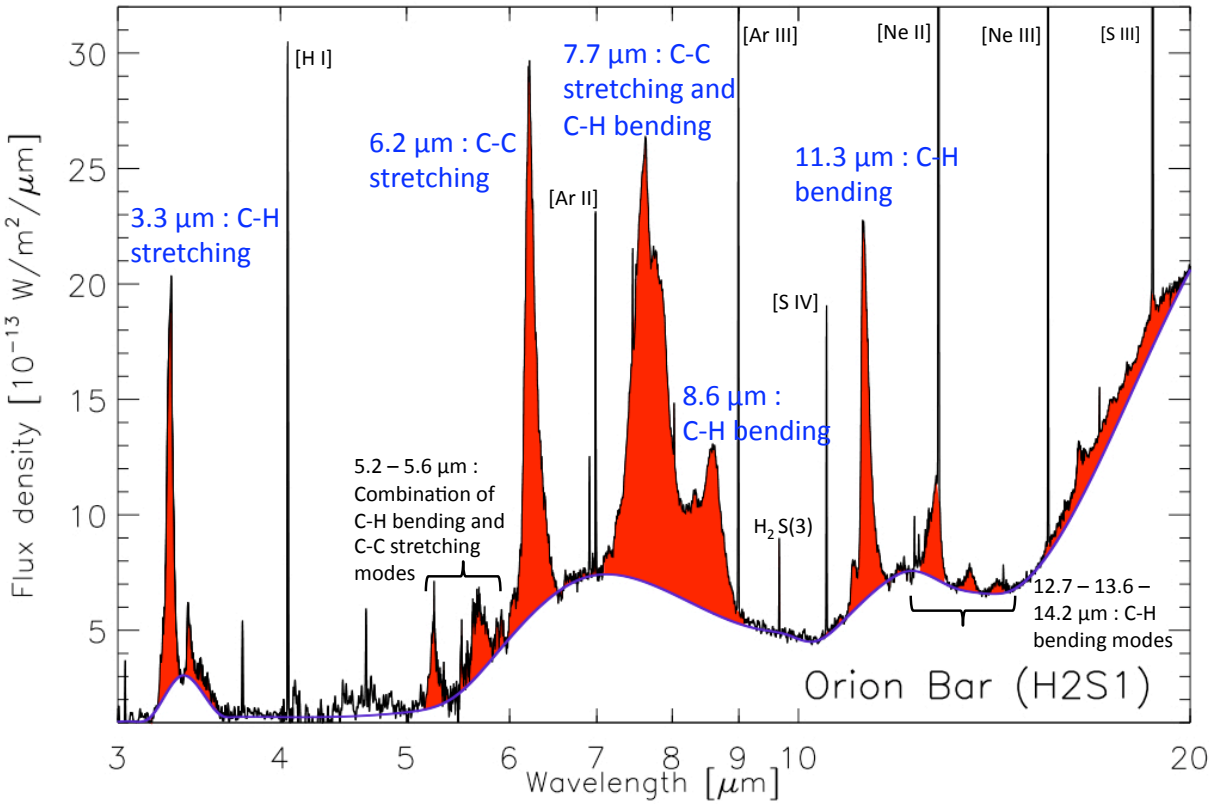

Figure I.8: *IR spectrum of the Orion nebula (image from Remy-Ruyer 2013, adapted from Peeters et al. 2004). The main PAH bands are in red. They are labeled with the vibration modes producing these features. Strong ionic fine-structure lines in the spectrum have also been identified.*

1 mm, emission by dust dominates the total emission. By taking into account all of these processes, it is possible to model the SED and decompose it into the different contributions from stars, dust and gas.

The most massive stars (in cyan) heat the gas and dust. Part of the energy (shown by the hashed areas) is absorbed by the gas and is re-emitted in particular through emission lines (in yellow). Another part of this energy is absorbed by dust and re-emitted as shown in blue. The dust emission in the H II region peaks around 30 μm indicating a warm dust component (average $T_d \sim 100$ K). In addition, we note that PAHs are photo-dissociated by the strong radiation field in these regions.

The red curve shows the emission from older and less massive stars, peaking at longer wavelengths compared to the more massive stars. Emission from the dust heated by these stars is shown in pink. We note that the peak of the emission is around 90 μm which indicates colder dust. Note that PAHs are also present in these regions. A component of cold dust (in green) can be identified, arising from grains embedded in molecular clouds and well shielded from the interstellar radiation field. The emission in the radio is due to accelerated charges in the ISM (free-free and synchrotron emission).

SED models, such as those presented in Galliano et al. (2011), used in this study, are designed to fit the observed SED and deduce the starlight intensity, the dust mass, the dust properties, etc. More details about the model we use in this study are given in Section III.1.1.

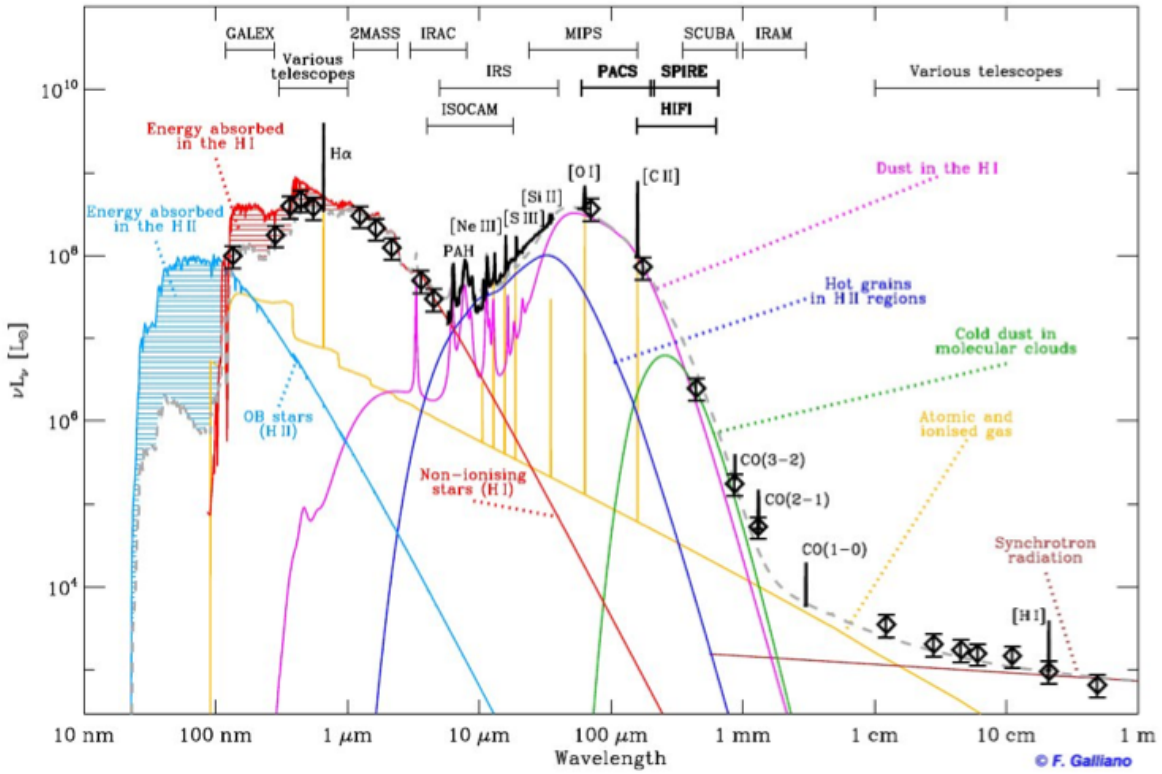

Figure I.9: *Example of a synthetic SED of a galaxy. Stellar spectra of ionizing stars and older stars are shown in blue and red colors respectively. Part of the stellar energy is absorbed by dust (hashed blue and red areas), causing extinction in the UV-optical, and reemitted in the IR (small grains in blue, big grains and PAHs in purple, cold dust in green), indicating the energetic balance throughout the UV to radio wavelength range. Cooling from the gas and free-free emission appears in yellow. Observations are overplotted with dark symbols.*

I.4 Gas heating and cooling

I.4.1 Main heating mechanisms

The gas of the ISM is mostly heated by the stellar radiation field through photo-ionization: an electron removes some of the interacting photon energy in the form of kinetic energy, which is then transferred to other atoms and electrons of the gas through collisions. In the H II regions, where energetic photons ($\geqslant 13.6$ eV) are present, H ionization dominates the heating of the gas, while in the H I regions, photo-ionization of PAHs and small dust grains dominates. In the molecular phase, the gas can be heated through the photo-dissociation of molecules and the photoelectric effect on dust grains and collisions. X-ray heating, cosmic-ray heating and heating through turbulence can also be important in particular environments, hosting SN, X-ray sources, active galaxy nucleus (AGN), etc. Two of the processes which dominate in PDRs, which are the focus of our study here, are described below.

Heating by photoelectric effect

The main heating mechanism in the neutral gas is due to the photoelectric effect on dust grains and PAHs. FUV photons absorbed by a grain create energetic electrons of several eV inside the grain.

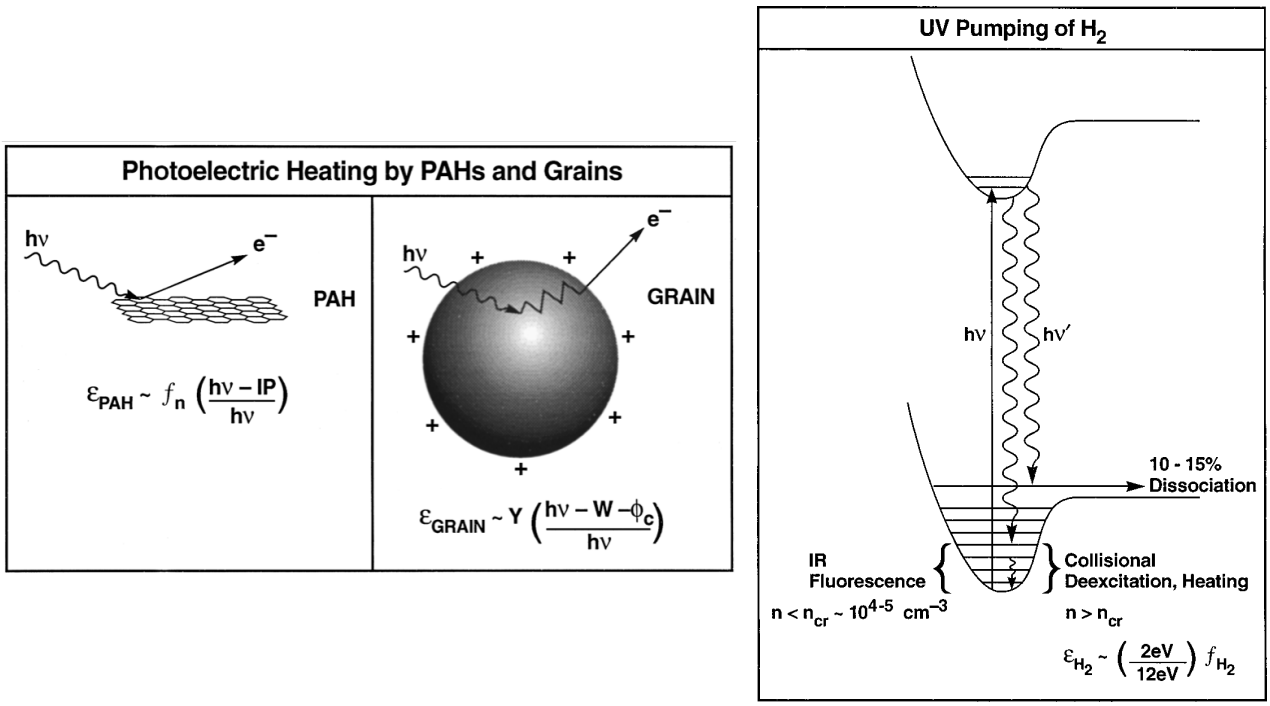

Figure I.10: *Left: schematics of the photoelectric effect on a PAH and a dust grain. For PAHs, the efficiency of this process, ϵ_{PAH}, is a function of the fraction of PAHs that can still be ionized by FUV photons, f_n. For dust grains, the efficiency, ϵ_{GRAIN}, is a function of the yield, Y. Right: schematic of the H_2 FUV pumping, dissociation and heating mechanisms in the PDRs. Absorption of a FUV photon followed by fluorescence can lead to a H_2 molecule in an excited vibrational level in the electronic ground level, which can then de-excite through collisions, thus heating the gas. A simplified expression of the heating efficiency of this process, ϵ_{H_2}, is indicated. $f(H_2)$ is the fraction of the FUV flux pumping H_2 ($13.6 \geqslant h\nu \geqslant 11$ eV). Figures from Hollenbach & Tielens (1999).*

These electrons diffuse through the grain, loosing energy through collisions. If they have enough energy, they are injected into the gas with excess kinetic energy, thus heating the gas. This is represented in Figure I.10. For dust grains, the electrons must overcome the work function W, which is typically ~ 5 eV, and the coulomb potential, ϕ_C, if the grain is positively charged. The efficiency of the heating is then a function of the yield, Y, which measures the probability that the electron escapes, and which is a complex function of the grain size, the FUV absorption length scale inside the grain and the photon energy. For PAHs, the electron must overcome the ionization potential, IP, in order to be injected in the gas phase. As a result, the efficiency of this process is dependent on the grain size and charge. The heating is done primarily by the smallest dust particles, the PAHs and the small grains, emitting primarily in the MIR.

Heating by H_2 pumping

FUV pumping is the second major heating source of the gas in the neutral medium. It results from the interaction of H_2 molecules with FUV photons with energies > 11.2 and 12.3 eV (Lyman-Werner electronic transitions). The absorption of a FUV photon pumps H_2 molecules to a bound electronic state. In 10-15% of the time, the H_2 molecule fluoresces back to the ground electronic state and dissociates. In the remaining 85-90% of the time, the H_2 molecule fluoresces back to an excited vibrational level in the electronic ground state. At low densities (below the critical density), the excited molecule cascades down to the ground vibrational state, through emission of IR photons. Alternatively, at higher densities ($\geqslant 10^4 - 10^5$ cm^{-3}; Martin & Mandy 1995) collisional de-excitation becomes an important heating mechanism. This is illustrated in Figure I.10.

I.4.2 Observational tracers

Gas emission

One of the main cooling processes of the gas is through collisionally excited line radiation. In the optical and UV, cooling lines probe the ionized state of the gas and extinction by dust. On the other hand, at IR and submm wavelengths, cooling lines from the ionized, atomic and molecular gas are only weakly affected by extinction and are good probes of the physical state and structure of the various gas phases. Critical densities[2], n_{crit}, and excitation potentials[3] of the fine-structure lines observed by the *Spitzer* and *Herschel* space telescopes are presented in Figure I.13 and Table I.3.

The FIR fine structure lines, in particular, are important diagnostics of the FUV flux, gas density, temperature and filling factor of the PDR and ionized regions (e.g. Tielens & Hollenbach 1985; Wolfire et al. 1990; Kaufman et al. 2006). A number of these FIR lines have been observed by the COsmic Background Explorer (*COBE*; Wright et al. 1991), the Infrared Space Observatory (*ISO*), the Kuiper Airborne Observatory (*KAO*) and the *Herschel* Space Observatory. Now, the Stratospheric Observatory for Infrared Astronomy (*SOFIA*) allows us to probe a wide range of emission lines. We examine here some of the characteristic of the main FIR fine structure lines which are used in this study.

- **[O III] 88 μm and [O III] 52 μm**

  The [O III] 88 μm and [O III] 52 μm lines correspond, respectively, to the $^3P_1$-$^3P_0$ and $^3P_2$-$^3P_1$

[2]For a two levels system, the critical density is defined as $n_{crit} = A_{ul}/\gamma_{ul}$, where A_{ul} is the Einstein coefficient for spontaneous emission between the upper (u) and the lower (l) level, and γ_{ul} is the collisional de-excitation rate coefficient between u and l. When the density is much larger than n_{crit}, collisions dominates the de-excitation process.

[3]We define the excitation potential as the energy required to create the specie.

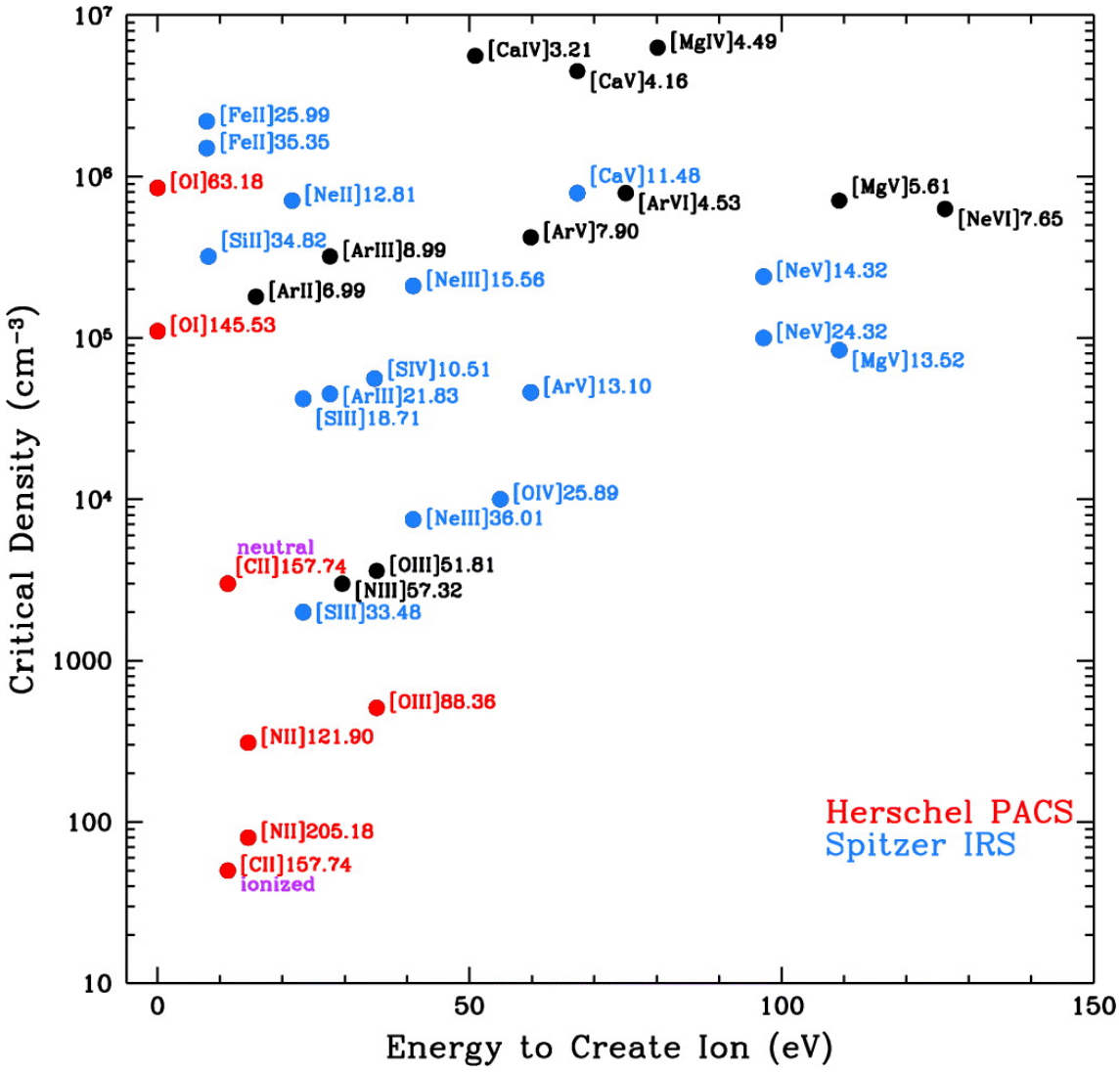

Figure I.11: *Excitation potentials as a function of critical densities for Herschel and Spitzer lines, from Kennicutt et al. (2011). The observation of these emission lines enable us to probe a wide diversity of environments, ranging several order of magnitudes in density and in energy.*

magnetic dipole transitions of O^{++}. O^+ has an ionization potential of 35.12 eV and the critical density for collisions with electrons (noted e^-) is 510 cm^{-3} for the [O III] $^3P_1$-$^3P_0$ transition (88 μm) and 3.5×10^3 cm^{-3} for the [O III] $^3P_2$-$^3P_1$ transition (52 μm). The formation of O^+ thus requires high energy photons and [O III] is found only in the ionized gas, preferentially in the H II regions rather than in the diffuse interclump medium. As both [O III] lines are at the same ionization stage, the ratio of these two lines is a good tracer of the electron density in the H II regions (e.g. Lebouteiller et al. 2012; see also Section IV.3.2), especially in the $\sim 10^2 - 10^4$ cm^{-3} regime, as presented in Figure I.12. The [O III] 52 μm line was not accessible by *Herschel* for our sample, but *SOFIA* can now detect this line.

In the Dwarf Galaxy Survey (DGS; Madden et al. 2013), which includes the LMC and SMC, Cormier et al. (2015) found that [O III] 88 μm is the brightest FIR line even on global galaxy scales. This is remarkable, since [C II] 158 μm is usually the brightest FIR fine structure line in more metal rich galaxies (e.g. Stacey et al. 1991; Malhotra et al. 1997; Brauher et al. 2008;

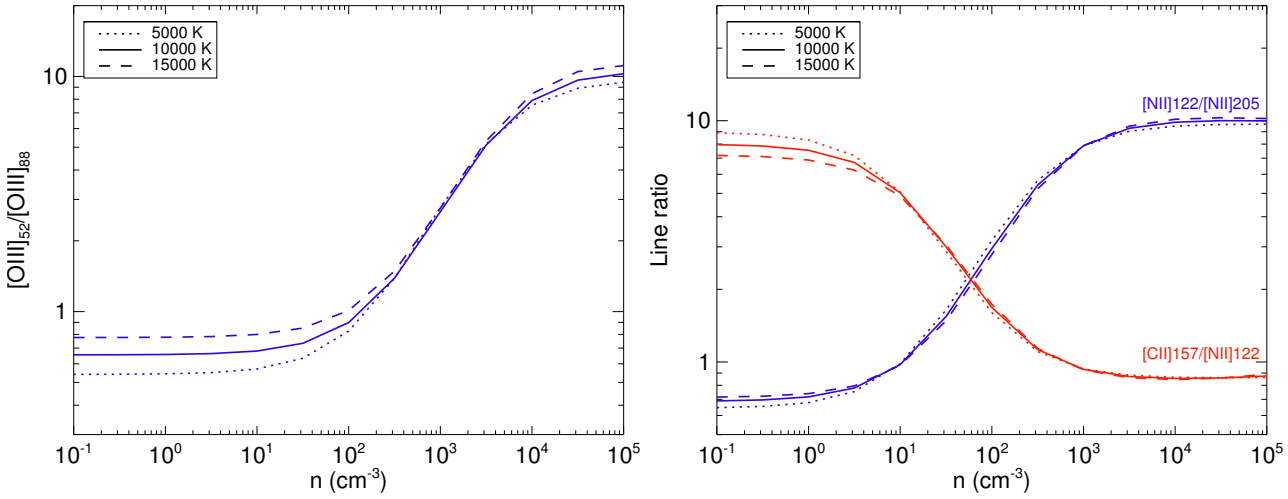

Figure I.12: *Left: Theoretical ratio [O III] 52 μm/[O III] 88 μm as a function of the electron density for three different gas temperatures. This can be used to determine the electron density in the highly ionized gas, in the density regime ≳ 100 cm^{-3}. Right: Theoretical ratios [N II] 122 μm/[N II] 205 μm (blue) and [C II] 158 μm/[N II] 122 μm (red) as a function of the electron density for three different gas temperatures. These pairs of lines can be used to determine the electron density in the moderately ionized gas and the contribution of the diffuse ionized gas to the [C II] emission.*

Maiolino et al. 2009; Stacey et al. 2010; Hailey-Dunsheath et al. 2010).

- **[N III] 57 μm**

  N^+ has an ionization potential of 29.60 eV. The critical density for collisions of with e^- is 3×10^3 cm^{-3} for the $^2P_{3/2} - ^2P_{1/2}$ transition. Hence, this line originates from the ionized gas only, and it is generally associated with H II regions. Since they are at two different ionization stages, the ratio of [N III] 57 μm/[N II] 122 μm is a good measure of the effective temperature of the ionizing stars (Rubin et al. 1994).

- **[N II] 122 μm and [N II] 205 μm**

  N^0 has an ionization potential of 14.53 eV, hence the transitions [N II] $^3P_2$-$^3P_1$ at 122 μm and [N II] $^3P_1$-$^3P_0$ at 205 μm are emitted only from the ionized gas. The critical densities with e^- are, respectively, 310 cm^{-3} and 48 cm^{-3}. Similarly to the [O III] lines, the ratio of these two lines is a good tracer of the electron density (Figure I.12). It is sensitive to more diffuse ionized gas, from ∼ 10 to ∼ 10^3 cm^{-3}. These lines have also been proposed as a SFR tracers (e.g. Zhao et al. 2013; Herrera-Camus et al. 2016).

- **[C II] 158 μm**

  The [C II] 158 μm line corresponds to the $^2P_3/2$-$^2P_1/2$ transition of C^+. It is one of the most important cooling lines of the ISM as carbon is the fourth most abundant element. It has been observed and studied in a wide variety of objects, from Galactic PDRs (Bennett et al. 1994) to high-redshift galaxies (e.g. Maiolino et al. 2009; Stacey et al. 2010; Hailey-Dunsheath et al. 2010; De Breuck et al. 2011). [C II] is bright and well detected in spiral (Crawford et al. 1985; Stacey et al. 1991) and in low-metallicity galaxies (Mochizuki et al. 1994; Poglitsch et al. 1995;

Madden et al. 1997; Hunter et al. 2001), while it appears to be faint for most ultra-luminous IR galaxies (ULIRGs; Luhman et al. 1998).

The ionization potential of C^o is 11.26 eV, below that of hydrogen (13.6 eV), which implies that C^+ can be found both in the ionized gas, and also in the neutral phase. The critical density of the [C II] line is 50 cm^{-3} for collision with e^- and 2.8×10^3 cm^{-3} for collisions with H atoms. Hence, [C II] can originate from the diffuse ionized gas as well as the diffuse neutral gas or the surface layers of PDRs. The interpretation of [C II] observations can thus be difficult and the [N II] lines are often used to disentangle the fraction of [C II] from the ionized gas from that of the PDR only, based on the theoretical ratio [C II]/[N II] in the ionized gas, shown in Figure I.12. Application of this is presented in more details in Section IV.1.2. The critical densities of collisions with e^- of [C II] and [N II] 205 μm as well as the energy of the transitions ($\Delta E/k$ = 91.3 K for [C II] and 70.1 K for [N II] 205 μm) are similar, thus their ratio is mostly dependent on the relative abundance of C^+ and N^+.

As [C II] traces PDRs as well as diffuse H I and H II regions, it has been proposed as a possible tracer of star formation (e.g. Stacey et al. 1991; Madden et al. 1997; Boselli et al. 2002), as an alternative to the widely-used CO(1-0) luminosity. De Looze et al. (2011) and Herrera-Camus et al. (2015), find a tight correlation between SFR and the [C II] luminosity for normal star-forming galaxies, however they note a deviation for more quiescent galaxies and ULIRGs. For dwarf galaxies, [O I] 63 μm is proposed to be a better SFR tracer than [C II] (De Looze et al. 2014).

- **[O I] 63 μm and [O I] 145 μm**

The ionization potential of O^0 is 13.62 eV, just above that of hydrogen. Thus, [O I] lines are found in the neutral phase. The critical densities for collisions with H atoms are 9.5×10^4 cm^{-3} and 4.7×10^5 cm^{-3} for the $^3P_0$-$^3P_1$ and $^3P_1$-$^3P_2$ transitions at 145 μm and 63 μm, respectively. The energies of the upper states (in temperature units) for these two transitions are $\Delta E/k$ = 228 K for the [O I] 63 μm line and $\Delta E/k$ = 325 K for the [O I] 145 μm line. Hence, [O I] arises mostly from the warm dense neutral medium. The ratio of the two [O I] lines is an indicator of the gas temperature (in the range ~50-500 K) and is a density tracer at high densities and high temperatures. The [O I] 63 μm line is, in general, brighter that the [O I] 145 μm line and one of the brightest PDR cooling lines, along with [C II] (e.g. Bernard-Salas et al. 2012).

The formation of CO and O_2 occurs at large A_V ($\approx 5-10$) so O^0 is present deep into the cloud. As a consequence, the [O I] lines, and in particular the lower level transition at 63 μm, can be affected by optical depth effects, thus limiting its diagnostic power.

- **[C I] 370 μm and [C I] 609 μm**

From the PDR models, C^o is found only in a relatively thin layer of gas, as a transition between C^+ and CO (e.g. Kaufman et al. 1999). The critical densities of the $^3P_2$-$^3P_1$ transition at 370 μm and the $^3P_1$-$^3P_0$ transition at 609 μm for collisions with H and H_2 are, respectively, 1.2×10^3 cm^{-3} and 4.7×10^3 cm^{-3}. The energies of the upper states are $\Delta E/k$ = 23.6 K above the ground state for the 370 μm line and $\Delta E/k$ = 62.5 K for the 609 μm line. As such, the ratio of the [C I] lines is a sensitive temperature probe at moderate densities. Observationally, [C I] lines are well correlated with CO, tracing the surface of the CO clumpy structures, filaments and clumps. [C I] lines are easily excited and may be a good tracer of H_2, perhaps better than the CO transition in certain cases, especially at high redshift or at decreased metallicity (e.g.

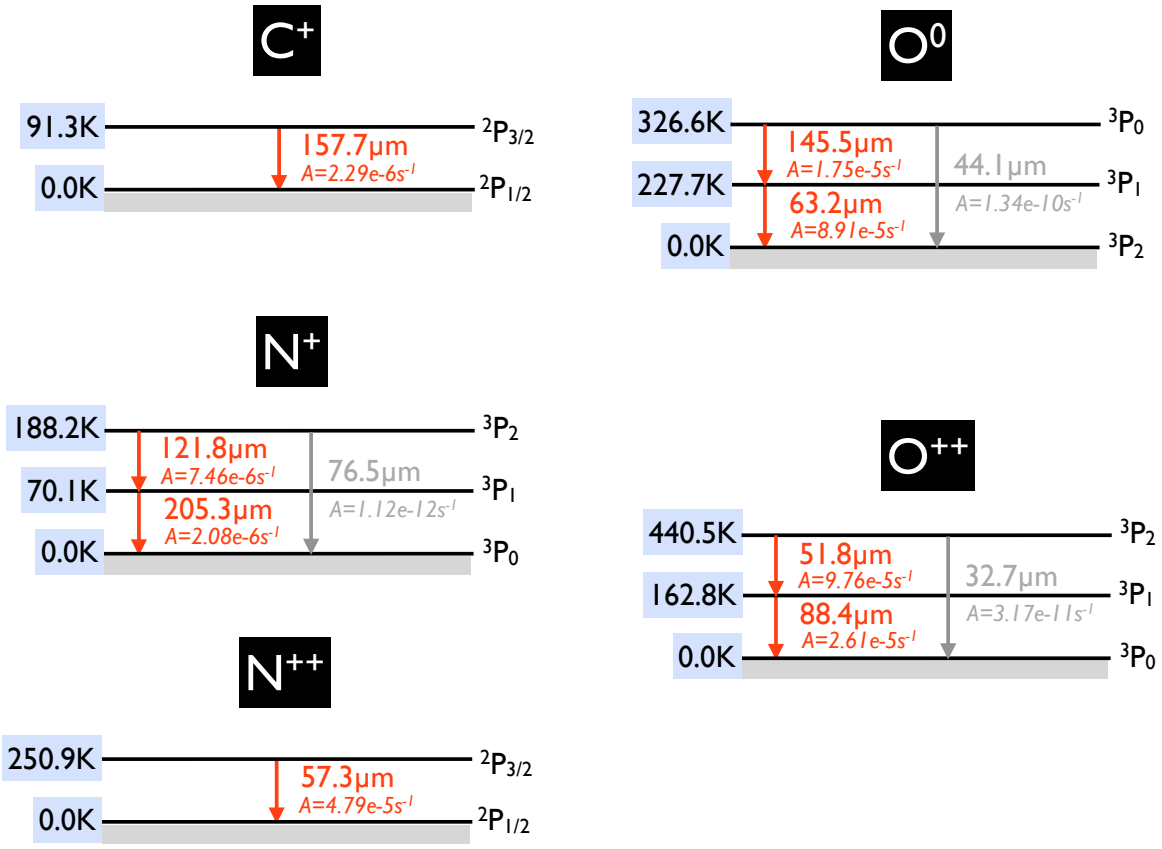

Figure I.13: *Electronic levels of the FIR fine structure lines of C^+, N^+, O^0 and O^{++}. Transitions observed with Herschel and SOFIA are indicated in red, along with their Einstein A coefficients for spontaneous emission. The energy of each level is given on the left in temperature units ($T = \Delta E/k$). From Cormier (2012).*

Papadopoulos et al. 2004; Glover & Clark 2016; Madden et al. in prep.).

The MIR fine-structure lines, observed by *ISO*, the *Spitzer* space telescope and *SOFIA*, are mainly ionic lines, providing diagnostics to the ionized gas.

- **[Ne II] 12.81 μm and [Ne III] 15.6 μm**

  The ionization potential of Ne^0 is 21.56 eV and that of Ne^+ is 40.96 eV. Both the [Ne III] 15.6 μm and [Ne II] 12.81 μm lines arise from the ionized gas only, and are usually associated with dense H_2 regions. Their critical densities for collisions with e^- are 7×10^5 cm^{-3} for [Ne II] and 3×10^5 cm^{-3} for [Ne III]. As a result, the ratio [Ne III]/[Ne II] is a good probe of the hardness of the radiation field, and is only weakly sensitive to the density. In addition, the energies of the transitions for [Ne III] and [Ne II] are similar (respectively, $\Delta E/k = 925$ K and $\Delta E/k = 1123$ K) and both lines are insensitive to temperature fluctuations in H_2 regions, where T$\sim 10^4$ K.

- **[S IV] 10.51 μm**

  S^{++} has an ionization potential of 34.79 eV and the critical density of the [S IV] 10.51 μm line is 5×10^4 cm^{-3}. Thus, this line arises from the ionized gas only and traces rather dense H II

regions. Since the critical density of this line is close to that of the [S III] 18 μm line, the ratio [S IV]/[S III] 18 μm is a good indicator of the hardness of the radiation field, and is weakly dependent on the density.

- **[S III] 18 μm and [S III] 33 μm**

  S^+ has an ionization potential of 23.34 eV and the critical densities of the [S III] 18 μm and [S III] 33 μm lines are, respectively, 2×10^4 cm^{-3} and 7×10^3 cm^{-3}. Thus, both [S III] lines are found in the ionized gas only and the ratio of these two lines gives a good measure of the electron density in the H II regions, in a somewhat denser regime than the ratio of the [O III] lines.

- **[Si II] 34.82 μm**

  The ionization potential of S^0 is 8.15 eV and the critical density of the [Si II] 34.82 μm line is 3.4×10^5 for collisions with H atoms and 1×10^3 for collisions with e^-. Similarly to C^+, the consequence of the ionization potential lower than that of hydrogen, is that S^+ can be associated both with the ionized gas and the neutral gas.

- **[Ar II] 6.99 μm**

  The ionization potential of Ar^0 is 15.76 eV and the critical density for collisions with electrons of [Ar II] 6.99 μm line is 4×10^5 cm^{-3}. [Ar II] arises only from the ionized gas. The ratio [Si II]/[Ar II] (respectively [C II]/[Ar II]) can be used to disentangle the fraction of [Si II] (respectively [C II]) arising from the PDRs from that arising from the ionized gas using a similar method as that for [C II] and [N II] (Section IV.1.2), if the density is known or can be assumed.

Molecular lines are critical probes of the molecular gas phase.

- **H_2 lines**

  Although H_2 is the most abundant molecule, it is usually very difficult to detect directly. Indeed, H_2 is a symmetric molecule, with no permanent dipole moment, so dipole transitions are forbidden and H_2 does not emit at long wavelengths (mm). However, rotational quadruple transitions ($\Delta J = \pm 2$) are allowed. They are divided into ortho-transitions (antiparallel nuclear spins, odd J numbers) and para-transitions (parallel nuclear spins, even J numbers). The MIR transitions of H_2 (3.4 to 28 μm) observed by the *Spitzer* space telescope are pure rotational transitions ($\Delta v = 0$) in the electronic ground state, while NIR transitions (1 to 4 μm) are rotational-vibrational transitions. These transitions require temperatures $\Delta E/k \gtrsim 510$ K and thus probe generally the warm neutral phases rather than the cold molecular cores.

  H_2 emission is detected in a variety objects, in particular in PDRs (e.g. Tielens & Hollenbach 1993) and in nearby and dwarf galaxies with *Spitzer* (e.g. Roussel et al. 2007; Hunt et al. 2010). H_2 can also be seen in absorption in the Lyman-Werner band electronic transitions (in the UV), from warm and cold diffuse gas in front of strong UV sources (e.g. in the LMC and SMC, respectively, by de Boer et al. 1998; Richter et al. 1998).

- **CO rotational lines**

  CO is the second most abundant molecule after H_2 and the ^{12}CO and ^{13}CO transitions in the FIR and submm are common tracers for molecular cloud conditions. CO molecules are primarily excited through collisions with H_2. The first rotational level ($J = 1$) is only 5.5 K above ground

level ($J = 0$), thus cooling by rotational transitions is more efficient than cooling by vibrational transitions at higher energy (> 3000 K). Rotational transitions are allowed for $\Delta J = \pm 1$ and the upper level energy and the critical density increase with the level transition. Low-J CO lines, i.e. from upper levels of $J \lesssim 3$ typically, are tracers of the cold molecular gas. At low densities ($\leqslant 10^4$ cm^{-3}) low-J CO emission lines are good diagnostics of the density, while at higher densities, they mostly probe the gas temperature. The lower-J CO transitions, CO ($J = 1-0$) and CO ($J = 2-1$), are often affected by opacity effects. In particular, ^{12}CO ($J = 1-0$) (also noted ^{12}CO(1-0) for simplicity) is usually considered to be fully optically thick and therefore traces the surface of the molecular clouds. Other CO isotopes (e.g. ^{13}CO or C^{18}O) are less affected by optical depth effects and can probe denser medium, deeper into the molecular cloud.

Low-J CO lines can be observed from the ground, by single-dish antennas (e.g. *APEX*, *IRAM*, Mopra, NANTEN2) and interferometers (e.g. *SMA*, *ALMA*, *ATCA*, *NOEMA*). High-J CO lines, which are affected by atmospheric absorption are mostly visible from space, with the *Herschel* Space Observatory.

Dust emission

Dust grains heated by the radiation field emit most of their energy in the MIR to submm wavelength range. The emission depends on the nature of the grains and on the intensity and hardness of the radiation field. Their emission is easily observed in photometry, in the following bands:
- 3.3 μm, 4.7 μm, 12 μm and 23 μm with the Wide-Field Infrared Survey Explorer (*WISE*);
- 3.6 μm, 4.5 μm, 5.8 μm and 8.0 μm with *Spitzer*/IRAC, where PAH features in particular can be observed;
- 24 μm, 70 μm and 100 μm with *Spitzer*/MIPS:
- between 2.5 μm and 16 μm with *ISO*/ISOCAM;
- 12 μm, 25 μm, 60 μm and 100 μm with *IRAS*;
- 70 μm, 100 μm, 160 μm with *Herschel*/PACS, probing the peak of the SED;
- 250 μm, 350 μm, 500 μm with *Herschel*/SPIRE, probing the cooler dust where most of the mass resides;
- longer wavelengths are also accessible from the ground (e.g. 870 μm band at *APEX*/LABOCA or 450 μm and 850 μm bands at *JCMT*/SCUBA).
Probing the full wavelength range is essential to accurately sample the SED and bring robust constraints on the dust properties in galaxies. Indeed, small, stochastically heated grains and warm dust contribute mostly to the MIR range, while cold dust emits at longer wavelengths.

I.5 Characteristics of dwarf galaxies

This study focuses on the physical conditions and structures of the gas in the ISM, and in particular on how the peculiar environment of dwarf galaxies (in terms of metallicity and radiation field) affects these properties. To investigate these issues, we are focusing on star-forming regions of our two closest neighbors, the Large Magellanic Cloud and the Small Magellanic Cloud.

Table I.3: Properties of the main fine-structure cooling lines.

Line	Transition	λ (μm)	E. P. (eV)	I. P. (eV)	ΔE/k (K)	n_{crit} (cm^{-3})
Herschel/PACS and *SOFIA*/FIFI-LS			(*a*)	(*b*)	(*c*)	(*d*)
[O I]	$^3P_1 - ^3P_2$	63.2	–	13.62	228	4.7×10^5 [H]
[O I]	$^3P_0 - ^3P_1$	145.5	–	13.62	99	9.5×10^4 [H]
[C II]	$^2P_{3/2} - ^2P_{1/2}$	157.7	11.26	24.38	91	2.8×10^3 [H], 50 [e]
[N II]	$^3P_2 - ^3P_1$	121.8	14.5	29.60	118	310 [e]
[N III]	$^2P_{3/2} - ^2P_{1/2}$	57.32	29.6	47.45	251	3×10^3 [e]
[O III]	$^3P_1 - ^3P_0$	88.3	35.1	54.94	163	510 [e]
[O III]	$^3P_2 - ^3P_1$	51.8	35.1	54.94	440	3.6×10^3 [e]
Herschel/SPIRE FTS						
[N II]	$^3P_1 - ^3P_0$	205.3	14.5	29.60	70	48 [e]
[C I]	$^3P_2 - ^3P_1$	370.4	–	11.26	23.6	1.2×10^3 [H, H_2]
[C I]	$^3P_1 - ^3P_0$	609.7	–	11.26	62.5	4.7×10^2 [H, H_2]
^{12}CO	$J = 4\rightarrow3$	650.3	11.09	14.01	55	3.7×10^4 [H, H_2]
	up to $J = 13\rightarrow12$	200.3	11.09	14.01	503	2.5×10^6 [H, H_2]
Spitzer/IRS						
[Ne III]	$^3P_1 - ^3P_2$	15.56	40.96	63.45	925	3×10^5 [e]
[S IV]	$^3P_{3/2} - ^3P_{1/2}$	10.51	34.79	47.22	1369	5×10^4 [e]
[S III]	$^3P_2 - ^3P_1$	18.7	23.34	34.79	769	2×10^4 [e]
[S III]	$^3P_1 - ^3P_0$	33.5	23.34	34.79	430	7×10^3 [e]
[Ne II]	$^3P_{1/2} - ^3P_{3/2}$	12.81	21.56	40.96	1123	7×10^5 [e]
[Si II]	$^2P_{3/2} - ^2P_{1/2}$	34.82	8.15	16.35	413	3.4×10^5 [H], 1×10^3 [e]
[Ar II]	$^2P_{1/2} - ^2P_{3/2}$	6.99	15.76	27.63	1600	4.0×10^5 [e]
H_2	(0,0) S(0)	28.22	4.48	15.43	510	7×10^2 [H]
H_2	(0,0) S(1)	17.03	4.48	15.43	1015	2×10^4 [H]
H_2	(0,0) S(2)	12.28	4.48	15.43	1682	2×10^5 [H]
Ground-based						
H_2	(1,0) S(1)	2.12	4.48	15.43	6951	3.6×10^4 [H]^e
H_2	(2,1) S(1)	2.25	4.48	15.43	12550	1.8×10^4 [H]^e
^{12}CO	J = 1→0	2600	11.09	14.01	5.5	4.7×10^2 [H, H_2]
^{12}CO	J = 2→1	1300	11.09	14.01	16.6	1.5×10^4 [H, H_2]
^{12}CO	J = 3→2	867	11.09	14.01	33.3	3.7×10^4 [H, H_2]

(*a*) Excitation potential. Energy required to create the specie.
(*b*) Ionization potential. Energy required to ionize the specie; or binding energy for H_2 and CO.
(*c*) Energy of the transition, given as $T = \Delta E/k$, required to populate the transition level.
(*d*) Critical densities are noted [e] for collisions with electrons (T = 10 000 K), [H] with hydrogen atoms (T = 100 K) and [H_2] with molecular hydrogen (T = 100 K).
(*e*) Critical density estimated at T = 1000 K.
References: Malhotra et al. (2001), Giveon et al. (2002), Tielens (2005), Osterbrock & Ferland (2006), Kaufman et al. (2006), Ferland et al. (2009), Stacey (2011) and Walker et al. (2015).

I.5.1 Definition and classification

Although there is no exact criteria defining a dwarf galaxy, they are commonly defined as small in size, with low surface brightness, low luminosity and low mass. Both luminosity and mass criteria can be used to separate dwarf galaxies from more "normal" galaxies such as the metal-rich spiral and starburst galaxies. However, since the luminosity can be directly observable, a threshold on the V-band magnitude[4] ($M_V \gtrsim -18$) is often used (Gallagher 1998; Grebel 1999). By comparison the Milky Way is M_V = -21 mag. In term of mass, dwarf galaxies are often less massive than $10^{10}\,M_\odot$, with a stellar mass content of less than $10^9\,M_\odot$, which is more than 2 orders of magnitudes less than the mass and stellar mass of the Milky Way. A wide variety of dwarf galaxies in the local universe has been identified, presenting different characteristics in term of star formation activity, ISM conditions, chemical enrichment histories... They can be distinguished by several morphological types (Dwarf Spirals, Dwarf Irregulars, Dwarf Spheroidals, Blue Compact Dwarf Galaxies...) as described in Grebel (2001), for example, depending on their shape and properties. However, the classification is not unique and some classes overlap. Reviews of the various morphological types and properties for dwarf galaxies have been written by Mateo (1998); Kunth & Ostlin (2000); Grebel (2001).

Even though dwarf galaxies are the dominant population of galaxies in the Universe (Marzke & da Costa 1997), their study is mostly limited to nearby galaxies due to their faint luminosity. For example, the Local Group, our galaxy group which includes the Milky Way and the Andromeda galaxy, comprises approximately 100 galaxies within a diameter of 3 Mpc, 70% of which are dwarf galaxies (McConnachie 2012). The dwarf galaxies in the Local Universe present a great variety of properties. They can have luminosities as low as $10^5\,L_\odot$, masses as low as $10^7\,M_\odot$, and sizes smaller than 5 kpc in term of R_{25}[5]. The metallicity in the dwarf galaxies of the local universe spans a large range, down to $12 + log(O/H) = 7.14$ ($\sim 1/40\,Z_\odot$).

I.5.2 LMC and SMC

The Large Magellanic Cloud (LMC) and the Small Magellanic Cloud (SMC) are both dwarf galaxies of the Local Group, orbiting the Milky Way. They are our closest neighbors. They are located at $\sim$ 50 kpc (Walker 2012) and ~61 kpc (Hilditch et al. 2005), respectively. Table I.4 summarizes the properties of the LMC and SMC, in comparison with the Milky Way.

Although the LMC has been considered to be an irregular galaxy for a long time, it shows clear signs of a bar structure, a flat rotating disk, and at least one spiral structure. As such the LMC can sometimes be classified as a dwarf spiral galaxy (dS; e.g. de Vaucouleurs 1955). The metallicity of the LMC is $\sim 0.5\,Z_\odot$ (Pagel 2003), close to the mean metallicity of the ISM during the epoch of the peak of star formation in the universe ($z \sim 1.5$; Madau et al. 1996). Based on the [Fe/H] abundance ratio derived from asymptotic giant branch (AGB) stars, Cioni (2009) show a shallow metallicity gradient in the LMC, from the center to the edges. This has been confirmed by the recent spectroscopic study of Feast et al. (2010). However, this gradient is shallow ([Fe/H] $\propto$ -0.01 R_{GC}; Feast et al. 2010), and we use an average value of $Z = 0.5\,Z_\odot$ for our study of the LMC star-forming regions, except for 30 Doradus, for which the elemental abundance ratios have been studied in detail by Pellegrini et al. (2011), using optical lines. The dust-to-gas mass ratio show variations across the galaxy and is a

[4]The absolute magnitude in band V is defined as $M_V = -2.5\log\left(\frac{L_V}{4\pi(10\,pc)^2}\right)$, where L_V is the luminosity in the V band, i.e. in the visible domain, around 550 nm. As a result, bright objects have a lower magnitude than dimmer objects.

[5]R_{25} is defined as the radius at which the surface brightness falls to a level of 25 mag.arcsec^{-2}.

factor of ~ 2-4 lower than the Milky Way value (Gordon et al. 2003). Two distinct stellar populations seem to be present, with very different distributions. Near-IR surveys, for example, suggest that the older stellar population is smoothly distributed (Westerlund 1997; van der Marel & Cioni 2001), while young stars trace out a single dominant spiral arm (Moretti et al. 2014). In HI (Stanimirovič et al. 1999), H_α (e.g. Kennicutt & Hodge 1986) and radio continuum (e.g. Dickel et al. 2005), the LMC exhibits a variety of structures such as filaments, shells and holes at all scales.

The SMC is classified as a dwarf irregular galaxy. Dwarf Irregulars (dIrr) are characterized by an irregular shape in the optical, with scattered bright HII regions. They are gas rich and the HI distribution can show complicated patterns (with clumps and shells for example), and can be more extended than their optical size for the most massive dIrrs. The SMC is a gas-rich galaxy (Westerlund 1991) and has a low metallicity ($0.2\,Z_\odot$; Russell & Dopita 1992), which seems constant throughout the galaxy (Cioni 2009). The stellar population distribution of the SMC is quite complex (Zaritsky et al. 2000; Cioni et al. 2000; Maragoudaki et al. 2001). The older stars ($\gtrsim 1$ Gyr) show a rather regular distribution, typical for a spheroidal body. On the other hand, the younger population of stars is widely asymmetric and distributed on a main body, called the "Bar", where two very bright HII regions, N66 and N76 (Henize 1956) are located to the northeast; and a "Wing" in the eastern part, including as well a few bright HII regions (N81, N83, N84, N88). This young stellar population is responsible for the characteristic shape of the SMC visible in Figure I.1.

The presence of the eastern wing of the SMC as well as the presence of a HI "Bridge" connecting the LMC and the SMC are indicative of interactions between the two Magellanic Clouds. The existence of young stars ($\sim 10^8$ yr) in and around the Bridge reveals star formation activity which could be triggered by tidal interactions (Vallenari et al. 1996). Tidal interactions between the Magellanic Clouds and our Milky Way are also visible as HI streams of gas known as the Magellanic Stream (Mathewson et al. 1974) and the Leading Arm (Putman et al. 1998). Asymmetries in the LMC disk and bar (e.g. van der Marel & Cioni 2001; Subramaniam 2003; Nikolaev et al. 2004; Haschke et al. 2012) and low metallicity stars with distinct kinematics discovered in the LMC field (Kunkel et al. 1997; Graff et al. 2000; Olsen et al. 2011; Casetti-Dinescu et al. 2012) can be explained by a recent collision between the Magellanic Clouds (Besla et al. 2012). Several models have been developed to reproduce the large scale structure of the Magellanic System, suggesting repeated tidal encounters between the LMC and SMC (e.g. Besla et al. 2010; Diaz & Bekki 2011). Hence, they are in gravitational interaction and several proofs indicate that a collision between the Magellanic Clouds has occurred in the past (e.g. Fujimoto & Murai 1985; Bekki et al. 2008; Hammer et al. 2015).

The study presented here focuses on star-forming regions of the LMC and SMC, allowing us to probe different environments, of different metallicities, with good spatial resolution, allowed by their proximity with the Milky Way. We will examine, in particular, the physical conditions in the PDRs and estimate the total quantity of molecular gas from our modeling, based on FIR fine structure lines and dust continuum observations.

I.5.3 Metallicity effect on the ISM

Dust properties

Dust has a major impact on the physics and chemistry of a galaxy. For one thing, less metals are available to form dust grains in dwarf galaxies. Thus, a direct consequence of the low metallicity of dwarf galaxies is a lower dust abundance, resulting in lower UV-attenuation and a rather porous ISM. Additionally, the properties of the dust in dwarf galaxies can differ from those of more metal-rich environments as described below.

Table I.4: Physical properties of the LMC, SMC. The Milky Way is added for comparison.

Physical properties	LMC	SMC	Milky Way
Morphological type	dIrr/dS	dIrr	barred spiral
Diameter [kpc]	8	3	~ 30
Metallicity [$Z_\odot$]	0.5	0.2	~ 1
Distance to MW [kpc]	50	61	–
Physical scale for 1′[pc]	14	18	–
Inclination angle	23-37°	62°	–
M_{HI} [$M_\odot$]	$4.4\times10^{8(a)}$	$4.0\times10^{8(a)}$	4.5×10^{9}
M_{tot} [$M_\odot$]$^{(b)}$	$2\times10^{10(c)}$	$7\times10^{9(c)}$	$\sim 10^{12}$
Stellar mass [$M_\odot$]	1.7×10^{9}	3.7×10^{8}	1.8×10^{11}
Star formation rate [$M_\odot$ yr^{-1}]	0.1 - 0.25	0.024-0.05	$\sim 1^{(d)}$
Dust-to-gas ratio	1.7×10^{-3}	$\sim 1\times10^{-4}$	$\sim 10^{-2}$

Unless otherwise mentioned, values referenced in the table are from Meixner et al. (2013) and references therein for the LMC and SMC; and from Tielens (2005) for the Milky Way. $^{(a)}$ Brüns et al. (2005) $^{(b)}$ Including dark matter $^{(c)}$ Bekki & Stanimirović (2009) $^{(d)}$ Robitaille & Whitney (2010)

- *Warmer dust* - Dust can be overall warmer in dwarf galaxies compared to more metal rich galaxies, shifting the peak of the dust emission to lower wavelength, sometimes well below 100 μm (e.g. SBS0335-052; Houck et al. 2004) while the peak of the dust SED is around 90-200 μm for more metal-rich galaxies. High global 60/100 μm flux ratios were already observed with *IRAS* (e.g. Melisse & Israel 1994) and then have been confirmed by *Spitzer* (e.g. Engelbracht et al. 2008) and *Herschel* observations for a larger number of galaxies (e.g. Madden et al. 2012; Rémy-Ruyer et al. 2013, 2015). The SED also often appears flatter, dominated by the contribution of stochastically heated warm dust grains in the H II regions. This overall warmer dust is a consequence of the harder and more intense radiation field and of the lower dust abundance in dwarf galaxies (e.g. Madden et al. 2006).

- *Grain composition* - As presented in Section I.3.1, the extinction curve depends on the nature and properties of the grains along the line of sight. The extinction curves presented in Figure I.5 for the Milky Way, the LMC and the SMC differ particularly in the UV, by the importance of the "UV-bump" at 2175Å and the slope in the UV. Weingartner & Draine (2001a) theoretically reproduce the observed extinction curves in the Magellanic Clouds with a mixture of silicate and carbonaceous grains (in the form of graphite), with a deficit in very small carbonaceous grains (below 0.02 μm, including the PAHs) in the SMC to explain the absence of 2175Å feature. Galliano et al. (2011) modeling of the dust in the LMC suggested that Milky Way-type grains are not necessarily an accurate description of the LMC dust, but rather propose amorphous carbons (in lieu of graphite) and silicates to explain the submm slope of the SED.

  In addition, the size distribution is also expected to vary. The high 24/12 μm flux ratio observed by *IRAS* and *Spitzer* characterizes a steep rise of the SED in the MIR and thus suggest a low abundance of PAHs and the presence of a larger quantity of small and very small grains in dwarf galaxies ($\sim$ 30Å; e.g. Sauvage et al. 1990; Galliano et al. 2003, 2005; Galametz et al. 2009). The hard radiation fields combined with the dust deficiency of the low-metallicity ISM can destroy PAHs and redistribute grains into smaller particles, hence modifying the dust size distribution. Moreover, in starbursting dwarf galaxies, shock waves produced by the numerous

SN can contribute to the fragmentation and erosion of big grains (e.g. Jones et al. 1996; Galliano et al. 2003, 2005).

- *Weak PAH features* - PAHs can be very faint in dwarf galaxies (e.g. Sauvage et al. 1990; Madden et al. 2006; Wu et al. 2006; Hunter & Kaufman 2007; Smith et al. 2007), or even not detected for metallicites below $\sim 1/5\,Z_\odot$ (Engelbracht et al. 2005). Again, the paucity of the ISM, the hard radiation field and the SN shocks are deemed responsible for the destruction of the PAHs. The phenomenon can affect the thermal balance of the ISM, since the PAHs are usually the main heating source of the gas via the photoelectric effect (Section I.4.1).

- *Submm excess* - For some dwarf galaxies, usual SED models fail to reproduce the total emission above $\sim 500\,\mu$m (e.g.Galliano et al. 2003, 2005; Galametz et al. 2009; Bot et al. 2010; Dale et al. 2012; Rémy-Ruyer et al. 2013). The origin of this excess remains unclear. The possibilities considered are: 1) very cold dust ($< 10\,$K; Galliano et al. 2005; Galametz et al. 2011); 2) an additional rapidly spinning dust component (e.g. Draine & Lazarian 1998; Bot et al. 2010 for the SMC); 3) a change of the grain optical properties (see e.g. Remy-Ruyer 2013 for more details); 4) cosmic microwave background (CMB) fluctuations, as suggested by Planck Collaboration (2011b) from LMC observations.

  As a result of this submm excess, dust masses could be biased as they are very sensitive to a potential cold component. Hence, in the hypothesis of a very cold dust component responsible for the submm excess, the derived dust masses, and dust-to-gas mass ratios would be significantly higher, often in conflict with the observed elemental abundances. For the LMC, the study of Galliano et al. (2011) find a submm excess up to 40% compared to that expected from SED models, spatially anti-correlated with the dust mass surface density and is most likely not due to massive amounts of very cold dust, nor from CMB fluctuations. However, the origin of the submm excess is still inconclusive. In star-forming regions of the LMC, in the N158-N159-N160 complex, Galametz et al. (2013) do not find any submm excess; and the weak submm excess found in N11 by Galametz et al. (2016) can be accounted for by non-dust contributions (CO line emission and free-free emission). Hence, the submm excess is mostly significant in low-surface density regions, while its origin remains elusive.

Gas properties

- *Star formation* - For nearby IR-bright and spiral galaxies, considering the total gas reservoir H I + H_2, Kennicutt (1998) derives a power law of index 1.4 for the relation between the star formation rate surface density and the total gas surface density (Equation I.4). However, variations of this index have been observed, depending on the type of object and scale length considered. In particular, the Schmidt-Kennicutt relation appears to break down at scales $\leqslant 0.3\,$pc (Schruba et al. 2010; Onodera et al. 2010). The threshold value determined by Kennicutt (1998) is also dependent on the sample studied. Hunter et al. (1998) show that this density threshold must be lower for dwarf irregular galaxies. Indeed, many dwarf galaxies, in particular the Blue Compact Dwarfs (BCDs) are known to be very actively forming stars, while they can fall below the gas density threshold of $\sim 10^{21}\,\mathrm{H\,cm^{-2}}$. The LMC and SMC host many very active star forming regions (such as 30 Doradus, N44 in the LMC, N66 in the SMC). The presence of a high fraction of young stars in dwarf galaxies, combined with the low metallicity ISM, results in an overall harder radiation file on galaxy-scales (Campbell et al. 1986; Galliano et al. 2003, 2005; Madden et al. 2006).

Different relations are found when targeting a particular galaxy or a particular environment. For example, Bolatto et al. (2011) find a steeper relation between the total gas surface density and the star formation rate density, with a power-law index of 2.2 for regions in the SMC. This is comparable to that found in the outer disks of spiral galaxies for example (Bigiel et al. 2010). Applying the Schmidt-Kennicutt relation to the SMC would lead to significantly overestimating the SFR by one or two orders of magnitude. Similarly, Chen et al. (2014) find a low SFR based on YSOs observations for the whole Magellanic Bridge, while individual clouds seem to follow the Schmidt-Kennicutt relation, suggesting an overall low efficiency of the cloud formation in the Bridge.

In theory, different slopes of the Schmidt-Kennicutt relation may be explained by different dominant star formation mechanisms (gravitational instabilities, collisions, etc; Bigiel et al. 2008). However, the role of each ISM phase, in particular of the HI reservoir, on the star formation is still not clear. For example, a detailed study by Bigiel et al. (2008) on nearby galaxies and starburst galaxies shows a linear correlation between Σ_{SFR} and Σ_{H_2}, while the atomic gas surface density correlate poorly with SFR. Besides, while star-forming dwarf galaxies can be in relative agreement with the Schmidt-Kennicutt relation for total gas, they do not follow well that for molecular gas only, if traced by CO (Cormier et al. 2014). Relations with other gas species (e.g. HCN, Gao & Solomon 2004) and SFR can also exist. On the other hand, recent studies show that molecules are not necessarily needed for triggering star formation, which happen preferentially on cold atomic or molecular high density clumps (Glover & Clark 2012). At very low metallicity (below a few percent solar), the chemical timescale for H_2 formation becomes larger than the thermal and free-fall timescales of the clouds, which means star formation can occur before molecules form.

- *Atomic gas* - Although the absolute HI content of dwarf galaxies is relatively low compared to more metal-rich systems, gas-rich dwarf galaxies can have a high fraction of atomic gas. This is the case, for example, for the SMC, where HI represents $\sim 20\%$ of the total mass (see Table I.4), while it is $\lesssim 0.2\%$ in the Milky Way. BCDs also show a high fraction of atomic gas ($\geqslant 30\%$ of the baryonic mass; Thuan & Martin 1981). Therefore, in these gas-rich galaxies, there is a large reservoir of gas, not yet converted into stars. Many dwarf galaxies show a broad HI distribution (e.g. Hunter et al. 2011), which extend well beyond the stars and which could potentially fuel the star formation for very long periods. However, the evidence that this gas has a major impact on the activity of the galaxy is still not clear (Hunter 1997; de Blok & Walter 2006).

  The extended HI can also show structures revealing external perturbations, such as past or present gravitational interaction or merger events, as is the case for the Magellanic System for example. Finally, HI observations provide information on the rotational velocities of the gas. Therefore with rotational curve models (e.g. Navarro et al. 1996) it is possible to reproduce the gas and stellar radial profile of a galaxy and estimate the dark matter halo mass. Dwarf galaxies tend to contain a larger fraction of dark matter, more concentrated in the halo than more massive galaxies (Brinks & Taylor 1994). However, this is not the case for the SMC (Bekki & Stanimirović 2009), where models of the HI observations suggest that the SMC could have lost most of its original mass through tidal interactions with the Galaxy and the LMC.

- *Cloud structure* - As stated before, dwarf galaxies can be actively forming stars and host a large reservoir of atomic H. Yet, molecular gas detection through CO observations is particularly challenging in dwarf galaxies (e.g. Taylor et al. 1998; Leroy et al. 2009; Schruba et al. 2012; Cormier et al. 2014). This discrepancy between a high star formation activity and an apparently

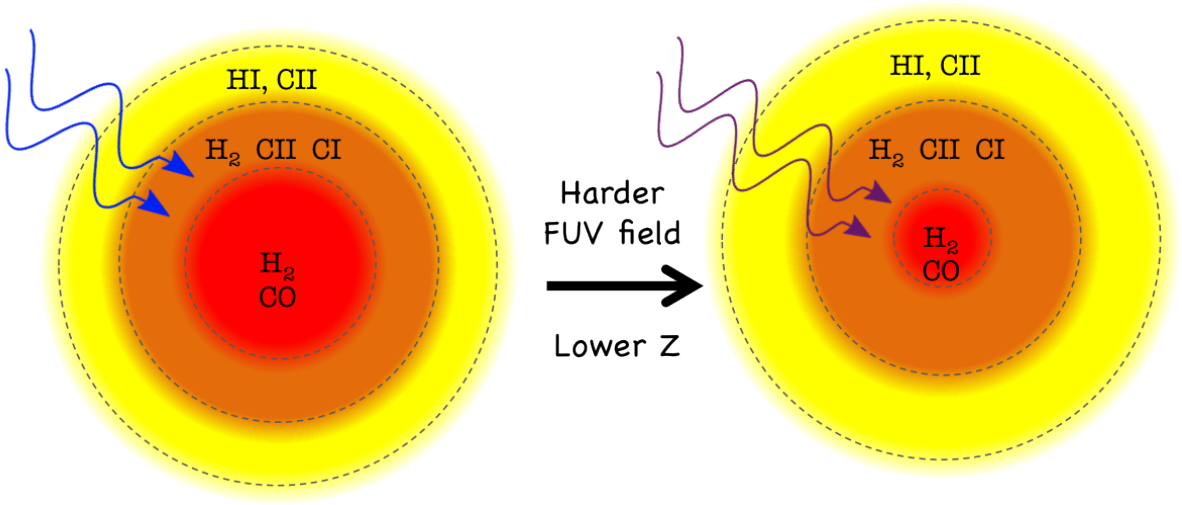

Figure I.14: *Illustration of the impact of the metallicity on the structure of a molecular cloud, inspired by Wolfire et al. (2010). The physical depths of the different layers of gas (H_I, H_2 without CO, and H_2 with CO in the molecular core) vary with the increased hardness of the radiation field and the decreased metallicity as the transitions are shifted deeper into the cloud.*

low reservoir of molecular gas raises the question of what effectively fuels star formation. Two hypothesis can be considered: either star formation occurs differently in low metallicity environments, or CO becomes a poor tracer of the total molecular gas content in these environments.

There is evidence for a lower CO content in dwarf galaxies, due to the chemical evolution and to the structure and physical conditions of the ISM. First, because of the reduced abundance of C and O elements. Then, the increased hardness of the interstellar radiation field in dwarf galaxies combined with the lower dust abundance (Madden et al. 2006) allow FUV photons to penetrate deeper into the clouds and photo-dissociate CO and other molecules, which are not abundant enough to be efficiently self-shielded (e.g. Wolfire et al. 2010; Shetty et al. 2011a). As a result, the $C^+/C^o/CO$ transition is shifted deeper into the cloud, where the shielding is sufficient for CO to survive, increasing the size of the PDR and reducing the relative size of the CO core (see Figure I.14). CO is then confined to small clouds of diameters of a few parsecs, which are difficult to observe in extragalactic environments. Moreover, PDR models at low metallicities (e.g. Kaufman et al. 1999; Wolfire et al. 2010) show the effects of the metallicity on the gas structure and on the gas temperature, which result in an enhanced emission from the higher-J CO transitions, for example.

- *The CO dark gas* - On the other hand, H_2 is efficient at self-shielding, contrary to CO and thus can be present in the C^o and C^+ emitting PDR envelope (Poglitsch et al. 1995; Madden et al. 1997; Röllig et al. 2006; Wolfire et al. 2010; Glover & Mac Low 2011; Glover & Clark 2016; Nordon & Sternberg 2016). This molecular gas not traced by CO is referred to as the "CO-dark" gas (Grenier et al. 2005; Wolfire et al. 2010; Krumholz & Gnedin 2011). In our galaxy, the presence of this dark component has been confirmed by several studies (e.g. Grenier et al. 2005; Planck Collaboration 2011a; Pineda et al. 2013; Langer et al. 2014). The recent study of Roman-Duval et al. (2014) based on *Herschel* photometric observations of the LMC and SMC find a fraction of CO-dark H_2 of 30%-100% in the LMC and 10%-40% in the SMC, in the regions where CO was not detected. Theoretical studies of Wolfire et al. (2010); Krumholz & Gnedin (2011); Glover & Clark (2012) show that the amount of H_2 outside the CO-emitting

core is controlled by the extinction, and thus increases as the metallicity decreases.

As a result, Equation I.5 is not valid anymore to quantify the total H_2 in low-metallicity environments. Although scaling of X_{CO} with metallicity have been suggested (Leroy et al. 2011; Genzel et al. 2011; Schruba et al. 2012), the precise calibration is still debated. A comprehensive review on the X_{CO} conversion factors in different environment is presented by Bolatto et al. (2013). In Chapter V, we examine the impact of different methods on the X_{CO} factor derived for the region of 30 Doradus in the LMC.

I.5.4 Concluding remarks on dwarf galaxy studies

Dwarf galaxies are the most abundant galaxy population, and show a wide range of properties, very different from more luminous metal-rich galaxies. Yet, they are a challenge to study and still pose a number of interesting questions in various domain, from cosmology to ISM processes.

In cosmology studies, dwarf galaxies play an important role because they are dominated by dark matter and thus provide constraints on the dark matter distribution predicted by simulations. Currently, simulations predict a larger number of small size dark matter halos at the present epoch than the observed number of dwarf galaxies (Moore et al. 1999). This "missing satellite problem" can be explained by the fact that some of these halos do not contain any visible matter and would thus be undetectable (Simon et al. 2007), or that they host very low surface-brightness dwarf galaxies, undetected up to now.

Galaxy evolution can be external, i.e. driven by the environment, or internal, i.e. driven by chemical enrichment. In the case of external evolution, gas inflows and outflows as well as merger events and gravitational interactions with companions are the main mechanisms. Although the scenario of dwarf galaxies being building blocks for more massive galaxies has been challenged, the continuous evolution of ISM properties between dwarf and massive galaxies seems to indicate a possible link between these two populations.

Additionally, there is a relation between the galaxy mass and its metallicity, the $M-Z$ relation. Indeed, the metallicity increases as the galaxy evolves through several cycles of star formation, and such a relation is expected. It was first observed in a sample of local dwarf galaxies by Lequeux et al. (1979), and later extended to ~50,000 local star-forming galaxies by Tremonti et al. (2004). This relation holds over 3 orders of magnitude in mass and a factor of 10 in metallicity. The $M-Z$ relation is also observed at high redshift (e.g. Savaglio et al. 2005; Maiolino et al. 2008; Henry et al. 2013; Salim et al. 2015), evolving until $z \sim 3$. Brooks et al. (2007) show that a mass-dependent star formation efficiency is needed to explain the $M-Z$ relation at low masses, using numerical simulations. This could explain the fact that low-mass galaxies are also metal-poor, because they have not yet converted a significant amount of their gas reservoir into stars due to a low star formation efficiency. Investigation of the ISM and star formation properties of dwarf galaxies (low mass and low metallicity) may provide clues on the physical origin of the $M-Z$ relation.

Another motivation for focusing on studies of dwarf galaxies is to try to understand the conditions for star formation in the primordial Universe. Indeed, since they have a low metallicity ISM, they can be considered to be chemically young objects, which have experienced only a few cycles of star formation. As it is currently not yet feasible to observe truly primordial environments due to instrumental limitations, dwarf galaxies provide the closest ISM conditions we can expect from early Universe objects in our neighborhood. Studying the evolution of the physical processes in the ISM, the evolution of the ISM structure and the star formation in these low metallicity environments can bring new insight on galaxy evolution in the primordial Universe. However, despite their low-metallicity, they often host an intermediate-age or old stellar population and therefore are not as pristine as early

Universe objects. The existence of a true link between local universe dwarf galaxies and primordial galaxies is therefore still uncertain.

Some of these issues can be investigated by studying dwarf galaxies in detail. As stated in Section I.5.3, the properties of the ISM of dwarf galaxies can be significantly different from more metal-rich environments. Recently, *Herschel* provided new constraints on the FIR-to-submm domain, with unprecedented sensitivity and wavelength coverage, opening new opportunities for the study of gas and dust in low-metallicity galaxies. Now, after the end of the *Herschel* mission, the Atacama Large Millimiter/sub-millimeter Array (*ALMA*) and the Stratospheric Observatory For Infrared Astronomy (*SOFIA*), covering a wide wavelength domain, will be able to extend and complement the *Herschel* discoveries.

In my thesis work, I have focused on the study of star-forming regions of the LMC and SMC. With the detailed view of the infrared ISM brought by *Herschel* in particular, I have analyzed the gas properties and structures of several active regions of the Magellanic Clouds. Due to their proximity, the Magellanic Clouds are the only low metallicity environments we can probe with spatial resolution of a few parsecs in the FIR with the current facilities. Thus, combining the fine-structure cooling lines from the PDRs and the molecular clouds, I probe the impact of the environment on the properties and structure of the ISM at resolved scales, and present a novel method to quantify the total amount of molecular gas. This approach brings new insights on the ISM structure and properties of these star-forming regions and is a first step to understand better unresolved studies of high-redshift galaxies.

Chapter II

Infrared to submillimeter observations of the Magellanic Clouds

Contents

II.1 The *Herschel* Space Observatory

II.1.1 The *Herschel* mission

In 1983, the InfraRed Astronomical Satellite (*IRAS*) was launched, inaugurating infrared space astronomy, and characterizing the full infrared sky. Before that, the Kuiper Airborne Observatory (*KAO*) was already operating in the stratosphere from an aircraft since 1974. It was followed by several other satellites such as the Infrared Space Observatory (*ISO*) in 1995 and the *Spitzer* Space Telescope in 2003. From 2009 to 2013, as the largest space telescope ever launched, *Herschel* Space Observatory had the best spatial and spectral resolution as well as access to complementary wavelength ranges, in particular the submm. Table II.1 compares several capabilities of these telescopes, along with the airborne observatory *SOFIA* (Stratospheric Observatory for Infrared Astronomy), successor of the *KAO*. In the near future (launch planned in 2018), we will have the largest IR telescope in space, James Webb Space Telescope (*JWST*), to probe the near-infrared (NIR) and mid-infrared (MIR) wavelength ranges.

Table II.1: Comparison of the capabilities of infrared telescopes

Telescope	Launch	Wavelength (μm)	Angular resolution (") at 100μm	Spectral resolution $R = \lambda/\triangle\lambda$	Sensitivity[a] (mJy)
KAO	1974	1-500	30	$\sim 10^4$	200
ISO	1995	2-240	60	$10^2 - 10^4$	10
Spitzer	2003	3-160	40	$10^2 - 10^3$	1
Herschel	2009	55-672	10	$10^2 - 10^7$	1
SOFIA	2011	0.3-240	10	$10^3 - 10^8$	10
JWST	2018	0.6-27	0.7[b]	$10^2 - 2.7 \times 10^3$	10^{-3}

Information taken from the *SOFIA* website: https://www.sofia.usra.edu/Science/telescope. [(a)] The sensitivity is given as 1-σ for 1 hour integration time at 100 μm (20 μm for *JWST*). [(b)] Angular resolution at 20 μm.

Herschel was a 3.5 meters telescope designed to observed the cold and obscured Universe in the far-infrared and submm wavelength range, from 55 to 672 μm. It was the fourth 'cornerstone' of the European Space Agency's Horizon 2000 mission (Pilbratt et al. 2010). The main scientific goals of the mission were to unveil how the first galaxies formed and how they evolve, to observe star and planet early stage formation and to understand the physical and chemical processes in the ISM.

The *Herschel* telescope operated from 2009 at the second Lagrange point of the Earth-Sun system (L2), thus unaffected by the earth atmosphere which partly absorbs the FIR-submm wavelengths. In space, the telescope was cooled radiatively to a temperature of approximately 85 K, protected by a large sunshade. The instruments were further cooled at least to 1.7K by helium to reach better sensitivity. The telescope was decommissioned in April 2013 after it ran out of liquid helium. It covered approximately 9.5% of the sky during its 3.5 years of operation.

The *Herschel* spacecraft was composed of a payload module, a superfluid helium cryostat, the telescope, the sunshield and the service module (see figure IV.1[1]). The cryostat housed the optical bench, with the three instruments:

[1]Images are from the *Herschel* Observer's Manual, available at http://herschel.esac.esa.int/Docs/Herschel/html/Observatory.html

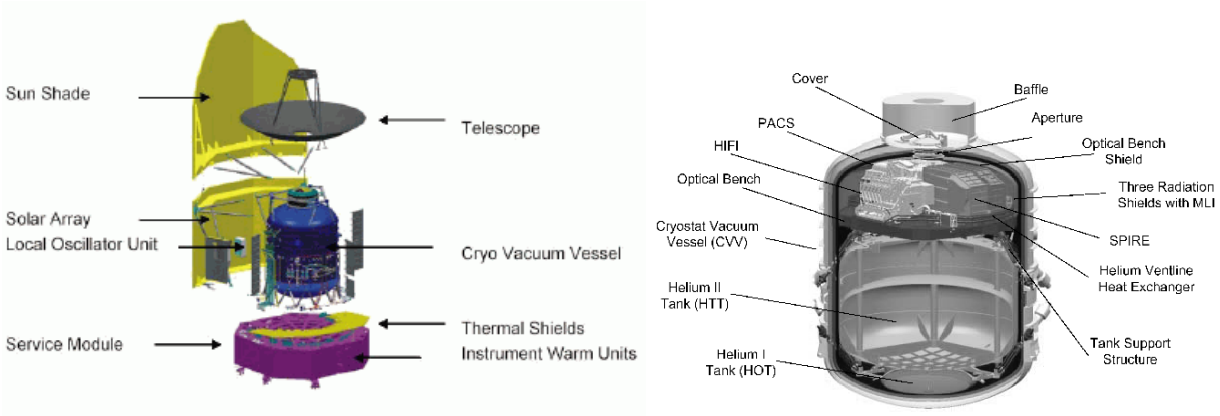

Figure II.1: *Schematic of the Herschel Space Observatory detailing the major components (left) and a schematic view of the cryostat, including the three instruments (right).*

- the **Photodetector Array Camera and Spectrometer** (PACS), consisted of two sub-instruments: a photometer and a medium resolution grating spectrometer. It was designed and build by a consortium led by Albecht Poglitsch (Poglitsch et al. 2010). Figure II.2[2] shows how the light is distributed between the different optical systems. PACS operated in the wavelength range from 55 to 210 μm.
- the **Spectral and Photometric Imaging REceiver** (SPIRE; Griffin et al. 2010) consisted of two sub-instruments: a three-band imaging photometer (at 250 μm, 350 μm and 500 μm) and an imaging Fourier Transform Spectrometer (FTS). The FTS operated in the wavelength ranges 194-313 μm and 303-671 μm.
- the **Heterodyne Instrument for the Far Infrared** (HIFI; de Graauw et al. 2010) was a heterodyne spectrometer in the wavelength bands 157–212 μm and 240–625 μm. Many chemical and dynamical questions could be addressed using HIFI's ability to observe thousands of molecular, atomic and ionized lines with high spectral resolution (resolving power of 10^3 to 10^7).

PACS and SPIRE instruments designs and capabilities are described in more details below. HIFI is not used in my study. Thus it will not be discussed further.

II.1.2 The PACS spectrometer

Design

The PACS integral-field spectrometer combined spectral and spatial coverage. It provides 5×5 spectra in a 2D field of view of $47'' \times 47''$. The principle of integral field spectroscopy is illustrated in Figure II.3 The light entering the spectrometer first passes through a slicer, transforming the 2D field into a 1D slit of 1×25 pixels. The light is then diffracted by a grating along the first order (for wavelengths between 102 and 201 μm), the second order (between 71 and 105 μm) or the third order (between 51 and 73 μm) to cover the full wavelength range. A dichroic beam splitter then separates the light from the first order, directed to the detector of the red band (102-201 μm), and from the two other orders, falling on the detector of the blue band (51-105 μm), after selection by a

[2]Images are from the PACS Observer's Manual, available at http://herschel.esac.esa.int/Docs/PACS/html/pacs_om.html

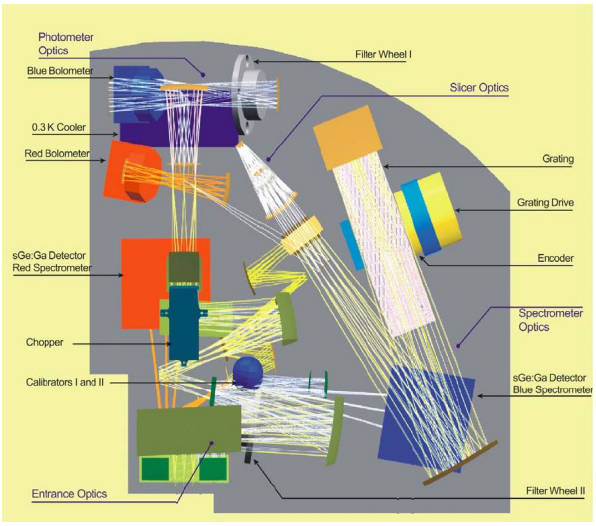

Figure II.2: *Schematic view of the optical layout of the PACS instrument.*

filter wheel. Simultaneous observations in the blue and red bands were possible. The detectors were Ge:Ga photoconductor arrays with 16×25 pixels (16 spectral elements for each of the 5×5 spatial elements, also called spaxels), as shown in the right panel of Figure II.3.

Scientific capabilities

Field-of-view and spatial resolution. Each spaxel had a projected size of 9.4″×9.4″ on the sky. This was a compromise between maintaining good spatial resolution at short wavelengths and obtaining efficient mapping capabilities at long wavelengths. A comparison between the observed spectrometer point spread function (PSF) measured on Neptune and the modeled PSF is presented in the left panel of Figure II.4 at 124 μm. The spectrometer was used over a large wavelength range. The spatial resolution, as determined by the full width half maximum (FWHM) of the beam profile, depended on the wavelength as shown in the right panel of Figure II.4. Below 115 μm, the spatial resolution was limited by the size of a pixel and was typically on the order of 9.5″. It then increased approximately linearly with the wavelength. The pointing accuracy was below 2″.

Spectral resolution. The spectral resolution of the instrument depends also on the wavelength and on the observed order, as shown in Figure II.5. The theoretical spectral power $\lambda/d\lambda$ was in the range $\approx$ 940-5500 (or $c\,d\lambda/\lambda \approx 55-320\,\mathrm{km\,s^{-1}}$). However, the spectral lines in standard environments are typically doppler broadened to 10-40 $\mathrm{km\,s^{-1}}$, and, in general, not resolved with PACS. The instantaneous spectral coverage of the 16 spectral pixels varied from 0.15 to 1.0 μm (corresponding to 600-2900 $\mathrm{km\,s^{-1}}$).

Sensitivity. Theoretical point source sensitivities for the different spectral orders as a function of the wavelength are presented in Figure II.5. The sensitivity was typically on the order of $7-10\times10^{-17}\,\mathrm{W\,m^{-2}}$ in the blue band and $3-4\times10^{-17}\,\mathrm{W\,m^{-2}}$ in the red band (sensitivity at 5-σ for 1 hour integration time). However, the actual in-flight performance depended on the observing mode. Absolute flux calibration was based on observation of $\sim$ 30 absolute flux sky calibration sources and determined with an accuracy of 11-12%. Relative flux calibration accuracies within a band are 10% for the blue band and 20% for the green and red bands.

Overlap from the grating order n+1 into the grating order n on the border of the grating orders caused spectral leakage. This was due to the finite steepness of the cut-off edges of the filter sorting

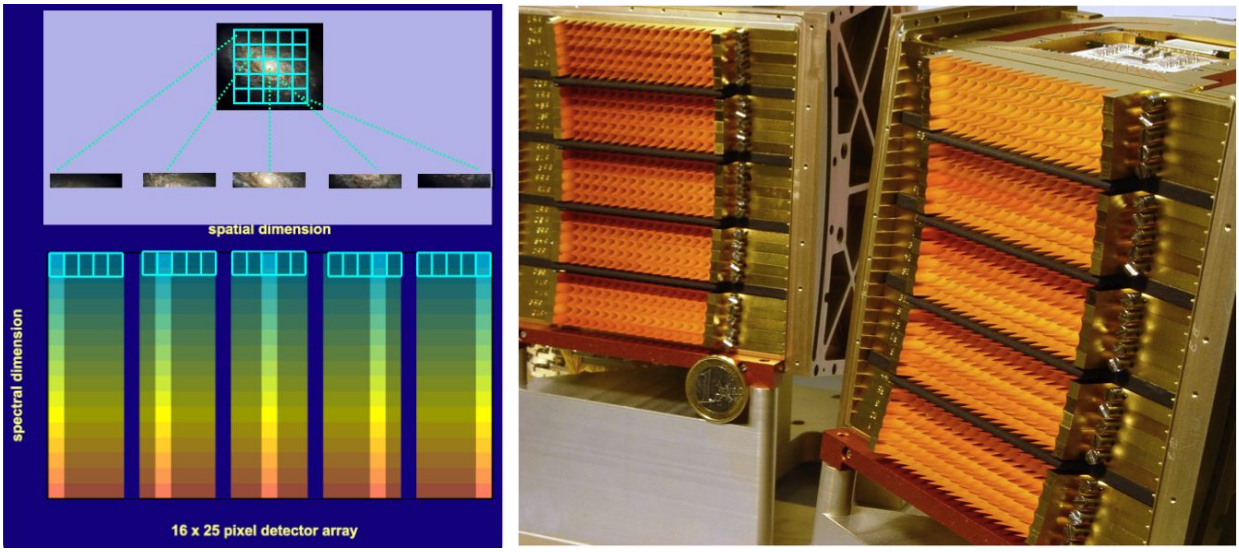

Figure II.3: *Left: illustration of the integral-field spectrometer concept. Right: picture of the blue- and red-band photoconductor arrays of the PACS spectrometer. Images are from the PACS Observer's Manual.*

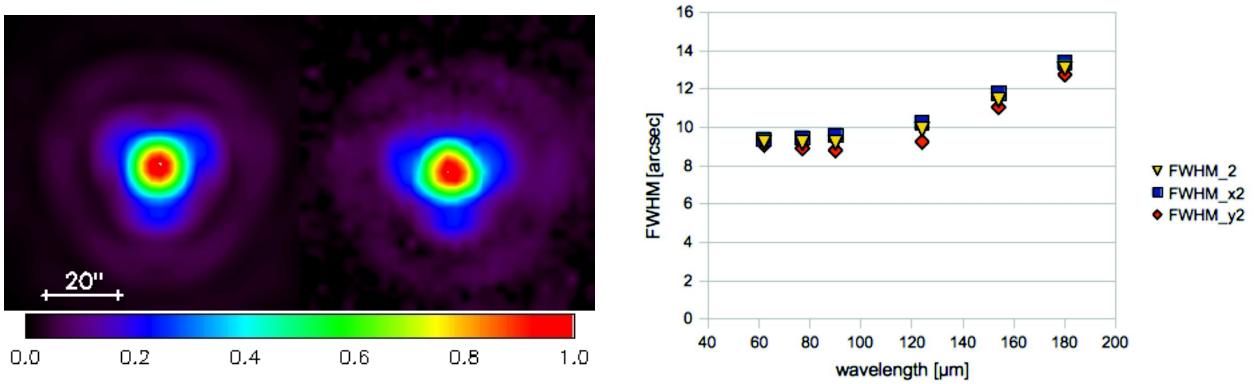

Figure II.4: *Left: calculated spectrometer PSF at 124 µm (left panel) and measurement on Neptune at the same wavelength (right panel). Both are normalized to the peak and the color bar is scaled by square root to make the faint wing pattern visible. Right: width of the PACS spectrometer beams as a function of wavelength. The PSF is fitted by an asymmetric Gaussian and the FWHMs are shown with blue squares in the x direction, red diamonds in the y direction and yellow triangles for the mean of the two. Images are from the PACS Observer's Manual.*

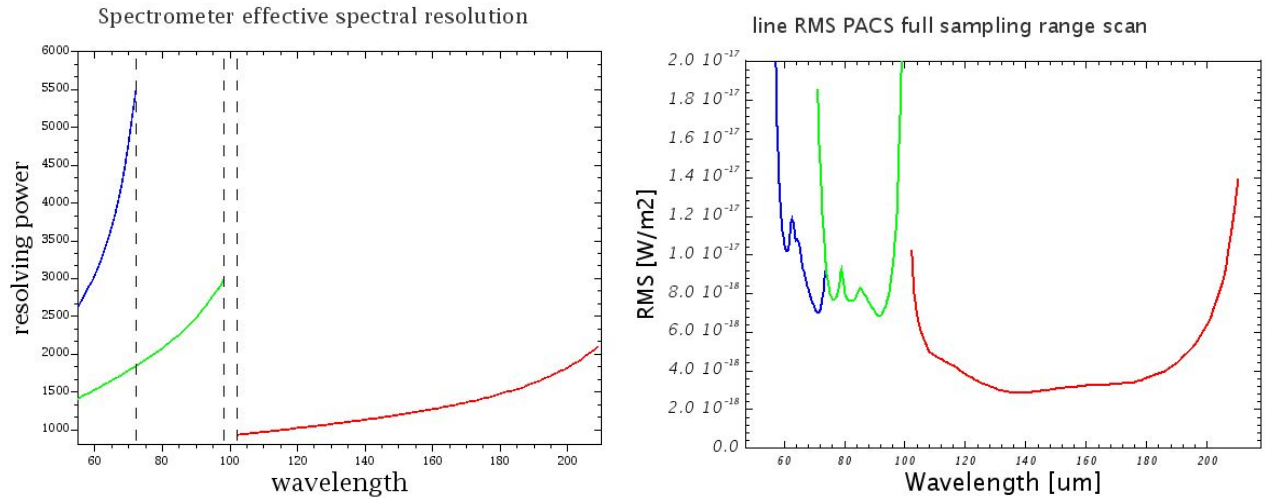

Figure II.5: *Left: resolving power ($\lambda/d\lambda$) of the PACS spectrometer for the three spectral orders as a function of the wavelength. Right: PACS point source line sensitivity at 5-σ in $W\,m^{-2}$ for the three different filters, as a function of the wavelength, for 1 hour integration time. Images are from the PACS Observer's Manual.*

the orders after the grating. In particular, the [N II] 205 μm line, at the border of the first order, was difficult to observe and to calibrate with PACS because of the contamination by the signal at the edge of the second order at 100 μm.

Observing modes

PACS spectrometer observations were carried out with two Astronomical Observing Templates (AOT), depending on the target properties:

- **The line spectroscopy AOT.** Narrow emission or absorption lines can be observed with a fixed angular range of the grating, which was optimized so that the full profile of the line is covered, along with continuum emission symmetrically on both sides of the line. The total wavelength range covered around the selected line was relatively short ($\approx 1\,\mu$m). Our observations were done using the line spectroscopy AOT.

- **The range spectroscopy AOT.** In order to observe several line features, broad lines, or when the precise line center is not known, it may be necessary to have a wider spectral coverage. This mode was more flexible and allowed scanning a wavelength range defined by the observer. It was completed by the SED mode, designed to cover the full PACS wavelength range at low spectral resolution (Nyquist sampling).

Both AOTs could use two observing modes in order to subtract the sky and telescope background. One or the other mode can be chosen, depending on the source characteristics.

- **Standard Chopping-nodding mode.** This mode could be used for single lines or larger wavelength ranges for sufficiently compact sources with a clean background within 6′. It was especially recommended for faint lines. The spectrometer performed up and down grating scans with 43, 46 and 48 grating steps in the first, second and third order respectively, so that a given wavelength was observed successively by all 16 spectral pixels. The resulting sampling density per resolution element was higher than three samples per FWHM of an unresolved line, at

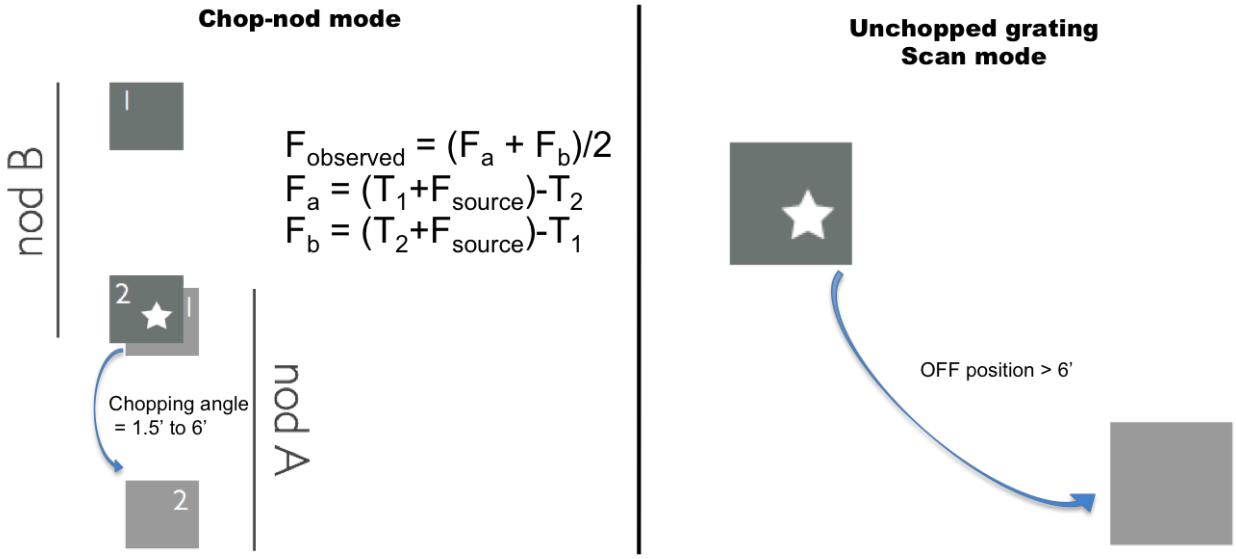

Figure II.6: *Left: telescope movements for the chopping-nodding mode. Right: telescope movements for the unchopped grating mode. Image from Cormier (2012).*

all wavelengths. The goal of the chopping was to remove the sky and telescope backgrounds by observing alternatively the source and an offset position, by moving a tilting mirror, called the chopper, at every grating position. In addition, since the telescope background is different at the optical angle of the two chop positions, it is necessary to repeat the grating scans and chopping at a second nod position, on the other side of the source (Fig. II.6). A sequence of line scan observations between the on-source position and an off-source position was done successively at both nod positions separated by 1.5′, 3′, or 6′, following the chopping pattern [on-off-off-on]-[on-off-off-on].

- **Unchopped grating scan mode.** This mode is an alternative to the standard mode if no emission-free area for the off position could be found within 6′ from the center of the source. This mode was recommended for spectral line mapping of extended objects for example, but not in the case of very faint lines. In this mode, the total observation time is spent on the source, and line scans are done with 75 grating steps in faint line mode and 50 steps in bright line mode, with at least three samples per resolution element. The up and down grating scans were faster and repeated twice. Additional time was spent on an off-source position, within 2° from the target, to remove the telescope background.

Line sensitivities were comparable for both modes. However, the continuum could be better recovered in the standard chopping-nodding mode. Our observations of extended regions in the LMC and SMC were done with the unchopped faint line or bright line mode. Pointed and mapping observations could be carried out with both modes.

II.1.3 The PACS photometer

Design

In photometry mode, the PACS instrument performed dual-band imaging, observing simultaneously the 160 μm red band (125-250 μm) with either the 70 μm blue band (60-85 μm) or the 100 μm green band (85-125 μm). The light was split into a long-wavelength (160 μm) and a short wavelength (70 and 100 μm) channel and was collected onto two bolometer arrays of 32×32 pixels (160 μm band) and 64×32 pixels (70 and 100 μm bands), covering a field of view of $\sim 1.75' \times 3.5'$ each.

Scientific capabilities

The PACS photometer PSF was diffraction-limited and dominated by the telescope. As seen in Figure II.7, it was characterized by a tri-lobe pattern, resulting from an imperfection of the mirror shape due to the secondary mirror tripod. The value of the FWHM in each band is summarized in Table II.2, along with the scan mapping mode sensitivity and the flux calibration uncertainties. The absolute flux calibration of the PACS photometer is based on models of 5 standard stars and more than 10 asteroids, covering in total a flux range of $\approx$ 100 mJy to 300 mJy. Calibration uncertainties are dominated by the calibration model uncertainties. The filter transmission for each of the three filters is presented in Figure II.7 as a function of the wavelength.

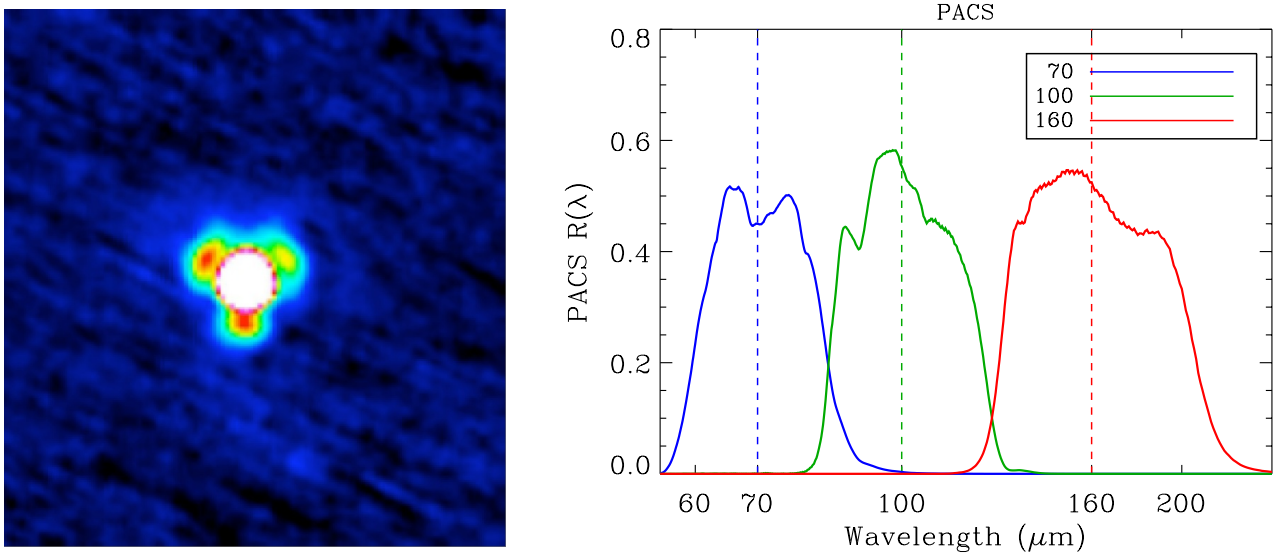

Figure II.7: *Left: the PACS photometer PSF in the green band ($\sim$ 100 μm); taken from the PACS Observer's Manual. Right: filter transmission curves of the PACS photometer. The reference wavelength for each filter is indicated by a dashed line.*

Observing modes

Three AOTs were used for the PACS photometric observations: the point-source mode in chopping-nodding technique, the scan-map technique and a parallel PACS/SPIRE scan technique mode. We describe here the second mode, which was the most frequently used *Herschel* observing mode and was used for our observations. It was the default mode to map large areas but it was also recommended for small fields and even point sources to achieve better sensitivities and more homogeneous coverage.

Table II.2: PACS photometer scientific specifications.

Band	Wavelength (μm)	Range (μm)	FWHM ($''$)	Scan mapping sensitivity 1σ-1 second (mJy)	Calibration accuracy
Blue	70	60 - 85	5.6	30.6	5%
Green	100	85 - 125	6.8	36.0	5%
Red	160	125 - 210	11.4	68.5	5%

The scan of a given sky area was carried out by moving the telescope at a constant speed along parallel lines (called *scan legs*). The number of scans, the scan leg length and separation and the orientation angle could be set by the observer. Our observations were carried out with $20''$/s speed, where the bolometer performance was best. As was recommended, we made combinations of two orthogonal scan directions for a better PSF and field reconstruction and to remove stripping effects.

II.1.4 The SPIRE spectrometer

Design

The SPIRE imaging Fourier Transform Spectrometer (FTS) worked as a Mach-Zehnder interferometer, covering the wavelength range between 194 and 671 μm. The incident radiation was split into two separate beams which traveled different paths before recombination on a detector as shown on the left panel of figure II.8[3]. The optical path difference (OPD) was created by a moving mirror (SMEC), and introduced a phase difference between the beams, causing constructive or destructive interferences between the two wavefronts. An interferogram of the signal as a function of the OPD was built by moving the mirror. This interferogram, $I(x)$, is the Fourier transform of the spectrum of the source, $B(\sigma)$, which can thus be reconstructed by calculating the inverse Fourier transform of the interferogram following:

$$B(\sigma) = \frac{1}{N} \sum_{x=-\infty}^{\infty} I(x) e^{-2i\pi\sigma x}; \tag{II.1}$$

where N is the number of resolution elements.

The two bolometer arrays covered overlapping bands of 194-324 μm for the SPIRE Short Wavelength spectrometer array (SSW) and 316-672 μm for the SPIRE Long Wavelength spectrometer array (SLW). They contained 37 (SSW) and 19 (SLW) hexagonally packed detectors as presented in the right panel of figure II.8[4], resulting in an unvignetted field of view of $2'$ in diameter.

Scientific capabilities

Spectral resolution. The instrumental line shape of all FTSs is a *sinc* function. The resolution element in frequency is given by $\Delta f = \frac{c}{2 \times \mathrm{OPD}_{\max}}$ where c is the speed of light and $\mathrm{OPD}_{\max}$ is the maximal optical path difference introduced by the mirror, equal to 12.8 cm for the high resolution (HR) mode and 0.6 cm for the low resolution (LR) mode of the SPIRE/FTS instrument. The resulting spectral

[3] Image from the SPIRE data reduction guide available at http://herschel.esac.esa.int/hcss-doc-14.0/

[4] Images are from the SPIRE Observers' Manual, available at http://herschel.esac.esa.int/Docs/SPIRE/html/spire_om.html

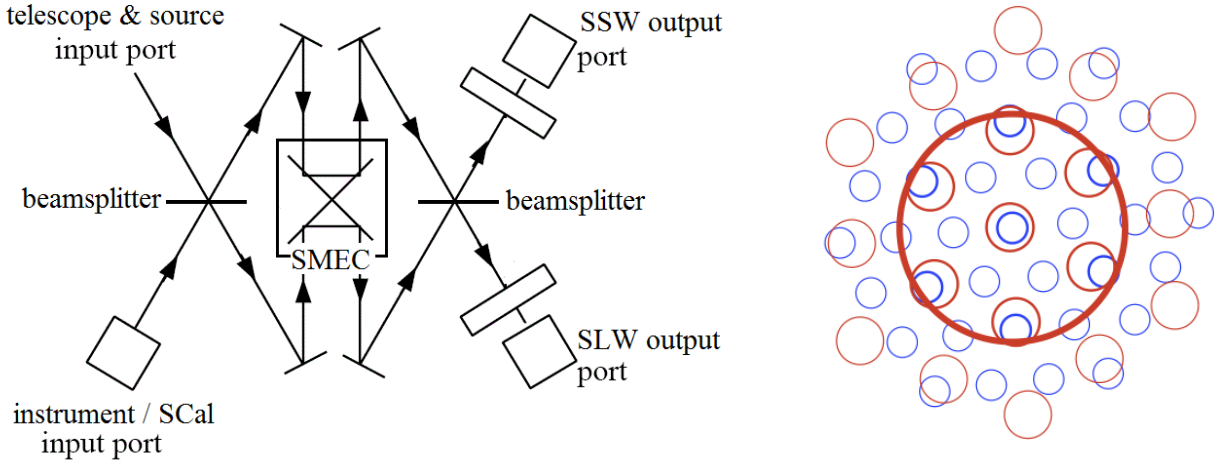

Figure II.8: *Left: schematic of the optical layout of the SPIRE FTS. Right: schematic view of the spectrometer bolometer arrays and how they overlaped on the sky. The SLW and SSW are represented respectively with red and blue circles. The bold red circle delineates the 2′ unvignetted field of view for FTS observations.*

Table II.3: SPIRE spectrometer scientific specifications.

Band	Range (μm)	Spectral resolution km s^{-1}	FWHM ($''$)	Line sensitivity 5σ-1 hour (W m^2 $\times$ 10^{-17})
SSW	194 - 324	280 - 450	16 - 20	1.56 - 2.15
SLW	316 - 672	440 - 970	30 - 43	0.94 - 2.04

element resolution was then of 1.2 GHz for the HR mode (respectively 25 GHz for the LR mode) and the FWHM for the best achievable resolution with the SPIRE HR mode was $\approx$ 1.5 Ghz.

Sensitivity. For an FTS, the line sensitivity is in principle independent of the spectral resolution for unresolved lines. However, it was recommended to adopt only the HR mode for line observations. The line sensitivity at 5σ for 1 hour integration time for this mode is reported in Table II.3 and was typically $\approx 1.5 \times 10^{-17}$ W m^2. The overall calibration accuracy is estimated to 6% for point sources and 7% in mapping mode.

Spatial resolution. Makiwa et al. (2013) have determined the FTS beam profile as a function of the frequency (Fig. II.9) based on Neptune observations. The point-source observations can be fitted by a Gaussian function in the SSW band. The profile in the SLW band was more complex and had to be modeled by a superposition of at least three Hermite-Gaussian functions.

Observing modes

Any given observation was defined by its spectral resolution (HR, LR or HR+LR), its pointing mode (single or mapping) and its spatial sampling (sparse, intermediate or full Nyquist sampling):

- **Spectral resolution.** Our observations where done with the HR mode, by scanning the SMEC to the maximum OPD. It was an efficient mode to observe simultaneously several lines of the CO rotational ladder for example (CO $J = 4-3$ to CO $J = 13-12$ have been observed in several regions of the LMC, including 30 Doradus).

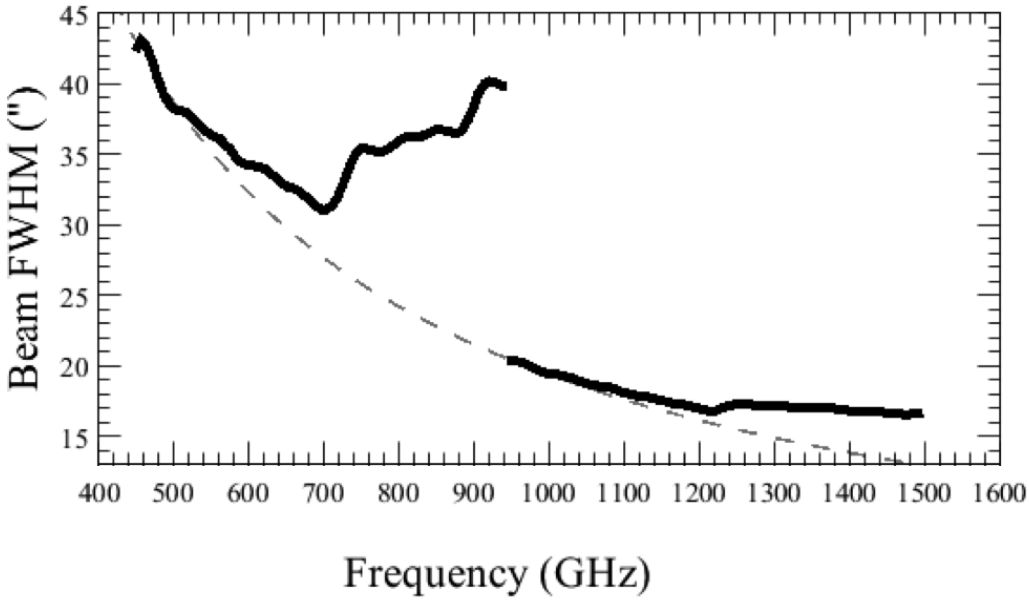

Figure II.9: *FWHM of the SPIRE FTS beam profile fitted by Makiwa et al. (2013) as a function of the frequency for the SWL and the SSL. The dashed line shows the expected FWHM for diffraction limited observations. The resulting FWHM of the fitted profile matches the value expected from the diffraction theory only at the low frequency end of each band. At higher frequencies, the superposition of several electromagnetic modes of propagation in the waveguides connecting the telescope beam to the detectors, results in larger effective beam sizes. The cut-off frequencies of the electromagnetic modes that are propagated are determined by the diameter of the waveguide. In particular, the waveguides are single-moded at the low frequency end of each band.*

- **Pointing mode.** The single pointing mode could be used to take spectra on the 2′ instrument field of view. For larger regions, the telescope was moved to various positions. In order to make efficient complete coverage of a region, the pointings were combined in a hexagonally packed design.

- **Spatial sampling.** The image sampling options are represented in Figure II.10. The sparse image sampling mode could be used to measure the spectrum of a compact source centered on the central detectors of the instrument. It required accurate pointing and precise knowledge of the source position. The fully Nyquist sampled spectroscopy of a region was done by moving a beam steering mirror into 16 different jiggling positions with 1/2 beam spacing. The final beam spacing for SSW and SLW was 8.1″ and 12.7″ respectively, and the resulting coverage for SLW and SSW is shown in the right panel of Figure II.10. The intermediate sampled mode was faster than the fully sampled mode. The beam stirring mirror was moved into 4 jiggling positions, with 1 beam spacing. The final beam spacing for SSW and SLW was 16.3″ and 25.3″ respectively, roughly equal to the FTS beam. The observations were thus sub-Nyquist sampled. The resulting coverage for SLW and SSW is shown in the right panel of Figure II.10. Our observations were made using the intermediate sampled mode.

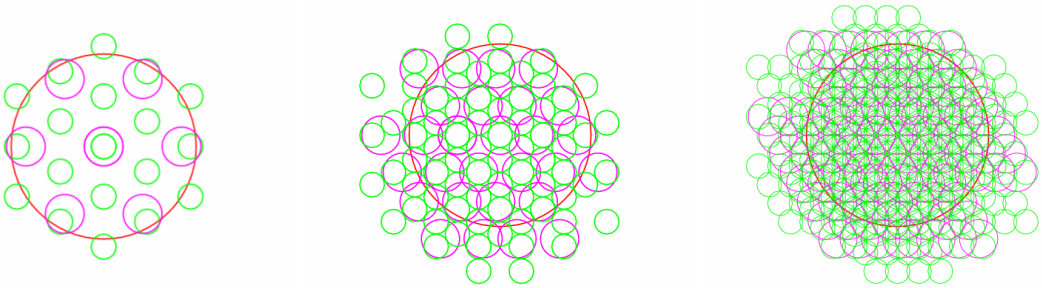

Figure II.10: *Illustration of the SPIRE/FTS sampling modes: sparse (left), intermediate (center) and full Nyquist sampling (right). The green and magenta circles indicate the positions of the observed spectra for the SSW and SLW respectively, only in the unvignetted area (2′; red circle).*

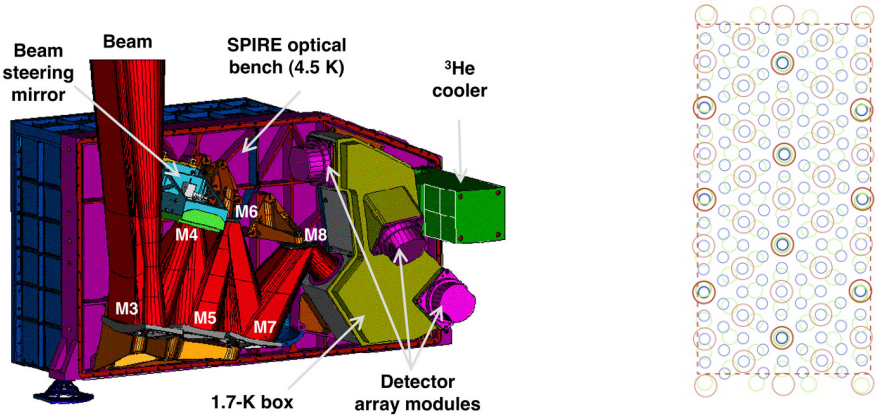

Figure II.11: *Left: photometer side layout of the SPIRE focal plane unit. Right: schematic view of the photometer bolometer arrays and how they overlap on the sky. The 250 µm, 350 µm and 500 µm bands are represented respectively by blue, green and red circles. The circle sizes correspond to the size of the FWHM of the beam. The dashed red rectangle delineates the 4′×8′ unvignetted field of view.*

II.1.5 The SPIRE photometer

Design

The SPIRE photometer performed broad-band photometry in three spectral bands simultaneously. The photometer layout is presented in figure II.11[5]. The three detectors are visible, as well as the ^{3}He cooler assuring the required operating temperature of ∼ 0.3 K for the five SPIRE detectors. The beam was separated by dichroic filters and focused onto three detector arrays composed of 139, 88 and 43 bolometers, centered approximately on 250, 350 and 500 μm.

[5]Images are from the SPIRE Observers' Manual, available at http://herschel.esac.esa.int/Docs/SPIRE/html/spire_om.html

Scientific capabilities

SPIRE photometer characteristics are presented in Table II.4. The beam was approximately gaussian and the spatial resolution was between 18″ and 36″ for the three bands. The absolute flux calibration was made on Neptune and estimated to ∼ 4%. It is combined with the relative calibration uncertainties of 1.5%. The SPIRE Observer's Manual advises to conservatively add these values linearly instead of quadratically, for a total uncertainty of 5.5%.

Table II.4: SPIRE photometer scientific specifications.

Band	Wavelength (μm)	Range (μm)	FWHM (″)	Beam areas (″^{2})	Scan mapping sensitivity 1σ-1 second (mJy)	Calibration accuracy
PSW	250	200 - 300	18.1	465	30.6	5.5%
PMW	350	270 - 430	24.9	822	36.0	5.5%
PLW	500	375 - 670	36.4	1768	68.5	5.5%

Observing modes

Three observing templates could be used for SPIRE photometric observations. The large map mode was used to cover areas larger than 5′ by scanning the telescope at the nominal speed (30″/s) or fast speed (60″/s). The direction of the scan was oriented at ≈ 42° compared to the orientation of the bolometer arrays and scan lines were separated by 348″ to provide overlap and good coverage for fully sampled maps in the three bands. Small area map mode was adapted for areas smaller than 5′. The map was done with only two cross scans with the telescope. A point source photometry mode, adapted for isolated point sources, also existed although it has never been used for science observations. In all three modes, observations were made in the three photometer bands simultaneously. For our sources in the LMC, the large map mode at nominal speed was used.

II.2 The observed sample

II.2.1 The Dwarf Galaxy Survey

Due to the better sensitivity of *Herschel* compared to previous IR telescopes, a wide range of low surface brightness objects, in particular low-metallicity dwarf galaxies, became accessible. Our observations come from several *Herschel* surveys. The *Dwarf Galaxy Survey* (DGS; PI: S. Madden) in particular is one of the three *Herschel* Garanteed Time Key Programs of the SPIRE Local Galaxies consortium (SAG2). The *Star formation and activity in infrared bright galaxies at 0<z<1* (SHINING; PI: E. Sturm) is a 333.5 h *Herschel* Garanteed Time Key Program of the PACS consortium, focussing mainly on ultra-luminous infrared galaxies (ULIRGS) and active galactic nuclei (AGN). It includes 85.5 h for dwarf galaxies observations, which are included as part of the DGS sample. Other smaller projects complement this sample. In total, during the 230 hours of this project, 50 dwarf galaxies have been observed with PACS and SPIRE instruments in the DGS. It includes local galaxies with a large metallicity range (down to 1/40 $Z_\odot$) and four orders of magnitude in star formation rates. The DGS aims at studying gas and dust properties in low metallicity ISM, with photometry and spectroscopy observations. An overview of this survey is presented by Madden et al. (2013).

Rémy-Ruyer et al. (2013, 2014, 2015) focus on the dust properties and the gas-to-dust mass ratio of 48 of the DGS sources. These studies reveal different grain properties and/or global environments of the low-metallicity galaxies compared to more metal-rich galaxies. The evolution of the chemical and dust properties results from a complex interplay between star formation activity, stellar mass and metallicity. Cormier et al. (2015) present the *Herschel* PACS spectroscopy observations of 48 galaxies in the DGS. This study reveals the more porous structure of low-metallicity galaxies compared to metal-rich galaxies on global galaxy scales. To investigate the effects of metallicity on the ISM, we zoom into the Magellanic Clouds, our nearest neighbors, also at low metallicity.

II.2.2 Observations of LMC and SMC

In total, in the LMC and SMC, 11 regions have been mapped with *Herschel*/PACS spectrometer as part of the DGS and Hony et al. Open Time 2 (OT2) program. The Hony et al. OT2 program also include SPIRE/FTS observations for 9 regions. An additional FTS pointing in 30 Doradus originates from the OT2 program by Indebetouw et al. A list of the lines observed with the PACS spectrometer and SPIRE/FTS is presented in Table II.5.

For all of these regions, *Herschel* photometry (HERITAGE; Meixner et al. 2010) as well as *Spitzer* photometry (SAGE; Meixner et al. 2006) observations are available. "HERschel Inventory of The Agents of Galaxy Evolution (HERITAGE) in the Magellanic Clouds" (P.I. M. Meixner) is a 285 h *Herschel* open time key program, to uniformly survey the LMC (8 °× 8.5 °) and SMC (5 °× 5 °and 4 °× 3 °) with PACS and SPIRE photometry and study the life cycle of matter in the ISM, through observation of dust, YSOs and the contribution of evolved stars. "Surveying the Agents of a Galaxy's Evolution" (SAGE; P.I. M.Meixner) is a 508 h survey of the LMC ($\approx 7° \times 7°$) in all of the IRAC and MIPS bands. SAGE was designed to detect the population of IR sources, including evolved stars and YSOs, and to map with high signal-to-noise ratio (S/N) the dust emission from all ISM phases, from diffuse to molecular clouds, PDRs and H II regions.

Both Magellanic Clouds have also been mapped in H I 21 cm with the Australian Telescope Compact Array and the Parkes 64m radio Telescope by Kim et al. (2003) for the LMC and Stanimirovič et al. (1999) for the SMC, at ∼1′ angular resolution. The Magellanic Cloud Emission-line Survey (MCELS, Smith & the MCELS Team 1998) is a deep imaging survey of the central 8 °× 8 ° of the LMC and of the central 3.5 × 4.5 ° of the SMC, with a ∼3″ angular resolution. Our study also relies on the ground-based CO(1-0) observations with the Mopra telescope, at 45″ resolution, of several GMCs in the LMC (Wong et al. 2011) and the SMC (Muller et al. 2010). These are results from the Magellanic Mopra Assessment (MAGMA) project which improves resolution for the largest GMCs compared to the full mapping of the LMC obtained by the 4 m NANTEN telescope at 1.6′ resolution (Fukui et al. 2008) and of the SMC at 2.6′ resolution (Mizuno et al. 2001). 32 GMCs have also been observed in ^{12}CO(3-2) and ^{13}CO(3-2) with the Atacama Submillimeter Telescope Experiment (ASTE) at ∼45″ resolution (Minamidani et al. 2011).

A detailed analysis of the PDRs and CO-dark gas in the 30 Doradus region, relying on these observations, is presented in Chapters IV and V. The other mapped regions are analyzed in Chapter VI.

II.3 Data processing

II.3.1 Data reduction

Herschel data are reduced using the *Herschel* Interactive Processing Environment (HIPE; Ott 2010).

Table II.5: *Herschel* spectroscopic observations of the LMC and SMC

Region	Program	PACS observations	SPIRE observations[a]
LMC-30Dor	DGS, Hony et al. (OT2) & Indebetouw et al. (OT2)	[C II], [O I]$_{63}$, [O I]$_{145}$, [O III]$_{88}$, [N II]$_{122}$	yes
LMC-N11A	DGS	[C II], [O I]$_{63}$	no
LMC-N11B	DGS & Hony et al. (OT2)	[C II], [O I]$_{63}$, [O I]$_{145}$, [O III]$_{88}$, [N II]$_{122}$	yes
LMC-N11C	DGS	[C II], [O I]$_{63}$, [O III]$_{88}$	no
LMC-N11I	DGS	[C II], [O I]$_{63}$, [O III]$_{88}$	no
LMC-N44	Hony et al. (OT2)	[C II], [O I]$_{63}$, [O I]$_{145}$, [O III]$_{88}$, [N II]$_{122}$	yes
LMC-N157	Hony et al. (OT2)	[C II], [O I]$_{63}$, [O I]$_{145}$, [O III]$_{88}$, [N II]$_{122}$	yes
LMC-N158	DGS & Hony et al. (OT2)	[C II], [O I]$_{63}$, [O III]$_{88}$	yes
LMC-N159W	DGS & Hony et al. (OT2)	[C II], [O I]$_{63}$, [O I]$_{145}$, [O III]$_{88}$, [N II]$_{122}$	yes
LMC-N159S	DGS	[C II], [O I]$_{63}$	no
LMC-N160	DGS & Hony et al. (OT2)	[C II], [O I]$_{63}$, [O I]$_{145}$, [O III]$_{88}$	yes
LMC-N180	Hony et al. (OT2)	[C II], [O I]$_{63}$, [O I]$_{145}$, [O III]$_{88}$, [N II]$_{122}$	yes
LMC-Diffuse	Hony et al. (OT2)	[C II], [O I]$_{63}$, [O I]$_{145}$, [O III]$_{88}$, [N II]$_{122}$	yes
SMC-N66	DGS	[C II], [O I]$_{63}$, [O III]$_{88}$	no
SMC-N83	Hony et al. (OT2)	[O I]$_{145}$	no

[a] When the SPIRE/FTS spectrum is available, the lines [N II] 205 μm, [C I] 370 μm, [C I] 609 μm and the CO transitions from $J = 4 - 3$ to $J = 13 - 12$ have been fitted.

The galaxies of the DGS (Madden et al. 2013) were observed between November 2009 and August 2011 and the HIPE environment has evolved considerably since then. Several versions of HIPE have been used for the data reduction, as described below. Detailed information about the HIPE pipeline can be found at http://herschel.esac.esa.int/hcss-doc-14.0/. We summarize here some of the main steps of the data reduction.

PACS spectroscopy

Data from the *Herschel* Science Archive (HSA) have been reprocessed from the raw data (level 0) to the spectral data cube (level 2) using HIPE v.12. For a given observation, each of the 25×16 pixels of the detector array contains the variation of the signal with time as the grating is moved. Detectors provide 8 measurements per seconds. Hence, for any observation of n seconds, data cubes originally cover $25 \times 16 \times 8n$ measurements.

In the first step of the pipeline (level 0 to level 0.5), the signal is converted to Volt s^{-1}, the wavelength is calibrated and the bad pixels (noisy or saturated for instance) are flagged. The astrometry and information from the instrument are read. The second step (level 0.5 to 1) is used to flag the

glitches and calibrate the flux. If the chop-nod mode is used, the signal from the chopped position is subtracted. At the end of this step, the data are reorganized as a $5\times5\times n_\lambda$ cube, containing one spectra for each of the 5×5 positions on the sky, for n_λ wavelength steps. In the next step (level 1 to level 2), outlier pixels are masked and a flat-field correction is applied. In the unchopped case, we apply an additional transient correction as described in Lebouteiller et al. (2012), which is more robust than the default procedure included in the pipeline. The off-spectra before and after the on-spectrum observation are averaged to get a good estimate of the continuum and then is subtracted from the on-signal. The individual spectral cubes of each raster position are saved as FITS files, including the coordinate information. Although additional steps to rebin the data and combine the different raster positions are included in HIPE, we choose to save the unrebinned data cubes to keep all of the spectral information.

The flux analysis is done using the IDL software PACSman version 3.63, written by Vianney Lebouteiller and described in Lebouteiller et al. (2012). The continuum only of each observation in each spaxel is first fitted by a polynomial curve of order 2. From this initial estimate, the continuum and the line are then fitted, assuming a gaussian instrument profile. This approximation is in general valid, although a slight deviation can be observed for a point source at the edge of the array. An example of the fit in shown in Figure II.12. Errors are not propagated in HIPE. They are calculated in the PACSman analysis as the dispersion of the measured flux density in a given wavelength bin. Errors are taken into account for the fit of the spectra.

The reconstruction of the total map is done from the fluxes at each spatial position. The data are projected on a new grid of 3″ sub-pixels. If several spaxels fall on the same sub-pixel, the contribution of each spaxel to the intensity of this sub-pixel is weighted by the distance to the center of the sub-pixel. The uncertainty on the nominal response of each spaxel (10%) is taken into account in the map projection procedure by doing a Monte-Carlo simulation.

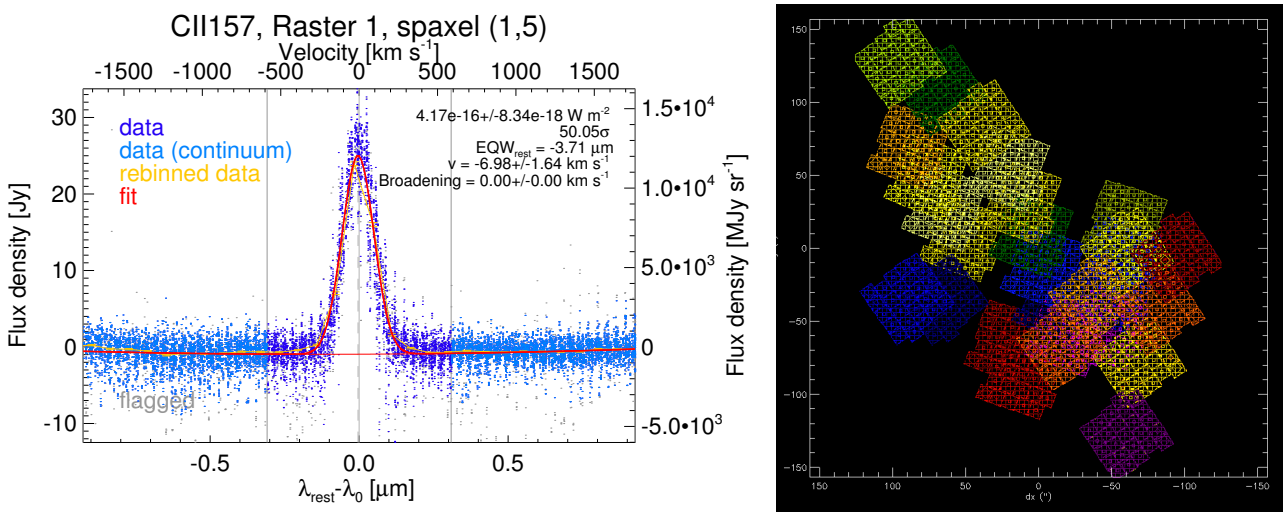

Figure II.12: *Left: Example of a fit with PACSman for one observation of [CII] 158 µm. The range of the spectrum used for the fit of the continuum only are in light blue, avoiding the line profile, and the final fit of the continuum and of the line are in red. Right: Raster projection of the [CII] observations of 30 Doradus in the LMC showing the overlapping PACS footprints.*

SPIRE spectroscopy

The FTS data have been processed using HIPE version 11.0.2825 and the SPIRE calibration version 11.0 (Fulton et al. 2010; Swinyard et al. 2014). The flux analysis is done using the data reduction script by Wu et al. (2015). The method is described by Lee et al. (2016) and it has been used to produce flux measurements of intermediate sampling SPIRE/FTS observations. The continuum and the line emission are first fitted with a combination of a parabola and *sinc* function respectively for each of the detectors. Contrary to the method used for PACS, the full spectra, not the integrated fluxes for every detectors, are projected on a common grid. The continuum-subtracted spectra are projected onto a grid of $15'' \times 15''$ pixels, which corresponds approximately to the jiggle spacing of the SSW observations. Where detectors fall onto the same $15'' \times 15''$ pixel, the overlapping spectra are weighted by their covering areas before summation. The integrated intensity is then derived for each pixel and the statistical errors are calculated based on the residual of the line measurement. Calibration errors of 10% are also added in quadrature, as suggested by the SPIRE Observer's Manual.

II.3.2 Convolution

An image, $I(x,y)$, observed by any instrument is the result of the convolution of the source, $S(x,y)$, by the instrumental response to a point source, called the Point Spread Function (PSF), $\Psi(x,y)$:

$$I(x,y) = \iint S(x,y)\Psi(x-x',y-y')dx'dy' = (S * \Psi)(x,y) \tag{II.2}$$

The PSF depends on the instrument, but also on the wavelength for the same instrument. In particular, the lines coming from the PACS spectrometer are observed with different instrumental PSF, at different resolutions (Sections II.1 and II.4). To be able to compare the observations taken with different instruments and/or at different wavelengths, i and j for example, we thus have to convolve the images, such that:

$$I_i(x,y) = (S * \Psi_i)(x,y) = (S * \Psi_j * K\{i \Rightarrow j\}) = (I_j * K\{i \Rightarrow j\}), \tag{II.3}$$

where the convolution kernel $K\{i \Rightarrow j\}$ must satisfy

$$\Psi_i = (\Psi_j * K\{i \Rightarrow j\}). \tag{II.4}$$

In this way, we reproduce the observations we would have if all of the lines were observed with the same PSF, which now allows us to compare them.

The convolution kernels between the different PACS photometry and spectroscopy channels have been calculated by Aniano et al. (2011) and are available, along with a convolution procedure, at http://www.astro.princeton.edu/~ganiano/Kernels.html. We use the procedure of Aniano for the convolution, modifying the first step in order to smooth the map and extrapolate the values of the pixels at the edge of the map to extend it. We remove the extrapolated pixels after the convolution. In this way, the values on the edges of the convolved map are more reliable.

II.4 Other infrared and submillimeter observatories

II.4.1 The *Spitzer* telescope

The *Spitzer* Space Telescope is an infrared space observatory launched in 2003 by NASA. The primary mirror is 83 cm and was cooled to 5.5 K until May 15th 2009, after which the liquid helium supply was exhausted. It continues today in its warm mission phase. Three instruments have been on-board the *Spitzer* telescope and are described below.

IRS

The InfraRed Spectrograph[6] (IRS) consisted of four separate modules (Short-Low, Short-High, Long-Low and Long-High) which provided low (R~60-130) resolution spectroscopic capabilities over 5.2 to 40 μm and moderate (R~600) resolution spectroscopic capabilities over 9.9 to 37 μm. The basic information of the modules is presented in Table II.6 and a schematic view of the IRS slits can be seen in Figure II.13.

Table II.6: IRS module characteristics, from the IRS Instrument Handbook.

Module	Wavelength range (μm)	Resolving Power R	Plate Scale (arcsec/pix)	Slit width (arcsec)	Slit length (arcsec)
SL1	7.46-14.29	61-120	1.8	3.7	57
SL2	5.13-7.60	60-127		3.6	
SL3	7.33-8.66				
LL1	19.91-39.90	58-112	5.1	10.7	168
LL2	13.90-21.27	57-126		10.5	
LL3	19.91-39.90				
SH	9.89-19.51	600	2.3	4.7	11.3
LH	18.83-37.14	600	4.5	11.1	22.3

IRAC

The InfraRed Array Camera (IRAC) is a four-channel imaging camera. It is now the only instrument still in service during the warm mission phase. It provides simultaneously 5.2″× 5.2″images at 3.6, 4.5, 5.8 and 8 μm. The four detector arrays are 256 × 256 pixels, with a pixel size of ~ 1.2″×1.2″. The main characteristics for the four IRAC channels can be found in Table II.7. The flux in channel 3 and 4 in particular can include a contribution from the major PAH features at 6.2 μm, 7.7 μm and 8.6 μm. This is discussed in more details in Section III.2.

Table II.7: IRAC module characteristics, from the IRAC Instrument Handbook.

Channel	Effective wavelength (μm)	Bandwidth (μm)	FWHM (″)
1	3.6	0.750	1.66
2	4.5	1.015	1.72
3	5.8	1.425	1.88
4	7.9	2.905	1.98

MIPS

The Multiband Imaging Photometer for Spitzer (MIPS) executed broad-band photometry simultaneously in three channels centered at 24, 70 and 160 μm. The main characteristics of the three detectors

[6]More information can be found in the IRS handbook, available at: http://irsa.ipac.caltech.edu/data/SPITZER/docs/irs/irsinstrumenthandbook/

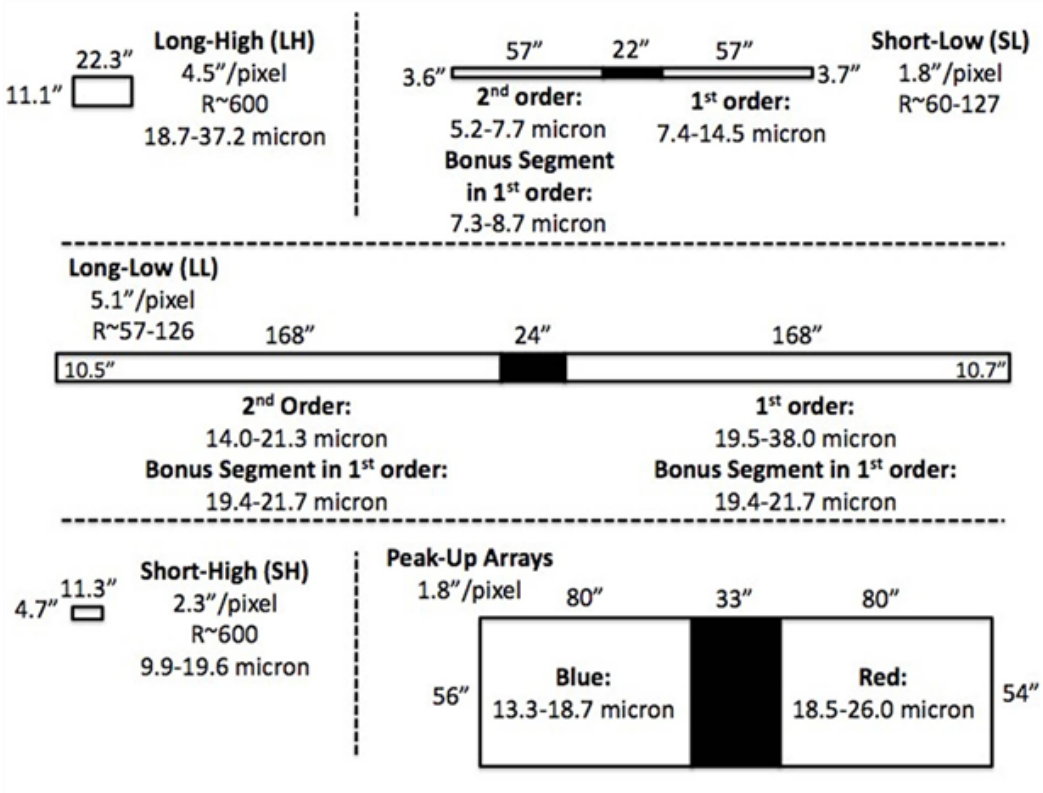

Figure II.13: *Schematic representation of the IRS slits. Note that the slits are not parallel in the Spitzer focal plane.*

are given in Table II.8.

Table II.8: MIPS module characteristics, from the MIPS Instrument Handbook.

Band	Wavelength range (μm)	Bandwidth (μm)	FOV ($'\times'$)	FWHM ($''\times''$)	Array size (pix $\times$ pix)	Pixel size ($''\times''$)
1	24	4.7	5.4×5.4	6	128×128	2.5×2.6
2	70	19	5.2×2.6	18	32×16	9.9×10.1
3	160	35	5.3×2.1	38	20×2	16×18

II.4.2 The *SOFIA* observatory

It was necessary to follow up on our *Spitzer* and *Herschel* observations with some FIR spectroscopy ([O III] 52 μm line, in particular) and to extend the PACS maps. For this, we used the Stratospheric Observatory For Infrared Astronomy (*SOFIA*), which is the largest airborne observatory in the world. It consists of a modified Boeing 747SP aircraft, carrying a reflective telescope with an effective diameter of 2.5 meters (Fig. II.14). The telescope has two Nasmyth foci: the IR focus, where the instruments are set, and an additional visible light focus for guiding. It is a partnership of NASA and the German Aerospace center (DLR). "First Light" flight was achieved in May 2010. Eight instruments, imagers and spectrographs, are available and can be separately mounted at the focal plane of the telescope. Their spectral coverage and spectral resolution are presented in Figure II.15. Guider cameras and a

water vapor monitor are also used for pointing corrections and calibration. The typical precipitable water vapor at 41,000 feet is of the order of 7 μm. We will only focus here on FIFI-LS, which has been used recently to complement our PACS observations of the star-forming regions 30 Doradus in the LMC (Section IV.3).

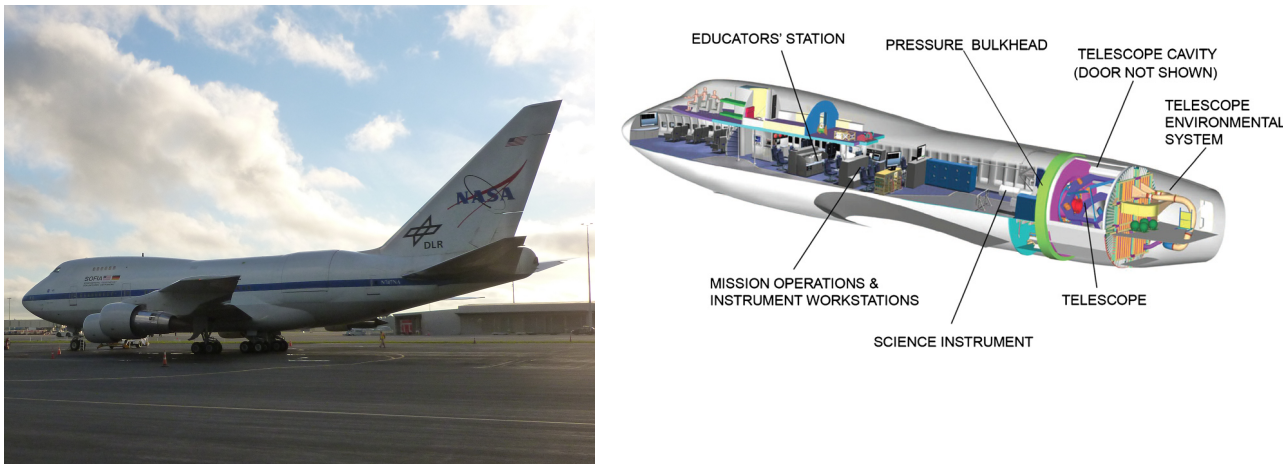

Figure II.14: *Left: SOFIA during the 2016 southern deployment in Christchurch, when I participated in the observations. Right: schematic of the SOFIA observatory (Krabbe et al. 2013). The telescope looks out of the left side of the airplane.*

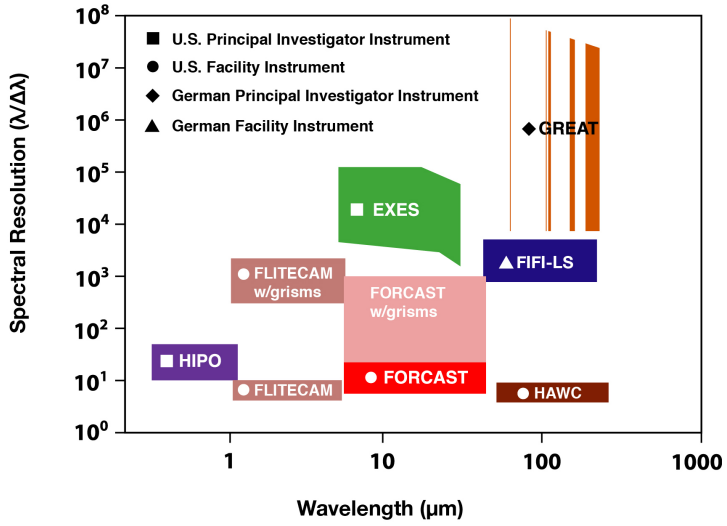

Figure II.15: *Spectral resolution and wavelength coverage of the different instruments available on SOFIA. EXES, FIFI-LS and GREAT are spectrometers. FLITECAM, FORECAST and HIPO are IR imagers and photometers. HAWC+ is an imaging photometer. FPI+, not represented here is an imaging photometer in the wavelength range 360-1100 nm.*

FIFI-LS

Description. The Field Imaging Far Infrared Line Spectrometer (FIFI-LS; P.I.: A. Krabbe) is an integral field far-infrared spectrometer. It consists of two independent grating spectrometers with medium resolution (R ~ 2200) operating at short wavelength (the blue channel ranges from 51 to 120 μm) and long wavelength (the red channel ranges from 115 to 203 μm). The two detectors consists of 16×25 photoconductor arrays configured as in the PACS detectors, with 16 spectral elements for each of the 5×5 spatial elements. The red channel covers a field of view on the sky of 1′×1′ and the blue array,

30″×30″ (Fig. II.16). The spatial resolution in both arrays is diffraction limited.

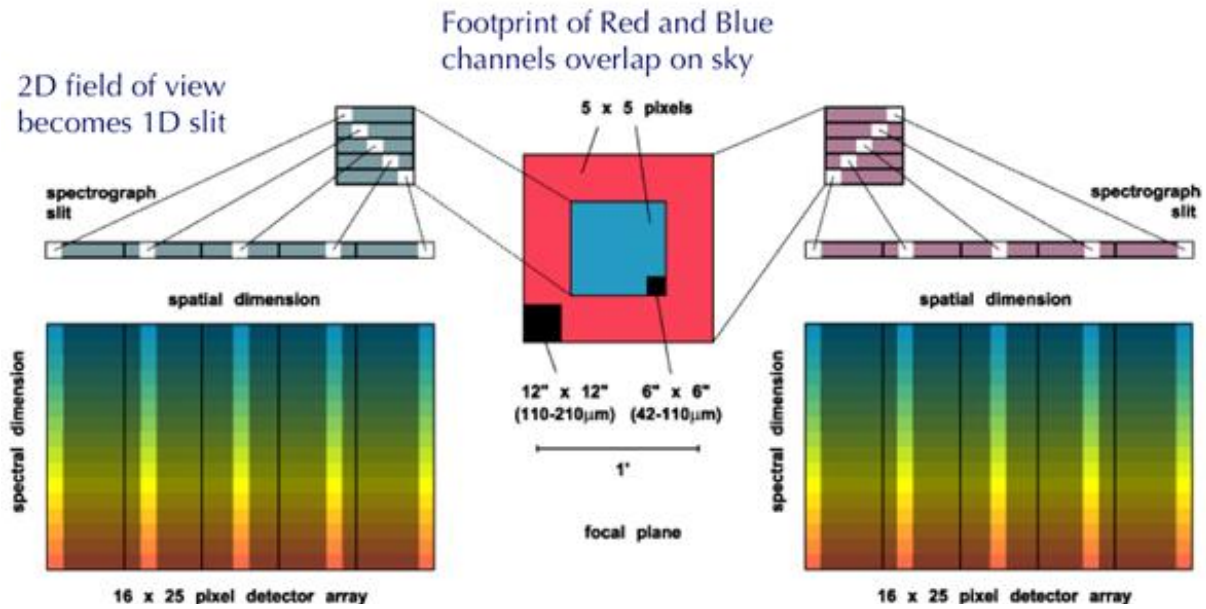

Figure II.16: *Concept of the integral field spectrometer FIFI-LS. The 5×5 spatial pixels in both, the red and the blue channel are optically rearranged to form a 1×25 spatial slit before entering the red and blue grating spectrometer.*

Comparison with PACS. In term of spatial coverage, spectral resolution and design, FIFI-LS is very similar to the PACS spectrometer. However, the useful short wavelength range of FIFI-LS exceeds that of PACS, and additional diagnostic lines (such as [O III] 52 μm) become available. Besides, due to the smaller pixel size in the blue channel, FIFI-LS provides better angular resolution for the short wavelengths. On the other hand, the execution time per observation and sensitivity differ considerably. The raw sensitivity of PACS for point source observations is about a factor of 8 times better than FIFI-LS, due to telescope temperature, atmospheric absorption and telescope diameter.

Observing modes. Subtraction of the high IR sky background is done by alternatively nodding the telescope and chopping the secondary mirror. The recommended observing mode is the Symmetric Chop, as for the PACS spectrometer. In this mode, the two off-source positions are symmetric to the on-source position and the source is observed 50% of the time. However, for extended sources, of more than $\sim 4'$, large chop throws can degrade the image quality due to the introduction of a coma, in particular at short wavelengths. In this case, the Asymmetric Chop mode can be used. The source is observed on the optical axis, and is unaffected by coma. Then, the off-source position can be observed by chopping the secondary mirror by several arcsecs, with no consequence of the coma on an empty-sky observation. The telescope is then nodded to an off-source position, where the same pattern is executed to efficiently remove the background contamination. In this scenario, the source is observed 25% of the total observing time.

For bright objects, where the estimated observing time is 10 s or less, the telescope moves dominate the total observing time. In this case, it is more efficient to observe two map positions and one off-source position per nod-cycle, using an asymmetric chop, hence limiting the overhead time. This mode is used for our observations of [O III] lines in 30 Doradus (Section IV.3).

We used the mapping mode for the LMC observations, which can be used either with the symmetric mode, or the asymmetric mode.

II.4.3 The *ALMA* interferometer

To follow up our *Herschel* observations and our modeling efforts in the LMC, we required higher resolution *ALMA* observations. The Atacama Large Millimeter/submillimeter Array (*ALMA*) is composed of the 12-m Array (fifty 12 m diameter antennas), and the Atacama Compact Array (ACA; twelve 7 m antennas and four 12 m antennas). It is located on the Chajnantor plain of the Chilean Andes, at an altitude of ≈ 5000 m (see Figure II.17). It operates imaging and spectroscopy at submm and millimeter wavelengths. *ALMA* can probe the cold dust and molecular gas in nearby and more high-redshift galaxies at high spatial and spectral resolution. The properties of the available bands for the recent *ALMA* cycle 3 are presented in Table II.9.

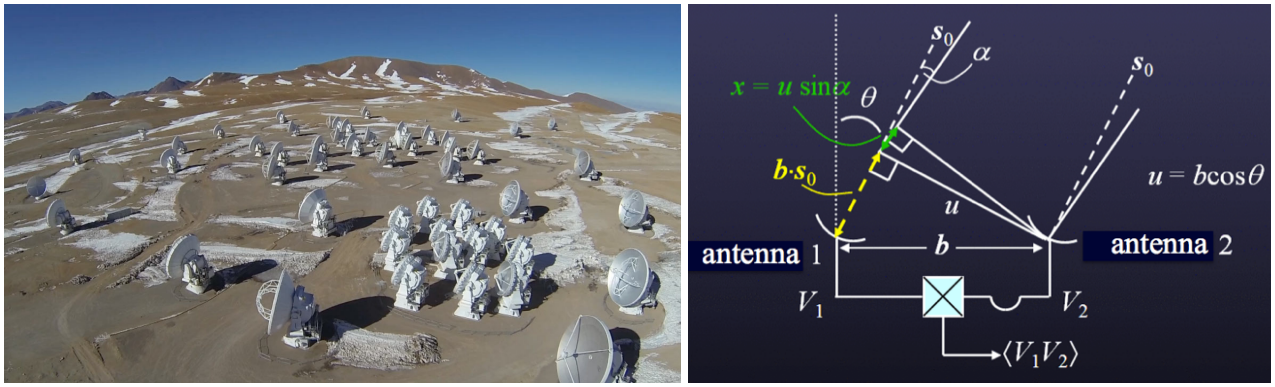

Figure II.17: *Left: The ALMA antennas on the Chajnantor plain. Right: Schematic of an 1-D two-antennas interferometer. Antennas 1 and 2 are separated by a baseline b and oriented in the direction s_0, forming and angle θ with the meridian. A point source is located at an angle α from the direction s_0. Interferometry details are given in the text.*

Table II.9: Properties of the available *ALMA* bands for the Cycle 3 (2015).

Cycle 3 Receiver Bands				Most Compact		Most extended	
Band (GHz)	Frequency (mm)	Wavelength (FOV, ″)	Primary beam (″)	Angular res. (″)	Max. Scale (″)	Angular res. (″)	Max. Scale (″)
3	84 - 116	2.6 - 3.6	73 - 53	3.8 - 2.8	21 - 22	92 - 66	1.25 - 0.91
4	125 - 163	1.8 - 2.4	49 - 38	2.6 - 2.0	20 - 15	62 - 47	0.84 - 0.65
6	211 - 275	1.1 - 1.4	29 - 22	1.5 - 1.2	12 - 9.0	36 - 28	0.50 - 0.38
7	275 - 373	0.8 - 1.1	22 - 16	1.2 - 0.86	9.0 - 6.6	48 - 36	0.64 - 0.47
8	385 - 500	0.6 - 0.8	16 - 12.0	0.84 - 0.65	6.4 - 4.9	84 - 64	2.2 - 1.7
9	602 - 720	0.4 - 0.5	10 - 8.5	0.53 - 0.45	4.1 - 3.4	53 - 45	1.4 - 1.2
10	787 - 950	0.3 - 0.4	7.8 - 6.5	0.41 - 0.34	3.1 - 2.6	41 - 34	1.1 - 0.87

Figure II.17 shows a schematic picture of an ideal 1-D interferometer with two antennas, separated by a baseline $b = L/\lambda$ in units of the observing wavelength, L being the distance between the antennas. The optical signal received by each antenna is converted into an electrical signal $V_1(t)$ and $V_2(t)$, in

volts. In the case presented in Figure II.17, both antennas are pointing toward a common sky location, s_0, oriented at a angle θ from the meridian. From the perspective of the source, the projected distance between the antennas is $u = b\,cos(\theta)$. Due to the geometrical configuration of the antennas and source, a plane wave coming from s_0 reaches antenna 1 after a delay of $\tau = b \cdot s_0/c = b\,sin(\theta)/c$, with c the speed of light, compared to antenna 2. An artificial delay equal to τ is electronically added into the signal path of antenna 2 so that the signals from both antennas arrive at the correlator with the same phase.

If there is an off-axis source, located at an angle α compared to s_0, the additional delays do not entirely compensate for the longer path length that the light has to travel to reach antenna 1. The extra path length is noted as $x = u\,sin(\alpha) = ul$ in unit of the observing wavelength, with $l = sin(\alpha)$ and results in a phase difference between V_1 and V_2. The voltage response of antenna 2 can then be written as:

$$V_2 = V_1 e^{2i\pi ul}. \tag{II.5}$$

We can generalize this to the two dimensions of the sky, introducing an angle β from the on-axis direction, in the plane perpendicular to plane of α, and $m = sin(\beta)$. We define $v = b\,cos(\phi)$ where ϕ is the angle of the position s_0 from the meridian, in the plane orthogonal to the plane of θ. Similarly to Equation II.5, the two-dimensional voltage response of antenna 2 can be written as:

$$V_2 = V_1 e^{2i\pi(ul+vm)}. \tag{II.6}$$

The signals from both antennas are multiplied and time-averaged by the correlator, resulting in an output signal:

$$\langle V_1 V_2 \rangle = \langle \iint V_1(l,m)\,dldm \iint V_2(l,m)\,dldm \rangle. \tag{II.7}$$

Assuming that signals from different parts of the sky are incoherent, Equation II.7 can be simplified as:

$$\begin{aligned} \langle V_1 V_2 \rangle &= \iint \langle V_1(l,m) V_2(l,m) \rangle\,dldm \\ \langle V_1 V_2 \rangle &= \iint \langle V_1(l,m)^2 \rangle\, e^{2i\pi(ul+vm)}\,dldm \end{aligned} \tag{II.8}$$

In addition, V^2 is proportional to the distribution of the intensity on the sky, $I(lm)$. The output of the correlator is called the complex visibility, $\mathcal{V}$, and is the Fourier transform of $I(lm)$:

$$\mathcal{V}(u,v) = \iint I(l,m)\, e^{2i\pi(ul+vm)}\,dldm. \tag{II.9}$$

As a consequence, the sky brightness distribution is also the Fourier transform of the complex visibility distribution:

$$I(l,m) = \iint \mathcal{V}(u,v)\, e^{-2i\pi(ul+vm)}\,dudv. \tag{II.10}$$

This is known as the van Cittert-Zernicke theorem.

The response of an interferometer with two antennas separated by a distance u are fringes separated by $1/u = \lambda/(L\,cos(\theta))$ in the case of Figure II.17. Hence the spatial scale seen by the interferometer at a given wavelength is proportional to the inverse of the distance between the antennas: antennas closer together measure emission on large scales while antennas further apart measure emission on smaller scales. Similarly, for a given baseline, the sampled scales are proportional to the observed wavelength. A given pair of antennas samples a single scale of the sky brightness distribution, measuring two visibilities in the uv-plane, one at (u, v) and its complex conjugate at (-u, -v). In

principle, the uv-plane should be completely sampled to recover the true sky brightness distribution. However, this is impossible, and to have a good reconstruction of the sky brightness distribution, the uv-plane has to be sampled efficiently. Then multiple antennas can be combined to form an array, with different distances and different angles from each other to avoid redundancy. An array of N antennas has $N(N-1)/2$ independent baselines, with each pair providing a single pair of samples in the uv-plane. The maximum baseline will set the resolution of the image and the minimum baseline will set the larger recoverable spatial scale in the image (Fig. II.18). The coverage of the uv-plane can be increased by taking advantage of the Earth's rotation. Although the physical distances between the antennas remain unchanged, their projected distances change depending on the altitude and azimuth of the target. The antennas can also be moved to a more compact or a more extended configuration to recover different spatial scales.

For the observations of [C I] 370 μm in band 10, for example, we used the Atacama Compact Array (ACA) to complement the 12-m array, to recover the large scales up to 5″ (~1.2 pc at the distance of the LMC), corresponding approximately to the size of the clumps we expect to see. However, this is much more time consuming. More details on this are given in Section V.4.

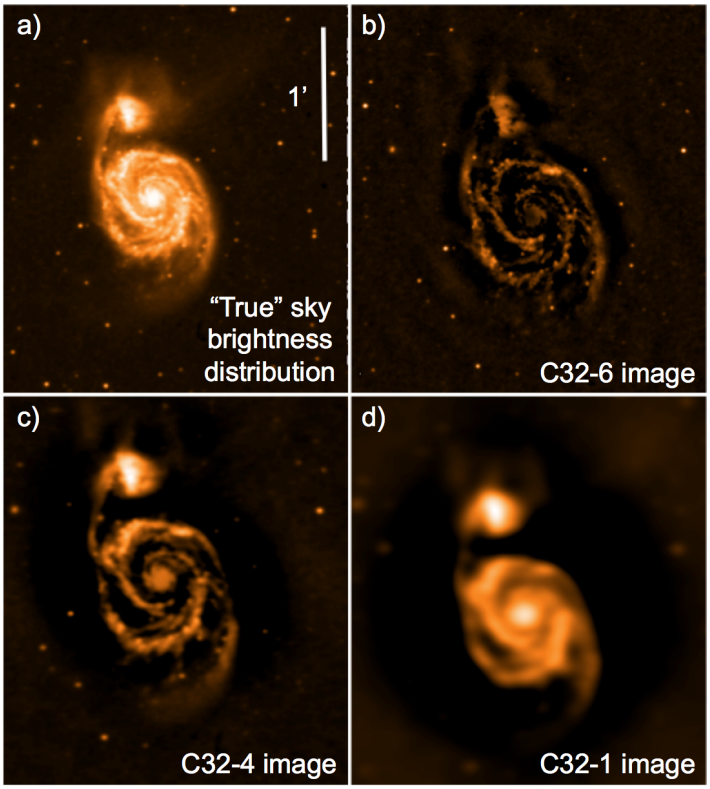

Figure II.18: *Simulation of spatial filtering for different ALMA configurations. Panel a shows an optical image of the galaxy M51. Panels b, c and d simulate the observation of M51 by ALMA , with a mosaic of 39 pointings, for three different minimum and maximum baselines of the antennas: 40.6 m and 1091.0 m for panel b (C32-6); 20.6 m and 556 m for panel c (C32-4) and 14.2 m and 81.4 m for panel d (C32-1). From ALMA Cycle 4 Technical Handbook.*

Chapter III

Modeling the interstellar medium

Contents

Modeling the ISM is a complex problem, involving many different scales, a wide range of wavelengths from the UV to the IR, and many physical processes have to be accounted for. In this chapter, we describe various existing models to explore the different ISM phases, from the modeling of the cold dust through spectral energy density (SED) fitting to the PDR models. With these models, we aim to understand better quantitatively what physical conditions can be at the origin of the observations of the interstellar medium.

III.1 Modeling the dust emission

Some fraction of the bolometric luminosity of a galaxy is absorbed by dust in the UV-optical primarily, and re-emitted in the MIR to FIR. Thus, the IR luminosity is strongly linked to the stellar population. The PDR models couple the emitted starlight intensity with the surrounding gas and dust. Therefore, the IR luminosity emitted by dust is one of the key elements to constrain the models.

III.1.1 SED modeling

The SED fitting model described in Galliano et al. (2011) is a semi-empirical model to fit the observed mid-IR to mm SEDs with a combination of realistic dust models, including very small grains (VSGs) and PAH features. At these wavelengths, most of the emission arises from large grains in equilibrium with the radiation field, and their spectrum depends only on the power they absorb (in other words, on their equilibrium temperature) and not on the details of the stellar spectrum nor their spatial distribution. This is not the case for small grains with radius $\lesssim 10\,\mathrm{nm}$, such as PAHs for example, which are out of thermal equilibrium (Draine 2003) and will be investigated separately in more details in Section III.2. The model developed by Galliano et al. (2011) can be decomposed into two steps:

1. *Focus on the microphysics.* First, the dust SED of one mass element of the ISM is modeled. It is controlled by the microscopic properties of grains and characterized by a given intensity of the radiation field.

2. *Reproducing the macrophysics.* Several mass elements, with a range of illumination conditions, are then combined to take into account the mixing of different environments in the beam.

SED of one mass element

The first step is to calculate the dust SED emitted by a single mass element of the ISM, illuminated by a uniform starlight intensity (U). We use here the spectral shape of the interstellar radiation field (ISRF) of the solar neighborhood as described by Mathis et al. (1983). This shape is likely to vary spatially throughout a galaxy like the LMC, but this will affect primarily the PAHs and the VSG spectra, and not the integrated FIR luminosity, which depends mainly on the intensity and hardness (or average temperature) of the radiation field.

The calculation of the shape of the dust SED for one mass element is based on the grain properties of the ISM. It depends on the composition of the grains (silicate, graphite, amorphous carbon...), on the elemental depletion onto grains, and on the size distribution for each type of grains. Several models for the dust compositions can be examined. We adopt here the "AC model" from Galliano et al. (2011), which is adapted from the standard model of Zubko et al. (2004). The model presented by Zubko et al. (2004) consists of a galactic grain composition made of PAHs (with updated optical properties from Draine & Li 2007), graphite and silicates. The size distribution for the different types

of grains is represented in Figure III.1. In the "AC model", the graphite in the standard model of the Milky Way is replaced by amorphous carbon. It is more adapted for the regions we model here, as the standard composition of grains fail to give physically realistic results for the LMC (Galliano et al. 2011).

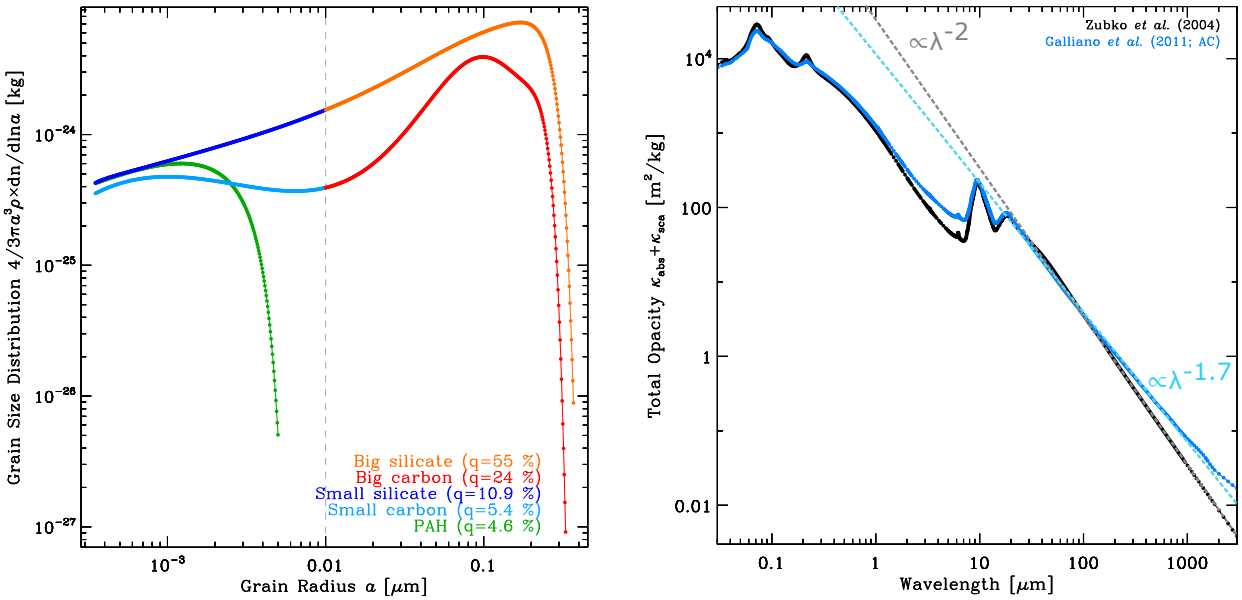

Figure III.1: *Left: size distribution for the different types of grains from the Zubko et al. (2004) model. Silicates are in dark blue and orange, carbon (in the form of amorphous for the LMC) in cyan and red and PAHs in green. The mass fraction of each component, q, is indicated. Right: total dust opacities as a function of wavelength for different dust compositions, which result in different dust opacities: the standard galactic dust model of Zubko et al. (2004) in black and a modified composition where graphite has been replaced by amorphous carbon (the "AC" model; Galliano et al. 2011) in blue. The resulting emissivities show a flatter slope in the submm for amorphous carbon ($\beta \propto \lambda^{-1.7}$, in blue) while the graphite has an emissivity index of -2 (in black)*

For each type and size of grain, and for a range of incident flux intensities, the temperature distribution, $p(T)$, of each grain is calculated by the method of Guhathakurta & Draine (1989), according to its cross section and heat capacity. Each grain emits a luminosity defined as:

$$L_\nu(\lambda) = \kappa_{abs}(a,\lambda) \int 4\pi B_\nu(T,\lambda) \frac{dp(T)}{dT} dT, \tag{III.1}$$

where $\kappa_{abs}(a,\lambda)$ is the opacity (in m^2 kg^{-1}) of a grain of radius a, which can be approximated at long wavelength by $\kappa_{abs}(a,\lambda_0)\left(\frac{\lambda}{\lambda_0}\right)^{-\beta}$ with β the emissivity index. The "AC model" results in a higher effective submm opacity ($\beta \approx 1.7$) compared to the standard model of Zubko et al. (2004) ($\beta \approx 2$). For the big grains ($a \gtrsim 0.01$ μm), $p(T)$ becomes close to a Dirac delta function and they are in equilibrium with the radiation field. We then combine the emission of all types of grains according to the dust composition and size distribution to have the uniformly illuminated templates of SED per mass unit for a range of U (see Figure III.2).

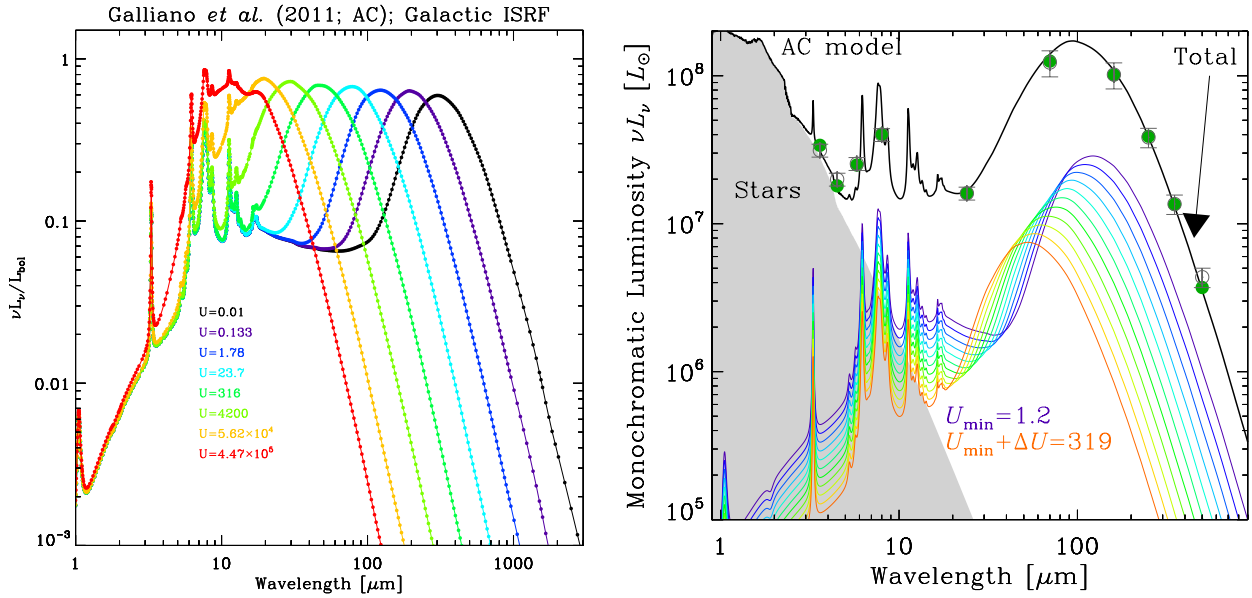

Figure III.2: *Left: uniformly illuminated SED templates, heated by the Mathis et al. (1983) ISRF for a range of starlight intensities (U). Right: decomposition of the SED of the LMC into a set of individual uniformly illuminated SEDs (from Galliano et al. 2011). Green points are Spitzer and Herschel fluxes from Meixner et al. (2006) and Meixner et al. (2010). The total model (in black) is the sum of the stellar component (grey filled area) and of the integral of a set of uniformly illuminated SEDs (in colors) characterized by* $U_{min} = 1.2$ *and* $U_{min} + \Delta U = 319$ *(in units of* $2.2 \times 10^{-5}\ W\,m^{-2}$*).*

Multiple SED components

For extragalactic environments in particular, we know that we are susceptible to mixing a range of environments and physical conditions in the beam for a given line of sight. Then we do not probe a single dust composition nor a single starlight intensity. In general, we have no information on the dust composition, so it is assumed to be homogeneous. We make the assumption that the distribution of the starlight intensity (U) per dust mass follows the empirical power law prescription by Dale et al. (2001):

$$\frac{dM_{dust}}{dU} \propto U^{-\alpha} \text{ with } U_{min} \lesssim U \lesssim U_{min} + \Delta U. \tag{III.2}$$

The parameters α, U_{min} and ΔU are determined by minimizing the χ^2 between the observations and the total modeled luminosity as in the example presented in Figure III.2 for the LMC. The other free parameters that are fitted by the model are the total dust mass M_{dust}, the fraction of PAHs f_{PAH}, the proportion of ionized PAHs f^+_{PAH} and f^-_{PAH} along with the stellar continuum at short wavelengths. The IR intensity is the integration of the resulting SED in a given wavelength range.

III.1.2 L_{TIR}/L_{FIR}

For the regions of the Magellanic Clouds we are studying here, the dust SED model is constrained by the IRAC bands at 3.6, 4.5, 5.8 and 8.0 μm, MIPS 24 and 70 μm and PACS 100 and 160 μm bands. MIPS 160 μm and SPIRE 250, 350 and 500 μm bands, at poorer resolutions, are not used to constrain the SED model for this study, to take advantage of the highest spatial resolution possible. All of the photometric observations are convolved to the same resolution, at $\approx 12''$, corresponding

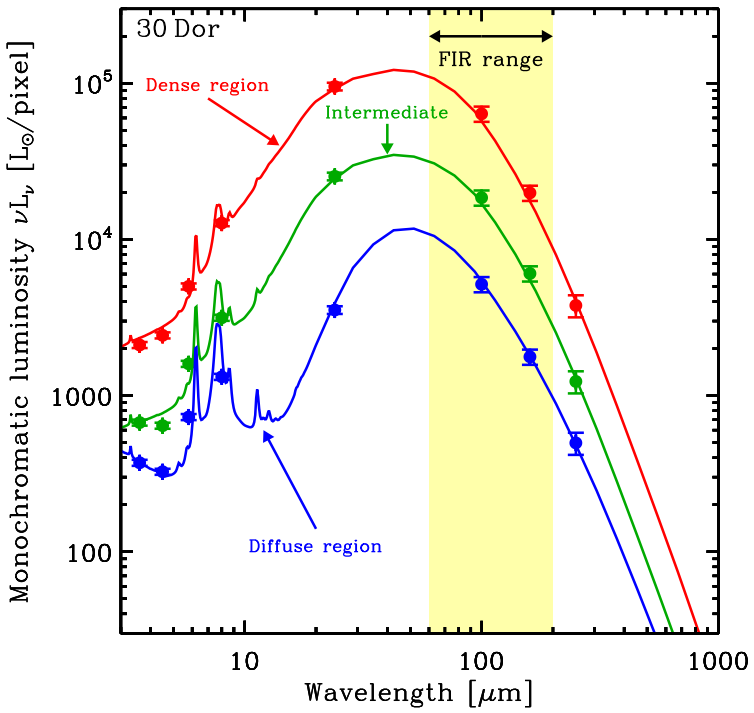

Figure III.3: *Examples of three SED modeling (solid lines) fitting the data points from the observations for three different pixels in the 30 Doradus map. A dense region (red), a diffuse region (blue) and an region at intermediate density (green) are represented. The integration wavelength range for L_{FIR} from 60 μm to 200 μm is delineated with a yellow band.*

to the angular resolution of the PACS [C II] map and similar to the resolution of the PACS 160 μm photometric observations. To do this, we use the convolution kernels developed by Gordon et al. (2008)[1].

For the PDR modeling, we are interested in the infrared luminosity, which is only marginally dependent on the precise dust SED model used, contrary to the other dust parameters. It mainly depends on the wavelength coverage and since the SED peaks at T $\lesssim$ 100 μm (see the example of 30 Doradus in Figure III.3), the fit is relatively well constrained with the above observations. Indeed, since the submm wavelengths have little effect on the infrared luminosity, we prefer to favor the spatial resolution given by the observations up to 160 μm and we do not include the SPIRE bands. The fit of the SED is then integrated between 3 μm and 1000 μm to calculate the total infrared luminosity (L_{TIR}) or between 60 μm and 200 μm to calculate the far-infrared luminosity (L_{FIR}). The advantage of using L_{FIR} compared to L_{TIR} is that the SED fit is better constrained and has less uncertainties in this limited wavelength compared to the fit including longer wavelengths, since we do not include data longward 160 μm. We will use L_{FIR} for the PDR modeling, but we compute L_{TIR} as well, for comparison with the literature.

[1]Convolution kernels which convert a higher resolution *Spitzer* (IRAC/MIPS) or *Herschel* (PACS/SPIRE) PSF to lower resolution PSF are available at: http://dirty.as.arizona.edu/~kgordon/mips/conv_psfs/conv_psfs.html

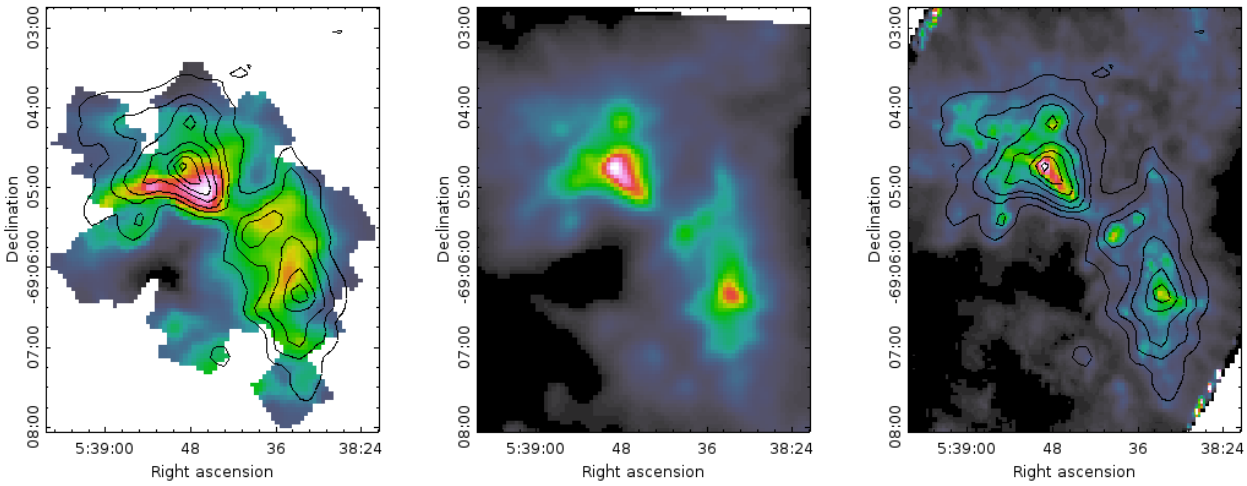

Figure III.4: *Comparison of the spatial distribution of a tracer of ionized gas, [O III] 88 µm (left), L_{FIR} (center) and a tracer of the neutral gas, PAHs (right) in the region of 30 Doradus. The contours of L_{FIR} are over-plotted in black on the [O III] and the PAHs maps.*

III.1.3 L_{FIR} associated with the PDRs only: L_{FIR}^{PDR}

As described in Section I.3.1 a fraction of L_{FIR} can be emitted from the grains in the ionized gas (both big grains in equilibrium with the ISRF and small warmer grains stochastically heated), and not only from the dust and PAHs in the PDRs. However, in Chapter IV we will model in particular the neutral atomic gas in the PDRs in the 30 Doradus nebula, which is a very active star forming region and where the gas is highly ionized over a large area. We then need to decompose L_{FIR} between an ionized gas component, and a component arising only from the PDRs to use L_{FIR} in the model.

The spatial distribution of L_{FIR} shows some features similar to the emission of the neutral atomic gas tracers ([O I], [C II], PAHs) and other features which seem to be spatially associated with ionized gas tracers ([O III], H_α, [S III]) as noted in Figure III.4 in the case of the 30 Doradus nebula. This supports the need to decompose L_{FIR} into a component from the neutral gas, L_{FIR}^{PDR}, and a component from the ionized gas, L_{FIR}^{IG}. In order to separate the emission from these two components, we assume that the PAH emission is a good proxy for the PDRs, following Tielens & Hollenbach (1993) and Sellgren et al. (1990), and that [O III] traces the ionized phase. We assume a linear relation such as:

$$L_{FIR} = L_{FIR}^{PDR} + L_{FIR}^{IG} = \alpha \times L_{PAH} + \beta \times L_{[O\,III]}. \quad \text{(III.3)}$$

For a given region, the pair of $(\alpha\,;\beta)$ values is calculated using a multiple linear regression using all of the pixels in the map. This decomposition implicitly assumes that the PAH-to-dust mass fraction is constant in PDRs and zero in H II regions. With this method, we are seeking a first order correction of the total L_{FIR} to be able to use it for the PDR modeling. The modeled L_{FIR} reproduces the observed L_{FIR} within 30% on average. We use this value to estimate the uncertainties on L_{FIR}^{PDR} for the PDR modeling. Other combinations of tracers were tested, using [C II] for the PDRs and H_α for the ionized gas for example, leading to similar values of L_{FIR}^{PDR} and L_{FIR}^{IG}.

III.2 PAHs

PAH emission, described in more details in Section I.3.2, is mostly concentrated in a few aromatic bands, and as such is not crucial to model accurately to have a good estimate of L_{FIR} needed for our

PDR modeling. However, PAHs play an important role in the photoelectric heating of the gas by providing photoelectrons (e.g.,Tielens & Hollenbach 1985; Bakes & Tielens 1994). Besides, PAHs are known to be destroyed in H II regions (e.g. Engelbracht et al. 2005; Madden et al. 2006), and even more dramatically in the porous low-metallicity medium of dwarf galaxies. Their efficiency in tracing the heating of the gas is investigated in the 30 Doradus region in Section IV.1.3. The spectrum of these grains depends on the hardness of the radiation field. They are stochastically heated, so the SED model described above will not be perfectly accurate for their detailed emission spectra. Different methods exist to measure the luminosity of the PAHs (L_{PAH}). We investigate two of them here. They are applied to the region of 30 Doradus and the results are compared in Section IV.1.3.

III.2.1 IRS spectra

The IRS spectrum, between 5 and 40 μm, contains PAH features, ionic lines, H_2 lines, and continuum from dust emission and stellar emission. We use the Mid-Infrared Line Extraction Software (MILES) to fit all of these components first individually and then simultaneously to have an accurate estimate of L_{PAH}. The atomic and molecular lines, unresolved, are first fitted one by one, assuming a Gaussian profile and a second order polynomial baseline:

$$F_\nu^{\text{line}}(\nu;i) = \frac{I_{\text{line}}(i)}{\sqrt{(2)}\pi\sigma(i)} \times \exp^{-\frac{(\nu-\nu_0(i))^2}{2\sigma(i)^2}} + a(i) \times \left[1 + b(i)\left(\frac{\nu}{\nu_0(i)} - 1\right) + c(i)\left(\frac{\nu}{\nu_0(i)} - 1\right)^2\right] \tag{III.4}$$

where the integrated line intensity, $I_{\text{line}}(i)$ and the three baseline parameters, $a(i)$, $b(i)$, $c(i)$ are allowed to vary. The line central frequency, $\nu_0(i)$, is fixed, as well as the line width, $\sigma(i)$ (fixed to the instrumental resolution) in this case.
Then, the dust continuum, the PAH emission bands and the stellar continuum are fitted simultaneously. The dust grain continuum is a linear combination of N_{grain} modified blackbodies with temperatures $T(i)$ and masses $M(i)$ are free to vary:

$$F_\nu^{\text{grain}}(\nu;i) = \frac{M(i)}{d^2}\frac{3}{4\rho(i)}\left(\frac{Q_{\text{abs}}(\nu;i)}{a}\right)B_\nu(T(i);\nu). \tag{III.5}$$

For 30 Doradus, two types of grains are taken into account, amorphous carbon and silicate, and realistic opacities $Q_{\text{abs}}(\nu;i)$ and specific volumes $\rho(i)$ are considered (Rouleau & Martin 1991; Jäger et al. 2003, respectively).
The stellar continuum, $F_\nu^\star(\nu)$ is modeled by a single starburst with PÉGASE (Fioc & Rocca-Volmerange 1997) at 5Gyr. However, the exact parameters are not critical, since we only fit the Rayleigh-Jeans slope longward of 5 μm.
The PAH emission bands are modeled with asymmetric Lorentzian profiles:

$$F_\nu^{\text{band}}(\nu) = I_{\text{band}}(i) \times \begin{cases} \dfrac{2}{1+\Delta\nu_{\text{long}}(i)/\Delta\nu_{\text{short}}(i)} \dfrac{\Delta\nu_{\text{short}}(i)}{\pi} \dfrac{1}{(\nu-\nu_0(i))^2+\Delta\nu_{\text{short}}^2(i)} \\ \dfrac{2}{1+\Delta\nu_{\text{long}}(i)/\Delta\nu_{\text{short}}(i)} \dfrac{\Delta\nu_{\text{long}}(i)}{\pi} \dfrac{1}{(\nu-\nu_0(i))^2+\Delta\nu_{\text{long}}^2(i)} \end{cases} \tag{III.6}$$

Each band in the 5-20 μm range (32 in total) is calibrated and the line profile ($\nu_0(i)$, $\Delta\nu_{\text{short}}(i)$, $\Delta\nu_{\text{long}}(i)$) is fixed. The only free parameter is the intensity of each band, $I_{\text{band}}(i)$.

The total model is defined as:

$$F_\nu^{\rm model}(\nu) = \left(F_\nu^\star(\nu) + \sum_{i=1}^{N_{\rm grain}} F_\nu^{\rm grain}(\nu;i) + \sum_{i=1}^{N_{\rm band}} F_\nu^{\rm band}(\nu;i) \right) \times P_{abs}(\nu) + \sum_{i=1}^{N_{\rm line}} F_\nu^{\rm line}(\nu;i). \quad \text{(III.7)}$$

The observed spectrum is then fitted with the complete model, using a minimum χ^2 method. Figure III.5 presents an example of the spectral decomposition for one pixel of the 30 Doradus map.

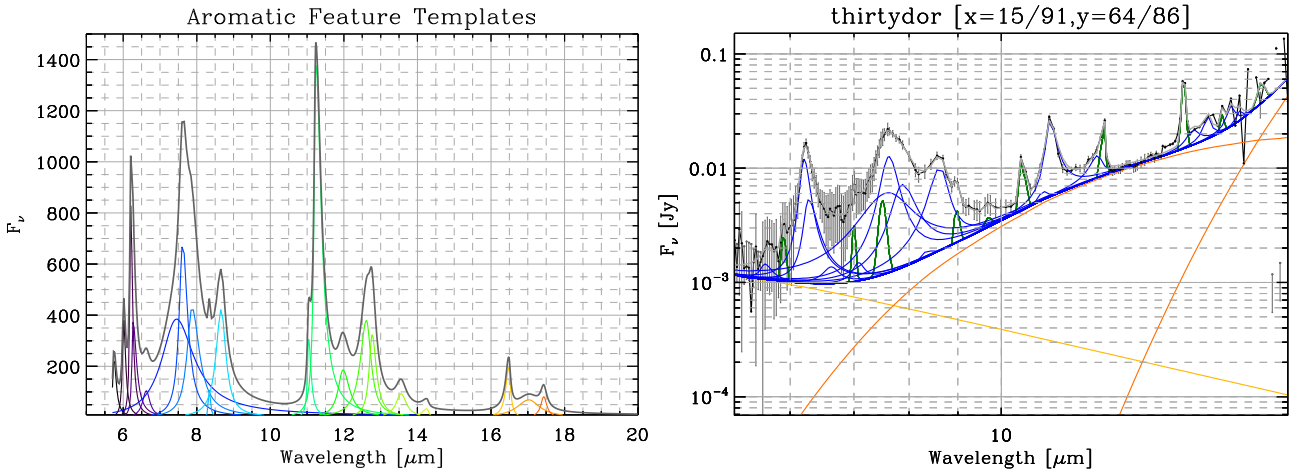

Figure III.5: *Left: calibrated profiles of the PAH emission features between 5 and 20 μm. Right: example of the spectral decomposition of an SED in 30Doradus. The observed IRS spectrum is in black. In blue are the PAH emission features, in green the atomic and ionized lines. The stellar continuum is represented in yellow and the modified blackbodies for the dust continuum in orange.*

The package PAHFIT (Smith et al. 2007), used by Indebetouw et al. (2009) for 30 Doradus for example, derives the PAH emission and the gas line with a method similar to that described here. However, for the weaker aromatic bands, some of which are not taken into account in PAHFIT, this method can be more accurate.

III.2.2 IRAC bands

The method described above, using the *Spitzer*/IRS observations, gives accurate results for quantifying the PAH emission. However, most of the LMC and SMC sources we are studying do not have IRS spectroscopy, but do have IRAC photometry. We determine a recipe to go from IRAC bands to PAHS, and then verify this recipe on 30Dor, where we have both IRS and IRAC photometry. We could then use this recipe to quantity the PAH emission from the IRAC bands for our other sources which have no IRS spectra.

This method uses the *Spitzer*/IRAC bands to calculate the total PAH emission from IRAC channel 3 or 4, following the approach of Lebouteiller et al. (2012) in the region N11 of the LMC. All four IRAC bands can contain both stellar and dust continuum emission, in various proportions. In addition, channels 1, 3 and 4 can have PAH features, although the 3.3 μm PAH band in channel 1 is much fainter than those in channels 3 and 4. Therefore, to estimate $L_{\rm PAH}$ from the IRAC bands, we assume that channel 3, centered at 5.0 μm, is dominated by the PAH band at 6.2 μm and dust continuum, and that

channel 4, centered at 8.0 μm, observes the PAH complex at 7.7 μm and 8.6 μm along with warm dust continuum. In addition, we assume that despite the possible presence of the faint PAH band at 3.3 μm, channel 1, centered on 3.6 μm, is mostly stellar and dust continuum and channel 2, centered at 4.5 μm, mostly dust continuum. These approximations are validated, in the region of 30 Doradus, by the comparison of L_{PAH} from the IRS spectra and the IRAC bands presented in Section IV.1.3.

All of the four IRAC bands are convolved to the resolution of channel 4 (~1.9″) using the convolution kernels calculated by Gordon et al. (2008). The pixels with a significant stellar contribution are masked. This is determined empirically based on the relative fluxes in the 2MASS-J band (1.25 μm), 2MASS-K band (2.17 μm), IRAC channel 1 and IRAC channel 2. Where the fluxes in the different bands are such that 2MASS-J band > 2MASS-K band > IRAC channel 1 > IRAC channel 2 and where the fluxes in channel 1 and channel 2 are higher than 20 RMS, the pixels are flagged as stars (this represents less that 1% of the pixels of our 30 Doradus map, for example). These are rather conservative criteria and in the remaining pixels, the fluxes in IRAC channels 1 and 2 are assumed to be dominated by dust emission.

The dust continuum emission can be approximated by fitting a power-law to IRAC channels 1 and 2 measurements, and thus extrapolated to estimate the dust continuum contribution to channels 3 and 4, assuming the possible stellar continuum in IRAC 1 and IRAC 2 is negligible. It would require using a proper stellar population model to correct for the stellar continuum and this would add additional uncertainties. Once the dust continuum emission is subtracted, we make the assumption that the remaining IRAC flux is only from PAH emission. This is justified, since, although some lines can be present in these wavelength ranges (e.g. [Ar II] 6.9 μm, [Ar III] 8.9 μm, [S IV] 10.5 μm, [Ne II] 12.8 μm, [Ne III] 15.6 μm, [S III] 18.7 μm), they are normally faint. From IRAC 3 we get a very good approximation of the PAH band at 6.2 μm. The estimation of the PAH bands at 7.7 and 8.6 μm is more uncertain since the underlying dust emission has to be extrapolated at higher wavelength.

To estimate the contribution of the PAH bands in IRAC 3 and IRAC 4, respectively, to the total PAH emission between ~5-14 μm (the PAH band at 3.3 μm is not included), we assume a MIR spectral PAH profile such as that seen in a starburst galaxy (Brandl et al. 2006). This is a relatively high S/N spectrum constructed based on the IRS spectra of 13 starburst galaxies. We subtract the brightest line emission as well as the dust continuum from the starburst template and estimate the fraction of the total PAH emission in the wavelength range 5-14 μm to ~ 10% in channel 3 and ~ 45% in channel 4 (Figure III.6). These numbers are highly dependent on the PAH template used, as PAH band ratios are expected to change in different environments. Indeed, as developed in more details in Section I.3.2, the bands at 6.2 μm, 7.7 μm and 8.6 μm, in particular, are emitted from different PAHs, under different excitation mechanisms. However it appears that the band ratios do not vary much in a given region (note, in particular, that the ratios ([C II]+ [O I] 145 μm)/L_{PAH} do not show large dispersion in 30 Doradus; see Section IV.1.3) so the absolute calibration is the main issue here. Since we have also modeled the PAH emission from the IRS spectrum in 30 Doradus, we were able there to adjust slightly the contribution of IRAC 3 and IRAC 4 to the total PAH emission to calibrate the L_{PAH} from the first method.

III.3 PDR modeling

Observations of gas line intensities reflect the physical conditions of the gas where they were emitted, but are also affected by the ISM along the line of sight. To model the line emission properly, it is then important to take into account the local processes taking place in the emitting clouds.

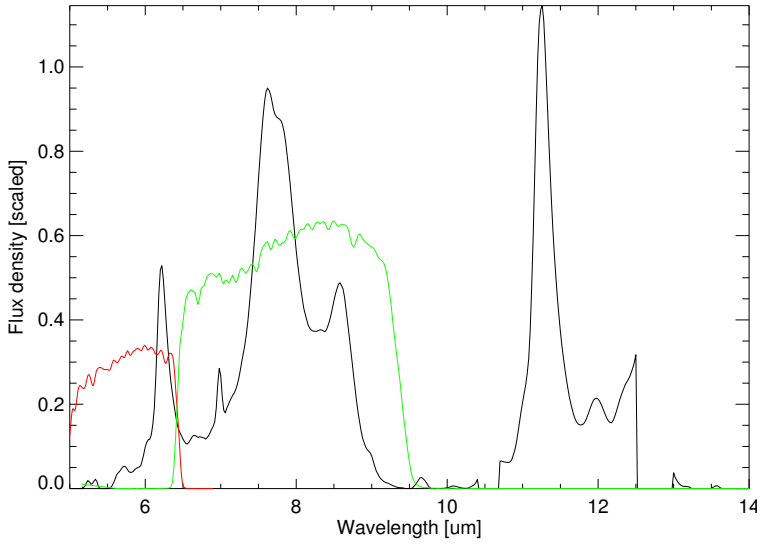

Figure III.6: *In black is the starburst template computed by Brandl et al. (2006), where the dust continuum and the bright line emission have been subtracted. The spectral responses of IRAC channels 3 and 4 are represented in red and green respectively.*

III.3.1 Radiative transfer notions

The propagation of light in an absorbing and emitting medium is described by the radiative transfer theory. When a radiation beam with intensity I_ν interacts with matter, several processes take place: absorption, emission and scattering. Absorption is characterized by a coefficient α_ν (in cm^{-1}) taking into account the gas and dust absorption and stimulated emission. Emission, noted ϵ_ν, is due to potential internal UV sources, and to spontaneous emission of gas and dust. The scattering coefficient is σ_ν (in cm^{-1}). The radiative transfer equation along the direction of propagation, measured by the optical path length, s, is then written as:

$$\frac{dI_\nu}{ds} = -(\alpha_\nu + \sigma_\nu)I_\nu + \epsilon_\nu + \sigma_\nu J_\nu, \tag{III.8}$$

where $J_\nu = \frac{1}{4\pi}\int I_\nu d\Omega$ is the mean intensity averaged over 4π steradian (sr).

Ignoring the scattering ($\sigma_\nu = 0$), it is convenient to define the source function, $S_\nu = \dfrac{\epsilon_\nu}{\alpha_\nu}$, and the optical depth measured along the path of a traveling ray, $d\tau_\nu = \alpha_\nu ds$. When integrated along a typical path through the medium, if $\tau_\nu < 1$, the medium is characterized as *optically thin*, or transparent; if $\tau_\nu > 1$, the medium is said to be *optically thick*, or opaque. With these notations, the solution to Equation III.8 can be written as:

$$I_\nu(\tau_\nu) = I_\nu(0)\,e^{-\tau_\nu} + \int_0^{\tau_\nu} e^{-(\tau_\nu - \tau')} S_\nu d\tau' \tag{III.9}$$

In the case of absorption and emission between a lower level (l) and an upper level (u) of randomly oriented emitters, the emissivity and the absorption coefficient are linked to the Einstein coefficients of spontaneous emission, A_{ul}, and stimulated emission and absorption, B_{ul} and B_{lu}:

$$\begin{aligned}\epsilon_\nu &= \frac{1}{4\pi} n_u A_{ul} h\nu \phi_\nu \\ \alpha_\nu &= \frac{1}{4\pi}(n_l B_{lu} - n_u B_{ul}) h\nu \phi_\nu,\end{aligned}$$

where n_l and n_u are the density of the lower and upper levels respectively. The line profile, ϕ_ν is assumed to be the same for absorption and emission. Hence, the source function, S_ν, can be expressed as:

$$S_\nu = \frac{n_u A_{ul}}{n_l B_{lu} - n_u B_{ul}}. \tag{III.10}$$

There is a coupling between the radiative transfer and the thermal balance, which determines the population of the excited levels. In a steady-state regime, for a two-level system with levels l and u, $\frac{dn_l}{dt} = \frac{dn_u}{dt} = 0$. The population of level u through collisional and radiative processes is balanced by the depopulation of level l. The statistical equilibrium equations can be written as:

$$n_u (B_{ul} \bar{J} + C_{ul}) = n_l (B_{lu} \bar{J} + A_{lu} + C_{lu}), \tag{III.11}$$

with $\bar{J} = \int J_\nu \phi_\nu d\nu$. C_{ul} and C_{lu} are the collisional coefficients. This simple case of a two-level system can be generalized to a more complex system where all excitation processes balance all de-excitation processes.

Approximation of LTE

In a cold and diffuse gas as it is often the case in astrophysics, thermal equilibrium between the matter and the radiation field does not usually takes place. However, a common approximation is to assume Local Thermal Equilibrium (LTE), in which case the matter is assumed to have thermodynamic equilibrium properties (not necessarily with the radiation) at the local temperature and density. In this case, the statistical distribution of particles in a two-level system is described by the Boltzmann distribution:

$$\frac{n_u}{n_l} = \frac{g_u}{g_l} e^{-h\nu_{ul}/kT_{ex}}, \tag{III.12}$$

thus defining the excitation temperature T_{ex}. The constants h and k are respectively the Planck constant and the Boltzmann constant; g_u and g_l are the degeneracies of the upper and lower levels. Moreover, there exist relations between the Einstein coefficients:

$$\begin{aligned} g_u B_{ul} &= g_l B_{lu} \\ A_{lu} &= \frac{8\pi h\nu^3}{c^3} B_{lu}. \end{aligned}$$

Combining Equation III.10 with Equation III.12 and the Einstein relations, we find:

$$S_\nu = B_\nu(T), \quad \text{with} \quad B_\nu(T) = \frac{2h\nu^3}{c^2} \frac{1}{e^{\frac{h\nu}{kT}} - 1}. \tag{III.13}$$

$B_\nu(T)$ is the Planck function describing the radiation field emitted by a black-body at the temperature T. In the LTE approximation, the solution to the radiative transfer equation depends only on the temperature profile and the density profile.

The LTE approximation is equivalent to assuming that the excitation temperature, T_{ex}, is equal to the kinetic temperature, T_{kin}, which measures the speed of the particles, following the Maxwell-Boltzman distribution. Hence, LTE can be a good approximation at high densities, where collisional excitations and de-excitation dominate. However, it is a strong assumption and does not produce accurate results in many environments.

III.3.2 Generalities and state of the art

The goal of a PDR model is to compute the structure and the physical conditions of the ISM. To do that, it requires calculating locally all of the physical properties of a cloud: pressure of the gas, temperature of the gas and dust, grain properties, relative abundances of the gas constituents along with their level population, etc. All of these properties depend in particular on the local radiation field, which is responsible for photo-chemical reactions, gas and dust heating, excitation of molecules, and thus are varying with the position in the cloud and the absorption along the line of sight between the edge of the cloud and this position. Computation of the structure of a cloud is typically done by solving the equations of the chemical equilibrium, the equations of the thermal equilibrium, and the UV radiative transfer. For a spatially finite model, this has to be done in an iterative way. Indeed all of these equations are coupled by multiple processes, as represented in Figure III.7.

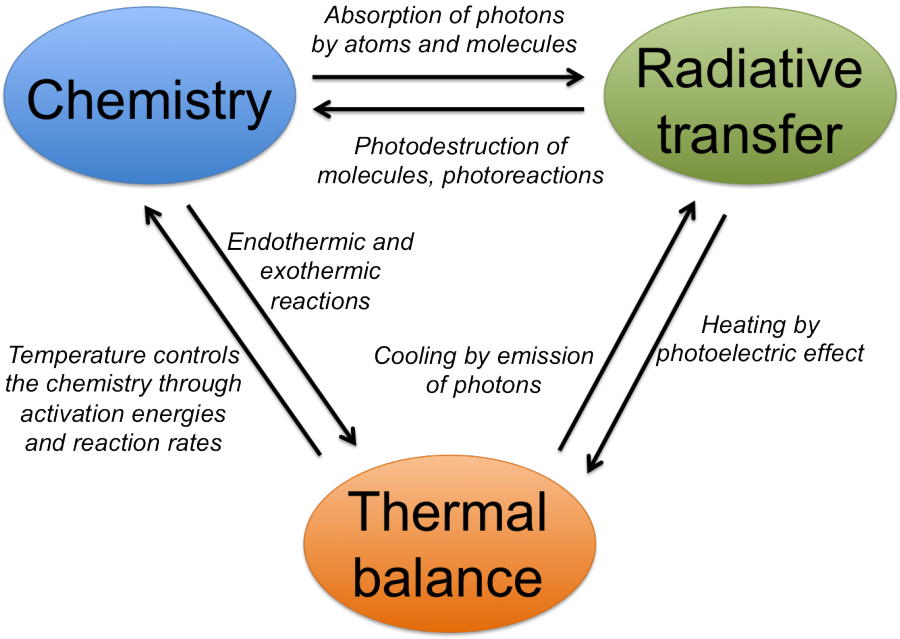

Figure III.7: *In the ISM, chemistry, radiative transfer and thermal balance are coupled through different processes. This is why the PDR code has to solve for the structure of the gas in an iterative way.*

The first PDR models were developed in the early 1970's (e.g. Hollenbach & Salpeter 1971) to examine in particular the transitions from H to H_2 and from C^+ to CO. From then, many models have been developed, some focussing more on some aspects of the chemistry or the physics, with various geometries, etc. The majority of these models have a steady state approach. Röllig et al. (2007) presented a detailed comparison of several existing PDR models to understand the differences between the results of the different codes and identify the limits of applicability for each of them.

III.3.3 Description and method of the Meudon PDR code

The Meudon PDR code considers a 1D stationary plane-parallel slab of gas and dust illuminated by an isotropic radiation field (from UV to radio) arising from one or both sides. The radiative transfer of the incident radiation field is first calculated throughout the cloud, making assumptions on the abundances and temperatures, and taking into account absorption by gas and dust and scattering and

emission by dust. Then, at a given location into the cloud, the local radiation field, I_ν, is known and the code solves the chemistry and the thermodynamic equilibrium alternatively until convergence. As radiative transfer depends on the thermal balance and chemistry, a second level iteration is needed. A constant hydrogen density, n_H or a constant pressure $P = n_H \times T$ can be assumed. In the isobaric case, the temperature is calculated, then the density is adjusted to maintain a constant pressure, and an additional iteration is made.

The version 1.4 of the Meudon PDR code is available at http://pdr.obspm.fr/PDRcode.html. Most of the description of the recent versions of the code has been done by Le Petit et al. (2006); Le Bourlot et al. (2012); Bron et al. (2014). We present here a summary of the treatment of the various processes taken into account by the code, including the specific characteristics of the development version 1.6.0 that we use for the modeling of the LMC regions. The updates of this version include in particular the computation of X-ray radiative transfer and the impact on the chemistry and thermal balance of the cloud (Godard et al. in prep).

Radiative Transfer

The incident radiation field is one of the elements impacting the radiative transfer results. The intensity of the incident FUV field is usually normalized to the value of the integrated ISRF between 912 and 2400 Å (corresponding to 6 to 13.6 eV, the energy range of the photons dominating the chemistry and thermal balance in the PDRs). The value measured by Habing in 1968 and equal to 5.60×10^{-14} erg cm^{-3} (Habing 1968) is often taken as a reference (in the PDR Toolbox for example). More recent values were calculated by Draine (1978; 1.046×10^{-14} erg cm^{-3}) or Mathis et al. (1983; 6.82×10^{-14} erg cm^{-3}; used in the Meudon PDR code). These are averaged values over 4π, for an isotropic field. The intensity of the incident radiation field interacting with the simulated cloud is a scaling of the ISRF, by a factor of G_{UV} (also noted G_0 or χ in other studies). The shape of the FUV field is also an important factor, controlling the hardness of the incident radiation field.

The incident radiation field is affected by several processes as described in Section III.3.1. *Continuum absorption* is due to both dust and gas. In the Meudon PDR code, as well as many other PDR codes, absorption by dust is directly calculated from the observed extinction curve for a given object, using the analytical fits of Fitzpatrick & Massa (1986, 1988, 1990).

Scattering by dust is included by taking into account a scattering coefficient, σ_λ, as well as an angular redistribution function. With this method, back scattering of photons by dust is well treated by the Meudon PDR code and it increases significantly the photodissociation rate of H_2 at the surface of the cloud compared to calculations with pure forward scattering (Röllig et al. 2007).

Gas line absorption depends on the populations of all of the different quantum states considered. The contribution of the absorption line from lower level l to upper level u to opacity at wavelength λ can be expressed as:

$$\alpha_{l \to u} = n_l B_{lu} H(\lambda), \tag{III.14}$$

where n_l is the density of the lower level population, B_{lu} is the Einstein coefficient and H the Voigt profile (Le Petit et al. 2006). This coefficient is calculated for every H_2 line ($\approx$ 20 000 for the Lyman lines and $\approx$ 10 000 for the Werner lines). Although it was not done for our models, it can also be calculated for CO and its isotopes.

For the *emission*, no UV source function is included. At UV wavelengths the radiative transfer considers only scattering or absorption followed by emission. Radiative transfer of (IR) dust emission and line emission is done consistently.

Chemical reactions

Two-body reactions in the gas phase and on grains are mainly considered. In the models we used for the LMC regions, the only process taking place on grains is the formation of H_2, although many more reactions on grains and ices can be taken into account in the Meudon PDR code. The goal here is to determine the abundance of each specie by taking into account the different formation and destruction processes. For each specie X, assuming a stationary state, solving the chemical balance results in solving:

$$\frac{dn(X)}{dt} = F_X - D_X = 0, \tag{III.15}$$

where F_X is the formation rate and D_X the destruction rate. F_X and D_X are combinations of the reaction rates of each reaction of formation and destruction involving specie X. Consequently, they depend on the temperature through the reaction rates. Thus an initial temperature is assumed, and iterations are done with the thermal balance. For a simple two-body reaction such as A + B $\rightarrow$ C + D, the reaction rate, k, is given by the generalized Arrhenius law, including a temperature dependent factor $\left(\frac{T}{300}\right)^{\beta}$:

$$k = \alpha \left(\frac{T}{300}\right)^{\beta} e^{-E_a/T}. \tag{III.16}$$

The values of α, β and E_a (activation energy) are determined theoretically or experimentally and available through data bases such as KIDA, for example (http://kida.obs.u-bordeaux1.fr/).

Formation of H_2. In the ISM, formation of H_2 through direct association of two H atoms is very inefficient. Indeed, this reaction generates ~ 4.5 eV so the molecule is created in its excited state $H_2^\star$. $H_2^\star$ cannot be de-excited easily to form H_2 because it is a symmetric molecule without a dipolar moment. Moreover, a three-body process, where the third body could remove the excess energy, is very rare. This is why H_2 is mainly formed on grains, and not in the gas phase. In one of the possible mechanisms (called Langsmuir-Hinshelwood mechanism), two H atoms are fixed on a grain physically, with Van der Waals bonds of low energy. This is called physisorption, the atoms are adsorbed on the grain surface but mobile. They then migrate from one site to another, forming an H_2 molecule when two H atoms meet and leave the surface. The efficiency of H_2 formation on grains was determined by laboratory experiments to be maximum for grain temperatures between ~ 7 K and 20 K approximately (Pirronello et al. 1999). Below 7 K, the grain is too cold and the atoms are frozen at the surface and they can not migrate. Above 20 K the grain is too warm and H atoms leave the surface before forming H_2. This mechanism is only efficient for big grains ($> 0.01\,\mu$m; Habart et al. 2004), which can carry a large fraction of physisorbed H atoms. However, observations from ISO and *Spitzer* (e.g. Habart et al. 2004, 2011) have shown that H_2 is present where grains are 20-30 K. Modifications of this mechanism, taking into account the grain surface irregularities, for example, (Chang et al. 2005; Cuppen & Herbst 2005) have been proposed to extend the range of efficient formation.

A second mechanism (called Eley-Rideal mechanism) was then investigated, as an alternative H_2 formation process, in particular at the edge of the PDR (Duley 1996; Habart et al. 2004; Bachellerie et al. 2009; Le Bourlot et al. 2012). Instead of physisorption, H atoms could be fixed on the grain by chemisorption. This implies higher energy bonds and the H atoms cannot move on the surface anymore, but another H atom from the gas phase can directly react with the chemisorbed H to form H_2. A schematic of both mechanisms can be seen on Figure III.8.

The formation of H_2 is a complex problem and a simple approximation is usually made in PDR models. The two processes of H_2 formation can be summarized as a single equation [H + H $\rightarrow$ H_2]

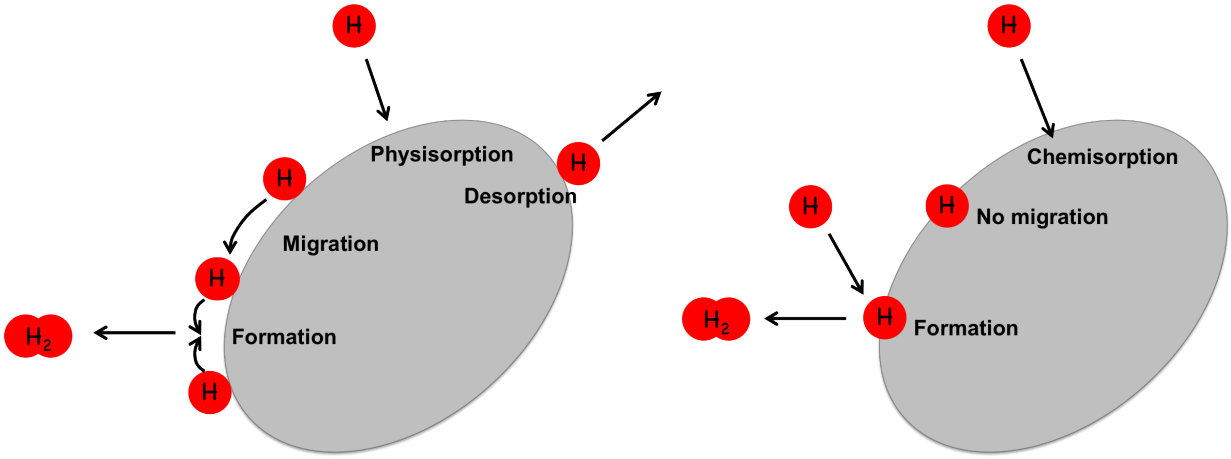

Figure III.8: *Diagram of the possible H_2 formation mechanisms on a grain. Left: Langmuir-Hinshelwood mechanism for H_2 formation. Right: Eley-Rideal mechanism. Adapted from Bron (2014).*

with a typical reaction coefficient $k = 3 \times 10^{-17}$ (Jura 1975; Gry et al. 2002):

$$\frac{dn(H_2)}{dt} = 3 \times 10^{-17} n(H) n_H \tag{III.17}$$

However, in the Meudon PDR code, these two mechanisms are treated in detail since version 1.4 (Le Bourlot et al. 2012). These calculations have been even more precisely developed further by Bron et al. (2014) but this is not used yet in the version of the code implemented here.

Thermal equilibrium: heating and cooling processes

Assuming a stationary state, solving for the thermal balance is equivalent to determining the temperature, T, by solving $\Gamma(T) = \Lambda(T)$ where Γ is the sum of the heating processes and Λ the sum of the cooling processes. This results in calculating the level population for all of the different species included in the code.

The photoelectric effect on grains and PAHs is usually the main heating source in the PDRs. The Meudon PDR code considers a distribution of grain sizes, where the properties are 30% the properties of carbon grains and 70% the properties of silicon grains, while the majority of the other PDR models considers only one size. Version 1.6, which we use for this study, uses the description of Weingartner & Draine (2001a) which includes more physics than the description of Bakes & Tielens (1994) used in the previous versions, but also depends more on the grain properties.

H_2 formation on grains releases approximately 4.5 eV. They are distributed as follows: 1/3 is converted into grain energy, 1/3 as internal energy of the molecule and 1/3 is used to heat the gas. H_2 can be excited or de-excited by collisions with other gas atoms/molecules. Since H_2 is very abundant, this process contributes to heating or cooling the gas. Kinetic energy released though the photodissociation or photoionization of the most abundant species (H_2, C, CO) also contributes to heating the gas

Other processes, such as *cosmic ray* ionization and *exothermic reactions*, contribute to gas heating (similarly, endothermic reactions contribute, although moderately, to gas cooling). *Collisions between*

gas and grains also have to be taken into account, since T_{gas} and T_{grains} are generally different, except at very high densities. Thus, gas heating or cooling occurs, depending on the temperature difference. *Mechanical heating* (also called turbulence heating), coming from the cascade of the energy from large scales to the smaller scales, is possible. However, this process is not very well constrained and is set to 0 in general in the Meudon PDR code.

Emission of photons by C, O, and CO (and its isotopes) is the main cooling source. Other species are also included, although this is mainly to calculate their line emission and they do not contribute much to the cooling of the gas. The quantum level populations of these species have to be determined to calculate the cooling rate from radiative transitions. The probability to go from a lower level l to an upper level u depends on the Einstein coefficients, on the local radiation field I, on the collision rates with H, H_2 and e^- mainly, on the chemical destruction D and formation, F_l. For each of the levels l and u of each specie, the code has to solve:

$$n_l \left[A_{lu} + B_{lu} I_{lu} + \sum_X k_{lu}^X n^X + D \right] = n_u A_{ul} + n_u B_{ul} I_{ul} + \sum_X k_{ul}^X n^X + F_l, \tag{III.18}$$

where n_l and n_u are the densities in levels l and u respectively, k^X is the collision rate with specie X and n^X is the density of the specie X (Gonzalez Garcia et al. 2008).

The particularity of H_2

The Meudon PDR code, as the photoionization code Cloudy for example, treats with great care the processes involving H_2, including many quantum levels in the calculations. Other PDR codes usually make the approximation of a two level system, with an additional virtual level. One of the resulting effects, as shown by Röllig et al. (2007), is an increased temperature at the surface of the cloud for the codes including the full H_2 description. This has consequences on the entire structure of the cloud, as the temperature is a crucial parameter for the thermal balance and the chemistry.

III.3.4 Other existing PDR models

I present here briefly the differences between a few PDR models that I have explored and their specific applications. A detailed PDR comparison study has been done by Röllig et al. (2007) with a focus on C^+/C^o/CO transitions and H_2 formation.

PDR Toolbox

The PDR Toolbox was developed by Michael Kaufman and Mark Wolfire, and the code is described in Kaufman et al. (1999, 2006). Model grids and an online fitting program are available through the web interface: `http://dustem.astro.umd.edu/pdrt/`. Given a set of IR spectral line intensities or ratios, the PDR Toolbox computes the best-fit FUV incident radiation field intensity and cloud density based on predictions of the PDR model. The geometry is fixed to a 1D plane parallel slab, with a total extinction $A_V^{max} = 10$, described by a constant hydrogen density, illuminated on one side by a unidirectional FUV radiation field. Standard parameters (gas phase elemental abundances, grain properties, turbulent doppler velocity of 1.5 km s^{-1}) are fixed and metallicities of 1 $Z_\odot$ and 3 $Z_\odot$ are available. The radiation field is a scaling of the Galactic interstellar radiation field (in units of the mean interstellar radiation field of Habing 1968). The available line intensity predictions include [C I], [C II], [O I], several CO and H_2 IR transitions, the IR dust continuum, [Si II] 35 μm and [Fe II] 26 μm.

Contrary to the Meudon PDR code, the complete radiative transfer is not calculated for the total spectrum, but L_{FIR} scales with G_{UV} ($L_{FIR} = \frac{2 \times G_{UV}}{4\pi}$). The adopted chemistry is also simplified, with a smaller number of species taken into account.

Cloudy

Cloudy is a photodissociation and photoionization code described in Ferland et al. (1998), Abel et al. (2005) and Ferland et al. (2013). The code is publicly available for download at http://www.nublado.org/. The shape and intensity of the external radiational field must be fully specified. It can be a simple blackbody, a scaling of the Galactic ISRF, a stellar spectrum from a stellar library or Starburst99 (Leitherer et al. 2010), a typical AGN SED, etc. Isotropic or uni-directional radiation fields can be defined. Moreover, several radiation fields can be combined as part of the total field interacting with the cloud. Default elemental abundances can be changed individually or by setting a metallicity value. Grain abundance can also be specified separately and the full rotational and vibrational treatment of the H_2 levels is calculated. The geometry is 1D spherical, although it can be made effectively plane-parallel by setting a large distance between the cloud and the source compared to the cloud thickness. Cloudy normally assumes an open geometry, where the covering factor of the cloud is small, and this can be changed to a closed geometry by increasing the covering filling factor until light escaping the gas on one side toward the central source always interacts with gas on the other side.

Cloudy has the advantage of treating the radiative transfer in both the ionized gas and the neutral gas continuously. It is particularly useful to do a self consistent model of all of the phases of the ISM. Especially, lines arising from several gas phases ([C II] or [Si II] for example) can be more easily interpreted since the possible contribution from the ionized gas is taken into account when doing the PDR modeling. For our study, as we concentrate on the study of the PDR, we chose to use the Meudon PDR code which is specialized in modeling only the neutral and molecular gas.

KOSMA-τ

The KOSMA-τ model was first developed by Sternberg & Dalgarno (1989) and is described in detail in Störzer et al. (1996). Updated versions are described in Röllig et al. (2006) and Röllig et al. (2013) for example. This model computes the physical and chemical structure for spherical clumps of radius R, illuminated by an external isotropic radiation field. The density profile is defined by a radial power law with an index α:

$$n(r) = n_0 \left(\frac{r}{R}\right)^{-\alpha}, \tag{III.19}$$

for $R_{core} \leqslant r \leqslant R$ and $n(r)$ constant for $r < R_{core}$. Typical values are $\alpha = 1.5$ and $R_{core} = 0.2R$ (Röllig & Ossenkopf 2013). The major difference compared to a standard plane-parallel PDR model is the finite cloud mass and the finite angular size of the cloud. Model grids are available at https://hera.ph1.uni-koeln.de/~pdr/. They offer predictions for several lines of [C II], [O I], [C I], ^{12}CO and ^{13}CO at various metallicities, densities, cloud masses and radiation fields (in units of the mean interstellar radiation field of Draine 1978). Contrary to the Meudon PDR code and Cloudy, which take into account rotational and vibrational levels of H_2, KOSMA-τ has a simplified treatment of H_2 with only the vibrational levels.

Three-dimensional PDR models

Most regions of the ISM have complex morphological structures and cannot be simply described by plane-parallel or spherical morphologies. For example, Stutzki et al. (1998) show that the clumpy structure of the ISM can be well represented by an ensemble of randomly positioned clouds, with a power-law mass distribution, and a power-law mass-size relation. As such, there is a need for 3D PDR codes to describe more accurately complex morphologies.

A pseudo-3D version of Cloudy, named Cloudy_3D, has been developed by Morisset et al. (2005); Morisset (2006) and is now integrated in pyCloudy[2]. This is not a fully 3D code: it considers radial radiation only. It combines a set of 1D Cloudy runs, corresponding to different angles, into a 3D cube. Shadowing or the effect of multiple stars in the field, for example, are then not taken into account. However, this pseudo-3D code has the advantage of being faster and less computational time consuming than a fully 3D code. The Meudon PDR code also offers the possibility to simulate a spherical cloud illuminated by an external isotropic field as a post-processing of the 1D model.

A 3D version of Kosma-τ is presented by Andree-Labsch et al. (in prep.). In this model, the 3D geometry of a PDR is described by a set of 3D pixels ("voxels") in which the fractal structure of the ISM is represented by a ensemble of spherical clumps, following a given clump-mass spectrum. The ensemble properties are position dependent and can vary between different voxels. The clump-averaged line intensities and optical depth, provided by the Kosma-τ model for each voxel, are then used to compute the PDR emission, accounting for the intrinsic velocities of individual clumps. Another example is the 3D-PDR code, described in Bisbas et al. (2012), which is an extension of the one-dimensional UCL PDR code (Bell et al. 2006). It is a 3D astrochemistry code able to treat PDRs with arbitrary geometries and density distributions. It solves the chemistry and the thermal balance self-consistently within a given 3D cloud. It can be used in combination with 3D photoionization codes such as Mocassin Accurso et al. (2016) or TORUS (TORUS-3DPDR; Bisbas et al. 2015).

The observations of the star-forming regions in the LMC and SMC we present here can be reproduced by plane-parallel models. A more complex geometry, taking into account a distribution of clouds of different masses and pressure in each pixel, illuminated by a central source and including the effect of scattering and shielding would be certainly more realistic. However, we now lack the observational constrains to model properly such a detailed scenario.

III.4 Application of the model to the data and caveats

We have used the Meudon PDR code to determine the physical conditions that reproduce the observations we collected with *Herschel*, *Spitzer* and ground-based telescopes. With these constraints on the radiation field, pressure, filling factor and size of the clouds, we are able to predict the total amount of H_2 gas in a cloud, characterize the fraction of H_2 outside the CO-emitting region and try to identify the best tracer of this CO-dark molecular gas. The Meudon PDR code was preferred over other PDR codes due to its focus on PDRs and very accurate modeling of H_2 formation and destruction processes. The Cloudy model will be used to interpret the observations of the ionized gas. We present here the method we used to constrain the physical parameters in the different regions of the LMC and the parameters we fixed. The results for 30 Doradus and the other LMC regions are presented in Chapters IV and VI.

[2]pyCloudy is the python version of Cloudy_3D, available at https://sites.google.com/site/pycloudy.

III.4.1 Input parameters

Incident radiation field

The 1D slab of gas can be illuminated from both sides, by an isotropic radiation field. The FUV spectra on both sides is a scaling of the Mathis field (Mathis et al. 1983), by a factor G_{UV}. We choose to maintain $G_{UV} = 1$ at the back side of the slab, to simulate the ISRF, while on the observer's side, illuminated by a stellar source, the radiation field can be varied between 1 and 10^6.

Although the inclination angle between the observer's line of sight and the perpendicular to the surface of the cloud can be varied, we choose to fix it to 0°. We do not have enough constraints to deduce this parameter from our observations and there is a degeneracy between this inclination angle, the filling factor and A_V^{max}, as detailed on Section III.4.3.

Abundances

The metallicity of the LMC is half of the solar metallicity (Pagel 2003; Rolleston et al. 2002), with no strong variations throughout the galaxy. Hence, for the elemental gas phase abundances in the model, we scale the standard values used in the Meudon PDR code for solar metallicity (Le Petit et al. 2006) by the LMC metallicity ($\approx 0.5\ Z_\odot$). However, the elemental gas phase abundances have been constrained by Pellegrini et al. (2011), relying on a detailed Cloudy modeling of the optical ionized gas line in 30 Doradus. Particularly, for 30 Doradus, we choose to use these abundances to have a more accurate ratio C/O, which can have important consequences on the cooling processes in particular. For the other regions of the LMC, where we do not have such precise constraints, we scale the standard ISM abundances by a factor 0.5 (see Table III.1).

Table III.1: Adopted gas phase abundances for some of the main elements for the half-solar metallicity model and the model adapted for the 30 Doradus nebula.

Gas phase abundances	Half-solar metallicity	30 Doradus
	$log(n(X)/n(H))$	
He	-1.30	-1.05
C	-4.19	-4.3
N	-4.43	-4.91
O	-3.80	-3.75
S	-5.02	-5.32

Other input parameters

Table III.2 summarizes the input parameters of the Meudon PDR code we use to model the LMC observations. The pressure (P, for an isobaric model), the density (n, for a constant density model), the intensity of the radiation field (G_{UV}) and the visual extinction (A_V^{max}, corresponding to the total cloud depth) can be varied in the given ranges. We take the standard Galactic value for the cosmic ray flux, noted ζ (Indriolo & McCall 2012; Indriolo et al. 2015). The PAH fraction ($f_{PAH} = 2\%$) is scaled with the metallicity, except for the 30 Doradus model, where we take 1%, as the result of the detailed SED fitting (see Section III.1.1). As the radiation field in 30 Doradus is expected to be intense, we also expect that PAHs are destroyed more efficiently.

Table III.2: Input parameters for the PDR model.

Parameter	Notation	Value
Pressure	P	$10^4 - 10^8$ cm^{-3} K
Density	n	$1 - 10^6$ cm^{-3}
Radiation field	G_{UV}	$1 - 10^5$
Total visual extinction	A_V^{max}	1 – 10 mag
Cosmic ray flux	ζ	3×10^{-16} s^{-1}
Metallicity	Z	$0.5 Z_\odot$
PAH fraction	f_{PAH}	2% - 1%
Dust-to-gas mass ratio	M_{dust}/M_{gas}	5×10^{-3}

III.4.2 Method

With the input parameters described above, we ran a large number of models for different sets of G_{UV}, P or n and A_V^{max}, for isobaric or constant density equation of state. The output quantities computed by the model include the integrated line intensities and L_{FIR}, ionic and molecular abundances, emissivities, and chemical and thermal structure of the cloud. For each line or line ratio in a given pixel (x,y), we compare the observed value, $I_j(x,y)$ with the predicted value, M_j and determine the best solution by minimizing the χ^2 distribution:

$$\chi^2 = \sum_{j=1}^{N} \left(\frac{I_j(x,y) - M_j}{\sigma_j(x,y)} \right)^2, \tag{III.20}$$

where $\sigma_j(x,y)$ is the uncertainty associated with the observed value $I_j(x,y)$.

G_{UV}, P (respectively n) and the area filling factor

We use line ratios preferentially to individual line intensities to constrain the best model parameters (see also e.g. Wolfire et al. 1990; Lord et al. 1996). Indeed, the model considers an infinite slab of gas, hence a filling factor of 1 in a given pixel. However, the area filling factor of the PDRs in the beam can be different from unity and individual lines predicted by the model must be multiplied by this (unknown) area filling factor to reproduce the observations. When using line ratios of species which are expected to be co-spatial in the cloud, this area filling factor is cancelled.

Together, ([O I] 145 μm+ [C II])/L_{FIR} and [O I] 145 μm/[C II], for example, give good constraints on G_{UV} and P (Figure III.9). Once G_{UV} and P are determined by minimizing the χ^2, the area filling factor can be estimated as:

$$\Phi_A = \frac{[\mathrm{C\,II}]_{predicted}}{[\mathrm{C\,II}]_{observed}}, \tag{III.21}$$

where $[\mathrm{C\,II}]_{predicted}$ is the intensity of [C II] predicted by the best solution model. Φ_A is proportional to the total surface covered by the PDRs along the line of sight. If there is only a single PDR along the line of sight for a given pixel, Φ_A is equal to the fraction of the beam covered by the PDR. On the other hand, if several PDRs are present along the line of sight, Φ_A is equal to the sum of their surfaces (assuming the FIR lines are optically thin) divided by the beam area, and can thus be higher than 1. The method is exactly the same for a constant density model. The 1-σ uncertainties on G_{UV}, P and Φ_A are given for a $\Delta\chi^2 = 2.30$ compared to the minimum χ^2 value.

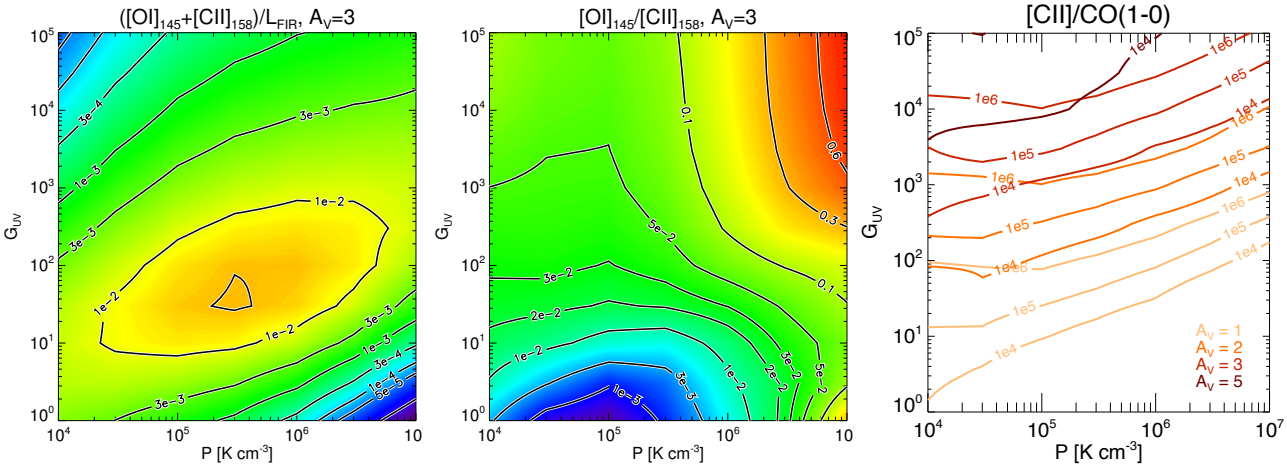

Figure III.9: *Left: ratio* $\frac{[O\,\textsc{i}]\ 145\,\mu m + [C\,\textsc{ii}]\ 158\,\mu m}{L_{FIR}}$ *emitted by a simulated PDR cloud of* $A_V^{max} = 3$*, as a function of* G_{UV} *and P. Center: ratio* $\frac{[O\,\textsc{i}]\ 145\,\mu m}{[C\,\textsc{ii}]\ 158\,\mu m}$ *for the same simulated cloud. This ratio is a good tracer of the pressure at high P and a good tracer of* G_{UV} *at low P. Right: ratio [CII]/CO(1-0) as a function of* G_{UV}*, P and* A_V^{max}*. The different colors represent the different* A_V^{max}*. Typical values of this ratio observed in the LMC are shown.*

Other ratios of PDR lines coming from the same regions and the same depth into the cloud could be used when available, such as [O I] 63 μm/[C II] or [C I] 609 μm/[C I] 370 μm for example. However, while the [C I] 370 μm was sufficiently detected with the SPIRE FTS, the [C I] 609 μm line was only barely detected in several of the observed LMC regions and [O I] 63 μm can be affected by optical depth effects (Section IV.1.2), so these ratios do not bring strong constraints on the model parameters.

Total depth of the cloud

Contrary to the ratios mentioned above, involving co-spatial lines, ratios of lines originating from different depths into the cloud depend greatly on the total size of the cloud. The variations of the predicted ratio [C II]/[C I] 370 μm as a function of G_{UV}, P and A_V^{max} are shown in Figure III.9. To constrain this parameter, we must use the ratio [C II]/[C I] 370 μm or [C II]/ CO for a low-J CO transition.

For a given pixel *i*, the best parameters $G_{0,i}$ and P_i are determined based on the ratios ([O I] 145 μm+ [C II])/L_{FIR} and [O I] 145 μm/[C II], independent of A_V^{max}. $A_{V,i}^{max}$ can then be interpolated so that the predicted ratio ([C II]/[C I] 370 μm)$_i$ matches the observed ratio ([C II]$_{i,obs}$ /[C I]$_{i,obs}$ 370 μm) for example. In practice G_{UV}, P (resp. n) and A_V^{max} are constrained simultaneously, by minimizing the χ^2.

As presented in Figure III.10, while at low A_V^{max} ($\approx$ 1 mag) and at high A_V^{max} ($\gtrsim$ 5-10 mag) an isobaric model and a constant density model predict the same line ratios, there can be differences of up to a factor of 10 on the predicted ratios at intermediate A_V^{max}. Indeed, for a given A_V^{max}, the density profile evolves differently as a function of depth into the cloud. In an isobaric model of moderate A_V^{max}, the density rises quickly as the temperature drops and CO lines are emitted at lower A_V compared to a model with a constant density. An isobaric model can be more appropriate to reproduce mid- to high-J CO lines, which can be difficult to reproduce with a constant density model (e.g. Plume et al. 2004; Habart et al. 2005), while lines arising from the surface of the PDR are not affected (Kaufman et al. 2006). Having similar A_V^{max} constrained by different ratios ([C II]/[C I] 370 μm, [C II]/ CO(1-0) or [C II]/ CO(3-2) for instance) can help determine the best adapted model for a given region.

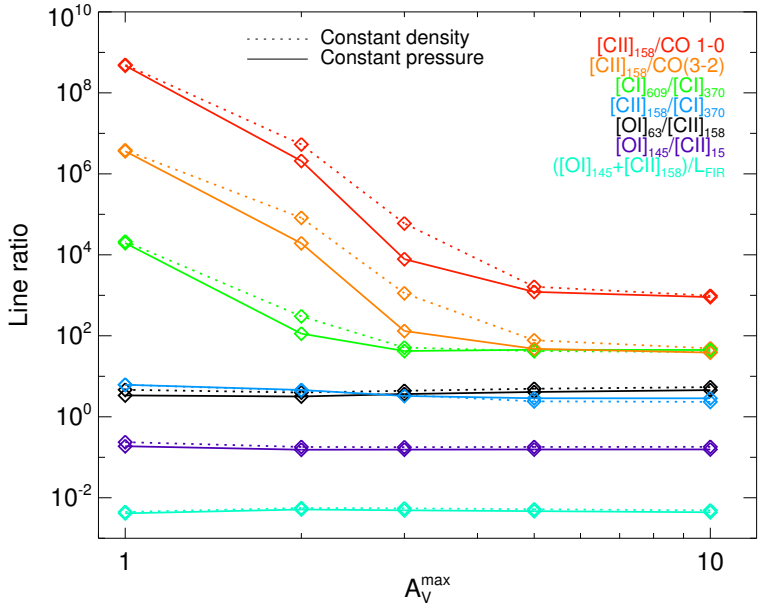

Figure III.10: *Variation of several line ratios for clouds of different* A_V^{max}*, from 1 to 10 mag, for two different equations of state. The solid lines represent constant pressure clouds, with* $P = 1 \times 10^6\ cm^{-3}\ K$*, illuminated by* $G_{UV} = 3000$*. The dashed lines represent constant density clouds, with* $n = 1 \times 10^4\ cm^{-3}$*, illuminated by* $G_{UV} = 3000$*.*

III.4.3 Limitations and caveats

Degeneracy

In many of the regions, as shown in Chapters IV and VI, we find two possible solutions with a low χ^2 value. One has a relatively higher G_{UV} and lower P while the other has a relatively lower G_{UV} and higher P. This can be understood easily by looking at the variations of the emitted ratio ([O I] 145 μm+[C II])/L_{FIR} as a function of G_{UV} and P (Figure III.9). The degeneracy remains in the constant density case.

Several lines of reasoning can help breaking this degeneracy. First, the low G_{UV}/high P solution necessarily requires a lower A_V^{max} (usually < 1 mag), while predicting a higher optical depth in [O I] 63 μm, which is not consistent. Another reasoning can help if there is already an idea of the separation between the source and PDR. For example, in the case of 30 Doradus, Pellegrini et al. (2011) predict a distance of a few parsecs between the central ionizing cluster, R136, and the ionized arc, based on optical line observations. Knowing the extreme radiation field emitted by the cluster, choosing the low G_{UV} solution would require putting the PDRs at a large distance of R136 (several tens of parsecs), so that the radiation field can be sufficiently attenuated. As a result, the high G_{UV}/low P solution is, in most cases, the preferred solution.

Geometry

The Meudon PDR code is a plane-parallel, 1D model, where the radiation field can be input differently on both sides of the cloud (see Figure III.11). However, it is possible to simulate spherical geometry in an isotropic radiation field by post-processing the plane-parallel 1D model. This is done by integrating the intensity of each transition over a sphere, where the abundance profiles of each specie are equal

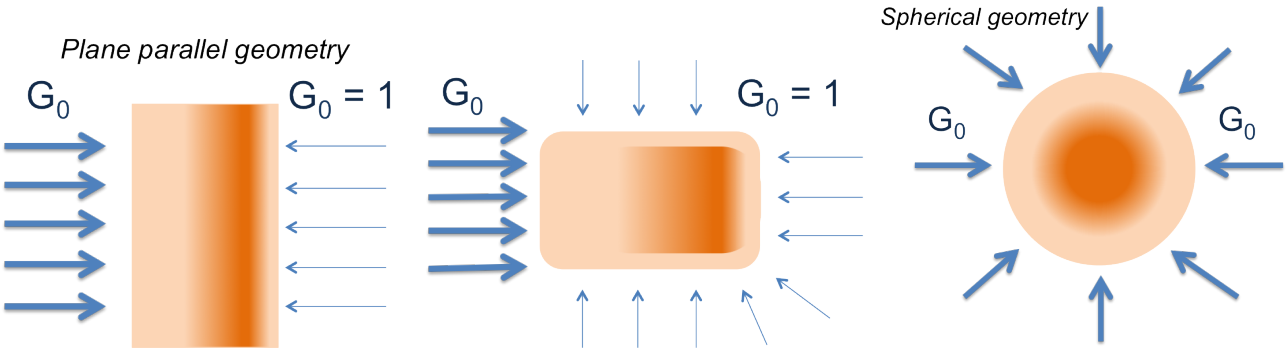

Figure III.11: *Schematic view of an infinite plane parallel PDR (left), a spherical geometry resulting from the wrap-around post-processing of the model (right) and the expected geometry close to R136 (center).*

to the computed abundance profile as a function of the distance to the surface for a plane parallel geometry. This is a geometrical approach, which is valid only if there is enough extinction ($A_V \gtrsim 5$). The impact of the geometry on the determination of A_V^{max} is described in the Appendix of Chevance et al. (2016), presented in Section IV.2.1. Choosing an isotropically illuminated sphere instead of a plane-parallel slab illuminated by a strong radiation on one side and $G_{UV} = 1$ on the other side, results in larger PDR clouds, with diameters approximately four times larger than the size of the optimal plane-parallel cloud.

After some tests, we chose not to use the spherical geometry for the final 30 Doradus PDR model. Indeed, although a spherical geometry can seem more realistic than an infinite slab of gas and dust, for the specific case of 30 Doradus and more generally close to star-forming regions, we do not expect the observations to be well reproduced by a spherical cloud in an isotropic radiation field, due to the proximity of a compact and intense ionizing source. The geometry of an individual cloud in 30 Doradus could be closer to that represented in the center panel of Figure III.11. More realistic modeling should take into account an ensemble of clouds of different sizes and at different distances of the ionizing cluster.

Inclination angle

In our modeling, A_V^{max} is determined by considering that the observer's line of sight is perpendicular to the surface of the PDR, which is not necessarily the case. The total extinction magnitude in V band can be independently determined for the dust mass derived from the SED modeling described in Section III.1.1. We call this value A_V^{dust}, which corresponds to the integrated extinction along the entire line of sight for each pixel, in contrast to A_V^{max}, which is the average depth of each PDR cloud in this pixel. A_V^{dust} includes all of the gas and dust in the line of sight, from the PDRs, but also from the ionized gas as well as from gas not associated with the studied PDR (foreground or background gas for example). These different parameters are represented in Figure III.12. If there is no significant contribution from the ionized gas and foreground and background, we then expect to have $A_V^{dust} = \Phi_A \times A_V^{\alpha}$, where A_V^{α} is the measured extinction for one cloud along the observer's line of sight which has an inclination angle of α. As noted in Section III.4.2, the area filling factor, Φ_A, is indeed proportional to the surface covered by the PDRs and the number of PDRs along the line of sight.

The inclination angle (the angle between the observer's line of sight and the perpendicular to the surface of the PDR) is related to the observation. It plays no role in the computation of the model,

but only in the post-processing aspect. The ratios of co-spatial lines are not affected and G_{UV} and P remain unchanged when assuming an inclination angle α between the observer's line of sight and the perpendicular to the PDR surface. The A_V^{max} we get from [CII]/CO for example in the PDR model is also unchanged, as it is a physical property of the cloud. Φ_A, however is expected to vary since the line of sight intercepts more matter that in the perpendicular case: Φ_A^α derived from the PDR model ($[CII]_{obs}/[CII]_{pred}$) decreases as α increases.

If we assume a different inclination angle β for the computation with the PDR model, we will get $\Phi^\beta = \Phi^\alpha \frac{cos(\alpha)}{cos(\beta)} \neq \Phi^\alpha$ and $A_V^\beta = \frac{A_V^{max}}{cos(\beta)} \neq A_V^\alpha = \frac{A_V^{max}}{cos(\alpha)}$. Eventually, we have $\Phi_A^\beta \times A_V^\beta = \Phi_A^\alpha \times A_V^\alpha = A_V^{dust}$ and it is not possible to determine the correct inclination angle. In the extreme case of the perpendicular case, we still have:

$$\Phi_A^0 \times A_V^{max} = \Phi_A^\alpha \times A_V^\alpha = A_V^{dust}. \tag{III.22}$$

There is clearly a degeneracy between the inclination angle, the filling factor and A_V. It is not possible to determine the inclination angle from these observations nor to confirm that the assumption of face-on PDR is correct. In the case of 30 Doradus, for example, we assume face-on PDRs and we find a good correlation between A_V^{dust} and $\Phi_A \times A_V^{max}$ (see Figure 18 of Chevance et al. 2016).

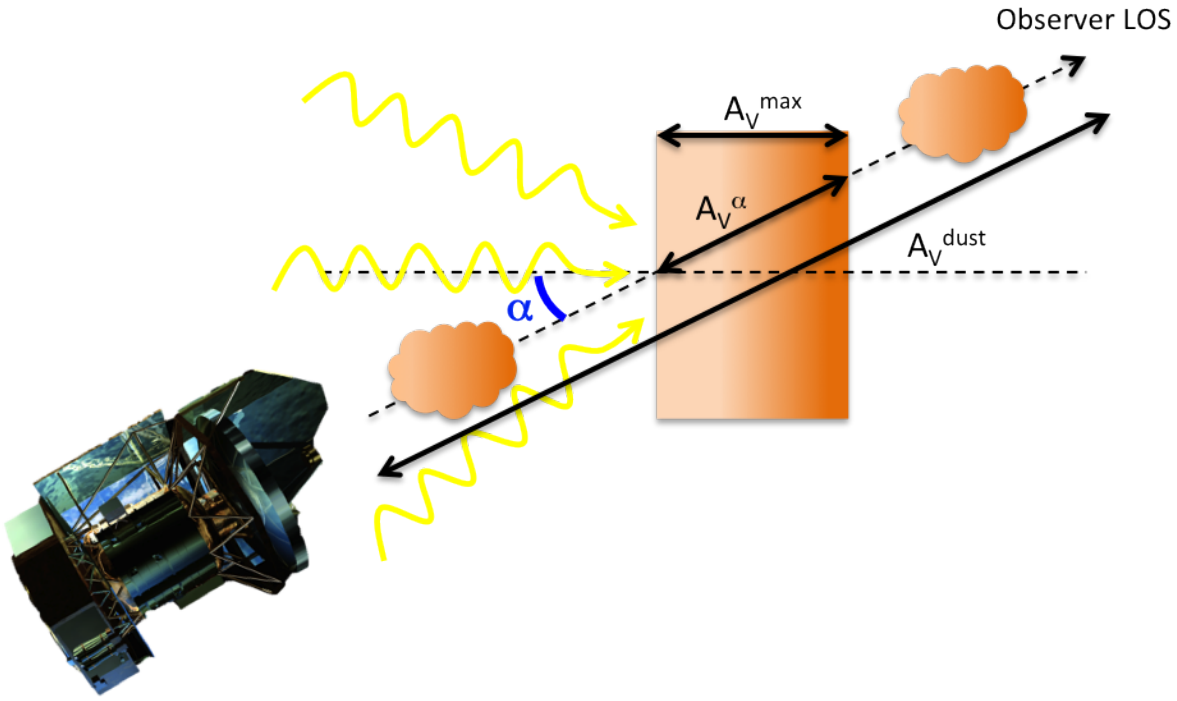

Figure III.12: *Schematic view of a PDR and comparison between the different A_Vs we can measure with various methods.*

Chapter IV

An extreme environment: 30 Doradus in the LMC

Contents

In this chapter, we apply the modeling described previously to the observations of the 30 Doradus nebula in the LMC. This extreme environment has been well studied over the entire wavelength spectrum. It is one of the best targets to study in detail, the impact of a strong radiation field on the surrounding half-solar metallicity ISM.

IV.1 The 30 Doradus nebula

IV.1.1 Description

The 30 Doradus nebula, also known as the Tarantula nebula, is a giant H II region and the brightest star-forming region in the LMC (Kennicutt 1984). First classified as a nebula by Nicolas-Louis de Lacaille in 1751, it has been intensively studied since then, from naked eye observations by Sir John Herschel, to infrared observations with the *Herschel* Space Observatory (see Figure IV.1). It is considered to be the largest and most massive H II region in the Local Group, with a diameter of 200 pc (15′; Lebouteiller et al. 2008). It is also one of the most active star-forming regions known in the Local Group, with a specific star formation rate (sSFR) of 6.6×10^{-7} yr^{-1} (Doran et al. 2013), which is approximately 2.4×10^{4} more that our Milky Way (sSFR = 2.71×10^{-11} yr^{-1}; Licquia & Newman 2015). The 30 Doradus nebula (hereafter 30Dor; Fig. IV.2), is an ideal target to study the interactions between gas, stellar radiation and dust at reduced metallicity (1/2 $Z_{\odot}$; Rolleston et al. 2002; Pagel 2003). Indeed, at 50 kpc (Walker 2012), the distribution and the structure of the gas can be studied with high spatial resolution (1″= 0.25 pc). The reduced metallicity of the LMC, along with its proximity, can give us detailed insight on how star formation proceeds at lower metallicity in comparison with our metal-rich Milky Way. Another interesting characteristic of the LMC is that it is a small galaxy (about 10^{10} M$_{\odot}$, which corresponds to $\sim 1/100$ the mass of the Milky Way), and is seen almost face-on, at a small inclination angle of $\sim 20°$- $35°$(Kim et al. 1998; van der Marel & Cioni 2001). There is less risk of source confusion due to this source orientation. All of these characteristics make 30Dor a perfect target to study in detail, the links between environment and star formation. Understanding the structure and the processes at play in this extreme region is essential for the interpretation of more distant starburst regions. The 30Dor nebula is often thought to be a testbed for higher redshift galaxies due to its reduced metallicity and massive starburst, and as such, a wealth of studies at all wavelengths have focused on this particular nebula.

Stellar population

The dominant star-forming cluster ionizing this region is NGC 2070, and in particular its dense center, Radcliffe 136 (R136; Feast et al. 1960), considered to be the nearest super star cluster (SSC). By comparison, NGC 3603, the most massive H II region known in our Milky Way, is approximately 10 times less massive than NGC 2070 (Moffat 1983). Selman & Melnick (2013) inferred a total stellar density in the core of R136 between $\rho_0 \sim 1.5\times10^{4}$ M$_{\odot}$ pc^{-3} and 10^{7} M$_{\odot}$ pc^{-3}. This is a young cluster of ∼1-2 Myr (de Koter et al. 1998; Massey & Hunter 1998), which hosts many extremely massive, hot and luminous stars with energy mostly radiated in the ultraviolet. More than 350 O and B0 type stars have been spectrally identified in 30Dor (Walborn et al. 2014). Based on a multi-wavelength study, Lopez et al. (2011) have shown that the direct radiation pressure from stars in R136 dominates the stellar feedback mechanisms within 75 pc of the cluster, compared to other possible sources of energy (classical warm H II gas, hot gas shock-heated by stellar winds or supernovae). More recently, a far ultraviolet spectroscopic survey of R136 (see Fig. IV.3) has been done with the *HST* Space Telescope

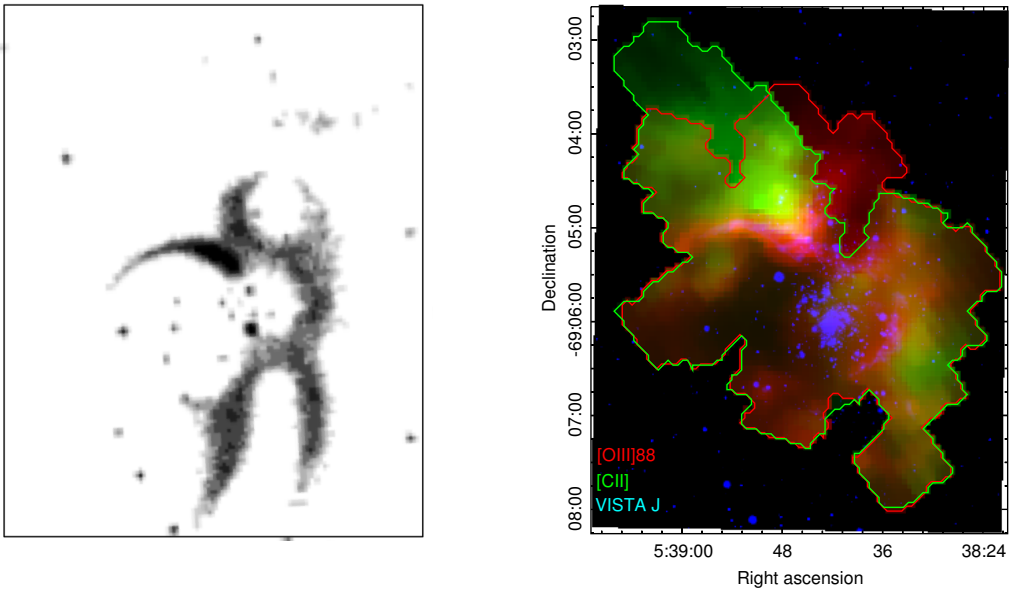

Figure IV.1: *Left: observation of the 30Dor nebula by Sir John Herschel in December 1835 from the Cape of Good Hope (Herschel 1847). Right: 30Dor nebula observed by the Herschel Space Observatory, revealing the ionized gas ([O III] 88 μm in red) and the PDRs ([C II] 157 μm in green) with the PACS spectrometer. The stars are observed with the Visible and Infrared Survey Telescope for Astronomy (VISTA; J-band, in blue).*

Imaging Spectrograph (STIS) by Crowther et al. (2016) providing spectral types for most of the bright sources in R136.

The ESO Large Program VLT-FLAMES Tarantula Survey (VFTS, Evans et al. 2011) has observed over 900 massive stars in 30Dor with optical spectroscopy from the VLT. Kinematics of the ionized gas was also obtained with this survey, and analyzed by Torres-Flores et al. (2013), revealing the presence of at least ten expanding structures in H_α, some of them previously unclassified. Although it has been previously considered to be an evolved H II region without major ongoing star formation, 30Dor shows evidence for current star formation. Walborn & Parker (1992) have established that 30Dor is a two-stage starburst region, with triggered star formation at the interfaces between the expanding central cavity and remnant giant molecular clouds to the west and northeast (Walborn & Blades 1997; Rubio et al. 1998; Johansson et al. 1998; Scowen et al. 1998; Walborn et al. 1999, 2002; Brandner et al. 2001). The Hubble Tarantula Treasury Project (HTTP, Sabbi et al. 2013) is using the capabilities of the *Hubble Space Telescope* (*HST*) to provide a multi-band view of R136 and study the properties of individual stars. These detailed observations make it possible to investigate the star formation history in this region. Cignoni et al. (2015) show for example that the star formation in 30Dor accelerated significantly ≈ 7 Myr ago, reaching a peak ≈ 1-3 Myr ago. Several young stellar objects (YSOs), still embedded in dust, have been discovered in this region. Gruendl & Chu (2009) and Whitney et al. (2008), in particular, have presented lists of bright *Spitzer* sources in the LMC from the program SAGE (Surveying the Agents of Galaxy Evolution; Meixner et al. 2006), including 30Dor. Ten YSOs in 30Dor were analyzed in more details by Walborn et al. (2013), revealing a wide diversity of sources.

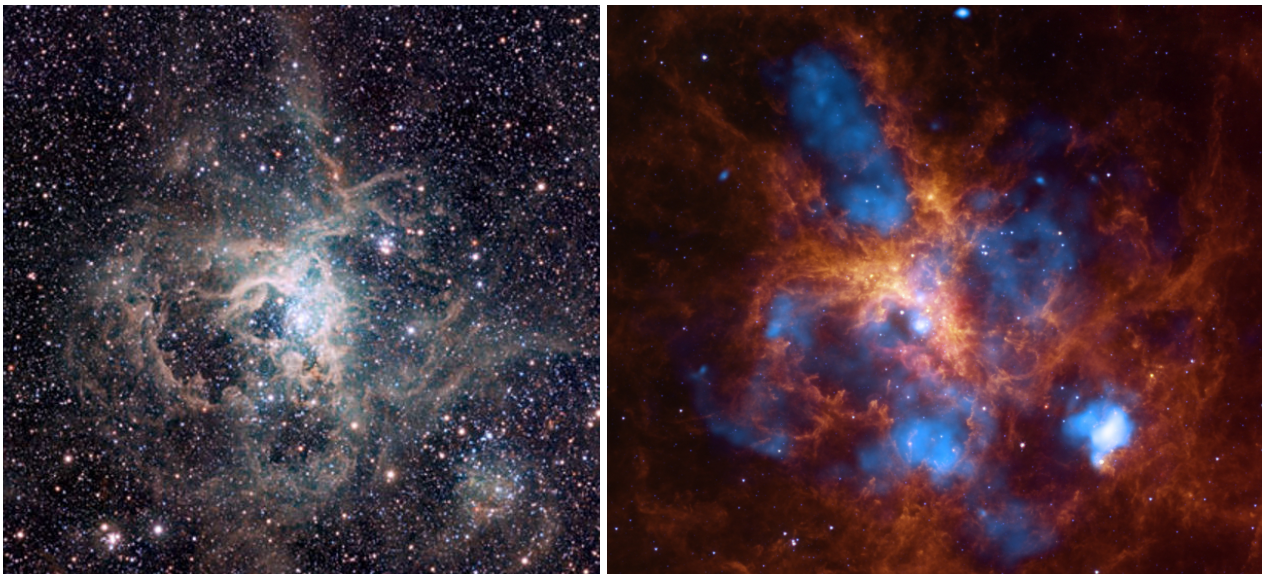

Figure IV.2: *Left: The 30Dor nebula was observed by VISTA as part of the VISTA Magellanic Cloud Survey at the Paranal Observatory in Chile (ESO). Right: 30Dor as seen in the X-ray (blue) with Chandra and IR (red) with Spitzer (Townsley et al. 2006a).*

Gas and dust

Ionized gas. 30Dor is part of the *Spitzer* SAGE survey (Surveying the Agents of Galaxy Evolution; Meixner et al. 2006) and the HERITAGE (HERschel Inventory of The Agents of Galaxy Evolution, PI: Meixner; Meixner et al. 2013) survey. Based in particular on the SAGE observations, Indebetouw et al. (2009) have studied the physical conditions of the ionized gas around R136, in particular the ionization parameter and the radiation temperature. The observations suggest that photoionization dominates over collisional excitation by shocks. The structure and chemical abundances of the ionized gas have been investigated by Pellegrini et al. (2010, 2011), revealing that, almost over the entire optical imaging and spectroscopic survey covering $140 \times 80\,\mathrm{pc}^2$, the cluster of O stars in R136 seems to be the dominant source of ionization. The dynamics and the large scale structure of the region are described by a system of X-ray bubbles, confined by the molecular gas and in pressure equilibrium with it. The elemental abundances in 30Dor have also been measured based on these observations.

Neutral and molecular gas. Models of the PDR conditions and structure have been done at 1′ (e.g. Stacey et al. 1991; Poglitsch et al. 1995; Kaufman et al. 1999) with observations at the Kuiper Airborne Observatory (*KAO*). These observations indicate a highly fragmented medium with low beam-filling factor of the CO molecular gas, while most of the H_2 molecular gas could be present in PDRs. More recently, Pineda et al. (2012) have derived the physical conditions of the gas (incident FUV intensity and average density) from the PDR to the molecular core in one pointing at the peak of the CO emission, using a clumpy PDR model. This study revealed a dense ($n_H = 10^5\,\mathrm{cm}^{-3}$), warm ($T = 160\,\mathrm{K}$ from CO and [C I] transitions) and clumpy medium, a consequence of the extreme FUV environment. Now, the new *Herschel* observations of 30Dor allow us to probe spatially in a 2′×2′ region, and in detail (12″ ∼ 3 pc scale) the physical conditions and the structure of the PDRs around R136 (Chevance et al. 2016; Sect. IV.2.1).

A number of studies have also analyzed the molecular gas content of this active star-forming region. Detection of ^{12}CO in 30Dor was first reported by Israel et al. (1982) and many studies of CO

Figure IV.3: *The R136 cluster seen by the Hubble Space Telescope. This is a combination of two images taken with the Wide Field Camera 3 and the Space Telescope Imaging Spectrograph (HTTP; Sabbi et al. 2013).*

since then have been carried out (Melnick & Rubio 1985; Israel et al. 1993; Johansson et al. 1998; Pak et al. 1998; Rubio et al. 1998; Ott et al. 2008; Pineda et al. 2009; Rubio et al. 2009). More recently, *ALMA* has made it possible to study in detail the molecular gas in the Magellanic Clouds and in particular in 30Dor, revealing a highly structured CO emission, mostly associated with sub-parsec dense clouds and filaments (Indebetouw et al. 2013). In the diffuse interclump gas, CO is significantly photo-dissociated, resulting in a higher X_{CO} factor. H_2 1-0 S(1) (2.12 μm) has also been observed directly with the Cerro Tololo Inter-American Observatory (CTIO) over the entire 30Dor region at 1″ angular resolution (Yeh et al. 2015). From the different regions viewed face-on or edge-on, it appears that the clumpy H_2 emission originates from the surface of the PDRs. The molecular gas content of 30Dor revealed by *Herschel* will be analyzed in details in Chapter V. Other more complex molecules, such as HCN and HCO^+ for example, are also detected in 30Dor with *ALMA* and the Australia Telescope Compact Array (ATCA; Anderson et al. 2014; Ott et al. 2008). They can exist in the core of the dense clumps, well shielded from the intense radiation field.

Dust grains and PAHs. Several studies have shown an increase of the VSG abundance around 30Dor (e.g. Bernard et al. 2008; Paradis et al. 2009, 2010), which could result from the destruction of big grains in shocks. Similarly, regions close to the surface of molecular clouds show an increased relative PAH abundance, which could be due to the destruction of VSG. However, the PAH abundance is relatively low in the close surroundings of the cluster R136, as is the case in other extreme environments, following on average a trend of decreasing PAH emission with decreasing metallicity and increasing ionizing radiation hardness (e.g. Madden 2000; Madden et al. 2006; Wu et al. 2006; Engelbracht et al. 2005). Around R136, though, the low PAH abundance could also be the hint for the presence of a cavity cleared out by the massive stars (Lebouteiller et al. 2011). Dobashi et al. (2008) found an increase of the apparent absorptivity of the dust from the outer regions of the LMC to 30Dor, which could be due either to a higher dust abundance close to the star-forming region, or to the presence of an additional gas component, not traced by HI and CO.

High energy. 30Dor is also very bright in X-rays. Townsley et al. (2006a,b) have studied this region based on observations of the Advanced CCD Imaging Spectrometer (ACIS) on the Chandra telescope, revealing complex diffuse X-rays structures (Fig. IV.2), such as super-bubbles filed with hot gas ($T \approx 7$ MK). Observations with the Fermi Gamma-Ray Space Telescope have detected an enhanced gamma-ray emission from 30Dor (Abdo et al. 2010; Foreman et al. 2015), originating probably from cosmic ray interactions.

IV.1.2 FIR empirical line diagnostics

FIR line ratios are important diagnostics of the gas conditions (see Sect. I.1). With the many spectroscopic and photometric observations of 30Dor with *Herschel* and *Spitzer*, we can analyze the correlations between several FIR tracers and obtain insight on the physical parameters of the ISM. We investigate different PACS line ratios as a function of L_{TIR}, which can be considered as a probe of star formation. We calculate the integrated intensity for each fine-structure line and L_{TIR} as described in Section III.1.2. We then compare the spatial information we have for 30Dor with the compact and extended sources of the DGS (see Section II.2.1) as described in Cormier et al. (2015) and more metal-rich galaxies from Brauher et al. (2008). We identify seven regions in 30Dor with various characteristics as shown in Figure 3 of Chevance et al. (2016; see Section IV.2.1).

Excitation of the gas

The line-to-L_{TIR} ratio is on average higher in the dwarf galaxies than in solar metallicity objects (e.g. Cormier et al. 2015). It can be seen in particular for the ratio [O III] 88 μm/L_{TIR} in the upper panel of Figure IV.4. The extended sources of the DGS in particular, where we zoom into star-forming regions, are among the highest points. If we zoom in on ~3 pc scales on 30Dor, we find even more extreme values of this ratio. Values of [O III] 88 μm/L_{TIR} in 30Dor cover a broad range between 6×10^{-3} and 4×10^{-2}. The regions where the ratio is the highest are not necessarily those closest to R136, but rather the more diffuse regions, where [O III] can be excited over large distances. The ratio [O III] 88 μm/L_{TIR} in 30Dor decreases with increasing L_{TIR} following the trend at galaxy scales for dwarfs and normal galaxies (Brauher et al. 2008; Cormier et al. 2015). This correlation can be explained by the lower dust extinction where L_{TIR} is lower, which allows UV photons to excite O^{++} on large spatial scales, resulting in higher [O III] emission.

[O III] 88 μm and [N II] 122 μm have similar critical densities (~ 300-500 cm^{-3}), but exist with very different excitation energies (35.5 and 14.5 eV respectively). Thus, the ratio of these two lines probes the hardness of the radiation field and are sensitive to the stellar effective temperature (Ferkinhoff et al. 2011). The middle panel of Figure IV.4 shows that the ratio [O III] 88 μm/[N II] 122 μm is on average higher in 30Dor than in all of the other sources of the DGS, in agreement with the expected hard radiation field close to the SSC R136. It spans almost one order of magnitude, between 200 and 1300. The highest values are found at the peak of the [O III] emission. [N II] 122 μm is relatively faint and as such was not observed in all of the DGS objects (Cormier et al. 2015). The region mapped in [N II] 122 μm with PACS in 30Dor is also much smaller than that mapped in [O III], [C II] and [O I].

The harder radiation field in 30Dor and in the other dwarf galaxies compared to the more metal-rich galaxies (Brauher et al. 2008; Figure IV.4), favors the excitation of [N III] relative to [N II] (the energy to create N^+ and N^{++} are respectively 14.5 eV and 19.6 eV) hence enhancing the ratio [O III]/[N II]. The ratio [O III] 88 μm/[N II] 122 μm is also sensitive to the abundance ratio O/N. Although no systematic trend of this ratio with the metallicity was found by Cormier et al. (2015) in

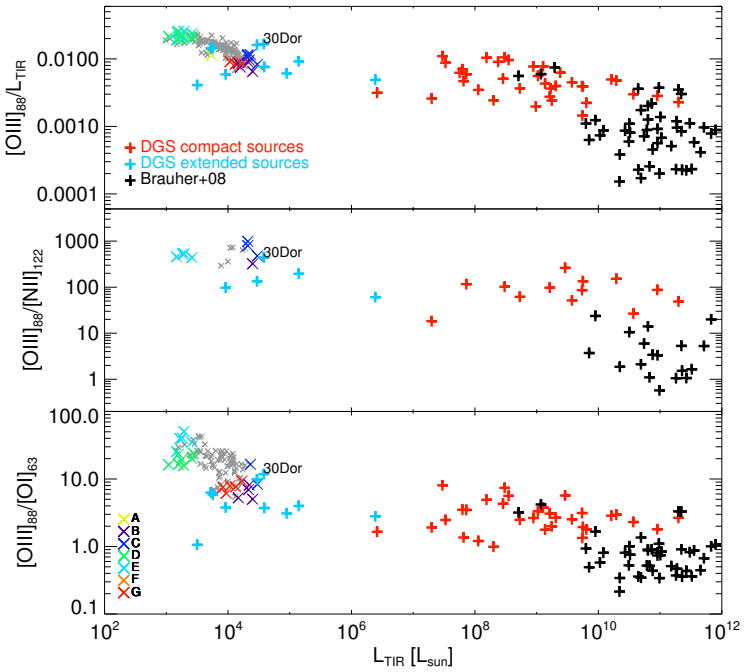

Figure IV.4: *PACS line ratios as a function of L_{TIR}. The crosses are for the Brauher et al. sample (black), the DGS sample (red for the compact sources and blue for the extended sources) and 30Dor (grey). The colored symbols correspond to the different discrete regions of 30Dor identified in Figure 3 of Chevance et al. (2016) (see Section IV.2.1). The yellow region (A) is located on the north east of R136, where [C II] is extended but where [O III] 88 µm seems fainter; the violet region (B) is located on the [C II] peak, and the blue region (C) is on the [O III] 88 µm peak; the green (D), cyan (E), and orange (F) regions probe more diffuse regions; the southwest peak of [C II] is in the red region (G). Top: [O III]/L_{TIR} as a function of L_{TIR}. Center: [O III]/[N II] 122 µm as a function of L_{TIR}. Bottom: [O III]/[O I] 63 µm as a function of L_{TIR}.*

the DGS sample, the abundance ratio O/N in 30Dor is about a factor of two higher than the solar ratio.

The bottom panel of Figure IV.4 presents the ratio [O III] 88 µm/[O I] 63 µm. [O I] 63 µm is one of the main coolants in resolved PDRs, while [O III] is a tracer of the ionized gas. This ratio is independent of the variations of the elemental abundances and thus can be considered as an indicator of volume filling factor of the PDRs in the ionized gas. This ratio is on average higher in the dwarf galaxies than in more metal-rich galaxies, highlighting a more porous medium, with a high filling fraction of ionized gas (Hunter et al. 2001; Cormier et al. 2015). The values observed in 30Dor are on average higher than those in the other dwarf galaxies and are spread over more than an order of magnitude (between 5 and 70), with the highest values found in the more diffuse regions. In 30Dor, as well as in other extended sources in the LMC (e.g. N11B; Lebouteiller et al. 2012) [O III] 88 µm is detected over large spatial scales, suggesting that high energy photons are able to excite the gas far from the ionizing source. We note a tendency of decreasing [O III] 88 µm/[O I] 63 µm with increasing TIR, showing a correlation between the volume filling factor of the PDR relative to the ionized gas and the presence of dust.

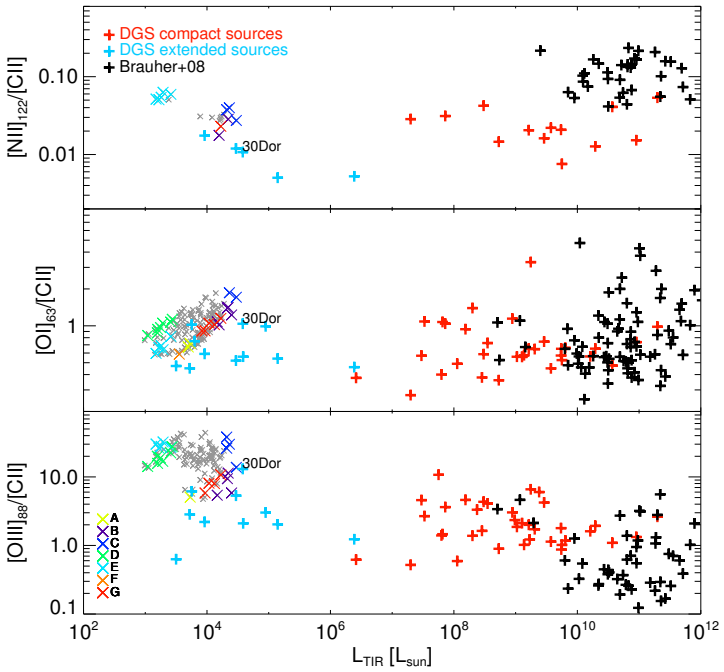

Figure IV.5: *Top: [N II] 122 µm/[C II] as a function of L_{TIR}. Center: [O I] 63 µm/[C II] as a function of L_{TIR}. Bottom: [O III]/[C II] as a function of L_{TIR}. The color coding is the same as in Figure IV.4*

Origin of [C II]

With an ionization potential for carbon of 11.3 eV, slightly lower than that of hydrogen, [C II] can originate from both the ionized gas and the neutral gas. As it is one of the brightest FIR fine-structure lines, it is important to identify the origin of [C II] and use it quantitatively in PDR models for example. Since the critical density of [C II] in the ionized gas is $\sim 50\,\mathrm{cm}^{-3}$ and since carbon becomes doubly ionized for energies higher than 24.5 eV, the physical conditions to produce [C II] emission in the ionized gas are close to those of [N II] 122 µm. Indeed, it requires 14.5 eV to singly ionize nitrogen, and 19.6 eV to doubly ionize it, and the critical density of [N II] 122 µm is $310\,\mathrm{cm}^{-3}$. Thus, [N II] 122 µm also originates from the low ionization, low density gas. There is only a negligible fraction of [C II] arising from the [N III] emitting gas, and [N II] 122 µm is a good tracer of the fraction of the [C II] emission arising from the ionized gas.

In the upper panel of Figure IV.5 we note that all of the dwarf galaxies have a ratio [N II] 122 µm/[C II] lower than the galaxies of the Brauher et al. metal-rich sample (Cormier et al. 2015). In 30Dor in particular, this ratio ranges between 0.02 and 0.06, with the highest values in the more diffuse regions where [C II] is relatively fainter. Oberst et al. (2006) show that [C II] originates from ionized gas only for ratios [N II] 122 µm/[C II] >0.1. The low values of the ratio [N II] 122 µm/[C II] observed in 30Dor in particular, suggest that [C II] originates mostly from the PDR gas. The highest value of [N II] 122 µm/[C II] (~ 0.06) can be found in the more diffuse regions. A more quantitative study is done in Section IV.2.1 and shows that ~90% of [C II] is emitted from the PDR in 30Dor.

The low ratio [N II] 122 µm/[C II] is also favored by the relatively faint [N II] 122 µm line in the dwarf galaxies. Indeed, the presence of N^{++} is favored in regions of high ionization as is the case for dwarf galaxies, and in particular for the extended regions of the DGS, chosen as active star-forming regions, so the ratio [N II] 122 µm/L_{TIR} is on average lower in dwarf galaxies than more metal-rich galaxies (Cormier 2012; Croxall et al. 2012).

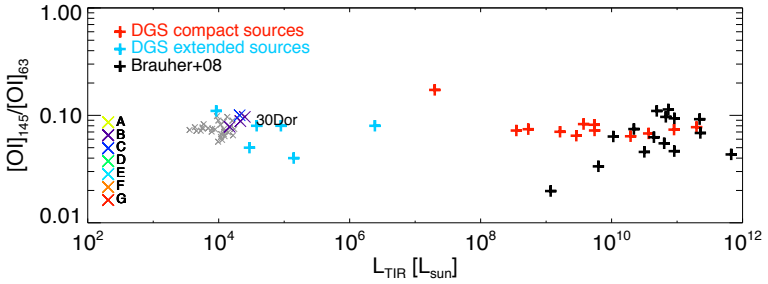

Figure IV.6: *[O I] 145 μm/[O I] 63 μm as a function of L_{TIR}. The color coding is the same as in Figure IV.4*

[O I] 63 μm and [C II] 158 μm can both trace, in principle, the neutral ISM. As shown in the middle panel of Figure IV.5 the range of values for the ratio [O I] 63 μm and [C II] 158 μm is similar for the dwarf galaxies as for the more metal-rich galaxies. There is no correlation with L_{TIR}. PDR studies show that [O I] 63 μm dominates in denser regions and in regions of intense radiation fields, while [C II] dominates in more diffuse regions (e.g. Wolfire et al. 2003; Kaufman et al. 2006), since the critical density and excitation energy are higher for [O I] 63 μm than for [C II]. Hence, the ratio [O I] 63 μm/[C II] is expected to increase with density and radiation field strength. Indeed, in 30Dor, the ratio ranges from 0.5 in the more diffuse regions, to 2 close to the peak of [O III] 88 μm, where the radiation field is expected to be the strongest. These values could actually be higher since [O I] 63 μm can be affected by optical depth effects (see below).

Contrary to more metal-rich galaxies where [C II] and [O I] 63 μm are dominant, [O III] 88 μm is often the brightest FIR line in the dwarf galaxies (e.g. Hunter et al. 2001; Cormier et al. 2015). In 30Dor in particular, [O III] 88 μm is brighter than [C II] throughout the entire PACS map. At $\sim$ 3 pc scale, the ratio [O III] 88 μm/[C II] shows extreme values up to 50, in particular at the peak of [O III] 88 μm and also in the more diffuse regions, due to the very extended [O III] 88 μm emission. This high ratio is also found over full galaxy scales (2.1 on average for the DGS galaxies; Cormier et al. 2015). This ratio is affected by variations in the abundance ratio of O/C. However, this abundance ratio is only a factor of two higher in 30Dor than the solar abundance ratio, so it cannot explain entirely the discrepancy between the high 30Dor values and the more moderate values of the Brauher et al. metal rich sample. As for the ratio [O III] 88 μm/[O I] 63 μm, these high values can only be achieved through a combination of a high stellar effective temperature and a high volume factor of the ionized gas compared to the PDRs.

Opacity of [O I] 63 μm

[O I] 145 μm is always fainter than [O I] 63 μm (by a factor of $\approx$ 10) for all galaxies in Cormier et al. (2015), resolved and integrated. The ratio [O I] 145 μm/[O I] 63 μm ranges between 0.05 and 0.11 in 30Dor, although the size of the map is limited here by the spatial coverage of the [O I] 145 μm PACS map. This is in the range of values found for the DGS galaxies and the Brauher et al. sample. Although the values are moderate, it may be important to take into account possible optical depth effects for the [O I] 63 μm line in the case of high [O I] 145 μm/[O I] 63 μm values ($\sim$ 0.1 or above).

These empirical considerations highlight the extreme environment in the 30Dor region compared to the normal galaxies of the Brauher et al. (2008) sample, and even among the metal-poor dwarf galaxies of the DGS sample (Cormier et al. 2015). The [O III] 88 μm emission line is the brightest FIR

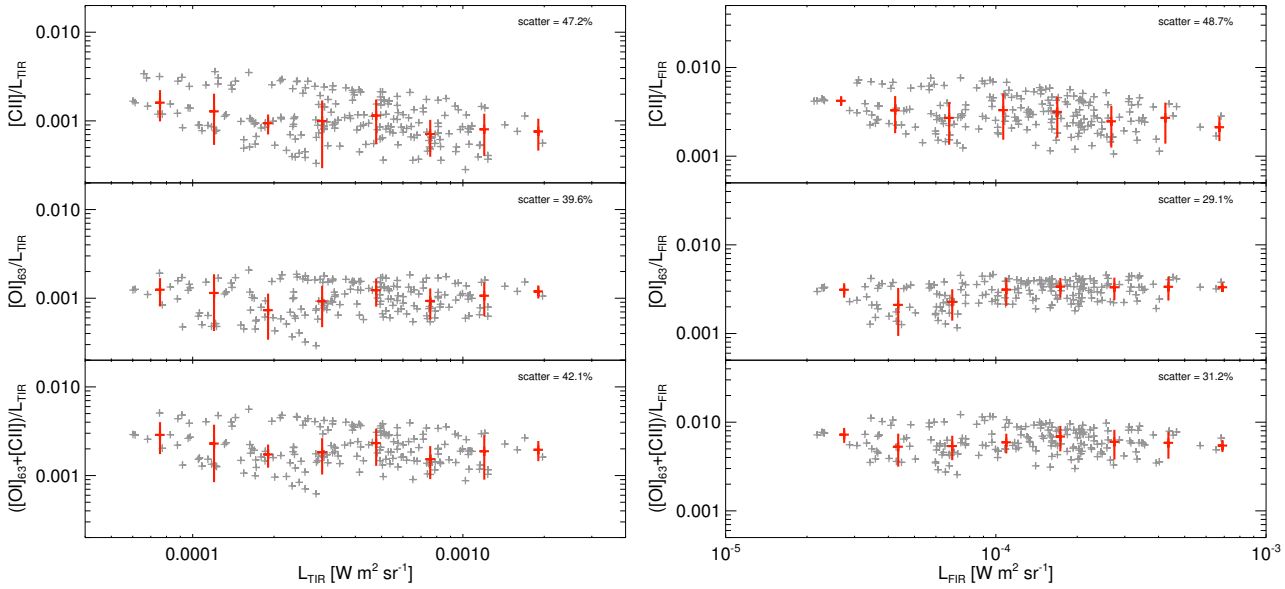

Figure IV.7: *Left: ratios [C II]/L_{TIR} (top), [O I] 63 μm/L_{TIR} (middle) and ([O I] 63 μm+[C II])/L_{TIR} (bottom) as a function of L_{TIR}. The [C II], [O I] and L_{TIR} maps are at 12″ resolution and have been rebinned to 12″. The different points can then be considered as independent pixels. In red are the median and the dispersion (1-σ) of the ratios in bins of 0.2 dex in L_{TIR}, chosen to include at least two points in each bin. Right: same for L_{FIR} instead of L_{TIR}.*

line over the entire mapped region, not the [C II] line as for other starburst galaxies. This is showing that the ISM is highly excited by the SSC R136 and probably very porous. The [C II] emission line originates from the PDRs for the most part. Section IV.2.1 presents more quantitative results by confronting the PACS observations with a PDR model.

IV.1.3 Photoelectric heating efficiency

The gas in PDRs and in neutral atomic clouds is mostly heated through collisions with electrons ejected from small dust grains through the photoelectric effect (e.g., Hollenbach & Tielens 1999; Weingartner & Draine 2001a). The efficiency of the photoelectric effect to heat the gas is then defined, at thermal equilibrium, as the ratio of photoelectric heating rate (Γ_{PE}, in erg cm^{-3} s^{-1}) over the power absorbed by the grains (P_{abs}, in erg cm^{-3} s^{-1}) through UV and optical photons:

$$\epsilon_{PE} = \frac{\Gamma_{PE}}{P_{abs}} \tag{IV.1}$$

(Rubin et al. 2009). The neutral gas, heated by photoelectrons ejected from small dust grains, cools through collisionally excited fine structure lines. [C II] and [O I] 63 μm are two of the main coolants of the neutral gas. Since the thermal radiation from radiatively warm dust peaks in the far-IR, L_{TIR} and L_{FIR} are good tracers of the dust heating. Therefore, the ratio of the gas cooling lines to the dust heating tracers can be considered to be a proxy for the fraction of the energy absorbed by dust that is transferred to the gas heating: the efficiency of the photoelectric heating.

Figure IV.7 presents the correlation between [C II], [O I] 63 μm and their sum with L_{TIR} and L_{FIR}. We note that there is a trend of decreasing [C II]/L_{TIR} (respectively [C II]/L_{FIR}) and a slight increase of [O I] 63 μm/L_{TIR} (respectively [O I] 63 μm/L_{FIR}) with increasing L_{TIR} (resp. L_{FIR}). This is due to different PDR conditions: [C II] is the dominant coolant in the most diffuse regions, while [O I] 63 μm

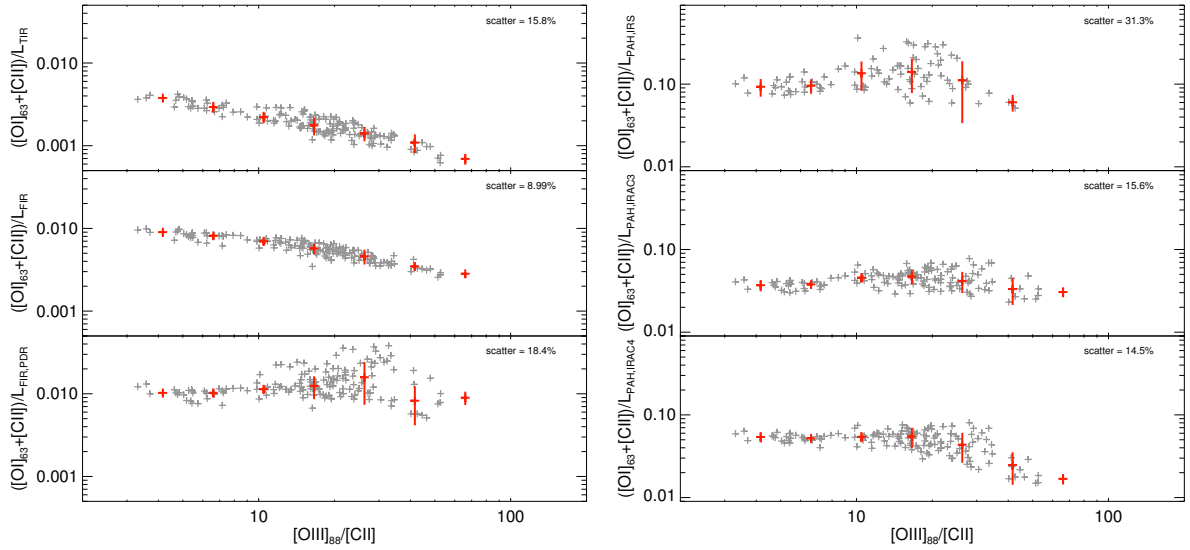

Figure IV.8: *Left: ([O I] 63 μm+[C II])/L_{TIR} (top), ([O I] 63 μm+[C II])/L_{FIR} (center) and ([O I] 63 μm+[C II])/L_{FIR}^{PDR} (bottom) as a function of [O III] 88 μm/[C II]. In red are the median and the dispersion (1-σ) of the ratios in bins of 0.2 dec in [O III]/[C II], chosen to include at least two points in each bin. Right: ([O I] 63 μm+[C II])/L_{PAH} as a function of [O III] 88 μm/[C II]. L_{PAH} is calculated from the IRS spectra (top), IRAC band 3 (center) and IRAC band 4 (bottom).*

dominates in denser regions and in regions of intense radiation field due to the different critical density and excitation energy (e.g. Wolfire et al. 2003; Kaufman et al. 2006). The sum of the contributions ([O I] 63 μm+[C II])/ L_{TIR} (resp. ([O I] 63 μm+[C II])/ L_{FIR}) is relatively flat with respect to L_{TIR} (resp. L_{FIR}).

The scatter is large: ~50% for [C II]/L_{TIR} and [C II]/L_{FIR} and ~ 40 – 30% for [O I] 63 μm/L_{TIR} and [O I] 63 μm/L_{FIR}. The dispersion for a given ratio is slightly smaller for L_{FIR} than for L_{TIR}. This dispersion is most probably due to the contamination of L_{TIR} and L_{FIR} from the big grains in equilibrium with the interstellar radiation field (ISRF) in the ionized gas phase. Indeed, as presented in left panel of Figure IV.8 there is a tight correlation between the ratio of the gas coolants over L_{TIR} or L_{FIR} and the ratio [O III] 88 μm/[C II], which is an indicator of the ionization state of the gas. Although L_{FIR} is integrated between a shorter wavelength range (60-200 μm) compared to L_{TIR} (3-1000 μm) there is still a substantial component coming from the ionized gas contributing to the dust continuum emission. The total IR emission must be corrected for this emission from the ionized gas to use L_{TIR} or L_{FIR} as a proxy of the gas heating in the neutral PDRs. To do that, we decompose linearly L_{FIR}, using the [O III] 88 μm emission as a proxy for the ionized gas and L_{PAH} as a proxy for the PDRs. More details on the method can be found in Section III.1.3. In this case (bottom left panel of Figure IV.8), although there is some scatter of the ratio ([O I] 63 μm+[C II])/L_{FIR}^{PDR}, there is no correlation with the ratio [O III] 88 μm/[C II] as we have subtracted the component from the ionized gas contributing to L_{FIR}. Alternatively, L_{PAH} might be a better proxy of the gas heating in this region.

Several studies (e.g. Croxall et al. 2012; Lebouteiller et al. 2012) have shown that the PAH emission can trace the ejection of photoelectrons in many environments, more effectively than the integrated dust emission. In 30Dor as well, we find that the scatter of the ratio ([O I] 63 μm+[C II])/ L_{PAH} is smaller than that of the ratio ([O I] 63 μm+[C II])/ L_{FIR} (≥20% and ~30% respectively) as shown in the left panel of Figure IV.9. This figure presents the correlation between ([O I] 63 μm+[C II])/ L_{PAH}

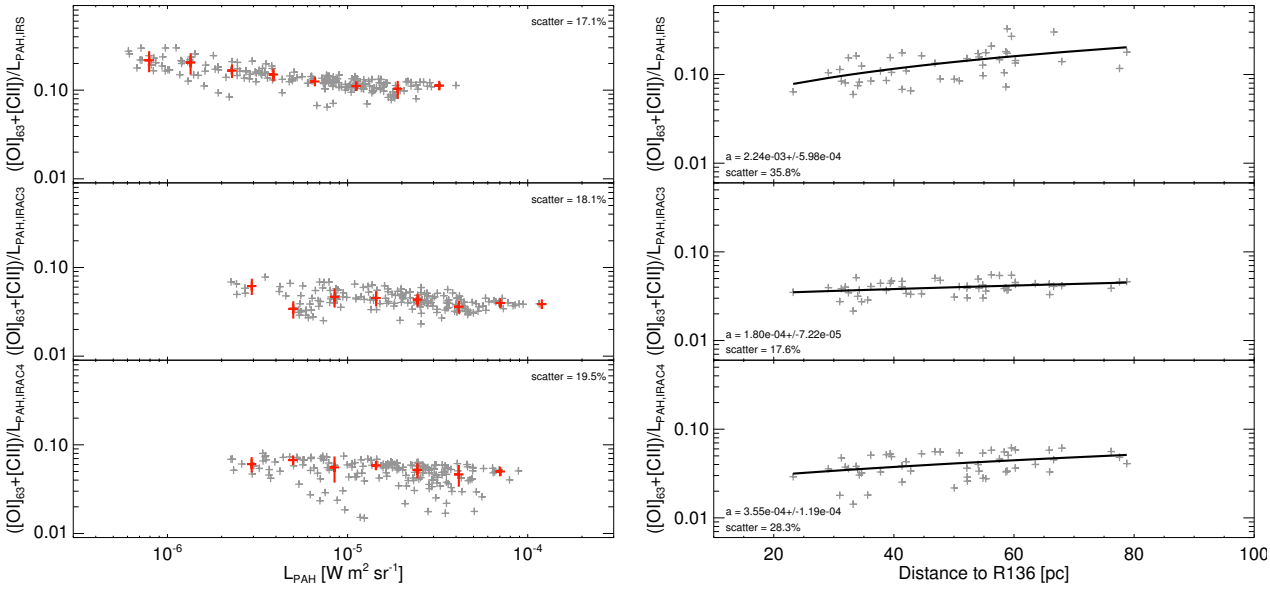

Figure IV.9: *Left: ([O I] 63 μm+[C II])/ L_{PAH} as a function of L_{PAH} for PAH emission in 30Dor, calculated from the IRS spectrum (top), IRAC channel 3 (center) and IRAC channel 4 (bottom). In red are the median and the dispersion (1-σ) of the ratios in bins of 12 pc, chosen to include at least two points in each bin. Right: Same ratios as a function of the distance in parsecs to the center of R136 from the PDR model (Sect. IV.2.1). The black line is a linear fit to the data.*

and L_{PAH} where L_{PAH} is calculated with the different methods presented in Section III.2 (from the fit of the IRS spectrum or from the IRAC3 or IRAC4 channels). The scatter is similar for all three methods, although the correlation is slightly tighter with the PAHs extracted from IRAC3 emission than from the extrapolation in IRAC4, and even tighter with the PAH spectral features from the IRS spectra. However, the absolute values are different, since they depend on the calibration chosen for the IRAC extrapolation, as discussed in Section III.2.

We can note from the left panel of Figure IV.9 that although the relation between ([O I] 63 μm+[C II])/ L_{PAH} and L_{PAH} is relatively flat, there is a tendency for higher ([O I] 63 μm+[C II])/L_{PAH} at low L_{PAH} values. This might be an effect of grain charging: the photoelectric effect is less efficient for ionized grains (e.g. Malhotra et al. 2001; Okada et al. 2013). As a consequence, the cooling line emission decreases relatively to the warm dust continuum close to the ionizing source, where grains are mostly ionized. On the other hand, as we go further from the ionizing source, grains are becoming more neutral and the photoelectric effect is more efficient, resulting in a higher ratio ([O I] 63 μm+[C II])/L_{PAH}. To test this assumption, we present in the right panel of Figure IV.9 the ratios ([O I] 63 μm+[C II])/ L_{PAH} as a function of the distance from R136 for the different estimates of PAH emission. The distance to R136 is derived from the results of the PDR modeling detailed in Section IV.2.1. Although the scatter is large, there is a tendency for increasing ([O I] 63 μm+[C II])/L_{PAH} with increasing distance (hence decreasing grain charging). Then variation of the grain charging probably contributes to the apparent variation of $\epsilon_{PE,PAH}$, although there might be another process at play here.

We find a similar efficiency in the photoelectric heating ($\sim$ 1%) due to small grains (probed by L_{FIR}) and due to PAHs (probed by L_{PAH}). Contrary to the result found by Lebouteiller et al. (2012) in the star-forming region N11-B in the LMC, dust components probed by L_{FIR}^{PDR} seem to dominate the gas heating in 30Dor over PAHs.

IV.2 PDR modeling of 30Dor

IV.2.1 Paper published in A&A, March 2016

In this paper we have conducted a detailed *spatial* modeling of the extreme 30Dor region in the LMC. We have confronted the mid-infrared (MIR) and far-infrared (FIR) fine structure line maps observed by *Spitzer* and *Herschel* with the Meudon photodissociation (PDR) code (Le Petit et al. 2006) to determine the impact of the ionization source on the surrounding ISM. The combination of the ionized gas, neutral gas and molecular gas tracers provides strong constraints on the models to estimate the size, pressure and filling factor of each phase, the fraction of CO-dark gas, the density structure, along with the distribution of the radiation field. By comparison of the distribution of the incident radiation field with the emitted radiation field by the stars, we have also been able to determine the three dimensional view of the region.

A&A 590, A36 (2016)
DOI: 10.1051/0004-6361/201527735

Astronomy & Astrophysics

A milestone toward understanding PDR properties in the extreme environment of LMC-30 Doradus⋆

M. Chevance[1,2], S. C. Madden[1], V. Lebouteiller[1], B. Godard[3], D. Cormier[4], F. Galliano[1], S. Hony[4], R. Indebetouw[5,6], J. Le Bourlot[3], M.-Y. Lee[1], F. Le Petit[3], E. Pellegrini[4], E. Roueff[3], and R. Wu[7]

[1] Laboratoire AIM, CEA/DSM – CNRS – Université Paris Diderot, IRFU/Service d'Astrophysique, CEA Saclay, 91191 Gif-sur- Yvette, France
e-mail: melanie.chevance@cea.fr
[2] Université Paris Diderot, Sorbonne Paris Cité, 75205 Paris, France
[3] LERMA, Observatoire de Paris & CNRS, 5 place Jules Janssen, 92190 Meudon, France
[4] Institut für theoretische Astrophysik, Zentrum für Astronomie der Universität Heidelberg, Albert-Ueberle Str. 2, 69120 Heidelberg, Germany
[5] Department of Astronomy, University of Virginia, PO Box 3818, Charlottesville, VA 22903, USA
[6] National Radio Astronomical Observatory, Charlottesville, VA 22904, USA
[7] Department of Astronomy, Graduate School of Science, The University of Tokyo, Bunkyo-ku, 113-0033 Tokyo, Japan

Received 12 November 2015 / Accepted 14 March 2016

ABSTRACT

Context. More complete knowledge of galaxy evolution requires understanding the process of star formation and the interaction between the interstellar radiation field and interstellar medium (ISM) in galactic environments traversing a wide range of physical parameter space. We focus on the impact of massive star formation on the surrounding low metallicity ISM in 30 Doradus in the Large Magellanic Cloud (LMC). A low metal abundance, which can characterizes some galaxies of the early Universe, results in less ultraviolet (UV) shielding for the formation of the molecular gas necessary for star formation to proceed. The half-solar metallicity gas in this region is strongly irradiated by the super star cluster R136, making it an ideal laboratory to study the structure of the ISM in an extreme environment.

Aims. Our goal is to construct a comprehensive, self-consistent picture of the density, radiation field, and ISM structure in the most active star-forming region in the LMC, 30 Doradus. Our *spatially* resolved study investigates the gas heating and cooling mechanisms, particularly in the photodissociation regions (PDR) where the chemistry and thermal balance are regulated by far-UV photons (6 eV < $h\nu$ < 13.6 eV).

Methods. We present *Herschel* observations of far-infrared (FIR) fine-structure lines obtained with PACS and SPIRE/FTS. We combined atomic fine-structure lines from *Herschel* and *Spitzer* observations with ground-based CO data to provide diagnostics on the properties and structure of the gas by modeling it with the Meudon PDR code. For each tracer we estimate the possible contamination from the ionized gas to isolate the PDR component. We derive the spatial distribution of the radiation field, the pressure, the size, and the filling factor of the photodissociated gas and molecular clouds.

Results. We find a range of pressure of $\sim 10^5$–1.7×10^6 cm^{-3} K and a range of incident radiation field $G_{\rm UV} \sim 10^2$–2.5×10^4 through PDR modeling. Assuming a plane-parallel geometry and a uniform medium, we find a total extinction $A_V^{\rm max}$ of 1–3 mag, which corresponds to a PDR cloud size of 0.2 to 3pc with small CO depth scale of 0.06 to 0.5 pc. At least 90% of the [C II] originates in PDRs in this region, while a significant fraction of the $L_{\rm FIR}$ (up to 70% in some places) can be associated with an ionized gas component. The high [O III]/[C II] ratio (2 to 60) throughout the observed map, correlated with the filling factor, reveals the porosity of the ISM in this region, which is traversed by hard UV photons surrounding small PDR clumps. We also determine the three-dimensional structure of the gas, showing that the clouds are distributed 20 to 80 pc away from the main ionizing cluster, R136.

Key words. ISM: general – photon-dominated region (PDR) – Magellanic Clouds – ISM: individual objects: LMC-30 Doradus – ISM: clouds – ISM: structure

1. Introduction

Galaxy evolution is dictated by progressive chemical enrichment, which is mostly achieved through a succession of star formation episodes. The effect of metal enrichment, on what we observe to be the star formation and interstellar medium (ISM) properties, remains elusive despite circumstantial evidence. For example, reduced metallicity is expected to have important consequences on the chemistry and the subsequent heating and cooling mechanisms of the gas and dust, directly affecting the transition of the atomic to molecular phase. In low metallicity environments, the transition between C^+/C/CO can be shifted further into the cloud in physical scale, leaving a relatively larger photodissociation region (PDR) and a smaller CO core compared to more metal-rich environments, such as the Milky Way (Kaufman et al. 1999). This effect on the molecular cloud structure manifests itself in an observed low CO luminosity in dwarf galaxies (e.g., Cormier et al. 2014; Schruba et al. 2012) and requires a higher CO-to-H_2 conversion factor, i.e., the

⋆ The reduced images are only available at the CDS via anonymous ftp to cdsarc.u-strasbg.fr (130.79.128.5) or via http://cdsarc.u-strasbg.fr/viz-bin/qcat?J/A+A/590/A36

X_{CO} factor (Schruba et al. 2012; Bolatto et al. 2013). The low observed CO luminosity could also possibly be explained by a higher star formation efficiency.

Dwarf galaxies in our local Universe are the closest environments we can explore in detail to witness the interplay between star formation and ISM under low metallicity conditions. Large surveys probing the cooling of dwarf galaxies are possible for the first time with the *Herschel* Space Observatory (Pilbratt et al. 2010; e.g., the Dwarf Galaxy Survey, DGS; Madden et al. 2013). Recent studies taking advantage of the *Herschel* sensitivity, have modeled the dust and gas properties of a wide range of low metallicity galaxies on integrated galaxy scales (e.g., Rémy-Ruyer et al. 2013, 2014, 2015; Cormier et al. 2012, 2015; Cigan et al. 2016) and find prominent differences between metal-rich and metal-poor galaxies. For example, from far-infrared (FIR) line ratios, Cormier et al. (2015) determined that radiation fields over global galaxy scales are harder in star-forming dwarf galaxies compared to more metal-rich galaxies. Furthermore, the filling factor of the ionized gas appears larger relatively to the neutral gas. As a consequence of the low metallicity and low extinction in dwarf galaxies, it is possible that a significant fraction of the molecular gas is not traced by CO, but may be residing in the C^+ or C^0 – emitting region; for example (referred to as the "dark gas" in Wolfire et al. 2010), this is quantified in low metallicity environments using C^+ by Poglitsch et al. (1995) and Madden et al. (1997) and, more recently, in our Galaxy by Langer et al. (2014) and Pineda et al. (2014).

The Large Magellanic Cloud (LMC) is our closest low metallicity galaxy neighbor (1/2 $Z_\odot$; Rolleston et al. 2002; Pagel 2003; 50 kpc; Walker 2012) allowing us to zoom into the ISM at the spatial resolution of ∼12″ (∼3 pc) with *Herschel*. We focus on 30 Doradus (hereafter "30Dor"), which is the most prominent star-forming region in the LMC and provides the best laboratory to study the impact of a super star cluster (SSC) on the ISM. The primary ultraviolet (UV) radiation source illuminating this region is the SSC R136, containing 39 O3 stars (Hunter 1999), which are often considered to be the most extreme star-forming region in the Local Group. The lower dust abundance of the LMC allows for deep penetration of the ionizing radiation, creating extended PDR regions and a more porous environment channeling the UV photons. Observations at the Atacama Large (sub)Millimeter Array (ALMA) from Indebetouw et al. (2013) revealed the clumpy structure of the molecular gas in 30Dor, showing small ^{12}CO filaments and clumps ($\lesssim$1 pc) covering about 15% of their map. We examine the PDR conditions in the neutral atomic gas using mainly [C II] and [O I] observed by *Herschel* in this region to unveil the spatial distribution of the radiation field and structure of the photodissociated gas and molecular clouds. The fraction of CO-dark gas based on this detailed study will be quantified in a following study (Chevance et al., in prep., hereafter Paper II).

Observations of the ionized gas were conducted with *Spitzer* and studied by Indebetouw et al. (2009). They showed in particular that photoionization dominates the ionization structure of the gas over shocks in the H II region around R136. A study of the fine structure lines of C^+ and O^0 in 30Dor has been previously carried out by Poglitsch et al. (1995) with the Kuiper Airborne Observatory (KAO) at a resolution of ∼55″ (∼13 pc). These authors found that a highly fragmented structure with high density clouds ($n = 10^3$–10^4 cm^{-3}), of low relative beam filling factor of CO compared to the PDR (4% of the clumps volume), bathed in ionized gas could explain the observed ratio [C II]/CO (i.e., ten times higher than the Galactic value). Moreover, most of the molecular gas may be present in the PDR and faint in CO. Now, the PACS observations provide better spatial resolution than the KAO data and include other important tracers with an improved signal-to-noise ratio (S/N). Pineda et al. (2012) investigated the CO and [C I] emission observed with the NANTEN2 4-m telescope in a 26″ beam, combined with the KAO observations of [C II] in 30Dor, and found likewise a very clumpy medium.

We present spectroscopic data of 30Dor in Sect. 2. Section 3 describes the observed maps and some preliminary results. In Sect. 4 we use PDR models to determine the physical parameters of the gas in PDR and we study the impact of metallicity and geometry on these parameters. We discuss our results and build a comprehensive 3D picture of the region in Sect. 5. Key results and conclusions are summarized in Sect. 6.

2. Observations and data preparation

2.1. Herschel PACS spectroscopy

We have mapped five fine structure lines, [C II] 158 μm, [N II] 122 μm, [O I] 63 μm, [O I] 145 μm, and [O III] 88 μm using the Photodetector Array Camera and Spectrometer (PACS; Poglitsch et al. 2010) toward 30Dor. Properties of these lines are presented in Table 1 and the maps can be seen in Fig. 1. These observations, described in Madden et al. (2013), are part of the *Herschel* key program, SHINING (P.I. E. Sturm). We also used two additional pointings east of R136, which were observed by Indebetouw et al (OT2) in [C II], [O I] 63 μm, [N II] 122 μm, and [O III] 88 μm. The details of the observations are shown in Appendix A.

The PACS array is composed of 5 × 5 spatial pixels (or *spaxels*) of 9.4″ covering a total field of view of 47″. The fine structure lines [O I] 63 μm, [O III] 88 μm, [N II] 122 μm, [O I] 145 μm, and [C II] were mapped with respectively 25, 25, 4, 11, and 31 raster positions, covering approximately a 4′ × 5′ region (56 pc × 70 pc). The observations were carried out in unchopped mode. The beam size is 9.5″ at 60 μm, and 12″ at 160 μm (PACS Observer's Manual 2011).

We refer to Cormier et al. (2015) for the full description of the PACS observations and data reduction, and we summarize some of the main steps here. The data are reduced with the *Herschel* interactive processing environment (HIPE) v12.0.0 (Ott 2010) from Level 0 to Level 1. The Level 1 cubes, calibrated in flux and wavelength, are then exported and processed with PACSman v3.61 (Lebouteiller et al. 2012) to fit the lines and create the individual maps. Each spectrum is fitted with a second order polynomial for the baseline and a Gaussian for the line. Finally the individual rasters are projected onto a common grid of 3″ × 3″ pixels (0.72 × 0.72 pc) to reconstruct the final maps. Uncertainties on the fit and projection are estimated using a Monte-Carlo simulation. All of the lines are well detected everywhere in the map (Fig. 1). The weakest line, [N II] 122 μm has a S/N between 5 and 30 for most of the mapped area. The emission line [O I] 145 μm has a S/N between 7 and 90 and the S/N is above 10 for all of the other lines.

The observed intensities match well those detected with the KAO by Poglitsch et al. (1995) with a lower spatial resolution (55″ for [C II] and [O I] 145 μm and 22″ for [O I] 63 μm). For example, they found a maximum [C II] intensity of 10^{-3} erg s^{-1} cm^{-2} sr^{-1}, and we measure a maximum intensity of 1.1×10^{-3} erg s^{-1} cm^{-2} sr^{-1} on PACS data convolved to the same resolution. They are also similar to the [C II] intensities measured by Requena-Torres (in prep.) using the German REceiver for

Table 1. Properties of lines and observations.

Instrument	Transition	λ (μm)	*FWHM* (arcsec)	Ionization energy (eV)	$n_{\rm crit}{}^a$ (cm^{-3})
PACS	[O I] $^3P_1$–$^3P_2$	63.2	9.5	–	4.7×10^5 [H]
	[O I] $^3P_0$–$^3P_1$	145.5	11.0	–	9.5×10^4 [H]
	[O III] $^3P_1$–$^3P_0$	88.3	9.5	35.1	510 [e]
	[C II] $^2P_{3/2}$–$^2P_{1/2}$	157.7	11.6	11.3	2.8×10^3 [H], 50 [e]
	[N II] $^3P_2$–$^3P_1$	121.8	9.9	14.5	310 [e]
SPIRE/FTS	[N II] $^3P_1$–$^3P_0$	205.3	16.6	14.5	48 [e]
	[C I] $^3P_2$–$^3P_1$	370.4	36.2	–	1.2×10^3 [H_2]
	[C I] $^3P_1$–$^3P_0$	609.7	38.6	–	4.7×10^3 [H_2]
Spitzer/IRS[b]	[S III] $^3P_2$–$^3P_1$	18.7	4.9	23.3	2×10^4 [e]
	[S III] $^3P_1$–$^3P_0$	33.5	8.9	23.3	7×10^3 [e]
	[Si II] $^2P_{3/2}$–$^2P_{1/2}$	34.8	9.4	8.1	3.4×10^5 [H], 1×10^3 [e]
	[Ar II] $^2P_{1/2}$–$^2P_{3/2}$	7.0	2.0	15.8	4.0×10^5 [e]
Mopra[c]	^{12}CO $J = 1 \rightarrow 0$	2600	43	–	1.8×10^3 [H_2]
ASTE[d]	^{12}CO $J = 3 \rightarrow 2$	867	22	–	3.2×10^4 [H_2]

Notes. [(a)] Critical densities are noted [e] for collisions with electrons ($T = 10\,000$ K), [H] with hydrogen atoms ($T = 100$ K), and [H_2] with molecular hydrogen ($T = 10$ K, in the optically thin limit). [(b)] Indebetouw et al. (2009); [(c)] Wong et al. (2011); [(d)] Minamidani et al. (2011).

Astronomy at Terahertz frequencies (GREAT; Heyminck et al. 2012) instrument on the Stratospheric Observatory For Infrared Astronomy (*SOFIA*).

2.2. Herschel SPIRE spectroscopy

The Spectral and Photometric Imaging Receiver (SPIRE) instrument includes an Imaging Fourier Transform Spectrometer (FTS) covering the wavelength ranges 194–324 and 316–672 μm (SPIRE Short Wavelength SSW and SPIRE Long Wavelength SLW arrays, respectively). The 30Dor nebula was observed with the SPIRE FTS in the high spectral resolution ($\Delta\nu \sim 1.2$ GHz), intermediate spatial sampling mode. In the intermediate spatial sampling mode, SLW and SSW are moved between four jiggling positions with a spacing of ~28″ and ~16″, respectively. The observations were performed on January 8, 2013 (observation IDs: 1342219550, 1342257932 and 1342262908) with a total integration time of ~15 400 s.

We process the FTS data using HIPE version 11.0.2825 and the SPIRE calibration version 11.0 (Fulton et al. 2010; Swinyard et al. 2013). We use the method from Wu et al. (2013) to derive integrated intensity images and their uncertainties. This script has recently been used to generate FTS spectral cubes for M83 (Wu et al. 2015). A combination of parabola (continuum) and sinc (emission) functions is used to model a spectral line. The spectra are then projected onto a grid that covers a 5′ × 5′ area with a pixel size of 15″ (roughly corresponding to the detector spacing for SSW). We perform a Monte-Carlo simulation with 300 iterations to estimate the uncertainties on the spectra, as described in detail in Lee et al. (in prep.). The S/N is between 1 and 8 for [N II] 205 μm and between 0.5 and 5 for [C I] 370 μm. The [C I] 609 μm is weaker and the S/N is below 2.

The maps of [N II] 205 μm and [C I] 370 and 609 μm are presented in Figs. 1 and 2. Properties of these lines are presented in Table 1. The CO transitions from $J = 4$–3 to $J = 13$–12 were also observed in 30Dor and will be presented in Lee et al. (in prep.).

2.3. Herschel and Spitzer photometry

To constrain the PDR models, we need to calculate the infrared luminosity, which requires photometry data from mid-infrared (MIR) to submillimeter. The PACS and SPIRE maps of the LMC at 100, 160 250, 350, and 500 μm were first published in Meixner et al. (2013) as part of the HERITAGE project. We also use the observations of 30Dor obtained as part of the *Spitzer* (Werner et al. 2004) Legacy program "Surveying the Agents of a Galaxy's Evolution" (SAGE; Meixner et al. 2006). We used the four channels of the Infrared Array Camera (IRAC; Fazio et al. 2004) at 3.6, 4.5, 5.8, and 8.0 μm and the Multiband Imaging Photometer for *Spitzer* (MIPS; Rieke et al. 2004) observations at 24 and 70 μm. The MIPS 24 μm map is saturated in several pixels. We use the *Spitzer* Infrared Spectrometer (IRS) spectra (Indebetouw et al. 2009; see also Sect. 2.4) to calculate the 24 μm synthetic photometry in the MIPS 24 bandpass and compare to the original map with excellent agreement in areas where the *Spitzer*/MIPS map is not saturated. Table 2 summarizes the photometry data we use to construct the infrared luminosity associated with their spatial resolution.

2.4. Spitzer/IRS spectroscopy

The *Spitzer*/IRS low-resolution data were initially presented in Indebetouw et al. (2009). The observed lines and their spatial resolution are listed in Table 1. We reduced again the low spectral resolution cubes with CUBISM (Smith et al. 2007a) as part of an effort to measure lines that have not been investigated yet in detail, in particular, the H_2 lines, [Si II], and [Ar II]. The resolving power of both short-wavelength/low-resolution (SL) and long-wavelength/low-resolution (LL) modules range approximately from 60 to 120 (*Spitzer* Observer's Manual 7.1 2006[1]). The maps of [Si II], [S III] 18 μm, and [S III] 33 μm are presented in Fig. 1.

We use the total emission of the polycyclic aromatic hydrocarbon molecules (PAHs), which has been fitted

[1] Available at http://ssc.spitzer.caltech.edu/documents/SOM

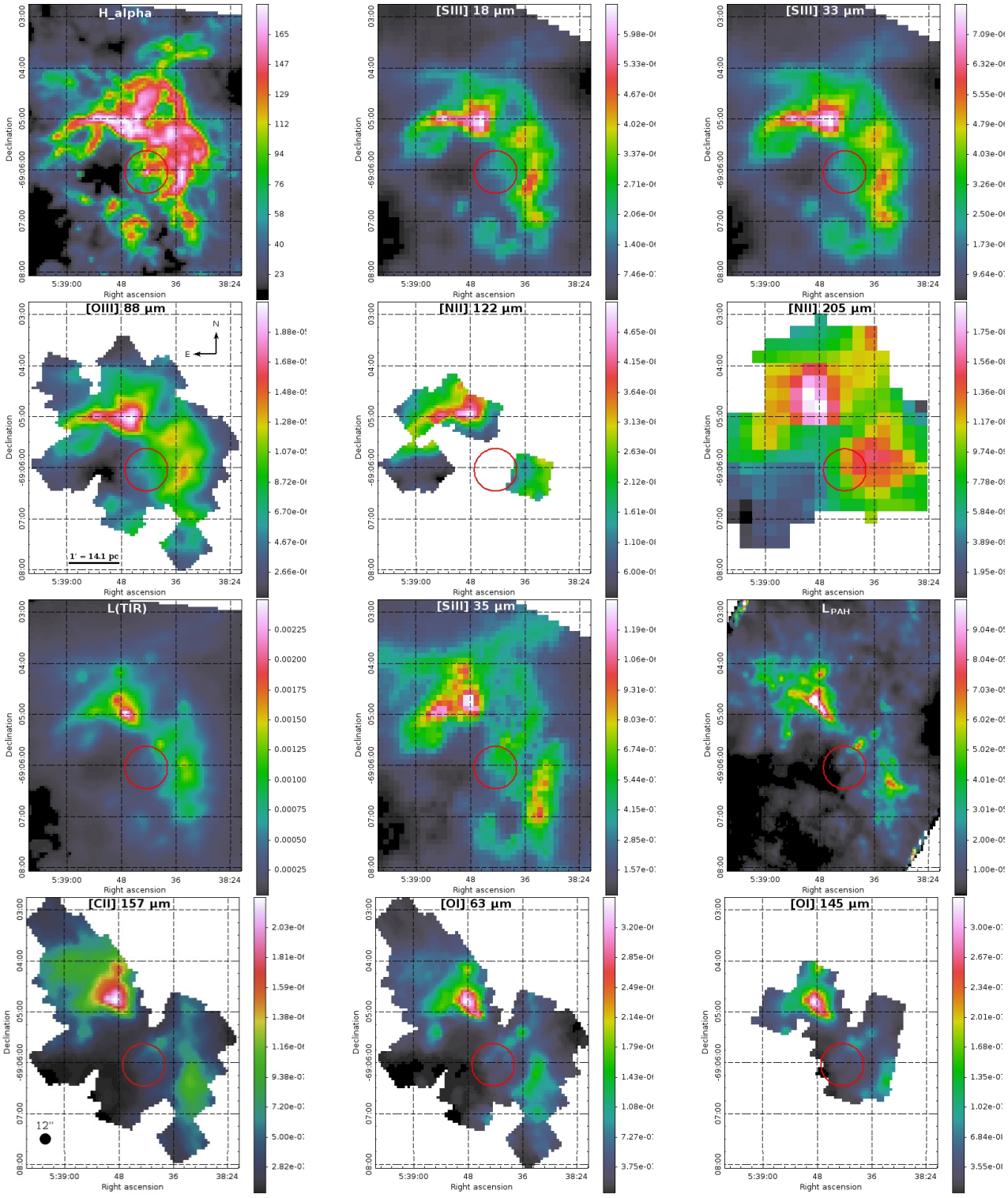

Fig. 1. Maps of PDR and ionized gas tracers from *Herschel* (PACS and SPIRE/FTS) and *Spitzer*/IRS observations of the 30Dor region in W m^{-2} sr^{-1}.The maps are shown at their original spatial resolution. The $L_{\rm TIR}$ map is the total infrared luminosity integrated between 3–1000 μm from our SED modeling. The red circle represents the location of the R136 cluster. Table 1 and Sect. 2 describe these observations in detail.

by Indebetouw et al. (2009) using the package PAHFIT (Smith et al. 2007b). Finally, we also use the *Spitzer*/IRS high-resolution spectra presented by Lebouteiller et al. (2008) to measure the H_2 lines.

2.5. Ground-based observations

Low-J CO transitions are required for additional constraints for the PDR modeling. We use the CO J = 1–0 transition observed

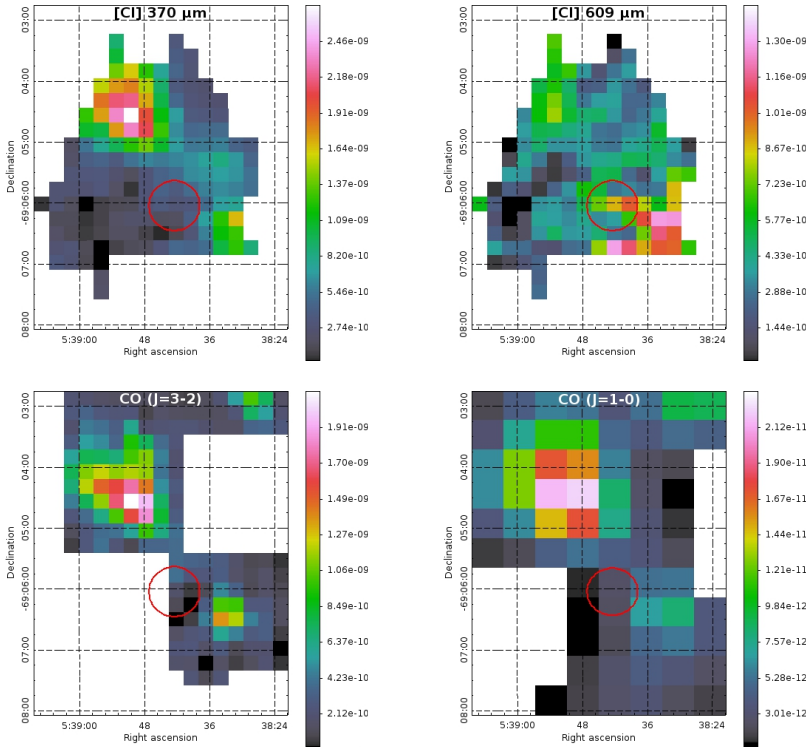

Fig. 2. *Top panels*: [C I] 370 μm (*left*) and [C I] 609 μm (*right*) SPIRE/FTS maps of 30Dor. *Bottom panels*: CO (3–2) ASTE map (*left*) and CO (1–0) Mopra map (*right*). All of the maps are shown at their original resolution, in W m^{-2} sr^{-1}. The circle shows the location of R136. Table 1 and Sect. 2 describe these observations in detail.

Table 2. Properties of the photometry data.

Instrument	λ (μm)	*FWHM* (arsec)
IRAC[a]	3.6	1.7
	4.5	1.7
	5.8	1.7
	8.0	1.9
MIPS	24	6
	70	18
PACS[b]	100	7.7
	160	12
SPIRE[b]	250	18
	350	25
	500	37

References. [(a)] SAGE (Meixner et al. 2006); [(b)] HERITAGE (Meixner et al. 2013)

with Mopra (Wong et al. 2011) and CO J = 3–2 observed with the Atacama Submillimeter Telescope Experiment (ASTE; Minamidani et al. 2011; see Fig. 2). The spatial resolutions for the Mopra and ASTE data are 42″ and 22″, respectively.

The H$_\alpha$ emission, which we use as a qualitative tracer of the ionized gas, was observed with the Cerro Tololo Inter-American Observatory (CTIO) Curtis Schmidt telescope as part of the Magellanic Clouds Survey (MCELS; priv. comm.; R. Leiton) at a resolution of ∼5″.

2.6. Convolution kernels

As we use line ratios of different wavelengths and different instruments (see Table 1), we must first convolve the maps to the same resolution. We add quadratically 12% uncertainties to the PACS maps to account for the absolute calibration uncertainties (PACS Observer's Manual v2.5.1). When we use only PACS observations, all of the maps are convolved to the resolution of PACS at 160 μm (12″ or ∼3 pc), using the kernels from Aniano et al. (2011).

When we combine PACS, SPIRE, and ground-based spectroscopy data together to include the [C I] and CO lines (see Sect. 4.4), all of the maps are smoothed to match the resolution of 42″ (∼10 pc) limited by the SPIRE long wavelength data. For this, we use the appropriate kernels to convolve a PACS point spread function (modeled by Aniano et al. 2011) to the SPIRE/FTS beam profile (fitted by a two-dimensional Hermite-Gaussian function) at the lowest resolution, essentially following the method by Gordon et al. (2008).

The photometry bands are used to determine the infrared luminosity with our spectral energy distribution (SED) model (see Sect. 2.7). Since we wish to perform the PDR analysis on the smallest possible scale (i.e., limited by the point spread function of the PACS [C II] map), we calculate the infrared luminosity at the resolution of 12″, which is also the resolution of the PACS 160 μm band. We compared this approximated infrared luminosity to that determined using all available bands, i.e., including the SPIRE bands (250, 300 and 500 μm). We find little difference on the integrated luminosity per surface area. Thus we include only the bands between 24 and 160 μm to fit the SED at the best spatial resolution possible.

2.7. Infrared luminosity maps

For each pixel of the map, we construct the full MIR to submm SED, to which we apply the dust SED model of Galliano et al. (2011, AC composition). This is a phenomenological SED fitting

procedure with which we derive a resolved total infrared luminosity ($L_{\rm TIR}$) between 3 and 1000 μm and a FIR luminosity ($L_{\rm FIR}$) between 60 and 200 μm. This model was designed to fit the *Herschel* broadband photometry of the LMC, still remaining consistent with the elemental abundances. The free parameters include the dust mass (from which the extinction magnitude in V band, $A_V^{\rm dust}$, can be derived), minimum starlight intensity, difference between the maximum and minimum starlight intensities, starlight intensity distribution power-law index, and PAH-to-total dust mass ratio $f_{\rm PAH}$. The final map of $L_{\rm TIR}$, which integrates the SED fit between 3 and 1000 μm, can be seen in Fig. 1. Contrary to other dust parameters, the infrared luminosity is very marginally model dependent. It depends mainly on the wavelength coverage of the photometric constraints used, which in our case is sufficient. For the PDR modeling (see Sect. 4) we use the $L_{\rm FIR}$ integrated between 60 and 200 μm. The SED model is better constrained in this limited wavelength range compared to the fit that includes longer wavelengths so this leads to fewer uncertainties on $L_{\rm FIR}$. However, even with no constraint longward of 160 μm, the $L_{\rm TIR}$ of 30Dor is still relatively well constrained, as the dust in this region is sufficiently warm to peak at much shorter wavelengths.

3. Data analysis

3.1. General morphology

Figure 1 shows the maps of H$_\alpha$, [O III], [S III], [N II], [C II], [Si II], and [O I] lines at their initial resolution. We also show the $L_{\rm TIR}$ (integrated between 3 and 1000 μm) and the PAH emission ($L_{\rm PAH}$). The emission of all lines is distributed in the northern and southern lobes around R136. The emission of all lines peaks near the same location within 5 pc toward the northern lobe with some inhomogeneous emission in the south. The spatial distributions of the [C I], CO(1–0), and CO(3–2) emission are presented in Fig. 2. They show two lobes of emission as well, and the peaks of both the [C I] and CO emission are shifted about 20″ north of the peak of [C II].

The [C II], [O I], and $L_{\rm PAH}$ follow each other approximately throughout the map. The [O I] 63 μm, [O I] 145 μm, and [C II] emission lines, as well as $L_{\rm PAH}$, are PDR tracers, although there may be a diffuse component as well, which could be contributing to the emission of [C II] (see Sect. 3.2).

The distributions of the H$_\alpha$, [O III] 88 μm, [S III], and [N II] lines have a structure that is different from the neutral PDR tracers [C II] and [O I]. The spatial distributions of [O III], [S III], and [N II] follow well the distribution of the ionized gas traced by H$_\alpha$ emission and show, in particular, a characteristic arm-like structure in the northeast of R136. The ionization potentials of O^{++} and S^{++} are 35 eV and 23.3 eV (see Table 1), respectively, so [O III] 88 μm and both [S III] 18 μm and [S III] 33 μm probe the highly ionized gas. The peak of [O III] is shifted from that of [C II] toward the south, in the direction of R136. The peak of [N II] 122 μm is located between the peaks of [O III] 88 μm and [O I], as expected from the values of the ionization potential of each species. [N II] traces the low density and low-excitation ionized gas (critical density for collision with electrons are ~310 cm^{-3} and ~48 cm^{-3} for [N II] 122 μm and [N II] 205 μm, respectively).

The distributions of [Si II] 35 μm and $L_{\rm TIR}$ emissions share properties both with the ionized gas ([O III] and [S III]) and the PDR tracers ([O I] and [C II]). The [Si II] 35 μm line and the $L_{\rm TIR}$ can in principle be used as a PDR tracer, but we also find in the maps some features that seem spatially associated with the ionized gas as well. This is discussed in Sects. 3.2 and 3.4.

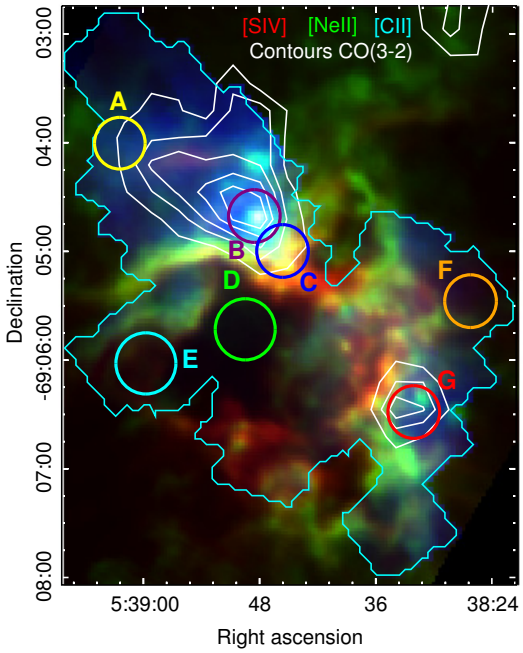

Fig. 3. Red: *Spitzer*/IRS [S IV] 10.5 μm (Indebetouw et al. 2009). Green: *Spitzer*/IRS [Ne II] 12.8 μm (Indebetouw et al. 2009). Blue: PACS [C II] 158 μm. The blue contours outline the limit of the [C II] map. We can identify the different layers of the gas from the highly ionized medium near the star cluster R136 to the clumpy molecular gas. The contours of the ^{12}CO(3–2) emission observed with ASTE (Minamidani et al. 2011) are indicated in white. The yellow region (A) is located on the northeast of R136, where [C II] is extended but where [O III] seems fainter. The violet circle (B) is located on the [C II] peak, and the blue circle (C) is on the [O III] peak. The green (D), cyan (E), and orange (F) circles probe more diffuse regions. The southwest peak of [C II] is in the red region (G).

Figure 3 shows the different layers of the ISM, from the ionization front near the stellar cluster, where the highly ionized gas traced by the [S IV] 10.5 μm emission is located, to lower ionization states ([Ne II] 15.6 μm) and then to the PDRs traced by [C II]. The CO peak is located close to the [C II] peak. This spatial disposition suggests that R136 dominates the photoionization. We can also see that the northern region seems to be shielded very well from ionizing UV photons, since [C II] is very extended in this direction while the tracers of the ionized gas show a sharp decrease on the other side of the H$_\alpha$ arc.

The [O III] 88 μm is the brightest FIR line in 30Dor, as in N11, the second largest H II region of the LMC (Lebouteiller et al. 2012), the dwarf galaxy Haro 11 (Cormier et al. 2012), and in most of the dwarf galaxies (Cormier et al. 2015), integrated over full galaxy scales. This was first noted in several dwarf irregular galaxies in Hunter et al. (2001). [O III] is brighter than [C II] by a factor of 2 to 60 throughout our 30Dor map. Figure 4 shows the ratio [O III]/$L_{\rm TIR}$ versus [C II]/$L_{\rm TIR}$ in 30Dor. Cormier et al. (2015) already noted the elevated [O III] 88 μm/$L_{\rm TIR}$ in dwarf galaxies compared to the normal galaxies of Brauher et al. (2008). Given that it requires 35 eV to ionize O^+ to O^{++}, this suggests the presence of high temperature stars throughout the region. The range of [C II]/$L_{\rm TIR}$ values covered in 30Dor is very broad (more than an order of magnitude) and they cover almost the entire

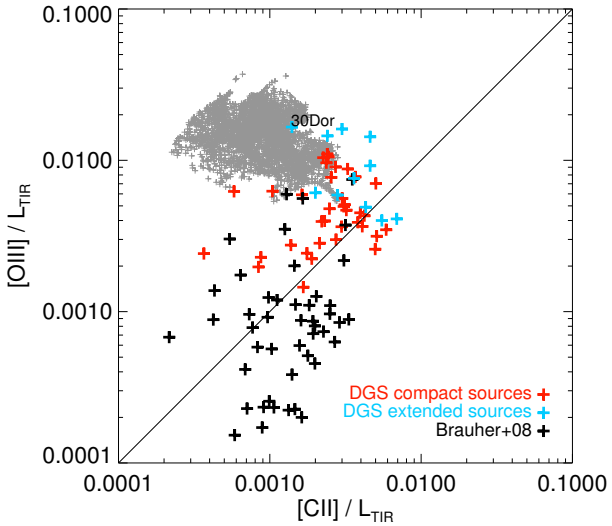

Fig. 4. [O III]/$L_{\rm TIR}$ versus [C II]/$L_{\rm TIR}$. The regions in 30Dor form the gray cloud with the high [O III]/$L_{\rm TIR}$ values. The DGS galaxies (Cormier et al. 2015) are represented by red (compact) and cyan (extended) symbols. The (mostly) metal-rich galaxies from Brauher et al. (2008) are represented by black symbols.

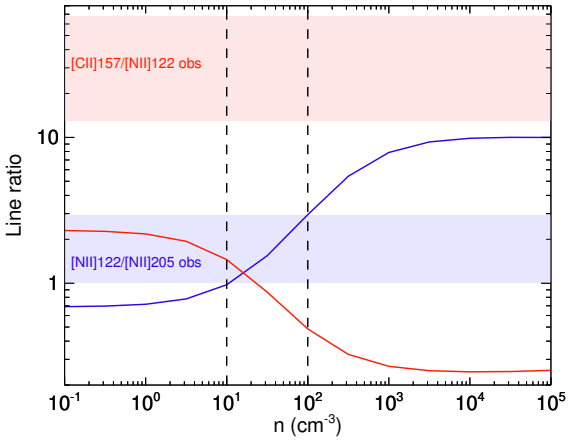

Fig. 5. Theoretical ratios [N II] 122 μm/[N II] 205 μm (blue) and [C II]/[N II] 122 μm (red) at the temperature of 10 000 K. Blue and red areas indicate our observed ranges for [N II] 122 μm/[N II] 205 μm and [C II]/[N II] 122 μm ratios, respectively. The observed values of the [C II]/[N II] ratio (in red) are much higher than the theoretical value in the ionized gas for the entire map, indicating that [C II] is mostly emitted in the PDRs and not in the ionized gas.

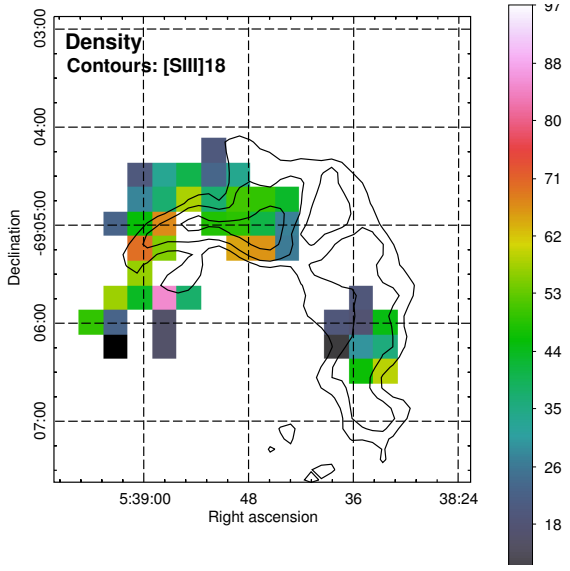

Fig. 6. Electron density in cm^{-3} calculated from the ratio [N II] 122 μm/[N II] 205 μm. The pixel size is 20″ (~5 pc). The black contours represent the emission of the ionized gas tracer [S III] 18 μm.

range of [C II]/$L_{\rm TIR}$ observed in the wide range of galaxy type in the Brauher et al. sample. The [O III]/$L_{\rm TIR}$ distribution is narrower (about a factor of 6 over the map). The regions with the highest $L_{\rm TIR}$ are the peaks of [O III] and [C II] (Fig. 3; regions C and B). The highest [C II]/$L_{\rm TIR}$ ratio is found in the northern part of 30Dor (near region A); this is because $L_{\rm TIR}$ decreases more rapidly than [C II] with increasing distance from the exciting sources.

In the regions where [C II] is the brightest, the line intensities of [O I] 63 μm and [Si II] are similar to the [C II] intensity. [O I] 63 μm is at least ten times brighter than [O I] 145 μm everywhere. The map of [N II] 122 μm is the smallest and this line is also the faintest of our PACS lines (at least 200 times fainter than [O III]), but the S/N throughout the region mapped is ≥5. The [N II] 205 μm emission is 1 to 3 times fainter than [N II] 122 μm.

3.2. Origin of C II and Si II emission

Because the ionization potential of C^0, 11.3 eV, is lower than 13.6 eV, the [C II] line can originate either from the PDRs or from the ionized gas. We thus need to investigate the possible contribution from the ionized gas and from PDRs to the [C II] emission before we can use it as a PDR tracer and a constraint for PDR modeling.

Following the analysis of Oberst et al. (2011), we use the fact that the ratio [C II]/[N II] 122 μm can be calculated theoretically in the ionized gas, and that [N II] originates only from the ionized gas. We calculate the fine-structure level populations of C^+ and N^+ as a function of the density using the theoretical collisional rates. We then apply a correction factor due to the ionic abundance fraction $\frac{C^+/C}{N^+/N}$. We used the MAPPINGS III photoionization grids (Allen et al. 2008) and found that this fraction depends little on the conditions (ionization parameter, starburst age, density) with a value around 0.85 ± 0.15. Finally, we scale the emission ratio with the observed elemental abundances of C and N in 30Dor from Pellegrini et al. (2011) listed in Table 3. The final ratio [C II]/[N II] 122 μm depends strongly on the electron density between 1 and 1000 cm^{-3}. Since the critical densities for [N II] 122 μm and [N II] 205 μm are 310 cm^{-3} and 50 cm^{-3}, respectively (Table 1), the ratio [N II] 122 μm/[N II] 205 μm is a good density tracer for the relatively low density ionized gas phase. We calculate the ratio [N II] 122 μm/[N II] 205 μm to determine the density using the theoretical curve from Bernard-Salas et al. (2012, see Fig. 5). This ratio depends only slightly on the temperature; we choose a typical temperature of 10 000 K. The calculated density presented in Fig. 6 ranges from 10 to 100 cm^{-3}. Our values fall in the low density regime of the [S III] line ratio, which is sensitive to high density ($n_{\rm crit}$ = 1.5×10^4 cm^{-3} for [S III] 18 μm and $n_{\rm crit}$ = 4.1×10^3 cm^{-3} for [S III] 33 μm), and does not provide a useful constraint.

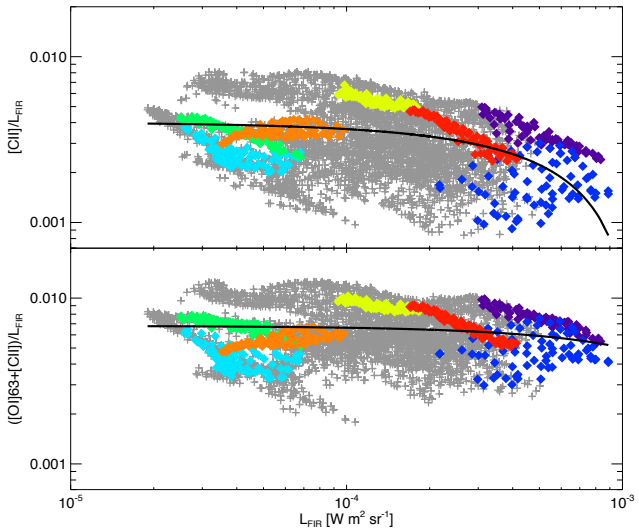

Fig. 7. *Top*: ratio of [C II]/$L_{\rm FIR}$ versus $L_{\rm FIR}$. The color symbols are associated with the regions defined in Fig. 3. The gray symbols are all of the other pixels of our 30Dor map. The black curve shows a linear regression of the data. *Bottom*: ratio of ([O I] 63 μm+[C II])/$L_{\rm FIR}$ versus $L_{\rm FIR}$.

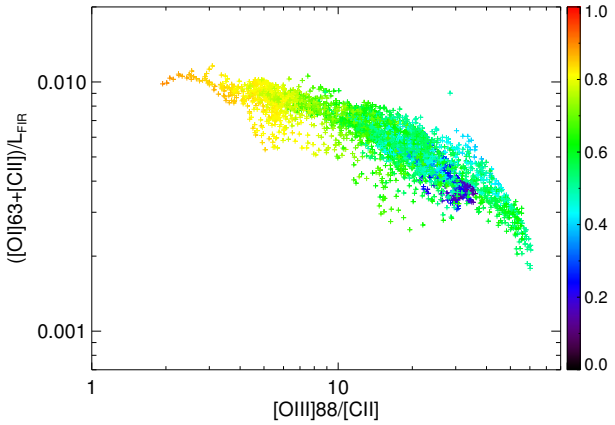

Fig. 8. Ratio of ([O I] 63 μm+[C II]) /$L_{\rm FIR}$ versus [O III]/[C II]. The color bar indicates the fraction of $L_{\rm FIR}$ expected to come from the PDRs (see Sect. 3.4).

If the [C II] emission originated in the low density ionized gas traced by [N II], the [C II]/[N II] 122 μm ratio would be ~0.5–1.3 (Fig. 5). However, the observed ratio is significantly higher by a factor of ~10 than this theoretical ratio in the ionized gas. At least 90% of the [C II] is expected to be emitted from PDRs in the entire mapped region. The [C II] emission can be considered to be a reliable tracer of the PDR gas in 30Dor.

Since the density is known and [Ar II] originates from the ionized gas, we can also calculate the theoretical ratio [C II]/[Ar II] in the ionized gas. Similarly, comparing the observed ratio [C II]/[Ar II] to the theoretical ratio in the ionized gas, we also deduce that a large fraction (>95%) of the [C II] emission originates from the PDRs.

[Si II] emission can also originate from PDR or ionized gas. We proceed with the same method to separate the emission of the ionized gas from that of the neutral gas. The critical density of [Si II] is close to that of [Ar II] (3.4×10^5 cm^{-3} and 4.0×10^5 cm^{-3}, respectively; see Table 1) and both the observed ratios of [Si II]/[Ar II] and [Si II]/[N II] are consistent with 60% to 90% of the [Si II] emission originating from the PDRs.

3.3. The photoelectric heating efficiency

The top panel of Fig. 7 shows the observed [C II]/$L_{\rm FIR}$ ratio as a function of $L_{\rm FIR}$ for every pixel of the PACS map. The ratio [C II]/$L_{\rm FIR}$ is often used to estimate the fraction of energy absorbed by dust that is used to heat the gas via the photoelectric effect (the photoelectric heating efficiency). This ratio ranges between 0.1% and 1% with a significant scatter, i.e., about one order of magnitude. We observe a tendency of decreasing [C II]/$L_{\rm FIR}$ as $L_{\rm FIR}$ increases (same trend as in Stacey et al. 2010) with a slope of -3.6 ± 0.2. However, when we add the [O I] 63 μm emission (lower panel of Fig. 7), we find a smaller dispersion (with a factor of 7) and also a flatter relation between ([O I] 63 μm+ [C II])/$L_{\rm FIR}$ and $L_{\rm FIR}$ with a slope of -1.4 ± 0.3 for the linear regression. Both [O I] and [C II] are contributing noticeably to the cooling of the gas, as shown in Lebouteiller et al. (2012).

Figure 8 shows that the decrease of the ratio ([O I] 63 μm+[C II])/$L_{\rm FIR}$ is mostly due to the ionized component in $L_{\rm FIR}$. Indeed, the ratio ([O I] 63 μm+[C II])/$L_{\rm FIR}$ is strongly correlated with the ratio [O III] 88 μm/[C II], and it decreases with increasing [O III] 88 μm/[C II], which is representative of the ionization state of the gas. If we subtract the infrared contribution from the ionized gas (as described in Sect. 3.4), we find that the ratio ([O I] 63 μm+[C II])/$L_{\rm FIR}$ is fairly constant and narrow.

3.4. The origin of the FIR emission

Although grains and PAHs in the PDRs contribute to the FIR emission, a fraction of $L_{\rm FIR}$ can also come from the H II regions, i.e., from big grains in equilibrium with the interstellar radiation field (ISRF). In this section, we inspect the origin of the $L_{\rm FIR}$ throughout the map to separate the fraction in the ionized gas component from that in the PDR component. We assume that the PAH emission traces the PDRs and [O III] traces the ionized phase. Indeed, we can see in Fig. 1 that the spatial distribution of the $L_{\rm FIR}$ shows features similar to the PAH emission or any other neutral atomic gas tracer ([C II], [O I]), while other features seem to be spatially associated with [O III] or any other ionized gas tracers (H_α, [S III]). To disentangle the fraction of $L_{\rm FIR}$ in the ionized gas, we assume a linear relation such as $L_{\rm FIR} = \alpha \times L_{\rm PAH} + \beta \times L_{\rm [O\,III]}$. The pair of ($\alpha$; β) values is calculated using a multiple linear regression using all of the pixels in the map and is equal to (5.4; 11.5). This decomposition implicitly assumes that the PAH-to-dust mass fraction is constant in PDRs and zero in H II regions. The left panel of Fig. 9 presents the correlation between [O III] 88 μm/$L_{\rm FIR}$ and $L_{\rm PAH}/L_{\rm FIR}$. The solid line on this plot shows the linear relation defined by $\frac{L_{\rm [O\,III]}}{L_{\rm FIR}} = \frac{1}{\beta} - \frac{\alpha}{\beta} \times \frac{L_{\rm PAH}}{L_{\rm FIR}}$. With this method, we are seeking a first order correction of the total $L_{\rm FIR}$ to be able to use it for the PDR modeling. The modeled $L_{\rm FIR}$ reproduces the observed $L_{\rm FIR}$ within 30% on average. We determine the proportion of $L_{\rm FIR}$ coming from the PDRs as $L_{\rm FIR}^{\rm PDR} = \alpha\ L_{\rm PAH}$. The result is presented on the right panel of Fig. 9. On the north side of the map, far from the ionizing cluster, up to 90% of the FIR emission is expected to come from the PDRs, while on the east of the map, near the R136 cluster, about 70% of the FIR emission is expected to come from the ionized gas. We subtract the estimated fraction of $L_{\rm FIR}$ emitted in the ionized gas, using $L_{\rm FIR}^{\rm PDR}$ for the PDR modeling.

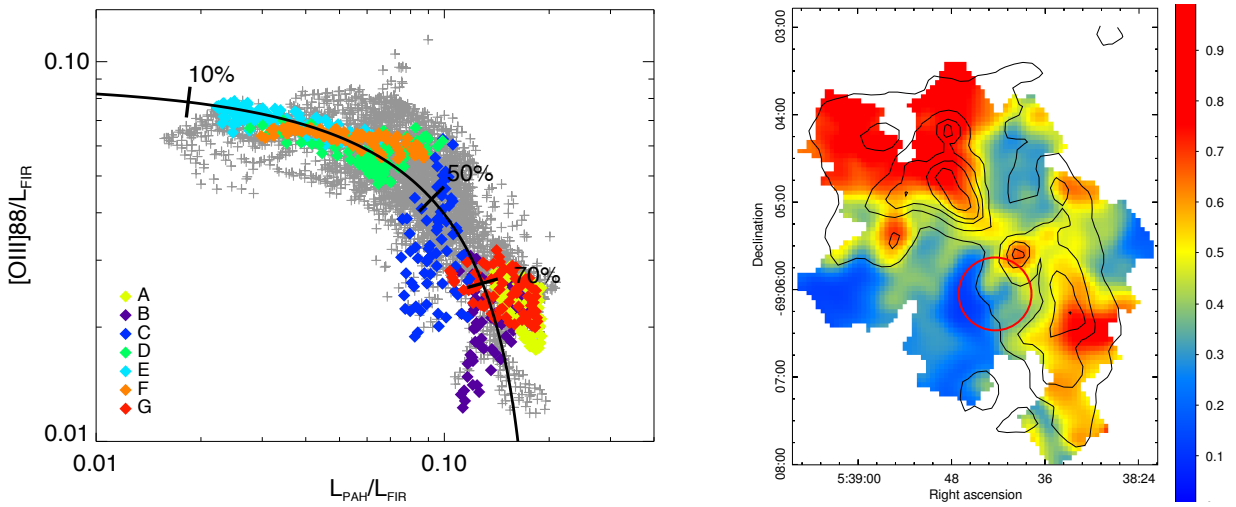

Fig. 9. *Left*: ratio [O III] 88 μm/$L_{\rm FIR}$ as a function of $L_{\rm PAH}/L_{\rm FIR}$. The color symbols are associated with the regions defined in Fig. 3. The gray symbols denote all of the other pixels of our 30Dor map. The solid curve shows the result of the multiple linear regression, using the values $\alpha = 5.4$ and $\beta = 11.5$. The values indicate the fraction of $L_{\rm FIR}$ coming from the PDR for three different positions on the curve. *Right*: ratio of $L_{\rm FIR}^{\rm PDR}/L_{\rm FIR}$. Black contours represent the total FIR emission. Close to the location of R136, only 20 to 30% of the $L_{\rm FIR}$ come from the PDRs.

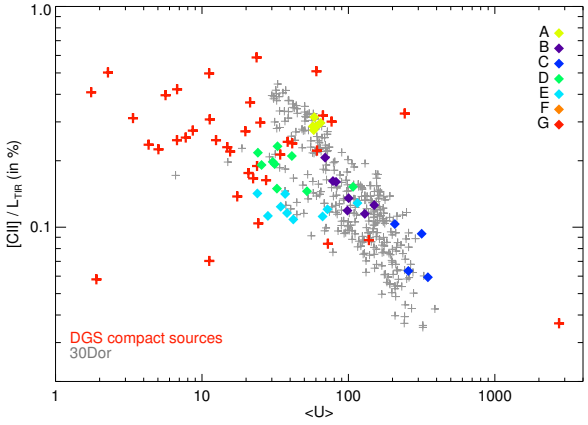

Fig. 10. Correlation between [C II]/$L_{\rm TIR}$ and $\langle U \rangle$ (average of the starlight intensity distribution). The red symbols are for the DGS galaxies (Cormier et al. 2015). The colored diamonds correspond to the regions of 30Dor illustrated in Fig. 3.

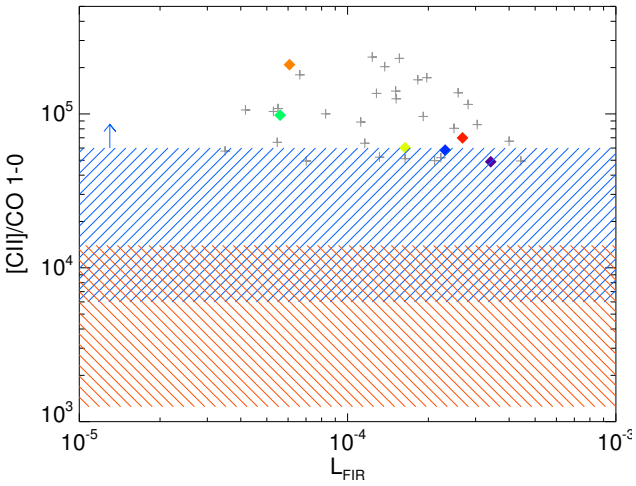

Fig. 11. Ratio of [C II]/CO(1–0) versus $L_{\rm FIR}$ at the scale of 30″. The dashed horizontal orange band indicates the observed ratio [C II]/C0(1–0) in star-forming regions of the Galaxy and metal-rich galaxies (Stacey et al. 1991). The dashed horizontal blue band indicates the range of observed ratios for six bright subsolar metallicity galaxies of the DGS (Cormier et al. 2014).

3.5. Line ratios: Empirical correlations

Far-infrared line ratios are useful diagnostics of the ISM conditions. We use these for PDR modeling (Sect. 4) and we inspect their distribution throughout 30Dor. In Figs. 10 and 11, we focus on different regions of 30Dor to inspect the local variations.

To study how the distribution of starlight affects the observed photoelectric heating efficiency, we compare the average modeled starlight $\langle U \rangle$ from the SED modeling (see Sect. 3.4) with [C II]/$L_{\rm TIR}$ (Fig. 10). We use the total $L_{\rm TIR}$ here since we do not know the fraction of the PDR component for the DGS sources. We compare our spatially resolved values with the distribution of $\langle U \rangle$ and [C II]/$L_{\rm TIR}$ from the integrated DGS compact sources of Cormier et al. (2015) and Rémy-Ruyer et al. (2014). More details and references can be found in Cormier et al. (2015). We see that 30Dor covers a large range in [C II]/$L_{\rm TIR}$ of approximately one order of magnitude and approximately one order of magnitude in $\langle U \rangle$.

There is a trend of decreasing [C II]/$L_{\rm TIR}$ as $\langle U \rangle$ is increasing, following the trend observed by Cormier et al. (2015), showing an apparent line deficit at high $\langle U \rangle$ values. This is probably an effect of the contribution of the ionized component to the infrared luminosity, as shown in Fig. 8. The [O III] peak (region C in Fig. 3) is the region with the highest $\langle U \rangle$: this is the closest region to R136 in physical distance (see Sect. 5.3); the gas is mostly ionized. This region also corresponds to the lowest [C II]/$L_{\rm TIR}$ ratio.

To compare one of the primary PDR coolants with the CO(1–0), we show in Fig. 11 [C II]/CO versus $L_{\rm FIR}$ at the resolution of 42″. [C II]/CO(1–0) throughout 30Dor is $\sim 5 \times 10^4 - 3 \times 10^5$. The observed range of the ratio [C II]/CO(1–0) is very broad. These values are about a factor 10 higher than the typical values for spiral or starburst galaxies (~2000–8000; Stacey et al. 1991; Negishi et al. 2001), and more in agreement with the

range of values measured for integrated dwarf galaxies as already noticed in Poglitsch et al. (1995), Madden et al. (1997), and Cormier et al. (2010, 2014). We note that low metallicity galaxies always show extreme [C II]/CO compared to the more metal-rich galaxies.

4. PDR modeling

In this section, we model the infrared observations of 30Dor using the Meudon PDR code and present results describing the properties of the gas.

4.1. The Meudon PDR model

The Meudon PDR code[2] is described in Le Petit et al. (2006), Le Bourlot et al. (2012), and Bron et al. (2014). It computes the atomic and molecular structure of interstellar clouds. The model considers a 1D stationary plane-parallel slab of gas and dust illuminated by a radiation field (from UV to radio) arising from one or both sides. The radiative transfer is solved in an iterative way at each point of the cloud by taking into account absorption by gas and dust and scattering and emission by dust. For the present work, we used a development version (v1.6.0) with updates that includes the computation of X-ray radiative transfer and the impact on the chemistry and thermal balance of the cloud (Godard et al., in prep.).

4.2. Input and output parameters

We describe here some of the configuration parameters of the model. We assume that the gas in each pixel can be modeled by a single cloud of pressure P, illuminated by a radiation field. The standard radiation field used in the Meudon PDR code is that observed in the solar neighborhood (Mathis et al. 1983) and is scaled with the parameter $G_{\rm UV}$ to control the intensity of the incident radiation field on each side of the cloud. For $G_{\rm UV}$ = 1, the integrated energy density between 911.8 Å to 2400 Å is 6.8×10^{-14} erg cm^{-3}. In the model we ran, $G_{\rm UV}$ ranges between 1 and 10^5 on one side and is fixed to 1 on the other side to expose this side to the general interstellar field. The pressure ranges between 10^4 and 10^8 cm^{-3} K. The pressure is constant throughout the cloud, however, we also explored a constant density model (Sect. 4.5). We investigated the possibility of adding X-rays in the model, but found that they are not needed to explain the PACS observed data (Sect. 5.5). The visual extinction of the entire cloud is varied from $A_V^{\rm max}$ = 1 magnitude to $A_V^{\rm max}$ = 10 magnitude. We estimate the mass fraction of PAHs from our SED modeling (Sect. 2.7). We find that $f_{\rm PAH}$ = 1% is adapted for 30Dor. We use elemental abundances as in Pellegrini et al. (2011) for He, C, N, O, Ne, Si, and S to reproduce the conditions in 30Dor as accurately as possible (see Table 3). The dust-to-gas mass ratio is fixed to 0.5×10^{-3} based on our SED modeling (Sect. 2.7).

The output quantities computed by the model include the integrated line intensities and $L_{\rm FIR}$, ionic and molecular abundances, emissivities, and chemical and thermal structure of the cloud. An example of the variations of the local gas phase abundances for some elements as a function of the depth into the cloud is presented in Fig. 12 for a typical cloud of $A_V^{\rm max}$ of 10 with a constant pressure of $P = 10^6$ cm^{-3} K, which is illuminated by a radiation field of $G_{\rm UV}$ = 3000.

[2] The Meudon PDR code is public and available online at the following address: http://ism.obspm.fr

Table 3. Input parameters for the PDR model.

Parameter	Notation	Value
Pressure	P	10^4–10^8 cm^{-3} K
Radiation field	$G_{\rm UV}$	1–10^5
Cosmic ray flux	ζ^a	3×10^{-16} s^{-1}
Total visual extinction	$A_V^{\rm max}$	1–10 mag
Metallicity	Z^b	0.5 $Z_\odot$
PAH fraction	$f_{\rm PAH}$	1%
Dust-to-gas mass ratio	$M_{\rm dust}/M_{\rm gas}$	5×10^{-3}
Gas phase abundances[c]		$\log(n({\rm X})/n({\rm H}))$
He		–1.05
C		–4.3
N		–4.91
O		–3.75
Ne		–4.36
Si		–5.51
S		–5.32

Notes. [(a)] Indriolo & McCall (2012), Indriolo et al. (2015); [(b)] Metallicity: 12+log(O/H) = 8.38 (Rolleston et al. 2002; Pagel 2003) and $({\rm O/H})_\odot = 4.9 \times 10^{-4}$ (Asplund et al. 2009); [(c)] Pellegrini et al. (2011).

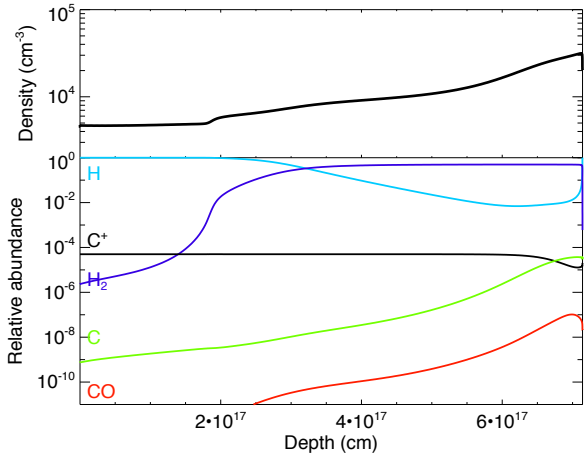

Fig. 12. *Top*: density profile as a function of the depth into the cloud in a simulated cloud of $A_V^{\rm max}$ = 2, $P = 10^6$ cm^{-3} K with $G_{\rm UV}$ = 3000 on the left side and $G_{\rm UV}$= 1 on the right side. *Bottom*: local gas phase relative abundances of C^+, C, CO, O, and H_2 for the same model.

We use [O I], [C II] and $L_{\rm FIR}^{\rm PDR}$ to constrain P and $G_{\rm UV}$ in the PDR model pixel by pixel. We consider here the observed [C II] emission without correction since the contribution from the ionized gas is low (Sect. 3.2) and we correct the $L_{\rm FIR}$ emission to remove the contamination from the component associated with the ionized gas (see Sects. 3.2 and 3.4). At first we let $A_V^{\rm max}$ vary freely as this set of tracers cannot constrain this parameter and it has no influence on the resulting best model. This is illustrated in Fig. 13, where we show the ratios $\mathcal{R}$ between several modeled line ratios and their observations for simulated clouds of different total depths. The ratios [O I]/[C II], ([O I]+[C II])/$L_{\rm FIR}$ are not very sensitive to $A_V^{\rm max}$, as is also the case for the ratio [C I] 609 μm/[C I] 370 μm.

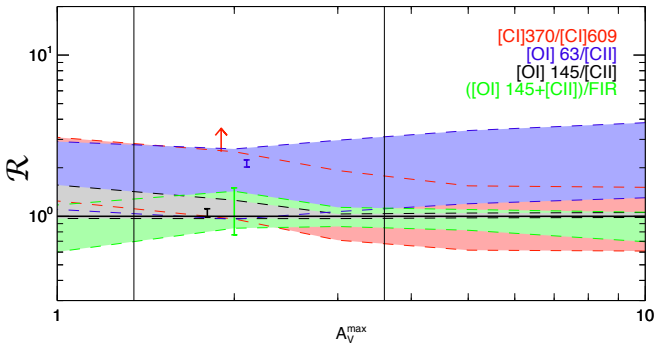

Fig. 13. Ratios, $\mathcal{R}$, of the modeled line ratios over the observed line ratios for [C I] 370 μm/[C I] 609 μm, [O I] 63 μm/[C II], [O I] 145 μm/[C II], and ([O I] 145 μm+[C II])/$L_{\rm FIR}^{\rm PDR}$, for simulated clouds of different $A_V^{\rm max}$ from 1 to 10 for 30Dor abundances. The width of the bands represents the dispersion of $\mathcal{R}$ throughout the map. The error bars due to uncertainties on the observations are plotted. The vertical lines indicate the range of $A_V^{\rm max}$ where the predictions of the model are compatible with the observed [C II]/CO(3–2) (see Fig. 17).

4.3. Pressure and incident radiation field

We find the best solution for the incident radiation field and the pressure using the observed line intensities as constraints. They are found by minimizing the χ^2 distribution

$$\chi^2 = \sum_{j=1}^{N} \left(\frac{I_j(x,y) - M_j}{\sigma_j(x,y)} \right)^2 , \quad (1)$$

where $I_j(x,y)$ is the observed value of the ratio i for a given pixel (x,y), $\sigma_j(x,y)$ is the uncertainty associated with this observed ratio, and M_j is the value predicted by the model for the ratio j. The value N is the number of constraints (independent ratios) that are used. Ratios of line intensities are used instead of absolute values. In this case, if species are cospatial in the cloud and there are no opacity effects, we can then ignore the effects of an area filling factor that differs from 1.0 and the presence of several clouds along the line of sight (see Sect. 5.1).

As an example, we present in Fig. 14 the values of $G_{\rm UV}$ and P that reproduce the observed values for the ratios ([O I] 145 μm+[C II])/$L_{\rm FIR}^{\rm PDR}$ in blue, [O I] 145 μm/[C II] in red, and [O I] 63 μm/[C II] in cyan for two pixels of the map of 30Dor at 12″ resolution, located in the regions D and C (Fig. 3). We can see in these figures that the constraint given by the ratio [O I] 63 μm/[C II] is never consistent with the other ratios within the error bars. This is likely due to optical depth effects in the [O I] 63 μm line, as we show later in this section. For this reason, we do not consider this line to be one of the constraints to the model.

First, we use the ratios ([O I] 145 μm+[C II])/$L_{\rm FIR}^{\rm PDR}$ and [O I] 145 μm/[C II] to constrain $G_{\rm UV}$ and P. Thus we are limited by the PACS resolution of 12″ and by the spatial coverage of the [O I] 145 μm map. We do not use the ratio [C I] 370 μm/[C I] 609 μm, which does not bring strong constraints on $G_{\rm UV}$ and P as the error bars are very large. We have then the same number of constraints and parameters. We can note from Fig. 14 that there is a degeneracy between a high $G_{\rm UV}$/low P solution and a low $G_{\rm UV}$/high P solution. The addition of the ratio [C II]/[C I] or [C II]/CO does not help to break this degeneracy since they are very dependent on $A_V^{\rm max}$ (Sect. 4.4). However, the high $G_{\rm UV}$/low P solution, highlighted with a green cross in Fig. 14, has a lower χ^2 and is preferred based on the following arguments. Indeed, the high P solution requires high optical depths in [O I] 63 μm ([O I] 63 μm is overpredicted by a factor of up to 9, see below), while the $A_V^{\rm max}$ (determined as in Sect. 4.4) would be very low (<1 mag). In addition, we found a pressure of $P = 10^5$–10^6 cm^{-3} K for a typical temperature of 10 000 K (see Sect. 3.2) in the ionized gas. We find a similar pressure in the PDR, suggesting that the gas may well be in pressure equilibrium. However, it must also be noted that Pellegrini et al. (2011) find a pressure that is somewhat larger using optical lines. Finally, a low $G_{\rm UV}$ solution results in large physical distances between the clouds and R136 (see Sect. 5.3), which is significantly larger (by a factor of ∼10 to 100) than the distances found in Pellegrini et al. (2011).

We find $G_{\rm UV}$ ranging between 10^2 and 3×10^4 throughout the region and P between 10^5 cm^{-3} K and 1.7×10^6 cm^{-3} K with $\chi^2 \sim 10^{-1}$ to 10^{-2} over the map[3] The best P and $G_{\rm UV}$ maps are represented in Fig. 15. The peaks of $G_{\rm UV}$ and P are almost cospatial. The maximum is located north of R136, at the southern edge of the [O III] peak. It shows that there is a void around R136 and that the radiation field is first interacting with any matter a few parsecs away from the cluster. Details regarding the structure around R136 are discussed in Sect. 5.3. The uncertainties associated with the observations, including calibration errors, lead to uncertainties on $G_{\rm UV}$ of +55%/-40% and on P of +/–12%.

The value of the observed ratio [O I] 63 μm/[C II] is lower than the ratio predicted by the model based on [C II], [O I] 145 μm and $L_{\rm FIR}^{\rm PDR}$ by a factor of 1.3–2.5. This discrepancy between the predicted and observed values may be due to optical depth effects of the [O I] 63 μm line (Tielens & Hollenbach 1985; Abel et al. 2007) or to absorption by cold gas along the line of sight (Liseau et al. 2006). As we can see from Fig. 16 on the left, the lowest values of the ratio $\frac{([\rm O\,I]\ 63\,\mu m/[C\,II])_{\rm observed}}{([\rm O\,I]\ 63\,\mu m/[C\,II])_{\rm predicted}}$ correspond to the locations of the highest pressure. Since the difference between the observations and model prediction seems to correlate spatially with the pressure here, it is probably not due to foreground absorption, but most likely from local effects. We can also note that the observed ratio [O I] 145 μm/[O I] 63 μm is larger than 0.1 in many pixels, which is an indication of optical depth effects in [O I] 63 μm (Tielens & Hollenbach 1985). In the best-solution model, the predicted ratio [O I] 145 μm/[O I] 63 μm is 0.04. The model accounts for the opacity of the lines for one cloud, but not between several clouds along the line of sight. If we examine one of the best solutions for region B ([C II] peak in Fig. 3), the model predicts an opacity of 0.6 for [O I] 63 μm at $A_V = 1$ while that of [C II] is still below 0.1. Thus, if we have several components along the line of sight, the [C II] intensity can be multiplied by the number of components, while the [O I] 63 μm intensity increases less than linearly.

4.4. Determination of A_V^{max} using [C II], [C I] and CO

In this section we investigate the influence of $A_V^{\rm max}$ (that is, the total depth of the cloud, in magnitude) on the line ratios predicted by the Meudon PDR code. In Fig. 17, we show the ratios $\mathcal{R}$ between several modeled line ratios and their observations for simulated clouds of different total depths. While the ratios [O I]/[C II], ([O I]+[C II])/$L_{\rm FIR}$ and [C I] 609 μm/[C I] 370 μm are not very sensitive to $A_V^{\rm max}$ (Fig. 13), the ratios [C II]/[C I] and [C II]/CO vary by several orders of magnitude with the total depth of the simulated cloud because they involve tracers that

[3] This is not a reduced χ^2 as we have as many constraints as free parameters.

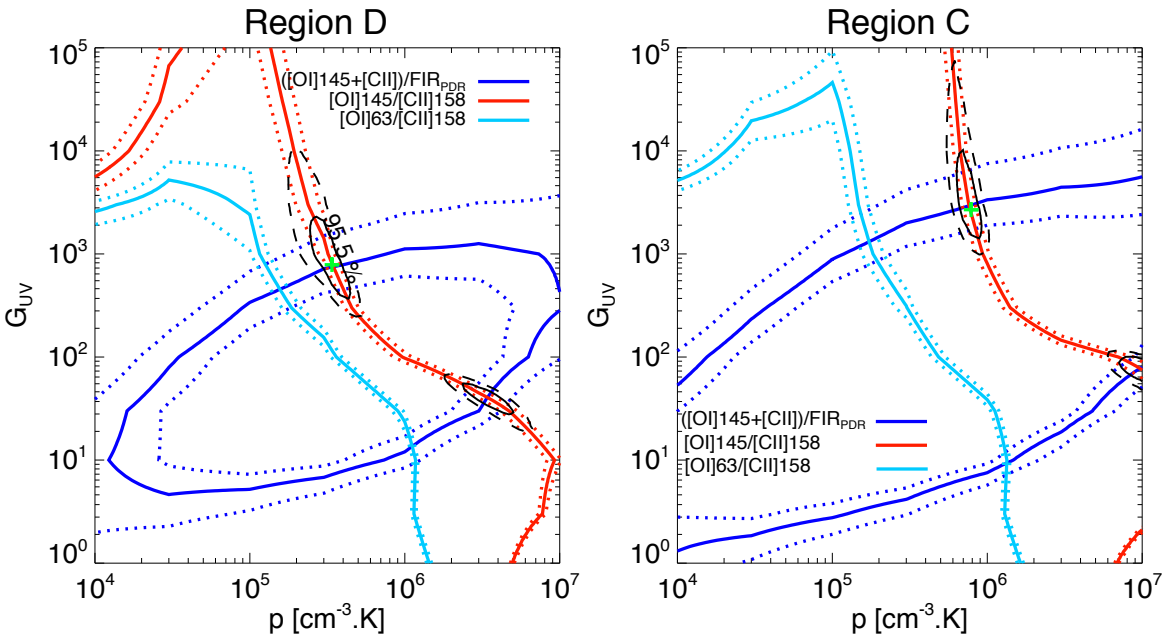

Fig. 14. Contour plots showing the parameters G_{UV} and P from our model, which reproduces the observed values of the ratios ([O I] 145 μm+[C II])/L_{FIR}^{PDR} (dark blue), [O I] 145 μm/[C II] (red), and [O I] 63 μm/[C II] (cyan). The dotted lines show the 1σ error on the observed ratios. The solid and dashed black contours represent the confidence intervals for 1 and 2σ, respectively. The green crosses indicate the best solutions for G_{UV} and P in each case, using ([O I] 145 μm+[C II])/L_{FIR}^{PDR} and [O I] 145 μm/[C II] as model constraints. *Left plot* is for a pixel representative of the region D (from Fig. 3). *Right plot* is for a pixel from region C (from Fig. 3), near the G_{UV} peak.

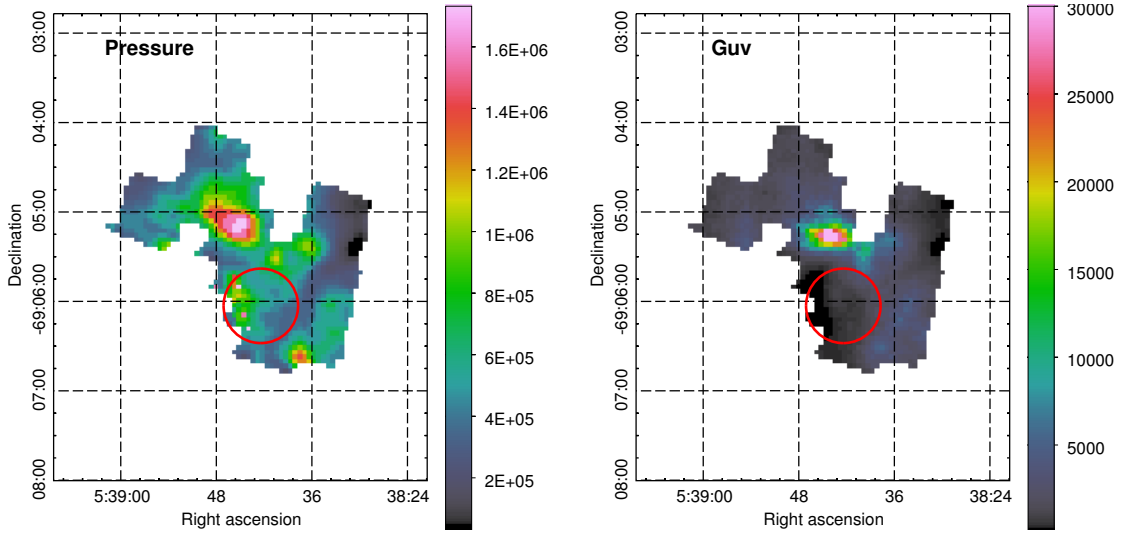

Fig. 15. *Left*: best pressure map (cm^{-3} K) of the 30Dor region; using ([O I] 145 μm+[C II])/L_{FIR}^{PDR} and [O I] 145 μm/[C II]. The total extinction for this model is A_V^{max} = 3. *Right*: best G_{UV} map (color bar in units of the Mathis field) for the same model. The red circle shows the location of R136.

originate from different depths into the cloud. The observed ratios [C II]/[C I], [C II]/CO(1–0) and [C II]/CO(3–2) can be reproduced with a cloud of $A_V^{max} \sim$ 1–3 mag per pixel of 30″ (7.2 pc) as shown in Fig. 17 with G_{UV} and P determined as described in Sect. 4.3. However we keep in mind that the determination of this parameter is strongly dependent on the geometry of the model. This is discussed in more detail in Sect. 5.2.

4.5. Isobaric versus isochoric case

We considered a constant density model to compare our results with our isobaric model and with previous PDR model results. We use the same set of line ratios and the same χ^2 method to find the best radiation field and density predicted by an isochoric model.

We find a similar map for G_{UV} compared to our isobaric model with a maximum of 20% difference between both cases. For the isochoric model, the density ranges between 3×10^2 to 1.4×10^4 cm^{-3} with a spatial distribution that is very similar to P in the isobaric case. This range of values is similar to those found by previous studies (e.g., Poglitsch et al. 1995; Bolatto et al. 1999; Röllig et al. 2006; Pineda et al. 2012). From the results of the isobaric model, we determine the density at the surface of the PDR. This initial density is about 1/2 to 2/3 the

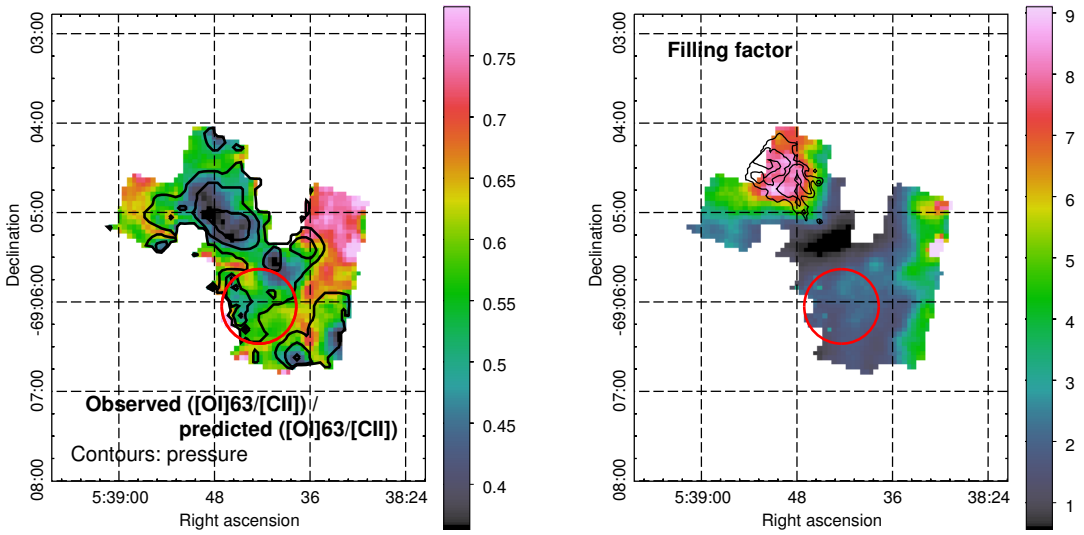

Fig. 16. *Left*: ratio of the observed [O I] 63 μm/[C II] ratio over the predicted [O I] 63 μm/[C II] ratio (color bar). The pressure contours of between 4.5×10^5 and 1.3×10^6 cm^{-3} K are indicated in black. The red circle shows the location of R136. *Right*: filling factor Φ_A between 0.6 and 9 (color bar). The lowest values are at the peak of G_{UV}. The black contours represent the ^{12}CO(2–1) emission from ALMA (Indebetouw et al. 2013)

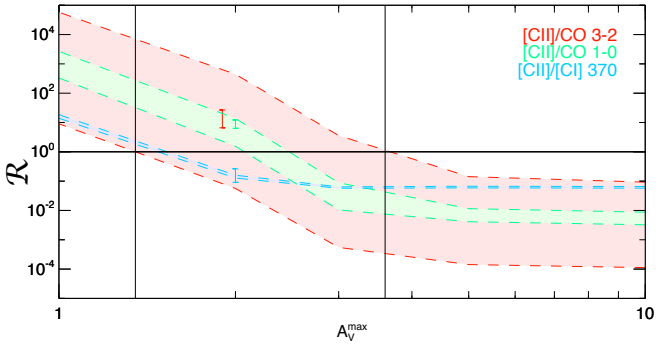

Fig. 17. Same as Fig. 13, for ratios [C II]/CO(3–2), [C II]/CO(1–0) and [C II]/[C I] 370 μm.

density determined with the isochoric model. In conclusion, the results from these two models are similar when applied to PDR line ratios.

However, the predictions of the models start to diverge deeper into the cloud, in particular for molecular lines. Indeed, for an isobaric cloud of A_V^{max} of 3, the density rises by about a factor of 10, as the temperature drops, between the surface of the PDR and the core of the cloud (Fig. 12). This implies that the CO lines are emitted at lower A_V in a isobaric model compared to an isochoric model. As a consequence, the A_V^{max} probed by the observed CO lines is lower for an isobaric model than for an isochoric model. For example, the A_V^{max} probed with the low-J CO transitions (J = 3–2 and J = 1–0) is slightly higher for the isochoric model (~2–4 mag) than the 1–3 mag we find with the isobaric model. In conclusion, choosing the isobaric case is important to reproduce the higher J transitions of CO and quantify the CO-dark gas (see Paper II), but it has few consequences for the results derived in this paper.

4.6. Model predictions for H_2 lines

The H_2 S(2) line is barely detected in the *Spitzer*/IRS low-resolution observations of 30Dor (Indebetouw et al. 2009). The model-predicted H_2 (0,0) $S(2)$ emission at 12.3 μm is 10 to 50 times lower than the upper limit from the observations. However, the emission from the high-resolution spectrum (Sect. 2.4) is in better agreement (by a factor of 2 to 5) with the model prediction.

Pak et al. (1998) measure H_2 (1, 0) $S(1)$ and (2, 1) $S(1)$ close to the CO (1–0) peak of 30Dor with a beam of 81″. We compare these observations to the predictions of our model at 81″ resolution. Our map does not fully cover the 81″ beam. However, we calculate lower limits of 6×10^{-6} and 3×10^{-6} erg s^{-1} cm^{-2} sr^{-1} on the H_2 (1, 0) $S(1)$ and (2, 1) $S(1)$ emission, respectively. There is a good agreement with the values measured by Pak et al. (1998) considering we are missing some fraction of their beam (10.8×10^{-6} and 4.0×10^{-6} erg s^{-1} cm^{-2} sr^{-1} respectively). Rubio et al. (1998) present H_2 (1, 0) $S(1)$ observations at 1.16″ resolution. Their peak value of $4–6 \times 10^{-5}$ erg s^{-1} cm^{-2} sr^{-1} is also consistent with our model results.

Yeh et al. (2015) presented an H_2 (1, 0) $S(1)$ map of the entire 30Dor nebula at 1″ resolution. The peak H_2 surface brightness in their region A is 9.15×10^{-5} erg s^{-1} cm^{-2} sr^{-1}. Our model predicts a maximum H_2 surface brightness of 5.3×10^{-5} erg s^{-1} cm^{-2} sr^{-1} located near the [C II] peak for a 12″ resolution. This is about a factor of 2 lower than the observed value, but it may be explained by the lower resolution used in our study and the fact that the H_2 emission could originate from clouds smaller than the PACS beam size.

5. Discussion

5.1. Filling factor

The model assumes that the PDR filling factor is unity, i.e., that the surface area of PDRs is equal to the beam area. If only part of the beam is covered or, on the contrary, if several clouds are present along the line of sight, the radiation emitted in the L_{FIR} and in cooling lines is different than the model prediction for optically thin lines. The filling factor is, respectively, lower or higher than 1.

We determined G_{UV} and P only using ratios of lines coming from the same phase of the ISM. Thus, they do not depend on

the filling factor because each line is affected by the same factor. The area filling factor, Φ_A, can then be estimated from the ratio of the observed intensity over the predicted intensity (for which $\Phi_A = 1$) for an individual line.

Both L_{FIR}^{PDR} and [C II] are emitted by PDRs and scale with the filling factor in the same way. Thus, we can determine Φ_A either with $\frac{[C\,II]_{observed}}{[C\,II]_{predicted}}$ (as in Wolfire et al. 1990) or similarly with $\frac{L_{FIR\ observed}^{PDR}}{L_{FIR\ predicted}^{PDR}}$. This result is presented in the right panel of Fig. 16. The parameter Φ_A is the smallest (about 0.6) near the peak of G_{UV} in region C (Fig. 3). The maximum value is ~9 in the northeast of the cluster. As stated earlier, an area filling factor greater than one means that several clouds covering the entire pixel are along the line of sight. This approach is marginally coherent near the peak of [C II] where the maximum filling factor is ~9. As noted in Sect. 4.3, considering that the opacity of [C II] is close to 0.1 at the [C II] peak, nine clouds on the line of sight add up to an opacity close to 1. As a consequence, the [C II] intensity does not add up linearly and this may call into question our assumption of optically thin [C II] at the [C II] peak location. Different PDR viewing angles can also affect this scenario and the number of components we derive is an upper limit.

This spatial distribution of the filling factor reflects the idea that the PDR clouds are smaller and/or less numerous where the radiation field is higher. The region mapped with ALMA by Indebetouw et al. (2013) corresponds to the region where the filling factor of PDRs is the largest in the map (see Fig. 16). The CO emission is highly structured, showing dense (10^3–10^5 cm^{-3}) clumps and filaments, on sub-parsecs scales, covering approximately 10% of the area of the map. They observed significant photodissociation of CO by radiation penetrating between the dense clumps, which can explain the increased X_{CO} factor determined for unresolved low metallicity clouds. Indebetouw et al. measure an X_{CO} factor that is two times the solar-metallicity value in the dense CO clumps. This value can be even higher, for unresolved studies, when possible interclump H_2 is included.

5.2. Clouds geometry

Indebetouw et al. (2013) observed the giant molecular cloud 30Dor-10, north of R136 with ALMA during Cycle 0 (it includes our regions B and C from Fig. 3). In the region mapped with ALMA, they measure a maximum diameter of 1.2 pc for the CO(2–1) clumps and a filling factor of about 10%. This could mean that the CO luminosity is dominated by small, bright clouds in the CO beam and the medium could be characterized by clumps/filaments of low volume filling factor with a physical size that is much smaller than our pixel size, implying that a plane-parallel geometry together with the high filling factor determined with [C II] may not be adapted to our observations.

Indeed, with the A_V^{max}, G_{UV}, and P previously determined in Sects. 4.4 and 4.3, we find that several plane-parallel clouds are required to reproduce the observed absolute intensities. Each of these clouds have a physical size of between 0.2 and 3 pc and an internal CO layer (estimated where the CO abundance is at least 50% of the maximum CO abundance) that ranges between 0.06 to 0.5 pc. The derived size scale is compatible with the ALMA observations. These results however depend on two main assumptions: the plane-parallel geometry and the uniformity of PDR clouds in each pixel.

With a plane geometry, the A_V^{max} of the simulated clouds determined here by comparison of the [C II] and CO emissions can be considered as a lower limit. Indeed, adopting a different geometry by post-processing the results of the model and wrapping the plane-parallel results on a spherical geometry results in a larger A_V^{max}. More details about this method can be found in Appendix B. When assuming a spherical geometry, bathed in an isotropic radiation field, a higher A_V (~20 mag at the center of the cloud) is needed to reproduce the CO observations. Such extinction corresponds to spherical clouds with diameters about four times larger than the size of the optimal plane-parallel clouds. Nevertheless, the results derived in Sect. 4.3 for G_{UV} and P are independent on the assumed geometry and remain unchanged.

We note that the extinction parameter can be determined independently from the dust mass surface density at a resolution of 22″ (Sect. 2.7). We can then compare A_V^{dust} derived from the dust map to A_V^{max} derived using the [C II]/[C I] and [C II]/CO ratios in our PDR models (Sect. 4.4). On the one hand, A_V^{dust} corresponds to the integrated extinction along the line of sight in each pixel. On the other hand, A_V^{max} is calculated for individual clouds, so for a meaningful comparison we need to scale by the number of components (i.e., the filling factor Φ_A; Sect. 5.1). While Φ_A is calculated at a relatively high spatial resolution (12″), the A_V^{max} for individual clouds is not constrained well owing to the poor spatial resolution (42″) and coverage of the [C I] and CO maps. In Fig. 18, we plot A_V^{dust} as a function of Φ_A (recalculated at a resolution of 22″) with several tracks showing the scaling with different A_V^{max} values. There is a remarkable correlation between A_V^{dust} and Φ_A, with most data points lying between the A_V^{max} = 1 and 3 lines, in agreement with the values determined with a plane-parallel geometry (Sect. 4.4). We emphasize that the determinations of A_V^{max} and Φ_A are independent from the determination of A_V^{dust}, as the two quantities are derived from different physical processes, and constrained by different observational sets. From Fig. 18, we infer that most clouds share similar A_V^{max} values at a spatial resolution of 22″. Moreover, the good agreement between A_V^{dust} (total extinction) and A_V^{max} (derived in the neutral gas of PDRs) suggests that (1) there is no significant contribution from the ionized gas in the A_V^{dust} determination, and (2) there is no significant contribution from foreground/background gas not associated with 30Dor and not accounted for by our PDR models. Our result not only strengthens the A_V^{max} range obtained in Sect. 4.4, but also suggests that this range remains valid at a resolution of 22″. While this result seems to favor plane-parallel geometry over spherical geometry, we wish to stress that we cannot easily derive the effective extinction corresponding to spherical clouds observed in any given pixel and that the large extinction probed at the center of the spherical cloud is not representative of this effective extinction.

Finally, we discuss the possible existence of clumps embedded in an interclump medium. Since the filling factor determined with [C II] in Sect. 5.1 may characterize an interclump medium surrounding small CO clumps, it is possible that the [C II] and the CO emission are not associated with the same structures. For example, a recent study of the N159 region by Okada et al. (2015) find that up to 50% of [C II] cannot be associated with the CO emission based on the velocity profiles of the lines. Testing the clumpiness of the medium would require us to adopt a distribution of clouds of different sizes and pressures, illuminated by a central source and including the effect of scattering and shielding, for each pixel of the map. Unfortunately, such a scenario cannot be properly modeled yet because of the lack of observational constraints.

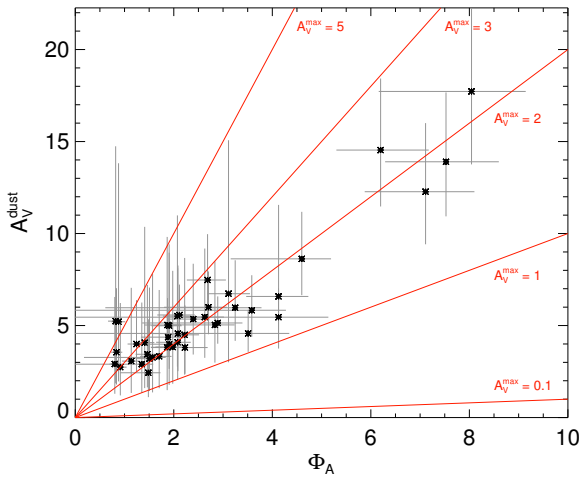

Fig. 18. Extinction derived from the dust mass $A_V^{\rm dust}$ is plotted against the filling factor $\Phi_{\rm A}$. The diagonal lines show different values of the extinction in individual PDR clouds ($A_V^{\rm max}$). The data points agree with $A_V^{\rm dust}$ for $A_V^{\rm max}$∼1–3.

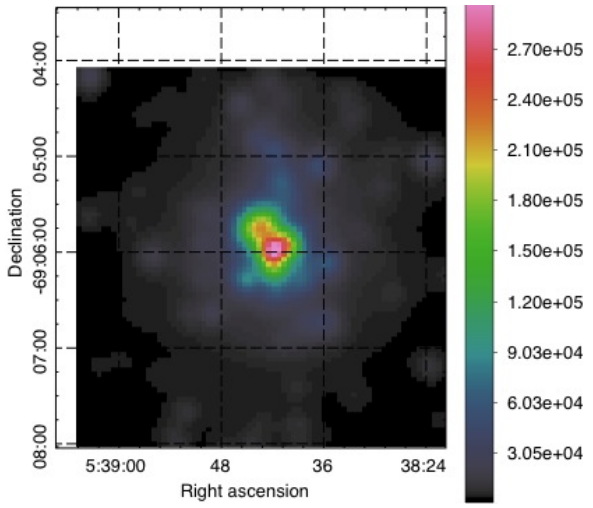

Fig. 19. Intensity of the emitted radiation field $G_{\rm stars}$ in the plane of R136 at 12″ resolution (color bar in units of the Mathis field).

5.3. Three-dimensional distribution of the gas

In this section, we determine the physical distance between the clouds and ionizing sources to reconstruct the 3D distribution of the gas. This is accomplished by comparing the incident $G_{\rm UV}$, predicted by the Meudon PDR code and the emitted radiation field, $G_{\rm stars}$. We define $G_{\rm stars}$ as the FUV radiation field computed from the known massive stellar population from the literature. We use catalogs of stars from Crowther & Dessart (1998) and Selman & Melnick (1999), including O and B stars and Wolf-Rayet (WF) stars. We use the temperature of the brightest optical sources and integrate over a blackbody between 912 and 2400 Å to be consistent with the definition of $G_{\rm UV}$ in the Meudon PDR code. We then use a $\frac{1}{R^2}$ relation, where R is defined as the physical distance from the center of the cluster, to calculate an average $G_{\rm stars}$ in each pixel of a cube centered on R136. We first make the assumption that all of the stars lay on the same plane, and derive the $G_{\rm stars}$ presented in Fig. 19. The maximum incident radiation field we expect on each point of the cube is then $G_{\rm stars}$, since no absorption is taken into account.

The ratios used to constrain $G_{\rm UV}$ and P are independent of the filling factor, since [O I] 145 μm, [C II] and $L_{\rm FIR}^{\rm PDR}$ are supposed to be almost cospatial in the PDR model. Thus, $G_{\rm UV}$ determined with the model is also independent of the filling factor. In that case, the incident radiation field, $G_{\rm UV}$, should be equal to the emitted radiation field, $G_{\rm stars}$, modulated by the distance to the R136 plane, assuming there is no absorption between the ionizing stars and the PDR (i.e., the distance to the plane calculated here is an upper limit on the actual distance). We can determine simultaneously four parameters: $G_{\rm UV}$, P, $\Phi_{\rm A}$, and z (the distance to the plane of R136) for each pixel of the map, using the following relations

$$L_{\rm FIR\ obs}^{\rm PDR} = \Phi_{\rm A} \times L_{\rm FIR\ pred}^{\rm PDR} \quad (2)$$

$$\mathrm{G_{stars}} = G_{\rm UV} \times \frac{z^2 + d^2}{d^2} \quad (3)$$

$$I_j = M_j, \quad (4)$$

where d is the projected distance between a pixel and the central source, $\sqrt{z^2 + d^2} = R$, I_j are the observed values of the line intensity ratios j, and M_j the ratios calculated by the PDR model (in erg s^{-1} cm^{-2} sr^{-1}). The parameters $G_{\rm UV}$ and $G_{\rm stars}$ are in units of the Mathis field, and $G_{\rm UV}$ and P are calculated as described in Sect. 4.3, using Eq. (4).

The physical distance R between PDR clouds and R136 is presented in Fig. 20. It ranges from ∼11 to 80 pc. The gas located close to R136 in the projected view is actually 40 to 80 pc away from the cluster. The bright arm-like structure in [O III], which, when projected, appears further from R136, is much closer to the star cluster as it is almost on the same plane. This is consistent with the distance calculated in Pellegrini et al. (2011) for the ionized gas using optical observations.

The physical distance described above was derived by assuming that all of the stars are located in the same plane. For comparison, we also considered a random distribution of the stars in the perpendicular direction, but maintaining a high density of stars within a 6 pc radius around the center of R136 in order to reproduce a spherical distribution. We performed a Monte Carlo simulation and calculated distances similar to our previous determination (<40% difference throughout the map). This is not surprising as most stars in R136 are in fact located in a ∼6 pc radius sphere. We used the Monte Carlo simulation to estimate a typical uncertainty on the physical distance of ∼4 pc.

5.4. Porosity of the ISM

The [O III] 88 μm line emission is detected over large spatial scales in 30Dor, as has already been noticed in other extended sources (e.g., in N11 by Lebouteiller et al. 2012) and, together with the small-scale CO clumps we see, may be indicative of a highly porous region. There is probably mixing of the ionized and neutral phases of the ISM throughout all spatial scales. This idea is supported by Fig. 21, which shows the ratio [O III]/[C II] as a function of $\Phi_{\rm A}$. We can see that these two quantities are strongly correlated. Indeed, a low area filling factor $\Phi_{\rm A}$ in a given pixel implies a small volume fraction occupied by PDRs. This means that there is less matter per unit volume to absorb the UV radiation and this radiation is able to travel further away. Region B from Fig. 3 (violet), at ∼40 pc from R136, has the lowest [O III]/[C II] ratio and the highest PDR filling factor. This is also where the [C II] peaks and the CO clumps reside (see contours in

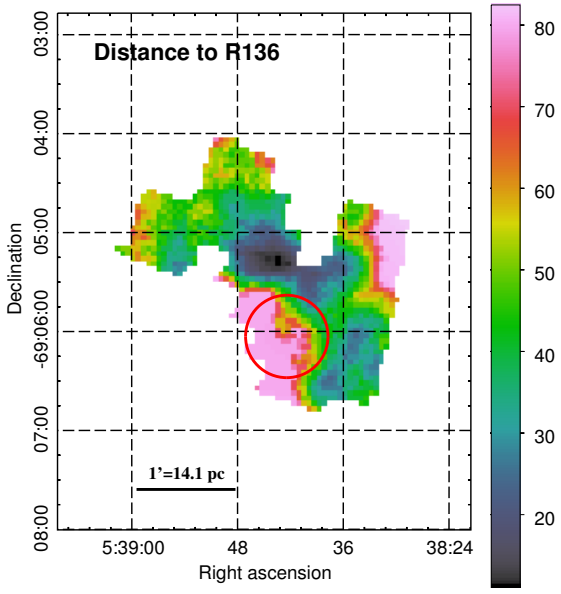

Fig. 20. Physical distance R (in pc) of the surface of the PDR to the center of R136. The red circle shows the location of R136.

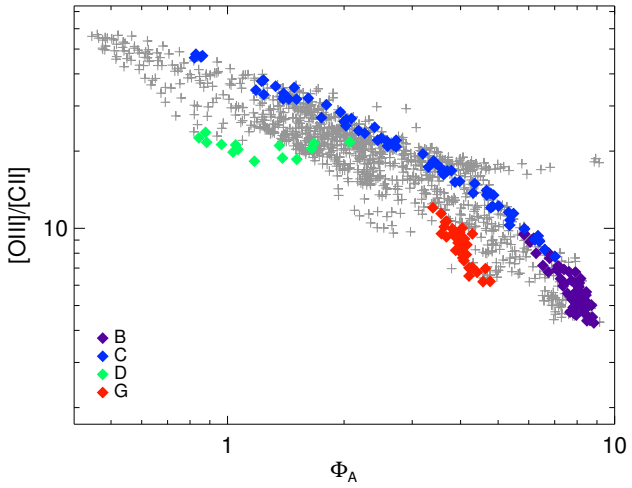

Fig. 21. Correlation between [O III]/[C II] and the PDR area filling factor. The color symbols are associated with the regions defined in Fig. 3. The gray symbols are all of the other pixels of our 30Dor map.

Fig. 16). In contrast, the ratio [O III]/[C II] is high (>10) in region D (green), which is one of the furthest region from R136 with a low Φ_A. The blue points of region C, which is the [O III] peak and near the G_{UV} and P peaks, show a large range of [O III]/[C II] and Φ_A. This is a region of widely varying ISM conditions. The ratio [O III]/[C II] as a function of the physical distance R or G_{UV} is a scatter plot, highlighting the fact that the proximity of the ionizing source is not the only controlling factor of the structure of the ISM.

Over the mapped area of 42 pc × 56 pc the PDR filling factor and the [O III]/[C II] ratio vary over one order of magnitude. The decrease in dust abundance and intense UV photons from the SSC conspire together to shape the surrounding porous ISM, filling it with hard photons and a relatively small filling factor of PDR clumps.

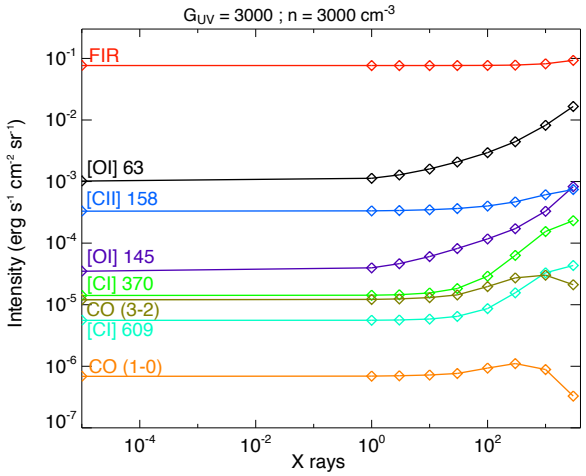

Fig. 22. Influence of the X-ray luminosity on the intensities of individual lines for a typical isochoric model with $G_{UV} = 3 \times 10^3$ and $n = 3 \times 10^3$ cm^{-3}. G_X is the X-ray luminosity integrated between 0.2 and 8 keV, given in unit of the Habing field (Habing 1968). This is to be compared with our results for G_{UV} (see Sect. 5.5).

5.5. Other sources of excitation

No evidence of any shock tracers has been found in 30Dor by previous studies so far (Indebetouw et al. 2009; Yeh et al. 2015). We investigate here the possibility for X-rays to be an important source of excitation of the gas in 30Dor. Townsley et al. (2006) studied the population of X-ray point sources (energy between 0.5 and 8 keV) in a 17′ × 17′ field around R136 with *Chandra*. Spectral fitting is performed on the brightest sources (49 in total). In particular, they determine a total X-ray luminosity, corrected for absorption, of $10^{36.95}$ erg s^{-1} for the brightest source in R136 (Mk 34) with an X-ray flux of 2×10^{-3} erg s^{-1} cm^{-2} sr^{-1} at a distance of 20 pc away, approximately at the ionization front. As presented in Fig. 22, such a low G_X, compared to the values of G_{UV}, does not have an important effect on the intensity of the individual lines for a given G_{UV} and density.

5.6. If 30Dor were unresolved

Studying resolved nearby galaxies can help us understand more distant unresolved targets. At a distance of 900 kpc, the entire region of 30Dor mapped in [O I] 145 μm with PACS (covering 56 pc × 70 pc) would fall in only one spaxel of the PACS spectrometer. This distance is comparable to the distance of the Andromeda galaxy (~780 kpc).

We integrate all of the tracers we have and perform the same study at this lower resolution with only one pixel. Using the same technique as Sect. 4.3, we find that all of the [C II] emission originates from the PDRs. Using the Meudon PDR code, we determine $G_{UV} = 1390$, $P = 6.18 \times 10^5$ cm^{-3} K, and $A_V = 2$–3. This is representative of a region of moderate G_{UV} and P in our detailed spatial study, such as region G in Fig. 3 or the ISM north of region B.

Even though our map is relatively small and centered on R136, the global solution is already biased toward the solution corresponding to regions with relatively low P and low G_{UV}. However, we have to keep in mind that the regions targeted with PACS are the most luminous around R136, especially for the [O I] 145 μm line. This implies that if we were to integrate an even larger area, the result would be presumably biased even

more to this diffuse and low G_{UV} regime. These two parameters could be even lower if we include more diffuse regions, which is the subject of a subsequent study in the LMC.

6. Conclusions

We have studied the ISM properties in the extreme environment of 30Dor in the LMC, around the super star cluster R136. We summarize our results as follow:

1. We presented and analyzed new *Herschel* PACS observations of 30Dor in [C II] 158 μm, [O I] 63 and 145 μm, [N II] 122 and 205 μm, and [O III] 88 μm over a 56×70 pc region of 30Dor. All of these lines are well detected and provide diagnostics on the structure of the ISM.
   The [O III] line is the brightest of the FIR lines, ranging from 2 to 60 times more luminous than [C II]. We propose that the [O I] 63 μm line is optically thick throughout the mapped region. We find that the [C II]/CO(1–0) luminosity ranges between 5×10^4 and 3×10^5 throughout the map. This range is larger than the broad range of ratios found from integrated DGS dwarf galaxies of Cormier et al. (2014).
2. Using the *Spitzer* and *Herschel* MIR to submm photometric observations, we model the full dust SED spatially around 30Dor and derive the infrared luminosity map. We find that the [C II] intensity ranges from 0.1 to 1% of the observed L_{FIR} throughout the region mapped.
3. Based on the electron density of the ionized gas (10 to 100 cm^{-3}) and the high value of the [C II]/[N II] ratio, we determined that at least 90% of the [C II] emission originates from the PDRs, which makes the [C II] intensity a valuable constraint for our PDR modeling.
4. We decomposed the L_{FIR} map to separate the component associated with the ionized gas from the PDR-only component. We find, in places, that ~70% of the L_{FIR} is not from PDRs, but associated with the ionized gas component, which we remove for the PDR modeling. We emphasize caution when applying the total L_{FIR} to PDR models without considering the origin of the L_{FIR}.
5. From the ratios ([O I] 145 μm + [C II])/L_{FIR}^{PDR} and [O I] 145 μm/[C II] we determined the spatial distribution of the radiation field and the pressure with the Meudon PDR code. The parameter G_{UV} ranges between 10^2 and 3×10^4 (in units of the standard radiation field defined in Mathis et al. 1983) and P ranges between 10^5 and 1.7×10^6 cm^{-3} K.
6. The total depth of the clouds is determined by including the ratios [C II]/[C I] or [C II]/CO in the modeling assuming that all of these tracers are associated with the same structures. We showed that in the 30Dor region, A_V^{max} in 30″ pixels is ~1–3 mag. This value should be considered a minimum value because of our assumption of a plane-parallel geometry.
7. We conducted a 3D model of the PDR gas around R136. A comparison of the incident radiation field determined from our PDR model, G_{UV}, with the emitted radiation field, G_{stars}, reveals that the PDR gas is distributed at various distances, ranging between 20 to 80 pc from the excitation source, R136.
8. The PDR area filling factor ranges between 0.6 (at the peak of G_{UV}) and 9 (at the peak of [C II]). The high value of the [O III]/[C II] ratio and its tight correlation with the filling factor rather than with the distance, highlight the porosity of the ISM, filled with hard photons around relatively small PDR clumps.

The combined effects of a half-solar metallicity gas with the intense excitation source R136 create the extreme environment we see in 30Dor. It has been shown that the structure of the gas in this region is dominated by photoionization. X-rays or shocks are not needed to reproduce the observed line intensities. Based on our findings in the present study, we speculate that the small size of the CO core inside the PDR clouds could explain the high [C II]/CO ratio we observe in low metallicity environments. The high value of the [O III] emission line suggests that a highly porous medium is a characteristic of the gas in low metallicity dwarf galaxies.

Acknowledgements. The authors would like to thank Annie Hughes for providing the CO(1–0) data and Akiko Kawamura for the CO(3–2) data. This research was made possible through the financial support of the Agence Nationale de la Recherche (ANR) through the programme SYMPATICO (Program Blanc Projet (NR-11-BS56-0023) and also through the EU FP7. SH acknowledges financial support from DFG programme HO 5475/2-1. PACS was developed by MPE (Germany); UVIE (Austria); KU Leuven, CSL, IMEC (Belgium); CEA, LAM (France); MPIA (Germany); INAFIFSI/OAA/OAP/OAT, LENS, SISSA (Italy); IAC (Spain). This development was supported by BMVIT (Austria), ESA-PRODEX (Belgium), CEA/CNES (France), DLR (Germany), ASI/INAF (Italy), and CICYT/MCYT (Spain). SPIRE was developed by Cardiff University (UK); Univ. Lethbridge (Canada); NAOC (China); CEA, LAM (France); IFSI, Univ. Padua (Italy); IAC (Spain); SNSB (Sweden); Imperial College London, RAL, UCL-MSSL, UKATC, Univ. Sussex (UK) and Caltech, JPL, NHSC, Univ. Colorado (USA). This development was supported by CSA (Canada); NAOC (China); CEA, CNES, CNRS (France); ASI (Italy); MCINN (Spain); Stockholm Observatory (Sweden); STFC (UK); and NASA (USA).

References

Abel, N. P., Sarma, A. P., Troland, T. H., & Ferland, G. J. 2007, ApJ, 662, 1024
Allen, M. G., Groves, B. A., Dopita, M. A., Sutherland, R. S., & Kewley, L. J. 2008, ApJS, 178, 20
Aniano, G., Draine, B. T., Gordon, K., & Sandstrom, K. M. 2011, PASP, 123, 1218
Asplund, M., Grevesse, N., Sauval, A. J., & Scott, P. 2009, ARA&A, 47, 481
Bernard-Salas, J., Habart, E., Arab, H., et al. 2012, A&A, 538, A37
Bolatto, A. D., Jackson, J. M., & Ingalls, J. G. 1999, ApJ, 513, 275
Bolatto, A. D., Wolfire, M., & Leroy, A. K. 2013, ARA&A, 51, 207
Brauher, J. R., Dale, D. A., & Helou, G. 2008, ApJS, 178, 280
Bron, E., Le Bourlot, J., & Le Petit, F. 2014, A&A, 569, A100
Cigan, P., Young, L., Cormier, D., et al. 2016, AJ, 151, 14
Cormier, D., Madden, S. C., Hony, S., et al. 2010, A&A, 518, L57
Cormier, D., Lebouteiller, V., Madden, S. C., et al. 2012, A&A, 548, A23
Cormier, D., Madden, S. C., Lebouteiller, V., et al. 2014, A&A, 564, A121
Cormier, D., Madden, S. C., Lebouteiller, V., et al. 2015, A&A, 578, A53
Crowther, P. A., & Dessart, L. 1998, MNRAS, 296, 622
Fazio, G. G., Hora, J. L., Allen, L. E., et al. 2004, ApJS, 154, 10
Fulton, T. R., Baluteau, J.-P., Bendo, G., et al. 2010, Proc. SPIE, 7731, 773134
Galliano, F., Hony, S., Bernard, J.-P., et al. 2011, A&A, 536, A88
Gordon, K. D., Engelbracht, C. W., Rieke, G. H., et al. 2008, ApJ, 682, 336
Habing, H. J. 1968, Bull. Astron. Inst. Netherlands, 19, 421
Heyminck, S., Graf, U. U., Güsten, R., et al. 2012, A&A, 542, L1
Hunter, D. A. 1999, in New Views of the Magellanic Clouds, eds. Y.-H. Chu, N. Suntzeff, J. Hesser, & D. Bohlender, IAU Symp., 190, 217
Hunter, D. A., Kaufman, M., Hollenbach, D. J., et al. 2001, ApJ, 553, 121
Indebetouw, R., de Messières, G. E., Madden, S. C., et al. 2009, ApJ, 694, 32
Indebetouw, R., Brogan, C., Chen, C. H. R., et al. 2013, ApJ, 774, 73
Indriolo, N., & McCall, B. J. 2012, ApJ, 745, 91
Indriolo, N., Neufeld, D. A., Gerin, M., et al. 2015, ApJ, 800, 40
Kaufman, M. J., Wolfire, M. G., Hollenbach, D. J., & Luhman, M. L. 1999, ApJ, 527, 795
Langer, W. D., Velusamy, T., Pineda, J. L., Willacy, K., & Goldsmith, P. F. 2014, A&A, 561, A122
Le Bourlot, J., Le Petit, F., Pinto, C., Roueff, E., & Roy, F. 2012, A&A, 541, A76
Le Petit, F., Nehme, C., Le Bourlot, J., & Roueff, E. 2006, ApJS, 164, 506
Lebouteiller, V., Bernard-Salas, J., Brandl, B., et al. 2008, ApJ, 680, 398
Lebouteiller, V., Cormier, D., Madden, S. C., et al. 2012, A&A, 548, A91
Liseau, R., Justtanont, K., & Tielens, A. G. G. M. 2006, A&A, 446, 561

Madden, S. C., Poglitsch, A., Geis, N., Stacey, G. J., & Townes, C. H. 1997, ApJ, 483, 200
Madden, S. C., Rémy-Ruyer, A., Galametz, M., et al. 2013, PASP, 125, 600
Mathis, J. S., Mezger, P. G., & Panagia, N. 1983, A&A, 128, 212
Meixner, M., Gordon, K. D., Indebetouw, R., et al. 2006, AJ, 132, 2268
Meixner, M., Panuzzo, P., Roman-Duval, J., et al. 2013, AJ, 146, 62
Minamidani, T., Tanaka, T., Mizuno, Y., et al. 2011, AJ, 141, 73
Negishi, T., Onaka, T., Chan, K.-W., & Roellig, T. L. 2001, A&A, 375, 566
Oberst, T. E., Parshley, S. C., Nikola, T., et al. 2011, ApJ, 739, 100
Okada, Y., Requena-Torres, M. A., Güsten, R., et al. 2015, A&A, 580, A54
Ott, S. 2010, Astronomical Data Analysis Software and Systems XIX, 434, 139
Pagel, B. E. J. 2003, in CNO in the Universe, eds. C. Charbonnel, D. Schaerer, & G. Meynet, ASP Conf. Ser., 304, 187
Pak, S., Jaffe, D. T., van Dishoeck, E. F., Johansson, L. E. B., & Booth, R. S. 1998, ApJ, 498, 735
Pellegrini, E. W., Baldwin, J. a., & Ferland, G. J. 2011, ApJ, 738, 54
Pilbratt, G. L., Riedinger, J. R., Passvogel, T., et al. 2010, A&A, 518, L1
Pineda, J. L., Mizuno, N., & Röllig, M. 2012, A&A, 544, A84
Pineda, J. L., Langer, W. D., & Goldsmith, P. F. 2014, A&A, 570, A121
Poglitsch, A., Krabbe, A., Madden, S. C., et al. 1995, ApJ, 454, 293
Poglitsch, A., Waelkens, C., Geis, N., et al. 2010, A&A, 518, L2
Rémy-Ruyer, A., Madden, S. C., Galliano, F., et al. 2013, A&A, 557, A95
Rémy-Ruyer, A., Madden, S. C., Galliano, F., et al. 2014, A&A, 563, A31
Rémy-Ruyer, A., Madden, S. C., Galliano, F., et al. 2015, A&A, 582, A121
Rieke, G. H., Young, E. T., Engelbracht, C. W., et al. 2004, ApJS, 154, 25
Rolleston, W. R. J., Trundle, C., & Dufton, P. L. 2002, A&A, 396, 53
Röllig, M., Ossenkopf, V., Jeyakumar, S., Stutzki, J., & Sternberg, A. 2006, A&A, 451, 917
Rubio, M., Garay, G., & Probst, R. 1998, The Messenger, 93, 38
Schruba, A., Leroy, A. K., Walter, F., et al. 2012, AJ, 143, 138
Selman, F., & Melnick, J. 1999, A&A, 549, 532
Smith, J. D. T., Armus, L., Dale, D. A., et al. 2007a, PASP, 119, 1133
Smith, J. D. T., Draine, B. T., Dale, D. A., et al. 2007b, ApJ, 656, 770
Stacey, G. J., Geis, N., & Genzel, R. 1991, ApJ, 373, 423
Stacey, G. J., Hailey-Dunsheath, S., Ferkinhoff, C., et al. 2010, ApJ, 724, 957
Swinyard, B. M., Polehampton, E. T., Hopwood, R., et al. 2013, MNRAS, 440, 3658
Tielens, a. G. G. M., & Hollenbach, D. 1985, ApJ, 291, 722
Townsley, L. K., Broos, P. S., Feigelson, E. D., et al. 2006, AJ, 131, 2140
Walker, A. R. 2012, Astrophys. Space Sci., 341, 43
Werner, M. W. W., Roellig, T. L. L., Low, F. J. J., et al. 2004, ApJS, 154, 1
Wolfire, M. G., Hollenbach, D., & McKee, C. F. 2010, ApJ, 716, 1191
Wolfire, M. G., Tielens, A. G. G. M., & Hollenbach, D. J. 1990, ApJ, 358, 116
Wong, T., Hughes, A., Ott, J., et al. 2011, ApJS, 197, 16
Wu, R., Polehampton, E. T., Etxaluze, M., et al. 2013, A&A, 556, A116
Wu, R., Madden, S. C., Galliano, F., et al. 2015, A&A, 575, A88
Yeh, S. C. C., Seaquist, E. R., Matzner, C. D., & Pellegrini, E. W. 2015, ApJ, 807, 117

Appendix A: PACS observations

Table A.1. Technical details on the observations.

OBSID	Coordinates	Lines	Observation date	Exposition time (s)	Rasters nb	Mode
1342222085	5h38m35,00s –69d05m39,0s	[O III]$_{88}$, [C II]$_{158}$	740	2513,0	4	faint line
1342222086	5h38m48,00s –69d06m37,0s	[O I]$_{63}$	740	908,0	2	faint line
1342222087	5h38m58,00s –69d04m43,0s	[O I]$_{63}$	740	1322,0	4	faint line
1342222088	5h38m58,00s –69d04m43,0s	[O III]$_{88}$, [C II]$_{158}$	740	2515,0	4	faint line
1342222089	5h38m48,00s –69d06m37,0s	[O III]$_{88}$, [C II]$_{158}$	740	1703,0	2	faint line
1342222090	5h38m56,66s –69d04m56,9s	[O I]$_{145}$	740	451,0	1	faint line, pointed
1342222091	5h38m34,92s –69d06m07,0s	[N II]$_{122}$	740	452,0	1	faint line, pointed
1342222092	5h38m45,00s –69d05m23,0s	[O I]$_{63}$	740	1734,0	6	faint line
1342222093	5h38m35,00s –69d05m39,0s	[O I]$_{145}$	740	1321,0	4	faint line
1342222094	5h38m45,00s –69d05m23,0s	[O III]$_{88}$, [C II]$_{158}$	740	3325,0	6	faint line
1342222095	5h38m46,10s –69d04m58,8s	[N II]$_{122}$	740	452,0	1	faint line, pointed
1342222096	5h38m45,00s –69d05m23,0s	[O I]$_{145}$	740	1735,0	6	faint line
1342222097	5h38m35,00s –69d05m39,0s	[O I]$_{63}$	740	1320,0	4	faint line
1342231279	5h38m38,00s –69d06m00,0s	[C II]$_{158}$	889	801,0	3	bright line
1342231280	5h38m30,00s –69d06m07,0s	[O III]$_{88}$	889	724,0	3	bright line
1342231281	5h38m30,00s –69d05m07,0s	[C II]$_{158}$	889	801,0	3	bright line
1342231282	5h38m55,00s –69d03m49,0s	[O I]$_{63}$, [C II]$_{158}$	889	1133,0	2	bright line
1342231283	5h38m30,.00s –69d06m07,0s	[O I]63, [C II]$_{158}$	889	1420,0	3	bright line
1342231284	5h38m56,00s –69d04m50,0s	[N II]$_{122}$	889	662,0	2	bright line
1342231285	5h38m40,00s –69d04m38,0s	[O III]$_{88}$	889	576,0	2	bright line

Notes. All of the observations were done in unchopped mode.

Appendix B: Spherical geometry

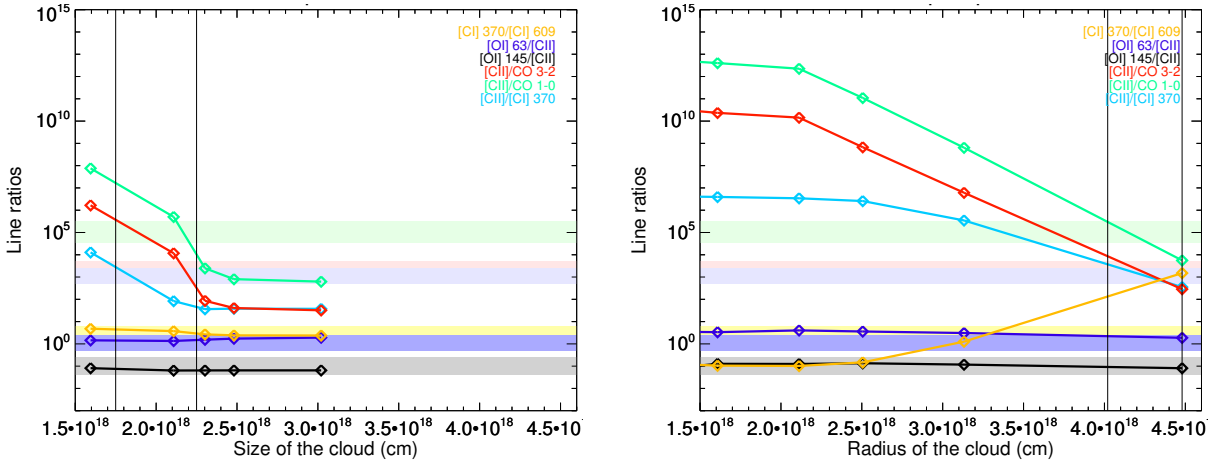

Fig. B.1. *Left*: ratios $\mathcal{R}$ of the modeled line ratios for [C I] 370 μm/[C I] 609 μm, [O I] 63 μm/[C II], [O I] 145 μm/[C II], [C II]/CO(3–2), [C II]/CO(1–0), and [C II]/[C I]370 μm, for simulated plane-parallel clouds of different sizes with $G_{\rm UV} = 1 \times 10^3$ and $P = 3 \times 10^5$ cm^{-3} K. *Right*: same for spherical clouds of different radius. The vertical lines indicate the range of radius where the predictions of the model are compatible with the observed [C II]/CO(3–2) and [C II]/[C I]370 μm.

The Meudon PDR code is a plane-parallel model. The code computes the abundance profiles of the various species and excited states in a plane-parallel system as a function of the distance to the surface of the cloud. It is possible to post-process the results of a simulation to wrap the structure and simulate a spherical cloud. To do that, we integrate the intensity of each transition over a sphere, where the abundance profiles of each species as a function of the distance to the surface of the sphere is equal to the computed abundance profile as a function of the distance to the surface for a plane-parallel geometry. The resulting line ratios as a function of the diameter of the sphere, for an integrated cloud illuminated by an isotropic field, are shown in the right panel of Fig. B.1.

This is approach is geometrical. It is not done to accurately model the physics of a spherical cloud, but to investigate the impact of the geometry on the integrated intensity, similar to the approach or Bolatto et al. (1999). Physically, this approach is only valid when there is enough extinction, i.e., for values of $A_V \gtrsim 5$. In addition, we wish to emphasize that the approach of computing a spherical cloud by wrapping the structure is not satisfactory in the case of clouds illuminated by a central stellar cluster since the radiation field seen by any cloud is not isotropic. The ideal model would be a model with clouds of various sizes located at various distances from a central radiation source.

IV.2.2 Complements to the paper

Determination of the 3D structure.

We develop here the method presented briefly in Chevance et al. (2016) for the determination of the 3D structure. The PDR modeling of 30Dor, applying the method described in Section III.4.2, enable us to compute G_{UV} at the surface of the PDRs, spatially. This value can be compared with the emitted radiation field by the massive stars, noted G_{stars} in order to determine the distance of the PDRs to the cluster. Assuming that there is no extinction between the ionizing stars and the PDRs, G_{stars} gives an upper limit to G_{UV} and the physical distance from the center of R136 can be calculated through the equation:

$$G_{stars} = G_{UV} \times \frac{z^2 + d^2}{d^2} \tag{IV.2}$$

where d is the projected distance in the plane of the sky between a pixel and the center of the cluster and z the distance in the perpendicular direction, along the line of sight. The distance z calculated here should be considered as an upper limit to the distance due to our hypotheses.

Although the the exact position of each star perpendicular to the plane of the sky is not known, R136 is compact (most of the stars are located within a 6 pc radius sphere) and as a first step, we assume that all of the stars are located in the same plane to calculate G_{stars}. The method is described in Section IV.2.1. As a second step, we use a more realistic approach, considering a random distribution of the stars in the perpendicular direction, but maintaining a high density of stars within a 6 pc radius around the center of R136 in order to reproduce a spherical distribution. We performed a Monte-Carlo simulation to investigate a wide range of possible 3D distributions of the stars. One realization is shown in the upper left panel of Figure IV.10. Both methods give similar 3D structure, with less than 40% difference for the absolute values.

The resulting distance z calculated with Equation IV.2 for each pixel of the mapped region of 30Dor is presented in a 3D view, with three different viewing angles in Figure IV.10. The physical distance between the center of R136 and the surrounding PDR clouds ($\sqrt{z^2 + d^2}$) ranges from $\sim$ 11 to 80 pc. The gas seems to be distributed as a large-scale shell around the ionizing cluster, consistently with the geometry derived from the ionized gas by Pellegrini et al. (2011) and in qualitative agreement with the expanding shells defined by Chu & Kennicutt (1994).

IV.3 Beyond *Herschel*/PACS : *SOFIA* observations

IV.3.1 Accepted *SOFIA*/FIFI-LS cycle 4 proposal

The proximity of this powerful starburst region provides a unique testbed to study the ISM impacted by the SSC, R136, at large scale, over tens of parsecs. With an international team, we proposed to use the FIFI-LS instrument on board NASA's Stratospheric Observatory for Infrared Astronomy (*SOFIA*) to follow-up on our *Herschel*/PACS observations of the FIR fine structure lines in 30Dor: [C II] 158 μm, [O I] 145 μm and [O III] 88 μm, along with [O III] 52 μm, which was not accessible with *Herschel*, but is crucial to determine the density of diffuse ionized gas. For *SOFIA* Cycle 4, 7 hours of Director Discretionary Time and 3 hours of Guaranteed Time have been allocated for this project (P.I. Chevance). I assisted in the flight series in New Zealand in June and July 2016 (Figure IV.14) and present the new data in Section IV.3.2.

Detailed PDR and photoionization modeling will be carried out using the Meudon PDR code and Cloudy, on $\sim$4 pc scales, which corresponds to the resolution of FIFI-LS ($\sim$15″ at 158 μm). These

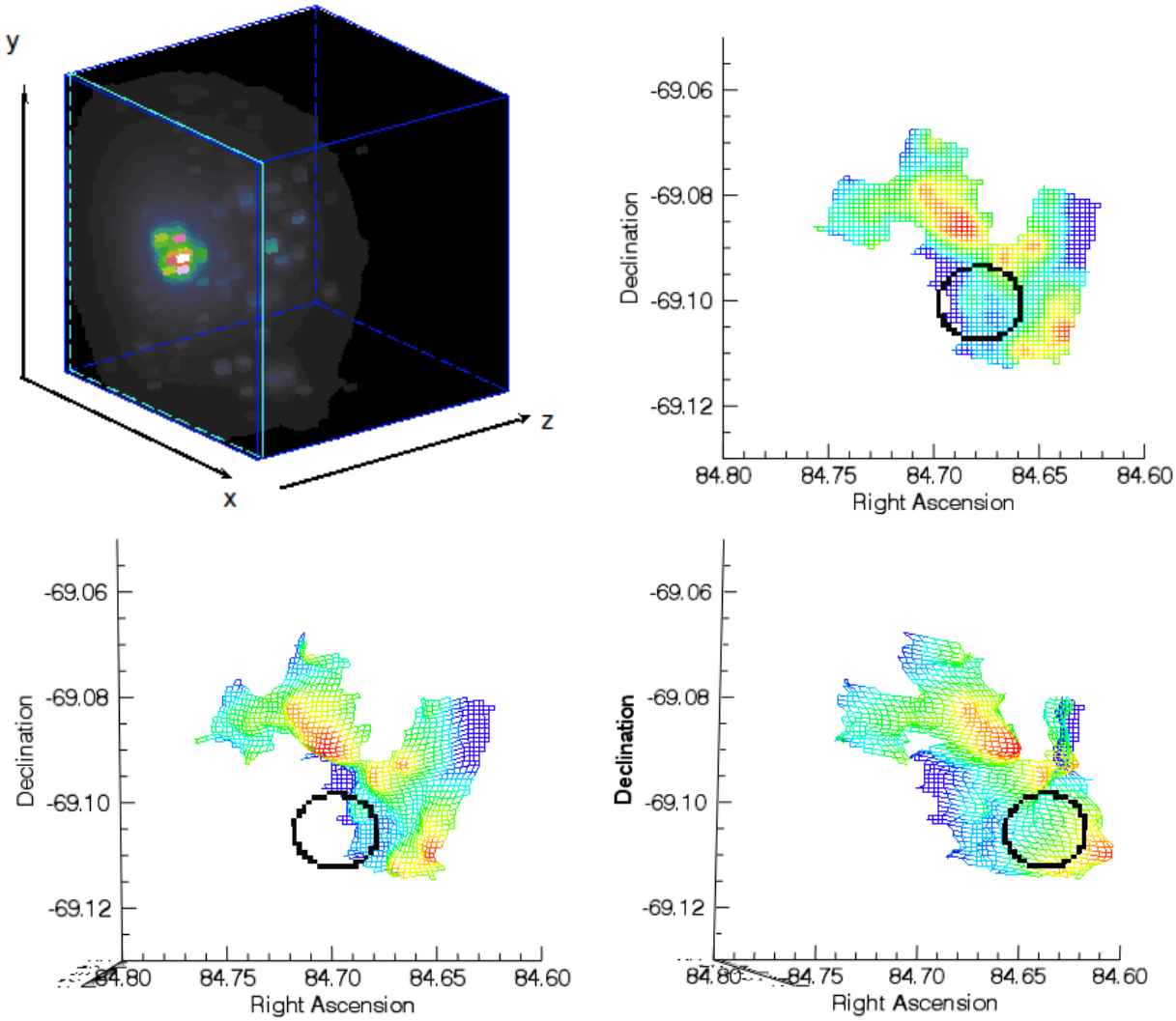

Figure IV.10: *Top left: Intensity of the emitted radiation field from the plane of R136 (x,y plane) to 50" beyond (along the z axis), at 12" resolution. Right and bottom left: 3D view of the distribution of the PDR around the SSC R136 (represented by a black circle in the plane z=0). The color scale represents the distance from the plane z=0, from 20 pc (red) to 70 pc (dark blue).*

new observations will be analyzed to elucidate the structure and properties of the different phases over the 90 pc × 75 pc region (6′ × 5′) - covering the full range of PDR and H II region conditions influenced by R136, and not just the central region (30pc × 30pc; 2′ × 2′) covered by *Herschel*/PACS (see Figure IV.11). The limited *Herschel* maps provide an incomplete picture of the region and our results are biased towards the more confined and bright central regions. Indeed, the influence of R136 on the ISM is expected to be dominant over ∼100 parsecs due to the high porosity of the medium (e.g. Lopez et al. 2011; Kawada et al. 2011), motivating this large field proposed for *SOFIA*.

The new *SOFIA* maps will allow us to chart the physical properties of the neutral and ionized phases influenced by the young massive star cluster. In particular, an important objective is to determine the density of the diffuse ionized gas, n_e, over the 30Dor region using the ratio of the two [O III] lines at 52 and 88 μm (see Fig. IV.13). We will also investigate the variations of the dust heating, primarily due to FUV photons in this region and traced by L_{FIR}. The ratio [C II]/L_{FIR}, which can be

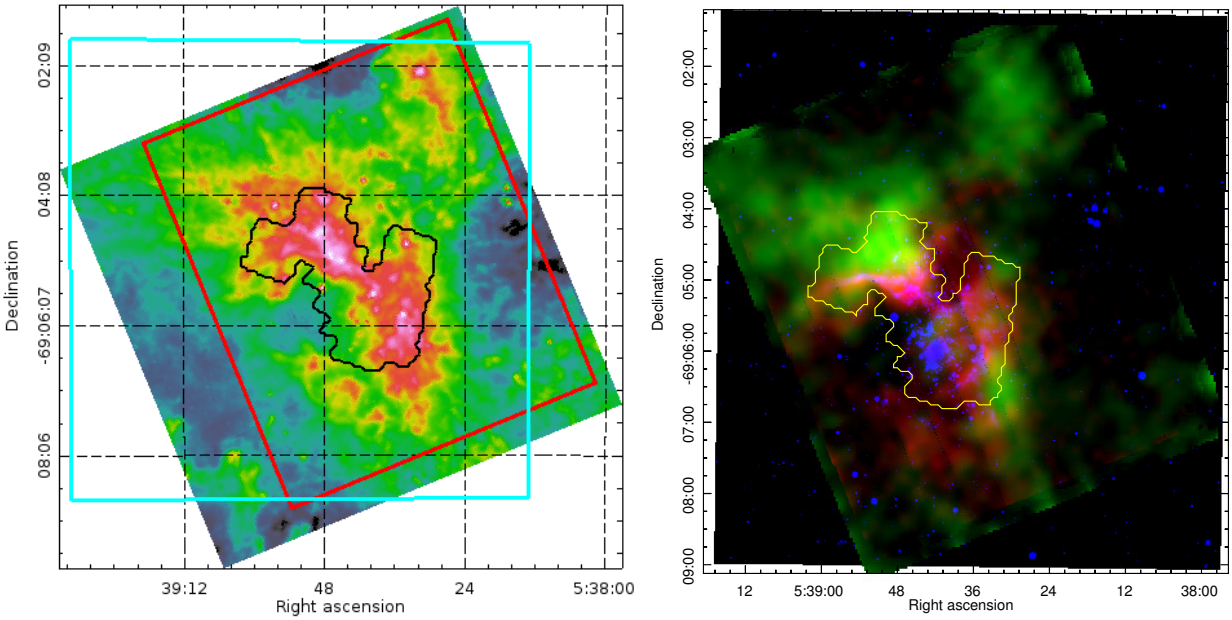

Figure IV.11: *Left: IRAC 8 µm image tracing mostly PAHs. The black and cyan contours outline the observed areas for [O I] 145 µm by PACS and for CO(1-0) by Mopra respectively. The red box is the selected area for the SOFIA observations of [C II] 157 µm and [O III] 52 µm and 88 µm. Right: Vista J band (blue), FIFI-LS [O III] 52 µm (red) and [C II] 158 µm (green). The yellow contour outlines the observed area for [O I] 145 µm by PACS.*

an indicator of the photoelectric heating efficiency (see Sect. IV.1.3) is depressed toward the peak of the modeled G_{UV}, where the shielding of molecular clouds has diminished. Models indeed indicate that a lower G_{UV} is needed to explain a high [C II]/L_{FIR} (Cormier et al. 2015). Moreover, this ratio should also depend on the PAH abundance which probably varies as a function of distance from the cluster. We will consistently model the gas and dust to test if these variations are driven by different local conditions, a different dust abundance or a different heating mechanism.

We will determine the distribution of G_{UV} and P with the new FIFI-LS observations and the Meudon PDR code, and probe the variations of A_V^{max} throughout the map with Mopra CO(1-0) data, which cover the entire $6' \times 5'$ targeted region. Our PDR solution maps (Figure 15 of Chevance et al. 2016 in Sect. IV.2.1) show several clumps in P and G_{UV}, indicating complex substructures with peaks of G_{UV} occurring near the western edge of our PACS map. In addition, for the limited regions already covered, more than 90% of the H_2 is not traced by CO (see more details in Sect. V.2.2). We expect such a high value since we probe the medium closest to the starburst, but how does that proportion of CO-dark gas vary further from the peak of G_{UV}? Our X_{CO} map hints at a decrease of CO-dark gas as CO increases, but the limited size of the PACS map does not cover the peak of the CO(1-0) emission. One of the most important objectives of this study will then be to characterize the evolution of the fraction of CO-dark gas with local gas conditions and proximity to R136.

In this extreme region, based on our modeling to date, we expect a predominance of the diffuse ionized gas and low filling factors for the dense clouds close to R136. This study will create and evaluate key diagnostics of the gas heating and cooling of a low-metallicity, resolved starburst region, and provide a legacy to the FIR community for studying similar but unresolved regions.

IV.3.2 Preliminary results

We observed [C II], [O III] 52 μm and 88 μm, [O I] 63 μm and 145 μm and [N III] 57 μm as part of *SOFIA*/FIFI-LS cycle 4. Observations were carried on between June 28th and July 4th 2016. The spectrum in each spaxel has been fitted by a linear component for the baseline and a gaussian for the line. We present here preliminary maps in Figure IV.12. A proposal has been re-submitted for *SOFIA* cycle 5 to follow-up on these observations and complete the [O I] 145 μm and [N III] 57 μm maps.

Data presentation

[O III] 52 μm and 88 μm are well detected over the entire map. Although the calibration has not been updated yet to take into account the most recent observations of the calibrators, the spatial distribution and the flux of [O III] 88 μm is in good agreement with the PACS measurements in the overlapping regions. Artifacts are visible in the [O III] 88 μm map due to the coarse spatial sampling: the blue array footprints are not overlapping on the sky. The spatial distribution of the [O III] 52 μm line is similar to that of the [O III] 88 μm line. In the small region mapped with [N III] 57 μm, simultaneously with [O I] 145 μm, we note that the spatial distribution matches that of the other tracers of the ionized gas, in particular the characteristic arm-like structure north of R136 (the ionization potential of N^+ is 29.6 eV).

The spatial distribution of [C II] matches that mapped with PACS, although the ratio of the FIFI-LS [C II] over PACS [C II] varies between 0.3 and 2 with this preliminary data treatment. In the north-west corner of the map, we observe bright [C II] emission, roughly coinciding with the peaks of L_{PAH} and ground-based CO emission. [O III] 88 μm and 52 μm are barely detected in this area.

As expected, [O I] lines are much fainter than the above FIR lines. [O I] 63 μm is mostly absorbed by the atmosphere and thus is difficult to detect, although we carried out a deep integration of this line. [O I] 145 μm is in principle $\sim$ 10 times fainter, but in a better transmission atmospheric window. Thus, the S/N is higher in the deep-integration region (outlined in red in Figure IV.12). [O I] 145 μm has also been observed simultaneously with [O III] 88 μm with a shorter integration time, thus only the brightest peaks are detected in the rest of the map.

Electronic density of the ionized gas

The critical density of [O III] 52 μm with electrons is $\sim 3.5 \times 10^3$ cm^{-3} and that of [O III] 88 μm is ~ 510 cm^{-3}. Thus, the ratio of these two line intensities is a strong function of the electron density between a few tens and a few 10^4 cm^{-3}, as visible in Figure IV.13. We apply a threshold in S/N to the [O III] 52 μm and keep the pixels with S/N > 3. We convolve the [O III] 52 μm map to the resolution of [O III] 88 μm ($\approx 7''$) and calculate the ratio [O III] 52 μm/[O III] 88 μm (Figure IV.13). We estimate an electronic density under 6×10^2 cm^{-3}. We note that some of the values are below the theoretical ratio for T between 5000 and 15000 K. These preliminary results may change with the updated calibration.

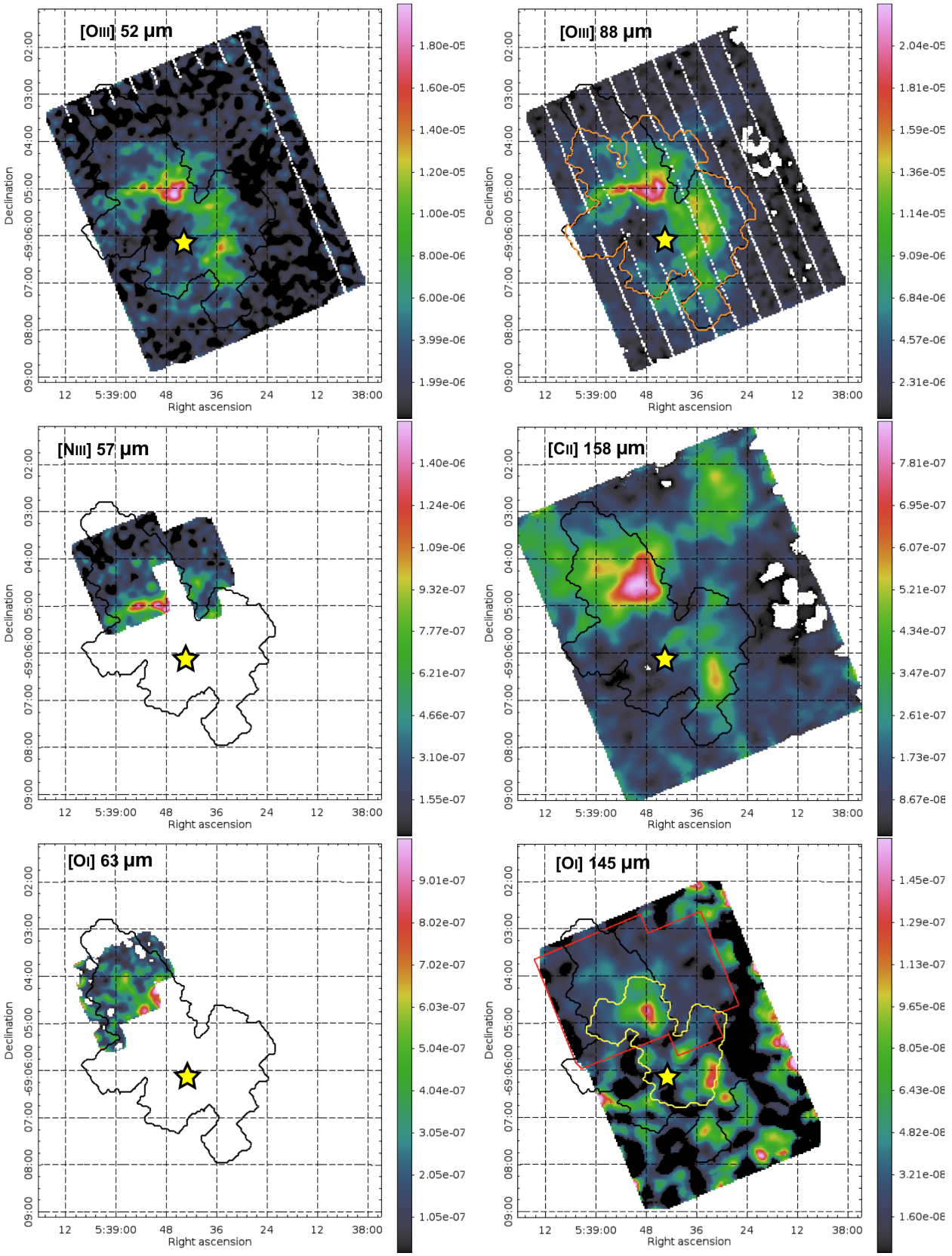

Figure IV.12: *FIFI-LS cycle 4 observations of the FIR fine structure lines [O III] 52 µm, [O III] 88 µm, [N III] 57 µm, [C II] 158 µm, [O I] 63 µm and [O I] 145 µm in 30Dor. The individual color scales indicate the line intensities in W m^{-2} sr^{-1}. The stars indicate the location of the center of R136 and the black contours outline the coverage of the PACS [C II] map. In the [O III] 88 µm map, the orange contour indicates the area mapped by PACS in [O III] 88 µm. In the [O I] 145 µm map, the yellow contour indicates the area mapped by PACS in [O I] 145 µm and the red contour outlines the FIFI-LS deep integration.*

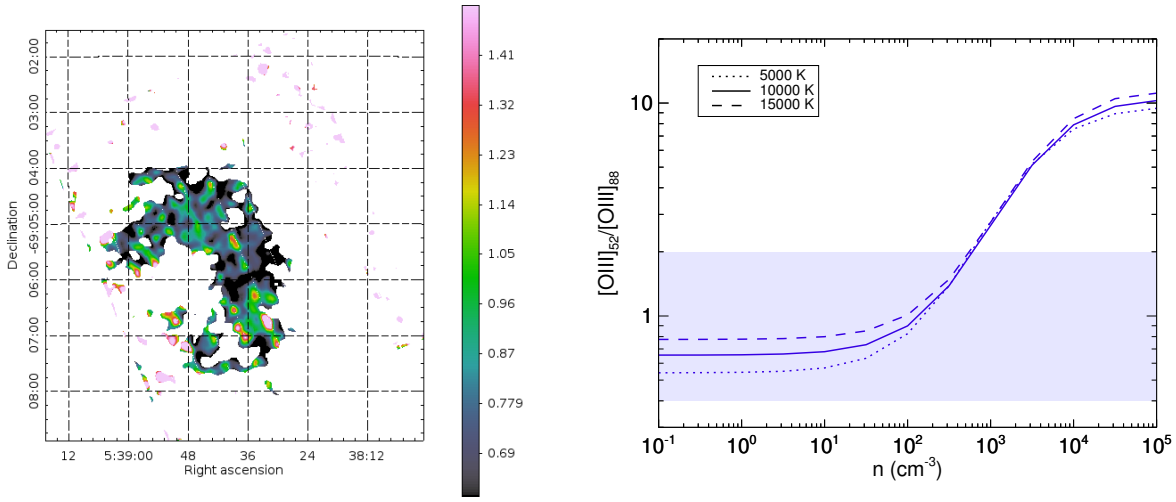

Figure IV.13: *Left: Observed ratio [O III] 52 µm/[O III] 88 µm from FIFI-LS maps. Right: Theoretical ratio [O III] 52 µm/[O III] 88 µm as a function of the electronic density for three different temperatures. The blue band indicates the range of our observed values in 30Dor.*

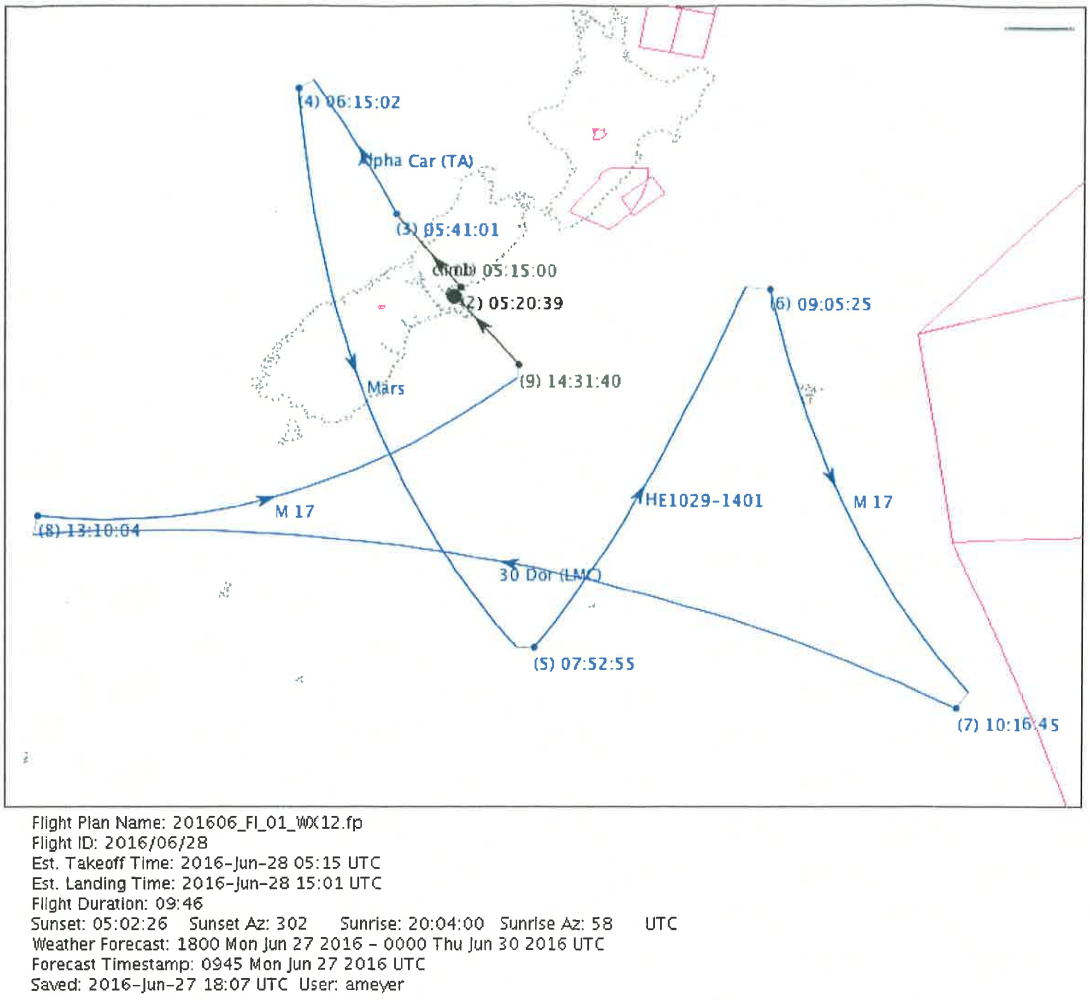

Figure IV.14: *Example of the flight plan for SOFIA observations of June 28th, 2016, from Christchurch.*

Chapter V

The "CO-dark" gas

Contents

Although H_2 is the most abundant molecule in the Universe and the primary ingredient for star formation, the bulk of the cold star-forming H_2 is, in general, not directly observable and various probes must be used to estimate the abundance of H_2. Stecker et al. (1975) reveals that H_2 mass dominates over HI in the inner Galaxy (< 7 kpc), using a combination of CO and gamma-ray observations. Most of the molecular gas in the Milky Way, approximately $1.3 \times 10^9\,M_\odot$ (Tielens 2005), is thought to be contained in giant molecular clouds. However, in low metallicity galaxies, little molecular gas is detected, raising questions about the processes of star formation in the early Universe. The results of the study carried out to quantify the CO-dark gas in 30Dor will be presented in our next paper.

V.1 H_2 as a tracer of the star formation

V.1.1 Observational approach

Observation of H_2

Star formation is fueled by molecular gas. The link between recent star formation and surrounding molecular gas reservoirs is well established for metal-rich galaxies in the Local Universe (Bigiel et al. 2008; Genzel et al. 2012; Bolatto et al. 2013). In particular, molecular hydrogen, H_2, which is the most abundant molecule in the ISM, plays an important role in this process. However, H_2 is a symmetric molecule, with no permanent electric dipole, and as such cannot be observed directly in the cold gas reservoir. We describe here some of the reasons why H_2 is so difficult to observe in the cold ISM.

- Molecules with identical atoms and non-zero spin can be found in two distinctive forms: *ortho* (with parallel nuclear spins) and *para* (with anti-parallel nuclear spins), between which transitions are forbidden: the probability for the **radiative ortho → para transition** at 84.4 μm is 7×10^{-21} s^{-1} (Lequeux 2005).

- **Electronic transitions** are permitted, but they are usually in the far-UV. For example, the Lyman band and the Werner band require energies of 11 eV and 14 eV, respectively. All of the electronic transitions of H_2 in particular are below 115 nm, requiring temperatures higher than 1.3×10^5 K.

- Only the stretching modes of the **vibrational transitions** are possible for diatomic molecules, and not the bending or deformation modes possible for more complex molecules. The lowest vibrational transition (at $\lambda = 2.22\,\mu$m) requires high energy to be excited with upper-level energy of $E/k \approx 6471$ K above ground level.

- The lowest **rotational transitions** of ortho-H_2 (at $\lambda = 28.22\,\mu$m) and para-H_2 (at $\lambda = 17.03\,\mu$m) have upper-level energies of $E/k \approx 510$ K and 1015 K respectively above ground level (Dabrowski 1984) and transition probabilities of 2.95×10^{-11} s^{-1} and 4.77×10^{-10} s^{-1}. Thus, they are only excited for high temperatures, $T \gtrsim 100$ K, and only few collisionally excited H_2 lines are emitted from PDRs, which are in general at lower temperatures.

CO as a tracer of H_2

However, other molecules are present in the ISM, such as CO, which is easily excited even at low temperatures. Contrary to H_2, CO has a permanent dipole moment of $\mu = 0.112$ Debye. Most measurements of the cold gas mass in the near and far Universe have taken advantage of the bright CO

emission, and in particular the isotopologue $^{12}C^{16}O$, which is the second most abundant molecule after H_2. In the following, we refer to $^{12}C^{16}O$ as simply CO. The abundance ratio CO/H_2 in the Milky Way is $\sim 10^{-4}$. The lowest rotational transition of CO, the CO $J = 1-0$ transition at 2.6 mm, in particular, can be observed from the ground. It corresponds to an excitation energy of $E/k \approx 5.6$ K and its transition probability is 7.4×10^{-8} s^{-1}. As a consequence, CO is excited to high rotational levels much more easily than H_2 in the cold neutral gas.

CO is frequently used as a tracer of the molecular gas mass in the Milky Way (e.g. Heyer & Dame 2015 and references therein). Indeed a simple relationship can be assumed between the observed CO (1-0) intensity and the column density of H_2 by applying a CO-to-H_2 conversion factor, X_{CO}, between these two quantities:

$$N(H_2)\,[\mathrm{cm}^{-2}] = X_{CO} \times I_{CO(1\text{-}0)}\,[\mathrm{K\ km\ s}^{-1}]. \tag{V.1}$$

Similarly, a CO-to-H_2 mass conversion factor, α_{CO}, can be applied between the observed CO luminosity and the mass of molecular gas:

$$M_{mol}\,[M_\odot] = \alpha_{CO} \times L_{CO(1\text{-}0)}\,[\mathrm{K\ km\ s}^{-1}\ \mathrm{pc}^2]. \tag{V.2}$$

X_{CO} and α_{CO} are related via the relation:

$$\alpha_{CO} \,/\, X_{CO} = m_{H_2} \times \frac{\Omega}{4\pi D^2}, \tag{V.3}$$

where m_{H_2} is the mass of one H_2 molecule in $M_\odot$, Ω is the source solid angle and D is the distance to the source. In our galaxy, $X_{CO,MW} = 2 \times 10^{20}$ cm^{-2} (K km s^{-1})$^{-1}$ and $\alpha_{CO,MW} = 4.3\,M_\odot$ pc^{-2} (K km s^{-1})$^{-1}$ are typical values of the CO-to-H_2 conversion factors (see Bolatto et al. 2013 for a review on the CO-to-H_2 conversion factor).

V.1.2 Theoretical approach

The virial theorem

The virial theorem is a useful mathematical tool to describe the global structure of a molecular cloud. It was first derived by Chandrasekhar & Fermi (1953) for magnetized clouds of gas. The review of McKee & Ostriker (2007) on the theory of star formation discusses the application of the virial theorem to molecular clouds. We present here the basics of this theorem.

The virial theorem is based on the equation of momentum conservation. In a Lagrangian description, i.e. for a system bounded by a closed surface with no mass flow across the surface, the virial theorem is written as:

$$\frac{1}{2}\frac{d^2 I}{dt^2} = 2(\mathcal{T} - \mathcal{T}_\mathcal{S}) + \mathcal{B} + \mathcal{W}, \tag{V.4}$$

where $I = \int r^2 dm$ has the dimensions of moment of inertia. In this expression, $\mathcal{T}$ is the total kinetic energy, including the thermal energy:

$$\mathcal{T} = \int_{V_{cl}} (\frac{3}{2}P_{th} + \frac{1}{2}\rho v^2) dV = \frac{3}{2}\bar{\rho}\sigma^2 V_{cl} \tag{V.5}$$

with σ^2 being the 1D mean square velocity (including a thermal and a turbulent term), V_{cl} the volume of the cloud, P_{th} the thermal pressure and $\bar{\rho}$ the mean density. $\mathcal{T}_\mathcal{S} = \oint P_{th}\mathbf{r}\cdot\mathbf{dS}$ is the surface kinetic

term, $\mathcal{B}$ is the magnetic energy and $\mathcal{W}$ is the gravitational energy, in general assumed to be equal to the gravitational self-energy:

$$\mathcal{W} = -\frac{1}{2}\sum_{1}\sum_{2\neq 1}\frac{Gm_1m_2}{|\mathbf{r}_1-\mathbf{r}_2|} = -\frac{G}{2}\int\int\frac{\rho(\mathbf{r}_1)\rho(\mathbf{r}_2)}{|\mathbf{r}_1-\mathbf{r}_2|}dV_2\,dV_1 \tag{V.6}$$

for any positions 1 and 2 in the cloud. The virial theorem can also be derived in the Eulerian case, which is more appropriate to describe turbulent clouds (McKee & Zweibel 1992).

Many studies make the approximation of the virial equilibrium, where $\ddot{I} = 0$. A system in equilibrium subjected to two forces, has approximately energy equipartition and both energies are of the same order of magnitude.

Application to the Giant Molecular Clouds

Equations V.1 and V.2 are highly simplified, not representative of the complexity of the ISM and covering a wide diversity of environments, geometry and dynamics. However, many observations in the Milky Way and nearby spiral galaxies, in particular, seem to follow these correlations (Figure V.1) and simple theoretical considerations show the origin of these relations. CO(1-0) is generally optically thick, thus its brightness temperature depends on the temperature of the surface, not on the total column density of the gas. For one GMC of projected radius R (in parsecs) and surface brightness temperature, T_B, L_{CO} is the product of its area and its integrated surface brightness. In the optically thick limit, and in the Rayleigh-Jeans approximation, assuming a Gaussian line profile, we have:

$$L_{CO} = \sqrt{2\pi^3}T_B\sigma R^2, \tag{V.7}$$

where σ is the CO(1-0) line width.

On the other hand, the total mass of a self-gravitating cloud is reflected in the velocity dispersion of the gas, which we can access through the width of emission lines. This can be calculated, in particular, for a virialized cloud in equilibrium, if the magnetic field can be neglected, in which case the potential energy is equal to twice the internal kinetic energy (Equation V.4). Following Bolatto et al. (2013), we assume that the volume density is inversely proportional to the distance to the center of the cloud: $\rho(r) \propto r^{-1}$. In this case,

$$M_{vir} = \frac{9}{2G}R\sigma^2 \tag{V.8}$$

with G the gravitational constant (see Section V.2.1).

Moreover, molecular clouds are observed to follow a size-line width relation (this is often referred to as the first Larson law; e.g. Larson 1981; Solomon et al. 1987; Scoville et al. 1987) so that

$$\sigma \approx CR^{0.5}. \tag{V.9}$$

For Milky Way GMCs, $C \approx 0.7\,\mathrm{km\,s^{-1}\,pc^{-0.5}}$ (Solomon et al. 1987) and this relation holds in extragalactic environments, although with different values of C (Blitz et al. 2007; Bolatto et al. 2008). Several studies have observed the correlation between the size and the velocity dispersion both for sub-systems of a given star forming region and between star-forming regions, showing that this relation holds up to entire GMC sizes and that turbulence is driven on large scales (e.g. Ossenkopf & Mac Low 2002; Brunt 2003). Heyer & Brunt (2004) argue that this relation demonstrates the universality of the turbulence in moderate density gas in molecular clouds.

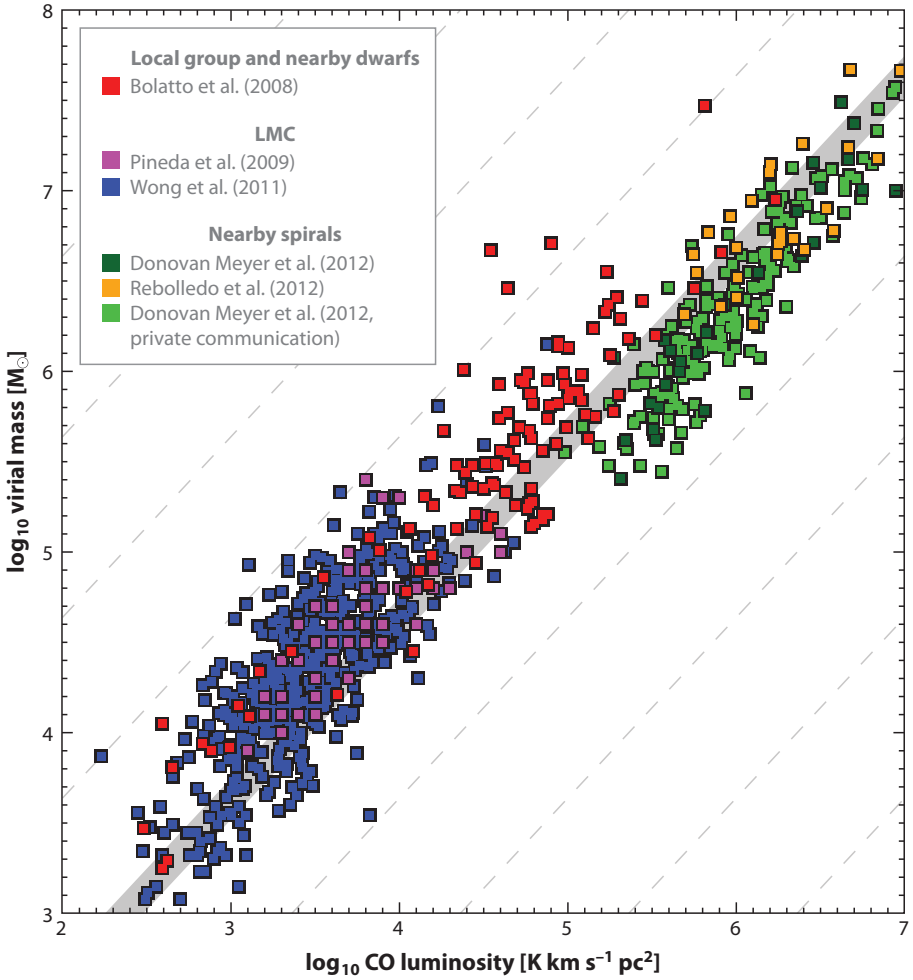

Figure V.1: *Correlation between the viral mass and the CO luminosity for a compilation of observations of extragalactic GMCs. The gray region delineates the Milky Way value of* $\alpha_{\rm CO} = 4.3 \pm 30\%\ M_\odot\ pc^{-2}\ (K\ km\ s^{-1})^{-1}$. *the dashed lined show constant* $\alpha_{\rm CO}$*values. Figure from Bolatto et al. (2013).*

Combination of Equation V.9 with Equations V.8 and V.7 leads to

$$\begin{cases} M_{vir} \propto \sigma^4 \\ L_{CO} \propto \sigma^5 \end{cases} \tag{V.10}$$

Hence, we obtain a relation between M_{vir} and $\rm L_{CO}$ for a single resolved GMC:

$$M_{vir} \approx \frac{9 \times C^{1.2}}{2G \times (2\pi^3)^{2/5}} \left(\frac{\rm L_{CO}}{T_B} \right)^{0.8} \tag{V.11}$$

Thus, for a GMC near virial equilibrium, which follows the size-line width relation and with approximately constant brightness temperature, we expect an almost linear relation between the virial mass and CO luminosity. The numerical coefficient is only a weak function of the density profile of the cloud. We note that this relation is not exactly linear and $\alpha_{\rm CO} = M_{vir}/\rm L_{CO}$ will always have a small dependance on the cloud mass, even if the assumptions above are verified.

In spite of the generally good correlation between the CO luminosity and the total molecular mass, at low extinction and low column density, CO becomes a poor tracer of H_2. For example, the

results from Planck Collaboration (2011a) suggest a component of H_2 emitting weakly in CO from the surface of the clouds, where the extinction is low ($0.4 \lesssim A_V \lesssim 2.5$) and where CO is photo-dissociated. Higher X_{CO} values are found at low A_V, where most of the carbon exists as C^+ or C^o, while molecular H_2 is present. CO is indeed easily photo-dissociated if not sufficiently shielded by dust and gas, while H_2 can be efficiently self-shielded (Section I.2.3). This discrepancy between CO and H_2 can result in a large amount of molecular gas not traced by the classic CO probe. This component is often referred to as the "CO-dark" gas (Grenier et al. 2005; Wolfire et al. 2010). The fraction of the CO-dark gas is likely to increase in low extinction environments, making the estimation of the total molecular gas mass via the classic X_{CO} factor unreliable. Theoretical studies (e.g. Wolfire et al. 2010; Feldmann et al. 2012) predict a strong dependency of the X_{CO} factor on metallicity, dust extinction and H_2 column density for GMC scales. The UV radiation field, however has a more moderate influence for a given hydrogen column density. The particular case of the low metallicity ISM is described below.

V.1.3 The case at low metallicity

Low metallicity galaxies are often characterized by higher and harder radiation fields (e.g. Madden et al. 2006), and a reduced dust content (e.g. Rémy-Ruyer et al. 2014), which change the structure of the ISM and may affect the star formation process. Star-forming low-metallicity galaxies are often outliers on the Schmidt-Kennicutt relation (e.g. Schruba et al. 2012; Galametz et al. 2009; Cormier et al. 2014). However, notorious uncertainties exist in a low-metallicity environments when inferring the H_2 reservoir from CO, potentially jeopardizing our interpretation of the evolution of star formation activity and gas mass at high-z (Daddi et al. 2010; Tacconi et al. 2010; Genzel et al. 2012). While CO seems to trace more or less satisfactorily the bulk of H_2 in solar metallicity galaxies, CO detection in dwarf galaxies is challenging, even for metallicities only a few times sub-solar. CO emission is disproportionately weak in the LMC and overall in low-metallicity galaxies (Hughes et al. 2010; Wong et al. 2011) with respect to the often-used star formation tracer [CII] 158 μm and far-infrared (FIR) luminosity (e.g. Madden et al. 2013; Cormier et al. 2014, 2015), as illustrated in Figure V.2. Low metallicity dwarf galaxies typically lie above the ratio [CII]/CO = 4000, while more metal-rich galaxies occupy another parameter space, below this ratio. We have added our spatial measurements for 30Dor, which have an extreme ratio [CII]/CO of approximately 80000, as also noticed by Stacey et al. (1991) and Poglitsch et al. (1995).

On the other hand, the star formation activity of some low-metallicity galaxies can be very high, as it is the case for the blue compact dwarf galaxies in particular. Several studies on low-metallicity galaxies have shown an increasing ratio of the star formation rates compared to the CO luminosities as the metallicity decreases (e.g. Taylor et al. 1998; Schruba et al. 2012). This could be the result either from an increased star formation efficiency or from the fact that CO fails at being an effective tracer of the total molecular gas in these environments. Is there truly a deficit of H_2 in low metallicity environments relative to their star formation activity, or do we lack an accurate picture of the gas reservoir under lower dust shielding conditions?

The molecular cloud structure gradually changes when the dust-to-gas mass ratio decreases. Reduced metallicity in the vicinity of star formation activity in particular has striking consequences on the nearby molecular cloud structure, as demonstrated in many theoretical studies (e.g. van Dishoeck & Black 1986; Maloney & Black 1988; Hollenbach & Tielens 1999; Röllig et al. 2006; Wolfire et al. 2010; Glover & Mac Low 2011; Krumholz & Gnedin 2011; Glover & Clark 2012; Sternberg et al. 2014). The photodissociation rate of CO is larger than that of H_2 at the cloud edge, and H_2 is self-shielded for a smaller column density as compared to CO, as explained in Section I.2.3. The depth

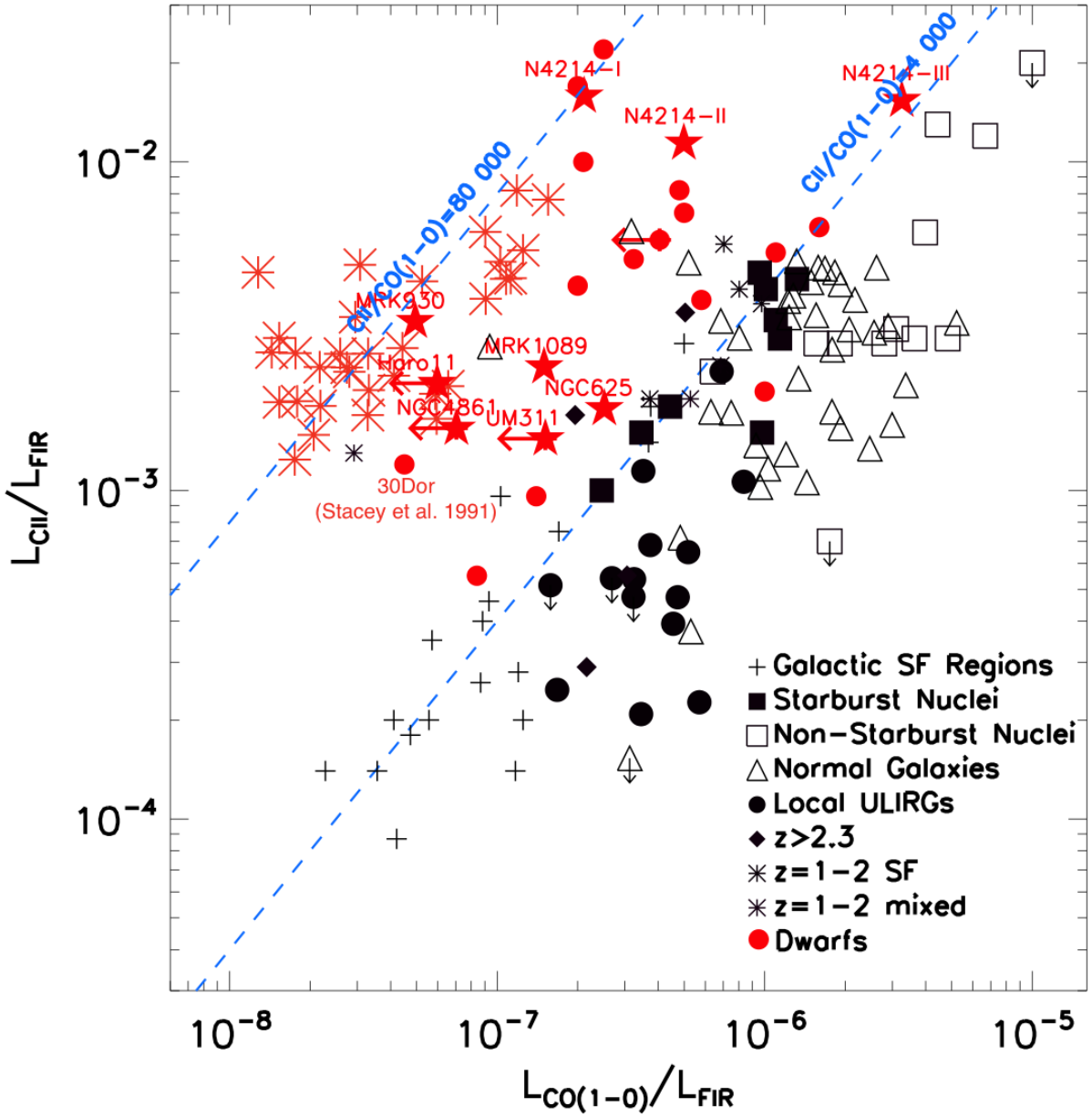

Figure V.2: *[CII]/L_{FIR} as a function of CO/L_{FIR}. Adapted from Stacey et al. (1991, 2010); Hailey-Dunsheath et al. (2010); Madden et al. (2013); Cormier (2012). In black are the normal and starburst galaxies (Stacey et al. 1991, 2010; Hailey-Dunsheath et al. 2010). They mainly lie under the dashed blue line representing [CII]/CO = 4000. The red circles and stars are the dwarf galaxies from the DGS sample (Madden et al. 2013). They mainly lie above [CII]/CO = 4000. The red asterisks are for 30Dor. They have an average ratio [CII]/CO ≈ 80000.*

at which CO can form is controlled by dust and thus depends strongly on the metallicity (e.g. van Dishoeck & Black 1986, 1988; Sternberg & Dalgarno 1995; Wolfire et al. 2010; Glover & Mac Low 2011; Feldmann et al. 2012). The combined effect of strong FUV radiation from the nearby young stars, low C and O abundance, and decreased dust abundance shifts the C^+/C^o/CO transition further into the cloud, resulting in a smaller CO core and a larger shell of C^o and C^+ which can host an important reservoir of H_2. Thus, X_{CO} is most probably subject to variations in different galaxies as well as

spatially within galaxies. This is schematically represented in the left panel of Figure V.3. Studies of Krumholz & Gnedin (2011) and Glover & Clark (2012) suggest that star formation does not require the presence of CO and can occur in the CO-dark gas. Several attempts, using various observational probes, have been made to determine observationally a relation between X_{CO} and the metallicity, as illustrated in the right panel of Figure V.3 (e.g. Bolatto et al. 2008; Leroy et al. 2011; Genzel et al. 2012; Schruba et al. 2012). This figure shows a large dispersion of the data and many uncertainties still remain on the dependance between X_{CO} and the metallicity. In addition, other factors, such as the radiation field, are also important and affect the value of X_{CO} as noted by Israel (1997). However, there is clear observational evidence of an increased X_{CO} factor when the metallicity decreases and models from Wolfire et al. (2010) and Glover & Mac Low (2011), for example, provide good fits to the observations (Bolatto et al. 2013).

As the metallicity decreases, the fraction of H_2 which is co-spatial with CO, decreases and the use of an X_{CO} factor at low metallicity implies extrapolation to the total molecular mass of a cloud only from its very central core. Hence, the reliability of CO as a tracer for H_2 becomes more uncertain at low metallicity and an increasing fraction of CO-dark gas is expected to be present. The total amount of molecular gas can be derived through different observational methods, each of them with advantages and drawbacks. We detail some of the most commonly used in Section V.2.1. We then apply the PDR method and the dust modeling to the region of 30Dor and compare the molecular gas mass thus derived to the molecular gas mass derived from the CO observations and the X_{CO} factor.

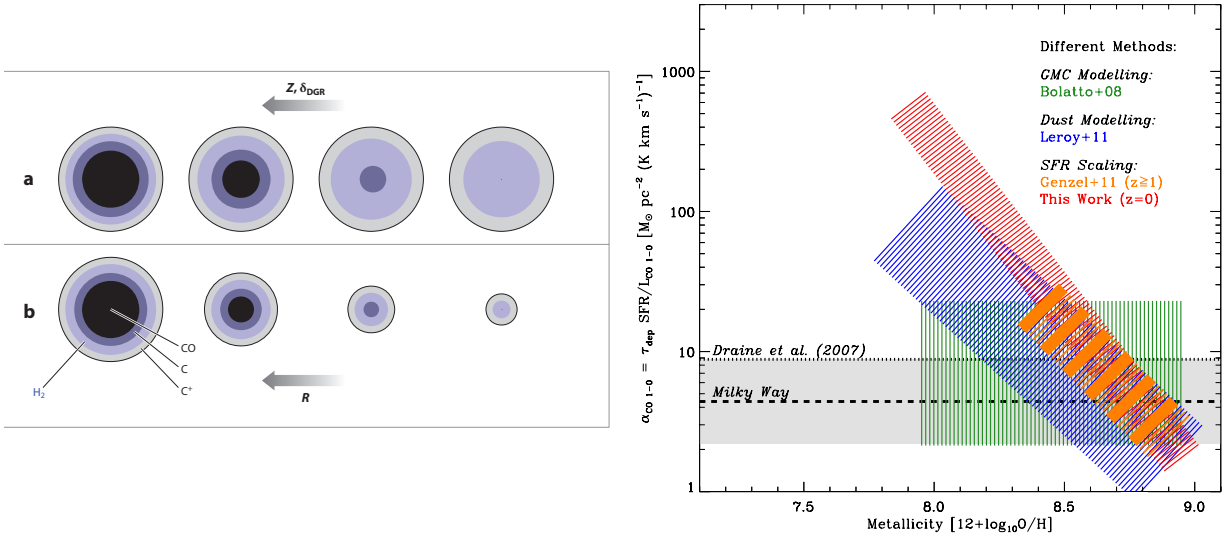

Figure V.3: *Left: figure from Bolatto et al. (2013). Top panel (a) illustrates the effect of decreasing the metallicity and the dust-to-gas mass ratio on the $C^+/C^o/CO$ transition and the size of the CO core. Bottom panel (b) illustrates the effect of decreasing the radius of the spherical clump or the column density for a given metallicity. Both cases result in an increased ratio H_2/CO. Right figure from Schruba et al. (2012) showing the observed trends of the α_{CO} factor with respect to the metallicity, deduced from different methods. The GMC modeling, based on the virial theorem and the dust modeling based on IR observations are developed in Section V.2.1. The dust modeling method relies on the gas-to-dust mass ratio to estimate the total gas mass from the measured dust mass. The third method assumes a relation between H_2 and the star formation to estimate X_{CO}. This is described in Section V.2.1. The width of the bands roughly indicates the scatter of individual measurements.*

V.2 Quantification of the CO-dark gas

In this section, we first investigate some of the common ways to estimate the total molecular gas mass (Section V.2.1). In particular, we will discuss the following approaches:

- estimation of the virial mass from velocity dispersion,
- estimation of the column density from CO isotopes,
- estimation of the H_2 mass via the dust mass,
- modeling the diffuse gamma-ray emission,
- assuming a constant star formation efficiency,
- modeling the structure of the cloud via PDR models.

Then, we compare two of these methods in the particular case of 30Dor (Section V.2.2).

V.2.1 Derivation of the molecular gas mass

Virial mass

In the case of a self-gravitational potential, for a uniform, unmagnetized sphere in virial equilibrium of mass M and radius R, Equation V.4 can be simply written as:

$$2\mathcal{T} + \mathcal{W} = 0. \tag{V.12}$$

with $\mathcal{T}$, the kinetic energy as in Equation V.5:

$$\mathcal{T} = \frac{3}{2}\bar{\rho}\sigma^2 V_{cl} = \frac{3}{2}M\sigma^2, \tag{V.13}$$

where $\bar{\rho}$ is the mean density, σ is the 1D velocity dispersion and V_{cl} is the volume of the cloud. The gravitational energy, $\mathcal{W}$, defined by Equation V.6 can be written in term of the gravitational potential Φ as

$$\mathcal{W} = \frac{1}{2}\int \rho(\mathbf{r})\Phi(\mathbf{r})d\mathbf{r} \quad \text{where} \quad \Phi(\mathbf{r}) = -G\int \frac{\rho(\mathbf{r}')}{|\,\mathbf{r}-\mathbf{r}'\,|}d\mathbf{r}'. \tag{V.14}$$

Using Poisson's equation, $\Delta\Phi = 4\pi G\rho$, and the fact that the gravitational field $\mathbf{g}$ is the opposite of $\overrightarrow{grad}(\Phi)$, in the spherical case, $\mathcal{W}$ can be written simply as

$$\mathcal{W} = -\frac{1}{8\pi G}\int |\,\mathbf{g}(\mathbf{r})\,|^2\, d\mathbf{r} = -\frac{1}{8\pi G}\int \left(\frac{GM(r)}{r^2}\right)^2 4\pi r^2 dr. \tag{V.15}$$

The solution of this equation depends on the density profile. For $\rho \propto r^{-k}$, with $k = 0$, 1 or 2,

$$\mathcal{W} = -GM^2\frac{3-k}{5-2k}. \tag{V.16}$$

Combining Equation V.12 with Equations V.13 and V.16 we obtain:

$$\begin{cases} M = \dfrac{5R\sigma^2}{G} & \text{for an homogeneous sphere} \\ M = \dfrac{9R\sigma^2}{2G} & \text{for a density profile in } r^{-1}. \end{cases} \tag{V.17}$$

Observationally, the velocity dispersion can be estimated from the line width, which combines thermal and turbulence broadening. A density profile $\rho \propto r^{-1}$ is commonly assumed (e.g. MacLaren et al.

1988). The individual cloud masses can then be derived from the virial theorem, assuming the clouds are spatially resolved.

Another parameter, convenient to define for this discussion, is the virial parameter:

$$a_{vir} = \frac{\mathcal{T}}{\mathcal{W}} = \frac{5R\sigma^2}{GM}. \tag{V.18}$$

There is a simple way of understanding this virial parameter: for clouds with $a_{vir} \gg 1$, kinetic energy dominates and the cloud would be rapidly dissipated, while for clouds with $a_{vir} \ll 1$ gravitational energy dominates and the cloud would collapse at the free-fall velocity. Roman-Duval et al. (2010) analyze the physical properties of 580 molecular clouds in the inner Galaxy, using ^{13}CO(1-0) and ^{12}CO(1-0) observations. They deduce an average virial parameter of ≈ 0.5, suggesting that the molecular clouds are gravitationally bound. In the LMC, however, Wong et al. (2011) have observed a large scatter of a_{vir}, roughly between 0.5 and 10 and showing no trend with the CO luminosity contrary to the finding of Heyer et al. (2001) in the outer galaxy, nor with the probability of hosting a YSO, raising doubts on the assumption of virialized clouds in the LMC.

Several studies have found good agreement between observations and the predictions deduced from the virial theorem. Solomon et al. (1987) have calculated the virial masses of 273 clouds in the Galactic disk and find a tight relation $M_{vir} \propto {L_{CO}}^{0.81}$, in close agreement with Equation V.11. This result was confirmed by Scoville et al. (1987). However, the turbulent nature of the interstellar clouds tends to suggest that they are probably not in virial equilibrium. Ballesteros-Paredes (2006) discusses the applicability of the most common assumptions of the virial theorem and shows that interstellar clouds are most likely out-of-equilibrium systems. Nevertheless, observed GMC properties can often be understood as consequences of approximate energy equipartition. Even if single clouds are not strictly in virial equilibrium, over a large sample, the assumption of virial equilibrium may be valid.

CO isotopologues

One of the common methods to determine the molecular mass is to use an optically thin tracer, such as transitions of CO or its isotopologues or other chemical species (e.g. CH; Magnani et al. 2003) and probe the column density of this specie in the cloud. This value is then converted into a total column density, assuming a conversion factor such as X_{CO}.

The fact that CO is rather abundant compared to H_2 ($\approx 10^{-4}$), and that CO transitions at millimeter wavelengths are relatively easy to detect, with a low critical density (4.2×10^3 cm^{-3} for CO(1-0) for example), allow an estimate of the column density of H_2 from CO column density. For regions with densities $< 10^2$ cm^{-3}, ^{12}C^{16}O can be used because the transitions are relatively bright and optically thin. However, at higher densities, due to its high fractional abundance, ^{12}C^{16}O becomes usually optically thick, and only lower limits on the total column density can be estimated. Therefore, less abundant isotopes, such as ^{13}CO or C^{18}O are better choices, since these transitions are in general optically thin.

The common method is to assume that the ^{12}CO emission is fully optically thick and in LTE (e.g. Pineda et al. 2008a; Wilson et al. 2009; Pineda et al. 2010; Indebetouw et al. 2013). The excitation temperature, T_{ex}, defined as the temperature at which we would expect to find the system with the observed ratio of level populations based on a Boltzman distribution, is then equal to the kinetic temperature, T_K (see Section III.3), and can be derived as follows. From Equation III.9, for a constant

source function S_ν, the measured specific intensity of a line can be written as:

$$I_\nu = (S_\nu - I_\nu(0))(1 - e^{-\tau_\nu}), \tag{V.19}$$

after subtracting the background intensity $I_\nu(0)$. For a filling factor of 1, the radiation temperature is defined as $T_R(\nu) = I_\nu \frac{c^2}{2\nu^2 k}$. Assuming the source function is a blackbody at T_{ex} and the background is mainly due to the 2.7 K microwave background radiation (which is a blackbody as well), we can write:

$$T_R(\nu) = T_0 \left(\frac{1}{e^{T_0/T_{ex}} - 1} - \frac{1}{e^{T_0/2.7} - 1} \right) (1 - e^{-\tau_\nu}), \tag{V.20}$$

where $T_0 = h\nu/k$. We focus here on the ^{12}CO(1-0) transition, although the same method can be applied to ^{12}CO(2-1) as in Indebetouw et al. (2013), for example. For $\nu(^{12}\text{CO(1-0)}) = 115.3$ GHz, $T_0 = 5.5$ K and when $\tau_\nu \to \infty$ (assuming an optically thick transition), T_{ex} can be derived from Equation V.20:

$$T_{ex} = T_K = \frac{5.5}{\ln\left(1 + \frac{5.5}{T_R^{12} + 0.82}\right)} = T, \tag{V.21}$$

where T_R^{12} is the measured ^{12}CO intensity in K. In the absence of background sources, the excitation temperature is only a function of the measured brightness temperature.

The second step is to calculate the column density of ^{13}CO (which is considered to be optically thin) from Equation V.20, assuming that the excitation temperature is the same for ^{13}CO and ^{12}CO. The ^{13}CO opacity per velocity bin is written as:

$$\tau_\nu^{13} = -ln\left(1 - \frac{T_R^{13}}{T_0^{13}} \left[\frac{1}{e^{T_0^{13}/T_{ex}} - 1} - \frac{1}{e^{T_0^{13}/2.7} - 1} \right]^{-1} \right), \tag{V.22}$$

with $T_0^{13} = h\nu(^{13}\text{CO(1-0)})/k = 5.3$K. With the approximation that all of the energy levels are populated under LTE conditions and if the molecular population is characterized by a single temperature T_{ex}, the total column density of ^{13}CO can be derived from:

$$N(^{13}\text{CO}) = 3.0 \times 10^{14} \frac{T_{ex} e^{T_0^{13}/T_{ex}} \int \tau_\nu^{13} d\nu}{1 - e^{T_0^{13}/T_{ex}}} \tag{V.23}$$

(Wilson et al. 2009).

This ^{13}CO column density is then converted into a ^{12}CO column density, generally assuming a single ^{12}CO/^{13}CO isotope ratio. However, this ratio, usually chosen equal to the ratio ^{12}C/^{13}C, is subject to variations between different regions, as shown by observational and theoretical studies (e.g. Langer & Penzias 1990; Milam et al. 2005; Szücs et al. 2014, and reference therein). In particular, there is evidence for an increasing ratio ^{12}C/^{13}C with the distance to the Galactic center (e.g. Langer & Penzias 1990; Wilson & Rood 1994; Savage et al. 2002; Milam et al. 2005). Indeed, nearly all of the observed ^{13}C is thought to be produced from ^{12}C in intermediate-mass (1.5-6 $M_\odot$) AGB stars (Iben & Renzini 1983; Clayton 2003), and the ratio ^{12}C/^{13}C can be considered as a probe of the galaxy chemical evolution (e.g. Milam et al. 2005; Ramstedt & Olofsson 2014). The next step to estimate the total column density is to assume an abundance ratio between H_2 and ^{12}CO. Once again, this ratio depends considerably on the environment and has high uncertainties (e.g. Shetty et al. 2011a,b; Glover & Mac Low 2011; Feldmann et al. 2012).

Finally, this result can be used to calculate the H_2 mass of a cloud by integrating over the surface of the cloud if the distance to the cloud is known. An additional factor ($\approx 36\%$) is added to take into account the other elements (helium and metals) and thus get the total molecular gas mass of the cloud.

Dust emission

Dust and gas are well mixed in the ISM. Thus, besides optically thin lines, dust emission is also a good indicator of the optical depth along the line of sight, which is proportional to the total gas column density, assuming a given gas-to-dust mass ratio (G/D) and constant dust properties. Under these assumptions, the FIR emission from dust is often used as a tracer of the gas distribution.

Several studies based on the Infrared Astronomical Satellite (IRAS) data showed that the dust emission at 100 μm was tightly correlated with the neutral atomic gas, in regions at low Galactic latitudes, away from molecular complexes (e.g. Boulanger & Perault 1988; Deul & Burton 1993). This correlation was later found to extend to high Galactic latitude regions, and at all wavelengths between 100 μm and 1 mm, making use of data from the Cosmic Background Explorer (*COBE*; Boulanger et al. 1996). A break in the correlation at high column densities ($N(\mathrm{H\,I}) \gtrsim 5\times10^{20}$ cm^{-2}) was identified by Boulanger et al. (1996), suggesting an increasing contribution from the molecular gas.

Observations of the dust SED can be modeled as described in Section III.1.1 to get the dust extinction, τ_v, or equivalently the dust mass, M_{dust}. Assuming approximately constant dust emissivity, these quantities are proportional to the total gas column density, N_H, or the total mass of gas, M_{gas} (mainly atomic and molecular hydrogen, but also a contribution of ionized hydrogen, helium and gaseous metals). We then define the gas-to-dust mass ratio $\mathrm{G/D} = \dfrac{M_{gas}}{M_{dust}}$, where $M_{gas} = M_{H^+} + M_H + M_{H_2} + M_{He} + M_{metals}$. M_{H^+} and M_H can be obtained, for example, from observations of H_α and H I 21 cm, respectively. $M_{metals} = Z \times M_{gas}$ and, assuming M_{He} scales with the total mass of gas independently from the metallicity, we have $M_{He} = Y_\odot M_{gas}$ with $Y_\odot = 0.270$ (Asplund et al. 2009). Hence,

$$M_{H_2} = \frac{G/D \times M_{dust}}{\mu_{gas}} - (M_{H^+} + M_H), \tag{V.24}$$

where $\mu_{gas} = \dfrac{1}{1 - Y_\odot - Z}$. The α_{CO} conversion factor can then be determined as the ratio of M_{H_2} and CO(1-0) luminosity (or similarly $\mathrm{X_{CO}}$, if $N(\mathrm{H_2})$ is calculated). In practice, G/D can be calibrated by measuring the dust emission and H I in regions where the gas is mainly atomic. A similar method has been used by Dame et al. (2001) using IRAS data, the Dwingeloo-Leiden H I survey and the Columbia survey of molecular gas in the Galactic plane, resulting in $\mathrm{X_{CO}} = 1.8\times10^{20}$ cm^{-2} (K km s^{-1})$^{-1}$. More recently, the Planck Collaboration (2011a) found that there were no significant variations of the G/D with Galactic radius and determine $\mathrm{X_{CO}} = 2.45\times10^{20}$ cm^{-2} (K km s^{-1})$^{-1}$.

This method has first been applied to extragalactic environments (LMC, SMC, and other irregular galaxies) by Israel (1997). The G/D was measured in atomic gas dominated regions of the galaxies, away from star-forming regions and CO clouds. This study shows that a higher $\mathrm{X_{CO}}$ is measured for low metallicity galaxies and that $\mathrm{X_{CO}}$ also shows a close to linear relation to the radiation field for a given galaxy. The dependency of dust-based $\mathrm{X_{CO}}$ with the metallicity was later confirmed by other studies with better sensitivity, resolution and wavelength coverage, making use of *Spitzer* and *Herschel* observations. In particular, Leroy et al. (2011) find a G/D scaling linearly with the metallicity and $\mathrm{X_{CO}}$ to be a strong function of the metallicity below 12+log(O/H) ~ 8.4 - 8.2.

The determination of the total $\mathrm{H_2}$ mass with this method is independent of CO observations. However, it is affected by several sources of uncertainties: this method is based on the assumption that gas and dust are well mixed and the resulting molecular mass is susceptible in particular to variations of the G/D ratio. We emphasize some of these sources of uncertainties below.

- *Determination of the gas-to-dust mass ratio.* G/D is believed to be fairly constant with the position in the galaxy. Therefore, it is often calibrated by measuring the ratio $M_{\rm HI}/M_{dust}$ at locations where neutral hydrogen is believed to dominate. Alternatively, the Galactic G/D of ~ 158 (e.g. Zubko et al. 2004) can be scaled by the metallicity. The G/D is typically assumed to be proportional to the inverse of the metallicity (e.g. Dwek 1998; Leroy et al. 2011), although steeper relations have also been measured (Muñoz-Mateos et al. 2009), in particular at low metallicities ($\lesssim 1/5\,Z_\odot$; Rémy-Ruyer et al. 2014). However, we know from Galametz et al. (2011) and Rémy-Ruyer et al. (2014) that there is substantial scatter in the gas to dust relation between galaxies even at a given metallicity. As a result, the determination of the G/D ratio is in general uncertain.
  Rather than assuming a G/D ratio, Sandstrom et al. (2013) determine simultaneously the values of $\alpha_{\rm CO}$ and G/D by minimizing the G/D scatter on $\sim$ kiloparsec regions of a sample of metal-rich disk galaxies from the KINGFISH survey. They find little variation of G/D, contrary to Rémy-Ruyer et al. (2014), but we note that the study of Rémy-Ruyer et al. (2014) covers 2 dec in metallicity, while the sample used by Sandstrom et al. (2013) covers a much reduced range (approximately a factor of 3), closer to the solar metallicity value. Roman-Duval et al. (2014) determine average $X_{\rm CO}$ factors for the LMC and SMC based on the assumption of a constant D/G between the diffuse and dense ISM. In both studies, any true variations of the D/G are degenerate with the amount of CO-dark gas in the beam.

- *Dust properties.* The determination of the dust mass is also uncertain and depends on the dust model used and on the wavelength coverage. Dale et al. (2012) report a difference of a factor of ≈ 2 between the dust masses derived from a single-temperature modified black-body fit and those using a more complex dust model (Draine & Li 2007) for the galaxies of the KINGFISH sample (Key Insights on Nearby Galaxies: A Far-Infrared Survey with *Herschel*; Kennicutt et al. 2011). Moreover, this discrepancy increases as the metallicity decreases, as noted by Rémy-Ruyer et al. (2015) for the galaxies of the DGS. In addition, the FIR emissivity of dust grains can also vary between galaxies as well as between different regions in a galaxy, and the exact dust composition (and emissivity) is generally not known, in particular for extra galactic environments. As a consequence, the dust mass can be underestimated by a large fraction (Galliano et al. 2011; Rémy-Ruyer et al. 2013).

- *Gas mass.* Several components have to be taken into account for the determination of the gas mass. Although one component can be negligible in some environments, the atomic gas and the ionized gas can contribute significantly to the gas mass and their determination can be uncertain as well. For example, Fukui et al. (2015b) argue that HI is dominated by an optically thick component, while it is usually considered to be optically thin. This could result in an average density of HI two times higher than the density derived with an optically-thin assumption. Optically thick cold HI gas could be misinterpreted as CO-dark molecular gas. However, this explanation was not validated for the Perseus molecular cloud by Lee et al. (2015). Another uncertainty comes from H_α luminosity, at visible wavelength, which thus must be corrected from possible foreground extinction.

Gamma-ray observations

Diffuse γ-ray emission is mainly produced through interaction of cosmic-ray particles with the ISM via three mechanisms: nuclear interactions producing neutral pions π^0 which decompose into two γ-ray photons with equal energies, Bremsstrahlung emission due to the electromagnetic scattering

of high-energy cosmic ray electrons by the ISM, and inverse Compton scattering of high-energy electrons and positrons by the low-energy photons of the interstellar radiation field (ISRF). A diffuse extragalactic emission is also identified. Since they are produced through interactions between cosmic rays and the interstellar gas or radiation, γ-rays at energies higher than 100 MeV trace effectively the gas mass of the ISM, with little dependance on its chemical or physical state. The ISM is transparent to cosmic rays. Therefore, this method is not limited to the molecular mass inside the CO-emitting clouds, but is sensitive to the total gas column density, independent of the dust properties or physical state of the gas (ionized, atomic or molecular).

Several studies have modeled the observed γ-ray emission, in particular in the Milky-Way (e.g. Grenier et al. 2005; Ackermann et al. 2012; Ade et al. 2015; Abrahams & Paglione 2015) and in the LMC (Abdo et al. 2010). At first order, γ-ray emission can be modeled as a linear combination of the gas column densities on the different phases along the line of sight.

$$I_\gamma = q_{\rm HI} N({\rm HI}) + q_{\rm CO} W(CO) + q_{\rm dust} I_{\rm dust} + q_{\rm IC} I_{\rm IC} + I_{\rm iso} + \sum_j S_j \tag{V.25}$$

The free parameters of the diffuse emission model are the emissivity per hydrogen atom, $q_{\rm HI}$ ($\rm s^{-1}$ $\rm sr^{-1}$), the emissivity per unit of CO(1-0) intensity ($W_{\rm CO}$), $q_{\rm CO}$ ($\rm cm^{-2}$ $\rm s^{-1}$ $\rm sr^{-1}$ (K km $\rm s^{-1})^{-1}$), the emissivity per unit of dust intensity (I_{dust}), $q_{\rm dust}$ ($\rm cm^{-2}$ $\rm s^{-1}$ $\rm sr^{-1}$ $\rm mag^{-1}$), and an isotropic intensity component $I_{\rm iso}$ ($\rm cm^{-2}$ $\rm s^{-1}$ $\rm sr^{-1}$). A model for the cosmic-ray propagation, with an estimated radiation field is generally used to derive the inverse Compton intensity map, $I_{\rm IC}$. The sum over j represents the combination of the known sources, either point-like or extended, including a free parameter (of flux normalization) independent for each of them.

Assuming a constant gamma-ray emissivity per hydrogen nucleus and assuming CO(1-0) is proportional to the total molecular column density, the $\rm X_{CO}$ factor can be determined as

$$X_{\rm CO} = \frac{q_{\rm CO}}{2 \times q_{\rm HI}}. \tag{V.26}$$

However, in some regions, a substantial residual γ-ray emission is observed (Grenier et al. 2005; Ackermann et al. 2011), revealing the presence of an unseen gas component, either atomic or molecular. This dark gas can represent a significant fraction of the total gas mass, in particular in cold molecular clouds (Planck Collaboration 2011a; Paradis et al. 2012; Pineda et al. 2013).

SFR scaling

The low ratio $\rm L_{CO}$/SFR measured in dwarf galaxies may result from a true deficit of $\rm H_2$ compensated by high star-forming efficiencies, or simply that CO becomes a poor tracer of the total molecular gas. Several studies of nearby spiral galaxies indicate a tight correlation between $\rm H_2$ and SFR on $\sim$ kpc scales (e.g. Kennicutt. et al. 2007; Bigiel et al. 2008; Leroy et al. 2008; Schruba et al. 2011), following the Schmidt-Kennicutt relation (see Section I.1.4). Moreover, there is growing evidence that star formation in molecular clouds, and in particular the star formation efficiency (SFE), is independent of the environment (e.g. Bolatto et al. 2008; Fukui & Kawamura 2010; Krumholz & Tan 2007). These results tend to favor the second hypothesis above, i.e. that CO is not accurately tracing the total molecular gas reservoir in dwarf galaxies.

Genzel et al. (2012) and Schruba et al. (2012) assume the universality of the Schmidt-Kennicutt relation and use an estimate of the recent SFR (e.g. a combination of FUV and 24 μm emission) to derive the $\rm H_2$ mass. They apply this method to a sample of low- and high-redshift galaxies and to a sample of dwarf galaxies, respectively. It is then possible to derive the variations of the $\rm X_{CO}$ factor

with metallicity, as represented in Figure V.3. This method requires the assumption of a constant relationship between H_2 and the SFR. One of the caveats is that any true variation of the SFE will be mis-interpreted as a variation of X_{CO}. Hunt et al. (2015) adopt a slightly different method, extending to lower masses the correlation between the depletion time (1/SFE) and the specific star formation rate, sSFR found by Saintonge et al. (2011). This results in a somewhat shallower dependance of α_{CO} with metallicity compared to that estimated assuming a constant τ_{dep} (Schruba et al. 2012; Genzel et al. 2012).

PDR modeling

Modeling accurately the entire structure of the cloud is important to determine the relative H_2 and CO emission. With a detailed model of the PDR as described in Section III.3, it is possible to compute the depths at which H_2 and CO form and to calculate the total mass of molecular gas. In the next section, we develop this method and apply it to the case of 30Dor, using the PDR modeling described in Section IV.2.1.

V.2.2 30Dor as a test bed

For the reasons already listed above (1/2 $Z_\odot$, proximity of the LMC, high radiation field, large number of observations covering a wide wavelength range), 30Dor is an ideal laboratory to examine the interaction between star formation and the surrounding ISM at low metallicity. In Section IV.2.1 we have built a complete PDR model using PACS and SPIRE observations (see Chapter IV; Chevance et al. 2016). In this section, we use this model to calculate the total mass of H_2 in 30Dor and determine the X_{CO} factor adapted for the region. We compare this value with the literature and investigate the impact of different methods and assumptions on the X_{CO} value.

Observations

Complementing the *Herschel* and *Spitzer* observations described in Section IV.2.1, we use ground-based observations of the molecular, atomic, and ionized gas. For the molecular gas, we use the CO ($J = 3 - 2$) transition observed with ASTE (Minamidani et al. 2011) at an angular resolution of 22″ (~ 5 pc) and the CO ($J = 1 - 0$) transition observed with Mopra (Wong et al. 2011) at 45″ (~ 10 pc). In order to compare our PDR results with the CO observations, we convolve the PACS data and L_{FIR} map to 22″ and 45″.

For the atomic gas, we use HI observations of the LMC from Kim et al. (2003) at a spatial resolution of 1′. H_α observations are from the Magellanic Cloud Emission Line Survey (MCELS; private communication R.Leiton) using the Cerro Tololo Inter-American Observatory (CTIO) Curtis Schmidt telescope. The angular resolution is $\sim 5''$.

The total H_2 reservoir via PDR modeling

In this section, we use the Meudon PDR code to calculate the mass of molecular gas in 30Dor. We use the method described in Section III.4.2 (and used in Chevance et al. 2016; Section IV.2.1) to find the best fit model to the PACS observations, now convolved at 22″ and 45″ resolution to combine them with [CI] and CO observations. Combining the PDR observations with [CI] or CO is necessary to derive the depth of the cloud, as explained in Section III.4.2. Indeed, [OI] and [CII] lines are co-spatial in the cloud and therefore are not sensitive to the geometry of the cloud. On the other hand, since,

[CI] and CO originate from deeper into the cloud, the ratios [CII]/CO or [CII]/[CI], for example, bring strong constraints on the parameter A_V^{max}.

We determine the spatial distribution of the incident radiation field, G_{UV}, the pressure, P, and the total visual extinction, A_V^{max}, at the resolution of 22″ based on *Herschel* far-infrared fine structure lines and CO (3-2) ground-based observations. The spatial variations and the absolute values of G_{UV} and P at 22″ are similar to those at 12″, except at the peaks, where we find lower values at 22″, due to the smoothing effect of the convolution. A_V^{max} ranges between 1.7 and 3.4 mag, with associated uncertainties of +14%/-10% on average. These values are determined for a parallel slab model and we keep in mind that this parameter is strongly dependant on the geometry of the model. From the Meudon PDR code with these new best-fit parameters at 22″ resolution, we deduce the column density and mass of molecular gas predicted by the model for each 15″×15″ pixel. We estimate the H_2 column density between 2.7×10^{21} and 3.4×10^{22} cm^{-2} and the H_2 mass approximatively between 50 and 550 $M_\odot$/pc^2, with uncertainties of +19%/-11% on average. The spatial distribution of the H_2 mass is presented in Figure V.4. The maximum value is located in region B in Figure 3 of Chevance et al. (2016), corresponding to the location of the [CII], CO(1-0) and CO(3-2) peak. It is also co-spatial with the CO(2-1) map observed with *ALMA* by Indebetouw et al. (2013).

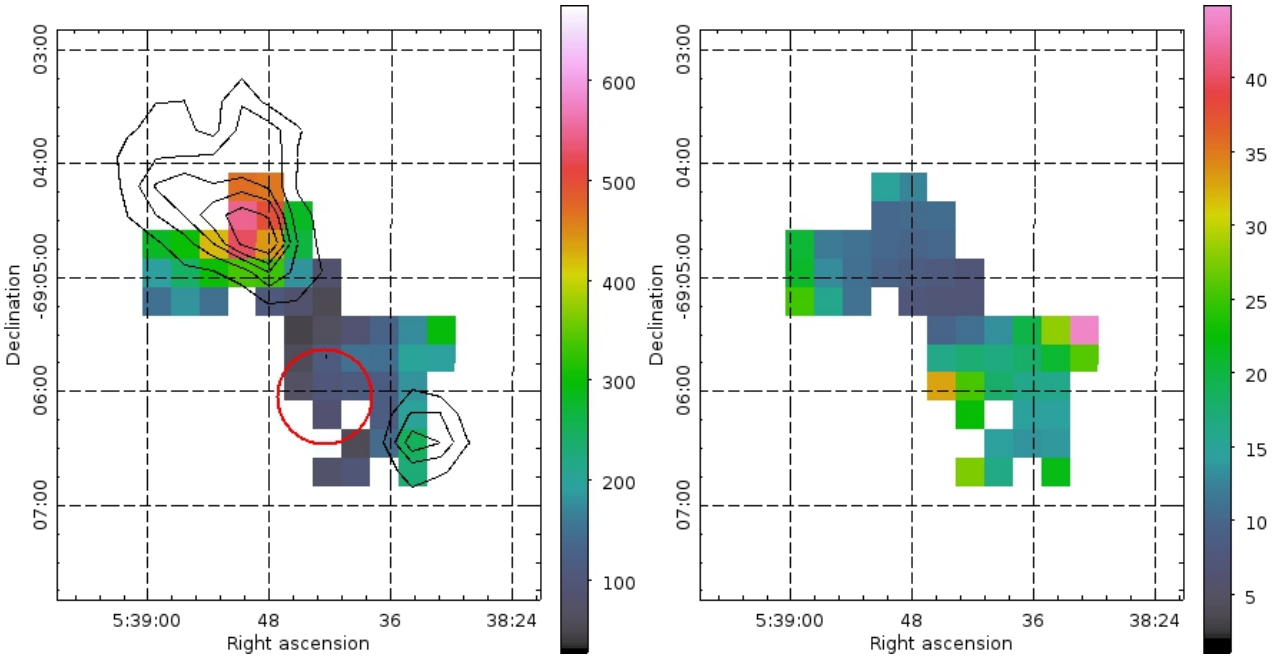

Figure V.4: *Left: Mass of H_2 (in $M_\odot$ pc^{-2}) predicted by the PDR model at 22″ angular resolution. The black contours outline the ^{12}CO (3-2) detected with ASTE (Minamidani et al. 2011). The red circle indicates the location of the SSC R136. Right: Ratio between our estimation of the X_{CO} factor adapted for 30Dor, $X_{CO,30Dor}$, and a standard value commonly used for the Milky Way, $X_{CO,MW}$= 2×10^{20} cm^{-2} (K km s^{-1})$^{-1}$.*

For the model at 45″, although the spatial resolution is degraded by a factor of ∼ 2, we obtain similar ranges of A_V^{max}, column density and mass. We compare the H_2 mass from this modeling with the mass of H_2 that we can infer from the CO(1-0) emission at 45″ resolution, using a standard Milky Way CO-to-H_2 conversion factor, $\alpha_{CO,MW}$ = 4.3 $M_\odot$ pc^{-2} (K km s^{-1})$^{-1}$ (corresponding to $X_{CO,MW}$ = 2×10^{20} cm^{-2} (K km s^{-1})$^{-1}$), which can be approximately applied down to metallicities of ∼ 0.5 $Z_\odot$ according to Bolatto et al. (2013). Slightly higher values have been proposed for the LMC (Leroy et al. 2011 determine $X_{CO} = 3.0\times10^{20}$ cm^{-2} (K km s^{-1})$^{-1}$ using a dust-based method; a scaling with

the metallicity is also possible as in Figure V.3) but these values are in any case uncertain and this should not affect our results by more than a factor of 2 since the LMC is not an extremely metal-poor environment. The H_2 mass resulting from this simple scaling of the CO luminosity with $X_{CO,MW}$ is only between 1 and 20% of the total H_2 mass predicted by our model. Between 80% and 99% of the total H_2 can then be characterized as "CO-dark" molecular gas in 30Dor.

As a result, it appears that the $X_{CO,MW}$ value is not adapted to quantify the total mass of H_2 in 30Dor and there is much more H_2 than that associated with CO only. We thus calculate the X_{CO} conversion factor adapted for this region, defined as:

$$X_{CO,30Dor} = \frac{N(H_2)_{model}}{I_{CO(1\text{-}0)}} \tag{V.27}$$

where $N(H_2)_{model}$ is the H_2 column density from the PDR model in cm^{-2} and $I_{CO(1-0)}$ is the observed CO(1-0) intensity in K km s^{-1}. The $X_{CO,30Dor}$ thus calculated ranges between $1.4{\times}10^{21}$ and $6.6{\times}10^{21}$ cm^{-2} (K km s^{-1})$^{-1}$ over the region we observed, a factor of 3 to 60 more than the commonly used $X_{CO,MW}$, suggested by Bolatto et al. (2013) for the LMC (Fig. V.4).

We find X_{CO} values ranging over a factor of 5 just within our limited 30Dor region. It is difficult to compare to other studies of different size scales. For example, Israel (1997) uses a dust modeling technique, with dust mass estimates based only on IRAS values to 100 μm and spatial sampling of 15′ ($\sim$ 235 pc) and determine X_{CO} factor higher than the range we find. Assuming a constant star formation efficiency, Schruba et al. (2012), based on Fukui et al. (2008) CO observations ($\sim$ 40 pc) find a X_{CO} value for the LMC which falls in the middle our range of values. Table V.1 summarizes these values.

The total H_2 reservoir via dust modeling

We convolve the *Spitzer*/IRAC (3.6, 4.5, 5.8 and 8.0 μm bands) and MIPS (24 and 70 μm bands) and the *Herschel*/PACS (100 and 160 μm bands) and SPIRE (250 μm band) photometry data at the resolution of 18″ (similar to the resolution of SPIRE at 250 μm). We use the full SED model from Galliano et al. (2011; AC composition) to estimate the amount of dust along the line of sight for each pixel. One of the outputs of the SED fitting procedure, described in Section III.1.1, is the resolved dust mass. Contrary to L_{FIR}, the dust mass is sensitive to the wavelength range over which the SED is fitted (e.g. Rémy-Ruyer et al. 2013). Therefore, incorporating the SPIRE 250 μm band, to probe the colder dust, was found to be a good compromise between the spatial resolution ($\sim$ 18″) and the reliability of the estimated dust mass. Tests confirmed that adding the SPIRE 350 μm band to the SED fit, results in a similar dust mass, but with a degraded resolution.

G/D for 30Dor is calculated using the broken power-law relationship between G/D and the metallicity defined in Rémy-Ruyer et al. (2014). We assume a constant G/D throughout the region. For 30Dor, $log(n(O)/n(H)) = -3.75$ (Pellegrini et al. 2011), which gives $(G/D)_{30Dor} = 4.5 \times 10^2$ from Rémy-Ruyer et al. (2014) relationship. We find a similar spatial distribution of molecular gas mass than with the PDR modeling (Fig. V.5), although with slightly higher values, leading to an X_{CO} factor of $2-8\times10^{21}$ throughout the region. This is higher than the maximum value of 6×10^{20} for the LMC derived by Roman-Duval et al. (2014). They use a different dust SED model than we do, to fit the same observations, i.e. a single-temperature blackbody modified by a broken power-law emissivity (Gordon et al. 2014), which has an impact on the dust mass derived. Moreover, the study of Roman-Duval et al. (2014) is done at 1′ resolution, and a degraded resolution tends to result in underestimated dust masses (Galliano et al. 2011).

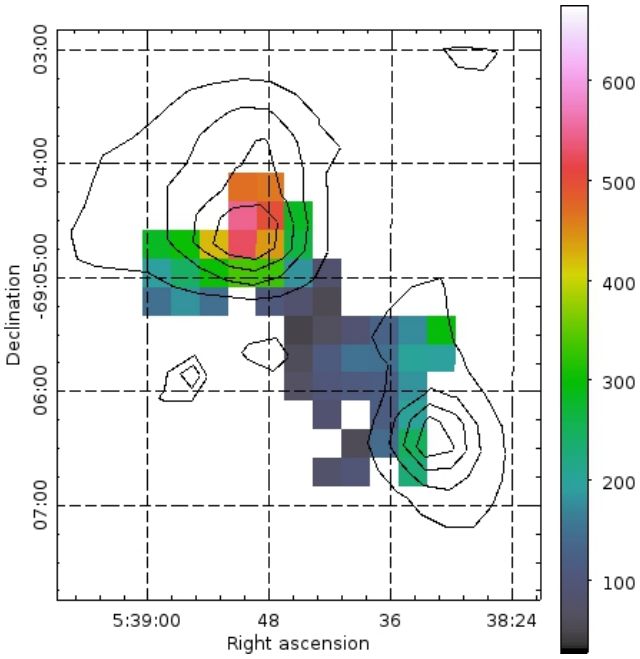

Figure V.5: *Contours showing the mass of molecular gas from the dust modeling overplotted on the molecular mass from the PDR modeling (same as Figure V.4). Contours levels are 300-500-700-900* $M_{\odot}/pc^2$.

A paper presenting this study on the quantification of the CO-dark molecular gas mass in 30Dor and including the effect of the resolution (see Section V.3) is currently in preparation for submission soon to A&A.

V.2.3 Concluding remarks

As described in Section V.1.3, the fraction of H_2 effectively probed by CO decreases when the metallicity decreases. CO traces only the central part of the molecular clouds and extrapolation to the total molecular mass becomes very uncertain. It is therefore imperative to resolve individual molecular clouds and to observe tracers corresponding to different depths into the cloud to disentangle the different components and probe the effect of the metallicity and environment on the structure of the gas. *ALMA* is the perfect instrument to achieve this goal in extragalactic environments (e.g. Indebetouw et al. 2013; Kepley et al. 2016). New *ALMA* observations of 30Dor are currently ongoing for Cycle 3 and described in Section V.4.

Other tracers could be more efficient at probing the total mass of H_2 than CO a reduced metallicity. Madden et al. (1997) suggest that a large fraction of H_2 is co-existing with [CII] in irregular galaxies. Based on theoretical results, Nordon & Sternberg (2016) find that the column density of C^+ associated with H_2 is larger than that associated with atomic hydrogen. They derive an analytical expression of the total molecular gas column density associated with C^+, which depends mostly on the metallicity. In the particular case of 30Dor, our PDR modeling results presented in Section V.2.2 show that, while [CII] is brighter than [CI], a larger fraction of the H_2 is residing in the C^o-region. Models by Offner et al. (2014) also reveal that [CI] may be a better tracer of the H_2 than CO. At decreased metallicities, the [CI] line is expected to better trace the total H_2 (e.g. Glover & Clark 2016; Madden et al. in prep). Papadopoulos et al. (2004) show in particular the interest of using [CI] as a tracer of the total molecular gas for high-redshift galaxies. Indeed, while ground-based observations of the [CI] lines

Table V.1: Comparison with other studies

Reference	X_{CO} [cm^{-2} (K km s^{-1})$^{-1}$]	Object	Physical size
Bolatto et al. (2013) *Review*	2×10^{20}	LMC, Milky Way	
Israel (1997) *Dust modeling*	8.4×10^{21}	30Dor	235 pc
Schruba et al. (2012)[a] *Constant SFE*	4.6×10^{21}	LMC	40 pc
Roman-Duval et al. (2014) *Dust modeling*[a]	$<6\times10^{20}$	LMC	15 pc
This study			
PDR modeling	$1.4-6.6\times10^{21}$	30Dor	10 pc
PDR modeling	2×10^{21}	30Dor	integrated (30 pc×30 pc)
Dust modeling (SED fitting from Galliano et al. 2011)	$2-8\times10^{21}$	30Dor	15 pc

[(a)] Based on Fukui et al. (2008) CO data.
[(b)] Single temperature blackbody modified by a broken-law emissivity.

in the local Universe are very difficult even with *ALMA* due to atmospheric absorption, they become more easily accessible in high-z galaxies, once redshifted to lower frequencies.

V.3 Calibrating molecular gas tracers for the high-redshift universe

V.3.1 Effect of spatial resolution

Except for the very nearby galaxies, the distance of extragalactic environments, resulting in fainter lines and a degraded spatial resolution, increases the difficulty to probe accurately the total gas mass. As a result, CO lines are generally used as molecular gas tracers through the X_{CO} factor for extragalactic studies. However, high-redshift galaxies, which are unique laboratories to test our understanding of the star formation in the early universe, cover a wide range of different environments and the calibration and reliability of X_{CO} is still debated. Mixing potentially very different environments in one beam could result in erroneous H_2 mass estimates. Spatial averaging on kpc scales seems to reduce the variations of X_{CO} with the H_2 column density compared to GMC scales, while the dependance on the metallicity is still observed (Feldmann et al. 2012).

This resolution effect has been studied for example by Galliano et al. (2011) on the dust mass estimates. This study reveals that the modeled dust mass from an SED model decreases significantly with a degraded resolution. In particular for the LMC, the spatially resolved dust mass is $\approx$ 50% higher than the value from modeling of the integrated galaxy. This is due to the fact that on large scales in the LMC, the contribution from warm regions dominates the energy distribution, while on small scales, cold regions can be modeled separately and thus more accurately taken into account. Indeed, on large scales, it is difficult to take into account the fainter, colder region, as the energy distribution is dominated by the brighter, warmer star-forming regions, thus biasing the model results toward lower dust masses.

The simple description of Section V.1.1 shows that CO can trace the H_2 mass for an individual GMC. On galaxy scales, we can find an equation similar to Equation V.11, and then use the X_{CO} factor, if we make a number of assumptions. If the individual clouds are virialized and if the brightness temperature is mostly independent of the cloud size, α_{CO} can be defined for an ensemble of clouds (Dickman et al. 1986). In this case, CO intensity is proportional to the number of clouds in the beam, as long as they do not overlap each other. This assumption can be critical in high density environments, as CO could be underestimated due to opacity effects. If the size distribution, the cloud surface density and the CO brightness temperature are approximately homogeneous throughout the galaxy, a uniform value of α_{CO} can be applied. As this is probably not the case, we can wonder what type of environment will dominate the observations. Are the results biased toward more diffuse regions, which are more extended, or toward denser regions and usually brighter regions?

V.3.2 30Dor in one pixel

Here we test the effect of size scale by assuming the LMC being further away. For example, at the distance of the Andromeda galaxy (~ 780 kpc; Ribas et al. 2005) the entire region of ~ 40 pc × 40 pc mapped here would fall in only one spaxel of the PACS spectrometer. We run another PDR model with integrated values of the ratios $\frac{[\mathrm{O\,I}]\ 145\,\mu\mathrm{m} + [\mathrm{C\,II}]}{\mathrm{L_{FIR}^{PDR}}}$, $\frac{[\mathrm{O\,I}]\ 145\,\mu\mathrm{m}}{[\mathrm{C\,II}]}$ and $\frac{[\mathrm{C\,II}]}{[\mathrm{C\,I}]\ 370\,\mu\mathrm{m}}$ as constraints. The integrated IR tracers are best reproduced by a PDR model with G_{UV}= 1390, P = 6.18×10^5 K cm^{-3} and A_V^{max} ~ 3. These values are similar to what we find as averages for the smaller scale models. The H_2 mass predicted by this particular model is 194 $M_\odot$ pc^{-2}. It represents a total H_2 mass of $1.2\times10^5 M_\odot$ over the entire PACS region. This is close to the value of $1.3\times10^5 M_\odot$ for the total H_2 mass estimated with the PDR model at 22″. Thus, we do not see any effect of the resolution on the total H_2 mass due to the resolution on large scales (between ~ 5 and 40 pc). However, we emphasize that the region probed here with *Herschel* is still relatively small and close to the SSC R136. We are biased toward the brightest PDR regions, and this could affect our results. The extended region mapped with *SOFIA* (Section IV.3.2) may reveal a different conclusion on larger scales (≈ 60 pc). X_{CO} is approximately 10 times higher than the standard Milky Way value for the integrated region.

On smaller scales, for resolved CO clouds with *ALMA*, Indebetouw et al. (2013) find an α_{CO} factor of 8.3 $M_\odot$ pc^{-2} (K km s^{-1})$^{-1}$, which is close to the Milky Way value scaled to the LMC metallicity, and lower than our result from the PDR modeling, between 30 and 140 $M_\odot$ pc^{-2} (K km s^{-1})$^{-1}$. However the value from Indebetouw et al. (2013) does not take into account a possible component of inter-clump H_2, which would increase the α_{CO} factor.

V.4 The need for high spatial and spectral resolution: *ALMA* observations

Deciding whether the difference in observed star forming properties corresponds to actual differences in the physical processes or not, requires detailed observations in low-Z environments. One way to answer this question would be to resolve the molecular gas and PDR transition zones, at a scale of ~0.1pc, which is approximately the size of the atomic-molecular gas transition observed in Orion for example (van der Werf et al. 1996). Such scales can now be reached with *ALMA* in the LMC. To support this, our PDR modeling results suggest significant reservoirs of CO-dark gas in the 30Dor region (see Sect. V.2.2). However, we are unable to identify the locations and physical conditions directly linked to the CO-dark gas fraction at small scales. At the limiting scale of our initial PDR study,

10 pc (Chevance et al. 2016; Section IV.2.1), a variety of environments are mixed within the beam. In particular, the importance of A_V in the determination of the CO-dark gas compels us to constrain A_V at molecular cloud scales ($\gtrsim 1$ pc) with *ALMA*. Having the capability to detail the structure of the PDR/molecular cloud at 0.1 pc scale will overcome the limitations associated with our large scale *Herschel* study.

[C I] typically appears for $A_V \approx 1-5$ from the recombination of C^+ with free electrons. The size of the [C I] layer thus strongly depends on the physical conditions and on parameters such as the PAH abundance (important for electron recombination; e.g., Le Bourlot et al. 1993; Wolfire et al. 2008), the elemental C and O abundance, and the FUV field penetration. Our PDR model results show that the [C I]/^{12}CO ratio is a sensitive tracer of the CO-dark gas fraction. Figure V.6 shows the relation between the ratio [C I] 370 μm/^{12}CO(2-1) and the fraction of CO-dark gas over H_2 traced by CO, for our set of simulated PDRs. There is a linear correlation between these two quantities over a wide range of physical conditions (A_V, G_{UV} and P). The tight correlation between [C I] 370 μm/CO(2-1) and the fraction of CO-dark gas provides an important motivation for an *ALMA* study. Thus, it is possible to determine the total molecular mass for any given cloud from combined observations of [C I] 370 μm and ^{12}CO(2-1).

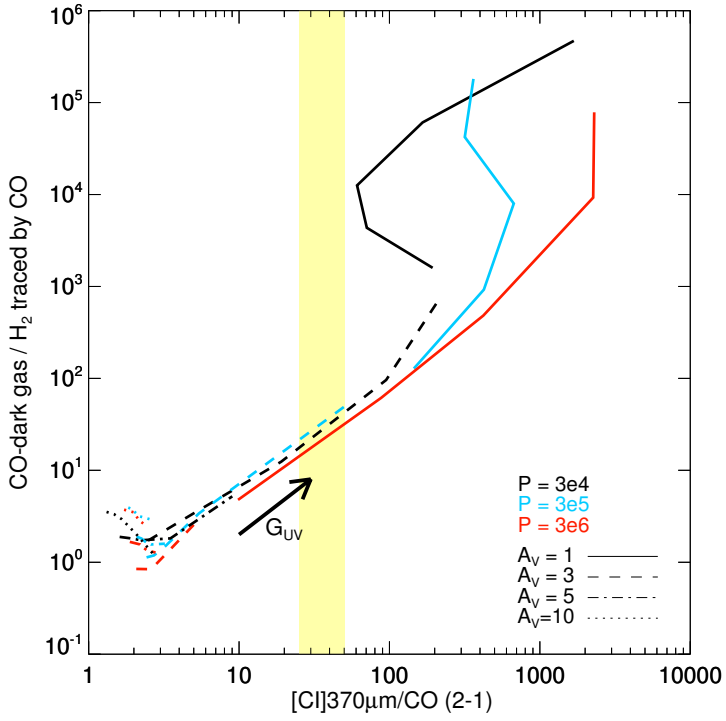

Figure V.6: *Diagnostic plot presenting the ratio of the CO-dark molecular gas over the CO-bright molecular gas as a function of [C I] 370 μm/^{12}CO(2-1), for a set of simulated clouds with 30Dor gas phase abundances, with different physical properties, modeled with the Meudon PDR code. The different line types designate the total A_V of the simulated cloud; the colors designate the pressure of the cloud. The range of G_{UV} is 30 to 3×10^3, increasing from bottom left to top right. These two quantities are well correlated over about two orders of magnitudes in [C I] 370 μm/^{12}CO(2-1), with a factor almost independent of A_V, P, and G_{UV}. The yellow vertical band shows the typical ratio [C I] 370 μm/^{12}CO(2-1) at 45″ resolution in the star-forming regions of the LMC observed with the Herschel/FTS.*

While it is difficult to distinguish [CI] and CO emitting regions in Galactic clouds, even at sub-pc resolution (e.g., Gerin & Phillips 2000), this paradigm truly holds for individual clouds with A_V sufficiently large to form CO. The *ALMA* [CI] and CO maps will probe the fractal distribution of sub-parsec clumps with a wide range of A_V, revealing in detail the relative spatial repartition of tracers at different depths. With the high velocity resolution provided by *ALMA*, we can also test other aspects of how the [CI] relates to the CO-emitting cores. For example, the dynamic state of clouds can be probed by comparing the virial masses determined with CO and [CI]. Although observations of molecular clouds on ≥ 10 pc scales follow a power-law relation between their size and velocity (Larson relationship; Larson 1981), a larger dispersion and a deviation of smaller clumps above the size-linewidth relation has been noted in the Milky Way and the LMC (e.g., Heyer et al. 2001; Hennebelle & Falgarone 2012; Indebetouw et al. 2013). Indebetouw et al. (2013) suggest that these observations can be explained either by the effect of the interclump pressure (Field et al. 2011), or by chaotic gravitational collapse of the clouds, in which gravity drives the turbulence.

To explore the spatial and velocity distribution of C^o and CO, we have proposed *ALMA* observations of 30Dor (P.I Chevance). This proposal was accepted for cycle 3 (A-rated) and observations have already partly been done (^{12}CO(2-1) and ^{13}CO(2-1) have been observed in the three targeted regions). We describe the observations planned and the goal of the proposal below.

Cycle 3 *ALMA* observations

We proposed to observe [CI] 370 μm simultaneously with CO(7-6) with *ALMA* band 10 and ^{12}CO(2-1) simultaneously with ^{13}CO(2-1) and C^{18}O(2-1) with *ALMA* band 6. We have selected 3 regions from within the Cycle 0 ^{12}CO(2-1) map (Indebetouw et al. 2013) where A_V is expected to lie between 1 and a few magnitudes. The Cycle 0 map already showed that the molecular gas is clumpy in 30Dor, even with the coarser resolution of band 6 in Cycle 0 ($2'' \sim 0.5$ pc), implying that the PDR modeling should use observational constraints at similarly small scales. With all of these tracers, we probe different depths into the cloud and discriminate the structure of the different tracers at low metallicity, not only in the molecular core, but also in the PDR envelope. We will compare the sizes in each tracer with each other as well as with the sizes and structure predicted from PDR models, and we will determine what local physical conditions control the CO-dark gas at these small scales. We added a continuum measurement in three bands. The secondary experiment we will perform consists of deriving an approximate dust mass (using the dust SED models of Galliano et al. 2011), which will then be combined to the total gas mass inferred by the models in order to determine the D/G resolved at 0.1 pc scales within our 3 regions. Driven by the predictive power of our models, we wish to test a new approach to quantify D/G spatially rather than simply assuming a uniform D/G (as explained in Section V.2.1). Observation of the continuum in several bands will allow us to distinguish between dust and free-free emission.

The three regions selected (fig V.7) have very different characteristics to answer these questions:

- *Region A* covers the previously detected CO (2-1) as well as the edge of the PDR, where CO clumps are not prominent and where we find the highest CO-dark gas fraction. It is a region where H_2 will be traced preferentially by [CI]. In this region, G_{UV} reaches 6×10^3 and P is greater than 10^6 K cm^{-3}.

- *Region B* is the peak of the [CII], [CI] and CO emission lines. In this region, G_{UV} is 3000 and P $\sim 8 \times 10^5$ K cm^{-3}. We already identified several ^{12}CO clumps in this region at $2''$ resolution.

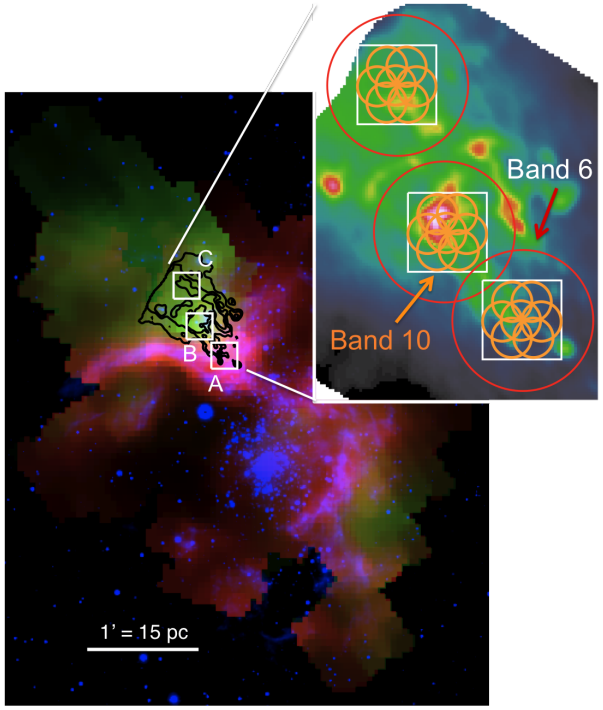

Figure V.7: *Herschel [C II] 158 μm (green) and [O III] 88 μm (red) and the VISTA K band (blue; Walborn et al. 2013). ^{12}CO(2-1) contours from ALMA cycle 0 are in black and the three proposed regions in 30Dor for Cycle 3 are outlined with white boxes. The insert shows the 7 pointings for Band 10 (orange) and 1 pointing for Band 6 (red) for each region, on the cycle 0 ^{12}CO(2-1) map of Indebetouw et al. (2009) at ∼ 2″ resolution.*

– In *Region C*, the CO(2-1) clumps are also prominent, but the G_{UV} and P are lower (resp. 800 and 3.5×10^5 K cm^{-3}) as well as the fraction of CO-dark gas.

With these observations we zoom into the structure of the PDR and map out the CO cores and photodissociated layers traced by C^o, resolved at ∼ 0.1 pc. We will apply the algorithm used by Indebetouw et al. (2013) for the cloud decomposition. The spatial (0.9″) and spectral (0.3 km.s^{-1}) resolution of *ALMA* allows us to compare the spatial and velocity structures of C^o and CO and their size-linewidth relation to see how the molecular cloud cores and the outer layers are related and identify the origin of C^o with a possible component from the interclump medium. We will calculate the physical properties of the clouds (P, G_{UV}, A_V^{max} and filling factor) by comparing the observations with the Meudon PDR code predictions for [C I] 370 μm, ^{12}CO(2-1), ^{13}CO(2-1) and the dust emission. We will derive H_2 column densities using ^{13}CO(2-1) and determine the H_2 mass assuming the clouds are virialized. We will then compare these virialized mass measurements with the H_2 determined by our PDR model, at 0.1 pc scales, and at 10 pc scale with *Herschel* and identify the effect of the resolution. In addition, from the observed ratio of [C I]/^{12}CO(2-1) at these resolved scales, we will quantify the CO-dark gas / H_2 traced by CO (Fig. V.6) and compare with that determined from the CO alone. The results in these three different regions in 30Dor will allow us to benchmark the use of the ratio [C I]/^{12}CO(2-1) as an indicator of the CO-dark gas reservoir.

Chapter VI

The effect of environment

Contents

30Dor is a very extreme environment and the properties derived for regions only a few parsecs away from the SSC R136 are probably very different from the rest of the LMC. In this chapter, we investigate the effect of the environment on the ISM structure and physical conditions. We also want to understand how the local conditions, such as metallicity, radiation field, ISM structure, A_V, etc, control the fraction of CO-dark molecular gas. We thus investigate the physical properties of the ISM in other star-forming regions of the LMC and SMC in order to compare them with the Tarantula Nebula and understand what drives the ISM properties on large scales.

VI.1 Presentation of the sample

VI.1.1 A large range of environments

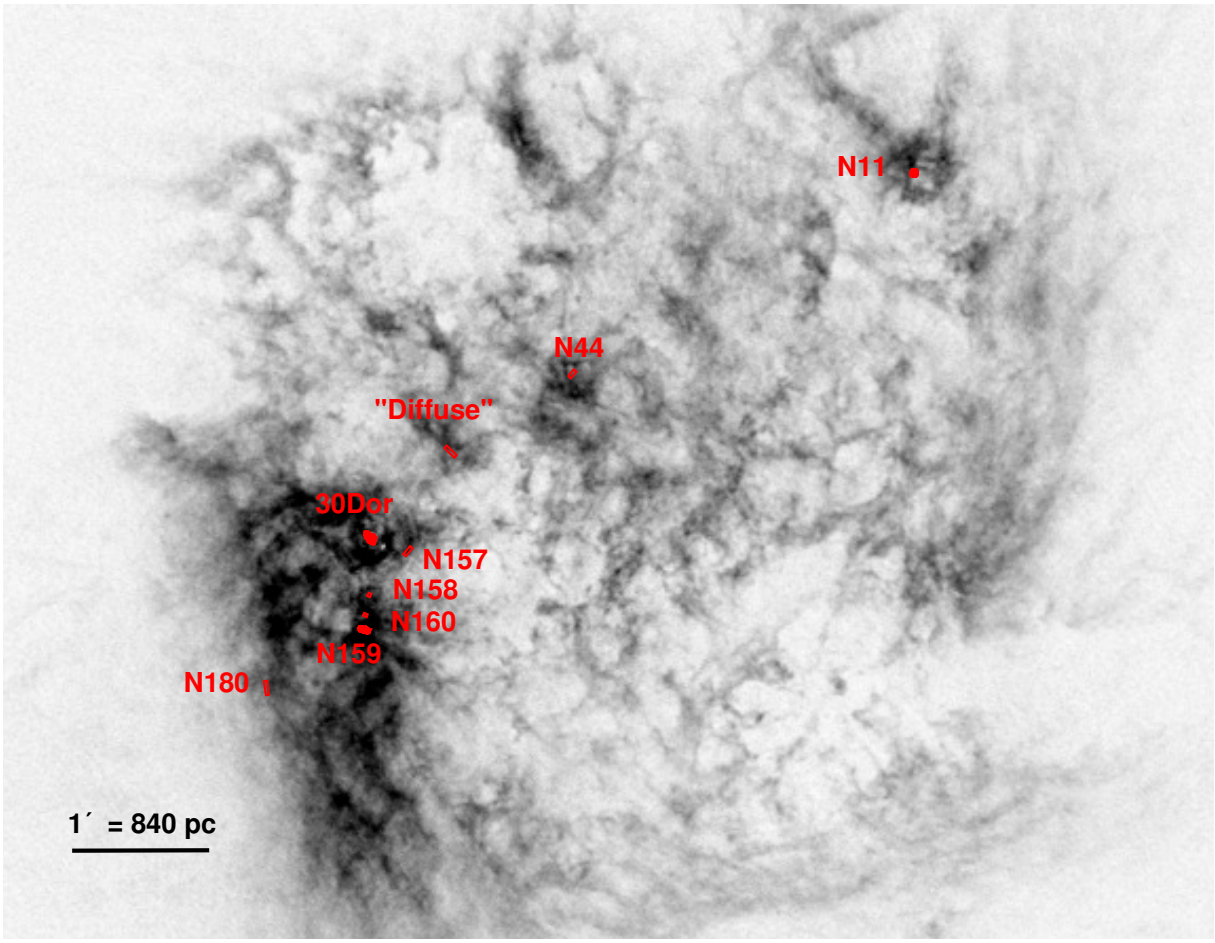

Figure VI.1: *H I map of the LMC (Kim et al. 2003). The spatial coverage of the PACS and SPIRE maps of the nine regions studied here are outlined in red.*

The metallicity of the LMC is considered to be fairly constant throughout the galaxy. Rolleston et al. (2002) for example have detected no significant metal abundance variations between different regions. A small metallicity gradient from the center to the outer regions is measured as a function of the distance to the center of the LMC, R_{CG} ([Fe/H] $\propto$ -0.01 R_{GC}; Feast et al. 2010; Cioni 2009). However, other physical conditions of the ISM, such as the density, the incident radiation field and the extinction, are varying greatly, resulting in different physical states and structures of the gas. On

the other hand, we can see the effect of metallicity on the structure of the gas by comparing regions of the LMC (~ 0.5 $Z_\odot$; Rolleston et al. 2002; Pagel 2003) and SMC (~ 0.2 $Z_\odot$; Russell & Dopita 1992). Despite a slightly larger distance (60.6 kpc for the SMC, Hilditch et al. 2005; 50 kpc for the LMC; Walker 2012) the spatial resolution achievable with PACS and SPIRE in the SMC still allows us to study in detail the PDR and molecular gas in star-forming regions and compare the LMC and SMC results.

The regions that we are studying here are part of two different *Herschel* observing programs. N11B, N158, N159, N160 and N66 are part of the DGS survey (Madden et al. 2013). The "Diffuse" region, N44, N157, N180 and N83 are part of Hony et al. (OT2). Except for N66, and N83, located in the SMC and shown in Figure VI.2, all of these regions are part of the LMC. Their positions are shown in Figures VI.1 and VI.2. PACS and SPIRE spectroscopic observations available from these surveys are listed in Table II.5. All of the LMC and SMC regions were mapped with PACS spectroscopy and contained within the *Spitzer* SAGE and *Herschel* HERITAGE photometry maps. The LMC regions were also observed with the SPIRE spectrometer (Lee et al., in prep). We describe here briefly the principal characteristics of these regions. The PACS maps, the maps of L_{FIR}, of [C I] 370 μm and CO(1-0) for each region are presented in Figures VI.14 to VI.22.

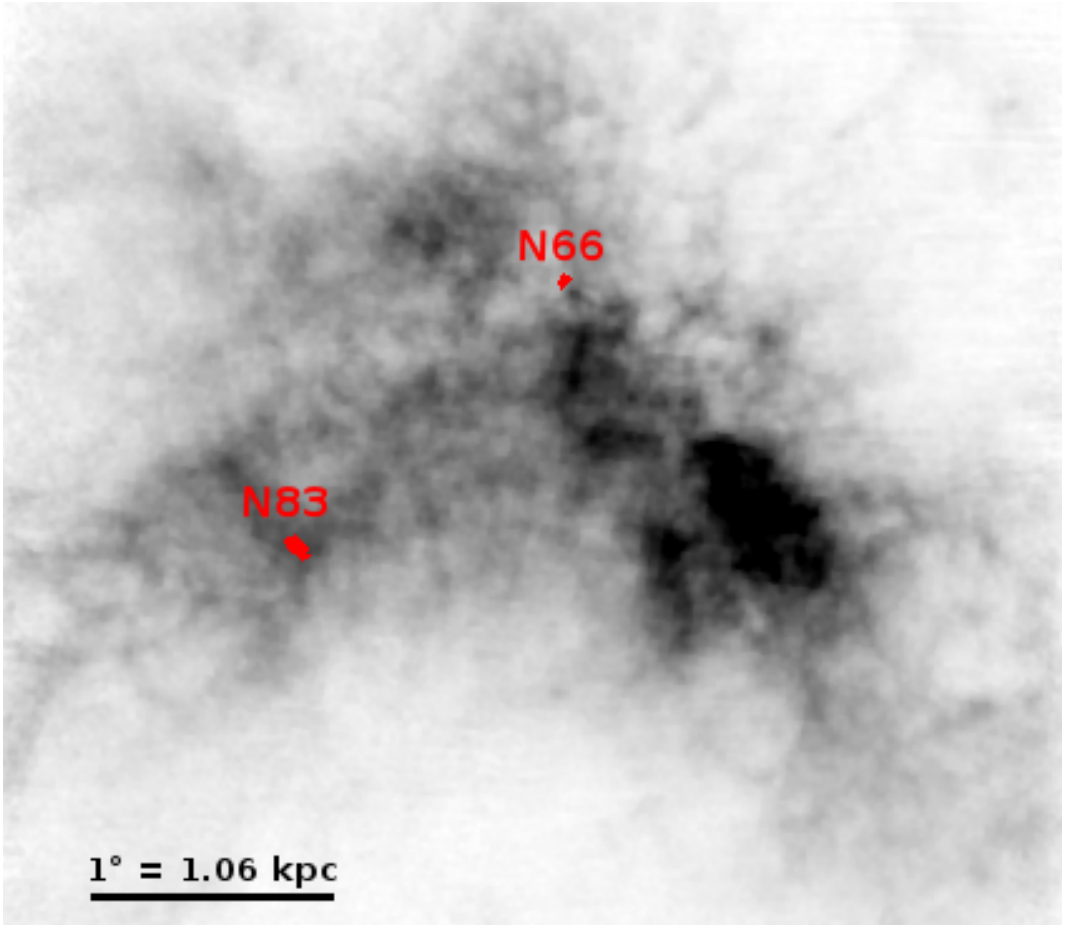

Figure VI.2: *H I map of the SMC (Stanimirovič et al. 1999). The spatial coverage of the PACS map N66 and N83 are outlined in red.*

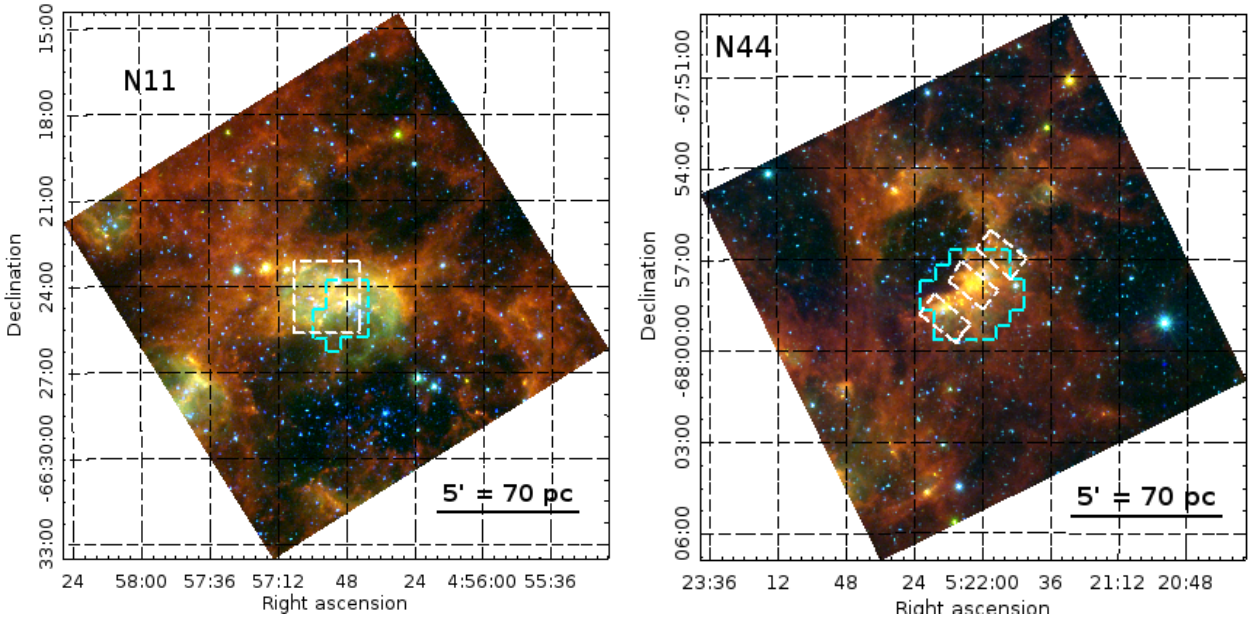

Figure VI.3: *Left: N11 in the LMC seen with Spitzer/IRAC 8 µm (red) showing PAHs and warm dust, Spitzer/IRAC 4.5 µm (green) showing the warmer dust, and 2MASS J-band (blue) showing the stars. The white contour outlines the PACS [O I] 145 µm map of N11B and the cyan contour, the FTS coverage. Right: same for the region N44 of the LMC.*

N11B

N11 (also DEM34; Henize 1956; Davies et al. 1976) is located on the north-west edge of the LMC, and is the second brightest H II region of the galaxy after 30Dor (Kennicutt & Hodge 1986). N11 consists of nine distinct nebulae (N11A to N11I; Rosado et al. 1996) distributed around a cavity of approximately 120 pc in diameter (80x60 pc, Lucke & Hodge 1970). This cavity has been excavated by the OB association LH9 (NGC1760), one of the main sources of ionization in this complex, located at the center of the void. LH9 association, which is ∼ 7 Myr (Mokiem et al. 2007), triggered a secondary, peripheral starburst (Lucke & Hodge 1970; Parker 1992; Walborn & Parker 1992) inducing these nebulae to distribute themselves around the H I shell. The presence of several YSOs has been spectroscopically confirmed (Seale et al. 2009; Woods et al. 2011). We note in particular the young OB association in N11B (LH10 $\lesssim 3$ Myr; Walborn et al. 1999), which is the sub-region studied here. X-ray point sources and diffuse soft X-ray emission have been noticed in observations with the *XMM-Newton* telescope and the *Suzaku* observatory (Nazé et al. 2004; Maddox et al. 2009).

Observations of CO(1-0), CO(2-1) and [C II] by Israel et al. (2003) and Israel & Maloney (2011) reveal a high [C II]/ CO ratio ($> 10^5$) and suggest a strong influence from the ambient radiation field. Israel & Maloney (2011) derive G_{UV} equivalent to ≈ 215 (in units of the Mathis field). As in 30Dor, [O III] is the brightest FIR line, suggesting a fragmented medium (Lebouteiller et al. 2012), and the gas-to-dust ratio in N11 is lower than that expected for the LMC metallicity (G/D = 180; Galametz et al. 2016), which could partially result from an underestimation of the X_{CO} factor. Using dust measurements from IRAS, H I and CO, Israel (1997) derives $X_{CO} = 2.1 \times 10^{21}$ cm^{-2} (K km s^{-1})$^{-1}$, a factor of 10 higher than $X_{CO,MW}$ based on dust modeling at 15′ resolution.

N44

Along with 30Dor and N11, N44 is one of the most active star-forming regions in the LMC. This bright H II region contains three OB associations (LH47, LH48 and LH49; Lucke & Hodge 1970) at different evolutionary states. The PACS data focus on the southwest edge of the supershell located around the LH47 cluster of massive ionizing stars (Stasínska et al. 1986; Meaburn & Laspias 1991), as outlined in Figure VI.3. The age of LH47 is estimated to be ~5-6 Myr by Will et al. (1997), with a possible older population ($\leqslant$ 10 Myr) inside the bubble (Oey & Massey 1995). In addition, a large number of massive YSOs, aged $\leqslant$1 Myr, has been identified on the rim of the shell (Lucke & Hodge 1970; Oey & Massey 1995; Whitney et al. 2008; Gruendl & Chu 2009; Chen et al. 2009; Carlson et al. 2012), suggesting triggered star formation by the expansion of the supershell. Diffuse X-ray emission, revealing the presence of $\approx 10^6$ K gas, has been observed in N44, well correlated with the H_α shell (Chu et al. 1993).

Bright H II regions are visible along the H_α shell and the southwest rim, coinciding with our PACS observations and also associated with ^{12}CO(1-0) molecular gas, as revealed by the NANTEN surveys (Fukui et al. 2001, 2008). Bright ^{12}CO(4-3) line, emitted from dense ($\approx 10^5$ cm^{-3}) clouds is detected in this region (Kim et al. 2004). From dust measurements and H I, at 15′ scale, Israel (1997) derives $X_{CO} = 1.3 \times 10^{21}$ cm^{-2} (K km s^{-1})$^{-1}$ a factor of 2 lower than that of N11. Using *Herschel* and *Spitzer* data, Hony et al. (2010) derive the dust column density, the PAH mass fraction and the mean radiation field energy density, on a 40′ × 40′ region around N44, as a function of the distance to the TIR peak (approximately where our region is centered), revealing significant PAH depletion toward the center of N44, close to the ionizing stars, and an inhomogeneous ISM around this region.

N157

The region N157 is located on the edge of the super-bubble called 30Dor C, shown in Figure VI.4. The super-bubble is powered by the OB association LH90 (Lucke & Hodge 1970), consisting of several clusters of ~ 3-8 Myr, and including several Wolf-Rayet (WR) stars (Testor et al. 1993). 30Dor C has the particularity of being the strongest non-thermal X-ray emitting super-bubble in the LMC (Bamba et al. 2004; Smith & Wang 2004; Yamaguchi et al. 2009). In particular, the western edge of 30Dor C, where N157 lies, shows strong hard X-ray emission (1-8 keV; Smith & Wang 2004) detected by the *XMM – Newton* telescope. Based on the study of multi wavelength observations, Kavanagh et al. (2015) recently bring evidence for a synchrotron origin to the X-ray emission from 30Dor C. This study also identifies for the first time a supernova remnant (MCSNR J0536-6913) interacting with 30Dor C and located ~15 pc from N157. In Section VI.2.1, we model relatively well the PDR tracers without including any additional X-ray component to the incident radiation field. However, X-rays penetrate deeper into molecular clouds while dissociating fewer molecules compared to UV. As a result, X-rays produce large column densities of warm molecular gas for a given irradiation energy (e.g. Meijerink & Spaans 2005) and may be required to explain the CO emission, for example, although this is not investigated in our study.

N158

N158-N159-N160 are parts of a large molecular cloud complex of ~ 400 pc from north to south, called 'the molecular ridge' and located ~ 500 pc south of 30Dor. The molecular ridge accounts for ~30% of the total molecular mass of the LMC (Mizuno et al. 2001).

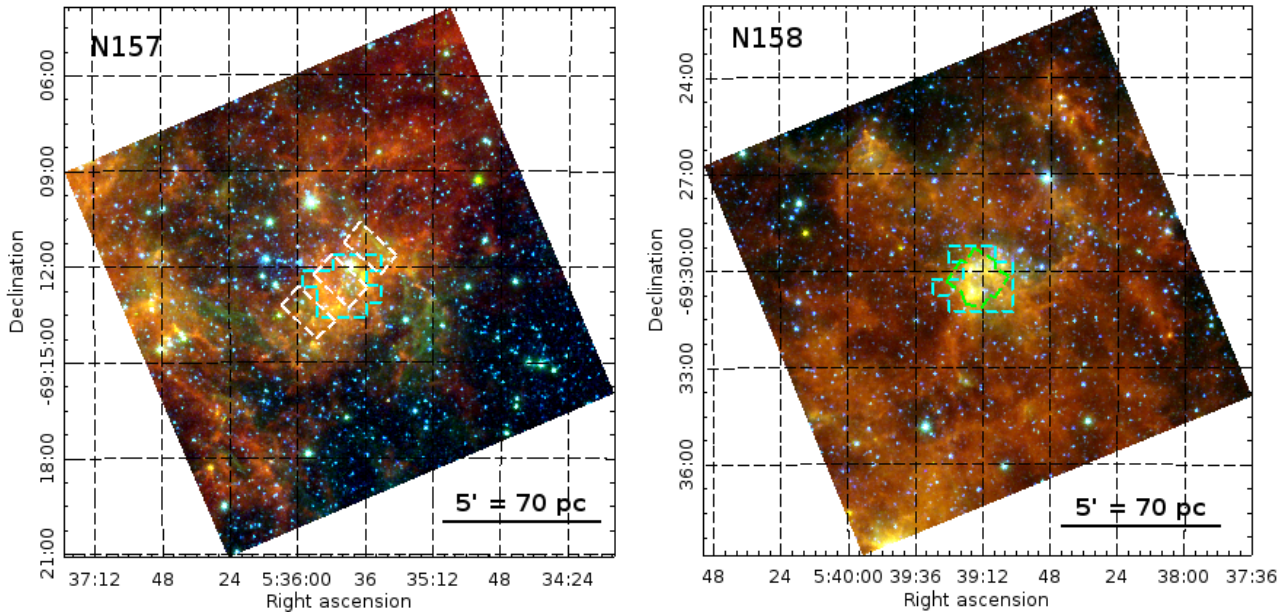

Figure VI.4: *Same as Figure VI.3 for the regions N157 (left) and N158 (right) of the LMC. [O I] 145 µm emission line was not observed by PACS in N158. Therefore, we outline here in green the spatial coverage of the PACS [O I] 63 µm map.*

Two OB associations were first discovered in the N158 H II region by Lucke & Hodge (1970). LH104, associated with the northern super-bubble, is dominated by a young stellar population of 2 to 6 Myr (Testor & Niemela 1998). LH101, associated with the southern H II region, which is shown in Figure VI.4, consists in two populations, one of ⩽2 Myr and the other one of ∼ 3-6 Myr. The HST/WFPC2 observations of N158 are discussed in detail in Fleener et al. (2010). They confirm the presence of 10 YSOs in the star-forming region NGC 2070 in the center of our PACS map, with a majority of early B to late O spectral types. Galametz et al. (2013) conduct a detailed study of the infrared/submm emission and modeled the SED of the N158–N159–N160 complex by combining observations from the *Spitzer* (3.6–70 µm), *Herschel* (100–500 µm) and Large APEX Bolometer Camera (LABOCA) (on APEX, 870 µm), and find a strong deficit of PAH emission in the vicinity of the H II regions, compared to our Galaxy,

N159 West

N159 (Figure VI.5) shows signs of intense on-going star formation such as protostars, masers and young massive stars (Deharveng et al. 1992; Meynadier et al. 2004). In particular, a large number of O- and B-type stars, YSOs, and ultracompact HII regions have been identified in N159 west (e.g., Jones et al. 2005; Fariña et al. 2009; Chen et al. 2010; Carlson et al. 2012). This region seems to be young, with the current star formation in N159 triggered by an expanding bubble blown by several O stars born 1-2 Myr ago (Jones et al. 2005).

The values of [C II]/CO is this region are less extreme than in 30Dor (∼ 5600; Israel et al. 1996; as compared to our finding of 5×10^4 to 3×10^5 in 30Dor). Pineda et al. (2008b) have constrained the radiation field (G_{UV}∼ 220) and the density (n ∼ 10^5 cm^{-3}) with a clumpy PDR model toward the peak of CO intensity. More recently, Okada et al. (2015) present spectrally resolved observations of N159 with GREAT on *SOFIA* and APEX, showing that a significant fraction of [C II] emission seems to trace neutral gas, not associated with the [C I] and CO gas. Galametz et al. (2013) have estimated a

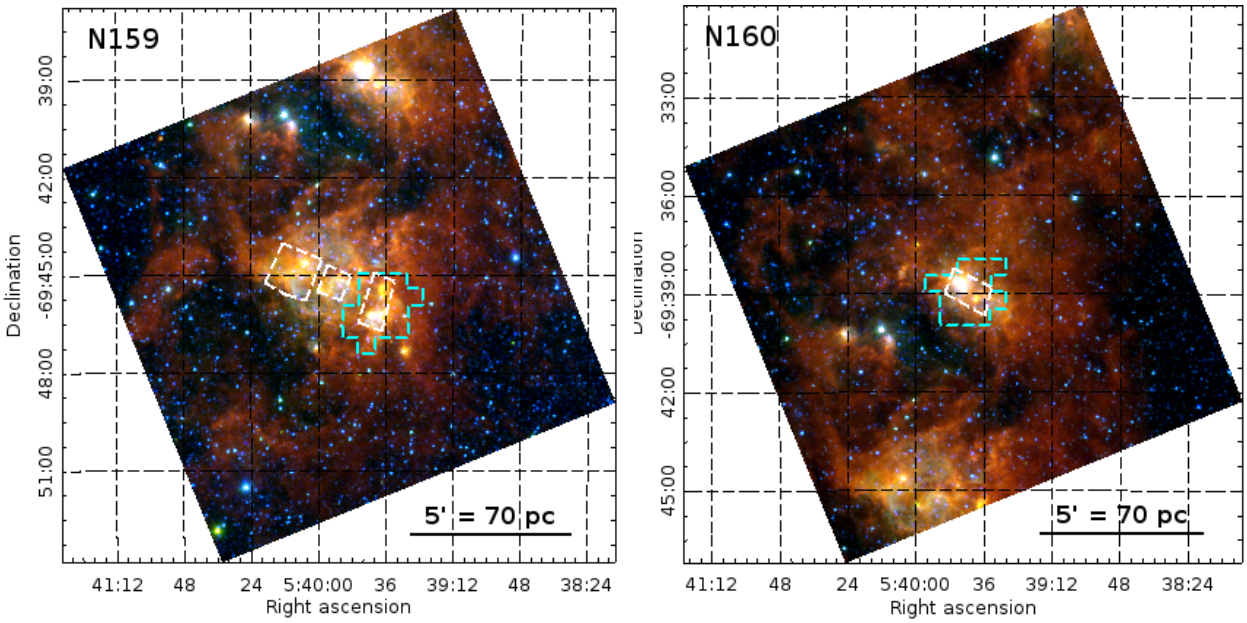

Figure VI.5: *Same as Figure VI.3 for the regions N159 (left) and N160 (right) of the LMC.*

G/D of ~ 356 based on LABOCA observations and CO(3-2) data and, assuming this value is constant throughout the region, derived an X_{CO} conversion factor of 5.4×10^{20} cm^{-2} (K km s^{-1})$^{-1}$. Analysis of the SPIRE/FTS CO transitions and PDR modeling of this region have been done by Lee et al. (2016). They suggest that shocks could be a significant heating source, in particular for the CO emission. It appears that ionization sources (including X-rays and cosmic rays) have a negligible contribution to the CO emission and that low-velocity shocks could be the main mechanism of the CO excitation. Recent *ALMA* observations have revealed that the ^{13}CO(2-1) emission is distributed along colliding filaments of 5-10 pc long (Fukui et al. 2015a) which could also be associated with the shocks seen in Lee et al. (2016).

N160

Massive star formation has been evolving in N160 (Figure VI.5) and several generations of stars have been formed prior to the current star formation (Oliveira et al. 2006). Several stellar clusters have been detected, mostly younger than 10 Myr, and only one of them seems to be older than 10 Myr (Nakajima et al. 2005). A detailed study of the YSOs in this region have been conducted by Carlson et al. (2012), who estimate a large SFR in this region (combined with N159), higher than in other active star-forming regions of the LMC such as N11 or N44.

Heydari-Malayeri et al. (2002) describe the stellar content and structure of N160 using *Hubble Space Telescope* observations, revealing a high activity from newborn massive stars, with bright emission ridges, arcs and filaments, sculpted by shocks and stellar winds. They resolve the ionization front between the molecular cloud and the H II region created by the star cluster, which appears to be particularly dust-rich.

N180

N180 (also DEM323; Davies et al. 1976; Figure VI.6) is a bright compact H II region, ionized by the OB association LH117, described by Massey et al. (1989). Bica et al. (1996) estimated the age of

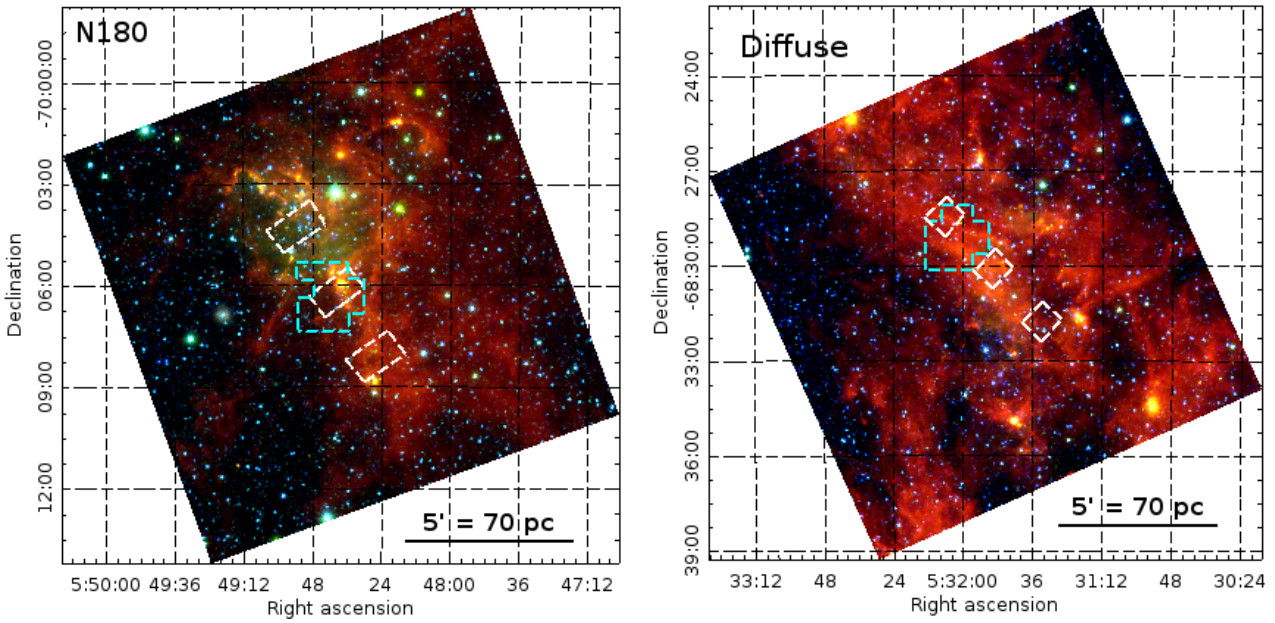

Figure VI.6: *Same as Figure VI.3 for the region N180 (left) and a more diffuse region (right) of the LMC.*

LH117 to be ⩽10 Myr. No X-ray emission is found toward N180 from XMM Newton observations (Snowden et al. in prep).

The effect of the OB association on the surrounding ISM can be seen in the distribution of PAHs, which show a decline in mass fraction where the radiation field is the highest, presumably indicating PAH destruction due to the hard radiation field. The internal kinematics of this H II region show local expansion around the massive stars, but no large-scale expansion or supernova remnant shocks have been detected (Nazé et al. 2001)

The "Diffuse" region

This region, shown in Figure VI.6, has been chosen to be more diffuse than the other LMC star forming regions. It does not contain massive OB associations and is still sufficiently bright to detect the FIR fine structure lines. It is included to compare and contrast with our brighter star forming regions.

N66

N66 is the largest and brightest nebula in the SMC (Henize 1956), covering an area of approximately 180″× 300″ on the sky, located within the main body of the SMC bar. The H_α luminosity is almost 60 times higher than that of the Orion nebula (Kennicutt 1984). N66 contains 33 O stars distributed across the H II region, which is about half the number for the entire SMC. Most of the ionization seems to be due to NGC346, the largest stellar concentration in the SMC (Dreyer 1888), with an age of ~3 Myr (Bouret et al. 2003). Several dozen O-type stars are confirmed in NGC 346 (Walborn & Blades 1986; Massey et al. 1989). The metallicity of the NGC346 cluster has been determined independently for individual O stars, forbidden line emission originating in the gas, and spectral models (Haser et al. 1998; Lebouteiller et al. 2008; Bouret et al. 2003) to be ~ 0.2 $Z_\odot$. Numerous other massive stellar clusters of similar ages, although somewhat fainter, are located across the region (Sabbi et al.

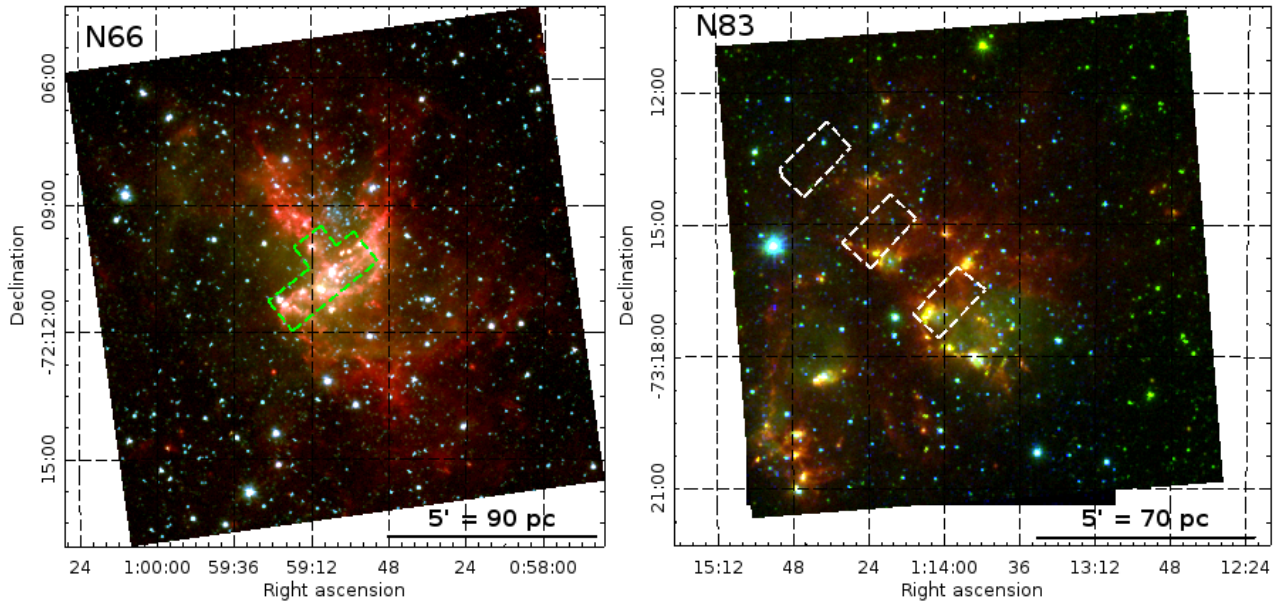

Figure VI.7: *Same as Figure VI.3 for the regions N66 (left) and N83 (right) of the SMC. The green contour overplotted on N66 outlines the PACS [O I] 63 μm coverage.*

2007). Gouliermis et al. (2006) built a stellar catalog from photometry observations using data of the Advanced Camera for Surveys (ACS) on board the HST. Star formation in N66 has been going on during the last 10 Myr and is currently ongoing, with about 100 embedded YSOs identified by Simon et al. (2007) and a further 263 candidate young stellar sources found by Gouliermis et al. (2010). Moreover, the region is characterized by several X-ray sources (Naze et al. 2003) and radio sources (Loiseau et al. 1987; Filipovi et al. 2002). This region is a typical example of mixed stellar populations in the low-metallicity environment of the SMC.

Spitzer photometry and spectroscopy observations have been presented by Lebouteiller et al. (2011) and Whelan et al. (2013), with particular emphasis on the PAHs, suggesting that PAH emission depends less on the metallicity than the dust emission, as the ratio $L_{PAH}/14\,\mu m$ is larger in N66 compared to that of 30Dor, for similar physical conditions. Rubio et al. (2000) showed a spatial correlation of the peaks of H_2, CO and PAH emission at 43″ resolution and suggest that the CO has been photo-dissociated across the region, existing only in small clumps. Israel & Maloney (2011) derive $G_{UV} \approx 1145$ for N66 using H_α measurements (a factor of ~ 7 lower using dust), and a ratio [C II]/CO of 6.4×10^4. More generally, over a sample of star-forming regions in the SMC, Israel & Maloney (2011) find [C II]/CO ranging between 10^4 and 8×10^4, with no clear trend of a higher ratio [C II]/CO in the SMC regions at lower metallicity compared to the LMC. More recently, Requena-Torres et al. (2016), based on GREAT on *SOFIA* and APEX observations of N66, showed that the bulk of the molecular gas mass in the SMC star-forming regions is relatively well traced by [C II]. We explore this further with our PACS observations and PDR modeling.

N83

Although the SMC Wing has a lower stellar and gas density that the bar, it contains some compact and intense H II regions such as the N83/N84 complex, presented in Figure VI.7, which is the most prominent H II region in the SMC Wing. It is illuminated by several early-type stars, and in particular the NGC456 stellar association (Testor & Lortet 1987). Israel & Maloney (2011) determined a G_{UV} approximately a factor of 3 lower in N83 than in N66. The X_{CO} factor has been determined to ≈

20-55 times the Galactic value by Leroy et al. (2009), using dust modeling. This is much more than the values determined from the virial masses via CO measurement (e.g. Bolatto et al. 2003; Israel et al. 2003), although the H_2 masses determined from dust and the dynamical masses from CO are both compatible with a model of a small CO core embedded in a larger H_2 cloud. As N83 was only observed in [O I] 145 μm with PACS, we do not attempt the modeling of this region.

VI.1.2 Line ratio empirical diagnostics

Excitation of the gas

For each region, L_{FIR} is derived as presented in Section III.1.1, using the dust SED fitting model of Galliano et al. (2011), at $\sim 12''$ resolution, from IRAC, MIPS and PACS photometry. As presented in Figure IV.4 for the integrated fluxes, the ratios [O III]/L_{FIR}, [O III]/[N II] and [O III]/[O I] in the Magellanic Clouds (MC) star-forming regions are higher than those of the more metal-rich galaxies of the Brauher et al. (2008) sample. This suggests the existence of hard radiation fields in these regions, due, for example, to the presence of high temperature stars, and a high filling factor of the ionized gas. This is also observed on smaller scales for each of the individual star-forming regions.

On resolved scales ($12''$), all of the regions have a ratio [O III]/L_{FIR} above 10^{-3} and up to 7×10^{-2} (Figure VI.8), while the galaxies of the Brauher et al. sample are generally between 10^{-4} and 3×10^{-3}. Some of these regions, in particular N44 and N159, clearly probe a wide variety of environments, as the ratio [O III]/L_{FIR} spans approximately one order of magnitude. This is mainly driven by a large range in [O III] 88 μm while L_{FIR} spans a more moderate range of values. N44 and N159 show among the lowest [O III]/L_{FIR} values in the sample, as well as the lowest [O III]/[O I] 63 μm values. Hence, the wide range of [O III] could be due to a wide range of filling factors of the PDR in the ionized gas.

Origin of [C II]

Figure VI.8 shows the ratio [O III] 88 μm/L_{FIR} as a function of the ratio [C II]/L_{FIR}. The total range of [C II]/L_{FIR} covered by all of the regions is about one order of magnitude, although each individual region spans a relatively restricted range of values (a factor of $\sim$ 2 or less), except for 30Dor, N11B and N160, showing more dispersed values. From this figure, we see that, for the majority of the regions, [O III] 88 μm is the brightest FIR fine-structure line, as opposed to [C II] more commonly for more metal-rich galaxies (e.g. Stacey et al. 1991). On the contrary, N180, the "Diffuse" region, and significant fractions of N44 and N157 show a ratio [O III] 88 μm/[C II] lower than unity. This suggests a higher filling fraction of the PDRs compared to the ionized gas in these regions. In the "Diffuse" region, we also expect the radiation field to be somewhat softer than in the other regions, as no massive star formation is present.

Except for N158, N160 and N66, all of the other regions are partially detected in [N II] 122 μm. We find a ratio [C II]/[N II] 122 μm $\geqslant$ 20 where [N II] is detected with good S/N for N159 and N180, and [C II]/[N II] 122 μm $\geqslant$ 30 for the "Diffuse" region, N11B, N44 and N157. However, the [N II] maps are generally of small spatial coverage, with moderate to low S/N and provide incomplete information. As in 30Dor (Chevance et al. 2016), and N11B (Lebouteiller et al. 2012), [C II] is expected to come mostly from the PDR in these star-forming regions of the MC, as we demonstrated in Section IV.1.2 for the similarly high values of [C II]/[N II] in 30Dor. This idea is also strengthened by the fact that, in Galactic star-forming regions, for example, the contribution of the ionized gas to the [C II] emission is small ($\lesssim$ 10%; e.g. Stacey et al. 1991), and this proportion is expected to decrease with metallicity,

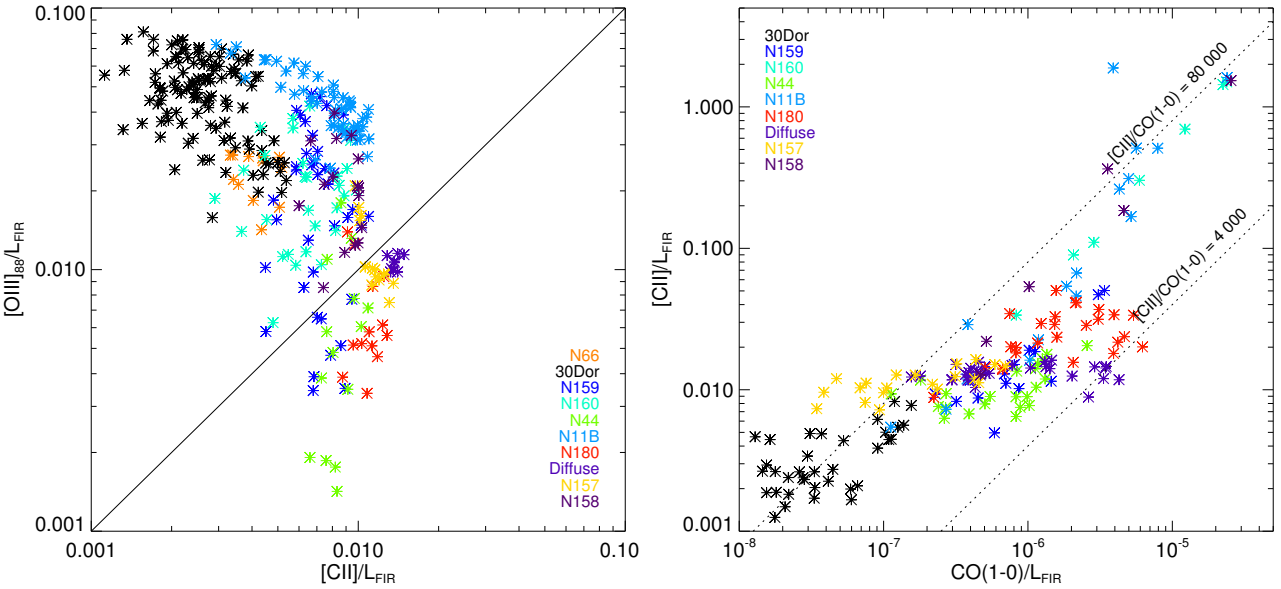

Figure VI.8: *Left:[O III]/L_{FIR} as a function of [C II]/L_{FIR} for the star-forming regions of the MC mapped with PACS. The solid line indicates the ratio [O III]/[C II] = 1. For most of the regions, [O III] is brighter than [C II]. Right: [C II]/L_{FIR} as a function of CO(1-0)/L_{FIR}. The dotted lines indicate the ratios [C II]/CO(1-0) = 4,000 and 80,000. This is the equivalent of Figure V.2 (integrated values for galaxies) for the spatially resolved star-forming regions of the LMC. Metal rich starbursts and spiral galaxies are mostly located below the [C II]/CO(1-0) = 4,000 ratio, while integrated dwarf galaxies, are located above this ratio, as do the individual regions studied here.*

since models show that the C^+ column in H II regions decreases with Z while the C^+ column in the PDR remains almost constant (Maloney & Wolfire 1997; Kaufman et al. 2006). Therefore, we do not attempt to correct for the (rather small) fraction of [C II] from the ionized gas when using the [C II] emission line as a tracer of the PDRs and as a constraint for the PDR model (Section VI.2.1).

As already noted, the ratio [C II]/CO(1-0) is generally higher in dwarf galaxies compared to metal-rich galaxies (e.g. Figure V.2; e.g. Stacey et al. 1991; Madden et al. 2013). Figure VI.8 (right) shows the ratio [C II]/L_{FIR} as a function of CO(1-0)/L_{FIR} for the MC, where the CO(1-0) observations for the LMC regions are from the Mopra telescope, at 43″ resolution (Wong et al. 2011). Individual star-forming regions of the LMC all show ratios [C II]/CO(1-0) higher than 4000, with a dispersion of 2 orders of magnitudes. There is a good correlation between increasing [C II]/CO(1-0) and increasing CO(1-0)/L_{FIR} in most of the regions, except for N11B, N160 and the "Diffuse" region. Israel et al. (1996) find variations of the [C II]/CO(1-0) ratio of almost 3 orders of magnitude between LMC clouds, as well, possibly reflecting the evolutionary states of the clouds. Indeed, more evolved regions such as 30Dor, N11B and N160 show higher [C II]/CO(1-0) ratios than more quiescent regions such as our "Diffuse" region and N159S from Israel et al. (1996), which have lower values. On the small scales probed here, wide ranges of the [C II]/CO(1-0) ratio are also visible within the individual regions (approximately one order of magnitude or more for 30Dor, N44, N157, N159, N180 and the "Diffuse" region). The CO(1-0)/L_{FIR} ratios in N11B and N158 span more than 2 orders of magnitude, with a comparatively smaller dispersion of the [C II]/CO(1-0) ratios.

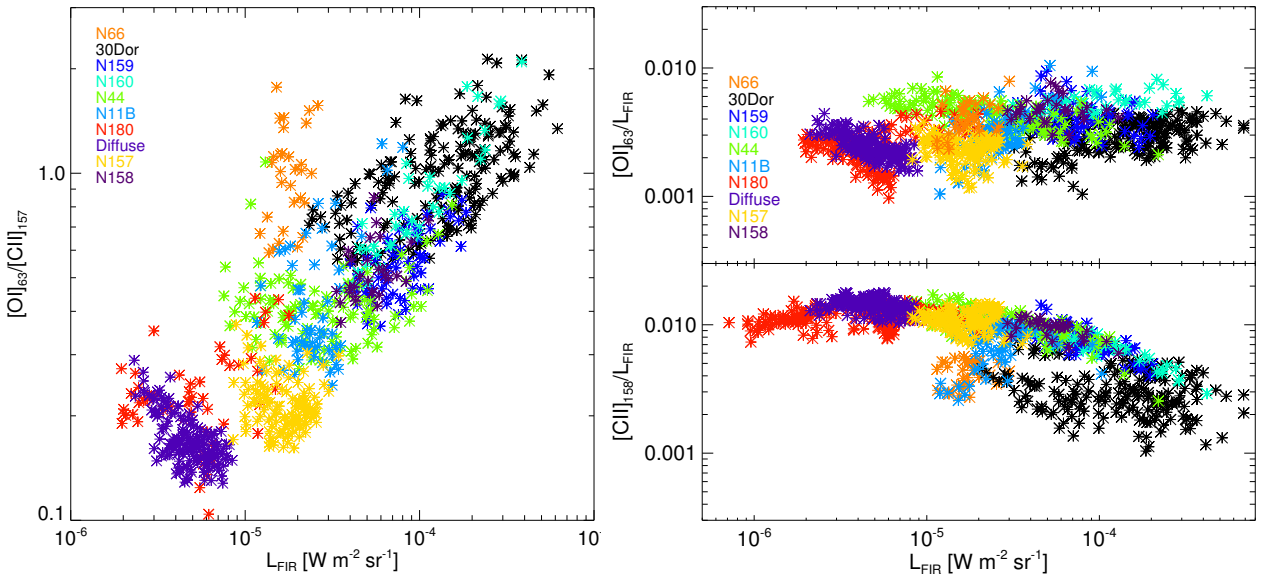

Figure VI.9: *Left: [O I] 63 μm/[C II] as a function of L_{FIR} for the star-forming regions of the MC mapped with PACS. Right: [O I] 63 μm/L_{FIR} and [C II]/L_{FIR} as a function of L_{FIR}.*

Photoelectric heating efficiency

From the considerations presented above, concluding the origin of [C II] from PDRs, [O I] 63 μm and [C II] can both trace the PDRs. Although no trend between [O I] 63 μm/[C II] and L_{TIR} was apparent in Figure IV.5 on global scales, we see in Figure VI.9 a clear correlation between the ratio of these two cooling lines and L_{FIR}, on $\sim$ 3 pc scales, for the selected LMC regions. On global scales, [O I] 63 μm/L_{FIR} and [C II]/L_{FIR} both decrease similarly with L_{FIR}, which cancels out any correlation of [O I] 63 μm/[C II] with L_{TIR} (e.g. Cormier et al. 2015). When zooming in to star-forming regions in the MC, the ratio [O I] 63 μm/[C II] is on average higher (see Figure IV.5), as expected, since [O I] 63 μm dominates the cooling over [C II] for high densities and high radiation fields (e.g. Wolfire et al. 2003; Kaufman et al. 2006), and the rather small regions targeted here are missing the [C II] emission from the more extended, diffuse regions. In addition, L_{FIR} is expected to scale roughly with the the intensity of the radiation field, which is in agreement with the correlation in the left panel of Figure VI.9.

This correlation is driven by the decreasing [C II]/L_{FIR} with increasing L_{FIR} , while [O I] 63 μm/L_{FIR} remains relatively flat with L_{FIR} as shown in the right panel of Figure VI.9. This is a first hint towards the results of the PDR modeling presented in Section VI.2.1. N66, of the SMC, seems to be slightly offset from the [O I] 63 μm/[C II] correlation of the LMC sources. This ratio is higher for a given L_{FIR}, suggesting a denser medium and a stronger radiation field in N66. The fact that we measure a given ratio [O I] 63 μm/[C II] for a lower L_{FIR} compared to the LMC sources could also be an effect of a reduced dust abundance in the SMC compared to the LMC. Indeed, G/D is estimated to be 1200 for the whole SMC, and 380 for the LMC (Roman-Duval et al. 2014), while the C/O elemental abundance ratio is only slightly lower in the H II regions of the SMC compared to those of the LMC (Pagel 2003).

As seen for the case of 30Dor (Figure IV.5), the correlation between [O I] 63 μm/[C II] and L_{FIR} is also visible for most of the individual regions where several environments are probed, such as 30Dor, N11B, N44, N158, N159, N160, N180. It is less clear for the "Diffuse" region and N157, which seem to be more homogeneous. Although there is a large scatter, this ratio probes the existence of widely different physical conditions in the PDRs.

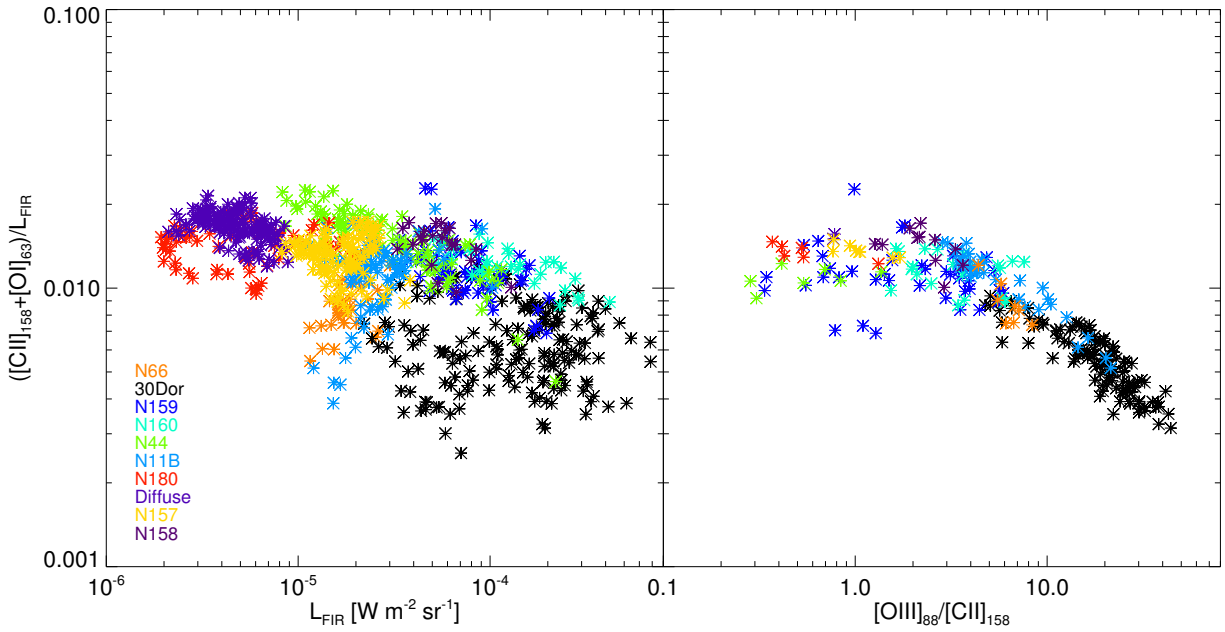

Figure VI.10: *Left: ([O I] 63 μm+[C II])/L_{FIR} as a function of L_{FIR} in the MC regions. Right: ([O I] 63 μm+[C II])/L_{FIR} as a function of [O III] 88 μm/[C II].*

Figure VI.10 shows the ratio ([O I] 63 μm+[C II])/L_{FIR} as a function of L_{FIR} for the individual star-forming regions of the MC. As noted in Section IV.1.3, this ratio can be considered to be a probe of the heating efficiency of the photoelectric effect on dust grains. The values measured here are around 1%. Globally, as well as for most of the individual regions, there is a significant scatter and we see a decrease of the ratio ([O I] 63 μm+[C II])/L_{FIR} with increasing L_{FIR}. 30Dor shows somewhat lower values of the ratio ([O I] 63 μm+[C II])/L_{FIR} ($\leqslant$ 1%) compared to the other regions. However, we show in Section IV.1.3 that a significant fraction (30 to 70% throughout the map) of L_{FIR} is arising from the ionized gas and needs to be subtracted to probe the heating efficiency of the photoelectric effect on dust grains in PDRs.

As in the case of 30Dor, we test the hypothesis that the scatter observed for the other MC regions is due to contamination of L_{FIR} by emission of grains in the ionized gas (right panel of Figure VI.10). For 30Dor, N11B, N158, N160 and N66, the ratio ([O I] 63 μm+[C II])/L_{FIR} shows a rather tight correlation with the ratio [O III] 88 μm/[C II], which is an indicator of the ionization state of the gas. For these regions, there seems to be a significant contribution from the ionized gas to L_{FIR}. On the contrary, there is no correlation between ([O I] 63 μm+[C II])/L_{FIR} and [O III] 88 μm/[C II] for N159 and the scatter cannot be explained only by contamination of L_{FIR} by the ionized gas.

VI.2 PDR modeling

VI.2.1 Analysis of the individual regions

As a first step, we use the Meudon PDR code to determine the spatial distribution of the parameters G_{UV} and P in each star-forming region of the LMC and SMC described above, at 12″ resolution. We

use the method described in Section III.4.2 to constrain the physical conditions of the gas in the PDRs using the ratios ([O I] 145 μm+[C II])/L_{FIR} and [O I] 145 μm/[C II]. The goal is to extend the method tested on 30Dor to other regions and try to understand what local parameters play an important role on the deduced quantities. We present here preliminary results of this study.

Input parameters

These other regions in the LMC and the SMC are in general not as well studied as 30Dor. In particular, their individual gas phase abundances are not known accurately for most of them. Therefore we use grids of models from the Meudon PDR code calculated at half-solar metallicity for the regions of the LMC and at $0.2\,Z_\odot$ for the SMC: the abundance of each element, as well as the abundance of dust, is decreased by a factor of 2 and 5 for the LMC and SMC, respectively, compared to the Milky Way value (see Table III.1). The difference of the abundance ratio C/O, in particular, between the Milky Way and the LMC, as well as variations of the G/D throughout the LMC, are thus not taken into account. For 30Dor, using the half-solar metallicity model instead of the model using the adapted 30Dor abundances results in a higher G_{UV} (by a factor of ~ 1.8) and a slightly higher pressure (by a factor of ~ 1.2). This is due to the fact that the predictions for the ratio [O I] 145 μm/[C II], which is the main constraint for the pressure, are mostly unchanged. However, the ratio ([O I] 145 μm+[C II])/L_{FIR}, which is the main constraint for G_{UV}, is shifted towards higher values for a given G_{UV} and P. Therefore, accurate relative elemental abundances should certainly be taken into account, if possible, for a more accurate study of the individual regions. However, we note that the resulting fraction of CO-dark gas (Section VI.3.1) is essentially unchanged.

Contrary to the study of 30Dor, for these regions, we are not able to use the method described in Section III.1.3 for the decomposition of L_{FIR} in a component arising from the ionized gas and a component arising from the neutral gas, for several reasons. Indeed, the IRS spectra are not available for all of the sources and therefore L_{PAH} cannot be calculated directly. Alternatively, the method presented in 30Dor to calculate L_{PAH} from the IRAC bands is partly built on empirical basis (for the masking of the pixels dominated by the stellar component for example) and would require more investigation before being applicable to other regions. Additionally, the spatial coverage of the [O III] 88 μm map is, in many cases (for the "Diffuse" region, N44, N157 and N180), only a single raster pointing, which is not sufficient to provide a reliable decomposition over the entire map. Therefore, to be consistent between the different regions and to be able to compare them, we decide to constrain the PDR model using the total L_{FIR}, keeping in mind that a fraction of L_{FIR} can arise from the ionized gas. We note here that the subtraction of L_{FIR}^{IG} from the total L_{FIR}, as we have done for the 30Dor modeling, is not commonly done in PDR models described in the literature: PDR models are often compared to the total L_{FIR}, although a fraction of it can come the the ionized gas phase.

To estimate roughly the fraction of L_{FIR} emitted from the ionized gas, we examine the following decomposition, equivalent to Equation III.3 we use for 30Dor:

$$L_{FIR} = L_{FIR}^{PDR} + L_{FIR}^{IG} = \alpha \times (L_{[O\,I]63} + L_{[C\,II]}) + \beta \times L_{[O\,III]88}. \quad \text{(VI.1)}$$

([O I] 63 μm+[C II]) is used as a tracer of the PDRs, instead of the PAH luminosity and [O III] 88 μm as a tracer of the ionized gas. For each region, the relation between [O III]/L_{FIR} and ([O I] 63 μm+[C II])/L_{FIR} is shown in Figure VI.11. In each panel, we specify the value ([O I] 63 μm+[C II])/L_{FIR} = 1% with a doted vertical line, which is a typical value for the photoelectric heating efficiency (e.g. Bakes & Tielens 1994; Weingartner & Draine 2001b). Ratios ([O I] 63 μm+[C II])/L_{FIR} below this value can suggest that dust grains probed by L_{FIR} do not dominate the neutral gas heating. This can indicate the

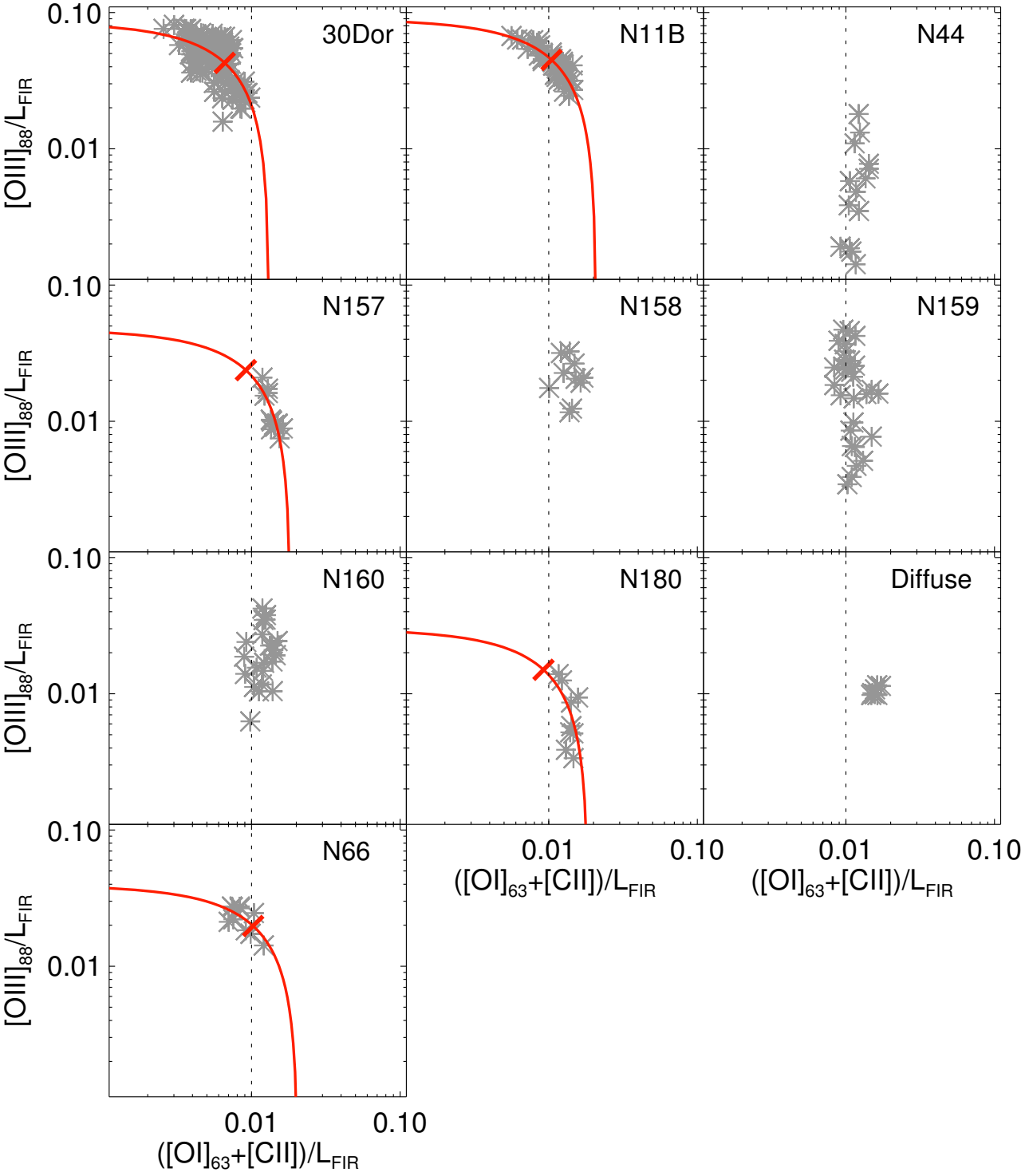

Figure VI.11: *[O III]/L_{FIR} as a function of ([O I] 63 µm+[C II])/L_{FIR} for the MC star forming regions. When possible, the best linear fit is represented in red (see text for details). At the position of the perpendicular red mark, 50% of L_{FIR} is expected to come from the PDR. The dotted vertical line indicates the value ([O I] 63 µm+[C II])/L_{FIR} = 1%.*

contribution of a significant component from the ionized gas to the total L_{FIR}, for example, thus not contributing to the heating of [O I] and [C II]. When the number of points is sufficient and where there is a dependency of ([O I] 63 μm+[C II])/L_{FIR} with [O III]/L_{FIR}, we fit a linear regression:

$$\frac{L_{[O\,III]88}}{L_{FIR}} = \frac{1}{\beta} - \frac{\alpha}{\beta} \times \frac{L_{[O\,I]63} + L_{[C\,II]}}{L_{FIR}}. \quad \text{(VI.2)}$$

This is represented by a solid red curve in Figure VI.11.

We note that most of the values ([O I] 63 μm+[C II])/L_{FIR} are above the 1% threshold. For N11B and N66, in particular, it seems that a significant fraction of L_{FIR} is due to a component from the ionized gas. However, the number of pixels for each region is small and there is a significant dispersion. Hence, the quantitative prediction of this diagnostic is limited and we do not try to apply a correction factor to L_{FIR} contrary to what we did for 30Dor.

In 30Dor, [O I] 63 μm is overestimated by our best model prediction by a factor of 2 to 3 throughout the map (Section IV.2.1; Chevance et al. 2016). We attribute this discrepancy to the optical thickness of the [O I] 63 μm line. As a result, [O I] 63 μm may not be a reliable constrain for the modeling and we prefer using [O I] 145 μm, when possible. The regions N158 in the LMC and N66 in the SMC have not been observed in [O I] 145 μm with PACS. We thus use the ratios ([O I] 63 μm+[C II])/L_{FIR} and [O I] 63 μm/[C II] as constraints for the models. To test possible optical depth effects of the [O I] 63 μm line, we also model the case where we increase the [O I] 63 μm line intensity by a factor of 2 (see below).

Results

The resulting spatial distributions for G_{UV} and P for each region are presented in Figures VI.14 to VI.22. As in 30Dor, the model-predicted [O I] 63 μm line intensity is over-estimated, by a factor of $\sim$ 1 to 3 throughout all of the regions. This factor is correlated with P, therefore this discrepancy is likely to be due to optical depth effects of the [O I] 63 μm line. For N158 and N66, where the [O I] 145 μm line was not observed with PACS, we have to keep in mind that [O I] 63 μm is probably under-estimated when using it as a model constraint.

The comparison between the ranges in G_{UV} and P for the different regions is shown in Figure VI.12. As expected, G_{UV} scales roughly with L_{FIR}. Some of these regions span a large range of G_{UV} and P. The region N11B, for example, probes a large range of environments: G_{UV} varies by more than 2 orders of magnitude throughout the map and P by more than an order of magnitude. On the contrary, although the 30Dor map is large, the ISM properties are relatively homogeneous there.

We see that the different star-forming regions studied populate a restricted range of the G_{UV}-P grid, with G_{UV} increasing with P. Ratios G_{UV}/P are on average between 10^{-3} and 10^{-4}. This can be due to the nature of the regions studied. Indeed, most of them are active star-forming regions, with signs of recent and current star formation. We see that the lower metallicity N66 shows a higher ratio G_{UV}/P and is offset from the correlation. However, when the [O I] 63 μm line intensity is multiplied by a factor of 2, for example, to take into account possible optical depth effects, we find a more moderate ratio G_{UV}/P and the model results for N66 move closer to the G_{UV}-P correlation. For N158, multiplying the [O I] 63 μm line intensity by a factor of 2 does change the values of G_{UV} and P significantly, although the ratio G_{UV}/P remains approximately constant.

Other types of environments, not observed here, could probe other regions of the G_{UV}-P plane. For example, infrared dark clouds (IRDC), which are thought to be the progenitors for massive stars and star clusters, are known to have high surface densities ($\sim 10^3 - 10^5$ cm^{-3}), similar to or above the

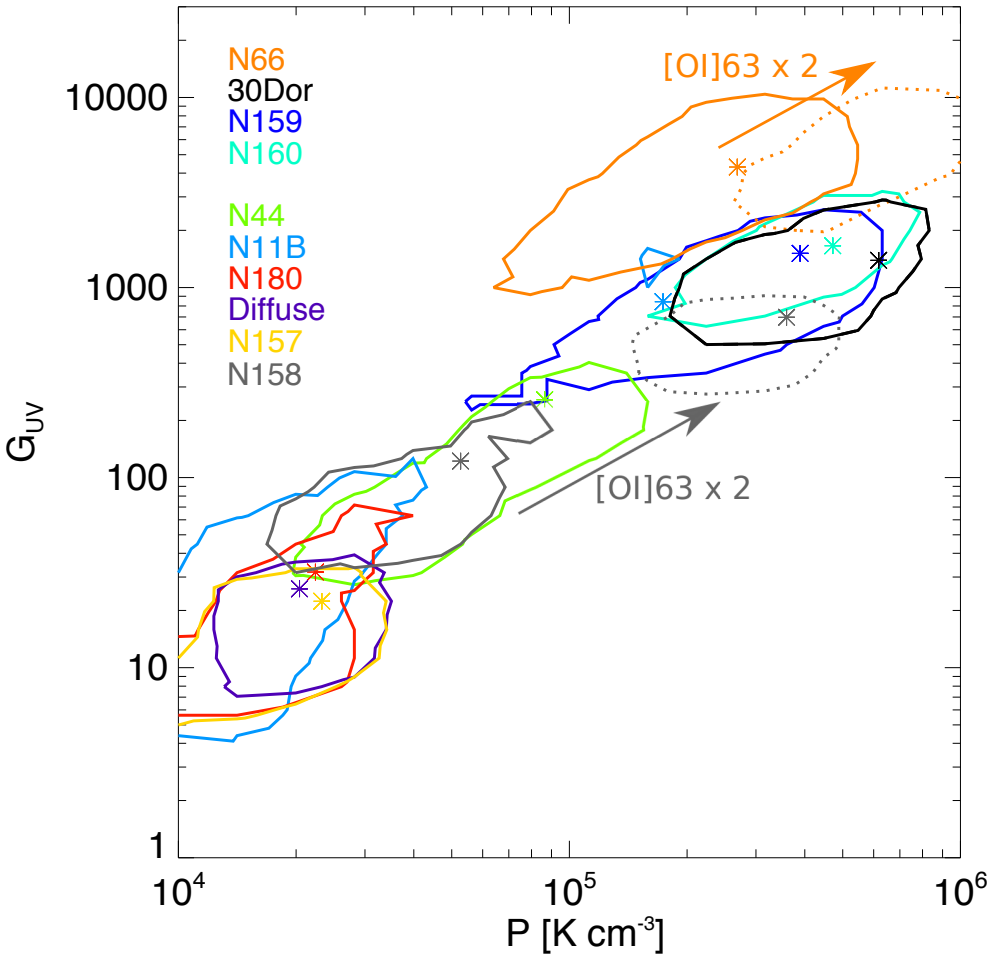

Figure VI.12: *Best model parameters, G_{UV} and P, for the star-forming regions of the LMC and SMC. The solid contours indicate the location of 75% of the pixels for a given region. The star symbols indicate the parameters of the best model set for each of the integrated maps. The dashed orange and grey contours indicate the location of 75% of the pixels for N66 and N158, respectively, if we assume that [O I] 63 µm is affected by opacity effect, and multiply the observed intensity by a factor of 2 correcting for this effect. Note that for N66 and N158, the optically thin [O I] 145 µm was not observed (see text).*

measured values for 30Dor. Beuther et al. (2014), for example, estimate the external radiation field, G_{UV}, for four IRDC, using the dust temperature, to approximately a few 10s to a few 100s. These objects, for example, would thus lie at the bottom right of the G_{UV}-P plane.

The position of each region in the G_{UV} -P plane, does not seem to be linked with the age of the region. Indeed, 30Dor, which contains an older population of 10-20 Myr (Selman & Melnick 2005) and N157, which is probably 1-2 Myr (Jones et al. 2005) have similar values of G_{UV} and P.

VI.2.2 Remarks on the resolution effect

One of the goals of this study is to determine what kind of environment dominates the properties of the ISM at large scale. If we do not have the high spatial resolution as we do here for the MC, for example when looking at high redshift galaxies, all of these different regions would be mixed into one single

beam, with the consequence of more diffuse gas and dust being included in the single beam as well. In this case, what kind of environment drives the galactic properties at large scales? In other words, what would be the resulting properties that we would derive for a mix of several environment? Would the integrated LMC have properties similar to 30Dor, which is the brightest source of the galaxy? Or would it be more like diffuse regions which represent the major part of the galaxy? Alternatively, it can also be a combination of these different environments.

On the scales of our star-forming regions (a few tens of parsecs), we test this effect by re-doing the PDR modeling with flux ratios integrated over the size of the overlapping area between the [O I] 145 μm and the [C I] 370 μm map (this is the area where we will be able to estimate the CO-dark molecular gas mass; see Section VI.3.1). The solution parameters thus determined are represented as star symbols for the integrated regions in Figure VI.12. We note that the parameters for the integrated observations are biased toward high P and high G_{UV} solutions compared to the distribution of most of the P and G_{UV} solutions for the maps, as indicated by the contours in Figure VI.12. This is particularly noticeable for N11B. A small number of pixels at high G_{UV} ($\sim 10^3$) and high P ($\sim 2\times10^2$ cm^{-3}) drive the integrated solution toward these values, while the large majority of the map have more moderate values ($G_{UV} \geqslant 100$ and P $\geqslant 10^4$ cm^{-3}).

Furthermore, our study is done at $\sim$ 3 pc resolution (12″). At these scales, there is a chance that the ISM is not homogeneous and that we mix dense clumps and a more diffuse inter-clump medium within the PACS beam (for example, CO clumps observed with *ALMA* in 30Dor can be less than 1 pc; Indebetouw et al. 2013). This is even more important for the estimation of the CO-dark molecular gas fraction, at 45″ ($\sim$ 10 pc) or more. Hence, although we have assumed in our study that the [C II], [C I] and CO emission are associated with the same structures, this is not necessarily the case. Indeed, the recent study of the N159 region by Okada et al. (2015), for example, reveals that up to 50% of the [C II] emission is not associated with the CO emission based on the velocity profiles of the lines. In this case, a two-phase model could be a more accurate way of describing the PDRs in the star-forming regions. However, testing the clumpiness of the medium requires many parameters to reproduce the geometry of the region: a distribution of clouds of different sizes and pressures, illuminated by a distribution of sources and including the effect of scattering and shielding, for each pixel of the map. Unfortunately, such a scenario cannot be properly modeled yet because of the lack of observational constraints.

VI.3 The CO-dark gas

VI.3.1 Preliminary results

We try to understand, in particular, the effect of different physical conditions affecting the CO-dark gas fraction, from the point of view of our PDR modeling, as we have demonstrated for 30Dor (Section V.2.2). Therefore, we integrate the observed emission lines over the areas were [O I] 145 μm (respectively [O I] 63 μm for N158 and N66) and [C I] 370 μm overlap. [C I] is necessary for this step to bring a constraint on A_V^{max}. These are the most constraining maps for the spatial coverage as [O I] 145 μm is often the smallest of the PACS map (apart from [N II] 122 μm), and since the SPIRE/FTS pointing for the [C I] does not necessarily cover the entire PACS maps (see Figures VI.3 to VI.7). We then calculate G_{UV}, P and A_V^{max} as described in Section III.4.2, using the ratios ([O I] 145 μm+[C II])/L_{FIR} and [O I] 145 μm/[C II] and [C II]/[C I] 370 μm as constraints. The results are presented in Table VI.1. We then calculate the total mass of H_2, M_{H_2}, and compare it with the molec-

Table VI.1: Results of the PDR modeling of the integrated regions of the Magellanic Clouds.

Region	G_{UV}	P [cm^{-3}]	A_V^{max} [mag]	M_{H_2} [$M_\odot\,pc^{-2}$]	$\alpha_{CO}/\alpha_{CO,MW}$	$M_{dark\ gas}$ [$M_\odot\,pc^{-2}$]	$F_{dark\ gas}$ %
Diffuse	26	2.04×10^4	1.2	93	2.84	60.4	65
N11B	842	1.74×10^5	1.9	77	2.62	47.8	62
N44	257	8.65×10^4	1.8	280	2.54	169.0	61
N157	240	2.33×10^4	0.9	297	14.60	276.0	93
N158[a]	122	5.27×10^4	1.2	312	13.50	289.0	92
N159	1513	3.89×10^5	2.1	143	1.19	22.7	16
N160	1659	4.70×10^5	1.7	132	3.81	97.2	74
N180	31.8	2.24×10^4	1.2	95.6	3.77	70.2	73
30Dor	1390	6.18×10^5	2.7	194	10.20	175.0	90
N66[a]	4305	2.69×10^6	3.0	35	–	–	–

Note that we could not determine the α_{CO} and $M_{dark\ gas}$ for N66 due to lack of observational constraints. [(a)] For the regions N158 and N66, we present here the results of the model constrained with the ratios ([O I] 63 μm+[C II])/L_{FIR} and [O I] 63 μm/[C II], because the [O I] 145 μm was not observed. We caution, though, that the [O I] 63 μm line is likely to be optically thick (see text).

ular gas mass obtained from the CO(1-0) luminosity and $\alpha_{CO,MW}$. The estimated α_{CO} adapted for the region, the mass of CO-dark molecular gas, $M_{dark\ gas}$, along with the fraction of dark gas, $F_{dark\ gas}$, for each region, are also listed in Table VI.1.

Except for N159, which has a moderate fraction of CO-dark molecular gas mass (16%), all of the other regions have $F_{dark\ gas} > 50\%$, which would be the result if X_{CO} was simply scaled with the metallicity ($0.5\,Z_\odot$ for the LMC). The fraction of CO-dark gas is not correlated with G_{UV} nor with the ratio G_{UV}/P. We do not see any trend of $F_{dark\ gas}$ with A_V^{max}, although we note that our sample spans a relatively small range in A_V^{max} (0.9 to 3 mag). On the other hand there could be a link between the fraction of CO-dark gas and the age of the region. For example, N159 is a relatively young star-forming region, and has a low $F_{dark\ gas}$, while 30Dor, N157 and N160, for example, are more evolved. However, our sample is relatively small and this still must be confirmed.

Our sample of star-forming regions in the LMC and SMC spans a relatively wide range of X_{CO}, from $1.2\,X_{CO,MW}$ to $14.6\,X_{CO,MW}$. For the large ensemble of GMCs in the LMC observed as part of the Magellanic Mopra Assessment (MAGMA) survey, Hughes et al. (2010) derive an average $X_{CO} = 4.7\times10^{20}\,cm^{-2}\,(K\,km\,s^{-1})^{-1}$, i.e. $2.35\,X_{CO,MW}$ from virial masse estimates, which is included in our range of X_{CO}. Our range of X_{CO} also includes the values found by Jameson et al. (2016) (~ 2 and $\sim 17\,X_{CO,MW}$ for the LMC and SMC, respectively), assuming a constant depletion time as well as the values of Leroy et al. (2011) (~ 1.5 and $\geqslant 12\,X_{CO,MW}$ for the LMC and SMC, respectively), using a dust-based method. Roman-Duval et al. (2014), based on dust modeling at 1′ resolution, determined a maximum value of $X_{CO} = 3\,X_{CO,MW}$ for the LMC (which is below our highest values of X_{CO}) and $X_{CO} = 20\,X_{CO,MW}$ for the SMC. However, for studies based on dust modeling, the assumption of a constant G/D as well as the wavelength range covered can affect the derived X_{CO}. In addition, as the effect of resolution is important, it is difficult to compare with other studies at different resolutions. For example, assuming a constant G/D of 350 across the N11 region, following Rémy-Ruyer et al. (2014) scaling of the G/D with the metallicity, Galametz et al. (2016) find a range of X_{CO} from $5.2\times10^{20}\,cm^{-2}\,(K\,km\,s^{-1})^{-1}$ up to $4.9\times10^{21}\,cm^{-2}\,(K\,km\,s^{-1})^{-1}$ (corresponding to 2.6

to 25 $X_{CO,MW}$) at 36″resolution. For N159, we find a value about 1/2 of that found by Galametz et al. (2013), who use a constant G/D at 45″ resolution. They find that the value $X_{CO} = 2.3\, X_{CO,MW}$ minimizes the scatter of the G/D.

These preliminary results show large fractions of molecular gas mass not coincident with the CO-emitting region ($16\% \leqslant F_{\rm dark\ gas} \leqslant 93\%$). This results in great local variations in the X_{CO} factors within the LMC. Although the metallicity of the LMC is not thought to vary much across the galaxy, this limited experiment demonstrates that the X_{CO} factor can vary over a factor of at least ~ 8 in selected regions. This work will continue to be finalized for presentation in a paper published in A&A.

VI.3.2 Proposal for *ALMA* cycle 4 observations

As was shown for 30Dor, high spatial and spectral resolution is crucial to resolve individual molecular clumps to probe the effective molecular mass, in particular in low metallicity environments. Thus, we proposed to observe [CI] 609 μm, ^{12}CO(2-1) and dust emission at $\approx 620\,\mu$m with *ALMA* in the LMC, to chart the PDR transition layers for C^o to the CO cores at 0.2 pc scales. This proposal has been accepted for cycle 4 observations, with priority grade B (P.I Chevance).

From our dust and PDR modeling on large scales (resp. 40″$\approx$ 10 pc and 20″$\approx$ 5 pc; Hony et al. 2010), we find that N44 and N159 probe a wide enough range of physical conditions and of CO-dark gas mass fractions (at such resolutions) to provide an ideal test for CO-dark gas determination at sub-parsec scales. These observations will bring enough constraints to probe the physical conditions of the individual sub-pc clouds by comparison with the Meudon PDR code predictions.

The proposed regions N44 and N159 show evidence for various fraction of CO-dark gas (61% and 16%, respectively) on $\approx$ 10 pc scales (40″). The spatial (0.9″) and spectral (0.3 km.s^{-1}) resolution of *ALMA* will allow us to compare the spatial and velocity structures of C^o and CO and their size-linewidth relation to see how the molecular cloud cores and the outer layers are related and identify the origin of C^o with a possible component from the interclump medium. We will calculate the physical properties of the clouds (P, G_{UV}, A_V and filling factor) by comparing the observations with the Meudon PDR code predictions for [CI] 609 μm, ^{12}CO(2-1), and dust emission around 620 μm. We will derive H_2 column densities using ^{13}CO(2-1) and determine the H_2 mass assuming the clouds are virialized. We will then compare these virialized mass measurements, at 0.2 pc scale, with the H_2 determined by our PDR model, at 10 pc scale with *Herschel*, and identify effects of the resolution. In addition, from the observed ratios [CI]/^{12}CO(2-1) at these resolved scales, we will quantify the CO-dark gas/H_2 traced by CO and compare with that determined from the CO alone. The results in these two very different environments will allow us to benchmark the use of the ratio [CI]/^{12}CO(2-1) as an indicator of the CO-dark gas reservoir.

For both regions, we choose to point at the [CI] 609 μm peak of the FTS map (Fig. VI.13). For N44 we select a 20″$\times$ 20″ region within the FTS beam, where the CO-dark gas is expected to be the most prominent based on our PDR modeling at 12″ resolution (Section VI.2.1). For N159, we also partly rely on the existing ^{12}CO(2-1) and ^{13}CO(2-1) *ALMA* observations at 1″ resolution (Fukui et al. 2015a). Furthermore, the population of YSOs and OB associations are known in these regions (Oey & Massey 1995; Whitney et al. 2008; Chen et al. 2009; Carlson et al. 2012; Sewiło et al. 2013), which will allow us to fold the effect of different evolutionary stages between the two regions into our study, with molecular clouds being increasingly photodissociated with time. Additionally the complex dust distribution and radiation field in both regions have been modeled in detail by us (Hony et al. 2010; Galametz et al. 2013), allowing us to put limits on the extinction and relate these to PDR ages.

This experiment will go beyond our *ALMA* cycle 3 observations of [CI] 370 μm and CO(7-6) in

the extreme 30Dor region, presented in Section V.4, to study the structure of the peak PDR region around the SSC R136.

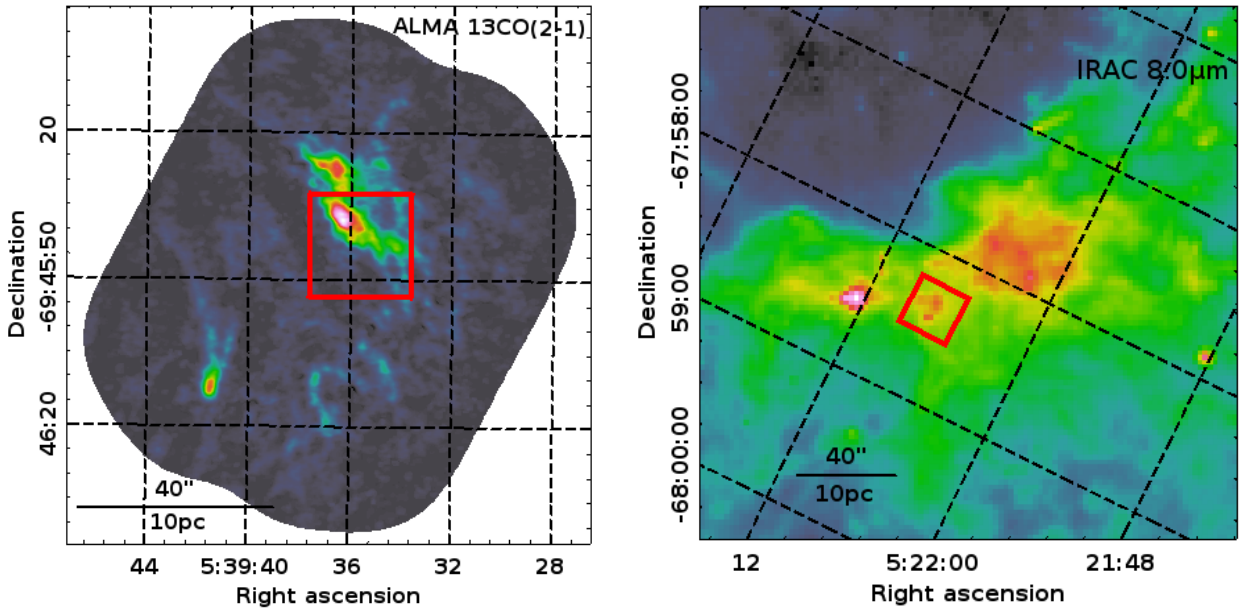

Figure VI.13: *Left: zoomed-in view of N159W with ALMA* ^{13}*CO(2-1) observations Fukui et al. (2015a) with the proposed region for [C*I*] 609 μm observations outlined in red. Right: position of the proposed [C*I*] 609 μm mosaic for N44 overlaid on the IRAC 8.0 μm map*

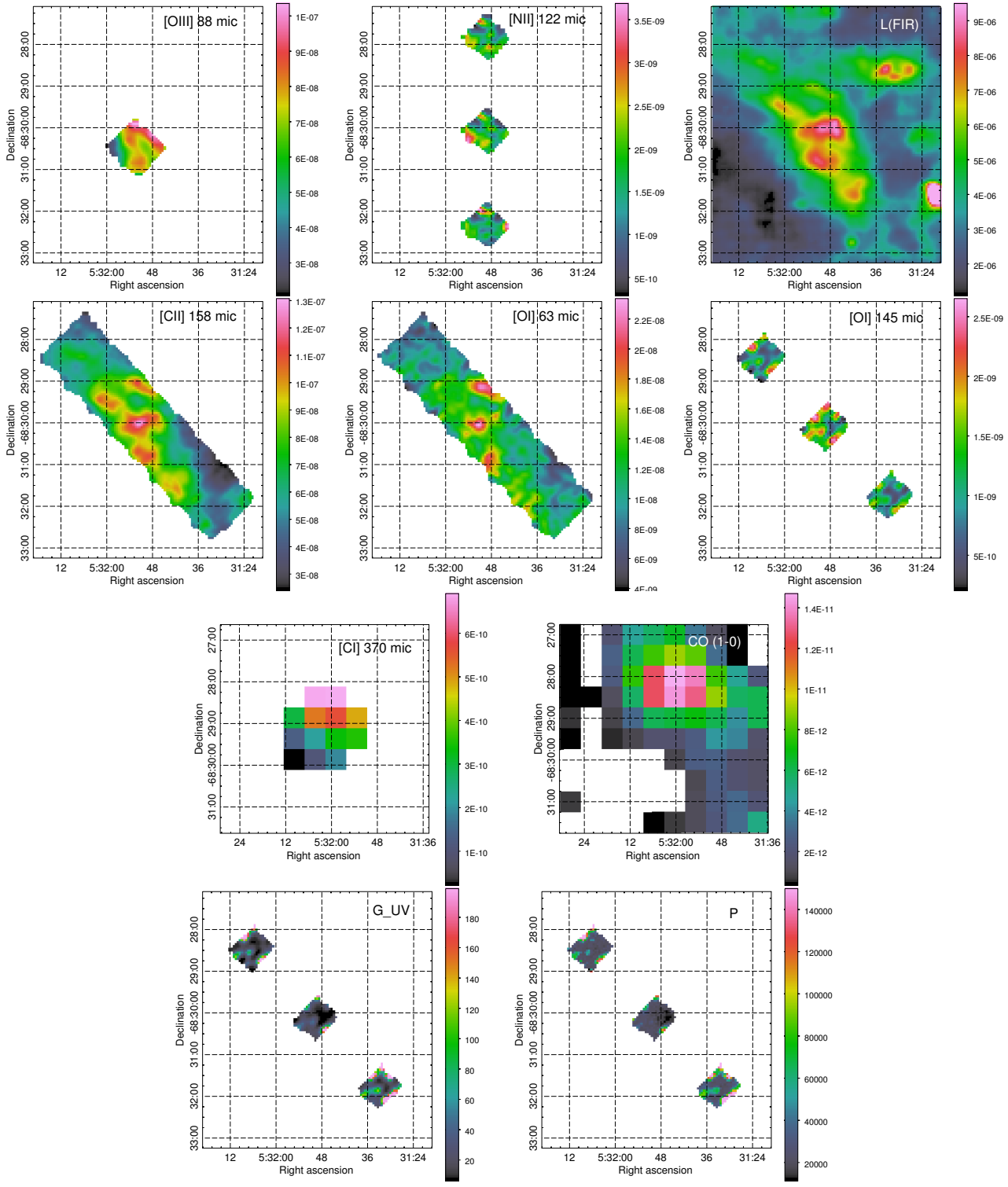

Figure VI.14: *Maps of the ionized gas tracers and PDR tracers from Herschel (PACS and SPIRE/FTS) and Mopra CO(1-0) observations (Wong et al. 2011) of the "Diffuse" region in the LMC, in W m^2 sr^{-1}. The two bottom panels show the preliminary results of our constant pressure PDR modeling of this region at 12″ resolution, G_{UV} (in units of the Mathis field, Mathis et al. 1983), and P in cm^{-3}.*

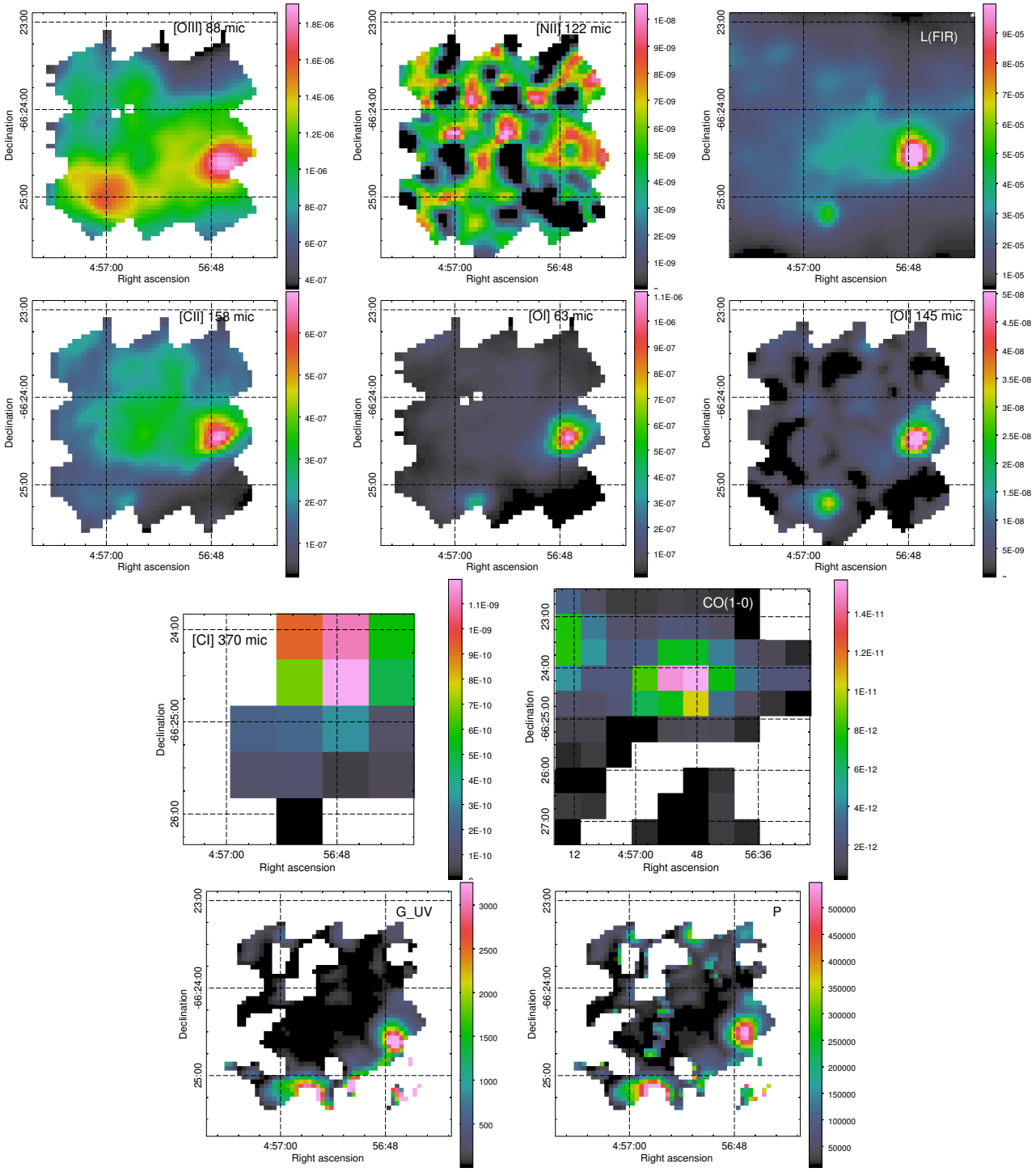

Figure VI.15: *Same as Figure VI.14 for N11B.*

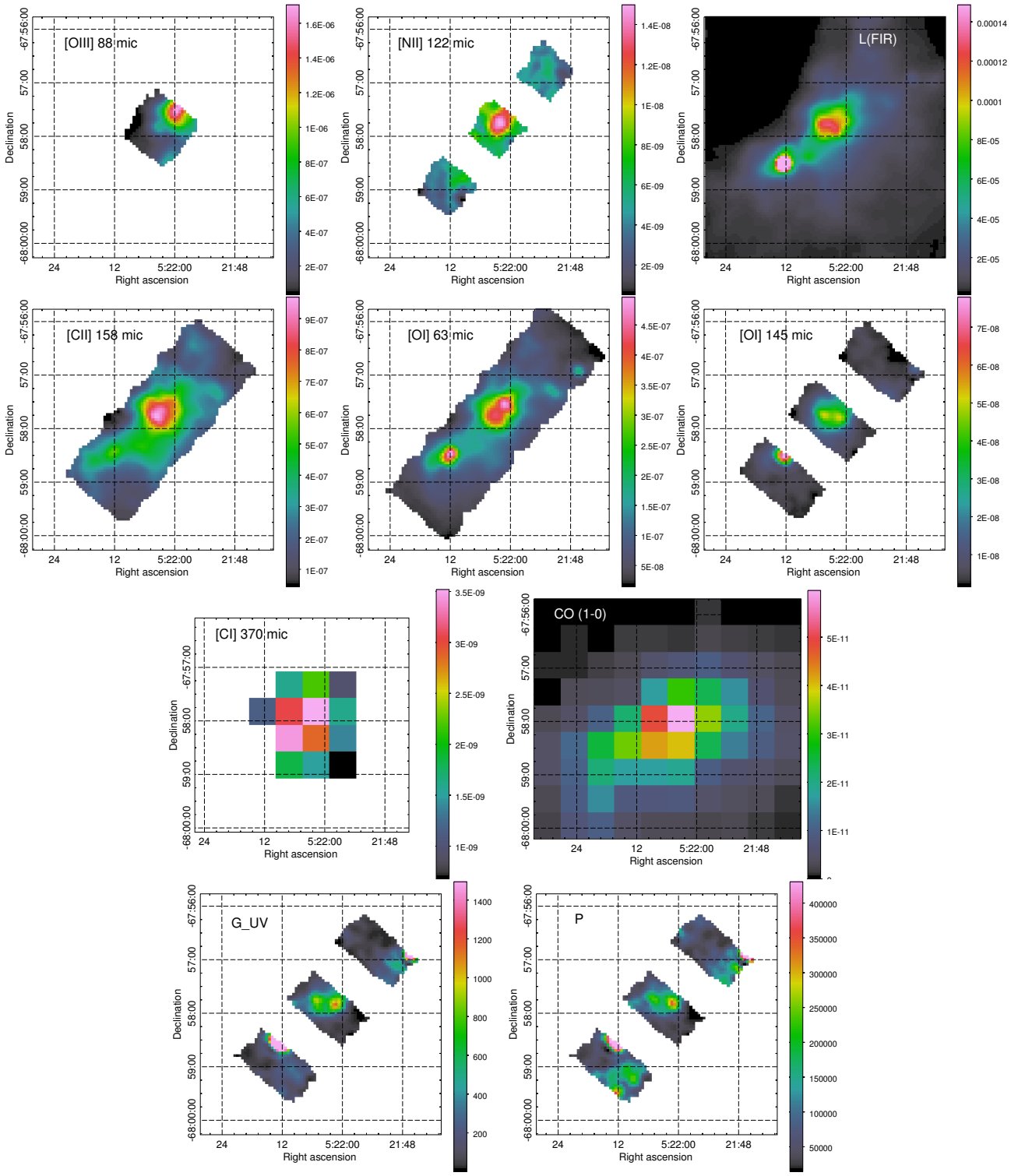

Figure VI.16: *Same as Figure VI.14 for N44.*

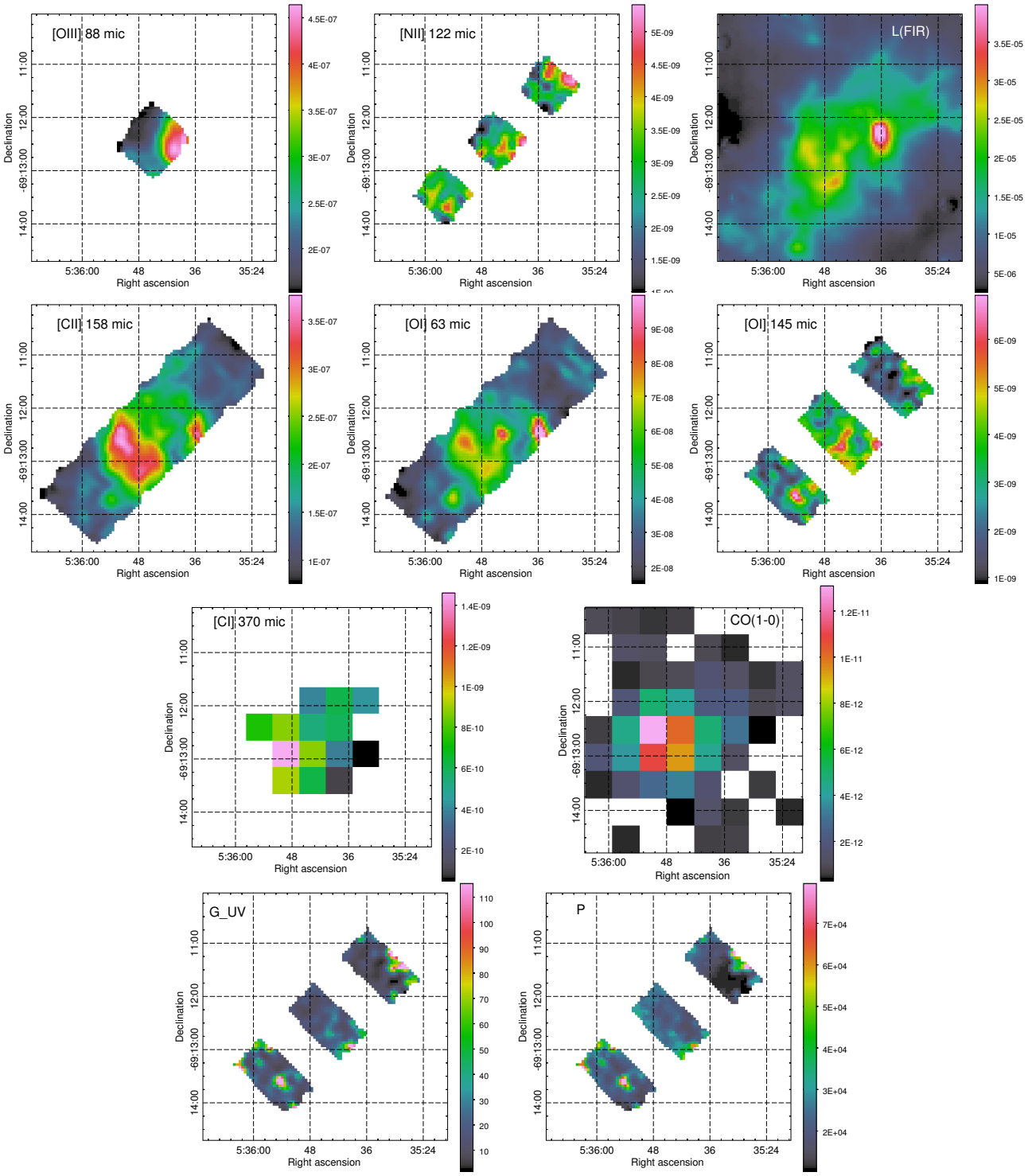

Figure VI.17: *Same as Figure VI.14 for N157.*

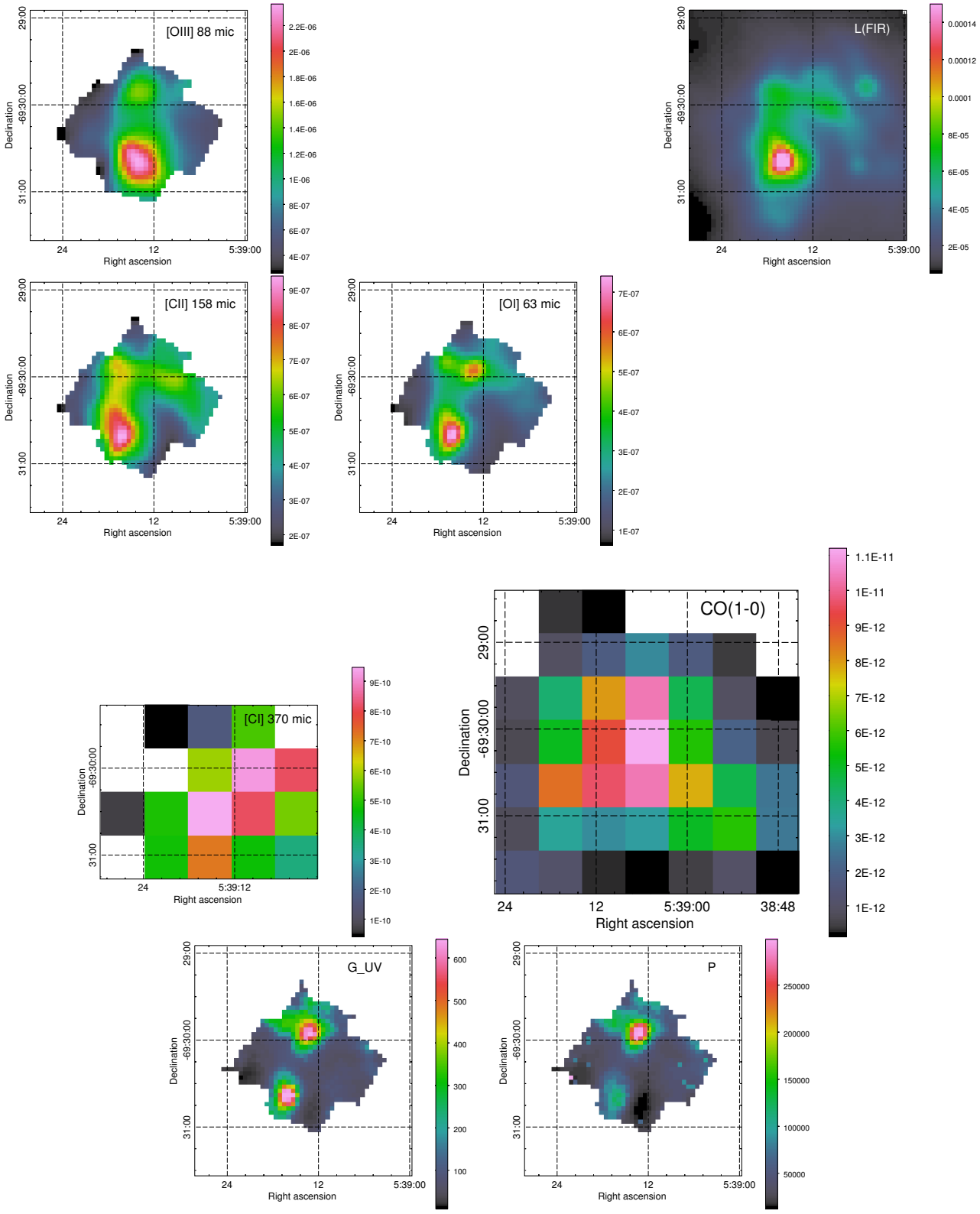

Figure VI.18: *Same as Figure VI.14 for N158*

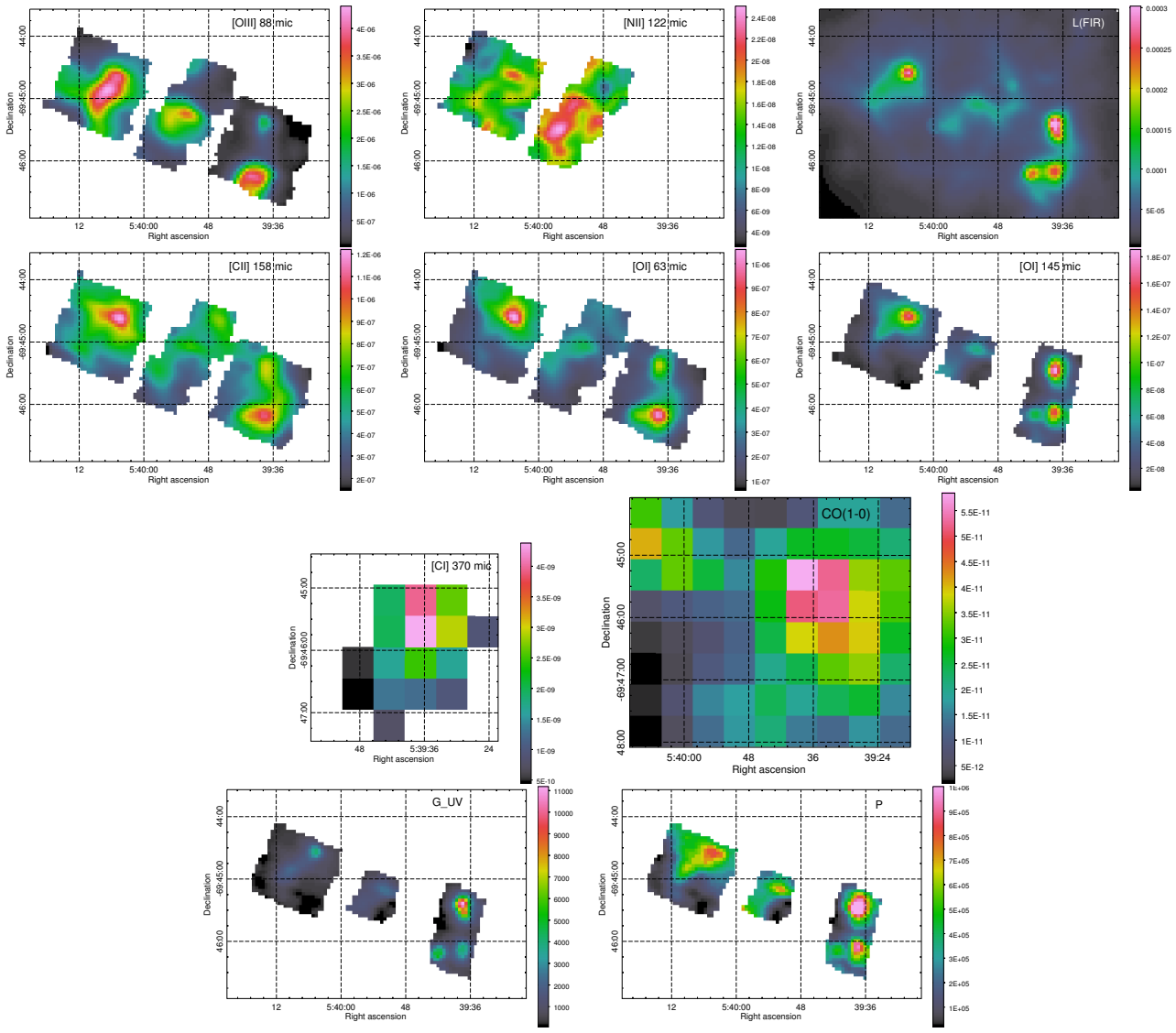

Figure VI.19: *Same as Figure VI.14 for N159.*

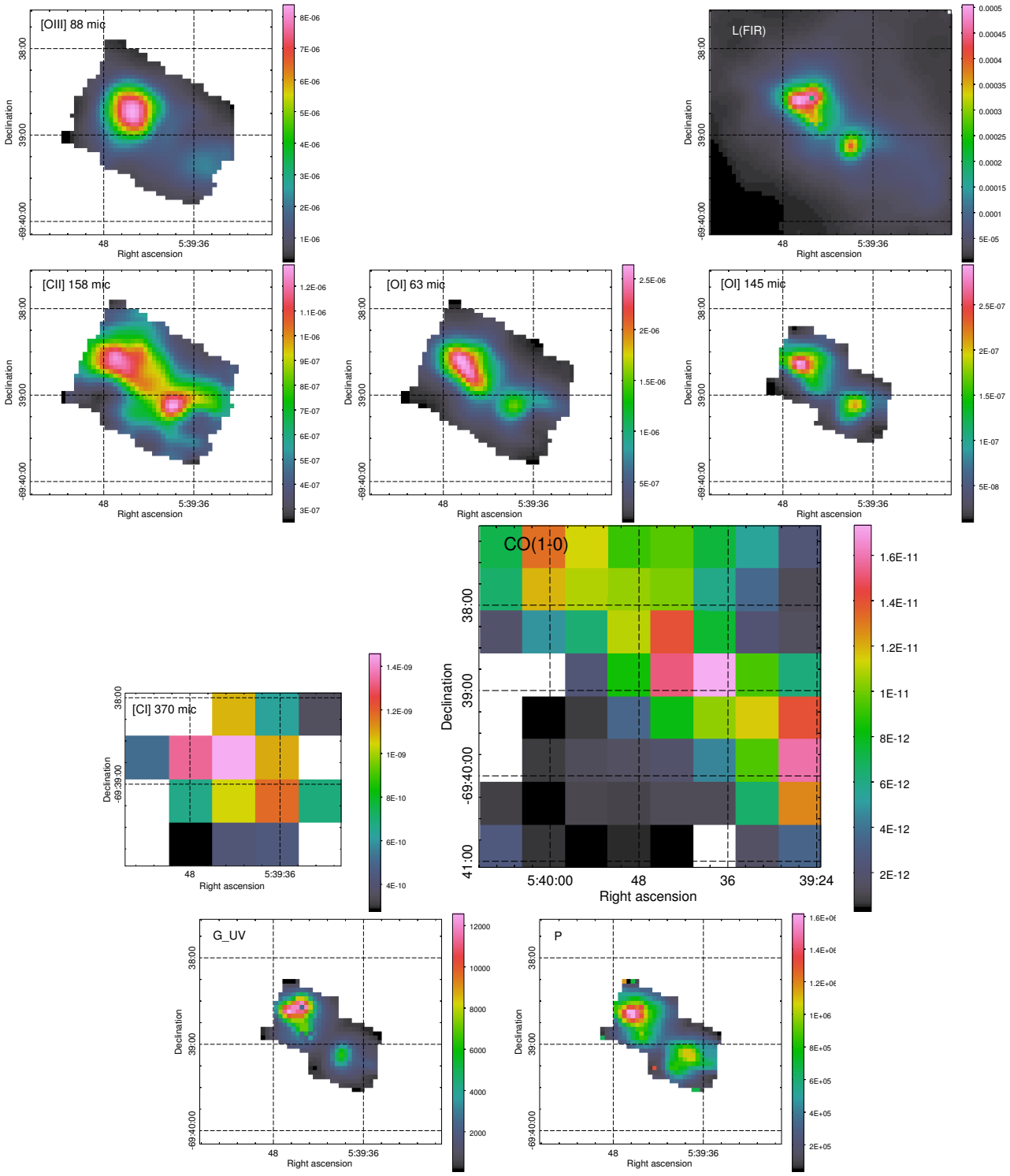

Figure VI.20: *Same as Figure VI.14 for N160.*

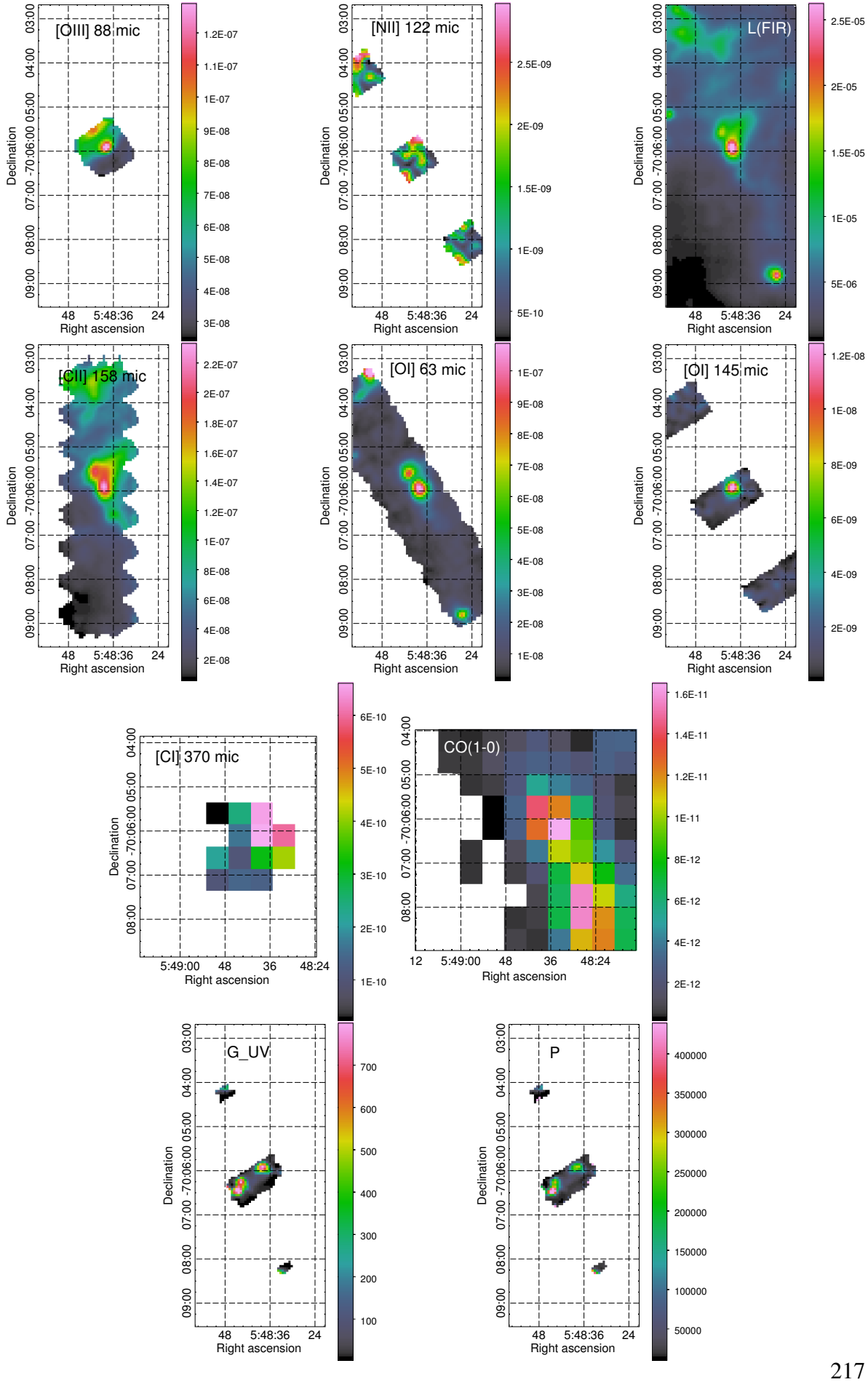

Figure VI.21: *Same as Figure VI.14 for N180.*

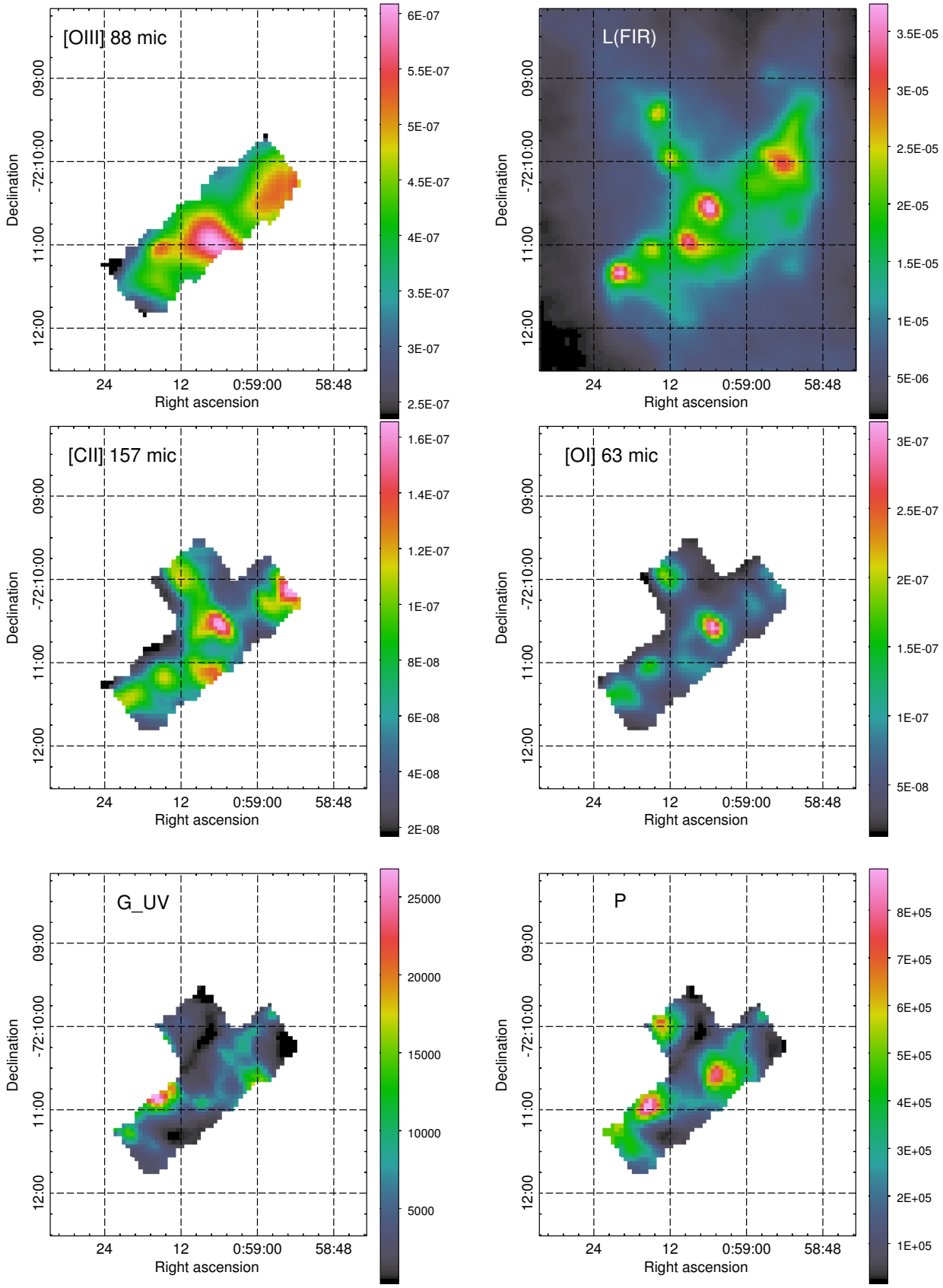

Figure VI.22: *Same as Figure VI.14 for N66.*

Conclusions and perspectives

Summary of the results

The goal of this work was to study in detail the physical conditions and the structure of the ISM in star-forming regions of the LMC and SMC. We investigated the impact of a strong radiation field on the low-metallicity environment, to understand better how the physical processes in the ISM are affected at reduced metallicity. The harder radiation fields and the reduced dust abundance in dwarf galaxies, compared to more metal-rich star-forming galaxies, affect the ISM structure and the star formation (e.g. Madden et al. 2006). We particularly focused on the photo-dissociation regions (PDRs), where an important reservoir of the molecular gas H_2, the primary ingredient of star formation, is expected to reside in low metallicity environments, undetected from the classical CO probe, as predicted by theoretical studies (e.g. Röllig et al. 2006; Wolfire et al. 2010; Glover & Mac Low 2011).

Our sample is based on the *Herschel* DGS sample (Madden et al. 2013), complemented by a few other regions from *Herschel* OT2 from Hony et al. The large wavelength domains observed by *Herschel* and *Spitzer* both in spectroscopy and photometry allow us to probe a wide diversity of ISM phases, from the ionized gas, to the PDR and molecular gas. With this complete dataset, we were able to determine the physical properties of the ISM in a number of LMC and SMC star-forming regions.

Dust and PDR modeling

After presenting the IR observations of our sample, I described briefly the dust SED model from Galliano et al. (2011), which we used in our study. This model allows us to estimate spatially, in particular, L_{FIR}, the mass of dust and the total extinction along the line of sight. I presented a method to disentangle the fraction of L_{FIR} emitted from the PDRs, which we can use as a constraint for the PDR modeling, to that from the ionized gas, using L_{PAH} and [O III] 88 μm emission line as tracers of these two gas phases.

I then presented the Meudon PDR code (Le Petit et al. 2006) and the method we used in this study to constrain the model parameters, G_{UV}, P and A_V^{max} with the observations. Using line flux ratios instead of individual lines allows us to ignore the effect of area filling factor different than unity, provided the lines are co-spatial. The ratios [C II]/[C I] or [C II]/CO are good tracers of the depth of the clouds, assuming the lines are associated with the same structure. Several caveats have been mentioned, related to the interpretation of the model results. First, there is a degeneracy between a high-G_{UV}/low-P and a low-G_{UV}/high-P solution. Then, the geometry used here for the PDR, a plane-parallel slab of gas and dust, is quite simple. However, for now, we lack the observational constraints for a more realistic scenario, taking into account a distribution of clouds with different sizes, illumi-

nated by a distribution of sources, including the effects of shielding and scattering,

Modeling of the PDRs in 30 Doradus

To start this study, we chose to focus on the 30Dor star-forming region in the LMC. In this extreme environment, the super star cluster R136 heats and ionizes the gas over tens of parsecs, producing an environment with no equivalent in our Galaxy. 30Dor is the brightest star-forming region of the LMC and has been observed in many wavelength ranges. The stellar population has been studied in detail (e.g. Whitney et al. 2008; Gruendl & Chu 2009; Sabbi et al. 2013; Walborn et al. 2014; Crowther et al. 2016) and the elemental abundances are known relatively accurately (e.g. Pellegrini et al. 2011). The proximity of the LMC, along with the angular resolution of *Herschel*/PACS spectrometer, allows us to probe the structure of the ISM with a spatial resolution of ~ 3 pc.

In low metallicity environments, we expect a higher fraction of the H_2 molecular gas to be outside of the CO-emitting cores, compared to more metal-rich environments. This potentially important reservoir of H_2 must then be located in the PDRs, co-spatial with C^o and C^+. Therefore, probing the physical conditions of the gas in the PDRs is a crucial step to quantify the total mass of molecular gas and start to understand better the star formation processes.

One of the first steps to trace the PDRs is to identify the origin of the bright [CII] line. Indeed, [CII] can, in principle, arise both from the PDRs and from the ionized gas, due to the relatively low ionization potential of carbon. The ratio of the [NII] lines observed by *Herschel*/PACS and *Herschel*/SPIRE FTS probes the electron density of the ionized gas, which in turn allows us to calculate the theoretical ratio [CII]/[NII] in the ionized gas. As the observed ratio in 30Dor is much higher than expected for the ionized gas only, we conclude that the major part of [CII] (> 90%) actually arises from the PDRs.

Combining the [CII] observations with other tracers of the PDR ([OI] and L_{FIR}), we were then able to determine spatially the incident radiation field and the pressure of the PDRs around R136 by comparing the observed line flux ratios to the predictions of the Meudon PDR code (Le Petit et al. 2006). In addition, we made an estimate of the area filling factor of the gas and of the depth of the clouds. Our results suggest that the [OI] 63 μm line is affected by opacity effects and is thus not a reliable constraint for the models in this region.

Comparing the incident radiation field obtained with the PDR model with the emitted radiation field, we proposed a 3-dimensional picture of the region. The PDRs are distributed at various distances around R136, between 20 to 80pc from the excitation source. The results of the modeling of the 30Dor region, presented in Chapter IV, have been published in Astronomy & Astrophysics (Chevance et al. 2016, A&A 590, A95)

Quantification of the CO-dark gas

Based on the PDR modeling of 30Dor described above, we calculated the total mass of H_2 predicted by our best fit model. We compared this value with the result of using the CO(1-0) luminosity, multiplied by a single conversion factor, $\alpha_{CO,MW}$, calibrated in the Milky Way. In 30Dor, as in other star-forming regions of dwarf galaxies, the combination of a strong radiation field and a low metallicity leading to a lower dust content, hence less shielding, results in CO photodissociation deep into the cloud. The CO molecule is expected to survive only in small dense cores, while H_2, which can more efficiently self-shield, exists in the PDRs.

This is verified with our study of 30Dor, where $\approx 90\%$ of the H_2 mass is not traced by CO using a Milky Way conversion factor. We thus derived a α_{CO} factor, adapted for 30Dor, on average a factor of

10 higher than the Galactic value. We also derived some higher values from our dust estimate, based on the SED fitting of 30Dor, assuming a constant gas-to-dust ratio throughout the region.

We note that the effect of the spatial resolution is important for the determination of the X_{CO} factor. When zooming in to a single GMC, more moderate values of X_{CO} can be found (e.g. Indebetouw et al. 2013). On the contrary, on larger scales ($\sim$ 10 pc or larger), more diffuse interclump medium, where H_2 can be present, but relatively free of CO, is included in the beam, driving X_{CO} towards higher values. A second first-author paper, presenting the quantification of the CO-dark gas in 30Dor is in preparation and will soon be submitted to A&A.

The effect of environment

We extended the method applied to 30Dor to other star-forming regions of the LMC and the SMC. The preliminary results of this study were presented in Chapter VI. The 10 regions studied here show a lot of contrast, in terms of star formation activity, stellar population, density and radiation field, as expected in galaxies on large scales. Modeling these regions on small scales is thus a first step toward understanding what drives the observed galaxy properties on global scales.

For each region, we have derived spatially the best model parameters, G_{UV} and P, combining the *Herschel* and *Spitzer* observations with the Meudon PDR code. For the integrated regions, we have estimated the total mass of H_2 molecular gas and compared it with the molecular gas mass derived from the CO(1-0) luminosity observed with Mopra (Wong et al. 2011), and a typical conversion factor $X_{CO,MW} = 2\times10^{20}$ cm^{-2} (K km s^{-1})$^{-1}$. The discrepancy between these two values reveals that CO is not a robust tracer of H_2 mass in these regions.

These preliminary results show significant reservoirs of H_2 not coincident with CO. We measured a large range of CO-dark molecular mass fractions, from 16% (in N159), up to $\sim$ 90% (for 30Dor, N158 and N157). More investigation is still needed to understand what physical parameters drive this value. Indeed, although the metallicity of the LMC is not thought to vary significantly across the galaxy, this experiment shows that the X_{CO} factor varies by a factor of $\sim$ 8 in the selected star-forming regions. Therefore, assuming a single X_{CO} or α_{CO} conversion factor for entire galaxies is probably rather simplified.

Perspectives

The impact of resolution

As we described in this study, spatial resolution is important for the derivation of the molecular gas mass. However, resolved observations are yet not feasible for high-redshift low-metallicity galaxies. The limited resolution and sensitivity of the IR, submm and millimeter observations makes it difficult to apply the methods described in Chapter V. For example, we have shown that, on large scales, the PDR model results are biased toward the densest regions. In addition, the dust mass is thought to be underestimated by $\sim$ 50% on galaxy scales compared to resolved studies (Galliano et al. 2011). Virial mass measurements are mostly limited to the Local Group galaxies (LMC, SMC, M31, M33, IC10, etc), where it is possible to resolve the population of GMCs (e.g. Vogel et al. 1987; Wilson & Scoville 1990; Wilson 1995; Leroy et al. 2006; Blitz et al. 2007; Fukui & Kawamura 2010). Only recently large coverage observations with high enough resolution to study the GMCs ($\sim$ 50 pc) became possible for spiral galaxies outside of the Local Group (e.g. Koda et al. 2009; Donovan Meyer et al. 2012, 2013;

Rebolledo et al. 2012, 2015).

As a result, detailed studies on resolved scales in nearby galaxies are necessary to understand and interpret the results at high redshift. The initial study presented here revealed a wide range of X_{CO} factors across the LMC from PDR modeling. Indeed, strictly speaking, X_{CO} is valid only for individual GMCs. On larger scales, variations of X_{CO} are expected, reflecting the local physical conditions of the ISM. The coming ALMA observations for 30Dor, N44 and N159, resolving the structure of the ISM at 0.2 pc scale, will help us understand better these variations and calibrate a method to derive the total H_2 mass in unresolved galaxies. Moreover, these high-resolution observations can help constrain a more realistic geometry for the models, taking into account the clumpiness of the medium.

In this study, we have evaluated key diagnostics of the gas heating and cooling of low metallicity resolved starburst regions. As a second step, it will now be interesting to see the effect of mixing all of these environments, along with more diffuse regions, in one beam, reproducing the wide range of environments existing in a galaxy in order to determine what properties (including total molecular gas mass) would be derived on global scales and understand what drives these properties. This will provide a legacy for studying similar but unresolved regions, in high-redshift galaxies.

Comparison with more metal-rich star-forming galaxies

Another follow-up on this study is the calibration of the CO-dark gas tracers at different metallicities. We have mostly focused here on star-forming regions of the LMC (and one in the SMC). Therefore, it will be interesting to extend our sample and compare these results with star-forming regions of the Milky Way, for example, or other more metal-rich galaxies in the Local Group, at similar spatial resolution. The increased dust abundances in more metal-rich star-forming galaxies, compared to the LMC, affect the ISM structure, and thus the fraction of CO-dark molecular gas. Models by Offner et al. (2014) and Glover & Clark (2016), for example, suggest that [CI] can be a good tracer of H_2, in particular at reduced metallicity. With [CI] and CO lines now accessible with high angular resolution with *ALMA*, it will be possible to calibrate these potential tracers of the molecular gas on a wide range of local environments, as a template for high-redshift galaxies. Tracing more accurately the total molecular reservoir of galaxies across cosmic times will give us clues to understand better galaxy evolution.

I will have the opportunity to continue exploring these topics related to stellar feedback and galaxy evolution during my post-doctoral position at the Astronomisches Rechen-Institut in Heidelberg University. My work will concerns the observational characterization of the cloud-scale physics of star formation and feedback in nearby and high-redshift galaxies, by combining large observational surveys of gas and star formation tracers in galaxies, from the Local Group to the high-redshift Universe, with state-of-the-art numerical simulations of star and galaxy formation.

New observational opportunities

Recently, new observatories have become (or will soon become) available for IR and radio observations. They allow us to probe the gas and dust with unprecedented resolution and sensitivity, which is crucial for faint dwarf galaxies and high-redshift galaxies, and will bring new insights on the issues of galaxy evolution. *SOFIA* observations of the FIR fine-structure lines, dust and PAH emission, for example, probe the ionized and neutral phases of the ISM. The model of 30Dor presented in Chapter IV will be extended to larger scales, based on the new *SOFIA* data, to derive the physical conditions of the gas, along with the fraction of the CO-dark molecular gas, as a function of the distance to the SSC R136. The new interferometers such as *ALMA* and the NOrthern Extended

Millimeter Array (*NOEMA*) offer now unprecedented resolution in the submm to radio wavelength ranges, and will soon ($\sim$ 2020) be complemented by the Square Kilometer Array (*SKA*). They allow us to trace, in particular, the atomic and molecular layers of the ISM (HI, [CI], CO, PAHs). Thus, they can probe the first stages of star formation, the dynamics and chemical evolution of nearby and higher redshift galaxies and galaxy formation in the early Universe. The James Webb Space Telescope (*JWST*), expected to be launched in 2018, will allow us to observe the valuable ionic lines, the H_2 lines and PAHs in the near- to mid-infrared wavelength domain, with an increased sensitivity and spatial resolution compared to the space telescope *Spitzer*. Finally, we hope to have *SPICA* as the next IR mission ($\sim$ 2027) which, with a cold 2.5m telescope, will give us 2 orders of magnitude better sensitivity than *Herschel* to observe the fainter and valuable MIR to FIR multiphase diagnostics, in many more distant galaxies.

Glossary

Acronyms

2MASS	Two Microns All Sky Survey
ACA	Atacama Compact Array
ALMA	Atacama Large Millimiter/sub-millimeter Array
AGB	Asymptotic Giant Branch
AGN	Active Galactic Nucleus
AOT	Astronomical Observing Templates
ASTE	Atacama Sub-millimeter Telescope Experiment
CTIO	Cerro Tololo Inter-American Observatory
COBE	Cosmic Background Explorer
DGS	Dwarf Galaxy Survey
(F)IR	(Far)-Infrared
FOV	Field-Of-View
FTS	Fourier Transform Spectrometer
(F)UV	(Far)-Ultraviolet
FWHM	Full Width Half Maximum
G/D	Gas-to-Dust mass ratio
GMC	Giant Molecular Cloud
HERITAGE	HERschel Inventory of The Agents of Galaxy Evolution
HIPE	Herschel Interactive Processing Environment
IRAC	InfraRed Array Camera
IRAS	InfraRed Astronomical Satellite
IRS	InfraRed Spectrograph
ISM	InterStellar Medium
ISO	Infrared Space Observatory
ISRF	InterStellar Radiation Field
KAO	Kuiper Airborne Observatory
LMC	Large Magellanic Cloud
MC	Magellanic Clouds
MCELS	Magellanic Cloud Emission Line Survey
MIPS	Multiband Imaging Photometer for *Spitzer*
MIR	Mid-Infrared
NIR	Near-Infrared
PACS	Photodetector Array Camera & Spectrometer
PAH	Polycyclic Aromatic Hydrocarbon
PDR	PhotoDissociation Region
PÉGASE	Projet d'Étude des Galaxies par Synthèse Évolutive

PSF	Point Spread Function
RMS	Root Mean Square
SED	Spectral Energy Distribution
SFE	Star Formation Efficiency
SFR	Star Formation Rate
sSFR	Specific Star Formation Rate
SMC	Small Magellanic Cloud
SN	Supernova
SOFIA	Stratospheric Observatory For Infrared Astronomy
submm	submillimeter
SSC	Super Star Cluster
S/N	Signal-to-Noise Ratio
SAGE	Surveying the Agents of a Galaxy's Evolution
SPIRE	Spectral and Photometric Imaging Receiver
TIR	Total Infrared
UKST	UK Schmidt Telescope
WR	Wolf-Rayet stars
YSO	Young Stellar Object

Notations

α_{CO}	CO-to-H_2 conversion factor in term of mass surface density
A_V	Visual extinction
A_V^{dust}	Visual extinction integrated on a line of sight
A_V^{max}	Visual extinction for one simulated cloud of the Meudon PDR code
A_V^{obs}	Observed visual extinction
c	Speed of light (3.00×10^8 m s^{-1})
ϵ_{PE}	Heating efficiency of the photoelectric effect
$\epsilon_{PE,FIR}$	Photoelectric heating efficiency on dust grains
$\epsilon_{PE,PAH}$	Photoelectric heating efficiency on PAHs
EP	Excitation Potential
eV	electron-Volt
G	Gravitational constant (6.67×10^{-11}m^{-3} kg^{-1} s^{-2})
G_{UV}	Incident ionizing radiation field (input parameter of the Meudon PDR code)
G_{stars}	Emitted radiation field
Γ_{dust}	Heating of the dust
Γ_{gas}	Heating of the gas
h	Planck constant (6.62×10^{-34} J s)
I_{CO}	CO intensity
IP	Ionization Potential

k_B	Boltzman constant (1.38×10^{-23} J K^{-1})
L_{FIR}	FIR luminosity integrated between 60 and 200 μm
L_{FIR}^{PDR}	Component of L_{FIR} originated from the PDRs
L_{TIR}	TIR luminosity integrated between 3 and 1000 μm
n	Density
n_{crit}	Critical density
P	Pressure
pc	parsec
Φ_A	Area filling factor
σ	Velocity dispersion
T_{ex}	Excitation temperature
T_{kin}	Kinetic temperature
X_{CO}	CO-to-H_2 column density conversion factor
s	Redshift
sr	Steradian
Z	Metallicity

Bibliography

Abdo, A. A., Ackermann, M., Ajello, M., et al. 2010, Astronomy & Astrophysics, 512, A7

Abel, N. P., Ferland, G. J., Shaw, G., & van Hoof, P. A. M. 2005, The Astrophysical Journal Supplement Series, 161, 65

Abrahams, R. D. & Paglione, T. A. D. 2015, The Astrophysical Journal, 805, 50

Accurso, G., Saintonge, A., Bisbas, T. G., & Viti, S. 2016, Accepted for publication in Monthly Notices of the Royal Astronomical Society, ArXiv eprint: 1607.03488

Ackermann, M., Ajello, M., Allafort, A., et al. 2012, Astronomy & Astrophysics, 538, A71

Ackermann, M., Ajello, M., Baldini, L., et al. 2011, The Astrophysical Journal, 726, 81

Ade, P. A. R., Aghanim, N., Aniano, G., et al. 2015, Astronomy & Astrophysics, 582, A31

Allamandola, L. J., Tielens, A. G. G. M., & Barker, J. R. 1985, The Astrophysical Journal, 290, L25

Anderson, C. N., Meier, D. S., Ott, J., et al. 2014, The Astrophysical Journal, 793, 37

Andree-Labsch, S., Ossenkopf-Okada, V., & Röllig, M. in prep., ArXiv eprint: 1405.5553

Aniano, G., Draine, B. T., Gordon, K., & Sandstrom, K. M. 2011, Publications of the Astronomical Society of the Pacific, 123, 1218

Asplund, M., Grevesse, N., Sauval, A. J., & Scott, P. 2009, Annual Review of Astronomy and Astrophysics, 47, 481

Babul, A. & Rees, M. J. 1992, Monthly Notices of the Royal Astronomical Society, 255, 346

Bachellerie, D., Sizun, M., Aguillon, F., et al. 2009, Physical Chemistry Chemical Physics, 11, 2715

Bakes, E. & Tielens, A. 1994, The Astrophysical Journal, 427, 822

Ballesteros-Paredes, J. 2006, Monthly Notices of the Royal Astronomical Society, 372, 443

Bamba, A., Ueno, M., Nakajima, H., & Koyama, K. 2004, The Astrophysical Journal, 602, 257

Bekki, K., Chiba, M., & McClure-Griffiths, N. M. 2008, The Astrophysical Journal, 672, L17

Bekki, K. & Stanimirović, S. 2009, Monthly Notices of the Royal Astronomical Society, 395, 342

Bell, T. A., Roueff, E., Viti, S., & Williams, D. A. 2006, Monthly Notices of the Royal Astronomical Society, 371, 1865

Bennett, C. L., Fixsen, D. J., Hinshaw, G., et al. 1994, The Astrophysical Journal, 434, 587

Bernard, J.-P., Reach, W. T., Paradis, D., et al. 2008, The Astronomical Journal, 136, 919

Bernard-Salas, J., Habart, E., Arab, H., et al. 2012, Astronomy & Astrophysics, 538, A37

Bertelli, G., Bressan, a., Chiosi, C., Fagotto, F., & Nasi, E. 1994, Astronomy and Astrophysics Supplement Series, 106, 275

Besla, G., Kallivayalil, N., Hernquist, L., et al. 2012, Monthly Notices of the Royal Astronomical Society, 421, 2109

Besla, G., Kallivayalil, N., Hernquist, L., et al. 2010, The Astrophysical Journal, 721, L97

Beuther, H., Ragan, S. E., Ossenkopf, V., et al. 2014, Astronomy & Astrophysics, 571, A53

Bica, E., Claria, J. J., Dottori, H., Santos, J. F. C., J., & Piatti, A. E. 1996, The Astrophysical Journal Supplement Series, 102, 57

Bigiel, F., Leroy, A., Walter, F., et al. 2008, The Astronomical Journal, 136, 2846

Bigiel, F., Walter, F., Blitz, L., et al. 2010, The Astronomical Journal, 140, 1194

Bisbas, T. G., Bell, T. A., Viti, S., Yates, J., & Barlow, M. J. 2012, Monthly Notices of the Royal Astronomical Society, 427, 2100

Bisbas, T. G., Haworth, T. J., Barlow, M. J., et al. 2015, Monthly Notices of the Royal Astronomical Society, 454, 2828

Blitz, L., Fukui, Y., Kawamura, A., et al. 2007, in Protostars and Planets V, ed. B. Reipurth, D. Jewitt, & K. Keil (Tucson: University of Arizona Press), 81

Bolatto, A. D., Leroy, A., Israel, F. P., Jackson, J. M., & Journal, T. A. 2003, The Astrophysical Journal, 595, 167

Bolatto, A. D., Leroy, A. K., Jameson, K., et al. 2011, The Astrophysical Journal, 741, 12

Bolatto, A. D., Leroy, A. K., Rosolowsky, E., Walter, F., & Blitz, L. 2008, The Astrophysical Journal, 686, 948

Bolatto, A. D., Wolfire, M., & Leroy, A. K. 2013, Annual Review of Astronomy and Astrophysics, 51, 207

Boselli, A., Gavazzi, G., Lequeux, J., & Pierini, D. 2002, Astronomy & Astrophysics, 385, 454

Bot, C., Rubio, M., Boulanger, F., et al. 2010, Astronomy and Astrophysics, 524, 12

Boulanger, F., Abergel, A., Bernard, J.-P. P., et al. 1996, Astronomy & Astrophysics, 312, 256

Boulanger, F. & Perault, M. 1988, The Astrophysical Journal, 330, 964

Bouret, J., Lanz, T., Hillier, D. J., et al. 2003, The Astrophysical Journal, 595, 1182

Brandl, B. R., Bernard-Salas, J., Spoon, H. W. W., et al. 2006, The Astrophysical Journal, 653, 1129

Brandner, W., Grebel, E. K., Barbá, R. H., Walborn, N. R., & Moneti, A. 2001, The Astronomical Journal, 122, 858

Brauher, J. R., Dale, D. A., & Helou, G. 2008, The Astrophysical Journal Supplement Series, 178, 280

Brinks, E. & Taylor, C. L. 1994, in ESO Conference and Workshop Proceedings, ed. G. Meylan & P. Prugniel (Garching: European Southern Observatory), 263

Bron, E. 2014, PhD thesis, Université Paris Diderot

Bron, E., Le Bourlot, J., & Le Petit, F. 2014, Astronomy & Astrophysics, 569, A100

Brooks, A. M., Governato, F., Booth, C. M., et al. 2007, The Astrophysical Journal, 655, L17

Brüns, C., Kerp, J., Mebold, U., Putman, M. E., & Haynes, R. F. 2005, Astronomy & Astrophysics, 67, 23

Brunt, C. M. 2003, The Astrophysical Journal, 583, 280

Calzetti, D., Kennicutt, R. C., Engelbracht, C. W., et al. 2007, The Astrophysical Journal, 666, 870

Campbell, A., Terlevich, R., & Melnick, J. 1986, Monthly Notices of the Royal Astronomical Society, 223, 811

Carlson, L., Sewilo, M., & Meixner, M. 2012, Astronomy & Astrophysics, 542, A66

Casetti-Dinescu, D. I., Vieira, K., Girard, T. M., & van Altena, W. F. 2012, The Astrophysical Journal, 753, 123

Chandrasekhar, S. & Fermi, E. 1953, The Astrophysical Journal, 118, 116

Chang, Q., Cuppen, H. M., & Herbst, E. 2005, Astronomy and Astrophysics, 611, 599

Chen, C.-H. R., Chu, Y.-H., Gruendl, R. A., Gordon, K. D., & Heitsch, F. 2009, The Astrophysical Journal, 695, 511

Chen, C.-H. R., Indebetouw, R., Chu, Y.-H., et al. 2010, The Astrophysical Journal, 721, 1206

Chen, C.-H. R., Indebetouw, R., Muller, E., et al. 2014, The Astrophysical Journal, 785, 162

Chevance, M., Madden, S. C., Lebouteiller, V., et al. 2016, Astronomy & Astrophysics, 590, A36

Chu, Y., Low, M.-M. M., Garcia-Segura, G., Wakker, B., & Kennicutt, Robert C., J. 1993, The Astrophysical Journal, 414, 213

Chu, Y.-H. & Kennicutt, R. C. J. 1994, The Astrophysical Journal, 425, 720

Cignoni, M., Sabbi, E., van der Marel, R. P., et al. 2015, The Astrophysical Journal, 811, 76

Cioni, M. R. L. 2009, Astronomy and Astrophysics (ISSN 0004-6361), 506, 1137

Cioni, M. R. L., Habing, H. J., & Israel, F. P. 2000, Astronomy and Astrophysics, 358, L9

Clayton, D. 2003, Handbook of Isotopes in the Cosmos, 326

Cormier, D. 2012, PhD thesis, Université Paris Diderot

Cormier, D., Madden, S. C., Lebouteiller, V., et al. 2015, Astronomy & Astrophysics, 578, A53

Cormier, D., Madden, S. C., Lebouteiller, V., et al. 2014, Astronomy & Astrophysics, 564, A121

Cowie, L. L., Songaila, A., Hu, E. M., & Cohen, J. G. 1996, Astronomical Journal v.112, 112, 839

Crawford, M. K., Genzel, R., Townes, C. H., & Watson, D. M. 1985, The Astrophysical Journal, 291, 755

Crowther, P. A., Caballero-Nieves, S. M., Bostroem, K. A., et al. 2016, Monthly Notices of the Royal Astronomical Society, 458, 624

Croxall, K. V., Smith, J. D., Wolfire, M. G., et al. 2012, The Astrophysical Journal, 747, 81

Cuppen, H. M. & Herbst, E. 2005, Monthly Notices of the Royal Astronomical Society, 361, 565

Dabrowski, I. 1984, Canadian Journal of Physics, 62, 1639

Daddi, E., Elbaz, D., Walter, F., et al. 2010, The Astrophysical Journal, 714, L118

Dale, D. a., Aniano, G., Engelbracht, C. W., et al. 2012, The Astrophysical Journal, 745, 95

Dale, D. A., Helou, G., Contursi, A., Silbermann, N. A., & Kolhatkar, S. 2001, The Astrophysical Journal, 549, 215

Dame, T. M., Hartmann, D., & Thaddeus, P. 2001, The Astrophysical Journal, 547, 792

Davies, R. D., Elliott, K. H., & Meaburn, J. 1976, Royal Astronomical Society, Memoirs, 81, 89

de Blok, W. J. G. & Walter, F. 2006, The Astronomical Journal, 131, 343

de Boer, K. S., Richter, P., Bomans, D. J., Heithausen, A., & Koornneef, J. 1998, Astronomy & Astrophysics, 338, L5

De Breuck, C., Maiolino, R., Caselli, P., et al. 2011, Astronomy & Astrophysics, 530, L8

de Graauw, T., Helmich, F. P., Phillips, T. G., et al. 2010, Astronomy & Astrophysics, 518, L6

de Koter, A., Heap, S. R., & Hubeny, I. 1998, The Astrophysical Journal, 509, 879

De Looze, I., Baes, M., Bendo, G. J., Cortese, L., & Fritz, J. 2011, Monthly Notices of the Royal Astronomical Society, 416, 2712

De Looze, I., Cormier, D., Lebouteiller, V., et al. 2014, Astronomy & Astrophysics, 568, A62

de Vaucouleurs, G. 1955, The Astronomical Journal, 60, 126

Deharveng, L., Caplan, J., & Lombard, J. 1992, Astronomy & Astrophysics Supplement Series, 94, 359

Dekel, a. & Silk, J. 1986, Astrophysical Journal, 303, 39

Deul, E. R. & Burton, W. B. 1993, in The Galactic Interstellar Medium, ed. D. Pfenniger & P. Bartholdi (Heidelberg: Springer-Verlag), 79

Diaz, J. & Bekki, K. 2011, Monthly Notices of the Royal Astronomical Society, 413, 2015

Dickel, J. R., McIntyre, V. J., Gruendl, R. A., & Milne, D. K. 2005, The Astronomical Journal, 129, 790

Dickman, R. L., Snell, R. L., & Schloerb, F. P. 1986, The Astrophysical Journal, 309, 326

Dobashi, K., Bernard, J.-P., Hughes, A., et al. 2008, Astronomy & Astrophysics, 484, 205

Donovan Meyer, J., Koda, J., Momose, R., et al. 2012, The Astrophysical Journal, 744, 42

Donovan Meyer, J., Koda, J., Momose, R., et al. 2013, The Astrophysical Journal, 772, 107

Doran, E. I., Crowther, P. A., de Koter, A., et al. 2013, Astronomy & Astrophysics, 558, A134

Draine, B. 2003, Annual Review of Astronomy and Astrophysics, 41, 241

Draine, B. T. 1978, The Astrophysical Journal Supplement Series, 36, 595

Draine, B. T. & Lazarian, A. 1998, The Astrophysical Journal, 494, L19

Draine, B. T. & Lee, H. M. 1984, Astrophysical Journal, 285, 89

Draine, B. T. & Li, A. 2007, The Astrophysical Journal, 657, 810

Dreyer, J. L. E. 1888, Memoirs of the Royal Astronomical Society, 49, 1

Duley, W. W. 1996, Monthly Notices of the Royal Astronomical Society, 279, 591

Duley, W. W. & Williams, D. A. 1981, Monthly Notices of the Royal Astronomical Society, 196, 269

Dwek, E. 1998, The Astrophysical Journal, 501, 643

Engelbracht, C. W., Gordon, K. D., Rieke, G. H., et al. 2005, The Astrophysical Journal, 628, L29

Engelbracht, C. W., Rieke, G. H., Gordon, K. D., et al. 2008, The Astrophysical Journal, 678, 804

Evans, C. J., Taylor, W. D., Hénault-Brunet, V., et al. 2011, Astronomy & Astrophysics, 530, A108

Fariña, C., Bosch, G. L., Morrell, N. I., Barbá, R. H., & Walborn, N. R. 2009, The Astronomical Journal, 138, 510

Feast, M. W., Abedigamba, O. P., & Whitelock, P. A. 2010, Monthly Notices of the Royal Astronomical Society: Letters, 408, 76

Feast, M. W., Thackeray, A. D., & Wesselink, A. J. 1960, Monthly Notices of the Royal Astronomical Society, 121, 337

Feldmann, R., Gnedin, N. Y., & Kravtsov, A. V. 2012, The Astrophysical Journal, 747, 124

Ferkinhoff, C., Brisbin, D., Nikola, T., et al. 2011, The Astrophysical Journal, 740, L29

Ferland, G. J., Fabian, A. C., Hatch, N. A., et al. 2009, Monthly Notices of the Royal Astronomical Society, 392, 1475

Ferland, G. J., Korista, K. T., Verner, D. A., et al. 1998, Publications of the Astronomical Society of the Pacific, 110, 761

Ferland, G. J., Porter, R. L., van Hoof, P. A. M., et al. 2013, Revista Mexicana de Astronomía y Astrofísica, 49, 137

Field, G. B., Blackman, E. G., & Keto, E. R. 2011, Monthly Notices of the Royal Astronomical Society, 416, 710

Filipovi, M. D., Bohlsen, T., Reid, W., et al. 2002, Monthly Notices of the Royal Astronomical Society, 335, 1085

Fioc, M. & Rocca-Volmerange, B. 1997, Astronomy & Astrophysics, 500, 521

Fitzpatrick, E. L. & Massa, D. 1986, The Astrophysical Journal, 307, 286

Fitzpatrick, E. L. & Massa, D. 1988, The Astrophysical Journal, 328, 734

Fitzpatrick, E. L. & Massa, D. 1990, The Astrophysical Journal Supplement Series, 72, 163

Fleener, C. E., Payne, J. T., Chu, Y.-H., Chen, C.-H. R., & Gruendl, R. A. 2010, The Astronomical Journal, 139, 158

Foreman, G., Chu, Y.-h., Gruendl, R., et al. 2015, The Astrophysical Journal, 808, 44

Fujimoto, M. & Murai, T. 1985, in The Milky Way Galaxy; Proceedings of the 106th Symposium, ed. H. van Woerden, R. J. Allen, & W. Burton (Dordrecht, D. Reidel Publishing Co.), 471–475

Fukui, Y., Harada, R., Tokuda, K., et al. 2015a, The Astrophysical Journal, 807, L4

Fukui, Y. & Kawamura, A. 2010, Annual Review of Astronomy and Astrophysics, 48, 547

Fukui, Y., Kawamura, A., Minamidani, T., et al. 2008, The Astrophysical Journal Supplement Series, 178, 56

Fukui, Y., Mizuno, N., Yamaguchi, R., Mizuno, A., & Onishi, T. 2001, Publications of the Astronomical Society of Japan, 53, L41

Fukui, Y., Torii, K., Onishi, T., et al. 2015b, The Astrophysical Journal, 798, 6

Fulton, T. R., Baluteau, J.-P., Bendo, G., et al. 2010, Proc. SPIE, 7731, 773134

Galametz, M., Hony, S., Albrecht, M., et al. 2016, Monthly Notices of the Royal Astronomical Society, 456, 1767

Galametz, M., Hony, S., Galliano, F., et al. 2013, Monthly Notices of the Royal Astronomical Society, 431, 1596

Galametz, M., Madden, S., Galliano, F., et al. 2009, Astronomy & Astrophysics, 508, 645

Galametz, M., Madden, S. C., Galliano, F., et al. 2011, Astronomy & Astrophysics, 532, 56

Gallagher, J. S. 1998, in Magellanic Clouds and Other Dwarf Galaxies, ed. T. Richtler & J. M. Braun, 25–36

Galliano, F., Hony, S., Bernard, J.-P., et al. 2011, Astronomy & Astrophysics, 536, A88

Galliano, F., Madden, S. C., Jones, A. P., et al. 2003, Astronomy and Astrophysics, 407, 159

Galliano, F., Madden, S. C., Jones, A. P., Wilson, C. D., & Bernard, J.-P. P. 2005, Astronomy and Astrophysics, 434, 19

Galliano, F., Madden, S. C., Tielens, A. G. G. M., Peeters, E., & Jones, A. P. 2008, The Astrophysical Journal, 679, 67

Gao, Y. & Solomon, P. M. 2004, The Astrophysical Journal, 606, 271

Genzel, R., Newman, S., Jones, T., et al. 2011, The Astrophysical Journal, 733, 101

Genzel, R., Tacconi, L. J., Combes, F., et al. 2012, The Astrophysical Journal, 746, 69

Gerin, M. & Phillips, T. G. 2000, The Astrophysical Journal, 537, 644

Giveon, U., Sternberg, A., Lutz, D., Feuchtgruber, H., & Pauldrach, A. W. A. 2002, The Astrophysical Journal, 566, 880

Glover, S. C. O. & Clark, P. C. 2012, Monthly Notices of the Royal Astronomical Society, 426, 377

Glover, S. C. O. & Clark, P. C. 2016, Monthly Notices of the Royal Astronomical Society, 456, 3596

Glover, S. C. O. & Mac Low, M.-M. 2011, Monthly Notices of the Royal Astronomical Society, 412, 337

Gonzalez Garcia, M., Le Bourlot, J., Le Petit, F., & Roueff, E. 2008, Astronomy & Astrophysics, 485, 127

Gordon, K. D., Clayton, G. C., Misselt, K. A., Landolt, A. U., & Wolff, M. J. 2003, The Astrophysical Journal, 594, 279

Gordon, K. D., Engelbracht, C. W., Rieke, G. H., et al. 2008, The Astrophysical Journal, 682, 336

Gordon, K. D., Roman-Duval, J., Bot, C., et al. 2014, The Astrophysical Journal, 797, 85

Gouliermis, D. A., Bestenlehner, J. M., Brandner, W., & Henning, T. 2010, Astronomy & Astrophysics, 515, A56

Gouliermis, D. A., Dolphin, A. E., Brandner, W., & Henning, T. 2006, The Astrophysical Journal Supplement Series, 166, 549

Gräfener, G. & Hamann, W.-R. 2008, Astronomy & Astrophysics, 482, 945

Graff, D. S., Gould, A. P., Suntzeff, N. B., Schommer, R. A., & Hardy, E. 2000, The Astrophysical Journal, 540, 211

Grebel, E. K. 1999, in The stellar content of Local Group galaxies, Proceedings of the 192nd symposium of the International Astronomical Union, ed. P. Whitelock & R. Cannon (San Francisco, CA: Astronomical Society of the Pacific)

Grebel, E. K. 2001, in Dwarf galaxies and their environment, ed. Klaas S. De Boer, R.-J. Dettmar, & U. Klein No. January, 45

Grenier, I. A., Casandjian, J.-M., & Terrier, R. 2005, Science, 307, 1292

Griffin, M. J., Abergel, A., Abreu, A., et al. 2010, Astronomy & Astrophysics, 518, L3

Gruendl, R. A. & Chu, Y.-H. 2009, The Astrophysical Journal Supplement Series, 184, 172

Gry, C., Boulanger, F., Nehm, C., et al. 2002, Astronomy & Astrophysics, 680, 675

Guhathakurta, P. & Draine, B. T. 1989, The Astrophysical Journal, 345, 230

Habart, E., Abergel, A., Boulanger, F., et al. 2011, Astronomy & Astrophysics, 527, A122

Habart, E., Abergel, A., Walmsley, C. M., Teyssier, D., & Pety, J. 2005, Astronomy and Astrophysics, 437, 177

Habart, E., Boulanger, F., Verstraete, L., Walmsley, C. M., & Pineau des Forêts, G. 2004, Astronomy & Astrophysics, 414, 531

Habart, E., Verstraete, L., Boulanger, F., et al. 2001, Astronomy & Astrophysics, 373, 702

Habing, H. J. 1968, Bulletin of the Astronomical Institutes of the Netherlands, 19, 421

Hailey-Dunsheath, S., Nikola, T., Stacey, G. J., et al. 2010, The Astrophysical Journal, 714, L162

Hainich, R., Pasemann, D., Todt, H., et al. 2015, Astronomy & Astrophysics, 581, A21

Hammer, F., Yang, Y. B., Flores, H., Puech, M., & Fouquet, S. 2015, The Astrophysical Journal, 813, 110

Haschke, R., Grebel, E. K., & Duffau, S. 2012, The Astronomical Journal, 144, 106

Haser, S. M., Pauldrach, A. W. A., Lennon, D., et al. 1998, Astronomy & Astrophysics, 330, 285

Henize, K. G. 1956, The Astrophysical Journal Supplement Series, 2, 315

Hennebelle, P. & Falgarone, E. 2012, Astronomy & Astrophysics Review, 20, 1

Henry, A., Scarlata, C., Domínguez, A., et al. 2013, The Astrophysical Journal, 776, L27

Herrera-Camus, R., Bolatto, A., Smith, J. D., et al. 2016, The Astrophysical Journal, 826, 175

Herrera-Camus, R., Bolatto, a. D., Wolfire, M. G., et al. 2015, The Astrophysical Journal, 800, 1

Herschel, J. F. W. 1847, Results of Astronomical Observations Made during the Years 1834, 5, 6, 7, 8, at the Cape of Good Hope (London: Smith, Elder, & Co.)

Heydari-Malayeri, M., Charmandaris, V., Deharveng, L., et al. 2002, Astronomy and Astrophysics, 381, 941

Heyer, M. & Dame, T. M. 2015, Annual Review of Astronomy and Astrophysics, 53, 583

Heyer, M. H. & Brunt, C. M. 2004, The Astrophysical Journal, 615, L45

Heyer, M. H., Carpenter, J. M., & Snell, R. L. 2001, The Astrophysical Journal, 20, 32

Hilditch, R. W., Howarth, I. D., & Harries, T. J. 2005, Monthly Notices of the Royal Astronomical Society, 357, 304

Hodge, P., Lee, M. G., & Kennicutt, R. C. J. 1989, Publications of the Astronomical Society of the Pacific, 101, 640

Hodge, P., Smith, T., Eskridge, P., MacGillivray, H., & Beard, S. 1991, The Astrophysical Journal, 379, 621

Hollenbach, D. & Salpeter, E. E. 1971, Astrophysical Journal, 163, 155

Hollenbach, D. J. & Tielens, A. G. G. M. 1999, Reviews of Modern Physics, 71, 173

Hony, S., Galliano, F., Madden, S. C., et al. 2010, Astronomy & Astrophysics, 518, L76

Hony, S., Gouliermis, D. A., Galliano, F., et al. 2015, Monthly Notices of the Royal Astronomical Society, 448, 1847

Houck, J. R., Charmandaris, V., Brandl, B. R., et al. 2004, The Astrophysical Journal Supplement Series, 154, 211

Hughes, A., Wong, T., Ott, J., et al. 2010, Monthly Notices of the Royal Astronomical Society, 406, 2065

Hunt, L. K., García-Burillo, S., Casasola, V., et al. 2015, Astronomy & Astrophysics, 583, A114

Hunt, L. K., Thuan, T. X., Izotov, Y. I., & Sauvage, M. 2010, The Astrophysical Journal, 712, 164

Hunter, D. 1997, Publications of the Astronomical Society of the Pacific, 109, 937

Hunter, D. & Kaufman, M. 2007, The Astronomical Journal, 134, 721

Hunter, D. A., Elmegreen, B. G., & Baker, A. L. 1998, The Astrophysical Journal, 493, 595

Hunter, D. A., Kaufman, M., Hollenbach, D. J., et al. 2001, The Astrophysical Journal, 553, 121

Hunter, D. A., Zahedy, F., Bowsher, E. C., et al. 2011, The Astronomical Journal, 142, 173

Iben, I. & Renzini, A. 1983, Annual Review of Astronomy and Astrophysics, 21, 271

Indebetouw, R., Brogan, C., Chen, C. H. R., et al. 2013, The Astrophysical Journal, 774, 73

Indebetouw, R., de Messières, G. E., Madden, S. C., et al. 2009, The Astrophysical Journal, 694, 32

Indebetouw, R., Whitney, B. A., Kawamura, A., et al. 2008, The Astronomical Journal, 136, 1442

Indriolo, N. & McCall, B. J. 2012, The Astrophysical Journal, 745, 91

Indriolo, N., Neufeld, D. A., Gerin, M., et al. 2015, The Astrophysical Journal, 800, 40

Israel, F. 1997, Astronomy & Astrophysics, 328, 471

Israel, F. P., de Graauw, T., Lidholm, S., van de Stadt, H., & de Vries, C. 1982, The Astrophysical Journal, 262, 100

Israel, F. P., Johansson, L. E. B., Lequeux, J., et al. 1993, Astronomy & Astrophysics, 276, 25

Israel, F. P., Johansson, L. E. B., Rubio, M., et al. 2003, Astronomy & Astrophysics, 406, 817

Israel, F. P. & Maloney, P. 2011, Astronomy & Astrophysics, 531, A19

Israel, F. P., Maloney, P. R., Geis, N., et al. 1996, The Astrophysical Journal, 465, 738

Izotov, Y. I., Stasińska, G., Meynet, G., Guseva, N. G., & Thuan, T. X. 2006, Astronomy and Astrophysics, 448, 955

Izotov, Y. I., Thuan, T. X., & Guseva, N. G. 2012, Astronomy & Astrophysics, 546, A122

Jäger, C., Dorschner, J., Mutschke, H., Posch, T., & Henning, T. 2003, Astronomy & Astrophysics, 408, 193

Jameson, K. E., Bolatto, A. D., Leroy, A. K., et al. 2016, The Astrophysical Journal, 825, 12

Johansson, L. E. B., Greve, A., Booth, R. S., et al. 1998, Astronomy and Astrophysics, 331, 857

Johnson, H. L. & Morgan, W. W. 1953, The Astrophysical Journal, 117, 313

Jones, A. P., Tielens, A. G. G. M., & Hollenbach, D. J. 1996, The Astrophysical Journal, 469, 740

Jones, T. J., Woodward, C. E., Boyer, M. L., Gehrz, R. D., & Polomski, E. 2005, The Astrophysical Journal, 620, 731

Jura, M. 1975, The Astrophysical Journal, 197, 575

Kaufman, M. J., Wolfire, M. G., & Hollenbach, D. J. 2006, The Astrophysical Journal, 644, 283

Kaufman, M. J., Wolfire, M. G., Hollenbach, D. J., & Luhman, M. L. 1999, The Astrophysical Journal, 527, 795

Kavanagh, P. J., Sasaki, M., Bozzetto, L. M., et al. 2015, Astronomy & Astrophysics, 573, A73

Kawada, M., Takahashi, A., Yasuda, A., et al. 2011, Publications of the Astronomical Society of Japan, 63, 903

Kennicutt, R. C. 1984, The Astrophysical Journal, 287, 116

Kennicutt, R. C., Calzetti, D., Aniano, G., et al. 2011, Publications of the Astronomical Society of the Pacific, 123, 1347

Kennicutt, R. C. J. 1989, The Astrophysical Journal, 344, 685

Kennicutt, R. C. J. 1998, The Astrophysical Journal, 498, 541

Kennicutt, R. C. J., Armus, L., Bendo, G., et al. 2003, The Publications of the Astronomical Society of the Pacific, 115, 928

Kennicutt., R. C. J., Calzetti, D., Walter, F., et al. 2007, The Astrophysical Journal, 671, 333

Kennicutt, R. C. J. & Hodge, P. W. 1986, The Astrophysical Journal, 306, 130

Kennicutt, R. C. J., Lee, J. C., Funes, S. J., J. G., Sakai, S., & Akiyama, S. 2008, The Astrophysical Journal Supplement Series, 178, 247

Kepley, A. A., Leroy, A. K., Johnson, K. E., Sandstrom, K., & Chen, C.-H. R. 2016, The Astrophysical Journal, 828, 50

Kewley, L. J., Dopita, M. A., Sutherland, R. S., Heisler, C. A., & Trevena, J. 2001, The Astrophysical Journal, 556, 121

Kim, S., Staveley-Smith, L., Dopita, M. A., et al. 1998, Astrophysical Journal, 503, 674

Kim, S., Staveley-Smith, L., Dopita, M. A., et al. 2003, The Astrophysical Journal Supplement Series, 148, 473

Kim, S., Walsh, W., & Xiao, K. 2004, The Astrophysical Journal, 616, 865

Koda, J., Scoville, N., Sawada, T., et al. 2009, The Astrophysical Journal, 700, L132

Krabbe, A., Mehlert, D., Röser, H.-P., & Scorza, C. 2013, European Journal of Physics, 34, S161

Krumholz, M. R. & Gnedin, N. Y. 2011, The Astrophysical Journal, 729, 36

Krumholz, M. R. & Tan, J. C. 2007, The Astrophysical Journal, 654, 304

Kudritzki, R. P., Pauldrach, A., & Puls, J. 1987, Astronomy & Astrophysics, 173, 293

Kunkel, W. E., Demers, S., Irwin, M. J., & Albert, L. 1997, The Astrophysical Journal, 488, L129

Kunth, D. & Ostlin, G. 2000, The Astronomy and Astrophysics Review, 10, 1

Lada, C. J. & Lada, E. a. 2003, Annual Review of Astronomy and Astrophysics, 41, 57

Langer, W. D. & Penzias, A. A. 1990, The Astrophysical Journal, 357, 477

Langer, W. D., Velusamy, T., Pineda, J. L., Willacy, K., & Goldsmith, P. F. 2014, Astronomy & Astrophysics, 561, A122

Larson, R. B. 1981, Monthly Notices of the Royal Astronomical Society, 194, 809

Le Bourlot, J., Le Petit, F., Pinto, C., Roueff, E., & Roy, F. 2012, Astronomy & Astrophysics, 541, A76

Le Bourlot, J., Pineau Des Forets, G., Roueff, E., & Flower, D. R. 1993, Astronomy & Astrophysics, 267, 233

Le Petit, F., Nehme, C., Le Bourlot, J., & Roueff, E. 2006, The Astrophysical Journal Supplement Series, 164, 506

Lebouteiller, V., Bernard-Salas, J., Brandl, B., et al. 2008, The Astrophysical Journal, 680, 398

Lebouteiller, V., Bernard-Salas, J., Whelan, D. G., et al. 2011, The Astrophysical Journal, 728, 45

Lebouteiller, V., Brandl, B., Bernard-Salas, J., Devost, D., & Houck, J. R. 2007, The Astrophysical Journal, 665, 390

Lebouteiller, V., Cormier, D., Madden, S. C., et al. 2012, Astronomy & Astrophysics, 548, A91

Lee, C., Leroy, A. K., Schnee, S., et al. 2015, Monthly Notices of the Royal Astronomical Society, 450, 2708

Lee, J. C., Gil de Paz, A., Kennicutt, R. C., et al. 2011, The Astrophysical Journal Supplement Series, 192, 6

Lee, M. G., Freedman, W., Mateo, M., et al. 1993, The Astronomical Journal, 106, 1420

Lee, M.-Y., Madden, S. C., Lebouteiller, V., et al. 2016, Accepted for publication in Astronomy & Astronophysics, ArXiv: 1606.04290

Leger, A. & Puget, J. L. 1984, Astronomy & Astrophysics, 137, L5

Leitherer, C., Ortiz Otálvaro, P. A., Bresolin, F., et al. 2010, The Astrophysical Journal Supplement Series, 189, 309

Lequeux, J. 2005, The Interstellar Medium, Astronomy & Astrophysics Library (Berlin/Heidelberg: Springer-Verlag)

Lequeux, J., Peimbert, M., Rayo, J. F., Serrano, A., & Torres-Peimbert, S. 1979, Astronomy and Astrophysics (ISSN 0004-6361), 80, 155

Leroy, A., Bolatto, A., Walter, F., & Blitz, L. 2006, The Astrophysical Journal, 643, 825

Leroy, A. K., Bolatto, A., Gordon, K., et al. 2011, The Astrophysical Journal, 737, 12

Leroy, A. K., Bolatto, A. D., Bot, C., et al. 2009, The Astrophysical Journal, 702, 352

Leroy, A. K., Walter, F., Brinks, E., et al. 2008, The Astronomical Journal, 136, 2782

Levesque, E. M., Kewley, L. J., & Larson, K. L. 2010, The Astronomical Journal, 139, 712

Licquia, T. C. & Newman, J. A. 2015, The Astrophysical Journal, 806, 96

Loiseau, N., Klein, U., Greybe, A., Wielebinski, R., & Haynes, R. F. 1987, Astronomy & Astrophysics, 178, 62

Lopez, L. A., Krumholz, M. R., Bolatto, A. D., Prochaska, J. X., & Ramirez-Ruiz, E. 2011, The Astrophysical Journal, 731, 91

Lord, S. D., Hollenbach, D. J., Haas, M. R., et al. 1996, The Astrophysical Journal, 465, 703

Lucke, P. B. & Hodge, P. W. 1970, The Astronomical Journal, 75, 171

Luhman, M. L., Satyapal, S., Fischer, J., et al. 1998, The Astrophysical Journal, 504, L11

MacLaren, I., Richardson, K. M., & Wolfendale, A. W. 1988, The Astrophysical Journal, 333, 821

Madau, P., Ferguson, H. C., Dickinson, M. E., et al. 1996, Monthly Notices of the Royal Astronomical Society, 283, 1388

Madden, S. C. 2000, New Astronomy Reviews, 44, 249

Madden, S. C., Galliano, F., Jones, A. P., & Sauvage, M. 2006, Astronomy & Astrophysics, 446, 877

Madden, S. C., Poglitsch, A., Geis, N., Stacey, G. J., & Townes, C. H. 1997, The Astrophysical Journal, 483, 200

Madden, S. C., Rémy, A., Galliano, F., et al. 2012, Proceedings of the International Astronomical Union, 7, 141

Madden, S. C., Rémy-Ruyer, A., Galametz, M., et al. 2013, Publications of the Astronomical Society of the Pacific, 125, 600

Maddox, L. A., Williams, R. M., Dunne, B. C., & Chu, Y. H. 2009, The Astrophysical Journal, 699, 911

Magnani, L., Chastain, R., Kim, H., et al. 2003, The Astrophysical Journal, 586, 1111

Maiolino, R., Caselli, P., Nagao, T., et al. 2009, Astronomy and Astrophysics, 500, L1

Maiolino, R., Nagao, T., Grazian, A., et al. 2008, Astronomy and Astrophysics, 488, 463

Makiwa, G., Naylor, D. A., Ferlet, M., et al. 2013, Applied optics, 52, 3864

Malhotra, S., Helou, G., Stacey, G., et al. 1997, The Astrophysical Journal, 491, L27

Malhotra, S., Kaufman, M. J., Hollenbach, D. J., et al. 2001, The Astrophysical Journal, 10, 766

Maloney, P. & Black, J. H. 1988, The Astrophysical Journal, 325, 389

Maloney, P. & Wolfire, M. 1997, in CO: Twenty-Five Years of Millimeter-Wave Spectroscopy, 299

Maragoudaki, F., Kontizas, M., Morgan, D. H., et al. 2001, Astronomy and Astrophysics, 379, 864

Martin, P. G. & Mandy, M. E. 1995, The Astrophysical Journal, 455

Marzke, R. O. & da Costa, L. N. 1997, The Astronomical Journal, 113, 185

Massey, P. & Hunter, D. A. 1998, The Astrophysical Journal, 493, 180

Massey, P., Silkey, M., Garmany, C. D., & Degioia-Eastwood, K. 1989, The Astronomical Journal, 97, 107

Mateo, M. 1998, Annual Review of Astronomy and Astrophysics, 36, 435

Mathewson, D. S., Cleary, M. N., & Murray, J. D. 1974, The Astrophysical Journal, 190, 291

Mathis, J. S., Mezger, P. G., & Panagia, N. 1983, Astronomy & Astrophysics, 128, 212

Mathis, J. S., Rumpl, W., & Nordsieck, K. H. 1977, The Astrophysical Journal, 217, 425

McConnachie, A. W. 2012, The Astronomical Journal, 144, 4

McKee, C. F. & Ostriker, E. C. 2007, Annual Review of Astronomy and Astrophysics, 45, 565

McKee, C. F. & Zweibel, E. G. 1992, Astrophysical Journal, 399, 551

Meaburn, J. & Laspias, V. N. 1991, Astronomy and Astrophysics, 245, 635

Meijerink, R. & Spaans, M. 2005, Astronomy and Astrophysics, 436, 397

Meixner, M., Galliano, F., Hony, S., et al. 2010, Astronomy & Astrophysics, 518, L71

Meixner, M., Gordon, K. D., Indebetouw, R., et al. 2006, The Astronomical Journal, 132, 2268

Meixner, M., Panuzzo, P., Roman-Duval, J., et al. 2013, The Astronomical Journal, 146, 62

Melisse, J. P. M. & Israel, F. P. 1994, Astronomy and Astrophysics Supplement Series, 103, 391

Melnick, J. & Rubio, M. 1985, Astronomy & Astrophysics, 151, 455

Meynadier, F., Heydari-Malayeri, M., Deharveng, L., et al. 2004, Astronomy & Astrophysics, 422, 129

Milam, S. N., Savage, C., Brewster, M. A., Ziurys, L. M., & Wyckoff, S. 2005, The Astrophysical Journal, 634, 1126

Minamidani, T., Tanaka, T., Mizuno, Y., et al. 2011, The Astronomical Journal, 141, 73

Mizuno, N., Rubio, M., Mizuno, A., et al. 2001, Publications of the Astronomical Society of Japan, 53, L45

Mochizuki, K., Nakagawa, T., Doi, Y., et al. 1994, The Astrophysical Journal, 430, L37

Moffat, A. F. J. 1983, Astronomy & Astrophysics, 124, 273

Mokiem, M. R., de Koter, A., Evans, C. J., et al. 2007, Astronomy & Astrophysics, 465, 1003

Moore, B., Ghigna, S., Governato, F., et al. 1999, The Astrophysical Journal, 524, L19

Moretti, M. I., Clementini, G., Muraveva, T., et al. 2014, Monthly Notices of the Royal Astronomical Society, 437, 2702

Morisset, C. 2006, in Planetary Nebulae in our Galaxy and Beyond, Proceedings of the International Astronomical Union, Symposium #234, ed. M. J. Barlow & R. H. Méndez No. 234 (Cambridge: Cambridge University Press), 467–468

Morisset, C., Stasinska, G., & Pena, M. 2005, Monthly Notices of the Royal Astronomical Society, 360, 499

Muller, E., Ott, J., Hughes, A., et al. 2010, The Astrophysical Journal, 712, 1248

Muñoz-Mateos, J. C., Gil de Paz, A., Zamorano, J., et al. 2009, The Astrophysical Journal, 703, 1569

Nakajima, Y., Kato, D., Nagata, T., et al. 2005, The Astronomical Journal, 129, 776

Navarro, J. F., Frenk, C. S., & White, S. D. M. 1996, Astrophysical Journal, 378, 496

Nazé, Y., Antokhin, I. I., Rauw, G., et al. 2004, Astronomy & Astrophysics, 418, 841

Nazé, Y., Chu, Y.-H., Points, S. D., et al. 2001, The Astronomical Journal, 122, 921

Naze, Y., Hartwell, J. M., Stevens, I. R., et al. 2003, The Astrophysical Journal, 586, 983

Nikolaev, S., Drake, A. J., Keller, S. C., et al. 2004, The Astrophysical Journal, 601, 260

Nordon, R. & Sternberg, A. 2016, Monthly Notices of the Royal Astronomical Society, 462, 2804

Oberst, T. E., Parshley, S. C., Stacey, G. J., et al. 2006, The Astrophysical Journal, 652, L125

Oey, M. S. & Massey, P. 1995, The Astrophysical Journal, 452, 210

Offner, S. S. R., Bisbas, T. G., Bell, T. A., & Viti, S. 2014, Monthly Notices of the Royal Astronomical Society: Letters, 440, L81

Okada, Y., Pilleri, P., Berné, O., et al. 2013, Astronomy & Astrophysics, 553, A2

Okada, Y., Requena-Torres, M. A., Güsten, R., et al. 2015, Astronomy & Astrophysics, 580, A54

Oliveira, J. M., Van Loon, J. T., Stanimirović, S., & Zijlstra, A. A. 2006, Monthly Notices of the Royal Astronomical Society, 372, 1509

Olsen, K. A. G., Zaritsky, D., Blum, R. D., Boyer, M. L., & Gordon, K. D. 2011, The Astrophysical Journal, 737, 29

Onodera, S., Kuno, N., Tosaki, T., et al. 2010, The Astrophysical Journal, 722, L127

Ossenkopf, V. & Mac Low, M.-M. 2002, Astronomy & Astrophysics, 326, 307

Osterbrock, D. E. & Ferland, G. J. 2006, Astrophysics of gaseous nebulae and active galactic nuclei (University Science Books)

Ott, J., Wong, T., Pineda, J. L., et al. 2008, Publications of the Astronomical Society of Australia, 25, 129

Ott, S. 2010, Astronomical Data Analysis Software and Systems XIX, 434, 139

Pagel, B. E. J. 1997, Nucleosynthesis and Chemical Evolution of Galaxies (Cambridge University Press), 392

Pagel, B. E. J. 2003, in Astronomical Society of the Pacific Conference Series, Vol. 304, CNO in the Universe, ed. C. Charbonnel, D. Schaerer, & G. Meynet, 187

Pak, S., Jaffe, D. T., van Dishoeck, E. F., Johansson, L. E. B., & Booth, R. S. 1998, The Astrophysical Journal, 498, 735

Papadopoulos, P. P., Thi, W. F., & Viti, S. 2004, Monthly Notices of the Royal Astronomical Society, 351, 147

Paradis, D., Dobashi, K., Shimoikura, T., et al. 2012, Astronomy & Astrophysics, 543, A103

Paradis, D., Reach, W. T., Bernard, J.-P., et al. 2009, The Astronomical Journal, 138, 196

Paradis, D., Reach, W. T., Bernard, J.-P., et al. 2010, The Astronomical Journal, 141, 43

Parker, J. W. 1992, Publications of the Astronomical Society of the Pacific, 104, 1107

Peeters, E., Allamandola, L. J., Hudgins, D. M., Hony, S., & Tielens, A. G. G. M. 2004, in Astrophysics of Dust, ed. A. N. Witt, G. C. Clayton, & B. T. Draine, Vol. 309 (San Francisco: Publications of the Astronomical Society of the Pacific), 141–162

Pellegrini, E. W., Baldwin, J. A., & Ferland, G. J. 2010, The Astrophysical Journal Supplement Series, 191, 42

Pellegrini, E. W., Baldwin, J. A., & Ferland, G. J. 2011, The Astrophysical Journal, 738, 54

Pilbratt, G. L., Riedinger, J. R., Passvogel, T., et al. 2010, Astronomy & Astrophysics, 518, L1

Pineda, J. E., Caselli, P., & Goodman, A. A. 2008a, The Astrophysical Journal, 679, 481

Pineda, J. L., Goldsmith, P. F., Chapman, N., et al. 2010, The Astrophysical Journal, 721, 686

Pineda, J. L., Langer, W. D., Velusamy, T., & Goldsmith, P. F. 2013, Astronomy & Astrophysics, 554, A103

Pineda, J. L., Mizuno, N., & Röllig, M. 2012, Astronomy & Astrophysics, 544, 84

Pineda, J. L., Mizuno, N., Stutzki, J., et al. 2008b, Astronomy & Astrophysics, 208, 14

Pineda, J. L., Ott, J., Klein, U., et al. 2009, The Astrophysical Journal, 703, 736

Pirronello, V., Liu, C., Roser, J. E., & Vidali, G. 1999, Astronomy and Astrophysics, 344, 681

Planck Collaboration. 2011a, Astronomy & Astrophysics, 536, A19

Planck Collaboration. 2011b, Astronomy & Astrophysics, 536, A17

Planck collaboration. 2016, Astronomy & Astrophysics, 586, A138

Plume, R., Kaufman, M. J., Neufeld, D. a., et al. 2004, Astrophysical Journal, 605, 32

Poglitsch, A., Krabbe, A., Madden, S. C., et al. 1995, The Astrophysical Journal, 454, 293

Poglitsch, A., Waelkens, C., Geis, N., et al. 2010, Astronomy & Astrophysics, 518, L2

Portas, A., Scott, T. C., Brinks, E., et al. 2011, The Astrophysical Journal Letters, 739, L27

Putman, M. E., Gibson, B. K., Staveley-Smith, L., et al. 1998, Nature, 394, 752

Ramstedt, S. & Olofsson, H. 2014, Astronomy & Astrophysics, 566, A145

Rebolledo, D., Wong, T., Leroy, A., Koda, J., & Meyer, J. D. 2012, The Astrophysical Journal, 757, 155

Rebolledo, D., Wong, T., Xue, R., et al. 2015, The Astrophysical Journal, 808, 99

Remy-Ruyer, A. 2013, PhD thesis, Université Paris-Sud

Rémy-Ruyer, A., Madden, S. C., Galliano, F., et al. 2014, Astronomy & Astrophysics, 563, A31

Rémy-Ruyer, A., Madden, S. C., Galliano, F., et al. 2013, Astronomy & Astrophysics, 557, A95

Rémy-Ruyer, A., Madden, S. C., Galliano, F., et al. 2015, Astronomy & Astrophysics, 582, A121

Requena-Torres, M. A., Israel, F. P., Okada, Y., et al. 2016, Astronomy & Astrophysics, 589, A28

Ribas, I., Jordi, C., Vilardell, F., et al. 2005, The Astrophysical Journal, 635, L37

Richter, P., Widmann, H., de Boer, K. S., et al. 1998, Astronomy & Astrophysics, 338, L9

Robitaille, T. P. & Whitney, B. A. 2010, The Astrophysical Journal, 710, L11

Rolleston, W. R. J., Trundle, C., & Dufton, P. L. 2002, Astronomy & Astrophysics, 396, 53

Röllig, M., Abel, N. P., Bell, T. A., et al. 2007, Astronomy & Astrophysics, 206, 28

Röllig, M. & Ossenkopf, V. 2013, Astronomy and Astrophysics, 550, 56

Röllig, M., Ossenkopf, V., Jeyakumar, S., Stutzki, J., & Sternberg, A. 2006, Astronomy & Astrophysics, 451, 917

Röllig, M., Szczerba, R., Ossenkopf, V., & Glück, C. 2013, Astronomy & Astrophysics, 549, A85

Roman-Duval, J., Gordon, K. D., Meixner, M., et al. 2014, The Astrophysical Journal, 797, 86

Roman-Duval, J., Jackson, J. M., Heyer, M., Rathborne, J., & Simon, R. 2010, The Astrophysical Journal, 723, 492

Rosado, M., Laval, A., Le Coarer, E., et al. 1996, Astronomy & Astrophysics

Rouleau, F. & Martin, P. G. 1991, The Astrophysical Journal, 377, 526

Roussel, H., Helou, G., Hollenbach, D. J., et al. 2007, The Astrophysical Journal, 959–981

Rubin, D., Hony, S., Madden, S. C., et al. 2009, Astronomy & Astrophysics, 494, 647

Rubin, R. H., Simpson, J. P., Lord, S. D., et al. 1994, The Astrophysical Journal, 420, 772

Rubio, M., Contursi, A., Lequeux, J., et al. 2000, Astronomy & Astrophysics, 359, 1139

Rubio, M., Garay, G., & Probst, R. 1998, The Messenger, 93, 38

Rubio, M., Paron, S., & Dubner, G. 2009, Astronomy & Astrophysics, 505, 177

Russell, S. C. & Dopita, M. A. 1992, The Astrophysical Journal, 384, 508

Sabbi, E., Anderson, J., Lennon, D. J., et al. 2013, The Astronomical Journal, 146, 53

Sabbi, E., Sirianni, M., Nota, a., et al. 2007, The Astronomical Journal, 133, 44

Saintonge, A., Kauffmann, G., Wang, J., et al. 2011, Monthly Notices of the Royal Astronomical Society, 415, 61

Salim, S., Lee, J. C., Davé, R., & Dickinson, M. 2015, The Astrophysical Journal, 808, 25

Sandstrom, K. M., Leroy, A. K., Walter, F., et al. 2013, The Astrophysical Journal, 777, 5

Sauvage, M., Vigroux, L., & Thuan, T. X. 1990, Astronomy & Astrophysics, 237, 296

Savage, B. D. & Sembach, K. R. 1996, The Astrophysical Journal, 470, 893

Savage, C., Apponi, A. J., Ziurys, L. M., & Wyckoff, S. 2002, The Astrophysical Journal, 578, 211

Savaglio, S., Glazebrook, K., Le Borgne, D., et al. 2005, The Astrophysical Journal, 635, 260

Schaller, G., Schaerer, D., Meynet, G., & Maeder, A. 1992, Astronomy and Astrophysics Supplement Series, 96, 269

Schmidt, M. 1959, The Astrophysical Journal, 129, 243

Schruba, A., Leroy, A. K., Walter, F., et al. 2011, The Astronomical Journal, 142, 37

Schruba, A., Leroy, A. K., Walter, F., et al. 2012, The Astronomical Journal, 143, 138

Schruba, A., Leroy, A. K., Walter, F., Sandstrom, K., & Rosolowsky, E. 2010, The Astrophysical Journal, 722, 1699

Scoville, N. Z., Yun, M. S., Sanders, D. B., Clemens, D. P., & Waller, W. H. 1987, The Astrophysical Journal Supplement Series, 63, 821

Scowen, P. A., Hester, J. J., Sankrit, R., et al. 1998, The Astronomical Journal, 116, 163

Seale, J. P., Looney, L. W., Chu, Y.-H., et al. 2009, The Astrophysical Journal, 699, 150

Sellgren, K., Tokunaga, A. T., & Nakada, Y. 1990, The Astrophysical Journal, 349, 120

Selman, F. J. & Melnick, J. 2005, Astronomy & Astrophysics, 443, 851

Selman, F. J. & Melnick, J. 2013, Astronomy & Astrophysics, 552, A94

Sewiło, M., Carlson, L. R., Seale, J. P., et al. 2013, The Astrophysical Journal, 778, 15

Shetty, R., Glover, S. C., Dullemond, C. P., & Klessen, R. S. 2011a, Monthly Notices of the Royal Astronomical Society, 412, 1686

Shetty, R., Glover, S. C., Dullemond, C. P., et al. 2011b, Monthly Notices of the Royal Astronomical Society, 415, 3253

Siebenmorgen, R., Voshchinnikov, N. V., & Bagnulo, S. 2014, Astronomy & Astrophysics, 561, A82

Simon, J. D., Bolatto, A. D., Whitney, B. a., et al. 2007, The Astrophysical Journal, 669, 327

Smith, D. A. & Wang, Q. D. 2004, The Astrophysical Journal

Smith, J. D. T., Draine, B. T., Dale, D. A., et al. 2007, The Astrophysical Journal, 656, 770

Smith, R. C. & the MCELS Team. 1998, Publications Astronomical Society of Australia, 15, 163

Solomon, P. M., Rivolo, A. R., Barrett, J., & Yahil, A. 1987, The Astrophysical Journal, 319, 730

Stacey, G. J. 2011, IEEE Transactions on Terahertz Science and Technology, 1, 241

Stacey, G. J., Geis, N., Genzel, R., et al. 1991, The Astrophysical Journal, 373, 423

Stacey, G. J., Hailey-Dunsheath, S., Ferkinhoff, C., et al. 2010, The Astrophysical Journal, 724, 957

Stanimirovič, S., Staveley-Smith, L., Dickey, J. M., Sault, R. J., & Snowden, S. L. 1999, Monthly Notices of the Royal Astronomical Society, 302, 417

Stasínska, G., Testor, G., & Heydari-Malayeri, M. 1986, Astronomy & Astrophysics, 170, L4

Stecker, F. W., Solomon, P. M., Scoville, N. Z., & Ryter, C. E. 1975, The Astrophysical Journal, 201, 90

Sternberg, A. & Dalgarno, A. 1989, The Astrophysical Journal, 338, 197

Sternberg, A. & Dalgarno, A. 1995, The Astrophysical Journal Supplement Series, 99, 565

Sternberg, A., Le Petit, F., Roueff, E., & Le Bourlot, J. 2014, The Astrophysical Journal, 790, 10

Störzer, H., Stutzki, J., & Sternberg, A. 1996, Astronomy and Astrophysics

Stutzki, J., Bensch, F., Heithausen, A., Ossenkopf, V., & Zielinsky, M. 1998, Astronomy & Astrophysics, 336, 697

Subramaniam, A. 2003, The Astrophysical Journal, 598, L19

Swinyard, B. M., Polehampton, E. T., Hopwood, R., et al. 2014, Monthly Notices of the Royal Astronomical Society, 440, 3658

Szücs, L., Glover, S. C. O., & Klessen, R. S. 2014, Monthly Notices of the Royal Astronomical Society, 445, 4055

Tacconi, L. J., Genzel, R., Neri, R., et al. 2010, Nature, 463, 781

Taylor, C. L., Kobulnicky, H. A., & Skillman, E. D. 1998, The Astronomical Journal, 116, 2746

Testor, G. & Lortet, M.-C. 1987, Astronomy & Astrophysics, 178, 25

Testor, G. & Niemela, V. 1998, Astronomy & Astrophysics Supplement Series, 130, 527

Testor, G., Schild, H., & Lortet, M. C. 1993, Astronomy & Astrophysics, 280, 426

Thuan, T. X. & Izotov, Y. I. 2005, The Astrophysical Journal Supplement Series, 161, 240

Thuan, T. X. & Martin, G. E. 1981, The Astrophysical Journal, 247, 823

Tielens, A. 2008, Annual Review of Astronomy and Astrophysics, 46, 289

Tielens, A. G. G. M. 2005, The Physics and Chemistry of the Interstellar Medium (Cambridge University Press)

Tielens, A. G. G. M. & Hollenbach, D. 1985, The Astrophysical Journal, 291, 722

Tielens, A. G. G. M. & Hollenbach, D. J. 1993, in Planetary nebulae: proceedings of the 155 Symposium of the International Astronomical Union, ed. R. W. Acker & Agnes (Dordrecht: Kluwer Academic Publishers), 155

Toomre, A. 1964, The Astrophysical Journal, 139, 1217

Torres-Flores, S., Barbá, R., Maíz Apellániz, J., et al. 2013, Astronomy & Astrophysics, 555, A60

Tosi, M., Aloisi, A., Mack, J., & Maio, M. 2007, Proceedings of the International Astronomical Union, 235, 65

Townsley, L. K., Broos, P. S., Feigelson, E. D., et al. 2006a, The Astronomical Journal, 131, 2140

Townsley, L. K., Broos, P. S., Feigelson, E. D., Garmire, G. P., & Getman, K. V. 2006b, The Astronomical Journal, 131, 2164

Tremonti, C. A., Heckman, T. M., Kauffmann, G., et al. 2004, The Astrophysical Journal, 613, 898

Vallenari, A., Chiosi, C., Bertelli, G., & Ortolani, S. 1996, Astronomy & Astrophysics, 309, 358

van der Marel, R. P. & Cioni, M.-R. L. 2001, The Astronomical Journal, 122, 1807

van der Werf, P. P., Stutzki, J., Sternberg, A., & Krabbe, A. 1996, Astronomy & Astrophysics, 313, 633

van Dishoeck, E. F. & Black, J. H. 1986, The Astrophysical Journal Supplement Series, 62, 109

van Dishoeck, E. F. & Black, J. H. 1988, The Astrophysical Journal, 334, 771

Verstraete, L. 2011, EAS Publications Series, 46, 415

Vink, J. S. & de Koter, A. 2005, Astronomy and Astrophysics, 442, 587

Vink, J. S., de Koter, A., & Lamers, H. J. G. L. M. 2000, Astronomy and Astrophysics, 362, 295

Vogel, S. N., Boulanger, F., & Ball, R. 1987, The Astrophysical Journal, 321, L145

Walborn, N. & Parker, J. 1992, The Astrophysical Journal, 399, L87

Walborn, N. R., Barbá, R. H., Brandner, W., et al. 1999, The Astronomical Journal, 117, 225

Walborn, N. R., Barbá, R. H., & Sewilo, M. M. 2013, The Astronomical Journal, 145, 98

Walborn, N. R. & Blades, J. C. 1986, The Astrophysical Journal, 304, L17

Walborn, N. R. & Blades, J. C. 1997, The Astrophysical Journal Supplement Series, 112, 457

Walborn, N. R., Maíz-Apellániz, J., & Barbá, R. H. 2002, The Astronomical Journal, 124, 1601

Walborn, N. R., Sana, H., Simon-Diaz, S., et al. 2014, Astronomy & Astrophysics, 564, A40

Walker, A. R. 2012, Astrophysics and Space Science, 341, 43

Walker, K. M., Song, L., Yang, B. H., et al. 2015, The Astrophysical Journal, 811, 27

Weingartner, J. C. & Draine, B. T. 2001a, The Astrophysical Journal, 548, 296

Weingartner, J. C. & Draine, B. T. 2001b, The Astrophysical Journal Supplement Series, 134, 263

Westerlund, B. E. 1991, in The Magellanic Clouds: Proceedings of the 148th Symposium of the International Astronomical Union, ed. R. Haynes & M. Douglas (Kluwer Academic Publishers), 15

Westerlund, B. E. 1997, The Magellanic Clouds (Cambridge University Press)

Whelan, D. G., Lebouteiller, V., Galliano, F., et al. 2013, The Astrophysical Journal, 771, 16

Whitney, B. A., Sewilo, M., Indebetouw, R., et al. 2008, The Astronomical Journal, 136, 18

Will, J.-M., Bomans, D. J., & Dieball, A. 1997, Astronomy and Astrophysics Supplement Series, 123, 455

Wilson, C. D. 1995, The Astrophysical Journal, 448

Wilson, C. D. & Scoville, N. 1990, The Astrophysical Journal, 363, 435

Wilson, T., Rohlfs, K., & Hüttemeister, S. 2009, Tools in radioastronomy, 5th edn. (Berlin: Springer-Verlag)

Wilson, T. L. & Rood, R. T. 1994, Annual Review of Astronomy and Astrophysics, 32, 191

Wolfire, M. G., Hollenbach, D., & McKee, C. F. 2010, The Astrophysical Journal, 716, 1191

Wolfire, M. G., McKee, C. F., Hollenbach, D., & Tielens, A. G. G. M. 2003, The Astrophysical Journal, 587, 278

Wolfire, M. G., Tielens, A. G. G. M., Hollenbach, D., & Kaufman, M. J. 2008, The Astrophysical Journal, 680, 384

Wolfire, M. G., Tielens, A. G. G. M., & Hollenbach, D. J. 1990, The Astrophysical Journal, 358, 116

Wong, T., Hughes, A., Ott, J., et al. 2011, The Astrophysical Journal Supplement Series, 197, 16

Woods, P. M., Oliveira, J. M., Kemper, F., et al. 2011, Monthly Notices of the Royal Astronomical Society, 411, 1597

Wright, E. L., Mather, J. C., Bennett, C. L., et al. 1991, The Astrophysical Journal, 381, 200

Wu, R., Madden, S. C., Galliano, F., et al. 2015, Astronomy & Astrophysics, 575, A88

Wu, Y., Charmandaris, V., Hao, L., et al. 2006, The Astrophysical Journal, 639, 157

Yamaguchi, H., Bamba, A., & Koyama, K. 2009, Publications of the Astronomical Society of Japan, 61, S175

Yeh, S. C. C., Seaquist, E. R., Matzner, C. D., & Pellegrini, E. W. 2015, The Astrophysical Journal, 807, 117

Zaritsky, D., Harris, J., Grebel, E. K., & Thompson, I. B. 2000, Astrophysical Journal, 534, L53

Zhao, Y., Lu, N., Xu, C. K., et al. 2013, The Astrophysical Journal, 765, L13

Zubko, V., Dwek, E., & Arendt, R. G. 2004, The Astrophysical Journal Supplement Series, 152, 211